Stress Analysis of Fatigue Cracks in Mechanically Fastened Joints

An analytical and experimental investigation

Stress Analysis of Fatigue Cracks in Mechanically Fastened Joints

An analytical and experimental investigation

PROEFSCHRIFT

ter verkrijging van de graad van doctor
aan de Technische Universiteit Delft,
op gezag van de Rector Magnificus prof.dr.ir. J.T. Fokkema,
voorzitter van het College voor Promoties,
in het openbaar te verdedigen op 17 juni 2005 om 10:30 uur
door Johannes Jacobus Maria DE RIJCK
ingenieur in de luchtvaart en ruimtevaart
geboren te Leiderdorp

Acknowledgements

A PhD thesis is looked upon as an achievement accomplished by a single person. However, this does not apply to the present thesis carried out in the Structures and Materials Laboratory of the Faculty of Aerospace Engineering. There is a long list of people who provide support in many different ways.

The first one I like to thank is Lt Col Scott Fawaz of the United States Air Force Academy. He introduced me to fatigue crack growth research, which led to a masters thesis on crack growth and continued to a larger research program for my doctors thesis. Although Scott resided on the other side of the Atlantic, we managed to stay in close contact and were able to discuss the research almost daily using the electronic highway. Scott Fawaz provided all the computational power, which was funded by the Department of Defense (DoD) High Performance Computing Modernization Program (HPCMP) initiative through the Department of Defense's High Performance Computing Modernization Office (HPCMO) for the Computational Technology Area (CTA): Computational Structural Mechanics at the Engineering Research and Development Center and Aeronautical Systems Center.

Secondly, I like to thank the people who created the spirit of the Structures and Materials Laboratory, Prof. Jaap Schijve, Prof. Boud Volgelesang and the late Prof. Ad Vlot. All three of them have had a large influence in providing the best possible research environment. Prof. Jaap Schijve who is invaluable in doing fatigue and damage tolerance research. He introduced the neutral line model which is further developed in my thesis. When I joined the Aerospace Materials of the laboratory one person was the personification of the laboratory, Prof. Boud Vogelesang who enthusiastically supported everybody in new ideas. His enthusiasm created the perfect "anything can happen" atmosphere in the laboratory, combined with a wonderful supporting staff. Without any doubt the influence of Ad Vlot goes beyond research in the laboratory. He introduced ethics and philosophy into the research driven environment. Technical progress can and will have an influence on the society, but being a researcher does not only mean doing research, inventing new and wonderful things; you also need to look at the impact on the society. Last but not least, Jos Sinke who took over for Ad Vlot as acting head of the Aerospace materials group in giving me the opportunity to continue my research after my NMIR period. Not forgetting, I also want to thank the Netherlands Institute for Metals Research for making it also financially possible.

As mentioned before, the Structures and Materials Laboratory's success depended on several factors. A very important one is the support staff: first of all Hannie van Deventer, Greetje Wiltjer en Peggy Peers, for not only solving all non-research related problems but also for creating enthusiastic social events. Secondly, Cees

Contents

Nomenclature

Latin

a	Misalignment	[mm]
a	Crack length	[mm]
a	Crack depth along elliptical axis	[mm]
a_{ave}	Average crack length	[mm]
A	Matrix	[-]
A^{-1}	Inverse of matrix A	[-]
$A_{al_{cracked}}$	Total area of aluminum removed due to fatigue cracks	[mm^2]
$A_{al_{pristine}}$	Pristine area of aluminum in Glare	[mm^2]
A_i	Cross sectional area of ith layer	[mm^2]
b	width of specimen	[mm]
b	Height of straight shank part of fastener hole	[mm]
B_{factor}	Correction of blunt notch for bending	[MPa]
C	Paris law constant	
c_1	Crack length along faying surface	[mm]
c_2	Crack length along free surface	[mm]
c_f	Fastener indicator	[-]
c_i	Distance to neutral line	[mm]
c_{LHS}	Crack length left side of the hole	[mm]
c_{RHS}	Crack length right side of the hole	[mm]
d	Fastener hole diameter	[mm]
d_1	Straight shank hole diameter	[mm]
d_2	Countersunk hole diameter	[mm]
da/dN	Crack growth rate	[μm/cycle]
d_{head}	Deformed fastener hole diameter	[mm]
D	Rivet diameter	[mm]
D_0	Initial rivet diameter	[mm]
D_a	Reaction Force	[kN]
e_i	Eccentricity	[mm]
E	Young's modulus	[MPa]
E_i	Young's modulus of ith layer	[MPa]
E_f	Young's modulus of fastener	[MPa]
f	Fastener flexibility	[mm/N]
F_{sq}	Rivet squeeze force	[kN]
$F_{sq\ calc}$	Calculated rivet squeeze force	[kN]
G	Shear modulus	[GPa]
G_i	Energy release rate	
h	Height	[mm]

H	Rivet height (protruding)	[mm]
H_0	Initial rivet height (protruding)	[mm]
H_{av}	Average rivet height (protruding)	[mm]
i	Counter	[-]
I	Moment of inertia	[mm^4]
I	Identity matrix	[-]
j	Counter	[-]
k_b	Bending factor	[-]
K	Strength coefficient Holloman	[MPa]
K_{2P}	Stress intensity factor for wedge loading	[MPa√m]
K_{brg}	Stress intensity factor for bearing	[MPa√m]
K_I	Stress intensity factor mode I	[MPa√m]
K_t	Stress concentration factor	[-]
$K_{t_{hole}}$	K_t for an open hole subject to tension in finite width sheet	[-]
$K_{t_{pin}}$	K_t for a pin loaded hole in a finite width sheet	[-]
K_{tb}	K_t for an open hole subject to bending in a finite width sheet	[-]
L	Length	[mm]
L_0	Total rivet length	[mm]
M_a	Reaction moment	[Nm]
M_i	Moment	[Nm]
$M_{internal}$	Internal moment	[Nm]
n	Joint designator	[-]
n	Strain hardening coefficient	[-]
n	Paris exponent	[-]
n	Number of load cases	[-]
n_{al}	Number of aluminum layers	[-]
n_j	Modular ratio	[-]
N	Number of cycles	[cycles]
p	Fastener row pitch	[mm]
P	Applied force	[kN]
P_{max}	Maximum applied force	[kN]
P_{min}	Minimum applied force	[kN]
Q	Shape factor	[-]
r	Number of fastener rows	[-]
r	Radius of fastener hole	[mm]
r	Distance to crack front	[mm]
R	R-ratio: S_{min}/S_{max}	[-]
s	Fastener collumn pitch	[mm]
s	Distance along the crack front	[mm]
S_{max}	Maximum applied stress	[MPa]
t_{al}	Thickness of aluminum layer	[mm]
$t_{prep,0}$	Thickness of all prepreg layers	

	in 0 degress	[mm]
$t_{prep,90}$	Thickness of all prepreg layers in 90 degress	[mm]
t_i	Thickness	[mm]
t_{tot}	Total thickness	[mm]
t_{total}	Total sheet thickness	[mm]
t_{sheet}	Sheet thickness	[mm]
T_i	Load transfer	[kN]
T_{factor}	Correction of blunt notch	[MPa]
u	Displacement in x-direction	[mm]
v	Displacement in y-direction	[mm]
V_0	Protruding rivet head volume	[mm³]
w	Displacement in y-direction	[mm]
w_i	Displacement neutral axis	[mm]
w_i	Element length along crack front	[mm]
W	Width	[mm]
W	Wronskian determinant	[-]
x	x-coordinate	[mm]
	Vector of unknows to be solved	[-]
y	y-coordinate	[mm]
	Vector of constants	[-]
y_i	Distance from center of ith layer to the neutral axis	[mm]
z	z-coordinate	[mm]
	Vector of constants	[-]
z_i	Distance from center of ith layer to the neutral axis	[mm]

Greek

α	Thermal expansion coefficient	[1/°C]
α_1	Stiffness ratio	[MPa]
β	Fastener rotation	[deg]
β_i	Boundary correction factor	[-]
β_t	Boundary correction factor for tensile load case	[-]
δ	Displacement	[mm]
$\delta_{f,i}$	Displacement of fastener	[mm]
Δ_i	Displacement of sheet	[mm]
Δ_i	Finite element length	[mm]
ΔS	$S_{max} - S_{min}$	[MPa]
ΔS_{eff}	Effective stress	[MPa]
ε^T	True strain	[-]
ε_{ult}	Ultimate strain	[-]
ε_x	Strain in x-direction	[-]

ε_y	Strain in y-direction	[-]
ε_z	Strain in z-direction	[-]
γ	Countersunk angle	[deg]
γ	Load transfer ratio	[-]
$\gamma_{,i}$	Stiffness ratio	[mm/N]
π	Pi	[-]
σ^T	True stress	[MPa]
σ_1	Stress in principle direction 1	[MPa]
σ_2	Stress in principle direction 2	[MPa]
σ_{AL}	Stress in aluminum layers	
σ_b	Bending stress	[MPa]
$\sigma_{bending}$	Bending stress	[MPa]
$(\sigma_b)_{anticlastic}$	Bending stress corrected for anticlastic curvature	[MPa]
σ_{brg}	Bearing stress	[MPa]
$\sigma_{BN_{Glare}}$	Blunt notch strength for pure tension	[MPa]
$\sigma_{BN_{al}}$	Blunt notch strength aluminum	[MPa]
σ_i	Remote stress for each load condition	[MPa]
$\sigma_{i_{BN}}$	XX, YY or XY material direction blunt notch strength	[MPa]
$\sigma_{i_{al}}$	Aluminum blunt notch strength	[MPa]
$\sigma_{i_{fiber}}$	Blunt notch strength prepreg layer	[MPa]
$\sigma_{pinload}$	Pinload stress	[MPa]
σ_{peak}	Peak stress at hole	[MPa]
$\sigma_{res_{cracked}}$	Residual strength of Glare laminate	[MPa]
σ_{sq}	Rivet squeeze stress	[MPa]
σ_t	Tensile stress	[MPa]
$\sigma_{tension}$	Tensile stress	[MPa]
σ_{tot}	Total stress	[MPa]
σ_{ult}	Ultimate stress	[MPa]
σ_x	Stress in x-direction	[MPa]
σ_y	Stress in y-direction	[MPa]
$\sigma_y(r,s)$	Stress distribution ahead of crack front	[MPa]
ν	Poisson's ratio	[-]
$\nu(r,s)$	Total displacement distribution behind crack front	[mm]
ν_{al}	Poisson's ratio aluminum layer	[-]
$\nu_{prep,0}$	Poisson's ratio prepreg in 0 degrees	[-]
$\nu_{prep,90}$	Poisson's ratio prepreg in 90 degrees	[-]
ν_f	Poisson's ratio fastener	[-]
ρ	Density	[kg/m^3]

1 Introduction

1.1   Two historical aircraft fuselage fatigue accidents

> **G-ALYP** *Ciampino this is George Yoke Peter passing flight level 260 for cruising altitude 360.*
> **ATC** *Hallo George Yoke Peter passing flight level 260.*
> **G-ALHJ** *George Yoke Peter from George How Jig understand you are passing 260 what's the cloud cover?*
> **G-ALYP** *George How Jig from George Yoke Peter did you get my…..*

The interruption on 10th January 1954 in the conversation [1] between the two British Overseas Airways Corporation (BOAC) aircraft was a result of the crash of the Comet G-ALYP, flight BA781, twenty minutes into its flight from Ciampino Airport, Rome, to London. Six possible causes for the accident were noted [2]; flutter of control surfaces, primary structural failure, flying controls, fatigue of the structure, explosive decompression of the pressure cabin and engine installation. From all these points the possibility of fatigue in the wing was assumed to be the cause of the failure. The lower frequent pressurization cycles of the fuselage were not believed to be the cause of the accident. After modification of the parts, which were supposed to be responsible for the crash, all Comets were reinstated into full service.

Two weeks after the reinstatement a crash near Napels of a second Comet, G-ALYY, on 8 April 1954 departing from Rome to Cairo, resulted in grounding all Comets for passenger transportation again. The accident occurred at a similar altitude and time after departure from Rome as in the case of the G-ALYP. This presented a major problem; all the modifications introduced did not prevent another disaster. After an extensive full-scale test program on a decommissioned Comet G-ALYU: the catastrophic explosive decompression of the pressurized fuselage of the Comet showed that the presence of small fatigue cracks in a pressurized fuselage is dangerous [2]. The Comet accidents were related to a poor design of the automatic direction finding (ADF) window at the crown of the fuselage. This window had a high stressed non-circular shape, resulting in an area susceptible to fatigue crack nucleation and growth.

It was several decades later when another astonishing accident occurred on 28 April 1988 involving an Aloha Airlines Boeing 737-200. The aircraft lost approximately 4.5 m of the fuselage skin due to poor maintenance, corrosion and fatigue, see Figure 1-1. In this case the fatigue crack grew through several bays for a large number of flights in a longitudinal lap-splice joint undetected by inspections to a total length of 4.50 m [3]. The problem of this Boeing 737-200 was related to the cold-bonded longitudinal lap-splice joint. This joint was designed to transfer the hoop stress introduced by the pressurization cycle through the bond line and rivets.

Due to the low durability of these bonded joints, the fasteners carried more load then anticipated. For aerodynamic purposes longitudinal lap-splice joints are usually manufactured with countersink fasteners. Countersunk fasteners, although highly favorable for aerodynamic consideration, introduce a higher stress gradient at the knife edge of the countersunk hole. And thus raising the possibility for faster crack nucleation at the fastener hole compared to straight shank holes.

In both cases fatigue cracks were involved; in the case of the Comets it was due to a poor design and a fatigue sensitive material and in case of the Aloha 737-200 it could also be attributed to significant fatigue damage not yet observed during inspections.
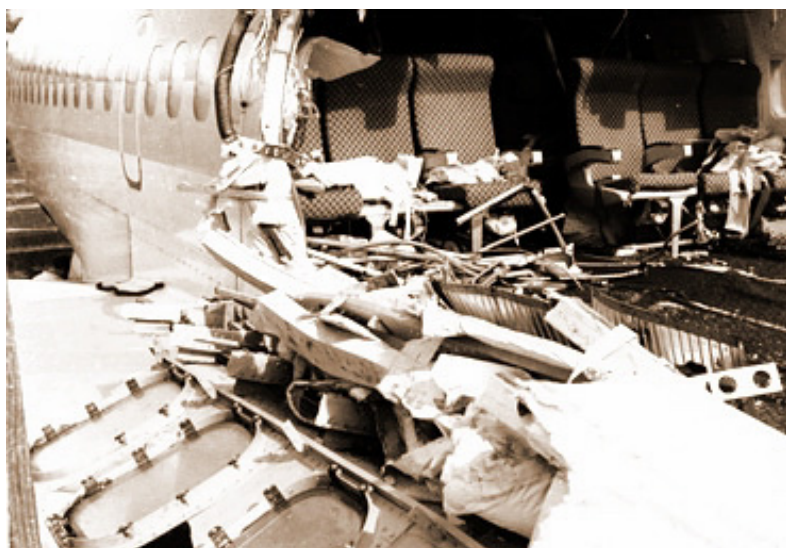
Figure 1-1   Catastrophic result of multiple side damage Aloha 737 200

These cases show the importance of fatigue resistant fuselage structures. The dominant load cycle for large passenger aircraft is the ground-air-ground (GAG) cycle. This means that the aircraft fuselage is pressurized and de-pressurized for each ground to air to ground transition, and thus creating a near constant amplitude fatigue cycle which can initiate fatigue. Dependent on the number of accumulated fatigue cycles, fatigue cracking can be a problem for a fuselage structure. The risk of a fatigue problem increases with the number of cycles if the hoop stress is above the endurance limit. Considering that a large number of commercial flying aircraft are reaching the Design Service Goal (DSG), special Service Life Extension Programs (SLEP) are implemented to extend the operational life of the aircraft resulting in an Extended Service Goal (ESG). *In these programs it is essential to know the fatigue crack growth behavior for the fuselage loading conditions. Using crack growth prediction models, an accurate estimation of the fatigue life of the fuselage should be given.*

In view of both the fatigue resistance and inspection of fuselage structure a look at metal-polymer laminates is an interesting option. In recent years, a number of studies on the behavior of these laminates, e.g. fiber metal laminates, has led to the

development of Glare. Glare is made of alternating layers of aluminum alloys (e.g. 2024-T3) and prepreg constituents consisting of S_2-glass fibers and FM94 epoxy resin. These polymer layers not only increase the damage tolerance of the material, but also fire resistance, impact, corrosion durability and fatigue properties [4]. The areas of interest are the fuselage joints, both longitudinal lap-splice and circumferential butt joints. *Since Glare was chosen as a skin material on the upper part of the A380 fuselage, more information on joint design with respect to both laminates and monolithic aluminum is required.*

The two italic sections above are combined into one research objective of the present thesis:

> **Develop structural analysis and life prediction methods for simple or complex, monolithic or laminated sheet and longitudinal or circumferential fuselage joints.**

1.2   Scope of present investigation

The two historical fuselage failures illustrate that similar accidents must be avoided which requires a profound understanding of the fatigue mechanisms involved, including analytical models to predict the fatigue behavior of a fuselage structure. Dealing with all aspects involved is obviously outside the scope of the present investigation, which mainly concentrates on fatigue of mechanically fastened joints of monolithic aluminum alloy sheet and fiber metal laminates.

In chapter 2 the boundaries of the research project are outlined.

Chapter 3 is used to re-introduce an analytical method developed in the late 1960's, namely the neutral line model. This model is rewritten to be applicable for laminates, using load transfer and fastener flexibility.

The objective of Chapter 4 is to find a relation between the resulting geometry of a rivet and the applied squeeze force. With this relation it is possible to assess the riveting quality, and thus the joint quality with respect to fatigue. As mentioned before, it is essential to be able to predict the crack growth behavior for aging aircraft.

In Chapter 5, stress intensity factors for cracks emanating from countersunk holes will be generated for crack growth predictions based on crack shapes found *in-service* as well as in the laboratory. When a crack reaches a certain length, the strength of a joint is the next question.

Chapter 6 will evaluate the available methods to calculate the residual strength in both monolithic and laminated joints. In support of the residual strength calculations, both crack nucleation and crack growth methods will be dealt with in the same chapter.

Finally, in Chapter 7 a summary of all findings will be given together with conclusions.

1.3 Literature

[1]   Transcript excerpt from sound file, copyright sound file by S. Hitchcock

[2]   Ministry of Transport and Civil Aviation, *Civil aircraft accident; report of the Court of Inquiry into the Accidents to Comet G-ALYP on 10th January, 1954 and Comet G-ALYY on 8th April, 1954*, London HMSO, 1955

[3]   Aircraft Accident Report: *Aloha Airlines, Flight 243, Boeing 737-200, N73711, near Maui, Hawaii, April 28, 1988, NTSB/AAR-89/03*, Washington DC: U.S. National Transportation Safety Board, 1989

[4]   Vlot, A. and J.W. Gunnink, (eds.); *Fibre Metal Laminates: an Introduction. Glare, The New Material for Aircraft*, Kluwer Acadamic Publishers, Dordrecht, 2001

2 Background

2.1   Introduction

The scope of the research project covers a wide variety of joint types and joining techniques for both monolithic and laminated sheet materials. Looking at an aircraft fuselage structure, a rather complicated system of parts can be observed, e.g. skin, tear-straps, stringers, frames and doublers. All these parts connect to each other via mechanically fastened or bonded joints, or a combination of both. In this chapter the topics of this research are described. The complex fuselage structure will be reduced to specimen level size for laboratory testing. As mentioned in Chapter 1 two materials are considered, monolithic aluminum 2024-T3 Clad and Glare.

Aluminum 2024-T3 is a well-known aluminum alloy used in the aircraft fuselage; Glare is a relatively new material for the aircraft manufacturers. Glare is a member of the fiber metal laminates family, the history and variants will be discussed in section 2.2 of this chapter. In section 2.3 a stepped approach is taken to simplify the fuselage structure for laboratory sized testing. A good interpretation of the loading conditions in a fuselage will allow for investigating each component's role in the structural assembly. Two specific types of joints are used in an aircraft fuselage as will be discussed in section 2.3. In section 2.4, characteristic variables of joints are reviewed. Section 2.5 describes the work done on crack growth characteristics for both aluminum alloy 2024-T3 and fiber metal laminates. Finally in section 2.6 the approach taken in this effort will be outlined.

2.2   Fiber Metal Laminates

Laminates have been around for some decades now; a good example of laminated primary structures in airplanes is the de Havilland Mosquito, Figure 2-1. This aircraft primary structure was fully manufactured from wood. In order to provide sufficient strength, the wood was laminated. The laminated fuselage structure was made of balsa wood between two layers of cedar plywood; the remaining airframe structure was primarily made of spruce, with plywood covering. This showed the remarkable strength of the optimized design process for this aircraft in the midst of a rising all metallic aircraft industry.

The step from bonding thin wooden layers together to bonding metal layers was made by a British engineer, Norman de Bruijne, working for de Havilland at the beginning of the 1940's [1]. De Bruijne, being an avid enthusiast of building wooden model aircraft, tried to connect wooden parts, with pressure applied on the wood to enable for good bonding. To apply the pressure, he used a hot plate press, and the adhesive flowed accidentally out between the wooden layers, he also bonded the metal plates of the press.
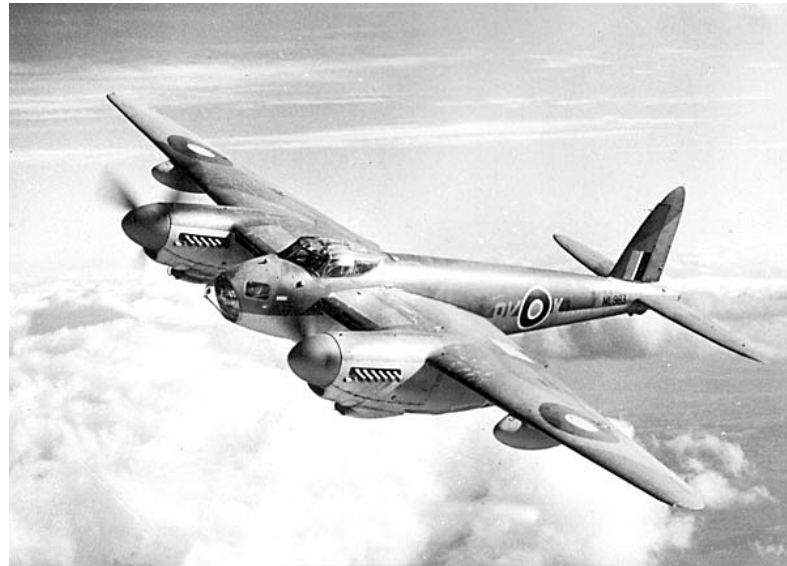
Figure 2-1   de Havilland Mosquito

Thus, he discovered something new: metal bonding. The next step in the development of laminates was attributed to Schliekelman from Fokker. He learned about the metal bonding process during his time at de Havilland. He convinced his superiors in 1952 that bonding was a technique that would benefit future aircraft, such as the Fokker F-27. Since Fokker did not have the large milling machines to produce sheets of aluminum that varied in thickness, Fokker decided to produce these sheets for the F-27 by means of bonding thin layers of aluminum together. This bonding process is basically similar to the process used for the de Havilland Mosquito. This started the research into the behavior of laminated aluminum sheets. Tests at the time showed a significant decrease in fatigue crack growth rate compared to monolithic aluminum sheets. In the early seventies, with increasing knowledge of the behavior of aluminum laminates, a tendency to reinforce metal structures with composites created the first fiber metal laminates. It was found that adding fibers to the adhesive further improved the fatigue performance of the aluminum laminates. The development of fiber metal laminates was characterized by the crack bridging effect of the fibers and thin aluminum layers. The first fiber metal laminate was named: ARALL (Arimid Reinforced ALuminum Laminates). The eighties were predominantly used for development and finding applications for ARALL, e.g. several experimental cargo doors for the C-17 military transport aircraft. Late in the eighties research led to the development of a new fiber metal laminate named Glare (GLAss REinforced). This research was initiated in order to overcome the problems found with ARALL in a fuselage structure. Under cyclic loading conditions similar to the ones found in an operational aircraft fuselage, the Aramid fibers around a crack would break subject to cyclic loading. Fiber pull out of the crack bridging fibers caused fiber buckling and cyclic buckling led to fiber failure. This eliminated the low crack growth rate advantages of ARALL [2].

Glare is built up from thin aluminum alloy 2024-T3 sheets with a thickness varying between 0.2 mm and 0.5 mm and prepreg layers, consisting of uni-directional S_2-glass fibers embedded in FM94 adhesive. Combining the aluminum layers and prepreg, several different grades of Glare can be manufactured. The number of prepreg layers between the aluminum layers can be varied as well as the orientation of the prepreg.

Table 2-1 lists the standard Glare variants available. The lay-up of the fiber direction is linked to the rolling direction of the aluminum sheets: the longitudinal rolling direction (*L*) corresponds to 0° and the longitudinal-transverse direction (*LT*) corresponds to 90°.

Table 2-1   Available Glare grades. Aluminum alloy 7475-T761 layers in Glare 1

Variant	Prepreg orientation between Al layers	Thickness of prepreg layer [mm]	Characteristics
Glare 1	0°/0°	0.25	fatigue, strength, yield stress
Glare 2A	0°/0°	0.25	fatigue, strength
Glare 2B	90°/90°	0.25	fatigue, strength
Glare 3	0°/90°	0.25	fatigue, impact
Glare 4A	0°/90°/0°	0.375	fatigue, strength in 0° direction
Glare 4B	90°/0°/90°	0.375	fatigue, strength in 90° direction
Glare 5	0°/90°/90°/0°	0.50	impact
Glare 6A	+45°/-45°	0.25	shear, off-axis properties
Glare 6B	-45°/+45°	0.25	shear, off-axis properties

As an example, Figure 2-2 shows the build-up of Glare 3. The prepreg layers between each aluminum layer consist of one prepreg layer in 0° and one in 90°. A variant is shown with three layers of aluminum alloy and two combined prepreg layers. Based on this composition the following notation for the Glare variant is:

Glare 3 – 3/2 – 0.3

Where 3   : is the Glare variant
        3/2   : is the number aluminum layers (3) and prepreg layers (2)
        0.3   : is the aluminum alloy sheet thickness

90° - direction
0° - direction
Al layer
Prepreg layer 0°
Prepreg layer 90°
Al layer
Prepreg layer 90°
Prepreg layer 0°
Al layer
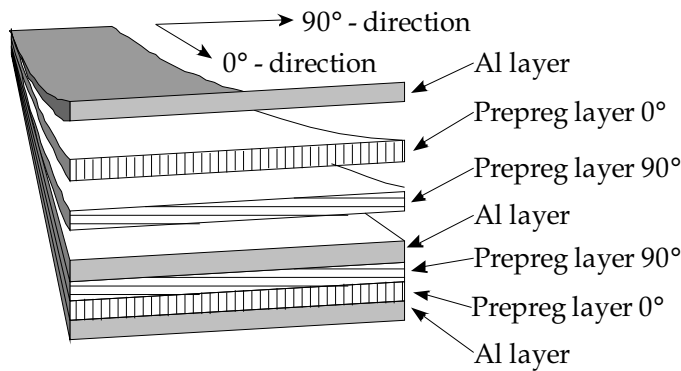
Figure 2-2   Fiber metal laminate with three aluminum layers and prepreg layers in 0° and 90°

2.3   From fuselage to laboratory sized test specimen

The first step is to understand the complex loading conditions in a fuselage structure. The pressurization of the fuselage causes the structure to expand outward like a simple balloon. The expansion creates a hoop stress in the circumferential and an axial stress in the longitudinal direction. Due to this complexity in structure, loading conditions and test set-up simplification to more simple test specimens is required. Using simple specimens enables isolation of specific parameters affecting the performance (e.g. secondary bending, out of plane displacements, crack growth, etc.) that otherwise would have been masked by other components in the structure. As discussed, the fuselage structure has biaxial loading, complex structure and a circular shape. Figure 2-3 shows a cut-out of a typical fuselage structure.

Butt strapp
Butt joint specimen
Stringer
Circumferential direction
Lap-splice joint specimen
Longitudinal direction
Skin
Frame clips
Frame
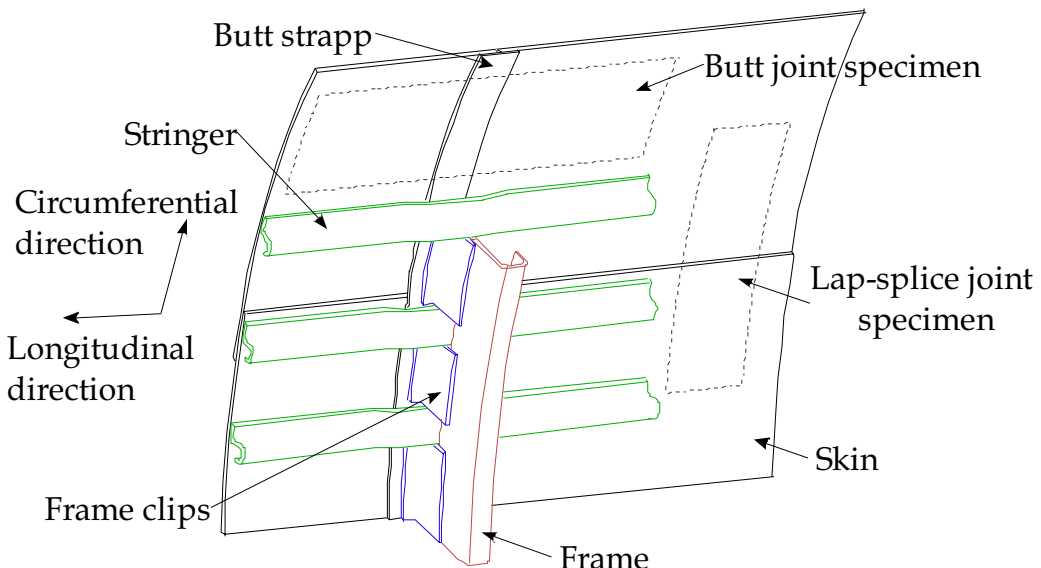
Figure 2-3   Cut-out section of fuselage structure, longitudinal lap-splice and circumferential butt joint with frame and stringers

With full pressurization, the skin and underlying structure will move outward. It is not too difficult to see that a frame or stiffener will not move the same distance as the skin would due to higher local stiffness, thus creating differences in outward movements and higher hoop stresses in the skin between the frames.

Setting up a test as large as a full-scale aircraft structure requires an enormous amount of time and money. Reducing the full-scale test to a more simple, easier to understand test specimen such as a barrel or fuselage panel including stiffeners and frames reduces the size of the test. However, the complexity in understanding the entire structure is similar to a full-scale test. Stepping down to the level of component testing to understand the behavior of the individual parts allows the researcher or designer to efficiently test multiple configurations of structural elements. Elimination of the stiffeners, frames and curvature reduces the structure to flat sheet longitudinal lap-splice and circumferential butt joints, Figure 2-3. When choosing uni-axially loaded longitudinal lap-splice and circumferential butt joints, see Appendix E, the above-mentioned fuselage characteristics are obviously not captured.

Specimen design should be based on what joint parameter is being studied during the test and what kind of experimental techniques are used. The sheet properties, joint geometry, and fastening system can have a large influence on the outcome and should be chosen with care. The effect of secondary bending introduced by the eccentricities of lap-splice and butt joints on the crack growth rate and crack shape needs to be investigated. The influence of the material properties on secondary bending is less significant. These aspects will be dealt with in more detail in Section 2.4.

Crack monitoring in joints is difficult since crack nucleation and crack growth occur at the faying surface, which is not visually inspectable until the crack penetrates as a through crack to the free surface. Non-destructive investigation (*NDI*) might reveal crack nucleation and crack growth in monolithic aluminum; but it is difficult to use eddy-current techniques for Glare. Schra et al. tried to show crack nucleation by means of high frequency testing, stiffness monitoring, eddy-current and visual inspections [2]. To obtain crack nucleation data using high frequency testing the specimen size is important. Lap-splice and butt joints shown in Appendix E are too large to fit into the servo-hydraulic testing machine set-up [3]. Monitoring the stiffness change as an indicator of crack nucleation proved to be not sensitive enough. The eddy-current inspections were inaccurate for cracks up to 2.5 mm lengths. Schra et al. used the eddy-current technique only for obtaining an indication that a crack was present. The work of Soetikno and others on crack nucleation and crack growth with respect to eddy-current inspections supports these observations [4],[5],[6]. To monitor crack growth in joints is a labor intensive test procedure. Removing the fasteners and checking the faying surface for possible cracks appeared to be the only option to monitor the crack growth in fiber metal laminate joints. It is also possible reconstruct the crack history post-test by using a

spectrum that marks the fracture surface during the test. A proven method for aluminum alloy joints is to use a marker load spectrum leaving visible marker bands on the fracture surface without influencing the fatigue crack growth rate [7]. The complete crack growth history can then be reconstructed using a scanning electron microscope. However, using a marker load spectrum for fiber metal laminate joints might well result in a difficult, if not impossible, task to reconstruct crack growth curves with a scanning electron microscope. Woerden noted that due to the small crack growth rates combined with plasticity effects around the crack tip and crack closure caused by the glass fibers the overall quality of the fracture surface is poor [8]. More on the effect of the glass fibers can be found in section 2.5.

The fasteners and the geometry of the structure have an influence of the fatigue crack growth. In order to observe the crack growth behavior of cracks growing from a hole subjected to tensile or combined tensile and bending loads a simple test specimen will suffice. For pure tensile loading, the flat sheet open hole specimen suffices. When looking at a combination of tensile and bending stresses, a combined tension and bending specimen is required. Obtaining crack growth data can be done by *in-situ* measurements and afterwards by fractographic reconstruction using a scanning electron microscope [7],[9],[10],[11],[12].

Stresses in joints can be obtained by different methods, well-known methods are:
1. Strain gage measurements
2. Finite element analysis
3. Photo-elastic analysis

Each of these methods has its advantages and disadvantages. Strain gage measurements can be done rather easily. The data obtained from these measurements are only the average strains of that very local area. Despite its simplicity it is impossible to obtain the strain data of the complete joint [13],[14]. Finite element analysis gives a more complete picture of the strain and stresses of the joint. However it is difficult to model such a joint completely. Modeling a complete joint results in a large finite element model and requires a full understanding of each individual component and interaction effect in the model. This increases the computational time that will be needed for a full finite element analysis [15]. Photo-elastic analysis gives the information needed to obtain the stresses in a joint. Photo-elastic fringes appear in the photo-elastic material bonded on the specimen surface. These photo elastic fringes can be digitally recorded; this gives the opportunity to record the regions of constant principal strains. The strains can then be identified and stresses can be assigned to these areas. The only disadvantage of this method is that only strains at the outer joint surfaces can be made visible.

Monitoring the stresses in lap-splice and butt joints for validation of the neutral line model, discussed in Chapter 3, can be done with strain gages. The neutral line model uses eccentricities inherent to joints to calculate tensile and bending stresses present in joints. By applying strain gages at some locations on the joint, the strain at

the surface can be monitored. These strains are converted to stress and these stresses can then be compared to stresses calculated using the neutral line model.

2.4 Joint variables

Two types of joints will be tested, longitudinal lap-splice and circumferential butt joints. Since only mechanically fastened joints are considered in the present investigation, the two main constituents of joints are the sheets and the fasteners. Joints in *in-service* situations will most likely incorporate a sealant or an adhesive layer between the mechanically fastened sheets. Early generations of aircraft have neither, sealant nor adhesive bonding present, e.g. KC-135, Boeing 707. Although the sealant is not applied to act as some sort of adhesive bonding, the presence of sealant does influence the load transfer. A brief discussion of the combination between adhesive bonding and mechanically fastening will follow. The sheet materials of interest here are aluminum alloy 2024-T3 and the fiber metal laminate Glare.

2.4.1 *Bonded and mechanically fastened joints*

In general a combination between adhesive bonding and mechanically fastened joints will not improve the joint performance compared to a well designed undamaged adhesive bonded joint [16]. The adhesive provides a much stiffer load path than the fasteners, which results in redundancy of the fasteners. An extra advantage of an adhesive is the prevention of fretting.

In the combination, the fasteners placed in conventional positions as in pure mechanically fastened joints, are located in minor shear stress areas. As long as the adhesive bond is undamaged, the fasteners will be moderately loaded. Only when disbonding occurs the combination will be effective. If the adhesive is totally disbonded and does not carry any more load, then the fasteners will prohibit the structure from failing. Research done by the National Aerospace Laboratory (NLR) and published by the Federal Aviation Administration (FAA) showed the improved fatigue life of a combination between riveting and adhesive (cold) bonded joints [17]. Modeling a combined adhesive and mechanically fastened joint is not a simple task. It is not as simple as a linear superposition of both solutions. Hart-Smith developed a Fortran code called A4EK for analyzing intact and flawed bonded-bolted step lap joints with linearly elastic adherent deformations [18].

2.4.2 *Material properties*

For a given joint design, the material of the joint dictates predominantly the fatigue crack nucleation, fatigue crack growth and residual strength behavior. Monolithic aluminum alloys are fatigue sensitive compared to fiber metal laminates, which in turn are more flexible (lower bending stiffness). The difference in stiffness can most profoundly be seen in the secondary bending behavior and the stresses through the thickness. Due to the different elastic moduli of the metal layers and fiber layers, the fiber metal laminates show a stepped or discontinuous stress distribution through

the thickness, see Figure 2-4. This results in higher stresses in the aluminum layers compared to monolithic aluminum. The influence of the material and geometry of the joint can easily be obtained by using the neutral line model [19]. This model provides the means to calculate stresses in the joint as a result of the eccentric load path.
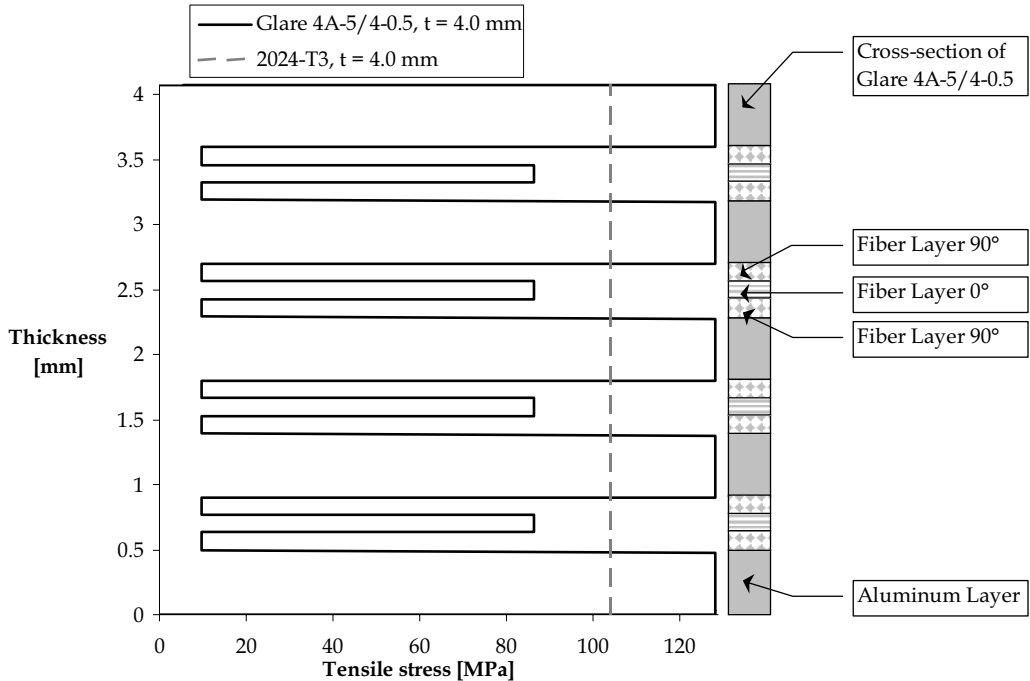
Figure 2-4   Comparison of stress distribution over the thickness in Glare and monolithic aluminum sheet. Applied stress is 104 MPa.

The parameters of interest in the test program are the static mechanical properties for the aluminum alloy 2024-T3 and Glare. The properties of the Glare variants are dependent on the static mechanical properties of the constituents, see Table 2-2.

Table 2-2   Properties of UD-prepreg and aluminum alloy 2024-T3 [20]

		Uni-Directional (*UD*) prepreg	2024-T3
Young's modulus, E_1	[GPa]	54.0	72.4
Young's modulus, E_2	[GPa]	9.4	72.4
Ultimate strength, σ_{ult}	[MPa]	2640	455
Ultimate strain, ε_{ult}	[%]	4.7	19
Poisson's ratio, ν_{12}	[-]	0.33	0.33
Poisson's ratio, ν_{21}	[-]	0.0575	0.33
Shear modulus, G_{12}	[GPa]	5.55	27.6
Density, ρ	[kg/m³]	1980	2770
Thermal expansion coefficient, α_1	[1/°C]	$6.1 \cdot 10^{-6}$	$23.4 \cdot 10^{-6}$
Thermal expansion coefficient, α_2	[1/°C]	$26.2 \cdot 10^{-6}$	$23.4 \cdot 10^{-6}$

The properties of the individual constituents of the fiber metal laminate can be used to calculate the global material properties if the laminate using the metal volume fraction (*MVF*) [21],[22].

The metal volume fraction is defined as the sum of all aluminum layers thicknesses over the total thickness of the laminate.

$$MVF = \frac{\sum_{1}^{n} t_{al}}{t_{tot}}$$

(2-1)

Where:

n : Number of aluminum layers
t_{al} : Thickness of aluminum layer
t_{tot} : Total thickness of laminate

The ratio *MVF* with a value of 1 means a 100% monolithic aluminum sheet, the value decreases when the amount of fibers increase. A theoretical value of 0 represents a complete sheet material made up of pure prepreg fiber layers. The *MVF* provides the means to calculate the basic properties; yield stress, ultimate strength, young's modulus, *G*-modulus, blunt notch strength and bearing strength. All these properties show a linear relation with the *MVF* [21],[22].

$$X_{lam} = MVF \cdot X_{al} + (1 - MVF) \cdot X_{prepreg}$$

(2-2)

Where:

X_{lam} : Laminate property
X_{al} : Aluminum layer contribution
$X_{prepreg}$: Fiber layer contribution

Figure 2-5 shows the significance of the *MVF* method. For the Glare grades shown, the differences between the calculated tensile yield strength and results obtained from tests are within –2% and +2%.
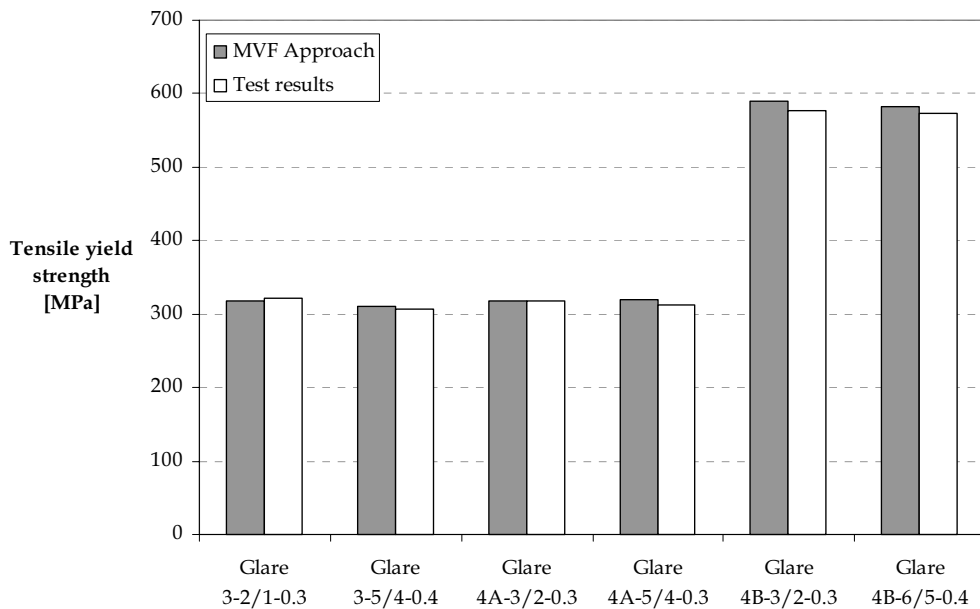
Figure 2-5 Tensile yield strength differences between MVF and test results for different Glare grades [23]

2.4.3 Fasteners

Various fastening systems are available; bolts, solid rivets. Titanium bolts, e.g. Hi-Loks, and solid rivets are used in this investigation. In this section, the effects of installing bolts and solid rivets on the sheet are discussed. The installation procedure will have little or no influence on bolts, for the solid rivet this is completely different. The installation of a solid rivet is characterized by large plastic deformations of the fastener.

Two types of bolts are available, clearance fit and interference fit. The clearance fit bolt has a different residual stress field, mostly caused by the clamping forces applied on the sheets. Since bolts will not expand in the fastener hole, residual stresses are caused by the fastening of the bolt with a certain torque. Interference fit fasteners provide a consistent torque and a collar that automatically detaches during fastening when the appropriate clamp-up stress or torque level is reached. The shape of the interference fit bolt causes a small plastic deformation of the hole during installation of the fastener. The diameter of the interference fit bolt is slightly larger then the diameter of the hole. A disadvantage of these interference fit fasteners is that during installation in fiber metal laminate sheets, local delamination around the fastener hole occurs [21].

The riveting process causes a residual stress distribution around the rivet hole. The force necessary to squeeze the rivet into shape causes plastic deformation of the rivet. This deformation will cause the rivet to expand in the rivet hole, and thus

create a deformation of the surrounding sheet material. After the riveting process, the residual stresses remain present around the installed rivet. It is this residual stress system that is responsible for better fatigue performance of the joint [14]. During this installation process the sheets are pressed together. This introduces surface contact stresses, which may result in a greater chance of fretting around the rivet hole. As shown by Müller [14], cracks may initiate away from the hole boundary.

A test program could give some indication of the effect of the deformations of the rivet head with regard to the rivet squeeze force. A simple relation between the deformations of the rivet head geometry and the squeeze force can be used to the quality control of the riveting process. Depending on the aircraft manufacturer the riveting processes are based on displacement controlled riveting machinery, e.g Airbus. This means that all rivets installed are checked against an earlier riveted specimen. Only a geometry check of the rivet head is done. So when a relation is known between the squeeze force and the rivet head geometry a better product quality can be achieved. The test program that will be used for this investigation should include a variation of the following parameters, countersunk, non-countersunk, rivet diameter, squeeze force and rivet material. The results of the investigation should present a relation between the formed rivet head and the squeeze force based on material properties and not on empirical obtained equations as was attempted in [14].

2.5   Crack growth characteristics

The crack growth characteristics of 2024-T3 aluminum alloy and fiber metal laminates made of 2024-T3 differ significantly. The fiber prepreg layers in the fiber metal laminates are insensitive to fatigue loading. The fatigue performance of fiber metal laminates is then a function of the fatigue sensitivity of the aluminum alloy layers.

The influence of the fibers on the fatigue properties of fiber metal laminates is twofold. Once a crack has been initiated in an aluminum alloy layer, another crack must still be initiated in a second layer, etc. For monolithic aluminum, the crack initiates and does not encounter any boundaries, in growing through the thickness. The fiber layers in fiber metal laminates are natural crack arresting layers within the material. The second advantage of the fiber prepreg layers is the fiber bridging effect. Two effects contribute to this advantage; the unbroken fibers in the cracked area still carry load over the crack, and secondly the bridging fibers restrain the crack opening displacement (*COD*). These two effects will reduce the stress intensity factor, *K*, at the crack tip significantly. Since *K* is the crack driving force, the crack growth rate of Glare is therefore low compared to the crack growth rate in monolithic aluminum. As discussed in section 2.4.2 the bending stiffness of Glare influences the stress distribution through the thickness. The aluminum alloy layers in Glare are more highly loaded than monolithic aluminum in the same area. This results in higher stresses in the aluminum layers in Glare. As a result, crack

nucleation occurs more rapidly than in monolithic aluminum. Fatigue cracks initiate in Glare earlier in the fatigue life compared to monolithic aluminum. This shows that a completely different approach is required for crack growth predictions in Glare. The prediction of crack growth in Glare is predominantly based on empirical evidence. However, crack growth predictions in monolithic aluminum are in the recent years more based on nearly exact stress intensity factors K_I using existing crack growth laws. Fawaz et al. produced the first exact K_I solutions for straight shank holes for part-elliptical through cracks emanating from a straight shank hole subject to general loading [25]. For the crack interaction effect, part-elliptical through cracks growing towards each other from straight shank holes, de Rijck provided three-dimensional K_I solutions [26].

Once the crack in a fiber metal laminate reaches a certain length, the crack growth slows down considerably, and it may even be arrested. This implies that the fatigue life is exceeding the fatigue life of monolithic aluminum. The crack growth in Glare is dominated by the crack bridging effect of the fibers resulting into a slow, constant fatigue crack growth rate.

Since the crack growth in laminates of this research focuses on joints, the ligament length between the fasteners plays a major role in the crack growth analysis. In monolithic aluminum, the crack growth rate is not influenced by the change in ligament area until the remaining net-section between the fastener holes is reduced by 50% [26],[27]. Glare joints however, still have the intact fibers in the net-section between the two fastener holes to carry the load. Failure of joints is related to the capacity to carry the load through the reduced net-section between the fasteners. The failure of a joint depends on the loading condition. Failure modes due to static loading are different from fatigue driven failures. The static failure modes are fastener shear, plate tension, bearing failure and plate shear (Figure 2-6).
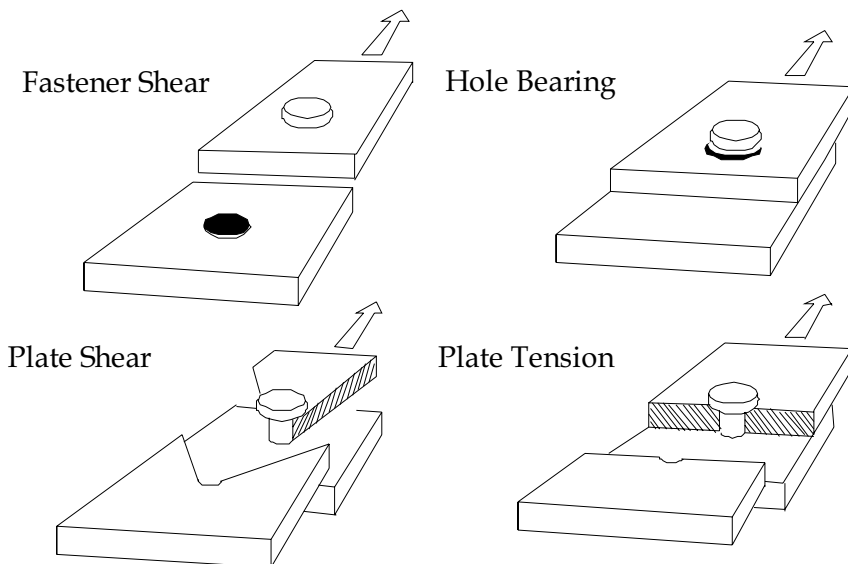
Figure 2-6   Occurring static failure modes in joints

2.6   Approach of the present investigation

The investigation reported in this thesis covers experimental and analytical work. The experimental work is used to explore theoretical problems while and at the same time the experimental results can be used to validate the theoretical analysis of the problems tackled in this thesis. The interest of the problems is focused on the stress distribution in the longitudinal lap-splice and circumferential butt joints in pressurized aircraft fuselages. The analysis includes the development of stress intensity factors for cracks at countersunk holes.

The theory for the calculations of the tensile and bending stresses in joints is based on the neutral line model. These results can be used as input for crack growth predictions for lap-splice joints. It will be shown that the accuracy can be improved by introducing load transfer characteristics of all fastener rows, which were ignored in the elementary neutral line model. A new internal moment model has been developed for that purpose. Several experiments have been carried out to validate the stress calculations for both monolithic aluminum and fiber-metal laminate joints.

The crack growth predictions in monolithic aluminum sheets of the joint specimens are based on the crack driving force characterized by the stress intensity factor K_I. An important part of the present investigation is the development of exact stress intensity factors, which can be used in available crack growth laws, e.g. the Paris equation. Results of research done in earlier years and experiments on both open hole and combined loading specimens are used for predictions. The experiments clearly show the characteristic shape found in aircraft service and the laboratory. A fractographic reconstruction of the crack shape en crack growth rates is possible by means of using a marker load spectrum.

The three-dimensional problem of stress intensity factors for crack emanating from a countersunk hole subject to tensile, bending and pin loading are developed with an indirect finite element analysis. In the analysis the nodal point output, nodal displacements and nodal forces are used to calculate K_I.

As observed in earlier investigations by Müller, the rivet squeezing force during the installation of the fastener can have an important influence of the crack nucleation period. A good relation between the formed rivet head and the squeeze force was not available at the time. New experiments have been carried out to derive a relation between the head geometry and the squeezing force for different types of rivets installed in both Glare and aluminum sheet material.

Because the endurance of a lap-splice joint is finally determined by a static failure of the fatigue crack damage joint, a new approach was developed for calculating the residual strength of Glare joints. The method is based on the metal content in the fiber-metal laminate material. Methods for crack nucleation and crack growth analysis in Glare joints are briefly discussed including the last stage of the life, which is a static failure of the joint.

2.7 Literature

[1] Vlot, A., *Glare; history of the development of a new aircraft material*, Kluwer Acadamic Publishers, Dordrecht, 2001

[2] Roebroeks, G., *Towards Glare – The development of a fatigue insensitive and damage tolerant aircraft material*, Delft University of Technology, 1991

[3] Schra, L. and H.J. ten Hoeve, *Feasibility of Eddy Current inspection for detection of fatigue crack nucleation in Glare joints, and a comparison of crack length measuring techniques*, National Aerospace Laboratory NLR, NLR-CR-2001-565, 2001

[4] Soetikno, T.P., *Residual strength of the fatigued 3 rows riveted Glare3 longitudinal joint*, MSc. Thesis, Delft University of Technology, Aerospace Engineering Department, May 1992

[5] Schijve, J., *Eddy-current inspection of visible cracks in a riveted lapjoint of ARALL-material*, Memorandum M-560, Delft University of Technology, Aerospace Engineering, March 1987

[6] Hughes, D., *Crack initiation in a GLARE3-5/4-0.4 riveted lap joint*, Delft University of Technology, Aerospace Engineering, September 1999

[7] Fawaz, S.A., *Fatigue Crack Growth in Riveted Joints*, Dis. Delft University of Technology, Delft University Press, 1997

[8] Woerden, H.J.M., *Fuselage Spectrum Fatigue Loading on Fiber metal Laminates*, MSc. Thesis, Delft University of Technology, Aerospace Engineering, October 1998

[9] Pelloux, W.R.A., and J. O'Grady, *Fractographic Analysis of Initiation and Growth of Fatigue Cracks at Rivet Holes*, Eds. S.N. Atluri, S.G. Sampath, and P. Tong, Structural Integrity of Aging Airplanes, Springer Series in Computational Mechanics, Berlin, Springer Verlag, 1991

[10] Piascik, R.S., and S.A. Willard, *The Characterization of Wide Spread Fatigue Damage in the Fuselage Riveted Lap Splice Joint*, NASA-TP-97-206257, 1997

[11] Schijve, J., *Fatigue of Structures and Materials*, Kluwer Acadamic Publishers, Dordrecht, 2001

[12] Schijve, J., *The Significance of Fractography for Investigations of Fatigue Crack Growth under Variable Amplitude Loading*, Series 07: Aerospace Materials 09, Delft university Press, 1998

[13] Fawaz, S.A., *Equivalent initial flaw size testing and analysis*, AFRL-VA-TR-2000-2034, June 2000

[14] Müller, R.P.G., *An Experimental and Analytical Investigation on the Fatigue Behaviour of Fuselage Riveted Lap Joints, The Significance of the Rivet Squeeze Force, and a comparison of 2024-T3 and Glare 3*, Dis. Delft University of Technology, 1995. Delft: NL, 1995

[15] Ryan, W.P., *An Experimental and Numerical investigation into the Manufacture and Service Behaviour of Riveted Joints*, Thesis University of Dublin, Trinity College, April 1999

[16] Clarke, J.L., *Structural Design of Polymer Composites*. EUROCOMP Design Code and Handbook, E&FN Spon, 1996

[17] Vlieger, H., and H.H. Ottens, *Uniaxial and Biaxial Tests on Riveted Fuselage Lap Joint Specimens*, DOT/FAA/AR-98/33, October 1998

[18] Hart-Smith, L.J., *Design methodology for bonded-bolted composite joints*, USAF Contract Report AFWAL-TR-81-3154, Vol. 1, February, 1982

[19] Schijve, J., *Some Elementary Calculations on Secondary Bending in Simple Lap Joints*, NLR-TR-72036, Amsterdam, NL, National Aerospace Laboratory, 1972

[20] de Vries, T.J., *Blunt and sharp notch behavior of Glare laminates*, Dis. Delft University of Technology, 2001

[21] Roebroeks, G.H.J.J., *The Feasibility of the Metal Volume Fraction Approach for the Calculation of the Glare Blunt Notch Strength*, TD-R-99-005, Structural Laminates Industries, Delft, 2000

[22] Roebroeks, G.H.J.J., *The Metal Volume Fraction Approach*, TD-R-00-003, Structural Laminates Industries, Delft, 2000

[23] IJpma, M.S., *Material design allowables and qualification*, In: Vlot, A., Gunnink, J.W. (eds.); Fibre Metal Laminates: an introduction, Kluwer Academic Publishers, Dordrecht, 2001, pp. 69-78

[24] Vissers, S.J.A., Detail Design of a Fuselage Crown Panel with a Butt Joint for the A3XX, MSc. Thesis: Delft 1998

[25] Fawaz, S.A., Andersson, B., and J.C. Newman, Jr., *Experimental Verification of Stress Intensity Factor Solutions for Corner Cracks at a Hole Subject to General Loading*, ICAF 2003, Luzern, Switzerland, 2003

[26] de Rijck, J.J.M., *Crack Interaction of Oblique Part-Elliptical Through Cracks*, MSc. Thesis Delft University of Technology, Aerospace Engineering, August 1998

[27] Pártl, O., and J. Schijve, *Multiple-site-damage in 2024-T3 alloy sheet*, Report LR-660, Faculty of Aerospace Engineering, January 1992

[28] Vlot, A. and J.W. Gunnink, (eds.); *Fibre Metal Laminates: an Introduction. Glare, The New Material for Aircraft*, Kluwer Acadamic Publishers, Dordrecht, 2001

3 Neutral Line Model

3.1 Introduction

Knowledge of the stresses at the most critical fastener row is essential in conducting static strength and damage tolerance analysis of mechanically fastened joints. The critical fastener location is most susceptible to fatigue crack nucleation and crack growth. For mechanically fastened lap-splice joints and butt joints in a fuselage structure a dominant load is introduced by the Ground-Air-Ground (GAG) pressurization cycle. The hoop load is transferred from one skin panel to the next via the fasteners in the lap-splice or butt splice joint. The hoop load is not collinear through the joint but is offset or eccentric. The eccentric path of the hoop load causes secondary bending. The total stress in the joint is then the membrane stress, the secondary bending stress and the bearing stress associated with the fastener loads on the holes. The secondary bending is highly dependent on the magnitude of the eccentricity and the flexural rigidity of the joint between the fastener rows. The theory used to derive the bending stresses is based on the advanced beam theory [1]. Schijve's simple, one-dimensional Neutral Line Model (NLM), is used to calculate the tension and bending stresses at any location in the joint that is most likely to develop fatigue crack nucleation and fatigue cracks [2],[3].

The elementary neutral line model is one-dimensional in such a way that the displacement of the neutral axis determines the behavior of the joint as a single structural element. The option of adding load transfer to the neutral line model is investigated in this chapter. Load transfer in both adhesively bonded lap-splice and butt joints is straightforward since the load transfer is continuous in the overlap region and not discrete as in mechanically fastened joints. For the latter type of joints, three approaches are available to implement the 'load transfer' into the neutral line model; (1) rivet rotation mentioned by Schijve [3], (2) adjusting flexural rigidity by Müller [4] and (3) adding an internal moment due to the eccentric load path. The latter approach is investigated in this thesis. The rivet rotation can account for added flexibility in a joint. According to Schijve, a relative low stress level can already cause plastic deformation [3]. Schijve showed that the small rotation introduced to account for this plastic deformation had a significant influence on the bending stresses calculated using the neutral line model. This finding was supported by research of de Rijck and Fawaz, which confirmed a significant influence of the fastener rotation on the bending stress [5]. The fastener rotation depends on both the material properties of the rivet and the applied loading. In [5] and [3] an arbitrary fastener rotation between 0 and 1° was chosen to account for the added flexibility. If a relation between the material properties, the applied load and the fastener rotation was available, then the method proposed by Schijve would be attractive. The method proposed by Müller is not evaluated here because this method is based on changing the actual flexural rigidity to a virtual flexural rigidity. The method is adequate for joints made of monolithic materials, but does not allow

for a correct calculation of the neutral line displacements for fiber metal laminates (FML) because both the elastic modulus and moment of inertia are changed.

In the present chapter, the elementary neutral line model is discussed in Section 3.2 and illustrated by analyzing secondary bending for the lap-splice joint shown in Figure 3-1. Since the sheets between the fastener rows are assumed to behave as an integral beam, no load transfer from one sheet to the other one occurs at the middle row.
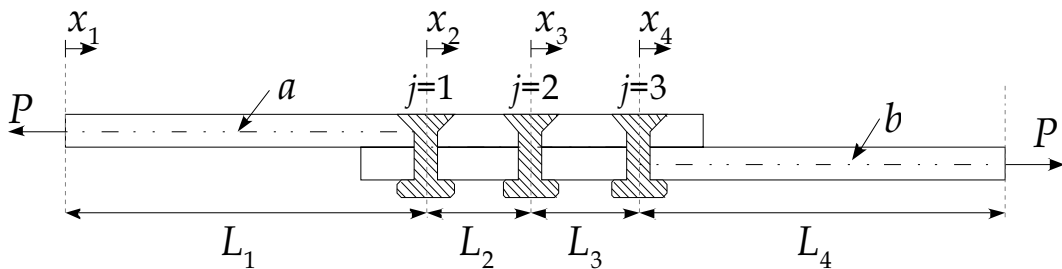
Figure 3-1   Nomenclature for lap-splice joint geometry

The variables presented in Table 3-6 will be used in Section 3.2. This will allow the reader to understand the background behind each step required for a neutral line model calculation in monolithic aluminum for a simple symmetric lap-splice joint. Also fastener flexibility and load transfer via fasteners will be introduced in the simple lap-splice joint.

Table 3-1   Lap-splice joint geometry variables

Width W [mm]	100.0
Skin length L_1 & L_4 [mm]	200.0
Skin length L_2 & L_3 [mm]	28.0
Skin thickness t_1 & t_2 [mm]	2.0
Applied force P [kN]	20.0
Skin material sheet a & b	AL 2024-T3 Clad

In section 3.3, the equations required for Schijve's neutral line model calculation are derived. Following this derivation, a neutral line model including load transfer, clamped edges and hinged end conditions is derived. The second derivation includes additions to the neutral line model allowing for a more realistic stress calculation. The additions required are the introduction of the fastener flexibility and internal moments. The internal moment as explained in section 3.4 is a function of the applied load and the fastener flexibility.

For fastener flexibility, several empirical equations exist. In Section 3.5, several widely used methods are described. In addition the fastener flexibility is directly

linked to the calculation of load transfer. A generic method to calculate the load transfer is also described in Section 3.5.

The section that follows discusses the implementation of fiber metal laminates into the neutral line model. Fiber metal laminates are sheets built up of thin aluminum and glass fiber layers. To find the location of the neutral axis a calculation is required taking into account the properties of each single layer. This is described in Section 3.6.

In Section 3.7 the geometric influences of the specimens will be described separately. This section shows the focus points required to compare calculations from the neutral line model with experimental results.

The results from the experiments and the neutral line model calculations are shown in Section 3.8, and in the last section the conclusion reached are presented.

3.2   Simple lap-joint model

In this section the neutral line model is discussed for the most simple symmetric lap-splice joint with three rows of fasteners as shown in Figure 3-2. In view of the symmetry $L_2 = L_3$, $L_1 = L_4$, $t_a = t_b$ and both sheets are made of the same sheet material ($E_1 = E_2$). If the specimen is loaded in pure tension, the neutral line becomes curved due to the eccentricities inherent to lap-splice joints.
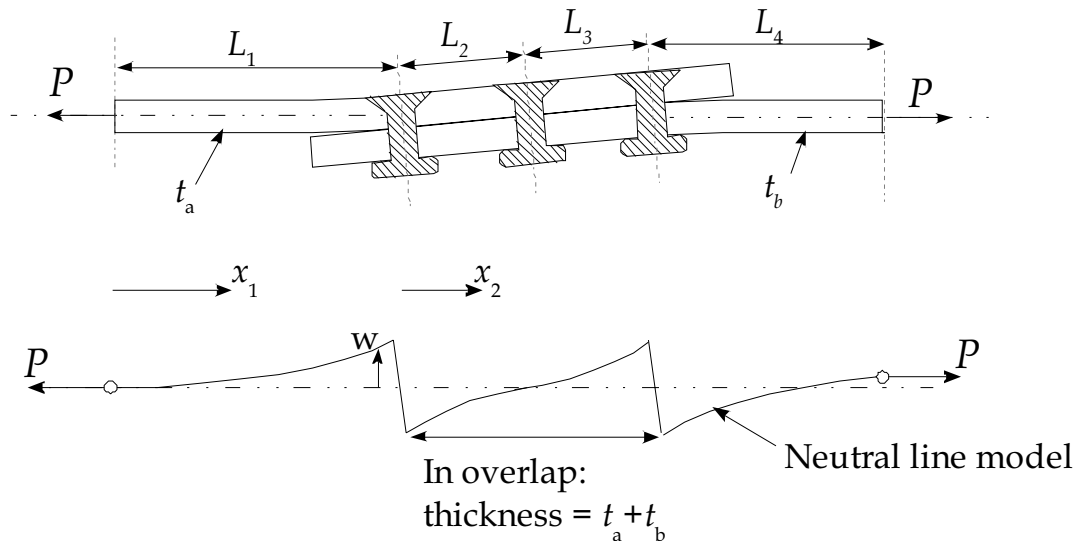
Figure 3-2   Secondary bending in a mechanically fastened lap-splice joint subject to tensile loading

23

In Section 3.2.1 the analysis is made for the elementary neutral line model. Because the two sheets between the two outer rows are assumed to behave as one integral sheet, load transfer does not occur by the middle row. It implies that the fastener flexibility is not considered. This is the model of Schijve [3].

In Section 3.2.2 the same lap-splice joint is analyzed, but this time considering fastener flexibility which is accounted for by introducing the new internal moment model.

3.2.1 The elementary neutral line model applied to the symmetric lap-splice joint

With the notations of Figure 3-2 the bending moment can be written as:

$$M_x = Pw \tag{3-1}$$

For sheet bending:

$$M_x = EI\frac{d^2x}{dx^2} \tag{3-2}$$

The differential equation thus becomes:

$$\frac{d^2w}{dx^2} - \alpha^2 w = 0 \tag{3-3}$$

with

$$\alpha_i^2 = \frac{P}{EI_i} \quad (i=1,2) \tag{3-4}$$

The solution is:

$$w_i = A_i \sinh(\alpha_i x_i) + B_i \cosh(\alpha_i x_i) \tag{3-5}$$

A_i and B_i are solved using the boundary conditions for a symmetric lap-splice joint of Figure 3-2. (A solution for more general boundary conditions is given in Section 3.3). The boundary conditions imply:

$$x_1 = 0 \rightarrow w_1 = 0$$

$$x_1 = L_1 \rightarrow (w_2)_{x_2=0} = (w_1)_{x_1=L_1} - e$$

$$x1 = L1 \rightarrow (\frac{dw_1}{dx_1})_{x_1=L_1} = (\frac{dw_2}{dx_2})_{x_2=0}$$

$$(w_2)_{x_2=L_2} = 0 \quad (symmetry)$$

(3-6)

The maximum secondary bending occurs at the first fastener row ($x_1 = L_1$). Defining the bending factor k_b as:

$$k_b = \frac{\sigma_{bending}}{\sigma_{tension}}$$

(3-7)

the solutions derived in [3] for $t_a = t_b$ and $L_2 = L_3$ is:

$$k_b = \frac{3}{1 + 2\sqrt{2}\left(\dfrac{T_2}{T_1}\right)}$$

(3-8)

with $T_i = \tanh(\alpha_i L_i)$. It was shown in [3] that for a long specimen, i.e. L_1 significantly larger then L_2, the value of T_1 is practically equal to 1. This implies that the effect of the length of the specimen on the secondary bending can be ignored, and the equation reduces to:

$$k_b = \frac{3}{1 + 2\sqrt{2}\tanh(\alpha_2 L_2)}$$

(3-9)

with:

$$\alpha_2 = \sqrt{\frac{3\sigma}{2t^2 E}}$$

(3-10)

The loading conditions at the ends of the specimen, i.e. far away of the overlap region, were also explored in [3]. If the hinged load introduction in Figure 3-2 is replaced by a fixed clamping ($dw/dx_1 = 0$ at $x_1 = 0$) the difference of the secondary bending at $x_1 = L_1$ with the hinged load introduction is negligible. This also applies

to a misalignment when the loads P at the two ends of the specimen are applied along slightly shifted parallel lines.

Values of the bending factor k_b calculated with (3-9) for different input data are shown in Table 3-6. The data in the first line of the table applies to the geometry of a typical specimen.

Table 3-2   Variation of input data for symmetrical lap-splice joint

L_1 [mm]	L_2 [mm]	t [mm]	E [N/mm²]	k_b for an applied stress of 100 MPa
200	28	2	72000	1.16
	18			1.43
	28	1		0.88
		2	210000	1.49

The results in the table show the following trends:
- If the row spacing L_2 is reduced from 28 mm to 18 mm, the bending factor increases from 1.16 to 1.43
- If the sheet thickness is reduced from 2 mm to 1 mm, the bending factor decreases from 1.16 to 0.88
- If the Elasticity Modulus is increased from 72000 MPa (Al-alloys) to 210000 MPa (steel) the bending factor increases from 1.16 to 1.49

These trends can be understood as being related to the bending flexibility of the overlap region and the eccentricity in the joint. It may well be expected that similar trends will also apply to lap-splice joints of fiber metal laminates, which also applies to the effects of specimen clamping (fixed or hinged and misalignment).

In [3] it was tried to account for some plastic deformation around the fastener holes as a result of the locally very high stresses. This was done by assuming that a small permanent bending deformation (angle β) occurred at the first and last rivet row. It implied that the boundary condition of equal slopes at $x_1 = L_1$ is replaced by:

$$\left(\frac{dw}{dx} \right)_{x_1 = L_1} = \left(\frac{dw}{dx} \right)_{x_2 = 0} + \beta \tag{3-11}$$

It turned out that even for $\beta = 1°$ a drastic reduction of the bending factor was calculated. In this simplified approach, load transfer by the middle fastener row did not occur, and fastener flexibility effects were not included. A more realistic approach is presented in the following section, which includes the analysis of the interrelated effects of fastener flexibility and load transfer by all fastener rows, again for the simple lap-splice joint of Figure 3-2.

3.2.2 *The internal moment model applied to the symmetric lap-splice joint*

In the previous section load transfer from one sheet to the other sheet of a lap-splice joint occurred only by the fasteners in the 1st and 3rd row because fastener flexibility was ignored and the two sheets between the outer rivet rows were considered as a single beam with a thickness of $t_a + t_b$. However, due to the high stresses in the sheets around the fastener holes, fastener flexibility will affect the load transmission and secondary bending. An "internal moment" model is presented for solving this problem. As an illustration of the model, it is discussed here for the simple symmetric lap-splice joint of Figure 3-1 with $L_2 = L_3$, $L_1 = L_4$, $t_a = t_b = t$ and both sheets are made of the same sheet material ($E_1 = E_2$). A more detailed and generalized analytical evaluation is given in Section 3.4 and 3.5

Because fastener flexibility is now considered load transmission from one sheet to the other sheet occurs by all three rows, also the middle row. The load transmitted by the three rows are T_1, T_2 and T_3 (see Figure 3-3), and because of the symmetry $T_3 = T_1$. Moreover, $P = T_1 + T_2 + T_3$ and thus:

$$P = 2T_1 + T_2 \tag{3-12}$$
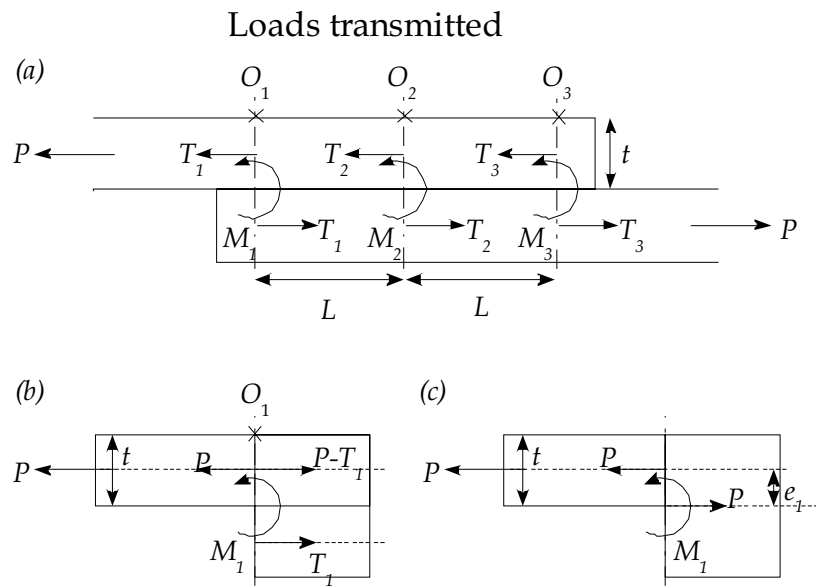
Figure 3-3 **Simple lap-splice joint with load transmission from the upper sheet to the lower sheet causing internal moments**

The loads in the various parts of the joint are indicated in Figure 3-3-a. In the elementary neutral line model the middle row did not contribute to load transmission ($T_2 = 0$) and as a consequence T_1 and T_3 were both equal to $P/2$. However, because of fastener flexibility, T_1 and $P-T_1$ are no longer equal to $P/2$, and thus different tension loads occur in the upper and lower segments of the overlap of

the joint. As a consequence an internal moment will be introduced at the fastener rows, M_1, M_2 and M_3, at the three fastener rows respectively. In view of symmetry $M_3 = M_1$. The internal moment M_1 at the first fastener row is indicated in Figure 3-3-b. As mentioned earlier, the loads in the upper and lower sheet are different due to the load transfer associated with different tensile elongations of the upper and lower sheet. In the neutral line model the upper and lower sheets between the 1st and 3rd rivet row, in the overlap region, are assumed to act as an integral beam subjected to secondary bending. However, the resultant force of the load transfer in Figure 3-3-b does not act at the neutral line of the overlap region. In order to account for this effect an internal moment is introduced, see Figure 3-3-c. In order to take the influence of the load transfer into the neutral line model, an internal moment is introduced in Figure 3-3-c. The moment M_1 clockwise about point O is:

$$-M_1 + T_1 \frac{t}{2} - T_1 \frac{3}{2}t = 0$$
$$M_1 = -T_1 t$$

(3-13)

This moment is associated with the influence of the load transfer of Figure 3-3-b and thus the neutral line model will behave as shown in Figure 3-3-c. For the moment in the second and third fastener row using the same principle follows that:

$$M_2 = -T_2 t$$
$$M_3 = -T_1 t$$

(3-14)

These moments generated by the load transfer take also a part of the moment introduced by the eccentricity e_1 into account. Since this moment is already a non-linear influence in the neutral line model, the influence should be removed from the internal moments. So what is actually needed is the Δmoment in each fastener row.

$$\Delta M_1 = -M_1 + Pe_1$$
$$\Delta M_2 = -M_2$$
$$\Delta M_3 = -M_3 + Pe_3$$

(3-15)

The calculation of T_1 and T_2 is based on the different elongations of the upper and lower sheet, which occurs as a result of the fastener flexibility. Due to some plastic deformation around the fastener holes some rotation of the fasteners occurs. This phenomenon is described here by a linear function between the applied load (P) transmitted by a row of fasteners and the displacement (δ) occurring in the joint due to plastic deformation around the fastener holes.

$$f = \frac{\delta}{P} \tag{3-16}$$

For the lap-splice joint, the symbol δ is the displacement of the lower sheet at a row relative to the upper sheet, while P is the load associated with the relevant internal moment (T_1 or T_2). The symbol f is an empirically obtained flexibility constant. For the first and the second row:

$$\begin{aligned}\delta_1 &= f \cdot T_1 \\ \delta_2 &= f \cdot T_2\end{aligned} \tag{3-17}$$

The fastener flexibility displacements and the tensile elongations of the upper and lower sheet (ΔL_{upper} and ΔL_{lower}) must be compatible, see Figure 3-4.
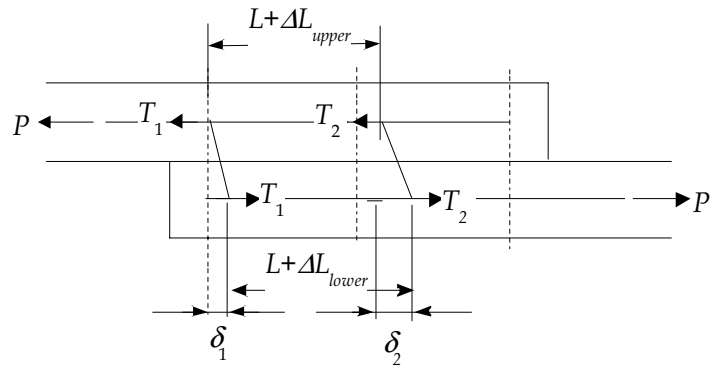
Figure 3-4   Force distribution when effected by fastener flexibility

The tensile elongations follow from the stress strain relation: $\varepsilon = \dfrac{\Delta L}{L} = \dfrac{S}{E} = \dfrac{load}{AE}$

$$\Delta L = \gamma \cdot load \ \text{ with } \gamma = \frac{L}{AE} \tag{3-18}$$

where A is the cross sectional area. For the lap-splice joint in Figure 3-4 it implies:

$$\begin{aligned}\Delta L_{upper} &= \gamma \left(P - T_1 \right) \\ \Delta L_{lower} &= \gamma \, T_1\end{aligned} \tag{3-19}$$

The compatibility between the tensile elongations and fastener flexibility displacements is easily obtained from Figure 3-4:

$$L + \Delta L_{upper} = \delta_1 + \left(L + \Delta L_{lower}\right) - \delta_2 \qquad \text{(3-20)}$$

With L = 28 mm, A = 200 mm² and E = 72000 N/mm² the γ-value is:

$$\gamma = 1.944 \cdot 10^{-6} \frac{mm}{N}$$

The empirical fastener flexibility according to Eqn. 3-73 to be discussed later is:

$$f = 3.523 \cdot 10^{-5} \frac{mm}{N}$$

The value of T_1 can now be calculated by substitution of Eqns 3-17 and 3-19 in 3-20, and T_2 follows from Eqn. 3-12. The results obtained are:

$$T_1 = \left(\frac{\gamma + f}{2\gamma + 3f}\right) P$$

$$T_2 = \left(\frac{f}{2\gamma + 3f}\right) P \qquad \text{(3-21)}$$

With the above-mentioned value of γ and f the results for T_1 and T_2 are:

$$T_1 = 7052$$
$$T_2 = 5896$$

Which leads to the load distribution in Figure 3-5. As a result of the fastener flexibility the first fastener row transmits 35 % (7052 N) of the load P, the second row 30 % (5896 N) and the third row again 35 %.
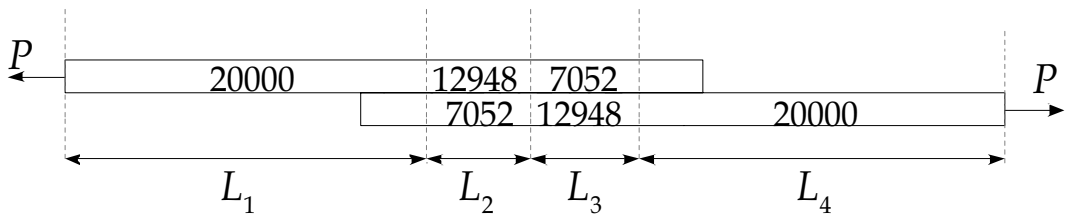
Figure 3-5 Calculated load transfer in the simple lap-splice joint accounting for fastener flexibility

In Section 3.4 the calculation of the internal moment is shown. The calculation of the internal moment is entirely dependent on the location of the neutral axis of the lap-splice joint. The internal moment is therefore a function of both the load transfer and the geometric lay-out of the joint. In case of a monolithic joint the neutral line is located at the center of each element of the lap-splice joint. The moments can then be calculated using e_1 = -t/2 and Eqn. (3-14) and (3-15):

$$\Delta M_1 = -5896 \, Nmm$$

$$\Delta M_2 = 11792 \, Nmm$$

$$\Delta M_3 = -5896 \, Nmm$$

With the internal moments known, the actual new neutral line model calculations can be made using Section 3.3.2. For the simple lap-splice joint used in the elementary neutral line model calculations in Section 3.2.1 a similar derivation of k_b will be presented.
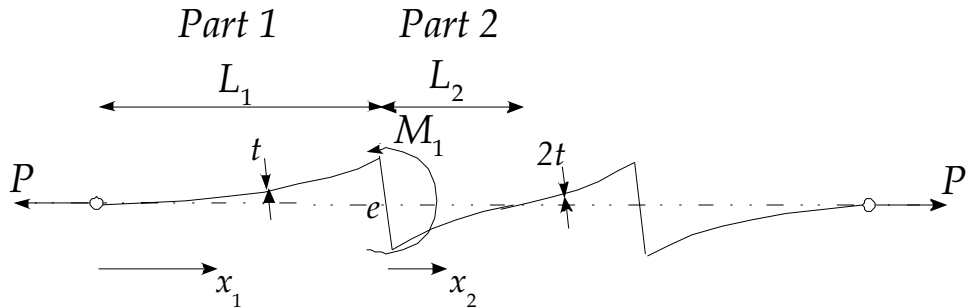
Figure 3-6   **Secondary bending in the simple symmetric lap-splice joint with the internal moments at the first fastener row**

For Part 1 in Figure 3-6 the equations for the bending moment and the displacements $w(x)$ are similar to the Eqn. (3-1) - (3-4) with the solution given in Eqn. (3-5). With the condition that $w(x_1) = 0$ for $x_1 = 0$, it is easily found that $B_1 = 0$. The equation for $w(x_1)$ thus becomes:

$$w(x_1) = A_1 \sinh(\alpha_1 x_1) \tag{3-22}$$

For Part 2 the internal moment ΔM_1 must be included:

$$M_{x_2} = Pw(x_2) - \Delta M_1 = EI_2\left(\frac{d^2 w}{dx_2}\right)_{x_2} \tag{3-23}$$

The solution of this differential equation is:

$$w(x_2) = A_2 \sinh(\alpha_2 x_2) + B_2 \cosh(\alpha_2 x_2) + \frac{\Delta M_1}{P} \qquad \text{(3-24)}$$

The boundary conditions at the first fastener row ($x_1 = L_1$ and $x_2 = 0$) are:

$$\left(w_{x_2}\right)_{x_2=L_2} = \left(w_{x_1}\right)_{x_1=L_1} + e_1 \qquad \text{(3-25)}$$

$$\left(\frac{dw}{dx}\right)_{x_1=L_1} = \left(\frac{dw}{dx}\right)_{x_2=0} \qquad \text{(3-26)}$$

At the end of Part 2 another condition for reasons of symmetry is:

$$\left(w_2\right)_{x_2=L_2} = 0 \qquad \text{(3-27)}$$

The constants A1, A2 and B2 can now be solved after substitution of Eqns (3-22) and (3-24) in Eqns. (3-25) to (3-27). With the boundary values of the hyperbolic function written as:

$$S_i = \sinh(\alpha_i L_i)$$
$$C_i = \cosh(\alpha_i L_i)$$
$$T_i = \tanh(\alpha_i L_i)$$

The three equations are:

$$B_2 = A_1 S_1 - \frac{\Delta M_1}{P} + e_1$$

$$A_2 = \frac{\alpha_1}{\alpha_2} A_1 C_1 \qquad \text{(3-28)}$$

$$A_2 S_2 + B_2 C_2 + \frac{\Delta M_1}{P} = 0$$

The most critical bending moment occurring at the first fastener row is obtained as:

$$M_{x_1=L_1} = EI\left(\frac{d^2 w}{dx^2}\right)_{x_1=L_1} \qquad \text{(3-29)}$$

32

With $\alpha_1^2 = \dfrac{P}{EI_1}$ the result for the bending factor becomes:

$$k_b = \frac{\sigma_{bending}}{\sigma_{tension}} = \frac{\dfrac{6M_c}{Wt^2}}{\dfrac{P}{Wt}} = \frac{6\alpha_1^2 A_1}{Pt} \tag{3-30}$$

After solving A_1 and realizing that $t_2 = 2t$ and $e = -t/2$ for the simple lap-splice joint, a further evaluation leads to:

$$k_b = \frac{\left(\dfrac{6\Delta M_1}{Pt}\right)\left(1 - \dfrac{1}{C_2}\right) + 3}{1 + \dfrac{T_2}{T_1}\sqrt{8}} \tag{3-31}$$

It should be noted that for $\Delta M_1 = 0$, i.e. no fastener flexibility and internal moments, Eqn. (3-31) reduces to the previous Eqn. (3-9). Results of the calculations of k_b with fastener flexibility (Eqn. (3-31)) are shown in Table 3-3 for similar values of L_1, L_2, t, E used previously.

Table 3-3 **Variation of input data for symmetrical lap-splice joint, f calculated using Eqn. (3-73) this also effects the load transfer through the fastener rows.**

L_1 [mm]	L_2 [mm]	t [mm]	E [N/mm²]	f [mm/N]	k_b for an applied stress of 100 MPa	
					With f	Without f
200	28	2	72000	3.542E-5	1.09	1.16
	18				1.39	1.43
	28	1		5.369E-5	0.64	0.88
		2	210000	1.214E-5	1.46	1.49

The comparison between the bending factors obtained with and without including fastener flexibility is made in the last two columns of Table 3-6. It turns out that the bending factor is reduced by the fastener flexibility which agrees with expectations about flexibility effects recalled earlier. However, the reduction is relatively small, just a few percent with one exception for $t = 1.0$ mm (reduction 27%).

The trends of k_b noted in the previous section do not change when the influence of load transfer is taken into account.

- Changing the overlap length from 28 mm to 18 mm still increases the bending factor k_b.
- A decrease in sheet thickness results in a decrease in bending stiffness and thus in a lower k_b.
- Increasing the Modulus of Elasticity for the joint results in a higher bending factor k_b.

The influence of the load transfer in the bending of the simple lap-splice joint is limited to a slight change in bending moment at the location of the highest bending loads. In this chapter it will be shown that this reduction of the maximum bending load increases the accuracy of the neutral line model.

In summary:

The crux of the present internal moment model is that the load distribution in the two sheets is related to deformations associated with fastener flexibility in order to arrive at compatibility equations from which the load distribution can be calculated. The load distribution then reveals the load transmitted by the fastener rows from which the internal moments can be derived.

In the present section, a calculation was made for the most simple case of a symmetric lap-splice joint to illustrate the basic procedure. Similar calculations can be made with the same model for other joints with a more complex geometry and other materials including fiber metal laminates.

3.3   Neutral line model for lap-splice joint

In this section a lap-splice joint will by used to show in a more generic way the 'classic' neutral line model and the present neutral line model, which includes the influence of load transfer. The influence of the boundary conditions will be taken into account and it is shown how to implement a variety of boundary conditions, such as hinged or clamped edges, internal moments about the fasteners, to represent a more complex structure.

3.3.1   Lap-splice joint with hinged clamping

The deflection of the neutral line, Figure 3-7, can be calculated with the advanced beam theory.
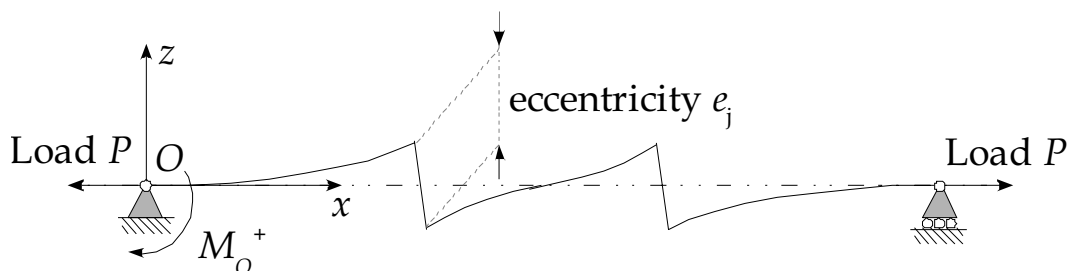
Figure 3-7   Deflection of neutral line

The displacements at any point along the beam are calculated with the following equation.

$$\left(M_x \right)_i = P w_i = \left(EI \right)_i \left(\frac{d^2 w}{dx^2} \right)_i \qquad \text{(3-32)}$$

The boundary conditions at the location of the fasteners include the eccentricity jump of the neutral line.

$$w_i + e_{j=i} = w_{i+1} \qquad \text{(3-33)}$$

At the location of the fasteners, the first derivative of the displacements (slope of the beam) is assumed to be equal at both sides of the fastener.

$$\left(\frac{dw}{dx} \right)_{x_i = L_i} = \left(\frac{dw}{dx} \right)_{x_{i+1} = 0} \qquad \text{(3-34)}$$

Eqn. (3-32) is a second order linear homogeneous differential equation valid for all parts of the lap-splice joint.

$$\left(\frac{d^2 w}{dx^2} \right)_i - \alpha_i^2 w_i = 0 \qquad \text{with} \qquad \alpha_i^2 = \frac{P}{(EI)_i} \qquad \text{(3-35)}$$

Solving Eqn. (3-35) for the out of plane displacement of the neutral line gives, see also appendix A.

$$w_i = A_i \sinh(\alpha_i x_i) + B_i \cosh(\alpha_i x_i) \qquad \text{(3-36)}$$

For the lap-splice joint shown in Figure 3-7, the solution can be obtained by decomposing the beam into four parts.
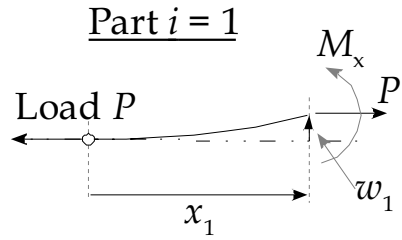
Figure 3-8   Deflection of neutral line for part *i* = 1

x_1 = 0;
At $x_1 = 0$ the displacement of the neutral line $w_1 = 0$. Then from Eqn. (3-36):

$$B_1 = 0 \qquad\qquad (3\text{-}37)$$
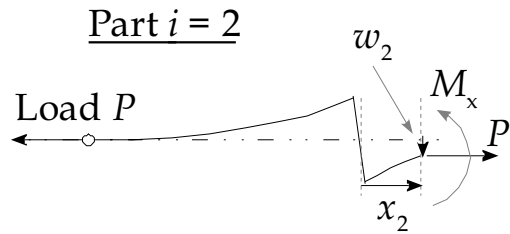
Figure 3-9   Deflection of neutral line for part *i* = 2

x_1 = L_1 and x_2 = 0;

Eqn. (3-33) shows that the displacement of the 2nd fastener is equal to the displacement of the 1st fastener plus the eccentricity e_1 of the lap-splice joint. Eqn. (3-34) provides a second 'connecting' equation with e_1 negative.

$$w_2 = w_1 + e_1$$
$$w_1 = A_1 \sinh(\alpha_1 L_1) + B_1 \cosh(\alpha_1 L_1)$$
$$w_2 = A_2 \sinh(\alpha_2 0) + B_2 \cosh(\alpha_2 0)$$

$$B_2 = A_1 \sinh(\alpha_1 L_1) + B_1 \cosh(\alpha_1 L_1) + e_1 \qquad\qquad (3\text{-}38)$$

$$\left(\frac{dw}{dx}\right)_{2,x_2=0} = \left(\frac{dw}{dx}\right)_{1,x_1=L_1}$$

$$\left(\frac{dw}{dx}\right)_{1,x_1=L_1} = A_1\alpha_1 \cosh(\alpha_1 L_1) + B_1\alpha_1 \sinh(\alpha_1 L_1)$$

$$\left(\frac{dw}{dx}\right)_{2,x_2=0} = A_2\alpha_2 \cosh(\alpha_2 0) + B_2\alpha_2 \sinh(\alpha_1 0)$$

$$A_2\alpha_2 = A_1\alpha_1 \cosh(\alpha_1 L_1) + B_1\alpha_1 \sinh(\alpha_1 L_1) \qquad \textbf{(3-39)}$$

Part i = 3
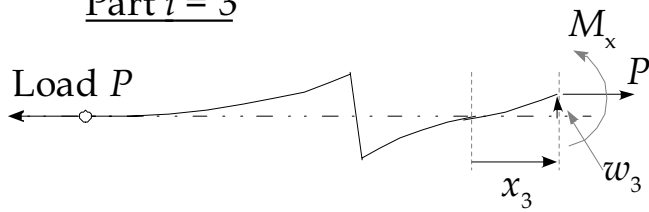
Figure 3-10 Deflection of neutral line for part i = 3

$x_2 = L_2$ and $x_3 = 0$;

The eccentricity jump at the 2nd fastener $e_2 = 0$. The following set of equations is obtained.

$$w_3 = w_2$$
$$w_2 = A_2 \sinh(\alpha_2 L_2) + B_2 \cosh(\alpha_2 L_2)$$
$$w_3 = A_3 \sinh(\alpha_3 0) + B_3 \cosh(\alpha_3 0)$$

$$B_3 = A_2 \sinh(\alpha_2 L_2) + B_2 \cosh(\alpha_2 L_2) \qquad \textbf{(3-40)}$$

$$\left(\frac{dw}{dx}\right)_{3,x_3=0} = \left(\frac{dw}{dx}\right)_{2,x_2=L_2}$$

$$\left(\frac{dw}{dx}\right)_{2,x_2=L_2} = A_2\alpha_2 \cosh(\alpha_2 L_2) + B_2\alpha_2 \sinh(\alpha_2 L_2)$$

$$\left(\frac{dw}{dx}\right)_{3,x_3=0} = A_2\alpha_3 \cosh(\alpha_3 0) + B_3\alpha_3 \sinh(\alpha_3 0)$$

$$A_3 \alpha_3 = A_2 \alpha_2 \cosh(\alpha_2 L_2) + B_2 \alpha_2 \sinh(\alpha_2 L_2) \tag{3-41}$$

Part $i = 4$
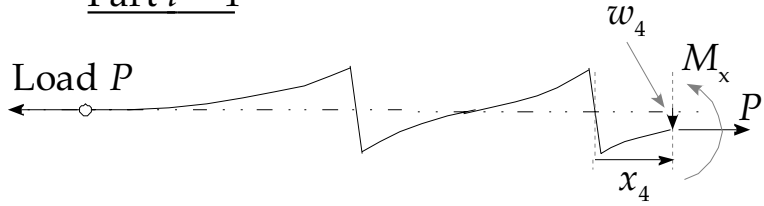
Figure 3-11 Deflection of neutral line for part $i = 4$

$x_3 = L_3$ and $x_4 = 0$;

$$w_4 = w_3 + e_3$$
$$w_3 = A_3 \sinh(\alpha_3 L_3) + B_3 \cosh(\alpha_3 L_3)$$
$$w_4 = A_4 \sinh(\alpha_4 0) + B_4 \cosh(\alpha_4 0)$$

$$B_4 = A_3 \sinh(\alpha_3 L_3) + B_3 \cosh(\alpha_3 L_3) + e_3 \tag{3-42}$$

$$\left(\frac{dw}{dx}\right)_{4,x_4=0} = \left(\frac{dw}{dx}\right)_{3,x_3=L_3}$$

$$\left(\frac{dw}{dx}\right)_{3,x_3=L_3} = A_3 \alpha_3 \cosh(\alpha_3 L_3) + B_3 \alpha_3 \sinh(\alpha_3 L_3)$$

$$\left(\frac{dw}{dx}\right)_{4,x_4=0} = A_4 \alpha_4 \cosh(\alpha_4 0) + B_4 \alpha_4 \sinh(\alpha_4 0)$$

$$A_4 \alpha_4 = A_3 \alpha_3 \cosh(\alpha_3 L_3) + B_3 \alpha_3 \sinh(\alpha_3 L_3) \tag{3-43}$$

$x_4 = L_4$;

At the hinged end location, the displacement $w_4 = 0$.

$$A_4 \sinh(\alpha_4 L_4) + B_4 \cosh(\alpha_4 L_4) = 0 \tag{3-44}$$

Eqns. (3-37), (3-39), (3-39), (3-40), (3-41), (3-42), (3-43) and (3-44) result in a system of eight equations that can be solved for A_i and B_i:

$$B_1 = 0$$
$$B_2 = A_1 \sinh(\alpha_1 L_1) + B_1 \cosh(\alpha_1 L_1) + e_1$$
$$A_2 \alpha_2 = A_1 \alpha_1 \cosh(\alpha_1 L_1) + B_1 \alpha_1 \sinh(\alpha_1 L_1)$$
$$B_3 = A_2 \sinh(\alpha_2 L_2) + B_2 \cosh(\alpha_2 L_2)$$
$$A_3 \alpha_3 = A_2 \alpha_2 \cosh(\alpha_2 L_2) + B_2 \alpha_2 \sinh(\alpha_2 L_2)$$
$$B_4 = A_3 \sinh(\alpha_3 L_3) + B_3 \cosh(\alpha_3 L_3) + e_3$$
$$A_4 \alpha_4 = A_3 \alpha_3 \cosh(\alpha_3 L_3) + B_3 \alpha_3 \sinh(\alpha_3 L_3)$$
$$A_4 \sinh(\alpha_4 L_4) + B_4 \cosh(\alpha_4 L_4) = 0$$

<div align="right">(3-45)</div>

After solving Eqn. (3-45), it is possible to calculate the bending moment at any location of the joint. For most lap-splice joints, as discussed earlier, the two outer fastener rows are the most critical. The bending moment is:

$$M(x) = Pw(x)$$

<div align="right">(3-46)</div>

The bending stress and the axial stress are:

$$\sigma_b = \frac{M(x)}{\frac{1}{6}Wt(x)^2}$$
$$\sigma_t = \frac{P}{Wt(x)}$$

<div align="right">(3-47)</div>

3.3.2 Lap-splice joint with fixed clamping and misalignment

In this section, the neutral line model will be expanded with fixed clamping conditions and misalignment, see Figure 3-12. It was shown by Schijve [3] that fixed clamping and misalignment could be discarded in certain cases.
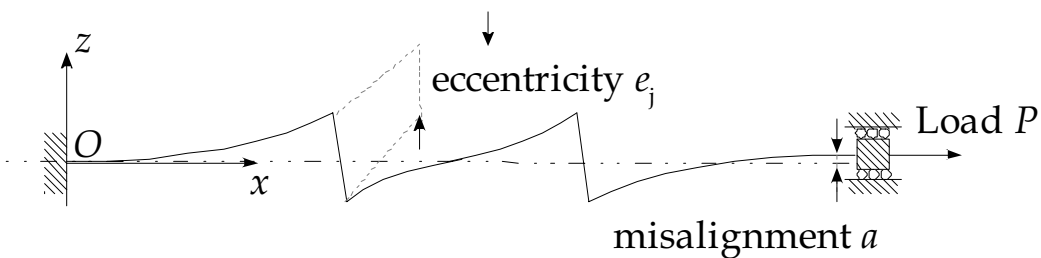
Figure 3-12 Deflection of neutral line with fixed clamping and misalignment

For completeness, the neutral line model is presented here for these boundary conditions. Figure 3-13 shows the free body diagram used to re-write Eqn. (3-32) to Eqn. (3-48).
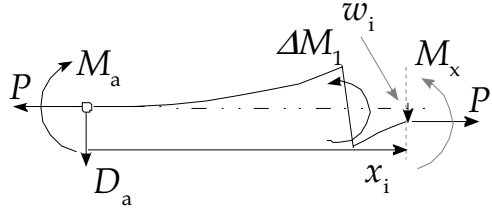
Figure 3-13 Free Body Diagram of lap-splice joint

Due to the boundary conditions a transverse load D_a and a clamping moment M_a occur at the end of the joint. As a result Eqn. (3-32) becomes:

$$\left(M_x\right)_i = M_a - \sum_i \Delta M_{Internal} + P w_i - D_a x_i = (EI)_i \left(\frac{d^2 w}{dx^2}\right)_i \tag{3-48}$$

The internal moment $\Delta M_{internal}$ is a function of the load transfer and fastener flexibility. The internal moment is located at the fasteners (ΔM_1, ΔM_2 and ΔM_3). At this location the displacement on the left and right hand side should be equal including the eccentricity jump.

$$w_i + e_{j=i} = w_{i+1} \tag{3-49}$$

The first derivative of Eqn. (3-49) gives

$$\left(\frac{dw}{dx}\right)_{x_i=L_i} = \left(\frac{dw}{dx}\right)_{x_{i+1}=0} \tag{3-50}$$

Rewriting Eqn. (3-48) a second order linear non-homogeneous differential equation is obtained

$$\frac{d^2 w}{dx^2} - \alpha^2 w_i = \alpha^2 \left(\left(\frac{M_a}{P} - \frac{\sum_i \Delta M_{Internal}}{P}\right) - \frac{D_a}{P} x_i\right) \tag{3-51}$$

The solution for this non-homogeneous equation is

$$w_i(x) = A\sinh(\alpha_i x_i) + B\cosh(\alpha_i x_i) - \left(\frac{M_a}{P} - \frac{\sum_i \Delta M_{Internal}}{P} \right) + \frac{D_a}{P} x_i \quad \text{(3-52)}$$
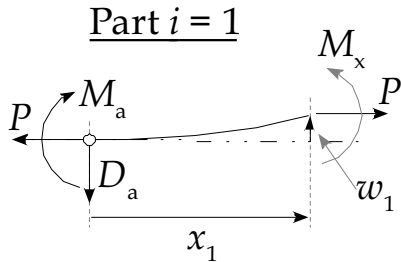
Figure 3-14 Deflection of neutral line for part $i = 1$

$x_1 = 0$;
At $x_1 = 0$ the displacement of the neutral line $w_1 = 0$ and a rotation cannot occur, which implies $\left(\dfrac{dw}{dx} \right)_{x_1=0} = 0$. Eqn. (3-52) gives

$$B_1 = \frac{M_a}{P}$$

$$A_1 \alpha_1 = \frac{D_a}{P}$$

(3-53)
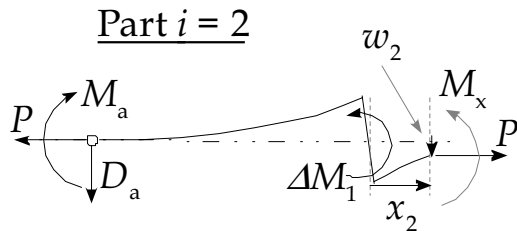
Figure 3-15 Deflection of neutral line for part $i = 2$

$x_1 = L_1$ and $x_2 = 0$;
The displacement of the 2nd part is equal to the displacement of the 1st part plus the eccentricity e_1. Using Eqn. (3-49) and (3-50) gives

$$w_2 = w_1 + e_1$$

$$B_2 = A_1 \sinh(\alpha_1 L_1) + B_1 \cosh(\alpha_1 L_1) - \frac{\Delta M_1}{P} + e_1 \qquad \text{(3-54)}$$

$$\left(\frac{dw}{dx}\right)_{2,x_2=0} = \left(\frac{dw}{dx}\right)_{1,x_1=L_1}$$

$$A_2\alpha_2 = A_1\alpha_1 \cosh(\alpha_1 L_1) + B_1\alpha_1 \sinh(\alpha_1 L_1) \qquad \text{(3-55)}$$
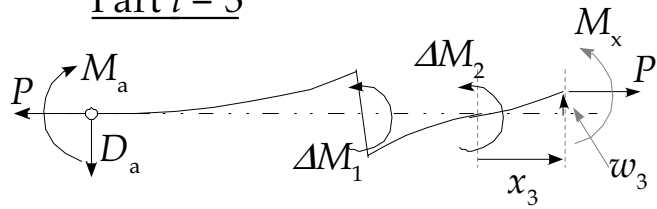
Figure 3-16 Deflection of neutral line for part i = 3

$x_2 = L_2$ **and** $x_3 = 0$;

$$w_3 = w_2$$

$$B_3 = A_2 \sinh(\alpha_2 L_2) + B_2 \cosh(\alpha_2 L_2) - \frac{\Delta M_2}{P} \qquad \text{(3-56)}$$

$$\left(\frac{dw}{dx}\right)_{3,x_3=0} = \left(\frac{dw}{dx}\right)_{2,x_2=L_2}$$

$$A_3\alpha_3 = A_2\alpha_2 \cosh(\alpha_2 L_2) + B_2\alpha_2 \sinh(\alpha_2 L_2) \qquad \text{(3-57)}$$
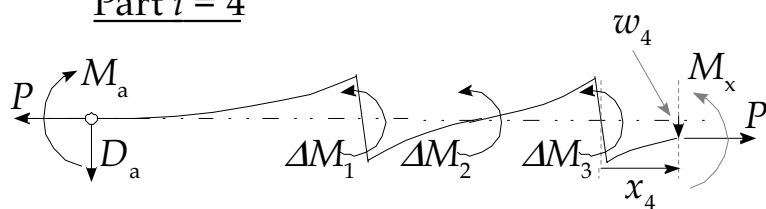
Figure 3-17 Deflection of neutral line for part i = 4

$x_3 = L_3$ **and** $x_4 = 0$;

$$w_4 = w_3 + e_3$$

$$B_4 = A_3 \sinh(\alpha_3 L_3) + B_3 \cosh(\alpha_3 L_3) - \frac{\Delta M_3}{P} + e_3 \qquad \text{(3-58)}$$

$$\left(\frac{dw}{dx}\right)_{4,x_4=0} = \left(\frac{dw}{dx}\right)_{3,x_3=L_3}$$

$$A_4\alpha_4 = A_3\alpha_3 \cosh(\alpha_3 L_3) + B_3\alpha_3 \sinh(\alpha_3 L_3) \qquad \text{(3-59)}$$

$x_4 = L_4$;
At the end of the lap-splice joint the displacement w_4 is equal to the misalignment
and the first derivative $\left(\dfrac{dw}{dx}\right)_{4,x_4=L_4} = 0$ due to the clamping.

$$w_4 = a$$

$$A_4 \sinh(\alpha_4 L_4) + B_4 \cosh(\alpha_4 L_4) = -\frac{D_a}{P}L_{tot} + \frac{M_a}{P} - \frac{\Delta\sum_i M_i}{P} + a \qquad \text{(3-60)}$$

$$\left(\frac{dw}{dx}\right)_{4,x_4=L_4} = 0$$

$$A_4\alpha_4 \cosh(\alpha_4 L_4) + B_4\alpha_4 \sinh(\alpha_4 L_4) = -\frac{D_a}{P} \qquad \text{(3-61)}$$

Summarizing the above equations gives a set of 10 equations with 10 unknowns. Solving the equations gives a solution for A_i, B_i, M_a and D_a.

$$B_1 = \frac{M_a}{P}$$

$$A_1 \alpha_1 = \frac{D_a}{P}$$

$$B_2 = A_1 \sinh(\alpha_1 L_1) + B_1 \cosh(\alpha_1 L_1) - \frac{\Delta M_1}{P} + e_1$$

$$A_2 \alpha_2 = A_1 \alpha_1 \cosh(\alpha_1 L_1) + B_1 \alpha_1 \sinh(\alpha_1 L_1)$$

$$B_3 = A_2 \sinh(\alpha_2 L_2) + B_2 \cosh(\alpha_2 L_2) - \frac{\Delta M_2}{P}$$

$$A_3 \alpha_3 = A_2 \alpha_2 \cosh(\alpha_2 L_2) + B_2 \alpha_2 \sinh(\alpha_2 L_2)$$

$$B_4 = A_3 \sinh(\alpha_3 L_3) + B_3 \cosh(\alpha_3 L_3) - \frac{\Delta M_3}{P} + e_3$$

$$A_4 \alpha_4 = A_3 \alpha_3 \cosh(\alpha_3 L_3) + B_3 \alpha_3 \sinh(\alpha_3 L_3)$$

$$A_4 \sinh(\alpha_4 L_4) + B_4 \cosh(\alpha_4 L_4) = -\frac{D_a}{P} L_{tot} + \frac{M_a}{P} - \frac{\Delta \sum_i M_i}{P} + a$$

$$A_4 \alpha_4 \cosh(\alpha_4 L_4) + B_4 \alpha_4 \sinh(\alpha_4 L_4) = -\frac{D_a}{P}$$

(3-62)

After solving the above equations it is possible to calculate the stress at any desired location of the joint. The bending moment is equal to:

$$M(x) = M_a - \sum_i \Delta M_{Internal} + Pw(x) - D_a x \qquad \text{(3-63)}$$

According to Eqn. (3-47) the bending stress and tensile stress become:

$$\sigma_b = \frac{M_a - \sum \Delta M_{Internal} + Pw(x) - D_a x}{\frac{1}{6} Wt(x)^2}$$

$$\sigma_t = \frac{P}{Wt(x)}$$

(3-64)

3.4   Internal moment due to load transfer

One of the assumptions made in Section 3.1 was that the sheets between the fasteners act as one integral beam. This assumption will not be contested here, but it

poses a problem with respect to the load path in a joint. In part *a* of Figure 3-18, separate sheets are replaced by integral parts. The force P will then follow the path of the neutral-axis.
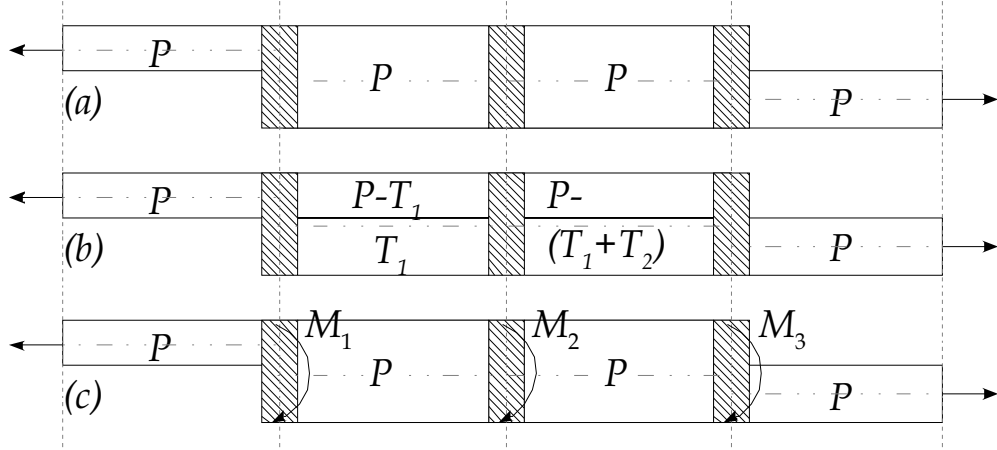
Figure 3-18 Representation of force distribution in lap-splice joint

The neutral axis location is determined by the geometry and material properties of the sheets. The jump in load path is inherent to multi-layer joints and creates the phenomenon known as secondary bending. Looking closer at the joint *a*, shown in Figure 3-18, it should be clear that the axial strain distribution through the thickness of each beam part is uniform, more precisely; the strain distribution through the thickness is continuous. A more physically correct representation is shown in Figure 3-18, *b*, the problem then is that the elongation of the two sheets are different due to the load differences and thus the strains at the faying side are not equal for both sheets, remember that the neutral line model assumes the overlap region to behave as a single beam element. This can be avoided by creating an internal moment that is representative of the load transfer represented in *b*, this solution is shown in Figure 3-18 *c*. Calculation of the internal moments is shown below. The moment clockwise about point O in Figure 3-19 is positive:

where
t_1, t_4 = Thickness of sheet
c_1, c_4 = Distance to neutral line
e_1, e_3 = Eccentricity jump
P = Applied load
T_1, T_2 = Load transfer
M_1, M_3 = Internal moments

45
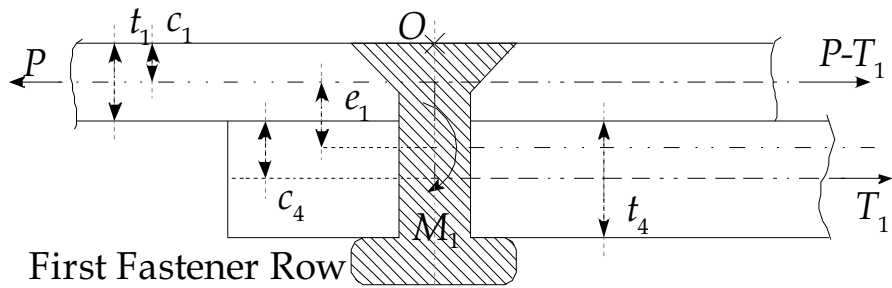
Figure 3-19 Load transfer in the first fastener row

$$\Sigma M_O = M_1 + Pc_1 - (P - T_1)c_1 - T_1(t_1 + c_4) = 0 \tag{3-65}$$

$$M_1 = (t_1 + c_4 - c_1)T_1 \tag{3-66}$$
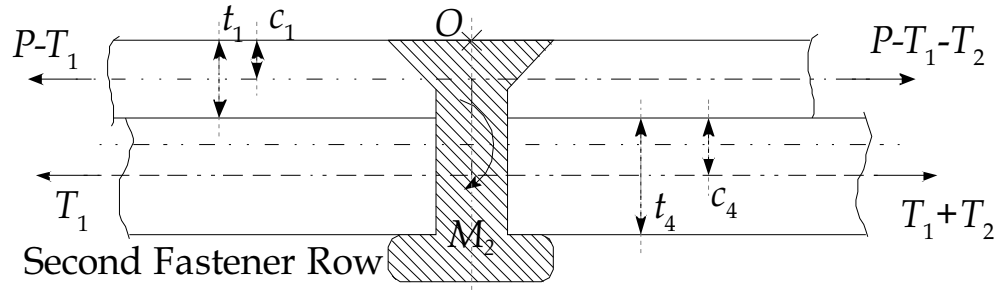
Figure 3-20 Load transfer in the second fastener row

$$\Sigma M_O = M_2 + T_1(c_4 + t_1) + (P - T_1)c_1 - (P - T_1 - T_2)c_1 - ...$$
$$... - (T_1 + T_2)(c_4 + t_1) = 0 \tag{3-67}$$

$$M_2 = (t_1 + c_4 - c_1)T_2 \tag{3-68}$$
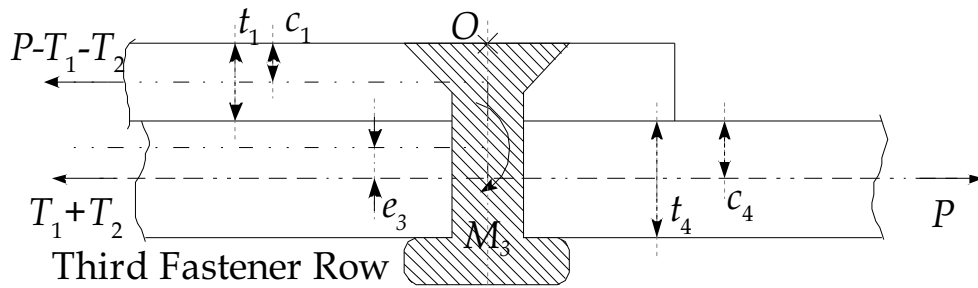
Figure 3-21 Load transfer in the third fastener row

$$\Sigma M_O = M_3 + \left(P - T_1 - T_2\right)c_1 + \left(T_1 + T_2\right)\left(t_1 + c_4\right) - P\left(t_1 + c_4\right) = 0 \qquad \textbf{(3-69)}$$

$$M_3 = \left(t_1 + c_4 - c_1\right)\left(P - T_1 - T_2\right) \qquad \textbf{(3-70)}$$

The internal moments are expressed as functions of the load transfer T_1 and T_2 and location of the neutral line.

3.5   Fastener flexibility and load transfer

Load transfer in joints, lap-splice joints or butt joints, depends not only on the number of fastener rows in a uniform distribution or a staggered fastener pattern but also on the fastener flexibility. Thus a geometric dependency and a material property dependency for all configurations of joints will exist.

3.5.1   Calculation of the fastener flexibility

Several empirical equations for fastener flexibility have been reported in the literature, which will be summarized.

The variables listed below are used in the Boeing, Grumman, Huth, Swift and Tate and Rosenfeld equations:

$$
\begin{aligned}
E_{1,2} \quad &= \text{Modulus of Elasticity}\\
E_f \quad &= \text{Modulus of Elasticity of fastener}\\
d \quad &= \text{Hole diameter}\\
t_{1,2} \quad &= \text{Sheet thickness}
\end{aligned}
$$

Boeing [6]:

$$f = \frac{2^{\left(\frac{t_1}{d}\right)^{0.85}}}{t_1}\left(\frac{1}{E_1} + \frac{3}{8E_f}\right) + \frac{2^{\left(\frac{t_2}{d}\right)^{0.85}}}{t_2}\left(\frac{1}{E_2} + \frac{3}{8E_f}\right) \qquad \textbf{(3-71)}$$

Grumman [7]:

$$f = \frac{(t_1 + t_2)^2}{E_f d^3} + 3.7\left(\frac{1}{E_1 t_1} + \frac{1}{E_2 t_2}\right)$$

(3-72)

Huth [8]:

$$f = \left(\frac{t_1 + t_2}{2d}\right)^a \frac{b}{n}\left(\frac{1}{t_1 E_1} + \frac{1}{n t_2 E_2} + \frac{1}{2 t_1 E_f} + \frac{1}{2 n t_2 E_f}\right)$$

(3-73)

Constants a and b are dependent on the type of joint, $n = 1$ is used for a single shear and $n = 2$ for a double shear joint.

Table 3-4   Equation parameters for Huth's formula

Type	a	b
bolted metallic	2/3	3.0
riveted metallic	2/5	2.2
bolted graphite/epoxy	2/3	4.2

Swift [9]:

$$f = \frac{5}{dE_f} + 0.8\left(\frac{1}{t_1 E_1} + \frac{1}{t_2 E_2}\right)$$

(3-74)

Tate and Rosenfeld [10]:

$$f = \frac{1}{E_f t_1} + \frac{1}{E_f t_2} + \frac{1}{E_1 t_1} + \frac{1}{E_2 t_2} + \frac{32}{9 E_f \pi d^2}\left(1 + v_f\right)\left(t_1 + t_2\right) +$$

$$+ \frac{8}{5 E_f \pi d^4}\left(t_1^3 + 5 t_1^2 t_2 + 5 t_1 t_2^2 + t_2^3\right)$$

(3-75)

where v_f represents the Poisson's ratio for the fastener. An extensive investigation into available methods determining the fastener flexibility has been done by Morris [11]. The results from Grumman, Eqn. (3-72), showed a remarkable resemblance to the newly found empirical formula for fastener flexibility found by Morris. Albeit that the new fastener flexibility is more applicable for geometries other then the base line specimens used by Morris.

$$f = \left(\left(\frac{2845}{E_1 t_1} + \frac{2845}{E_2 t_2} \right) + c_f \left(\left(\frac{500}{E_f t_1} + \frac{1000}{E_{ST_1} t_1} \right) \left(\frac{t_1}{d} \right)^2 + \left(\frac{500}{E_f t_2} + \frac{1000}{E_{ST_2} t_2} \right) \left(\frac{t_2}{d} \right)^2 \right) \right) \cdot$$

$$\cdot \left(\frac{d_{head}}{d} \right)^{-0.34} \left(\frac{s}{d} \right)^{-0.5} \left(\frac{p}{d} \right)^{0.34} e^{0.3r} \tag{3-76}$$

where

$E_{1,2}$	= Modulus of Elasticity
$E_{ST1,2}$	= Modulus of Elasticity in thickness direction
E_f	= Modulus of Elasticity of fastener
d	= Hole diameter
d_{head}	= Deformed fastener head
p	= Row pitch
r	= Number of rows
s	= Fastener pitch
$t_{1,2}$	= Sheet thickness
c_f	= 1 for aluminum rivets
	= 8.2 for countersunk aluminum rivets
	= 13.1 for titanium Hi-Loks

All the above equations were empirically derived from many experimental results. Morris questions the accuracy of the available fastener flexibility equations since the equations show similar trends but produce very different results. Morris concludes that the base to derive a suitable empirical equation should originate from more tests to reach a general understanding of experimental values for fastener flexibility. More research allows for an understanding of parameters currently neglected in the majority of equations, such as joint configuration, type of fasteners, type of fastener head, fastener fit clamping force and condition of faying surfaces. To calculate the load transfer in a lap-splice or butt joint, the fastener flexibility is required. Although the accuracy of the fastener flexibility can be improved, as a first approximation the results suffice for the load transfer calculation.

3.5.2 Calculation of the load transfer

Now that the flexibility f is known for each fastener, the load transfer can be calculated using the method described in this section. Figure 3-22 shows the nomenclature for the load transfer calculation of a simple lap-splice joint with sheet a, sheet c and an internal doubler with n rows of fasteners.
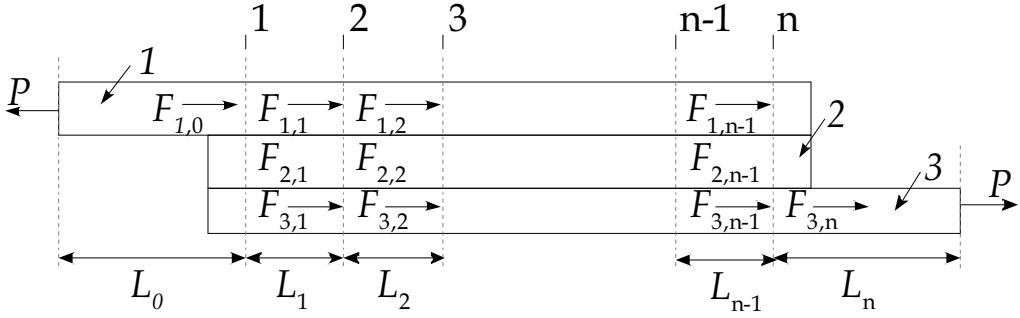
Figure 3-22 Model parameters for fastener flexibility

Based on work done by Swift, flexibility is defined as the total deflection of the joint δ, divided by the applied load P:

$$f = \frac{\delta}{P} \tag{3-77}$$

Figure 3-23 is a cut-out from a spliced joint showing the displacements due to the loads in several layers. From displacement compatibility, the following equation can be constructed for the first two layers, j and $j+1$:

$$L_{1,i} + \Delta_{1,i} + \delta_{f1,i+1} = L_{2,i} + \Delta_{2,i} + \delta_{f1,i} \tag{3-78}$$
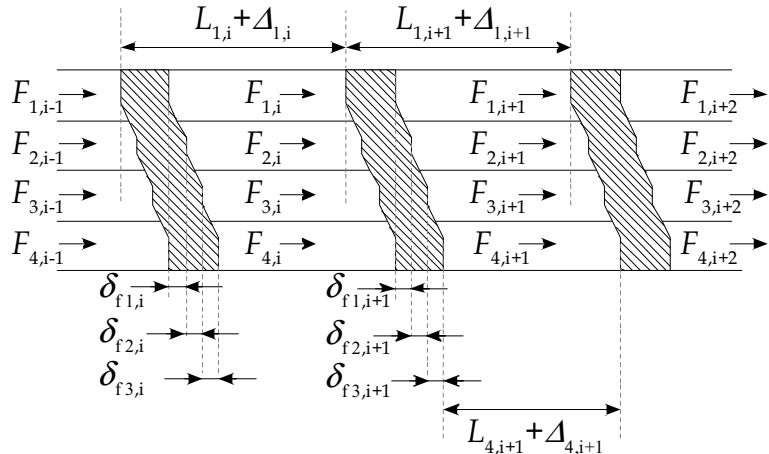
Figure 3-23 Fastener flexibility expressed in displacements and forces

Where $L_{j,i}$ represents the length of the ith element in layer j, $\Delta_{j,i}$ and $\Delta_{j+1,i}$ represent the elongation of sheet j and sheet $j+1$ respectively and $\delta_{fj,i}$ and $\delta_{fj,i+1}$ represent the displacement of the ith and the $(i+1)$th fastener of the jth layer. For m layers, $m-1$ equations can be constructed:

$$L_{2,i} + \Delta_{2,i} + \delta_{f2,i+1} = L_{3,i} + \Delta_{3,i} + \delta_{f2,i}$$

$$L_{3,i} + \Delta_{3,i} + \delta_{f3,i+1} = L_{4,i} + \Delta_{4,i} + \delta_{f3,i}$$

$$\vdots$$

$$L_{m-1,i} + \Delta_{m-1,i} + \delta_{fm-1,i+1} = L_{m,i} + \Delta_{m,i} + \delta_{fm-1,i}$$

$$(3\text{-}79)$$

So, for four layers as shown in Figure 3-23 three equations can be constructed. The displacement of fastener i can be found by using Eqn. (3-77) using the force responsible for the fastener displacement, e.g. the load passing through the ith fastener for each layer.

$$\delta_{f1,i} = \left(F_{1,i-1} - F_{1,i} \right) f_i$$

$$\delta_{f2,i} = \left\{ \left(F_{1,i-1} - F_{1,i} \right) + \left(F_{2,i-1} - F_{2,i} \right) \right\} f_i$$

$$\delta_{f3,i} = \left\{ \left(F_{1,i-1} - F_{1,i} \right) + \left(F_{2,i-1} - F_{2,i} \right) + \left(F_{3,i-1} - F_{3,i} \right) \right\} f_i$$

$$\vdots$$

$$\delta_{fm-1,i} = \left\{ \left(F_{1,i-1} - F_{1,i} \right) + \left(F_{2,i-1} - F_{2,i} \right) + \ldots + \left(F_{m-1,i-1} - F_{m-1,i} \right) \right\} f_i$$

$$(3\text{-}80)$$

Substitution of this equation into Eqn. (3-78) and Eqn. (3-79) results in the following equations

$$L_{1,i} + \Delta_{1,i} + \left(F_{1,i} - F_{1,i+1} \right) f_{i+1} = L_{2,i} + \Delta_{2,i} + \left(F_{1,i-1} - F_{1,i} \right) f_i$$

$$L_{2,i} + \Delta_{2,i} + \left\{ \left(F_{1,i} - F_{1,i+1} \right) + \left(F_{2,i} - F_{2,i+1} \right) \right\} f_{i+1} =$$
$$= L_{3,i} + \Delta_{3,i} + \left\{ \left(F_{1,i-1} - F_{1,i} \right) + \left(F_{2,i-1} - F_{2,i} \right) \right\} f_i$$

$$\vdots$$

$$L_{m-1,i} + \Delta_{m-1,i} + \left\{ \left(F_{1,i} - F_{1,i+1} \right) + \left(F_{2,i} - F_{2,i+1} \right) + \ldots + \left(F_{m-1,i} - F_{m-1,i+1} \right) \right\} f_{i+1} =$$
$$= L_{m,i} + \Delta_{m,i} + \left\{ \left(F_{1,i-1} - F_{1,i} \right) + \left(F_{2,i-1} - F_{2,i} \right) + \ldots + \left(F_{m-1,i-1} - F_{m-1,i} \right) \right\} f_i$$

$$(3\text{-}81)$$

The basic equation for an elongation of a beam is shown below.

$$\Delta_{j,i} = \frac{F_{j,i} L_{j,i}}{E_{j,i} A_{j,i}} = F_{j,i} \gamma_{j,i}$$

$$(3\text{-}82)$$

Combining the above two equations, results in:

$$L_{1,i} + F_{1,i}\gamma_{1,i} + \left(F_{1,i} - F_{1,i+1}\right)f_{i+1} = L_{2,i} + F_{2,i}\gamma_{2,i} + \left(F_{1,i-1} - F_{1,i}\right)f_i$$

$$L_{2,i} + F_{2,i}\gamma_{2,i} + \left\{\left(F_{1,i} - F_{1,i+1}\right) + \left(F_{2,i} - F_{2,i+1}\right)\right\}f_{i+1} =$$
$$= L_{3,i} + F_{3,i}\gamma_{3,i} + \left\{\left(F_{1,i-1} - F_{1,i}\right) + \left(F_{2,i-1} - F_{2,i}\right)\right\}f_i$$
$$\vdots$$
$$L_{m-1,i} + F_{m-1,i}\gamma_{m-1,i} + \left\{\left(F_{1,i} - F_{1,i+1}\right) + \left(F_{2,i} - F_{2,i+1}\right) + \ldots + \left(F_{m-1,i} - F_{m-1,i+1}\right)\right\}f_{i+1} =$$
$$= L_{m,i} + F_{m,i}\gamma_{m,i} + \left\{\left(F_{1,i-1} - F_{1,i}\right) + \left(F_{2,i-1} - F_{2,i}\right) + \ldots + \left(F_{m-1,i-1} - F_{m-1,i}\right)\right\}f_i$$

(3-83)

Regrouping and rewriting gives the following equations, which results in a system of *m*-1 equations for a *m*-layers lap-splice joint.

$$- F_{1,i-1}f_i + F_{1,i}\left(\gamma_{1,i} + f_i + f_{i+1}\right) - F_{1,i+1}f_{i+1} - F_{2,i}\gamma_{2,i} = L_{2,i} - L_{1,i}$$

$$- F_{1,i-1}f_i + F_{1,i}\left(f_i + f_{i+1}\right) - F_{1,i+1}f_{i+1} - F_{2,i-1}f_i - F_{2,i+1}f_{i+1} +$$
$$+ F_{2,i}\left(\gamma_{2,i} + f_i + f_{i+1}\right) - F_{3,i}\gamma_{3,i} = L_{3,i} - L_{2,i}$$
$$\vdots$$

(3-84)

$$- F_{1,i-1}f_i + F_{1,i}\left(f_i + f_{i+1}\right) - F_{1,i+1}f_{i+1} - F_{2,i-1}f_i + F_{2,i}\left(f_i + f_{i+1}\right) -$$
$$- F_{2,i+1}f_{i+1} + \ldots - F_{m-1,i}f_i + F_{m-1,i}\left(\gamma_{m-1,i} + f_i + f_{i+1}\right) - F_{m-1,i+2}f_{i+1} -$$
$$- F_{m,i}\gamma_{m,i} = L_{m,i} - L_{m-1,i}$$

The set of equations above can be put in equation form as shown below ($M_i\vec{P}_i = \vec{L}_i$)

$$M_i = \begin{bmatrix} -f_i & \left(\gamma_{1,i} + f_i + f_{i+1}\right) & -f_{i+1} & 0 & -\gamma_{2,i} & & & & & \\ -f_i & \left(f_i + f_{i+1}\right) & -f_{i+1} & -f_i & \left(\gamma_{2,i} + f_i + f_{i+1}\right) & -f_{i+1} & 0 & -\gamma_{3,i} & & \\ \vdots & & & & & & & & \ddots & \\ -f_i & \left(f_i + f_{i+1}\right) & -f_{i+1} & -f_i & \left(f_i + f_{i+1}\right) & -f_{i+1} & \cdots & -f_i & \left(\gamma_{m-1,i} + f_i + f_{i+1}\right) & -f_{i+1} & 0 & -\gamma_{m,i} \end{bmatrix}$$

$$\vec{P}_i = \begin{bmatrix} F_{1,i-1} \\ F_{1,i} \\ F_{1,i+1} \\ F_{2,i-1} \\ F_{2,i} \\ F_{2,i+1} \\ \vdots \\ F_{m,i-1} \\ F_{m,i} \\ F_{m,i+1} \end{bmatrix} \qquad \vec{L}_i = \begin{bmatrix} L_{2,i} - L_{1,i} \\ L_{3,i} - L_{2,i} \\ \vdots \\ L_{m,i} - L_{m-1,i} \end{bmatrix}$$

Once this matrix is completely filled the expansion for n-1 rows can be done, where the matrix M_i is a sub-matrix of the complete set of equations:

$$A\vec{F} = \vec{L}; \qquad \begin{bmatrix} M_1 & & & & \\ & M_2 & & & \\ & & M_3 & & \\ & & & \ddots & \\ & & & & M_{n-1} \end{bmatrix} \begin{bmatrix} \vec{P}_1 \\ \vec{P}_2 \\ \vec{P}_3 \\ \vdots \\ \vec{P}_{n-1} \end{bmatrix} = \begin{bmatrix} \vec{L}_1 \\ \vec{L}_2 \\ \vec{L}_3 \\ \vdots \\ \vec{L}_{n-1} \end{bmatrix} \qquad \textbf{(3-85)}$$

Using the following relation between the matrix A and its inverse matrix A^{-1} the forces can be calculated.

$$A\vec{F} = \vec{L}$$
$$A^{-1}A\vec{F} = A^{-1}\vec{L} \qquad \textbf{(3-86)}$$
$$\vec{F} = A^{-1}\vec{L}$$

Depending on the boundary conditions and the geometric shape of the joint, Eqn. (3-85) with $(n$-1$)(m$-1$)$ equations can be solved for the unknown forces. For a three-layer ($m = 3$) and three-row ($n = 3$) lap-splice joint where the row distance between the fasteners is equal, the 4x9 matrix presented below needs to be solved.

$$
\begin{bmatrix}
-f_1 & (\gamma_{1,1}+f_1+f_2) & -f_2 & 0 & -\gamma_{2,1} & 0 & 0 & 0 & 0 \\
-f_1 & (f_1+f_2) & -f_2 & -f_1 & (\gamma_{2,1}+f_1+f_2) & -f_2 & 0 & -\gamma_{3,1} & 0 \\
0 & -f_2 & (\gamma_{1,2}+f_2+f_3) & -f_3 & 0 & -\gamma_{2,2} & 0 & 0 & 0 \\
0 & -f_2 & (f_2+f_3) & -f_3 & -f_2 & (\gamma_{2,2}+f_2+f_3) & -f_3 & 0 & -\gamma_{3,2}
\end{bmatrix}
\begin{bmatrix}
F_{1,0} \\ F_{1,1} \\ F_{1,2} \\ F_{2,0} \\ F_{2,1} \\ F_{2,2} \\ F_{3,0} \\ F_{3,1} \\ F_{3,2}
\end{bmatrix}
$$

<div align="right">(3-87)</div>

The system to be solved has 9 unknowns; and without proper boundary conditions, the system cannot be solved. The applied load is introduced via sheet $F_{1,0} = P$. This means that for all other sheets left of the first fastener the loads are zero, $F_{2,0} = 0$, $F_{3,0} = 0$. All the middle parts must be in equilibrium, the forces in each separate sheet in section *1* and *2* must be equal to applied force P, $F_{3,1} = P\text{-}F_{1,1}\text{-}F_{2,1}$ and $F_{3,2} = P\text{-}F_{1,2}\text{-}F_{2,2}$. This leaves 4 unknowns and 4 equations.

$$
A =
\begin{bmatrix}
(\gamma_{1,1}+f_1+f_2) & -f_2 & -f_2 & 0 \\
(\gamma_{3,1}+f_1+f_2) & -f_2 & (\gamma_{2,1}+\gamma_{3,1}+f_1+f_2) & -f_2 \\
-f_2 & (\gamma_{1,2}+f_2+f_3) & 0 & -\gamma_{2,2} \\
-f_2 & (\gamma_{3,2}+f_2+f_3) & -f_2 & (\gamma_{2,2}+\gamma_{3,2}+f_2+f_3)
\end{bmatrix}
$$

<div align="right">(3-88)</div>

$$
\bar{F} =
\begin{bmatrix}
F_{1,1} \\ F_{1,2} \\ F_{2,1} \\ F_{2,2}
\end{bmatrix}
$$

<div align="right">(3-89)</div>

$$
\bar{P} = P
\begin{bmatrix}
f_1 \\ \gamma_{3,1}+f_1 \\ 0 \\ \gamma_{3,2}
\end{bmatrix}
$$

<div align="right">(3-90)</div>

The three matrices shown above can be solved using the inverted matrix of A.

$$A\vec{F} = \vec{P}$$
$$A^{-1}A\vec{F} = A^{-1}\vec{P} \tag{3-91}$$
$$\vec{F} = A^{-1}\vec{P}$$

With the four forces known, the two remaining unknown forces can be calculated

$$F_{3,1} = P - F_{1,2} - F_{2,1}$$
$$F_{3,2} = P - F_{1,2} - F_{2,2} \tag{3-92}$$
$$F_{3,3} = P$$

3.5.3   The significance of the fastener flexibility on the load transfer

The results from the empirically obtained formulæ for fastener flexibility are subject to question by Morris [11]. Using the equations derived in Section 3.3.2, one can show the influence of the magnitude of the fastener flexibility.

Skin = Al 2024-T3
W = 100 mm
P = 20 kN
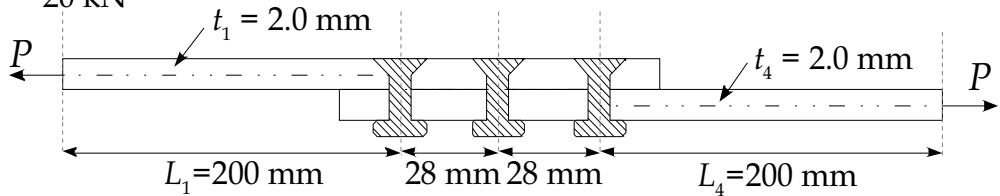
Figure 3-24 Lap-splice joint geometry for fastener flexibility and load transfer calculation

To show the influence for this geometry, the fastener flexibility selected is the value proposed by Huth:

$$f_{huth} = 3.523 \cdot 10^{-5} \frac{mm}{N}$$

Table 3-5 shows the changes in load transfer when the fastener flexibility is increased by 100% and 300% respectively. For the first fastener, a relative increase of 100% results in a load change of 2.6% and 4.1% for the second fastener row.

Table 3-5   **Differences in load transfer with significant changes in fastener flexibility**

	Load with f_{huth} [N]	Load with $2 \cdot f_{huth}$ [N]	Load with $4 \cdot f_{huth}$ [N]
1ste fastener	7052	6871	6772
2nd fastener	5896	6258	6456
3th fastener	7052	6871	6772

A fastener flexibility increase of 300% changes the load transfer in the first fastener by 5.8% and 8.7% for the second fastener row. These small changes compared to the large increase in magnitude of the fastener flexibility shows the relative small influence of the fastener flexibility. As long as the fastener flexibility does not cover all possible geometries, a quantitative indication of the load transfer can be obtained using any of the equations mentioned in Section 3.5.1. The fastener flexibility is needed for an educated guess of the load transfer for three or more rows of fasteners.

3.6   Fiber Metal Laminates and the neutral line model

In principle nothing changes in the equations mentioned in the previous parts of this chapter deriving a *NLM* for fiber metal laminates. The difference between monolithic materials and *FLM*s is associated with the calculation of the modulus of elasticity and the location of the neutral axis of the sheet material. The neutral axis is usually calculated in a manner similar to that for monolithic materials, dividing the sheet thickness by two. Calculating the location of the neutral axis does not account for asymmetric *FML* lay-ups that are available. Asymmetric sheet lay-up also means that the eccentricity is not accurately calculated. The modulus of elasticity of the *FML* is based on the relationship between the number of thin aluminum sheets and the number of prepreg layers.

3.6.1   Calculation of the location of the neutral axis

For monolithic materials the neutral axis location can be rather simply determined:

$$c_i = \frac{t_i}{2}$$

(3-93)

Where t_i is the thickness of the ith sheet, see Figure 3-25.
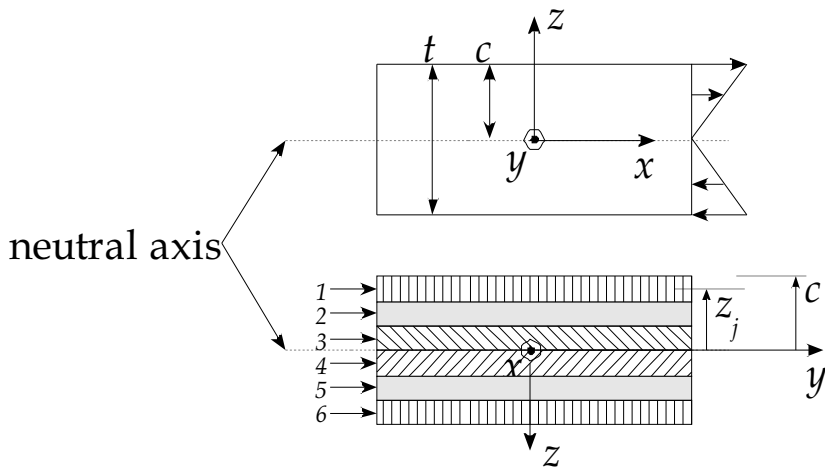
Figure 3-25 Definition of placement of neutral axis and the distance from the neutral axis to the point stress calculation y for monolithic and FML sheets

The calculation of the position of the neutral axis for laminated materials is somewhat more complicated. The differences in layer properties and possible asymmetry should be taken into account. Figure 3-25 shows a cross-sectional area of several layers combined into a laminate.

The position of the neutral axis, where the strain and normal stress are zero, can be found from the condition that the resultant axial force on the cross-sectional area under bending is zero. The following integral is evaluated over this cross-sectional area of the different layers. Each layer can also have a different thickness and modulus of elasticity.

$$\sum_j E_j \int_j z_j dA_j = E_1 \int_1 z_1 dA_1 + E_2 \int_2 z_2 dA_2 + \ldots = 0 \tag{3-94}$$

where
E_i = Modulus of Elasticity of ith layer
A_i = Cross sectional area of ith layer
z_i = Distance from centre of ith layer to the neutral axis
j = Total of layers in material

According to [1], Eqn. (3-94) can be used to locate the neutral axis for a beam of multiple layers. Eqn. (3-94) can now be rewritten in the following format using the transformed-section method:

$$E_1 \sum_j \left(n_j \int_j z_j dA_j \right) = E_1 \left(n_1 \int_1 z_1 dA_1 + n_2 \int_2 z_2 dA_2 + ... \right) = 0$$

$$E_1 \sum_j n_j z_j A_j = E_1 \left(n_1 z_1 A_1 + n_2 z_2 A_2 + ... \right) = 0$$

(3-95)

With the modular ratio $n_j = \dfrac{E_j}{E_1}$. From Figure 3-25 a relation for y_j can be found:

$$z_j = c_i - \sum_1^j t_{j-1} - \frac{t_j}{2}$$

(3-96)

Combining Eqn. (3-95) and Eqn. (3-96) gives one equation with the unknown c_i. With c_i known the moments of inertia for a monolithic and laminated sheet can be determined.

3.6.2 Calculation of stresses

To calculate the stresses at a distance y from the neutral axis for a monolithic sheet subjected to bending stresses the following equation is used (see Figure 3-17 for definition of y):

$$\sigma_b = \frac{M(x) z_j}{I_{c_i}}$$

(3-97)

With $M(x) = Pw(x)$ or $M(x) = M_a - \sum_i M_{Internal} + Pw(x) - D_a x$ depending on the boundary conditions.

For laminated sheets (b is width of sheet), with the position of the neutral axis known, the moment of inertia for each separate layer needs to be determined.

$$I_j = \frac{1}{12} b t_j^3 + A_j z_j^2$$

(3-98)

The moment of inertia for the entire laminate can then be determined taking the earlier mentioned modular ratio n_i into account.

$$I_{c_i} = \sum_1^j n_j I_j$$

(3-99)

For both monolithic and laminated materials, the longitudinal strain varies linearly through the thickness such that the strain at the bottom of a layer equals the strain at the top of the underlying layer. The stresses for a laminated material can be calculated taking into account the differences in elastic properties for the various layers. The stress distribution can be calculated by multiplying the strains, 1-D Hooke's law, by the appropriate elastic properties for a specific layer [1].

$$\sigma_b = \frac{M(x)z_j E_j}{\sum E_i I_i} = \frac{M(x)z_j E_j}{E_1 I_{c_i}} \tag{3-100}$$

3.7 Experiments

The new neutral line model will be validated by comparison with experiments. A number of joints were instrumented with strain gages to obtain load versus strain plots. Strain data of four different joints were available from [12]. These joints resemble real structures that have been used in commercial aircraft for many years. One four-fastener row lap-splice joint is used for validation purposes. To obtain additional information for the validation effort, four aluminum joints and four Glare joints were used. These specimens are equipped with a number of strain gages, see Figures E-3 – E-6, and tested in a MTS servo-hydraulic testing machine, see Figure 3-26.

Figure 3-26 25 Tons MTS servo-hydraulic testing machine

Before the results from the neutral line model are compared in Section 3.8 to the stresses calculated from the strain gage data, several remarks should be considered first. The length of the sheets, the boundary conditions and the internal moments influence the calculated stress in the neutral line model.

3.7.1 Influence of internal moment

The most important improvement made to the neutral line model is the implementation of the load transfer via the internal moment at the fasteners. The results for the lap-splice joint from Figure 3-27 are shown in Figure 3-28.

Skin = Al 2024-T3
W = 100 mm
P = 20 kN
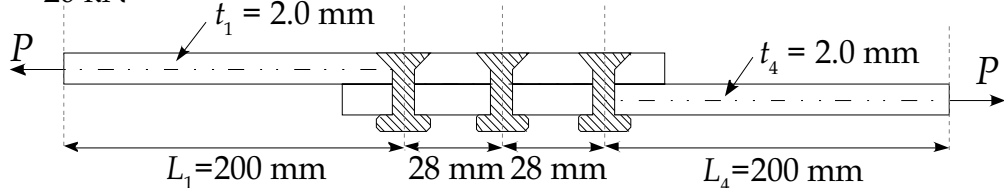
Figure 3-27 Lap-splice joint geometry used for parameter study

The differences are most significant in the overlap region; smaller differences are found at the critical fastener row, about 5.5%. The differences are a result of the implementation of the load transfer. The classic neutral line model did not include the load transfer as confirmed by the un-interrupted line of symbols in the overlap region. Half of the applied load is transferred to the lower attached sheet through the first fastener row, and the middle fastener does not transfer any load. As explained before, the use of the fastener flexibility model accounts for a quantitative approach to calculate the load transfer including the second fastener, or in case of joints with more than three fastener rows all of the middle fastener rows. When the load transfer is accounted for, the middle row fasteners transmits some part of the total applied load, thus lowering the load transfer at the outer fasteners. This distribution of the loads over all fastener rows lowers the stress at the outer fasteners as can be seen in Figure 3-28. The small reduction of secondary bending at the outer fastener rows was already mentioned in Section 3.2.2.
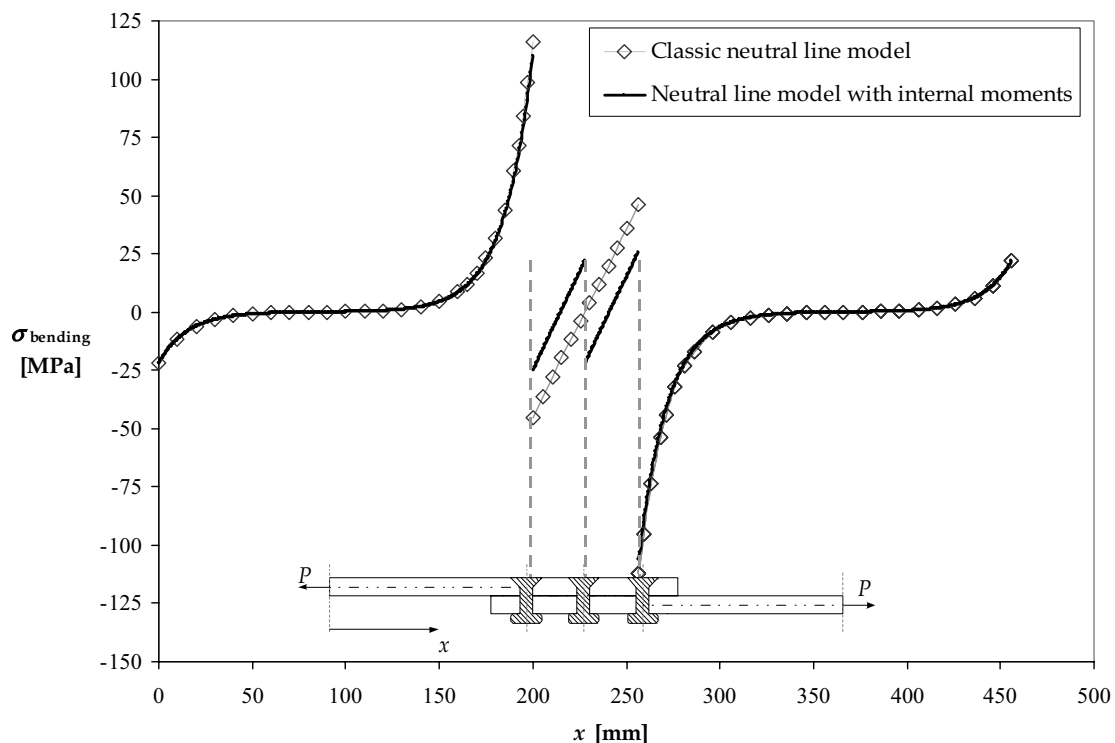
Figure 3-28 Effect of the internal moment on the bending stress

Usually extra structural elements such as stiffeners and doublers are found in real life fuselage constructions, a way to account for these effects is discussed below.

3.7.2 *Influence of attached stiffeners and doublers*

The influence of attached stiffeners and doublers depends on the geometric shape and location of attachment to the joint [5]. The examples shown in Figure 3-29 show four common joint configurations seen in aircraft fuselage structures. Type Ia is a lap-splice joint with an added stiffener at the 2nd fastener row, Type IIa is a butt joint with an added doubler and stiffener. Both Type Ib and Type IIb are simple representations of the a-Type joints.
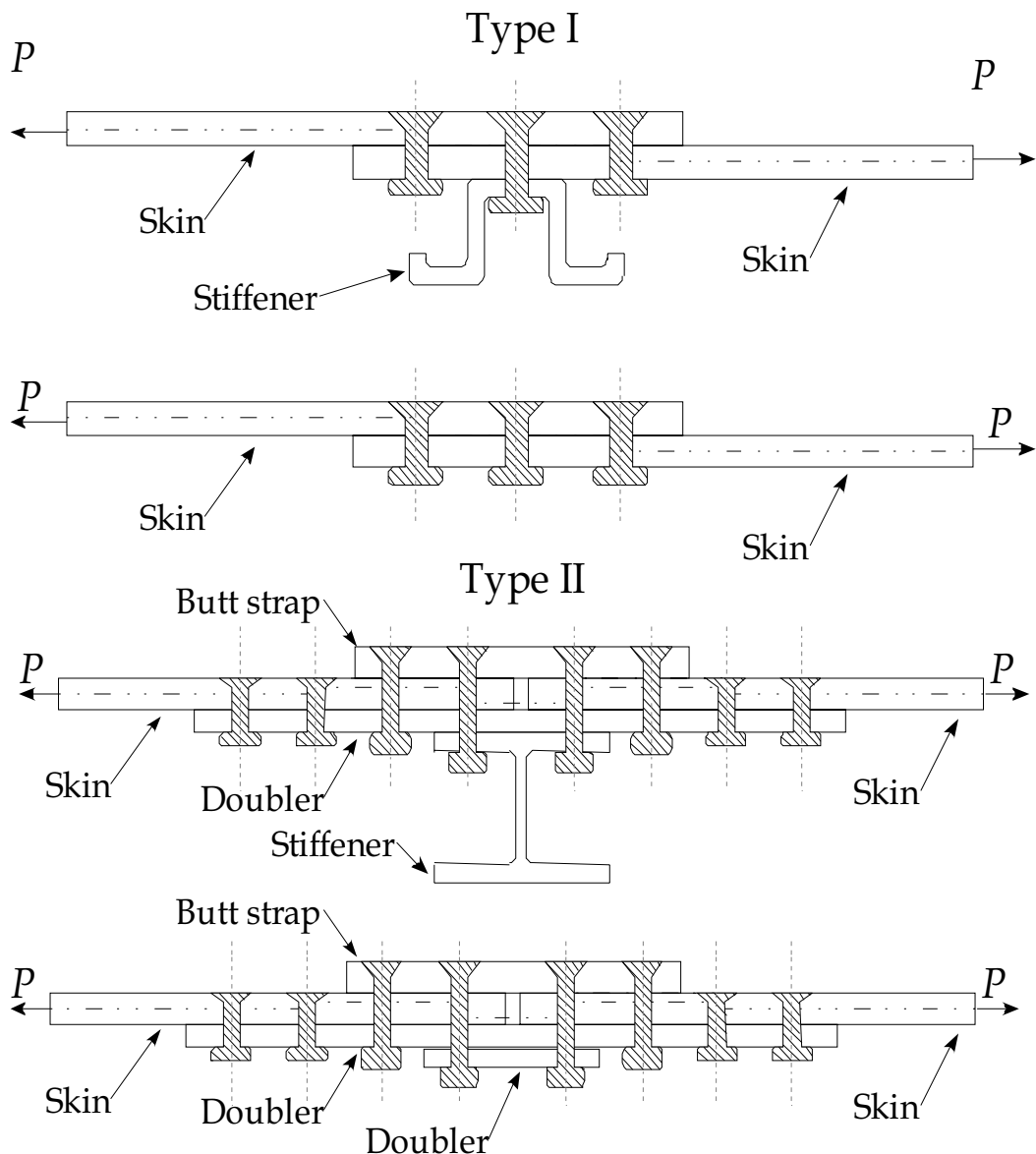
Type I

Type II

Figure 3-29 Examples of how to implement stiffeners into the neutral line model

Type Ia

For the Type Ia joint where the stiffener is attached to only one fastener row, the influence of the stiffener is limited to bending in width direction. However, the flanges of the stiffener do not contribute to the bending stiffness of the lap-splice joint in loading direction (P in Figure 3-29). The only part that might have some influence, locally, is the part of the stiffener-base attached directly to the lap-splice joint. Thus, the attached stiffener can be idealized as a doubler attached to the lap-splice joint via a single fastener. The question now is, does this doubler have some effect on the stiffness of the lap-splice joint? For any doubler attached via one fastener row to a joint, the influence on the bending stiffness is limited to the area

around the fasteners. Due to the clamping force of the installed fastener, an increased stiffness is created around the fastener. This shifts the bending stress away from the hole. Crack nucleation may even start away from the bore of the hole at the location of maximum bending stress [4]. In order not to complicate the neutral line model it is assumed that the extra doubler does not contribute significantly to the bending behavior of the lap-splice joint. The simplification of Type Ia results in a simple lap-splice joint shown in Figure 3-29 as Type Ib. This simplification of the lap-splice joint with attached stiffener has been verified by de Rijck and Fawaz [5].

Type IIa

This type is not essentially more complicated than the Type Ia lap-splice joint in Figure 3-29. This butt joint has a butt strap, a doubler, and a stiffener attached via two fastener rows. Again the stiffener is attached to the joint to provide more bending stiffness in width direction of the joint, but the web of the stiffener does not contribute to the bending stiffness of the butt joint. It is then easy to see that the stiffener can be idealized as another doubler attached via two fastener rows. This doubler provides extra flexural rigidity for the butt joint. The idealization of a butt joint with a stiffener attached to a simple butt joint is verified by de Rijck and Fawaz [5] and results in the Type IIb butt joint.

Depending on the contribution of the attached stiffeners to flexural rigidity of lap-splice and butt joints, attached stiffeners can be represented by simple beam elements replacing complicated geometric additions. Parts of stiffeners not contributing to the bending stiffness of the joint can be omitted from the neutral line model.

3.7.3 Strain measurements

The well known $\sigma(E)$ relations for plane stress according to [13] (Hooke's law) are:

$$\sigma_x = \frac{E}{(1-v^2)}\left(\varepsilon_X + v\varepsilon_y\right)$$

$$\sigma_y = \frac{E}{(1-v^2)}\left(\varepsilon_y + v\varepsilon_x\right)$$

(3-101)

This applies to isotropic material. For anisotropic materials (e.g. fiber metal laminates) the following equations are valid [14].

$$\sigma_x = \frac{1}{1-v_{xy}v_{yx}}\left(E_x\varepsilon_x + v_{xy}E_y\varepsilon_y\right)$$

$$\sigma_y = \frac{1}{1-v_{xy}v_{xy}}\left(E_y\varepsilon_y + v_{yx}E_x\varepsilon_x\right)$$

(3-102)

Strain measurements were carried out on two types of specimens (1) lap-splice joint, see Figure 3-33, and (2) single butt strap joint, see Figure 3-31. The specimens and the location of the strain gages are described in more detail in Appendix E. For the non-overlap parts of the joints it is assumed that the lateral contraction away from the overlap and from the clamping was practically unconstrained and thus:

$$\sigma_x = E\varepsilon_x \tag{3-103}$$

For the overlap region, the stress state is different. A 2-dimensional finite element analysis showed not only a load transfer in line with the applied load but also a load transfer perpendicular to the applied load [15]. This behavior was most profoundly visible at the outer fastener columns; this is in full agreement with the findings by Müller [4]. The stresses in the overlap region will not be equal in the upper and lower sheet, due to the differences in load transfer. The overlap region does not only have the thickness of both sheets which influences the lateral contraction but also a difference in stress. This difference in lateral contraction will create shear loading perpendicular to the loading direction on the rivets, which will be translated as a load transfer perpendicular to the loading direction. Having a load transfer perpendicular to the loading direction introduces a σ_y depending on the Poisson ratio v. For the overlap region, strains in the two directions ε_x and ε_y are required to calculate normal stress, σ_x. For isotropic materials:

$$\sigma_x = \frac{E}{(1-v^2)}\left(\varepsilon_x + v\varepsilon_y\right) \tag{3-104}$$

And for anisotropic materials:

$$\sigma_x = \frac{1}{1-v_{xy}v_{yx}}\left(E_x\varepsilon_x + v_{xy}E_y\varepsilon_y\right) \tag{3-105}$$

Standard practice for Glare is to calculate v_{xy} and v_{yx} using the rule of mixtures

$$v_{Glare,xy} = \frac{t_{al}}{t_{tot}}v_{al} + \frac{t_{prep,0}}{t_{tot}}v_{prep,0} + \frac{t_{prep,90}}{t_{tot}}v_{prep,90}$$

$$v_{Glare,yx} = \frac{t_{al}}{t_{tot}}v_{al} + \frac{t_{prep,0}}{t_{tot}}v_{prep,90} + \frac{t_{prep,90}}{t_{tot}}v_{prep,0} \tag{3-106}$$

with:

v_{al} : Poisson ratio aluminum (0.33)

$v_{prep, 0}$: Poisson ratio prepreg in 0 degrees (0.33)

$v_{prep, 90}$: Poisson ratio prepreg in 90 degrees (0.0371)

t_{al} : Thickness of all aluminum layers

$t_{prep, 0}$: Thickness of all prepreg 0 degrees layers

$t_{prep, 90}$: Thickness of all prepreg 90 degrees layers

t_{tot} : Total thickness of sheet material

3.8 Results

The neutral line model is used to design fatigue test specimens with a prescribed ratio of bending to tensile stress. Using the neutral line model allows for an accurate stress calculation at any location in the specimen resulting in a rather straight forward procedure for specimen design. Validation of the neutral line model is shown by Fawaz and de Rijck in [16] (specimens used in the investigation of chapter 5 will be described here). From several tests the neutral line model's applicability will be validated; this will be done by comparing calculated stresses with stresses obtained through strain gage measurements. The Glare specimens used to obtain strain gage data are also used for residual strength testing. The aluminum specimens tested after the residual strength tests for Glare are also equipped with strain gages perpendicular to the loading direction. The strain gage data from the Glare specimens showed some differences between the calculations and the calculated stresses obtained from the strain gage data.

3.8.1 Combined tension and bending specimen

The combined tension and bending specimen was designed as part of an experimental and analytical study of fatigue crack growth in mechanically fastened joints in fuselage structure. Fatigue performance is of concern in fuselage structures [16], [17]. The influence of tension and bending on fatigue crack growth is investigated. More details on the specimen production can be found in chapter 5. Here, some more details of the results from [16] will be discussed, see Figure 3-30 for the combined tension and bending specimen. At the centre of the specimen, tensile and bending loads at a countersunk hole are developed, making up the combined loading found in fuselage joint structures. The investigation by Fawaz and de Rijck included finite element analysis, stress analysis using the neutral line model, and strain gage measurements. They found good agreement between the finite element analysis and the neutral line model calculated stresses. The differences found were 3% for the tensile stresses and 5% for the bending stresses for a remote stress of 100 MPa. Similar values were obtained when comparing the finite element analysis results with the measured strain data.
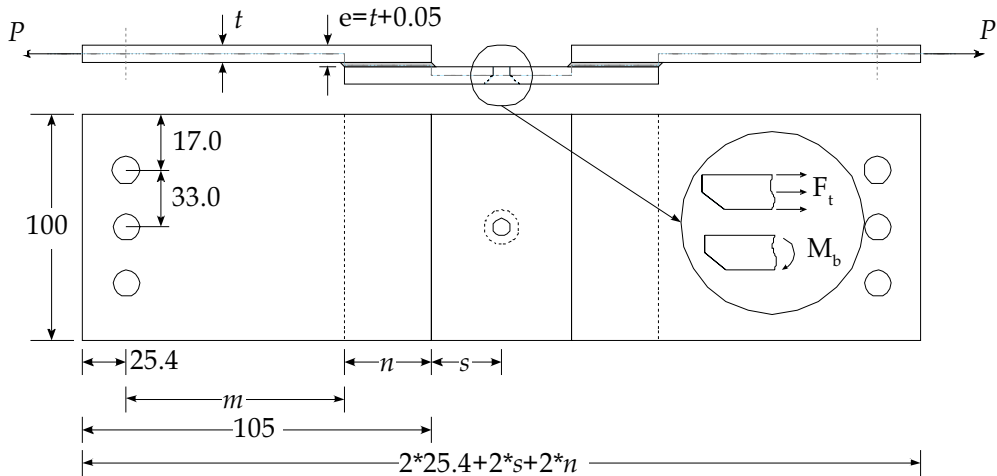
Figure 3-30 Combined tension and bending specimen, variables *m*, *n* and *s* can be varied to change the stress state at the area of interest

3.8.2 *Lap-splice and butt joints*

Fawaz and de Rijck have also shown that the neutral line model works for the combined tension and bending specimens [16]. Schijve was the first to show that the neutral line model can provide an easy means to calculate stresses in lap-splice and butt joints. The additions and changes made to the neutral line model in this thesis provides a method to calculate stresses at any location for different materials other than monolithic aluminum, such as Glare.

In the following sections, a comparison is made between the new neutral line model and the measured stresses, starting with an aluminum lap-splice and butt joint equipped with strain gage pattern II (see Appendix E for Figure E-4 and Figure E-6). Then the two remaining aluminum joint results will be presented followed by the calculations done for the Glare joints. For all results shown in Section 3.8.2.1 and Section 3.8.2.2 the results are for strain measurements from a single side lap-splice and butt joints. The results for the strain gages on the other side of the joints compare in the some order to the neutral line model calculations.

3.8.2.1 Strain measurements ε_x and ε_y

In Section 3.6.3 the equations to calculate stresses from the strain data were presented. The influence of the stress perpendicular to the loading direction, σ_{yy}, has generally been neglected in research on the neutral line model. To get a better understanding of σ_{yy} on fatigue crack growth, two specimens were equipped with strain gages perpendicular to the loading direction. Unfortunately this was not done for all specimens. Figure 3-31 and Figure 3-32 show the results from the neutral line model calculation including load transfer, misalignment and clamped edges.
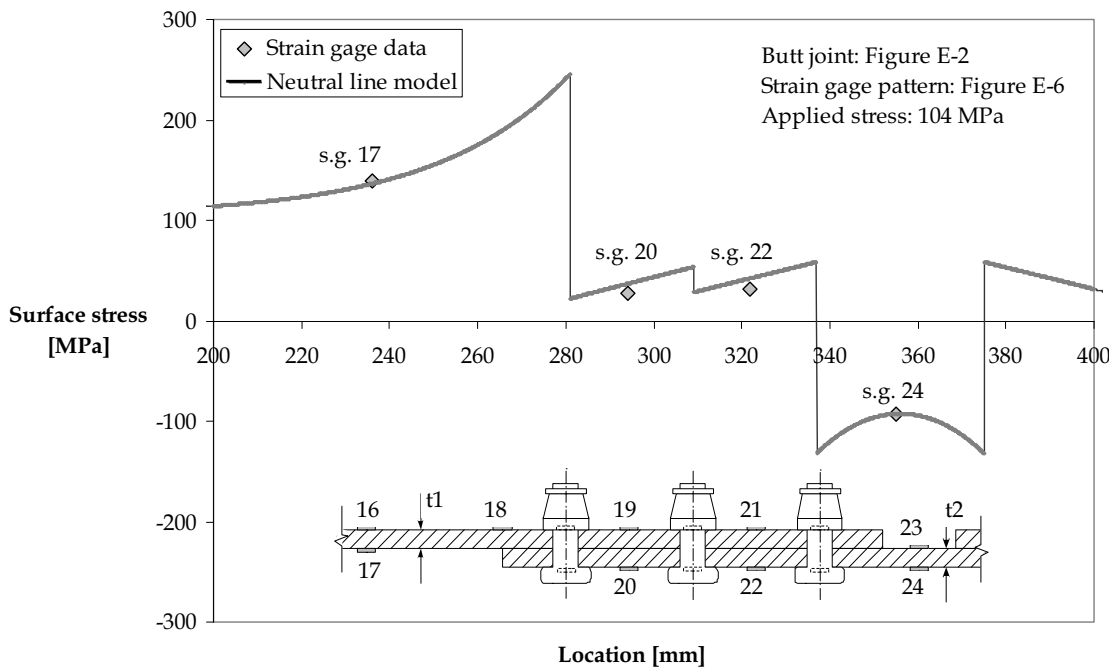
Figure 3-31 Butt joint validation results from strain gages at the lower side of the butt splice joint, sheet thickness $t_1 = 4.0$ mm, $t_2 = 4.0$ mm and material Al 2024-T3 Clad (AL_BJ_40_40_40)

The symbols in Figure 3-31 and Figure 3-32 are the stresses calculated, in x direction, obtained from the strain measurements in both x and y direction using Eqn. (3-104) at the lower and the upper side of the specimen respectively. The stresses shown are corrected for the one dimensional stress calculation of the neutral line model. Outside of the overlap region the stress prediction is within 3% of the measured data. Unfortunately the stress calculation in the overlap region shows a relatively large difference between the measurements and calculations (10 – 20%). Again it is important to realize that the neutral line model is a one dimensional model not taking the stresses in width direction into account.

According to Müller [4] it must be concluded that the load transfer is not limited to the loading direction of the joint. In the overlap region a load transfer is present perpendicular to the loading direction. This is mainly caused by the Poisson's ratio as a result of the rivet/sheet interaction. With $v = 0.0$, there is no lateral strain in the joint and thus no load transfer perpendicular to the loading direction. The joints tested have a non-zero Poisson's ratio and will experience load transfer in lateral direction. The second joint equipped with strain gages in both directions, is a lap-splice joint shown in Figure 3-33. The influence of the load transfer is more significant for this joint, because of the differences in sheet thickness. The sheets of the butt joint in Figure 3-31 all have a thickness of $t = 4.0$ mm, the lap-splice joint shown in Figure 3-33 has sheets thickness' of $t = 2.0$ mm and $t = 2.5$ mm.
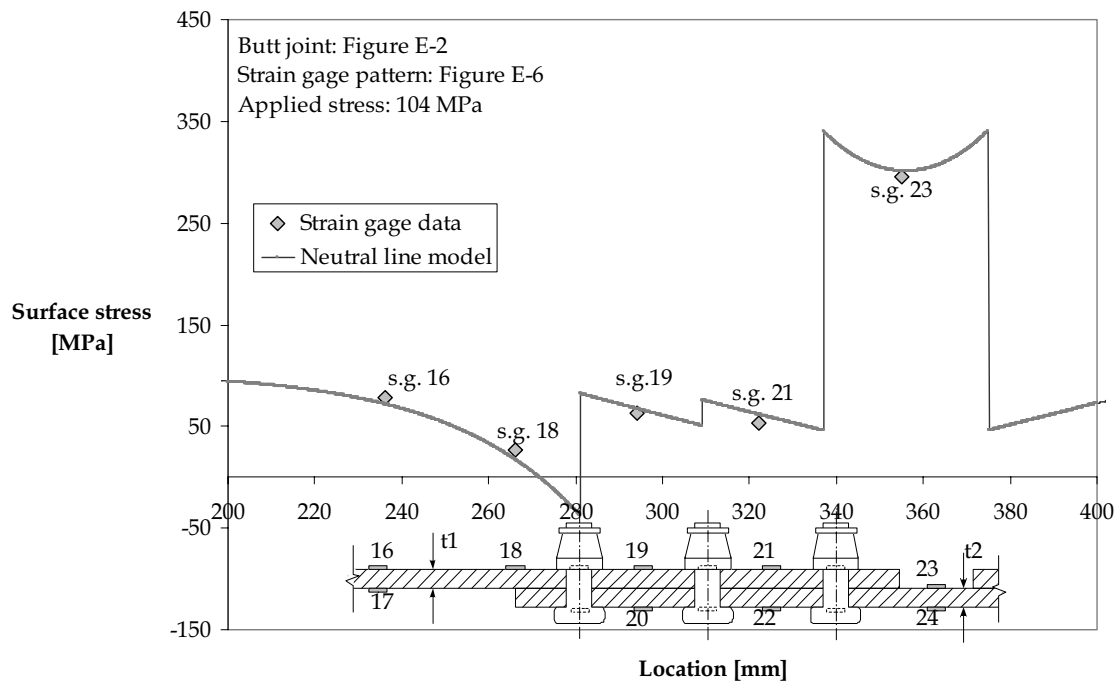
Figure 3-32 Butt joint validation results for strain gages at the upper side of the butt splice joint, sheet thickness t_1 = 4.0 mm, t_2 = 4.0 mm and material Al 2024-T3 Clad (AL_BJ_40_40_40)
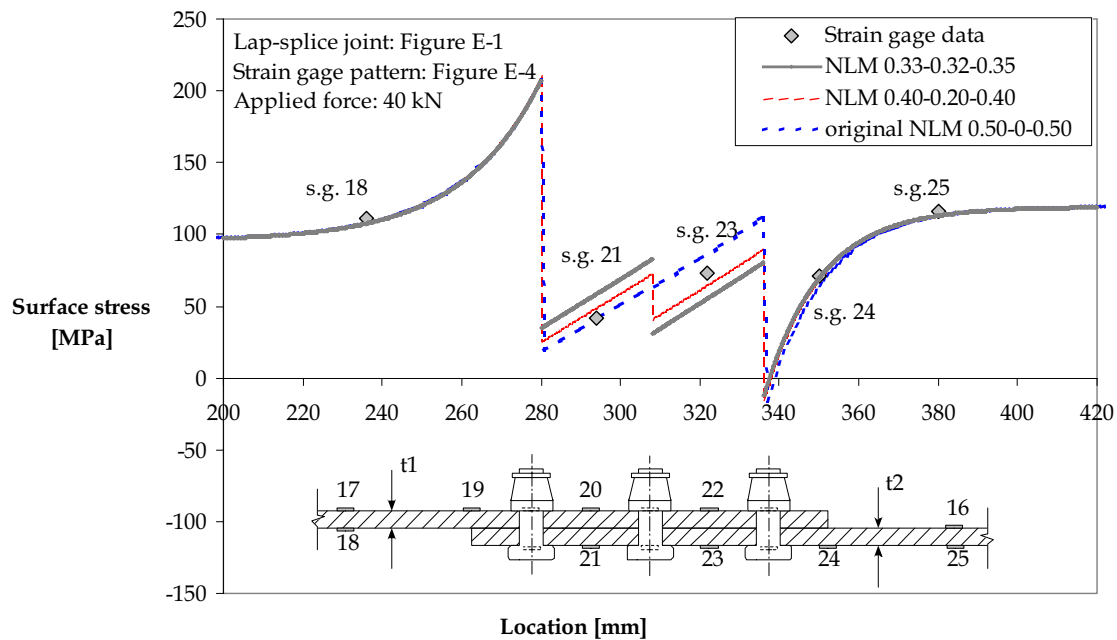
Figure 3-33 Lap-splice joint validation results, sheet thickness t_1 = 2.0 mm, t_2 = 2.5 mm and material Al 2024-T3 Clad (AL_LJ_25_20)

From [11], one could conclude that the empirical fastener flexibility equations do not catch the correct flexibility. As stated earlier, a lack of understanding of each parameter that could be of influence to the fastener flexibility might produce some uncertainties with respect to the accuracy of the fastener flexibility calculations. In section 3.5.3 it is shown that the influence of the fastener flexibility is of minor significance in the load transfer calculation. Therefore the empirical equation, Eqn. (3-72), is used for all fastener flexibility calculations. For the lap-splice joint mentioned above, the load transfer using the fastener flexibility gave a load transfer of 33% for the first fastener row, 32% for the second fastener row and 35% for the third fastener row. Having more accurate fastener flexibility results might solve only part of obtaining the correct load transfer ratios. Choosing a load transfer of 40%-20%-40% gives better results for the overlap region, but with improved fastener flexibility this arbitrary value might be accurately calculated. This shows that other influences in the overlap region play a more significant role. A portion of the load transfer will not go through the fasteners from sheet to sheet, but will be transferred by means of friction by the clamping action of the fasteners.

The calculated stresses for strain gage locations 18, 24 and 25 outside the overlap region are within 3.5% of the measured data. Again for the overlap region two comments can be made, not all loads will pass through the location of the strain gages and the load transfer is based on empirical equations.

How important are the stresses in the overlap region? The highest stresses occur outside the overlap region, and these stresses can be calculated within an accuracy of 3.5%. The stresses in the overlap region are of importance when the geometry of the joint results in high stresses in the overlap region. Figure 3-34 shows such a geometry that will have a high bending stress at the location of the middle fastener row.
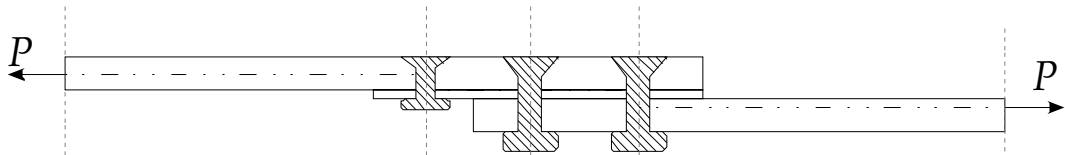
Figure 3-34 Lap-splice joint geometry with high loaded middle fastener row

3.8.2.2 Strain measurements ε_x

The output of the neutral line model is bending and tensile stresses parallel with the applied load. Therefore all specimens are equipped with strain gages parallel with the applied load. All stresses in width direction are not taken into account. The two specimens discussed in the last section were fitted with extra strain gages to measure the strains perpendicular to the loading direction to understand the influence of the lateral direction strains. For comparison, the aforementioned two joints will be used to show the difference in stresses obtained from the strain gage

data when the effect of the width is neglected. Figure 3-35 shows the results of a comparison between the calculated normal stress σ_x and the stress obtained from the strain gage measurements. Small differences can be found when comparing the stresses σ_x with the stresses shown in Figure 3-31. The lateral strain ε_y influence on the surface stress is present in the overlap region between the fasteners. More pronounced is the difference of the surface stresses found on the butt strap.
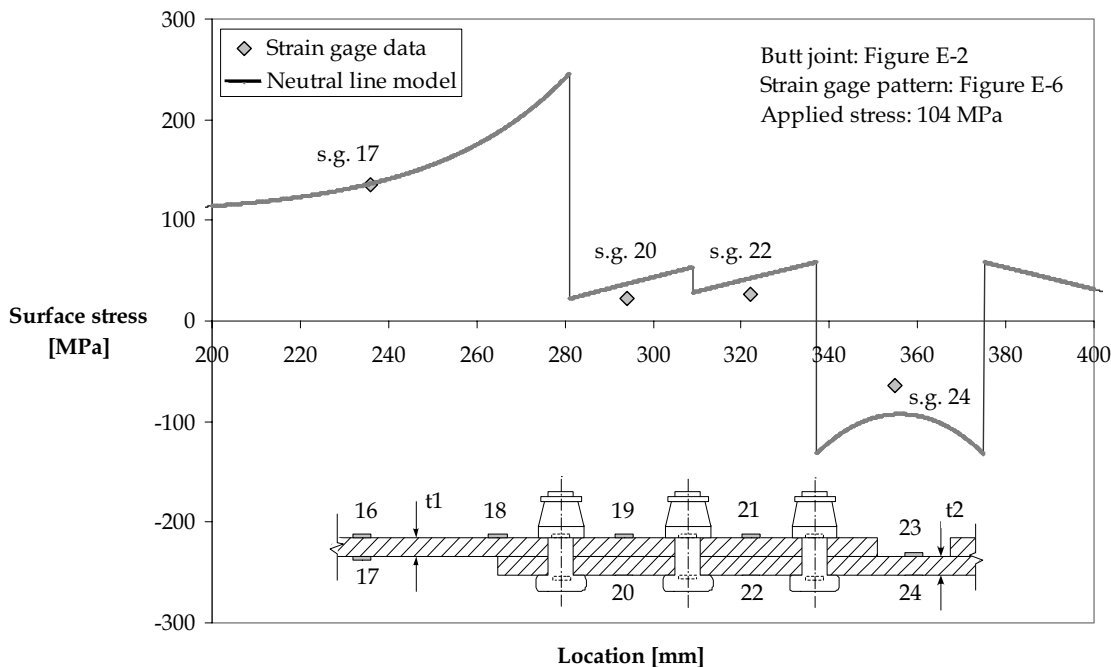
Figure 3-35 Butt joint surface stress representation for strain gages at the lower side of the joint, sheet thickness $t_1 = 4.0$ mm, $t_2 = 4.0$ mm and material Al 2024-T3 Clad (AL_BJ_40_40_40)

Figure 3-35 clearly shows the influence of the ε_y strains perpendicular to the loading direction. Correction of the strain data using Eqn. (3-104) is not possible since ε_y is not available.

The best results are obtained by comparing the calculated stresses with the stresses obtained from the strain gage measurement in both x and y direction. When looking at the most critical fastener rows, the outer fastener row, of the two joints used for validation, the results in both sections are within 4% of the measured values. The results of the overlap region for both the lap-splice and butt joint appear to show the correct behavior. The results of the two remaining aluminum joints are shown in Figure 3-36 and Figure 3-37. In Figure 3-36, strain gage at location 23 appeared to be faulty and the result is therefore not included. In Figure 3-37, strain gage at location 24 did not produce any results and is also not included. The influence of the load transfer in the overlap region is significant.
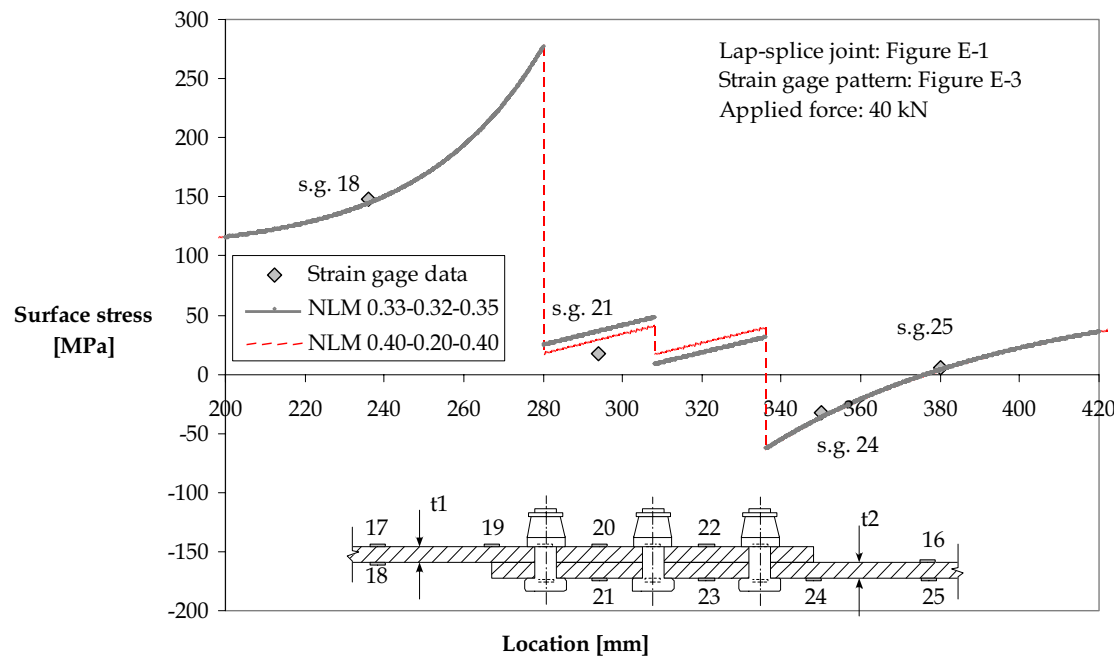
Figure 3-36 Lap-splice joint surface stress representation for strain gages at the lower surface, sheet thickness t_1 = 4.0 mm, t_2 = 6.4 mm and material Al 2024-T3 Clad (AL_LJ_40_64)
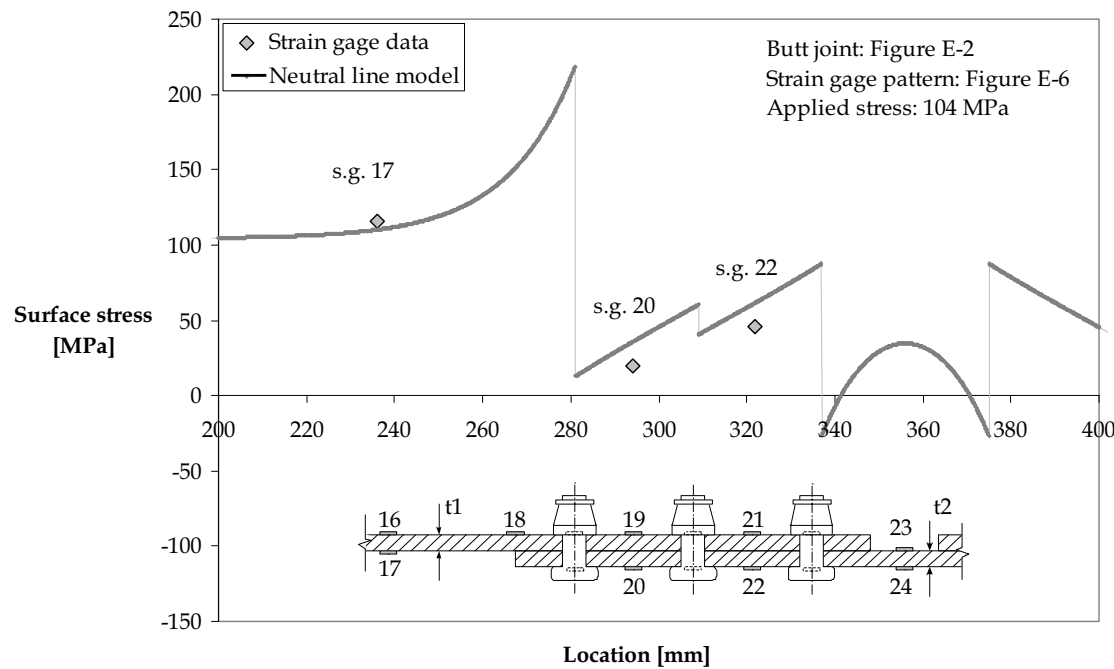
Figure 3-37 Butt joint surface stress representation for strain gages at the lower surface, sheet thickness t_1 = 2.0 mm, t_2 = 2.0 mm and material Al 2024-T3 Clad (AL_BJ_20_20_20)

Taking into account that no strains were measured perpendicular to the loading direction, the magnitude of the load transfer perpendicular to the loading direction is unknown. Recall that in joints a small portion of the load finds its way not through the fasteners but through friction by the clamping action of the fastener of the two sheets around the fasteners. Figure 3-36 and Figure 3-37 show that even without the strain ε_y known, the results out of the overlap region of a lap-splice or butt splice joint prove to be accurate.

The Glare specimens shown in the following Figure 3-38 to Figure 3-41 have strain gage patterns not including strain gages perpendicular to the loading direction. Four butt joints are used to obtain strains to validate the neutral line model to calculate stresses for fiber metal laminate joints. Figure 3-38 is a Glare butt joint representative of a large fuselage aircraft. The Glare sheet thickness $t = 4.25$ mm, resulting in large eccentricities and thus large bending stresses for all four Glare specimens. Glare 2 has a uni-directional lay-up, the fibers are embedded in the laminate in 0° or 90° to the loading direction. Glare 3 has a cross-ply lay-up, 50% of the fibers in 0° and 50% in 90° to the loading direction.
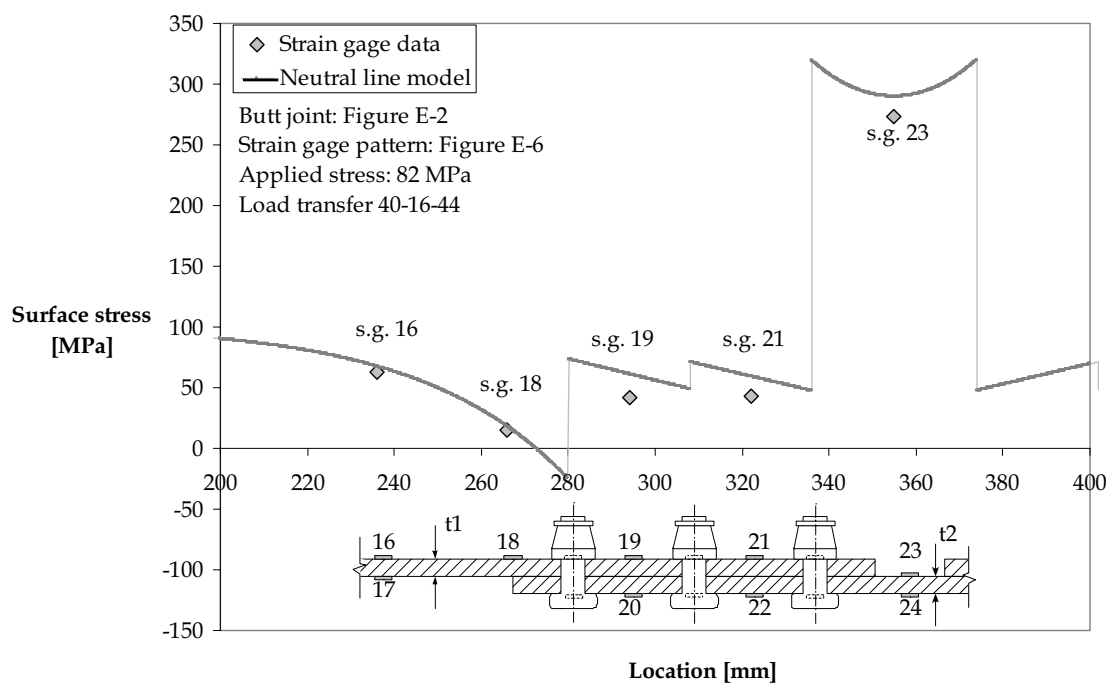
Figure 3-38 Butt joint surface stress representation for strain gages at the upper surface, sheet thickness $t_1 = 4.25$ mm, $t_2 = 4.25$ mm and material sheet 1 is Glare 3-6/5-0.5 and sheet 2 is Glare 2B-6/5-0.5 (GL_BJ_A1)
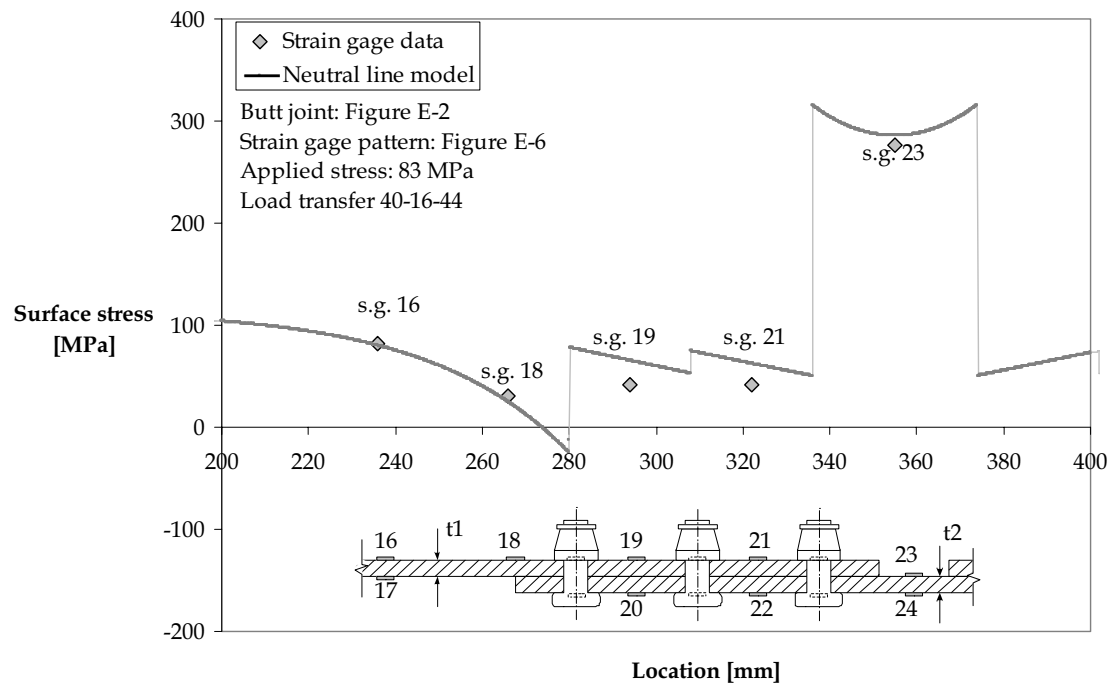
Figure 3-39 Butt joint surface stress representation for strain gages at the upper surface, sheet thickness t_1 = 4.15 mm, t_2 = 4.15 mm and material sheet 1 is Glare 3-8/7-0.3 and sheet 2 is Glare 2B-8/7-0.3 (GL_BJ_A2)
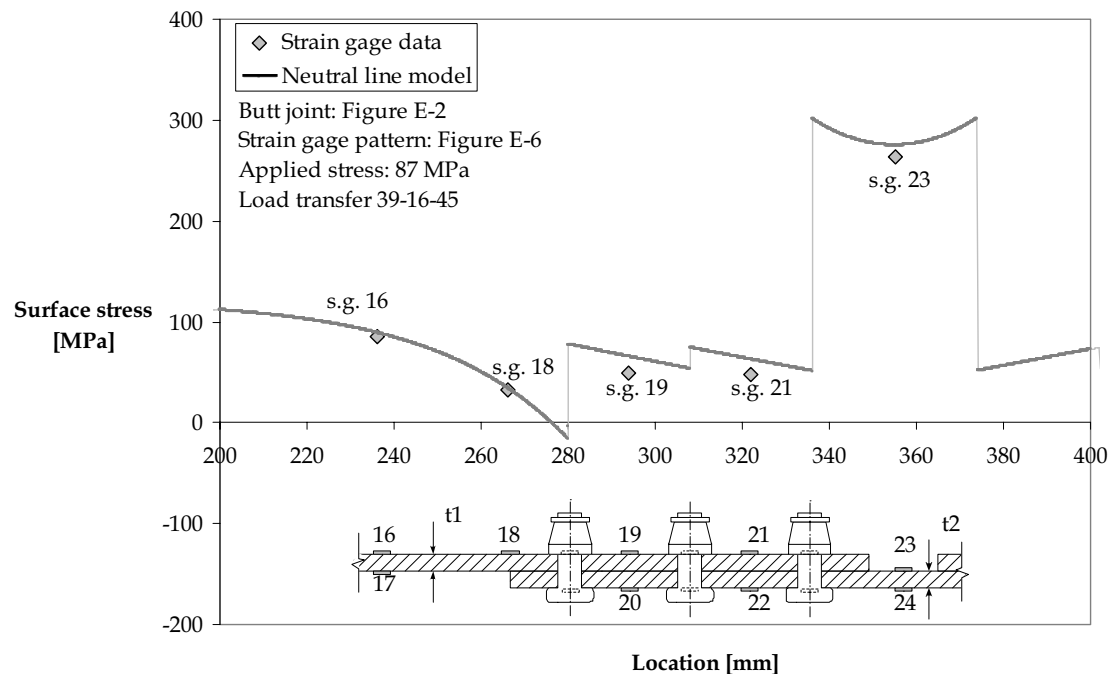
Figure 3-40 Butt joint surface stress representation for strain gages at the upper surface, sheet thickness t_1 = 4.00 mm, t_2 = 4.25 mm and material sheet 1 is Glare 4A-5/4-0.5 and sheet 2 is Glare 2B-6/5-0.5 (GL_BJ_A4)
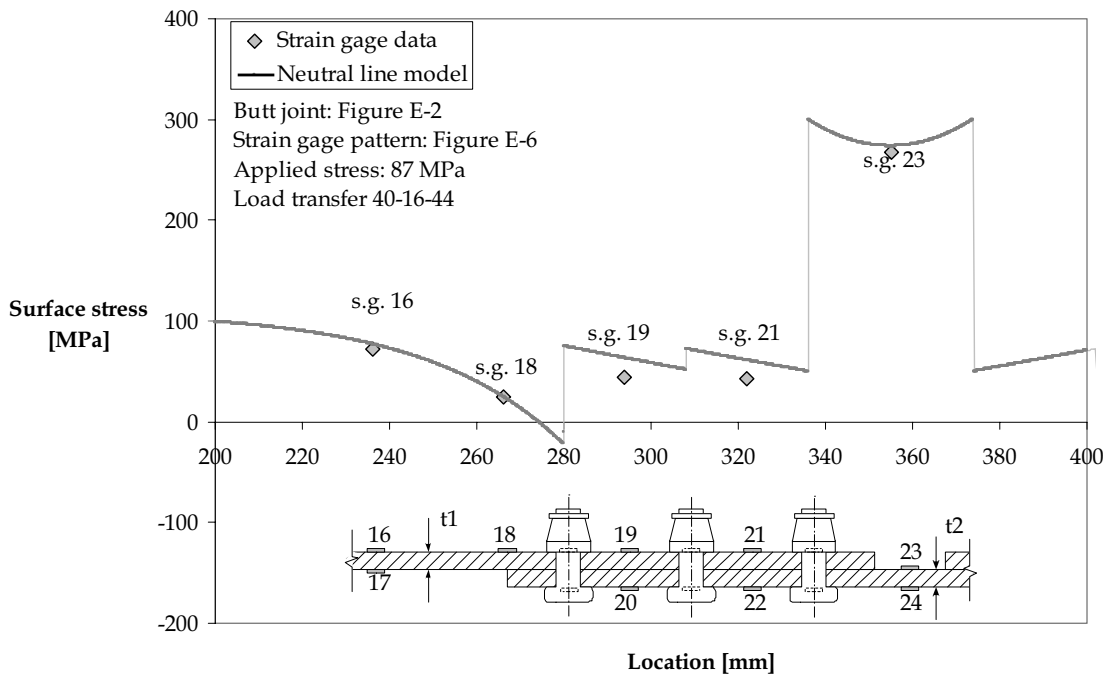
Figure 3-41 Butt joint surface stress representation for strain gages at the upper surface, sheet thickness t_1 = 4.00 mm, t_2 = 4.25 mm and material sheet 1 is Glare 4B-5/4-0.5 and sheet 2 is Glare 2B-6/5-0.5 (GL_BJ_A5)

Glare 4 is also a cross-ply but with 33% in 0° and 66% in 90° or 33% in 90° and 66% in 0°. More information on Glare can be found in Chapter 2. The butt straps for all butt joints are Glare 2 uni-directional sheets. This means that all fibers are in the direction of the applied load. The fibers therefore will carry a significant amount of load. For all Glare grades shown in Figure 3-38 to Figure 3-41 the calculated stresses outside the overlap region compare well to the stresses obtained from measured data. For all specimens the stresses are within 10% and for specimens GL_BJ_A4 and GL_BJ_A5 the stresses are within 6%.

The results shown in Figure 3-42 are from a four rivet row lap-splice joint with extra doublers and a longitudinal stiffener attached with only one fastener row. Strain gages for this joint were attached one inch to the right of row *A*. The results for this specimen were obtained by Fawaz [12]. Four different joints were used to obtain strain gage data. In [5] the results of the joints are compared to the calculated stresses from the neutral line model, using a fastener rotation factor. Since the fastener rotation is a parameter difficult to relate to geometric or material properties, the method used for this specimen is based on the load transfer calculation. With the method described in this chapter, the load transfer distribution over the four fastener rows is as follows; 25% load transfer from the skin-material into the doubler. The second fastener row transfers again 25% load from the skin and doubler sheet to the other sheet and doubler. Each fastener row carries 25% of the applied load. As shown for the other joints before, the stresses outside the overlap

74

region are predicted with great accuracy, even for this more complicated joint with doublers.
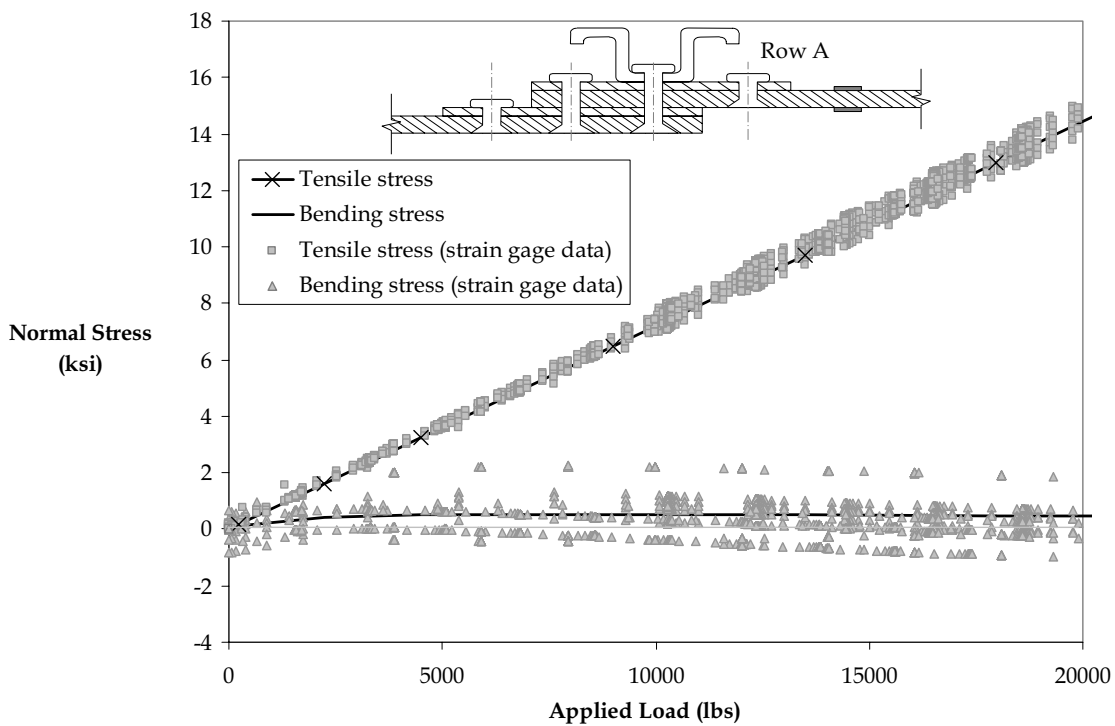
Figure 3-42 Normal stress one inch to the right of row *A*

3.8.2.3 Empirical correction for ε_y

A simple empirical relation between the total surface stress and the combined bending and tension stress has been found resulting in a better correlation between the strain gage measurements and the calculated neutral line model stresses of the overlap region and the butt strap. The neutral line model surface stress calculation then changes into:

$$\sigma_{total} = \sigma_{bending}\left(1 - v^2\right) + \sigma_{tension} \tag{3-107}$$

This correction only needs to be applied to the overlap and butt strap region, the accuracy of the neutral line model outside the overlap and butt joint region has already been demonstrated. Figure 3-43 shows the results of this correction. For the overlap region this gives a minor change of the results. This is related to the lower bending stresses in the overlap region. In the butt strap however, the bending stresses are significantly higher than the bending stresses in the overlap region. This is where the bending correction influence is effective.
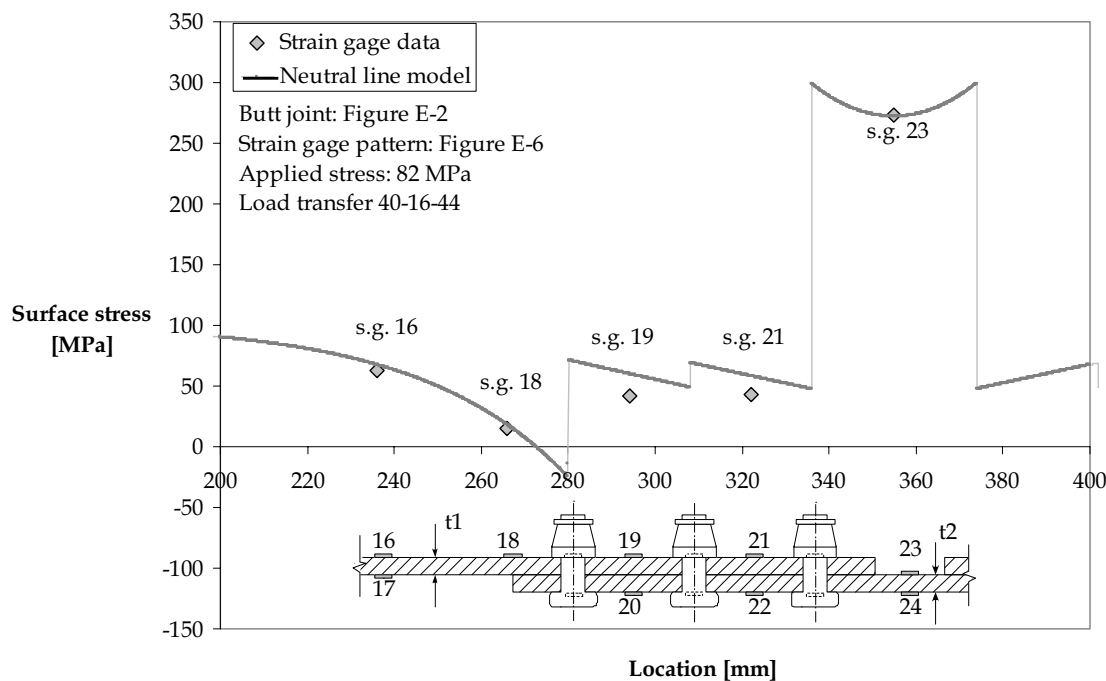
Figure 3-43 Butt joint surface stress representation for strain gages at the upper surface, sheet thickness t_1 = 4.25 mm, t_2 = 4.25 mm and material sheet 1 is Glare 3-6/5-0.5 and sheet 2 is Glare 2B-6/5-0.5 (GL_BJ_A1)

Table 3-6 contains the stresses at strain gage location 23 for all Glare butt splice joints. The influence of the bending stress correction in the butt strap increases the agreement between the strain gage measurements and the calculated stresses. The empirical correction provides a simple means to take some influence of the unknown ε_y into account. The results for the aluminum butt joint show that a large improvement can be made with this correction, although the difference is still large compared to the comparison with strain in both directions.

Table 3-6   Results of s.g. 23 with respect to the neutral line model with and without empirical bending stress correction

	s.g. 23 [MPa]	NLM [MPa]	% [-]	NLM[1] [MPa]	% [-]
GL_BJ_A1	272.9	289.8	6.2	271.9	0.4
GL_BJ_A2	275.8	304.1	10.3	285.5	3.5
GL_BJ_A4	263.4	293.2	11.3	275.1	4.4
GL_BJ_A5	267.4	291.6	9.1	273.6	2.3
AL_BJ_40_40_40	269.1	301.0	11.9	283.3	5.3
[1] Neutral line model with bending correction according to Eqn. (3-107)					

3.9 Conclusions

The internal moment is a good representation of the load transfer occurring in multiple row joints. The calculation of the load transfer can be made for complicated lap-splice and butt joints. Although the experimental and the calculated results differed in the overlap region, the improvement made with this method provides a base for further research into improved fastener flexibility equations.

The influence of the empirically found fastener flexibility on the load transfer is of less importance then previously thought.

Application of the neutral line model is also possible for fiber metal laminates and possibly composite joints.

Adding doublers and stringers does not offer complications. Only those parts adding bending stiffness to the joint need to be taken into account.

The limitation of the neutral line model is the one-dimensional solutions it provides.

Calculating stresses in the overlap region of joints is a problem that cannot be covered by the 'neutral line model' at the moment. A better understanding of the stresses through the entire joint may give insight for improvements. Also obtaining strain data at the faying surface will help to improve this understanding.

With all the additions made available, the neutral line model is still a very powerful tool to use in the early stages of joint design. It gives a good picture of the stresses in a joint. Since the stresses in the overlap region are small compared to the large stresses at the critical fastener rows, the differences found between the stresses calculated in the overlap region and the stresses obtained from measured data does not reduce the usefullness of this tool.

3.10 Literature

[1] Gere, J.M., and S.P. Timoshenko, *Mechanics of Materials*, Chapman & Hall, London, 1991

[2] Hartman, A., and J. Schijve, *Invloed van de afmetingen van geklonken lapnaden en enkele stripnaden op secundaire buiging*, NLR-TR-68026, Amsterdam, NL, National Aerospace Laboratory, 1968

[3] Schijve, J., *Some Elementary Calculations on Secondary Bending in Simple Lap Joints*, NLR-TR-72036, Amsterdam, NL, National Aerospace Laboratory, 1972

[4] Müller, R. P. G., *An Experimental and Analytical Investigation on the Fatigue Behaviour of Fuselage Riveted Lap Joints, The Significance of the Rivet Squeeze Force, and a Comparison of 2024-T3 and Glare 3*. Dis. Delft University of Technology, 1995

[5] de Rijck, J.J.M., and S.A. Fawaz, *A Simplified Approach for Stress Analysis of Mechanically Fastened Joints*, 4th joint DoD/FAA/NASA Conference on Aging Aircraft, 2001

[6] Unpublished reports of the Boeing Co., Renton, WA

[7] Kroes, R.A., *Description of the Computer Program SLAPJO*, Fokker report SF-63, 1992

[8] Huth, H., *Influence of Fastener Flexibility on the Prediction of Load Transfer and Fatigue Life for Multiple-Row joints*, ASTM STP 927, 1986, pp. 221-250

[9] Swift, T., *Development of the Fail-Safe Design Features of the DC-10*, ASTM STP 486, 1971, pp. 164-214

[10] Tate, M.B., and S.J. Rosenfeld, *Preliminary Investigation on Loads Carried by Individual Bolts in Bolted Joints*, NACA TN-105, 1946

[11] Morris, G., *Defining a standard formula and test-method for fastener flexibility in lap-joints*, Delft, to be published

[12] Fawaz, S.A., *Equivalent initial flaw size testing and analysis*, AFRL-VA-WP-TR-2000-3024, June 2000

[13] Timoshenko, S.P., and J.N. Goodier, *Theory of Elasticity*, McGraw-Hill Kogakusha Ltd., Tokyo, 1970

[14] Lekhnitskii, S.G., *Theory of Elasticity of an anisotropic elastic body*, Holden day inc., San Fransico, 1963

[15] de Rijck, J.J.M., *Investigation of Load Transfer within a Cracked Lap Joint and Butt Joint*, British Aerospace, R&T/B5607/66238, March 1998

[16] Fawaz, S.A., and J.J.M. de Rijck, *A Thin-Sheet, Combined Tension and Bending Specimen*, Experimental Mechanics, Vol. 39, No. 3, September 1999, pp. 171-176

[17] Fawaz, S.A., *Fatigue Crack Growth in Riveted Joints*, Dis. Delft University of Technology, Delft University Press, 1997

4 Riveting

4.1 Introduction

Large structures are usually an assembly of smaller parts joined together by a variety of production techniques. There are two important joining methods, namely: adhesive bonding and mechanically fastening. Mechanically fastened joints are an interesting subject to investigate. A large field of different parameters need to be taken into account, such as the fastener material and geometry, sheet material and installation process. The present investigation focuses on solid rivets installed in aluminum and Glare. The expansion of the solid rivet in the rivet hole is important with respect to the fatigue properties of joints. Müller showed that a properly riveted joint using a high squeeze force can have an extended fatigue life that is three times the fatigue life of a joint with a low squeeze force [1]. The expanding rivet inside a fastener hole will create a compressive residual stress around the hole and this will delay fatigue crack nucleation. For non-riveted fasteners cold working of the hole will result in similar compressive stresses around the fastener hole. Müller showed the importance of knowing the correct squeeze force used to form the driven head of a rivet. Measurements of the formed rivet head, diameter or protruding height, can then be used to check the force used to form the rivet. In order to establish a relation between the squeeze force and the final geometry of the driven head a follow up on research by Hilling and Müller was initiated by Schijve [2]. Schijve wanted to establish a direct link between the driven rivet head and the applied squeeze force as was suggested by Hilling [3] and later by Müller [1]. The efforts of Schijve did not result in a direct and simple relation between the driven head and the applied squeeze force, but showed a correlation between different parameters of the riveting process. Further investigation into the forming of the rivet head was done by Kandemir [4]. This chapter contains analysis of experimental results, based on the changing shape of the rivet and the material and geometrical properties of the rivet and the sheets. Using new experimental data and existing data from Müller, a direct and simple relation between the formed rivet head and squeeze force is found.

To understand the basic parameters present in the riveting process, the rivet installation is discussed in section 4.2. In section 4.3, the riveting variables such as the rivet material, rivet geometry and sheet properties are explained. In Section 4.4 an experimental setup based on the findings and results from both Müller and Schijve is introduced. In combination with the experimental data of Kandemir and results from Müller and Schijve, discovering a relationship between the riveting variables is the main purpose of section 4.5. From these relationships a direct link between the squeeze force and the driven head geometry of the rivet is discussed in section 4.6. Section 4.7 concludes with some remarks and recommendations.

4.2 Rivet installation

Rivet installation used to be a labor-intensive process, drilling the holes and inserting the rivet. Non-automated riveting involves installing the rivet and using a riveting gun to hammer the rivet into place. The quality of the rivet installation is therefore mainly dependent on the riveting gun operator. Improvements were made with the introduction of the machine controlled riveting process, which greatly decreased the variability of the installation of the rivets. The now frequently used machine controlled riveting process is based on applying a hydraulic squeezing force to the rivet head. With displacement controlled riveting, when a certain displacement is reached the rivet is assumed to be fully deformed and installed. For force controlled riveting, the rivet is fully installed when a predefined force is reached. In difficult to access areas, the manual riveting process is still used. The manual process is also used for *in-service* riveted repair patches applied to the aircraft structure when cracks are found. For quality control, it is essential to know exactly what force is used to form the rivet head. As was shown by Müller the riveting force has a significant effect on the fatigue properties of riveted joints.

The forming of the rivet is shown in Figure 4-1; in all stages large plastic deformations are present. Figure 4-1 is a picture of a two-dimensional finite element analysis to show the rivet installation process and the interaction between rivet and sheets. In the first stage *A*, the rivet is deformed by the squeeze force and expands within the fastener hole. Only a small amount of material flows into the fastener hole, this leads to stage *B*. In this stage, the rivet expands the material around the fastener hole and starts to deform into a barrel shaped cylinder outside the fastener hole.
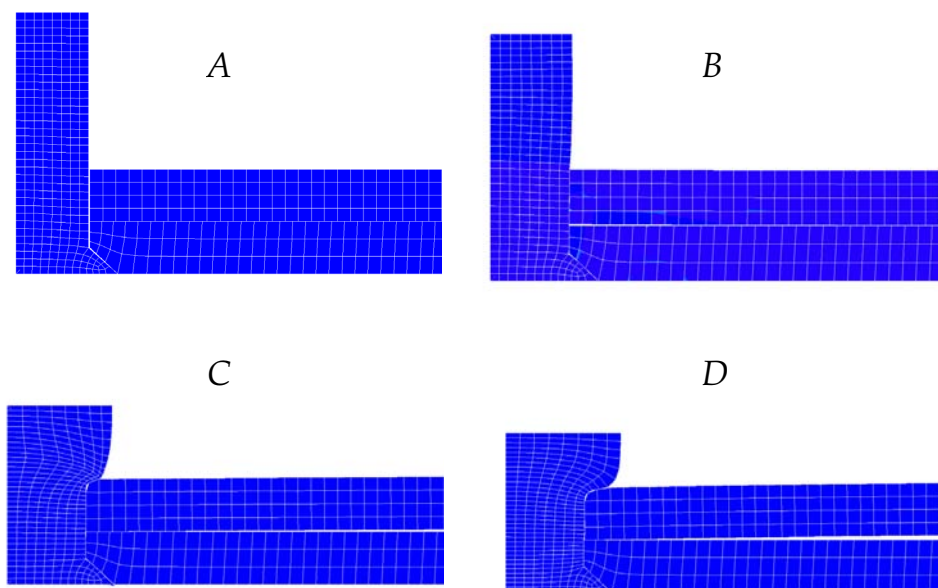
Figure 4-1 **The riveting process, A = inserting the rivet, B = applying squeeze force and filling the hole, C = plastic deformation around the rivet and D = relaxation of the installed rivet.**

Stage *C* shows clamping forces introduced as a result of forming the rivet head. Localized plastic deformations have occurred in and around the fastener hole. In the last stage *D*, the forming tools are retracted and the rivet and sheets are allowed to elastically recover. Depending on the elastic recovery of the sheets and rivet, a compressive clamping force is partly introduced permanently in the sheets. In addition some compressive clamping is a result from friction between the rivet and the hole shank during rivet squeezing.
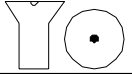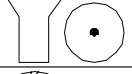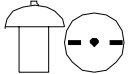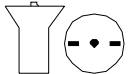
4.3   Rivet material and geometry variables

The riveting variables investigated in the experimental program can be divided into three categories; the rivet material, rivet geometry, and the combination of the sheet material and geometry. The squeeze force is directly related to all of these variables. Depending on the applied squeeze force, the rivet material will deform, but a difference may occur between protruding and countersunk rivets [1]. The behavior of the sheet is depending on the applied squeeze force.

4.3.1 Overview of the riveting material and rivet type

Four different rivet materials have been used; see Table 4-1. The *AD*-rivet can be used without any extra heat treatment; it has already undergone a heat treatment and is anodized.

Table 4-1   **Overview of riveting materials and rivet types.** *DD* and *E* rivets are used in ref [1]

Designation	Material	Composition	Type	Marker
AD	2117-T4	Al with 2.5% Cu, 0.3% Mg	NAS 1097	
			EN 6101	
			MS 20470	
D	2017-T4	Al with 4% Cu, 0.5% Mn, 0.5% Mg	NAS 1097	
DD	2024-T4	Al with 4.5% Cu, 0.6% Mn, 1.4% Mg	EN 6101	
E	7050-T73	Al with 6.2% Zn	NAS 1097	
2017A	2017A	Al with 4% Cu, 0.5% Mn, 0.5% Mg	MS 20470	
			EN 6101	

The *D* and *DD* rivets need an additional heat treatment without which the rivets tend to develop high internal stresses during the riveting process and cracking of the rivet can occur. The additional heat treatment for the *D* and *DD* rivets takes place at a temperature of 500 °C for 20 to 30 minutes [4], [5]. After this heat treatment, the rivets are instantly cooled down to room temperature by submersion in water with temperature of 25 °C, also called the "as quenched" condition (*W*). The rivets are then very soft and can easily be deformed in the riveting process. The *D* rivets have to be used in the riveting process within one hour after the cooling down cycle. The *DD* rivet must be used within ten minutes. To keep the heat treated rivets in the *W* state, the rivets must be stored at a temperature of 0 °C. The 2017A rivets have the same composition as the *D* rivets with exception of the Ti+Zr content. The grain size is smaller. The 2017A rivets are used for higher shear strength and can be used without any heat treatment prior to installation.

The rivet type designation explanation for the types in Table 4-1 can be found in Appendix F.2.

4.3.2 *The rivet geometry*

An obvious difference of the geometry of the rivets can be seen in the head shape, protruding or countersunk. Müller did observe a difference in the hole filling between the two types of rivets. The protruding head rivet geometry resulted in a more homogenous hole expansion whereas the countersunk rivet resulted in a larger hole expansion at the side of the driven head. The length of the shank of the rivet is measured, for protruding head rivets, from below the head to the end of the shank and for countersunk rivets, from the top of the countersunk head to the end of the rivet shank. The application length is determined by the following rules of thumb [5]; the combined sheet thickness plus $1.5\,D_0$ for protruding head rivets or $1.0\,D_0$ for countersunk heads, see Figure 4-2 for definition of D_0 and H_0. If the thickness of the combined sheets is larger then 7.0 mm the length of the rivet should be increased by an extra 1.0 mm.
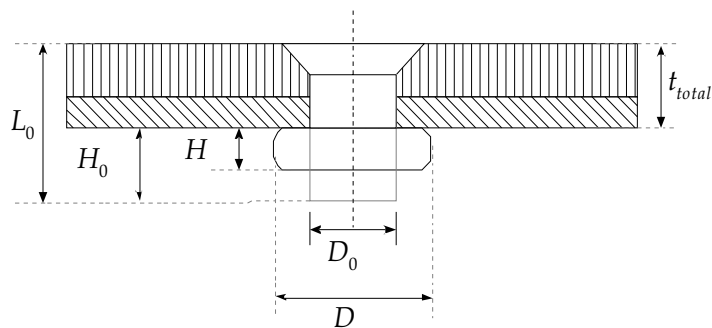
Figure 4-2   Rivet dimensions diameter D_0 and height H_0

To avoid the risk of insufficient hole filling by forming the rivet, the maximum combined sheet thickness should be less then three to four times D_0. This shows the initial shank height H_0 cannot be chosen independently from the rivet diameter D_0.

4.3.3 The sheet material and hole geometry

The sheet material is of similar importance as the rivet material itself. Looking at the riveting process in Figure 4-1 shows that the rivet expansion in the fastener hole is directly related to the material properties of the sheet material. Rivet expansion in aluminum 2024-T3 sheet material will be different from the rivet expansion in aluminum 7075 sheet material and Glare laminates. The differences are related to the material properties of the three mentioned sheet materials, differences in Elasticity Modulus. As mentioned before, the flow of rivet material into the fastener hole is small, therefore it is expected that the influences of the sheet material on the riveting parameters will be negligible. Schijve concluded in [2] when looking at data for riveting with respect to the sheet thickness that the small flow of material in the fastener hole will not greatly affect the final dimensions of the formed rivet head, and thus not play an important role in determining a relation between the squeeze force and the dimensions of the driven head.

4.4   Experimental setup

With results from Müller [1] and Schijve [2], the specimen shown in Figure 4-3 will be used to obtain a large amount of driven head dimensions data. Three different rivet diameters are used, $D_0 = 4.0$, 4.8 and 5.6 mm in combination with a large variety of rivet types. The complete test matrix is given in Table 4-2, listing the sheet material and rivet data. Different rivet materials are used to find a possible effect of the rivet material, and to take the rivet material properties into account in the relation between the squeeze force and the formed rivet head. Different rivet lengths are chosen to show an influence of the initial rivet geometry on the final rivet shape. Differences in sheet material are chosen to observe possible differences in hole filling, and the minor influence of the hole filling on the forming of the rivet head as was found by Müller [1] and Schijve [2].
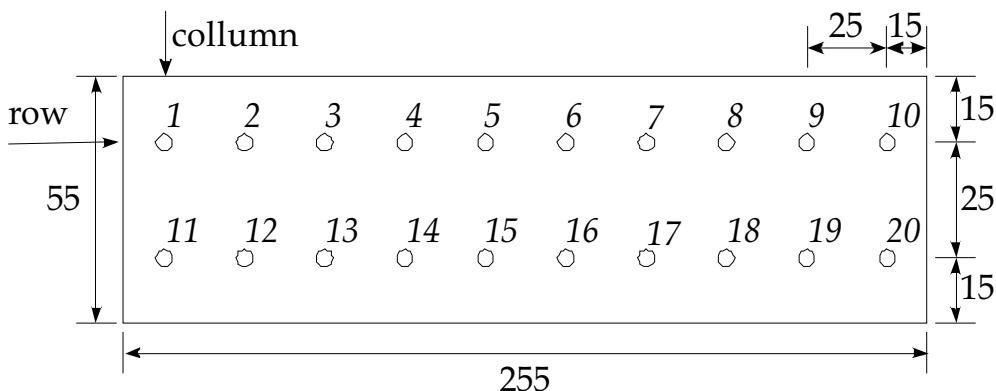
Figure 4-3   Two sheet specimen with two rows of rivets (all dimensions are in mm)

Table 4-2   Configurations for driven head dimension measurements, see Table 4-1 and Appendix F for rivet type clarification. [(1)] Total thickness of combined sheets

| Sheet material | t [mm][(1)] | Rivets | | | | | |
		D_0 [mm]	L_0 [mm]	H_0/D_0	Mat.	Rivet Code	Code
2024-T3 clad	4.00	4.0	9.5	1.38	*AD*	NAS 1097 *AD* 5-6	A.1
	4.00	4.8	11.1	1.48	*D*	NAS 1097 *D* 6-7	A.2
	6.30	5.6	16.0	1.73	*2017A*	EN 6101*D* 7-10	A.3
	4.00	4.0	9.5	1.38	*D*	NAS 1097 *D* 5-6	A.4
	4.00	4.0	8.0	1.00	*AD*	EN 6101*AD* 5-6	A.5
	4.00	4.0	9.0	1.25	*AD*	EN 6101*AD* 5-5	A.6
	4.00	4.0	10.0	1.50	*2017A*	EN 6101*D* 5-6-5	A.7
	4.00	4.0	9.0	1.25	*AD*	MS20470 *AD* 5-5-5	A.8
	4.00	4.8	11.0	1.46	*2017A*	EN 6101*D* 6-7	A.9
	4.00	4.8	11.0	1.46	*AD*	EN 6101*AD* 6-7	A.10
	4.00	4.8	11.1	1.48	*AD*	NAS 1097 *AD* 6-7	A.11
	4.00	4.8	9.0	1.04	*AD*	EN 6101*AD* 6-5-5	A.12
	4.00	4.8	10.0	1.25	*AD*	MS20470 *AD* 6-6-5	A.13
Glare 3-3/2-0.3	2.80	4.8	10.0	1.50	*2017A*	MS20470 *D* 6-6-5	G.1
Glare 3-6/5-0.4	7.30	4.8	13.0	1.19	*2017A*	MS20470 *D* 6-8	G.2
Glare 3-6/5-0.4	7.30	4.8	16.0	1.81	*2017A*	MS20470 *D* 6-10	G.3
Glare 3-8/7-0.5	11.50	4.8	16.0	0.94	*2017A*	MS20470 *D* 6-10	G.4
Glare 3-8/7-0.5	11.50	4.8	20.0	1.77	*2017A*	MS20470 *D* 6-12-5	G.5
Glare 4B-3/2-0.3	3.30	5.6	14.0	1.91	*2017A*	EN 6101*D* 7-9	G.6
Glare 3-3/2-0.3	2.80	5.6	13.0	1.82	*2017A*	EN 6101*D* 7-8	G.7
Glare 3-6/5-0.4	7.30	5.6	13.0	1.02	*2017A*	EN 6101*D* 7-8	G.8
Glare 4B-6/5-0.5	9.75	5.6	16.0	1.12	*2017A*	EN 6101*D* 7-10	G.9

Manufacturing of the specimens is done in the following manner. The holes are drilled 0.1 mm larger, according to Fokker specifications [4], then the nominal diameter of the rivets listed in Table 4-2. The two rows in each specimen are filled with one specific type of rivet and a force controlled riveting machine is used to complete each specimen. Using a force controlled riveting machine allows for a well-defined riveting quality of all specimens.

The riveting force used for a specimen depends on the initial rivet diameter D_0. To find a relation between the applied squeeze force and driven head geometry, a sequence of increasing squeeze forces was used for each of the two rows present in a specimen. Each specimen thus delivers a double set of measured driven head dimensions for a range of squeeze forces. Three different rivet diameters are used, requiring different squeeze forces. The squeeze forces are applied in a force controlled riveting machine capable of reproducing the riveting process for each specimen. The force controlled riveting machine is shown in Figure 4-4. The

accuracy of the riveting machine is constant. In the load train a load cell is built in to measure the applied load by the force driven piston. Each rivet is therefore installed with a known squeeze force.

Figure 4-4   Force controlled hydraulic riveting machine

The squeeze force for rivets with D_0 = 4.0 mm starts at 5 kN which is increased with steps of 2.5 kN up to 22.5 kN maximum. The squeeze force for rivets with D_0 = 4.8, is increased with steps of 5 kN from 5 kN to 40 kN. The final rivet diameter used in this investigation D_0 = 5.6 mm, this rivet is squeezed into shape using squeeze forces of 10 kN and 20 kN before steps of 5 kN going up to a maximum of 50 kN are used. The squeeze forces and the magnitude of the steps is related to the rivet diameter in order to include squeeze stress values similar to data found in the open literature on similar research [1], [2], [3].
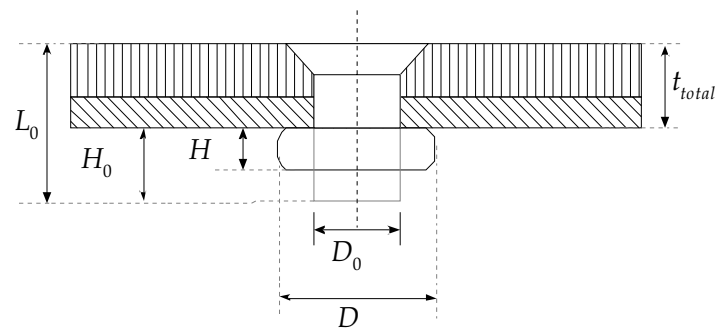
Figure 4-5   Rivet dimensions before and after riveting, with diameter D_0 and height H_0 initial values before riveting. D and H are the values for the diameter and height after the riveting process is completed

The dimensions of the driven rivet head are measured using a digital caliper providing an accuracy of 0.01 mm. Three measurements were made on each rivet head, two of the driven head diameter D, one in the width direction of the specimen and the second one perpendicular to the first measurement in the length direction of the specimen. Due to the force controlled riveting process very low scatter of the measured diameter D was found, this allowed for only two measurements of the rivet diameter D to obtain accurate geometry data. The third measurement is taken of the driven rivet head height H. Since two identical rows with respect to the squeeze force and rivet type are used, a duplicate set of measurements is obtained. All data from these measurements can be found in Appendix F.3.

4.5 Relation between riveting variables

As mentioned before, there are three categories in which the riveting variables can be separated; the rivet material, rivet geometry and the combination of sheet material and sheet geometry. The complete test matrix in Table 4-2 showed several sheet thicknesses and sheet materials, three different rivet diameters D_0, and a variety of different H_0/D_0 values. The measured values, for each load increment are the rivet diameter D and rivet length H.

4.5.1 Rivet material

Both Müller and Schijve reported a rivet material influence on the squeeze parameters. Results reported by Schijve and from the present measurements are shown in Figure 4-6. The results reported by Schijve dealt with AD (2117-T4), DD (2024-T4) and E (7050-T73) rivets. Added to this investigation are the rivet material designations D (2017-T4) and 2017A.

The data in Figure 4-6 show an increase of the driven diameter D for an increasing squeeze force. This figure also shows clearly the formability of the different rivet materials. Clear from this figure is the influence of the rivet material; the softer rivet materials obtain a larger deformation with respect to the squeeze force. The similar results obtained with AD-rivets and 2017A-rivets is related to the composition of the aluminum alloy. The D-rivet is made of 2017-T4 aluminum alloy, the 2017A-rivet is based on the same composition as the D-rivet with a different grain size effecting the ability to use the 2017A-rivet without any heat treatment and resulting in a different shear strength. The D-rivet without heat treatment should require a higher squeeze force to obtain a similar diameter D value, resulting in a shift of the curve down to the DD-rivets and E-rivets.
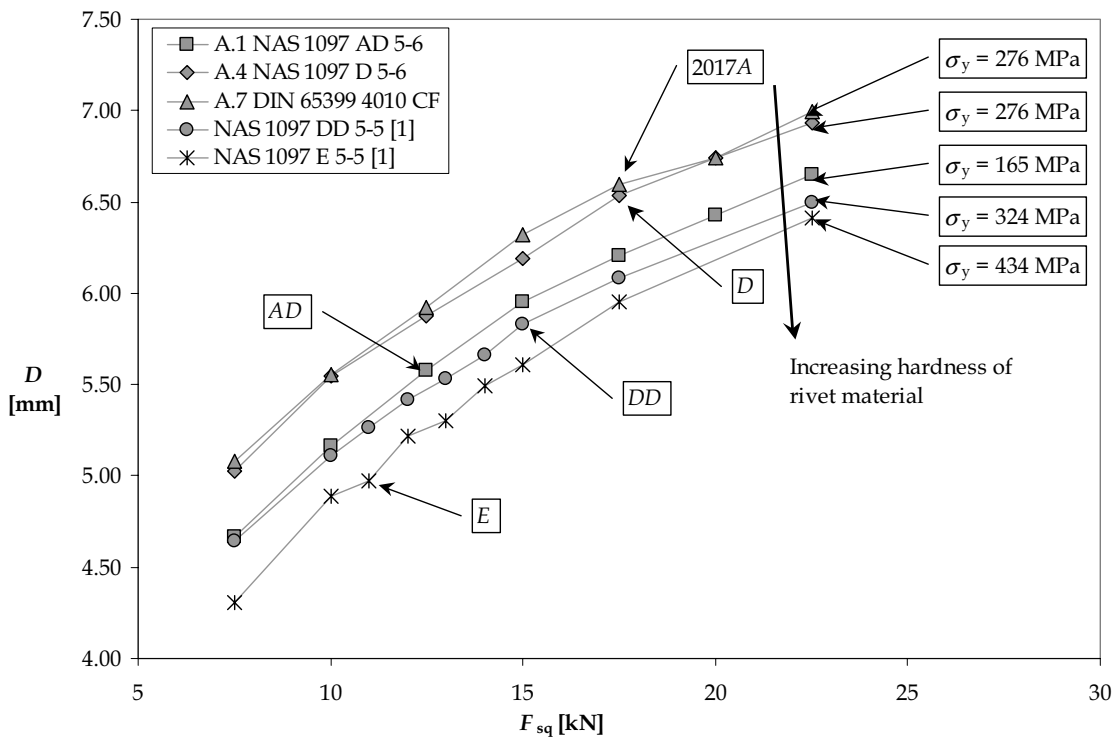
Figure 4-6 **Driven head diameter D as function of the squeeze force F_{sq}, for five different rivet materials. Hole diameter $D_0 = 4.0$ mm and $1.38 < H_0/D_0 < 1.50$, the sheet thickness for the results from [1] are half the total thickness of specimens A.1, A.4 and A.7 of 4.0 mm. Sheet material with countersunk holes for all specimens shown is 2024-T3**

4.5.2 *The sheet material*

In the test matrix shown in Table 4-2 the influence of the sheet material is not taken into account as a parameter to be investigated. This is based on the results published by Müller [1] and later Schijve [2]. Because of the minimum amount of rivet material that flows into the rivet hole during the rivet squeezing process, the influence of the type of sheet material can be neglected in determining a relation between the geometry of the driven rivet and the squeeze force. Assuming that the driven head has a cylindrical shape. The volume of the rivet head is:

$$V = \frac{1}{4}\pi D^2 H \qquad \textbf{(4-1)}$$

Before squeezing started the volume of the protruding shank is:

$$V_0 = \frac{1}{4}\pi D_0{}^2 H_0 \qquad \textbf{(4-2)}$$

The ratio V/V_0 for an increasing squeezing force as obtained in seven different test series is plotted in Figure 4-7. The ratio remains approximately 1.00, this confirms that the volume changes inside the hole are negligible. Some elastic deformation inside the hole will remain after squeezing. However, the plastic strains occurring during squeezing are much larger then the elastic strains. Ignoring the elastic strain, a constant V/V_0 ratio should be expected because the volume strain during plastic deformation is generally observed to be practically zero.
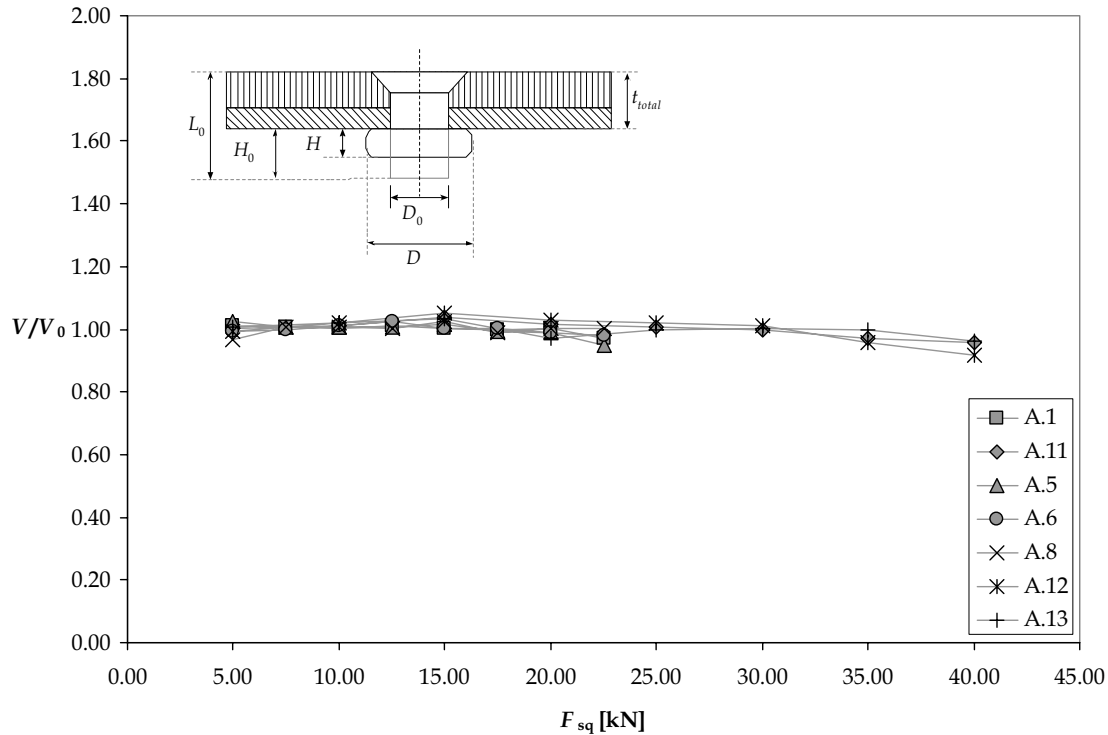
Figure 4-7   **Negligible volume changes in forming of the driven rivet heads as observed in seven different test series**

4.5.3 *Rivet shape*

With the knowledge that the volume V_0 of the protruding rivet head remains nearly constant during the forming of the rivet head, a relation between the rivet diameter D and the protruding rivet head H is obtained by rewriting Eqn. (4-2).

$$H = \frac{4V_0}{\pi D^2}$$

$$D = 2\sqrt{\frac{V_0}{\pi H}}$$

(4-3)

Figure 4-8 shows the results of calculated rivet height H values for measured rivet head diameter D. Since the initial rivet height H_0 and rivet diameter D_0 are known, the volume V_0 can be calculated for each rivet. The graph confirms that the constant volume concept gives accurate results.
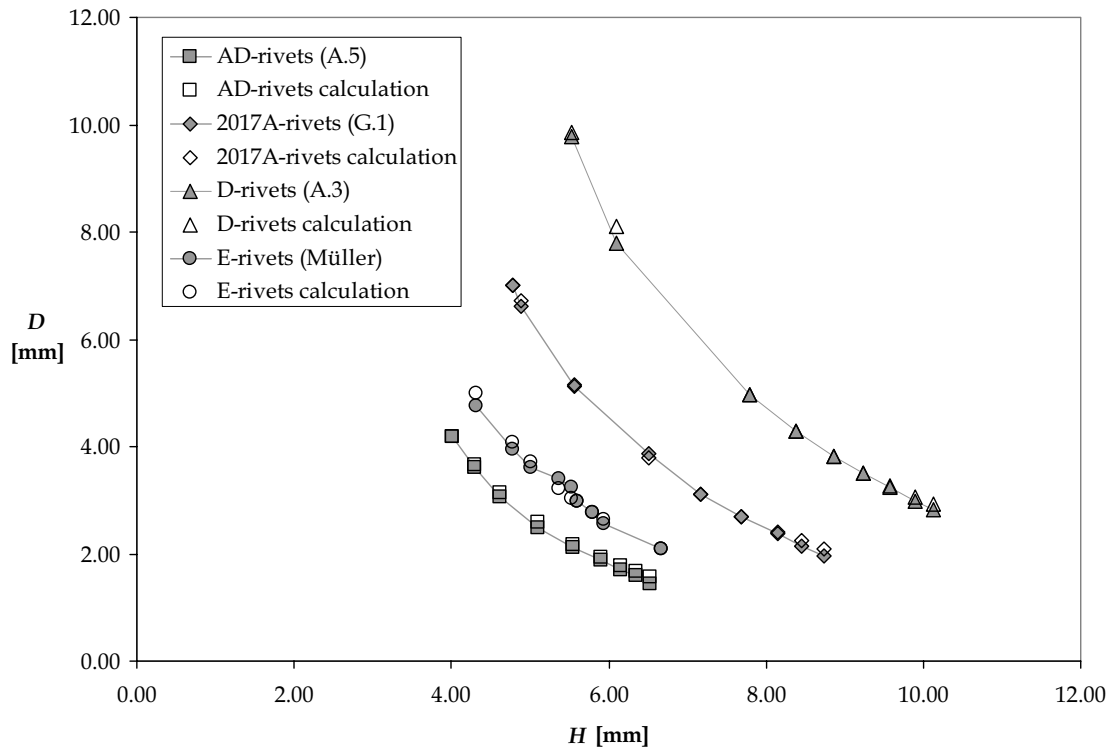
Figure 4-8 **Measured and calculated rivet head diameter D as a function of the measured rivet head height H (four test series)**

Figure 4-9 shows the relation between the driven rivet head dimensions D, H and the squeeze force F_{sq} for $D_0 = 4.0$ and 4.8 mm respectively. Figure 4-9 clearly shows that a higher squeeze force is required to deform the rivets with initial diameter $D_0 = 4.8$ mm. Both the protruding and countersunk head rivets display a similar D vs. F_{sq} curve and H vs. F_{sq} curve for the same D_0. The measurements for the protruding head rivets, A.8 D, A.8 H, A.13 D and A.13 H, are into the same range as for all the countersunk rivet head measurements. This is related to the limited amount of rivet material of the shank that flows into the hole area. The measurements are grouped nicely together. This grouping implies that the influence of the shape of the rivet, being countersunk or protruding, may therefore be safely ignored in the relation between the driven head and the squeeze force. The rivet head shape, countersunk or protruding rivets, does not affect the forming of the driven rivet head significantly. This confirms the findings by Müller and Schijve about the influence of the rivet shape.

Scatter of the results of the D measurements is fairly small, which may be associated with a similar rivet diameter and a similar total sheet thickness for all specimens of 4.00 mm. Differences between the H measurements are a result from the differences in the D_0/H_0 ratio for the specimens in Figure 4-9, varying from 1.00 to 1.50. In order to account for the effect of both the initial diameter D_0 and initial height H_0, the measurements will be normalized to H/H_0 and D/D_0 values. This will shift the lines for the diameter closer together and the height measurements closer to one another. The effect for the measured height will be most significant because, the initial rivet height H_0 shows more variability than the rivet diameter, see Table 4-2.
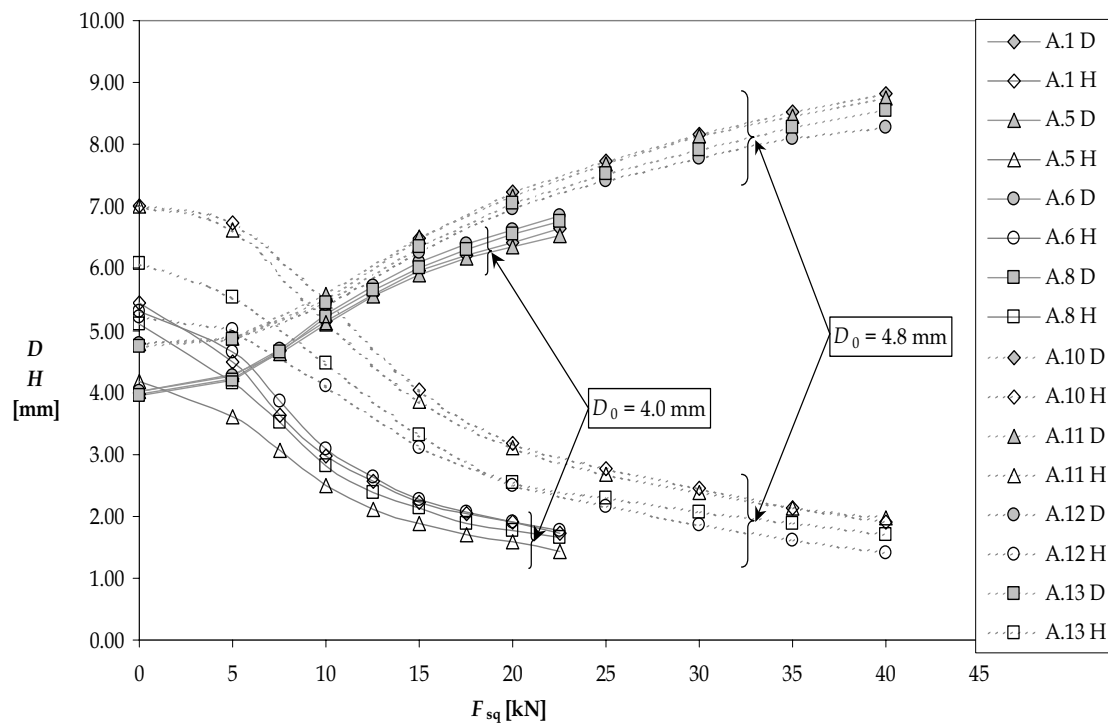
Figure 4-9 **Relation between the rivet dimensions of the driven head and F_{sq} for specimens with a total sheet thickness 4.0 mm; number A.1, A.5, A.6, A.8, A.10, A.11, A.12 and A.13. All specimens are countersunk rivets with exception of specimen A.8 and A.13 representing the results for protruding AD rivets**

The effect of the differences in squeeze force can be taken into account by using a squeeze stress σ_{sq}. This squeeze stress is defined as the true stress, i.e. the stress value associated with the actual deformed area.

$$\sigma_{sq} = \frac{F_{sq}}{\frac{1}{4}\pi D^2} \tag{4-4}$$

The normalized dimensions of the driven rivet head as a function of the squeeze stress for the data of Figure 4-9 are shown in Figure 4-10. The normalized measurements are now converging which is favorable to establish a relationship between the squeeze force and the driven head dimensions.
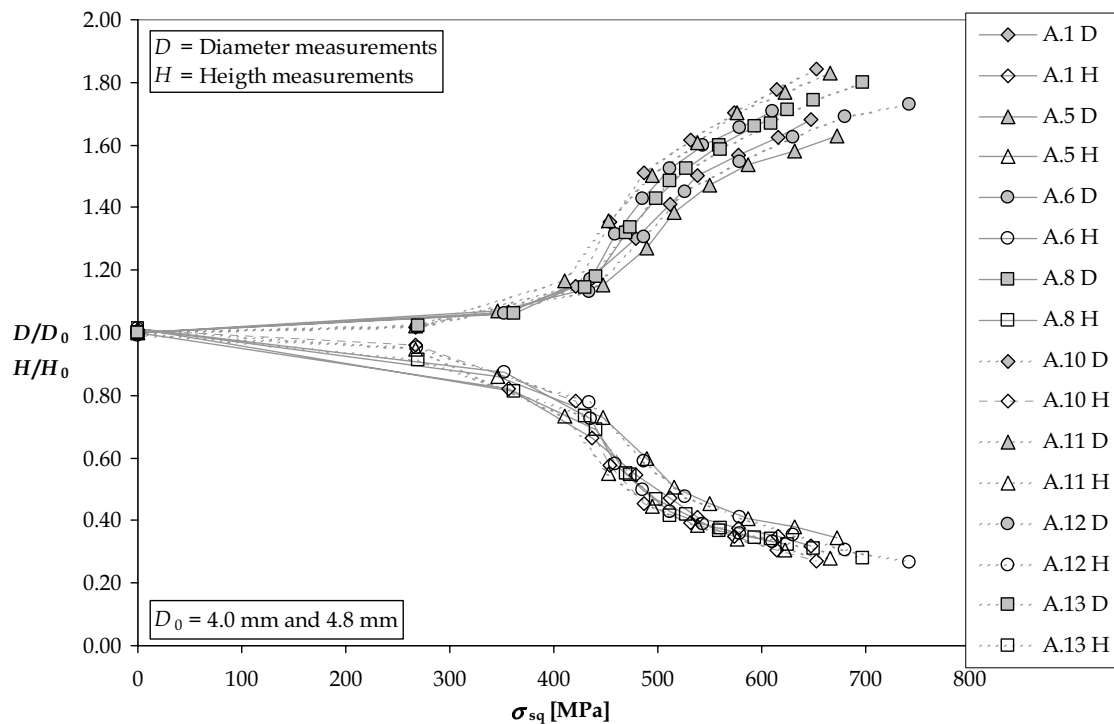
Figure 4-10 Relation between the normalized rivet dimensions of the driven head and σ_{sq} for specimens with a total sheet thickness 4.0 mm; number A.1, A.5, A.6, A.8, A.10, A.11, A.12 and A.13. All specimens are countersunk *AD* rivets with exception of specimen A.8 and A.13 representing the results for protruding *AD* rivets

Figure 4-11 gives a representation of the results for the few *D*-rivets used in this investigation. Figure 4-12 shows the results for the driven head dimensions for both aluminum and Glare sheet material. In both figures, the driven head dimensions are normalized using the initial dimensions of the rivets used. Although only two measurements are plotted in Figure 4-11 the trend is expected to be similar to the measurements of the driven rivet heads shown in both Figure 4-10 and Figure 4-12.
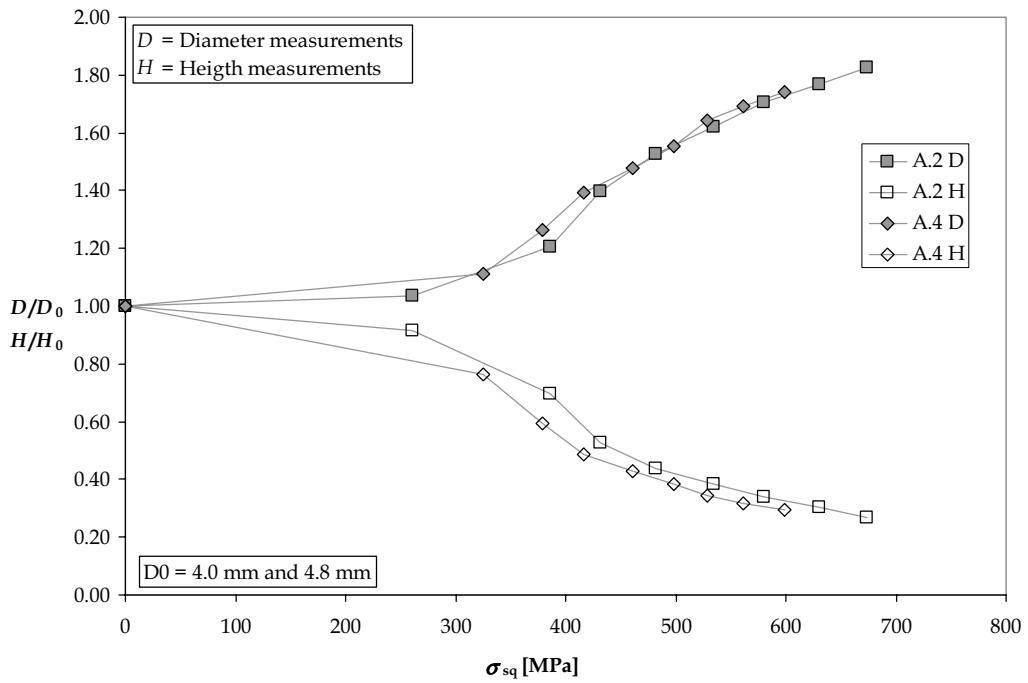
Figure 4-11 Relation between the normalized rivet dimensions of the driven head and σ_{sq} for specimens with a total sheet thickness 4.0 mm; number A.2 and A.4. All specimens are countersunk D rivets
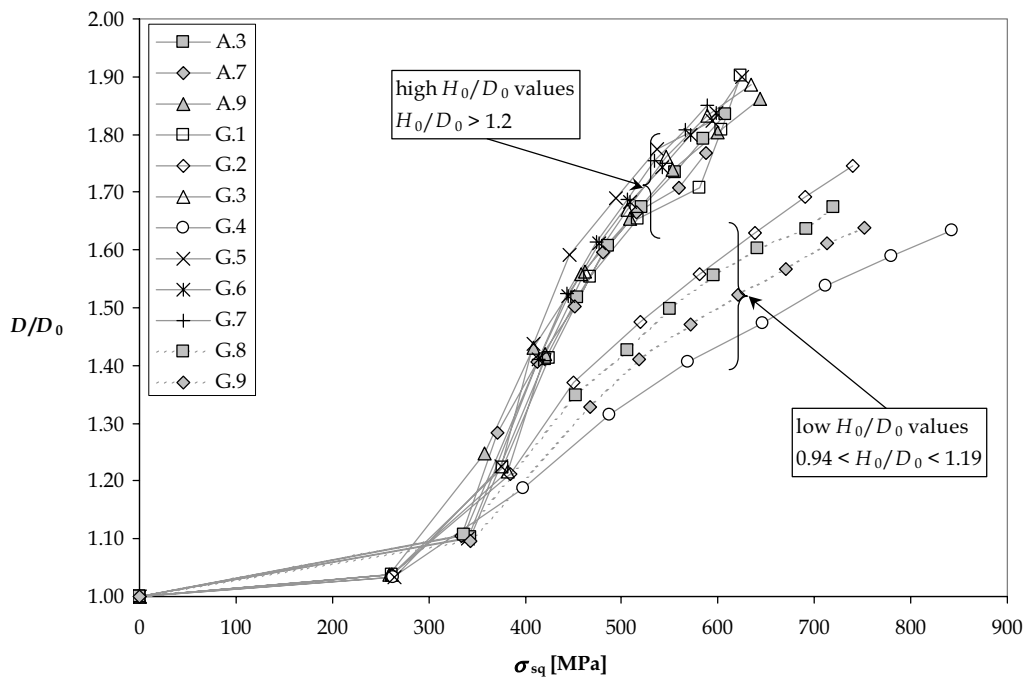
Figure 4-12 Relation between the normalized rivet dimensions D/D_0 of the driven head and σ_{sq} for specimens with different sheet materials and different total sheet thickness; A.3, A.7 and A.9 are aluminum sheets and G.1 to G.9 are different Glare grades. G.1, G.2, G.3, G.4 and G.5 are protruding head rivets, A.3, A.7, A.9, G.6, G.7, G.8 and G.9 are countersunk rivet results for protruding 2017A rivets

For low H_0/D_0 ratios, see Figure 4-12, the driven head measurements D deviate from the general trend. Curves G.2, G.4, G.8 and G.9 represent the low H_0/D_0 ratio. For $H_0/D_0 > 1.40$ the protruding rivet height has no influence on the diameter ratio D/D_0. For a small protruding rivet height ($H_0/D_0 < 1.40$) an influence of the squeeze force on the formed rivet head shows up clearly. This difference is most significantly observed in Figure 4-12, with the 2017A-rivets and in lesser detail in Figure 4-10 representing the AD-rivets. From the normalized driven head height H/H_0, the influence of the H_0/D_0 ratio is not present. Figure 4-13 shows the rivet dimensions H/H_0 the influence of the low H_0/D_0 ratios does not show up as clearly as is seen in Figure 4-12.
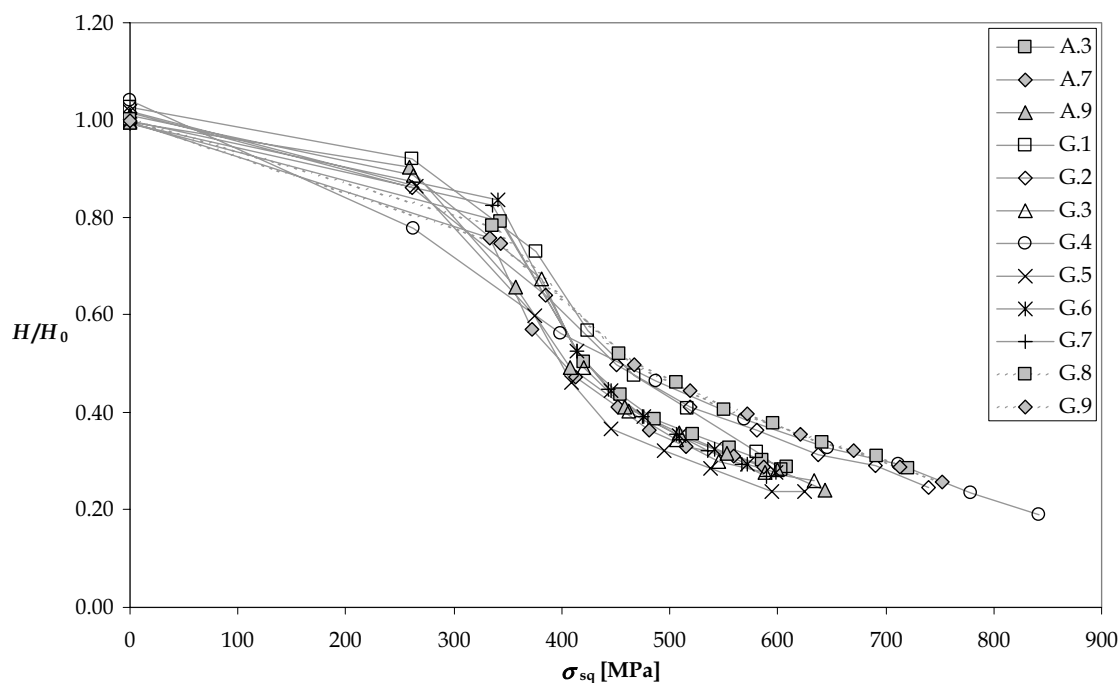
Figure 4-13 Relation between the normalized rivet dimensions H/H_0 of the driven head and σ_{sq} for specimens with different sheet materials and different total sheet thickness; number A.3, A.7 and A.9 are aluminum sheets and G.1 to G.9 are different Glare grades. Specimen number G.1, G.2, G.3, G.4 and G.5 are protruding head rivets, specimen numbers A.3, A.7, A.9, G.6, G.7, G.8 and G.9 are countersunk rivets representing the results for protruding 2017A rivets. Results for G.2, G.4, G.8 and G.9 are for low H_0/D_0 values.

4.6 Relation between F_{sq} and the driven head dimensions

Obtaining an empirical relation between the squeeze force and driven head dimensions is not a simple task. The riveting process is a highly non-linear forming process. The observation of a constant volume for the rivet protruding the sheets as observed in section 4.5.2 and 4.5.3 can help to derive a relation between the squeeze stress and the deformation of the rivet head.
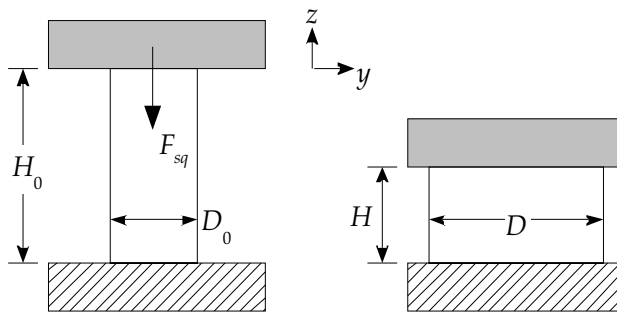
Figure 4-14 Idealized deformation of the driven rivet head based on the constant volume requirement in compression

Figure 4-14 shows an idealized forming of the protruding rivet head. The final shape of the rivet in the idealized situation differs from the actual shape, which is like a barrel. The idealized shape is used to derive the relation between the squeeze force and formed rivet head.

The constant volume requirement is satisfied according to Figure 4-7, and therefore the following equation is valid [6]:

$$\varepsilon_x + \varepsilon_y + \varepsilon_z = 0 \tag{4-5}$$

For uniform compression as shown in Figure 4-15 the true uniform strain is:

$$\varepsilon_z{}^T = \ln\left(\frac{H_i}{H_0}\right) \tag{4-6}$$

And for the true stress for cold forming according to the Holloman model for uniform plastic deformation the equation is:

$$\sigma_{sq} = K\left(\varepsilon_z{}^T\right)^n \tag{4-7}$$

where K is the strength coefficient and n the strain-hardening exponent.
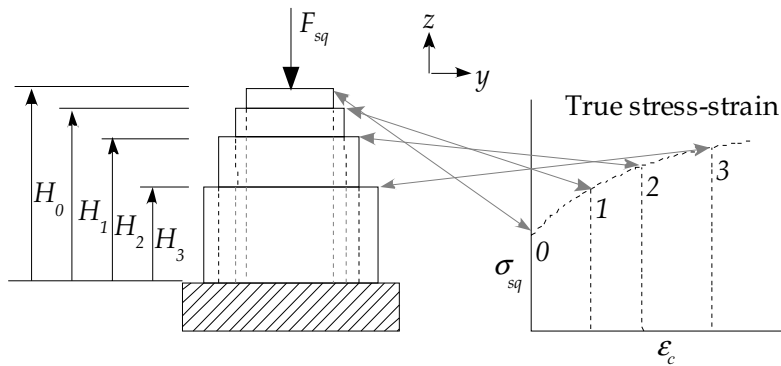
Figure 4-15   Relation between deformed rivet head and true stress-strain curve

With Eqn. (4-6) and (4-7), a relation between the formed rivet head and the squeeze force is found. The true strain ε^T is a function of the change in the protruding rivet height H, and since Eqn. (4-3) shows a relation between the rivet height H and the rivet diameter D, the true strains can also be expressed as a function of rivet diameter D.

$$\varepsilon^T = \ln\left(\frac{H}{H_0}\right) = \ln\left(\frac{4V_0}{\pi D^2 H_0}\right) = 2\ln\left(\frac{D_0}{D}\right) \tag{4-8}$$

Eqn. (4-7) contains two constants dependent on the aluminum alloy, K is the strength coefficient and n the strain-hardening exponent. The strain hardening coefficient n may have values from $n = 0$ (perfectly plastic solid) to $n = 1$ (elastic solid), K is the true stress at $\varepsilon^T = 1.0$. For most metals n has values between 0.10 and 0.50. For the alloys used in this investigation no proper strength coefficient K and strain hardening coefficient n for the Holloman equation were found in the literature. So values are estimated using true stress-strain data obtained from the rivet squeeze force and geometry measurements.

Table 4-3   Empirically derived constants for true stress strain curves

Aluminum alloy	K [MPa]	n
2117-T4	600	0.30
2017-T4	600	0.45
2024-T4	550	0.30
7050-T73	350	0.30
2017A	600	0.45

Combining Eqn. (4-4), (4-7) and (4-8) provides a relation between the applied squeeze force and the deformed rivet head height H and the rivet diameter D, or entirely as a function of the rivet diameter D.

$$F_{sq} = \frac{1}{4}\pi D^2 K \left(\ln\left(\frac{H}{H_0} \right) \right)^n$$

$$F_{sq} = \frac{1}{4}\pi D^2 K \left(2\ln\left(\frac{D_0}{D} \right) \right)^n$$

(4-9)

With Eqn. (4-9), a comparison between test measurements (F_{sq}, H, D) and the analytical results can be made. The following three figures, Figure 4-16 - Figure 4-18 show a good correlation between the analytical and measured data.
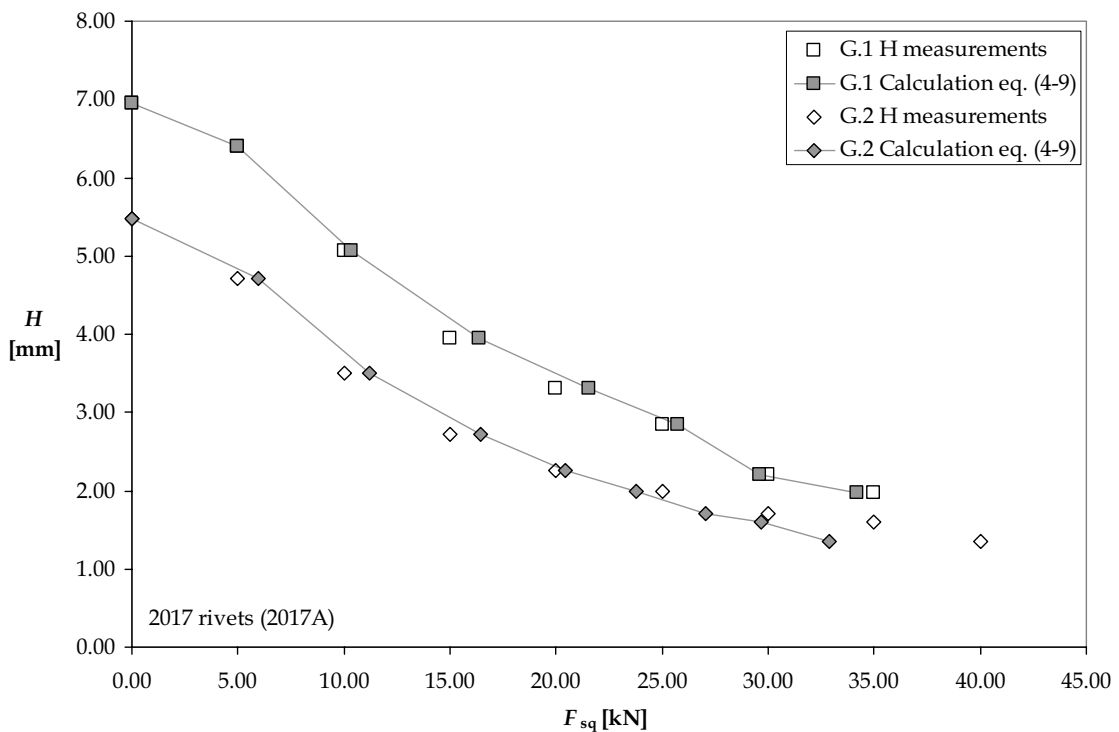
Figure 4-16 Rivet height H change vs. rivet squeeze force F_{sq} for two sets of specimens, calculated and measured values

96
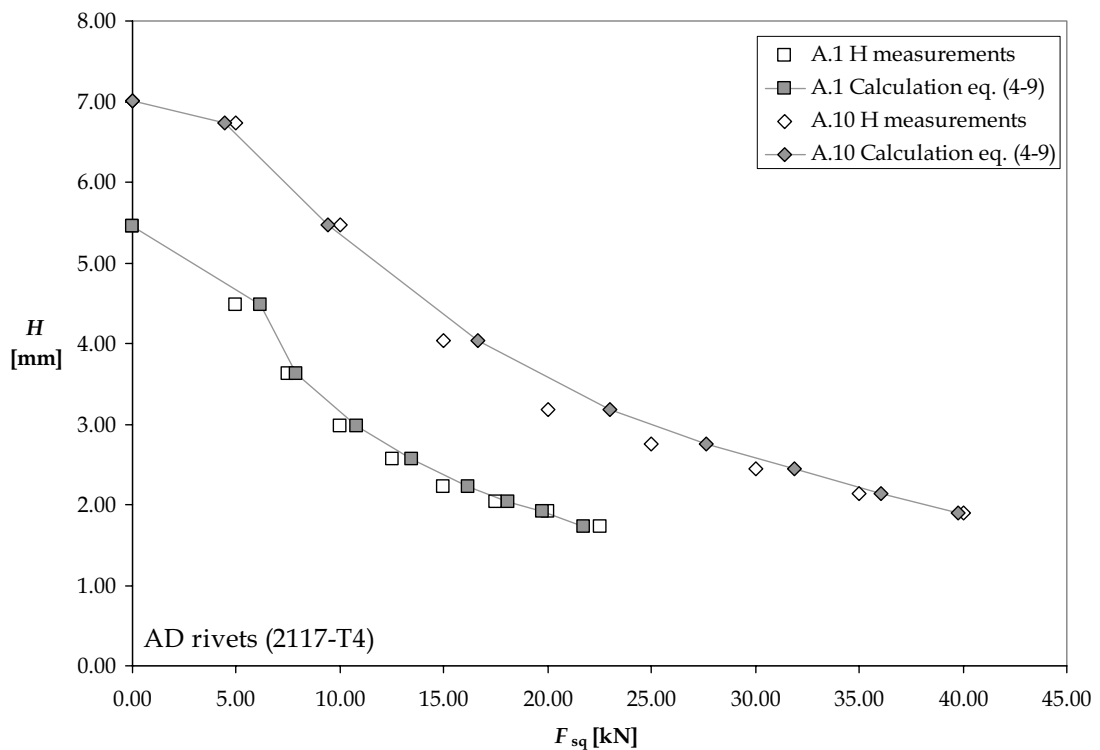
Figure 4-17 Rivet height *H* change vs. rivet squeeze force *F*$_{sq}$ for two sets of specimens, calculated and measured values
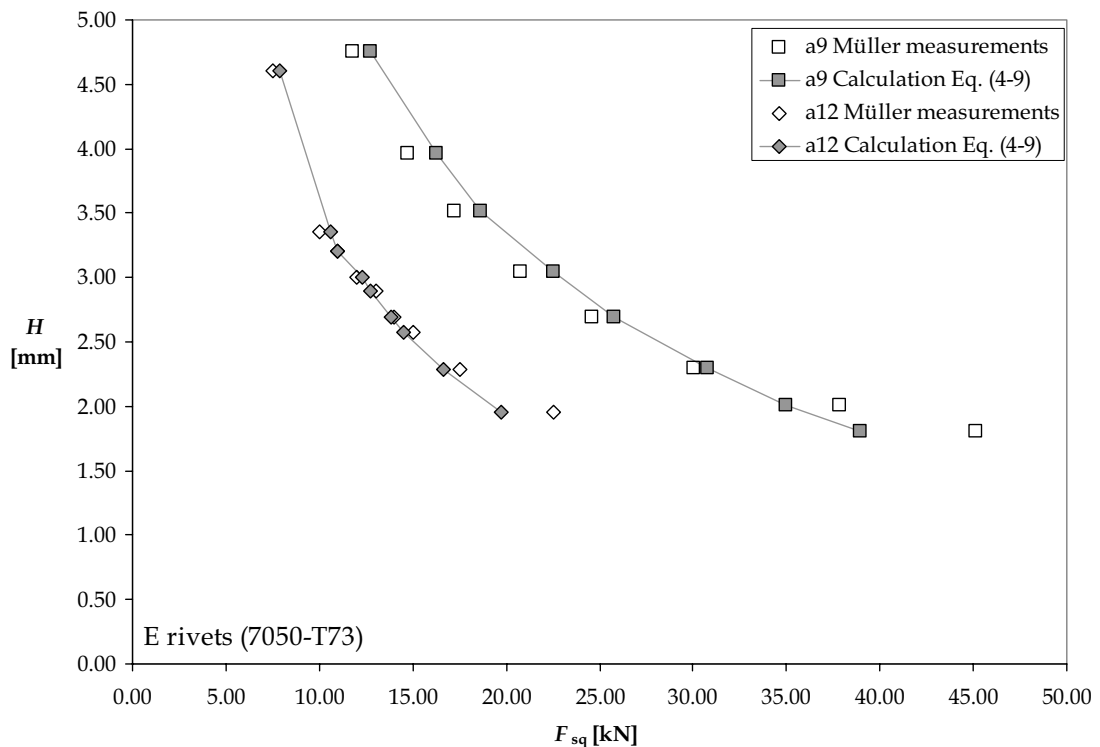
Figure 4-18 Rivet height *H* change vs. rivet squeeze force *F*$_{sq}$ for two sets of specimens, calculated and measured values

Eqn. (4-9) is valid for all rivet materials used in this investigation, the agreement for the *2017A*, *AD* and *E* rivets are generally good. However in Figure 4-16 series G.2 shows a large difference between the results of Eqn. (4-9) and the measured data. Figure 4-12 can help to explain this large difference for the G.2 test specimen. In this figure four test specimens, G.2, G.4, G.8 and G.9, showed a somewhat different deformation behavior than for the other rivets which is associated with a low H_0/D_0 (< 1.2), well outside the range of the rule of thumb for countersunk rivets as explained in section 4.3.2. According to this rule the shank length should be in the order of magnitude:

$$L_0 = t_{sheet} + D_0 + 1.0 \qquad\qquad\qquad (4\text{-}10)$$

For G.2 the initial rivet diameter $D_0 = 4.75$ mm and the total combined sheet thickness $t_{sheet} = 7.30$ mm gives a required rivet length $L_0 = 13.05$ mm (minimum $H_0/D_0 = 1.21$). The actual rivet length $L_0 = 12.85$ mm and actual $H_0/D_0 = 1.15$. Although the differences are minimal, the results in forming of the rivet head differ significantly. These deviating results can be understood by considering the relative amount of rivet material that flows into the rivet hole. For rivets with low H_0/D_0 values, the amount of rivet material that flows into the rivet hole is relatively large compared to rivets with higher H_0/D_0 values. The assumption that the volume of the protruding rivet head during plastic deformation is constant is therefore not valid for low H_0/D_0 values. Figure 4-19 shows the normalized volume reduction for the low H_0/D_0 value rivets.
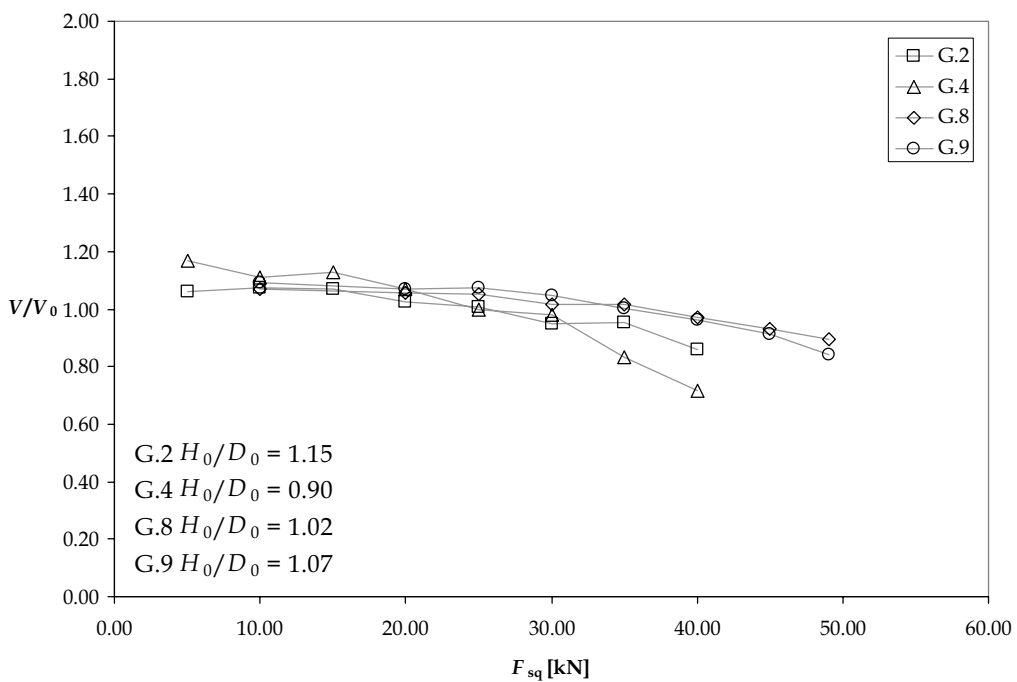
Figure 4-19 Volume reduction for low H_0/D_0 value rivets

4.7   Conclusions

The riveting process is a non-linear deformation process characterized by large plastic strains. The relation between the deformed rivet head and the applied squeeze force for the rivet materials *AD*, *D*, *DD* and *E* presented in this chapter allows for a good representation of the riveting process. The simple equations found can help to evaluate the riveting process when riveting forces are not known. With the initial rivet dimensions known and measuring the final shape of the deformed rivet head, the squeeze force can be calculated within a 10% accuracy for rivets with $H_0/D_0 > 1.2$.

For rivets with low $H_0/D_0 < 1.2$, the material flow of the forming rivet head into the rivet hole occurs throughout the complete forming process. The assumption that the volume of the deformed rivet head remains constant is for these rivets not valid. The simple equations derived in this chapter are therefore not valid.

The results presented in this chapter allows for the conclusion that once the strength coefficient *K* and strain hardening coefficient *n* are known for a rivet material; the equations presented in this chapter are valid for those rivet materials.

Since no accurate strength coefficient *K* and accurate strain hardening coefficient *n* for rivet materials were available during the investigation, it is not known if these values will increase the accuracy of the results presented in this chapter.

The assumption that the forming of the rivet head results in a completely cylindrical head differs significantly form the real barrel shape of the formed rivet. A more accurate volume and strain analysis can help to improve the relation between the formed rivet head *H*, *D* and the squeeze force F_{sq}.

4.8   Literature

[1]   Müller, R.P.G., *An Experimental And Analytical Investigation on the Fatigue Behaviour of Fuselage Riveted Joints, The Significance of the Rivet Squeeze Force, and a Comparison of 2024 T3 and Glare*, Dis. Delft University of Technology, Delft University Press, 1995

[2]   Schijve, J., *Some considerations on the correlation between the rivet squeezing force and the dimensions of the driven rivet head*, M-847, Aerospace Engineering, Delft University of Technology, March 1998

[3]   Hilling, B., *Driven rivet heads, definition of a squeeze parameter SQ (in German)*, Daimler-Benz Aerospace, Airbus, Report No.: DA-BRE-97-101, February 1997

[4]   Kandemir, Z., *A study on the geometry of the riveted head*, TZ-report Aerospace Engineering, Delft University of Technology, 2000

[5]   "Klinkverbindingen", Handleiding LR-27, 1980

[6]   Ludema, K.C., R.M. Caddel, and A.G. Atkins, *Manufacturing Engineering, Economics and Processes*, Prentice-Hall, Inc., 1987

5 Stress Intensity Factors

5.1 Introduction

The goal of the investigation reported in this chapter is to calculate accurate stress intensity factors for fatigue cracks emanating from open holes in sheet specimens loaded under pure tension and under combined tension and bending. The K values are used for crack growth predictions. The tension and bending case is of interest because it applies to various typical joint configurations in a pressurized aircraft fuselage. Due to the eccentricity of the neutral line of a joint, secondary bending will be present if the joint is loaded in tension.

Initially, fatigue cracks at the edge of a hole start as a part-through the thickness crack, which later becomes a through-the-thickness crack, a so-called through crack. But also for a through crack, the shape of the crack front is usually curved. Under combined tension and bending the crack length measured at both sides of the sheet will obviously be different. As a consequence, the geometry of fatigue cracks is an important variable of the present study.

The fatigue tests were carried out on specimens of AL 2024-T3 clad sheet material with three different thicknesses. In each specimen a single open countersunk hole was present. The specimens are described in Section 5.2 followed by a discussion on techniques to measure crack growth and to determine the shape of the crack front. The calculation of K values with a finite element analysis is discussed in Section 5.3. Some general comments on the K values are offered in Section 5.4. The results of the newly calculated stress intensity factors are presented in Section 5.5 and the crack growth predictions compared to test results are given in Section 5.6. The main findings of the present chapter are summarized in Section 5.7.

5.2 Experimental investigation

A thorough experimental investigation has been completed to document the crack growth shape and behavior for two dominant load conditions found in large aircraft fuselage joints: tensile and bending load conditions. These two load conditions dominate the crack shape and growth [1], [2]. Although bearing is very important for small cracks, the influence of pin loading has not been included in the experimental program. A special combined tension and bending specimen has been used to investigate the crack shape and crack growth behavior in different thickness aluminum sheets. In addition, using a special designed load spectrum allows for post-test fractographic crack reconstruction using a scanning electron microscope (SEM). Crack history reconstruction is also possible with a long working distance optical microscope [3]. The influence of the sheet thickness, load condition, and load spectrum are investigated in this section.

5.2.1 Fatigue specimens

All tests were carried out on a 100 kN MTS servo-hydraulic, closed loop machine shown in Figure 5-1. During all tests, the temperature and the relative humidity were recorded to determine that all tests were carried out under similar environmental conditions.

Figure 5-1   **100 kN MTS servo-hydraulic testing machine with combined tension and bending specimen**

As mentioned in Section 5.1 two load conditions usually found in large fuselage joint designs are tension and secondary bending. The tensile stresses are introduced by pressurization of the fuselage and secondary bending stresses develop by the eccentric load path inherent in fuselage joint design. Both load conditions influence the shape of cracks. Uniaxial tension fatigue tests are simple. However, to introduce secondary bending in an uniaxial test frame is challenging. A cyclic bending stress requires a more complicated test specimen [4], [5] or a complicated test fixture [6]. In [7] and chapter 3, it has been shown that a unique tension and bending (TB) specimen for testing thin sheet aluminum is possible. Extensive investigation into the behavior of this specimen showed a very good correlation between strain gage measurements, stresses calculated using the neutral line model, and finite element analysis [7]. Two series of test specimens were manufactured from six sheets of 2024-T3 clad aluminum alloy. Three different sheet thicknesses representing fuselage skin thicknesses were available for this test program, namely 1.0, 1.6 and 2.0 mm. Table 5-1 gives the number of specimens and some important parameters of the joint design. The countersunk geometry is not mentioned in Table 5-1. For both the tensile and TB-specimens, the angle of the countersunk was $\gamma = 100°$, diameter $d_1 = 4.80$ mm and width $W = 100$ mm, are equal.

Table 5-1   Parameters for 27 tension and 27 combined tension and bending specimens

No. of Specimens	3	3	3	3	3	3	3	3	3
Sheet thickness t [mm]	1.0			1.6			2.0		
Ratio b/t	0.05	0.25	0.50	0.05	0.25	0.50	0.05	0.25	0.50
Ratio r/t	2.4			1.50			1.20		
b [mm]	0.05	0.25	0.50	0.08	0.40	0.80	0.10	0.50	1.00

In order to create a realistic comparison to a fuselage lap-splice joint, the sheet orientation was chosen to match the orientation used in actual aircraft structures. The specimens were therefore tested in TL-orientation. Thus the crack growth is parallel to the grain (rolling) and perpendicular to the applied load direction.

The open hole tension specimen is used as a baseline test specimen. The results from this type of specimen serve as a baseline for the combined tension and bending tests. More specifically, the combined loading tests will show the influence of the bending stress on the crack growth behavior. The test matrix displayed in Table 5-1 shows that for both specimen types, similar tests will be performed, thus the bending will be the cause of any differences in crack growth behavior. Figure 5-2 shows the specimen geometry for the open hole tension specimen. The hole is centrally located in the sheet.
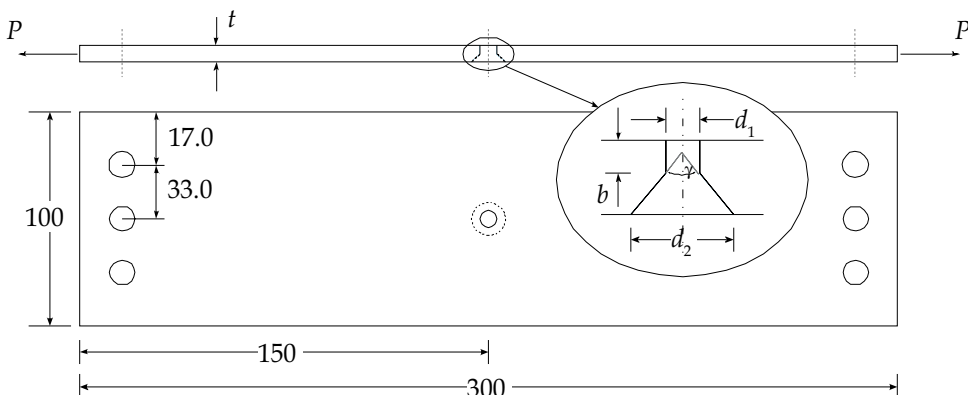
Figure 5-2   Open hole tension specimen with countersunk notch detail. All dimensions are in mm, were b is the height of the straight shank part and γ is the total countersunk angle

The production of the TB-specimen, shown in Figure 5-3, is as follows. The first step is to rid the aluminum parts of all grease and dirt over the area that will be bonded. This is done by placing the parts in a degreasing bath (P3RST™ 40 g/l) for twenty to thirty minutes, then the parts are placed in running distilled water for approximately five minutes. The next treatment step is acid etching; this will remove a few microns of the oxide layer from the surface in order to create a proper bonding surface. This treatment is done by immersing the aluminum parts for 20

minutes in a solution of Chromium acid (55 g/l), Sulfuric acid (275 g/l) and water at an average temperature of 60-65 °C. The final cleaning step is placing the parts for at least ten minutes in clean running water.
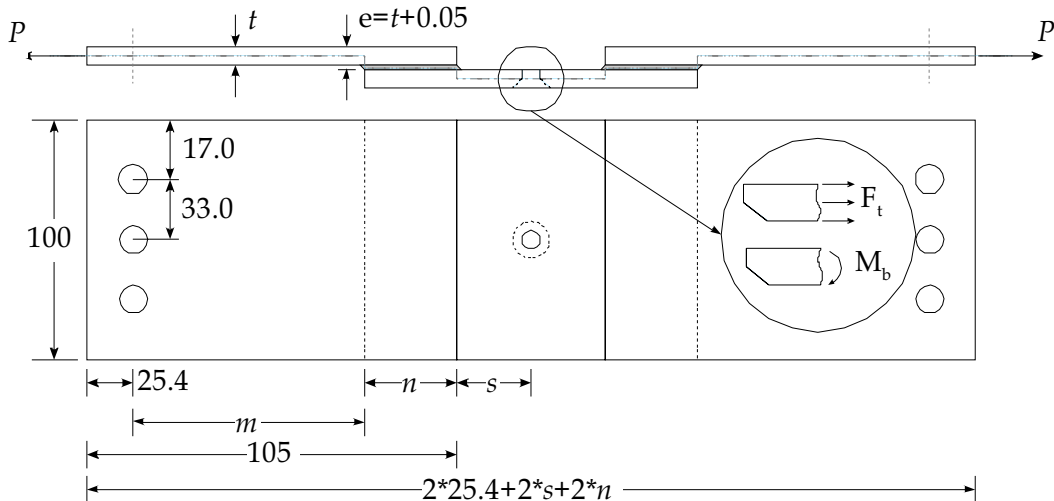
Figure 5-3   **Open hole tension and bending specimen. With *m*, *n* and *s* can be varied to change the bending factor k_b. All dimensions are in mm and all sheets are of equal thickness**

Following the surface treatments and drying of the parts the final step in manufacturing of the specimens can take place. If the time between the surface treatments and bonding of the separate parts is more then twelve hours, the oxide layer that was removed will slowly return on the surface. When that happens, the parts may not be properly bonded. The same process is used as pretreatment for AF-163X by Fawaz and de Rijck, [1] and [7], since none of those bonded joints failed when subjected to tensile stresses up to 200 MPa. The surface preparation is assumed to be adequate. The combined tension and bending specimens for this research were manufactured using FM-73M. Since none of the bonded joints failed, the surface preparation also suffices for FM-73M. The adhesives used by Fawaz and de Rijck and in this investigation have similar properties.

Following the surface preparation and drying of the specimen parts, each of the three aluminum parts were bonded together using an autoclave, see Figure 5-4, at an elevated temperature of 120 °C and 3 bar for 130 minutes. All specimens were manufactured in one autoclave cycle thus limiting possible manufacturing process variations. From the MIL-HNBK-5G [8] the influence of the cure cycle reduces the ultimate tensile strength by 1% and the yield strength by 4% of the sheet material. A reduction of 1% and 4% is not significant, and therefore the influence on the crack growth mechanism is assumed to be very small.
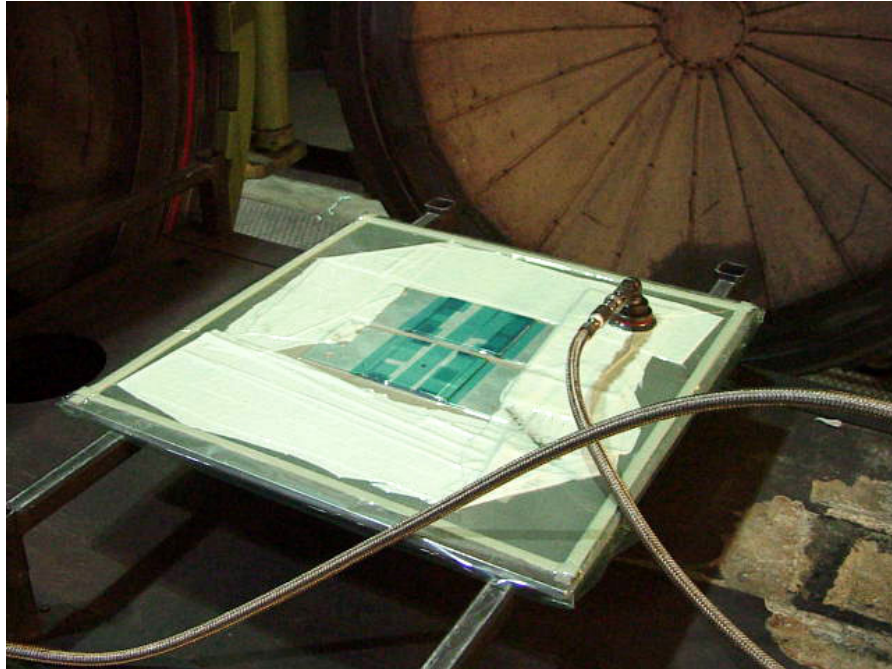
Figure 5-4 **Combined tension and bending specimen preparation for autoclave cycle**

By choosing the dimensions *m*, *n* and *s* as indicated in Figure 5-3 the appropriate bending stress could be obtained with great accuracy. The ratio of the normal stress caused by bending to the normal stress caused by membrane loading is referred to as the bending factor k_b defined as:

$$k_b = \frac{\sigma_{bending}}{\sigma_{tension}}$$ (5-1)

For the present test program the k_b values used (k_b=0.5) is a little higher then occurring in *in-service* applications [9]. It is chosen to induce a noticeable amount of bending stress into the test specimen. According to Fawaz and de Rijck, the degree of bending can easily be controlled by the geometry variable *s* [7]. A parametric study in [7] showed the influence of *s* on the bending at the center of the specimen. Parameters *m* (= 54.6 mm) and *n* (= 25 mm) are fixed and parameter *s* was varied to obtain the desired value for k_b at an applied maximum stress of 100 MPa. Table 5-2 gives the values of parameter s for three different sheet thicknesses.

Table 5-2 **Values of parameters for combined tension and bending specimens**

t [mm]	s [mm]
1.0	13.1
1.6	23.3
2.0	30.5

In order to initiate cracks simultaneously at both sides of the open hole, two small starter notches were introduced at opposite edges of the hole by a small score made by a knife blade (<0.05 mm). The starter notches were located at the lower side of the sheet, see Figure 5-5. In a lap-splice joint this side is the faying surface where two sheets are clamped together.

Crack shape 1   Crack shape 2   Crack shape 3
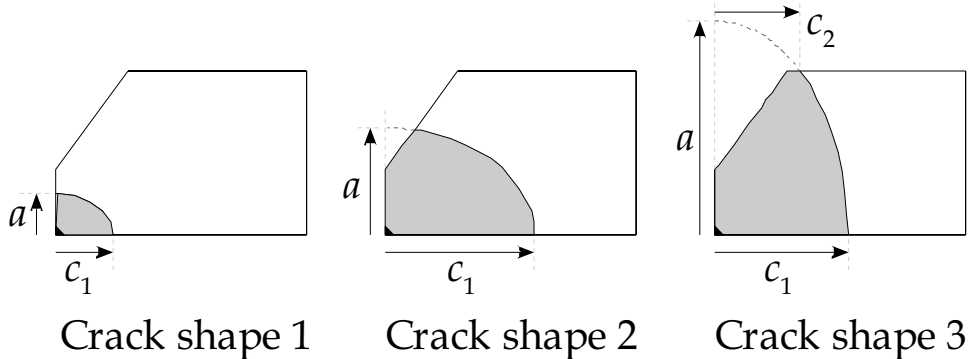
Figure 5-5   **Parameter definition of three different cracks, crack 1 is a corner crack, crack 2 is also a corner crack, but has penetrated the countersunk surface and crack 3 is a through the thickness crack. All cracks originated from small starter notch at the intersection of the straight shank and the lower surface**

5.2.2 *Crack measurements*

Crack length measurements were made by visual observations while the shape of the crack front was studied by post-test fractographic analysis in the SEM. Crack length measurements by the electric Potential Drop Method (ePDM) are attractive for through cracks with crack fronts perpendicular to the sheet surface [10]. However, in the present investigation ePDM observations would have been problematic for two reasons. First, initially part through cracks are present while the countersunk shape of the hole gives an additional complication. Secondly, secondary bending leads to slant crack fronts.

The visual *in-situ* crack length measurements were made with a traveling optical microscope (40x) and a tic-mark ruler on the specimen (accuracy 0.125 mm). Measurements were made at both sides of the sheet, c_1 and c_2, see Figure 5-5. This was done for cracks at both sides of the hole which implies four cracks tips to be monitored. All *in-situ* crack length measurements are compiled in Appendix C.

Fatigue is cyclical slip and is manifested as fatigue striations as shown in Figure 5-6, [11].
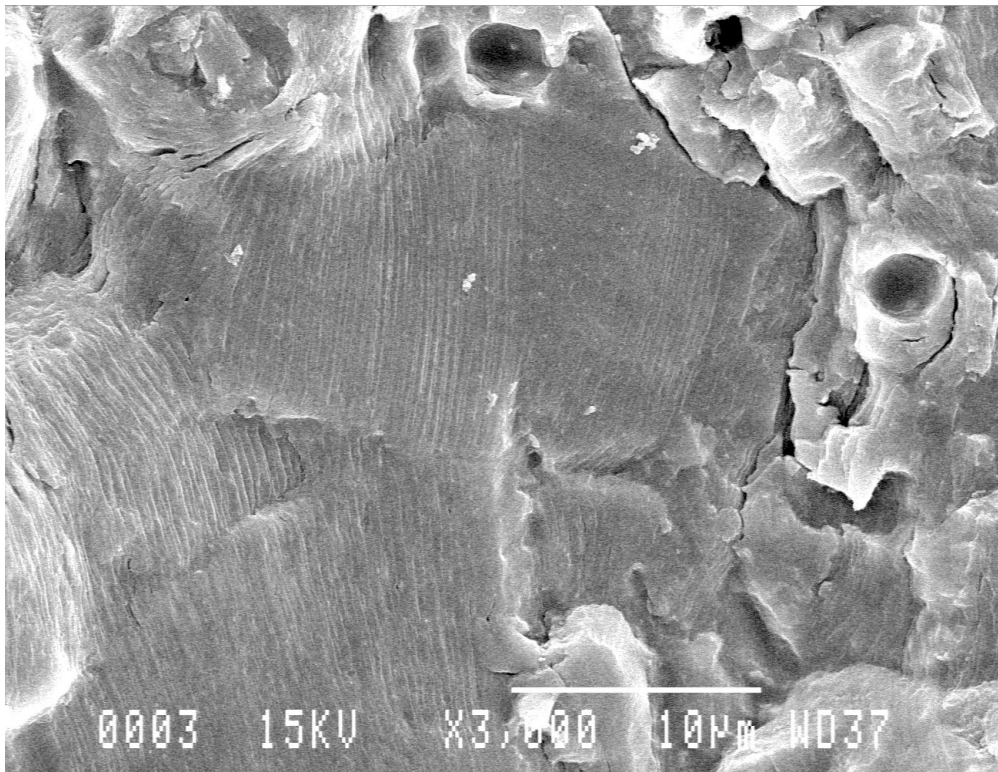
Figure 5-6   Visible striations on fracture surface

The shape of the crack front was analyzed by fractogrpaphic observations of striation patterns in the SEM. An example is given in Figure 5-6. Although local crack growth rates can be estimated from striation spacings, it is difficult to obtain crack front shapes from the striations only and to correlate these observations with the applied number of cycles. However, by applying so-called marker loads crack front shapes were introduced during previous investigations [1],[2],[12],[14] and crack front shapes could be deduced from SEM observations of the marker loads. It then is important to be sure that the effect of the marker loads on the crack growth is insignificant. Adding periodic larger cycles (overloads) to constant-amplitude base line cycles can introduce marker striations that can easily be observed as shown by Schijve [13]. However, he also found systematic crack growth retardation during the base line cycles.

Fawaz [2] successfully used the marker load spectrum shown in Figure 5-7 in crack growth tests on the present tension/bending specimen. The spectrum was previously used Piasick and Willard [14] to investigate crack fronts obtained in riveted lap joints. The spectrum includes batches of cycles with a smaller amplitude than the base line cycles and in those batches periodic blocks of 10 base line cycles.
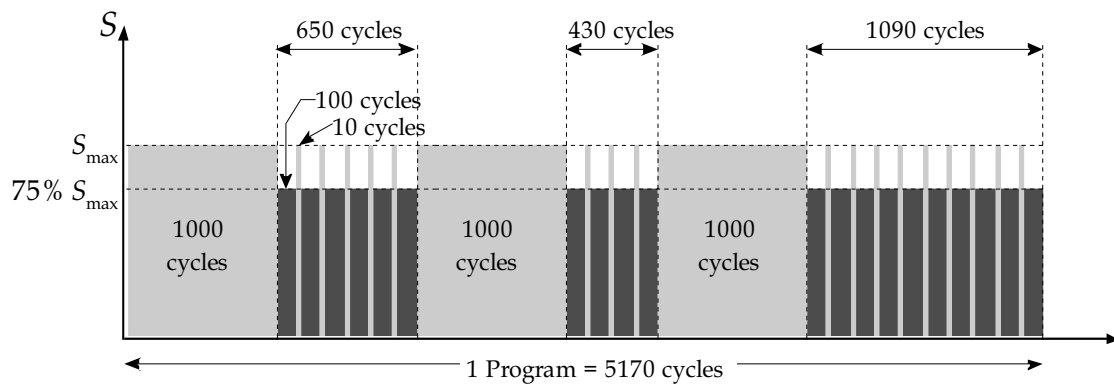
Figure 5-7   Blocked marker load spectrum

By having different numbers of those blocks (6, 4 and 10 respectively) the reconstruction of the the crack growth life should be possible. The spectrum was also used in the present tests. A *SEM* picture is shown in Figure 5-8 where the three different batches of marker loads are indicated by arrows. It should be pointed out that a full reconstruction of the advancing crack front requires many hours, and in some cases the marker loads are difficult to point out (10 block in Figure 5-8).
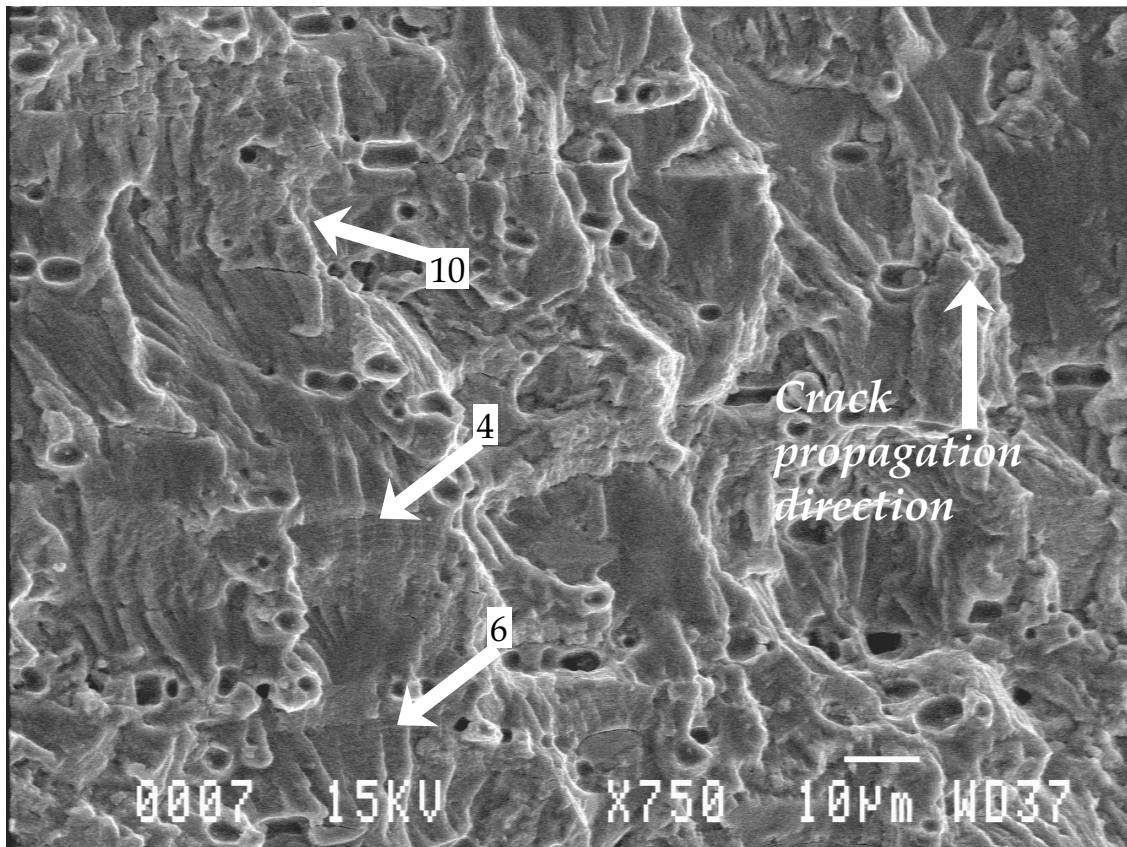
Figure 5-8   Visible marker bands on fracture surface, σ_t = 100 MPa and σ_b = 50 Mpa

The lower load levels (75% σ_{max}) will show up as dark lines or featureless bands on the fracture surface. The lower load levels have a smaller crack growth per cycle, so the striations are closer together and are not discernable at the same resolution used to find the 6-4-10 groups of marks. These "darker" bands are groups of 100 fatigue striations that can be seen at high magnification (5000x). The usefulness of marker bands is evident when some striations are not visible due to irregularities or damage on the fracture surface. Thus the missing mark can be deduced since the marker order is known. If for example, a band of ten is missed, then logically from the spectrum the following marker band should be a marker band with six distinct darker lines (six marker band). Figure 5-8 shows the usefulness of the marker load spectrum, the band of ten is difficult to detect. Using the spacing between the six and four marker band provides the location of the ten marker band. Although some very clear marker bands are visible, see Figure 5-8, for larger crack lengths the striation spacing increases rapidly. This makes it almost impossible to make the distinction between the marker bands and the baseline cycles. The fracture surface at larger crack lengths is dominated by micro voids due to the high ΔK. To avoid having problems determining the last marker band, the crack growth tests were stopped at a point were it was expected that the micro voids did not dominate the fracture surface. The experience of fractographic crack growth reconstruction obtained by de Rijck in [1] supported this approach. It was attempted to stop all tests after a ten marker band. The reconstruction begins then by finding the final ten-marker band, see Figure 5-9, and moving backwards to the edge of hole of the specimen. In order to reconstruct the crack shape as accurate as possible, several measurements were done to find the crack shape through the thickness.

Fawaz showed that the same marker load spectrum, as shown in Figure 5-7, did not influence the fatigue crack growth rate [2]. For the present test program almost all tests were done using $R = 0.1$, which differs from the R-ratio used by Fawaz ($R \cong 0$).

The following text will show that for $R = 0.1$ the influence of the marker loads is also negligible according to Elber's plasticity induced crack closure concept [15].

$$\left.\begin{aligned} S_{max} &= 100\ MPa \\ S_{min} &= 10\ MPa \end{aligned}\right\} \rightarrow R = 0.1, \Delta S = 90\ MPa \tag{5-2}$$

Using Elber's empirical U-ratio, which is only dependent on the stress ratio R:

$$U(R) = \frac{\Delta S_{eff}}{\Delta S} = 0.5 + 0.4R = 0.54 \rightarrow \Delta S_{eff} = 0.54\Delta S = 48.6\ MPa \tag{5-3}$$

$$S_{op} = \left(S_{max}\right)_{baseline\ cycles} - \left(S_{eff}\right)_{baseline\ cycles} = 51.4\ MPa \tag{5-4}$$
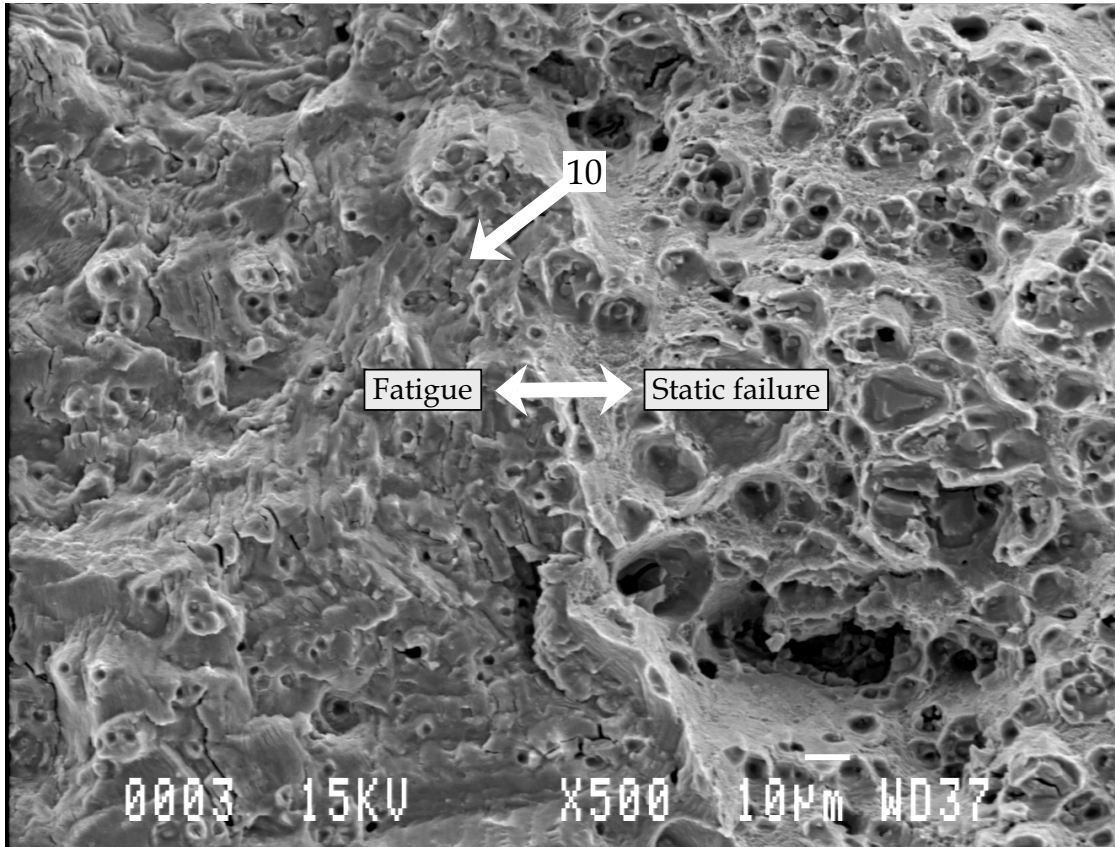
Figure 5-9   Last detectable marker band at the fatigue dominated fracture surface. Distinct line between fatigue dominated fracture surface and static failure.

Elber found that S_{op} remains approximately constant during a constant amplitude fatigue test. If S_{op} is constant then:

$$\left(\Delta S_{eff}\right)_{small\ cycles} = \left(S_{max}\right)_{small\ cycles} - S_{op} = 75 - 51.4 = 23.6\ MPa \tag{5-5}$$

$$\frac{\left(S_{eff}\right)_{small\ cycles}}{\left(S_{eff}\right)_{baseline\ cycles}} = 0.4856 \tag{5-6}$$

The relation between the da/dN and ΔK_{eff} can be described with the Paris relation where ΔK is replaced by ΔK_{eff} [16]. The concept of Elber is based on the fact that the fatigue crack growth rate depends on ΔK_{eff} only. Substituting ΔK_{eff} for ΔK:

$$\frac{da}{dN} = C\Delta K_{eff}^{n} = C\left(\beta\Delta S_{eff}\sqrt{\pi a}\right)^{n} \tag{5-7}$$

$$\frac{\left(\dfrac{da}{dN}\right)_{small\ cycles}}{\left(\dfrac{da}{dN}\right)_{baseline\ cycles}} = \left(\frac{\left(\Delta S_{eff}\right)_{small\ cycles}}{\left(\Delta S_{eff}\right)_{baseline\ cycles}}\right)^{n} = 0.4856^{n} \qquad\text{(5-8)}$$

With the Paris exponent $n = 3.3$, being the slope of the line plotted in Figure 5-10, the ratio between the crack growth of the hundred marker load cycles and the baseline cycles is then:

$$0.4856^{n} = 0.4856^{3.3} = 0.092196 \approx 9\% \qquad\text{(5-9)}$$

This means that the crack growth during the marker band of hundred cycles is about 9% of hundred baseline cycles, thus corresponds to 9 baseline cycles. With this information, the marker load spectrum can be corrected for the lower stress cycles in the spectrum. One program, which consists of 5170 cycles, reduces to 3354 baseline cycles. To validate the reduction method, two constant amplitude tests and four marker load tests were done. The results are shown in Appendix B, including the open-hole tension specimen in Figure B-1. Saw cuts were applied to all specimens to speed up the test and to reduce the scatter in nucleation time. Figure 5-10 shows a good agreement between constant amplitude tests and the marker load spectra tests. After correcting for the marker load, similar crack growth rates were obtained.
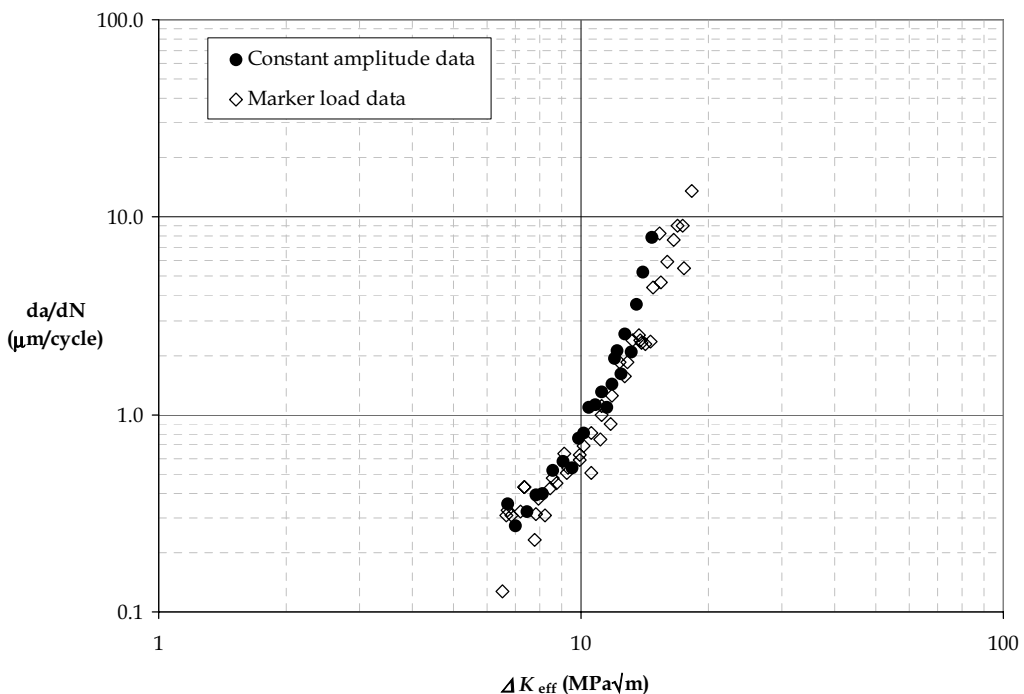
Figure 5-10 Crack growth rates of the tests corrected for the marker loads. Comparison with the constant amplitude tests

5.2.3 Influence of specimen thickness

The influence of the specimen thickness was investigated by Broek and Schijve [17]. They tested 2024-T3 specimens with thicknesses of 0.6, 1, 2, 3 and 4 mm and measured systematically faster crack growth in thicker specimens. The generally accepted explanation is associated with the plane strain/plane stress condition at the crack tip. More plane strain in a thicker specimen will cause smaller plastic zones, probably larger ΔK_{eff} values, and thus faster crack growth. The thickness effect has been explored for the Al 2024-T3 clad sheet materials used in the present research. The three thicknesses involved are 1.0, 1.6 and 2.0 mm respectively. The results in Figure 5-11 for tests at $R = 0.1$ and $S_{max} = 100$ MPa confirm that a thickness effect is present. This should be accounted for in the predictions.
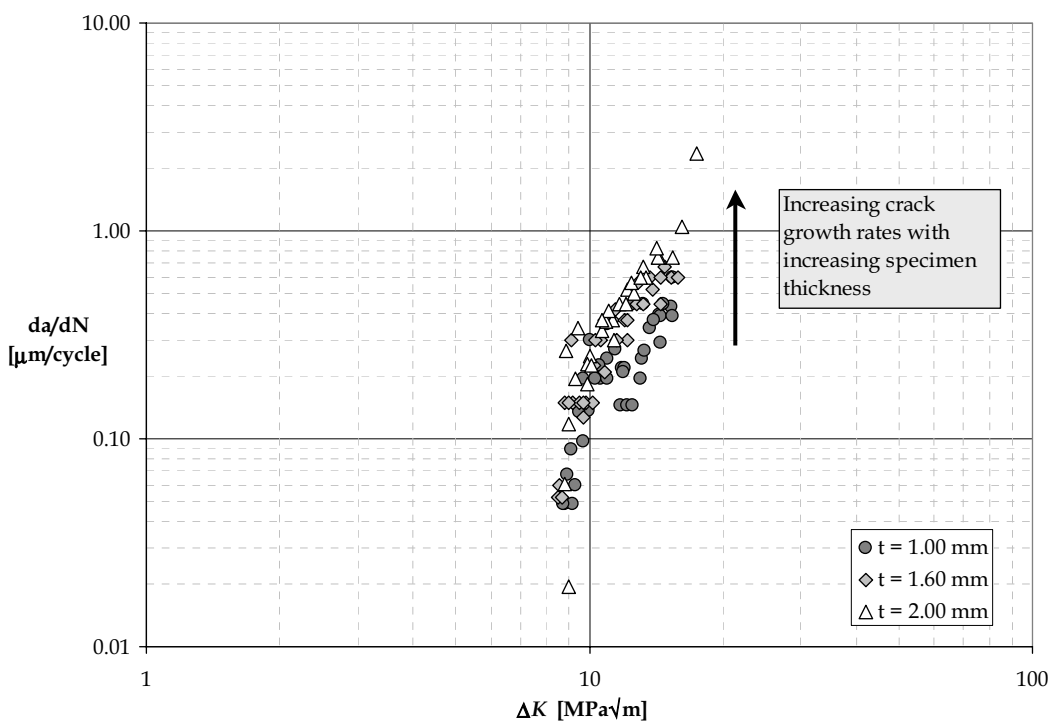
Figure 5-11 Crack growth rate data for three different specimen thicknesses

5.2.4 Crack shape

The crack shape throughout the growth history is of importance to verify the newly developed K solutions for cracks emanating from countersunk holes. As mentioned in section 5.2.2, the crack will most likely nucleate as a corner crack in a fastener hole at a location in a joint near or at the surface subjected to the highest strains. Whether the crack nucleation is due to fretting, inclusions or high stresses, this behavior is observed in *in-service* aircraft and in full-scale fatigue tests. Baldwin used both open-hole and lap-splice joint coupon specimens taken from a section of a retired USAF KC-135 [18] and showed the typical crack shape documented earlier

by Fawaz [2] and later again in [3], see Figure 5-12. Harris et al. also showed crack nucleation at the bore of the countersunk hole at the high stress side [19]. Vlieger and Ottens [20] carried out fatigue tests on representative longitudinal lap joints found in commercial aircraft. This research showed crack growth starting at the straight shank portion of the countersunk hole. Schijve presents in [21] a number of literature references on the subject of multiple side damage supporting the findings of crack growth characteristics for countersunk holes.
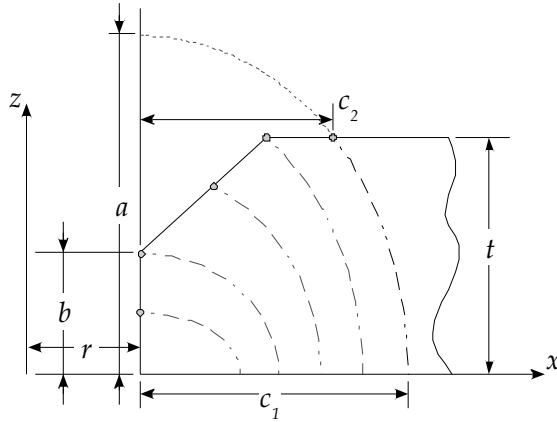
Figure 5-12 Definition of crack shape parameters

Müller [22] observed that the crack nucleation site could shift away from the edge of the fastener hole. Due to high squeeze stresses during the fastener installation process, a residual stress field is introduced around the fastener hole. This in combination with the secondary bending present in lap-splice joints, moves the most critical location away from the fastener.

After nucleation, the crack will grow to adapt the shape of a corner crack. For all the tension and combined tension and bending tests, the crack growth history was reconstructed using a SEM. Figure 5-13 shows the crack history of cracks growing from the straight shank part of the countersunk hole. To determine the crack shape parameter a/c_1 for the open-hole tension specimens can be difficult, mainly due to the fact that the cracks do not have a perfect quarter-elliptical crack shape. The effect of the plane stress at the surface of the specimens causes locally more crack-tip plasticity and thus more crack closure. As a result the crack front will be lagging behind at the sheet surface, see Figure 5-13. It is therefore not always possible to fit a curve that assumes a part-elliptical crack shape with the a-axis on top of the straight shank part of the hole and the c_1-axis on top of the lower surface as illustrated in Figure 5-12. For the tension specimens when the crack is still a very small corner crack, the crack growth in the thickness direction is somewhat faster then along the lower sheet surface. This results in an increasing a/c_1 ratio for corner cracks in the straight shank part of the countersunk hole. Once the crack penetrates the countersunk edge, the $a/c_1 \approx 1$ remains fairly constant. For fully through the thickness cracks, the crack at the free surface, crack length c_2, is trying to catch up with c_1. This behavior causes the a/c_1 ratio to increase.
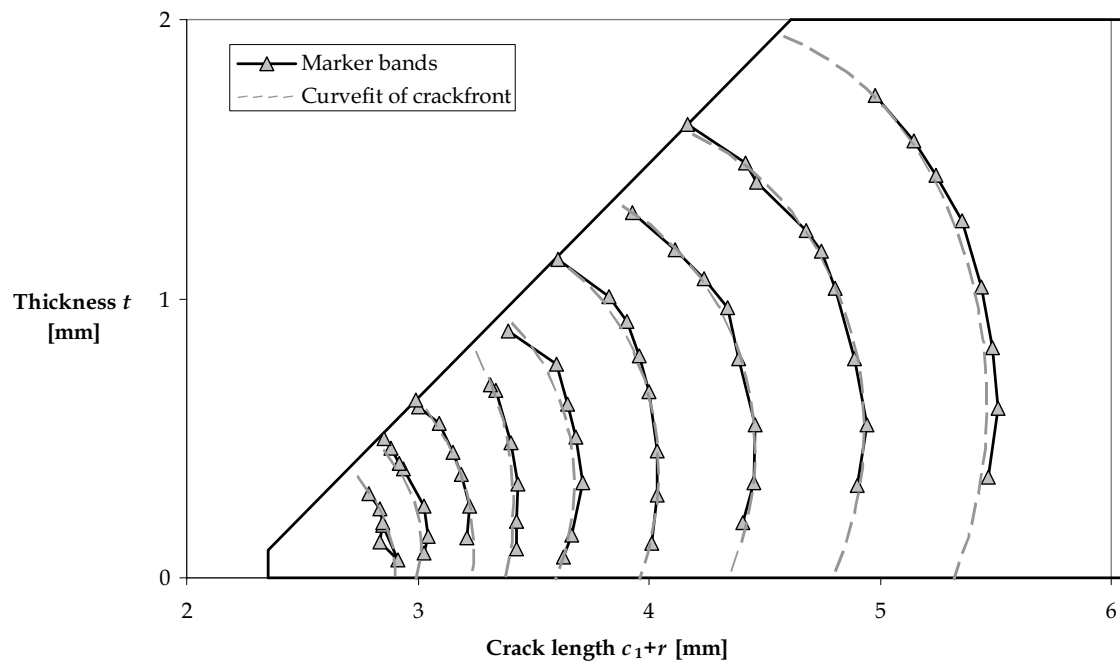
Figure 5-13 Crack fronts reconstructed for pure tension from marker bands
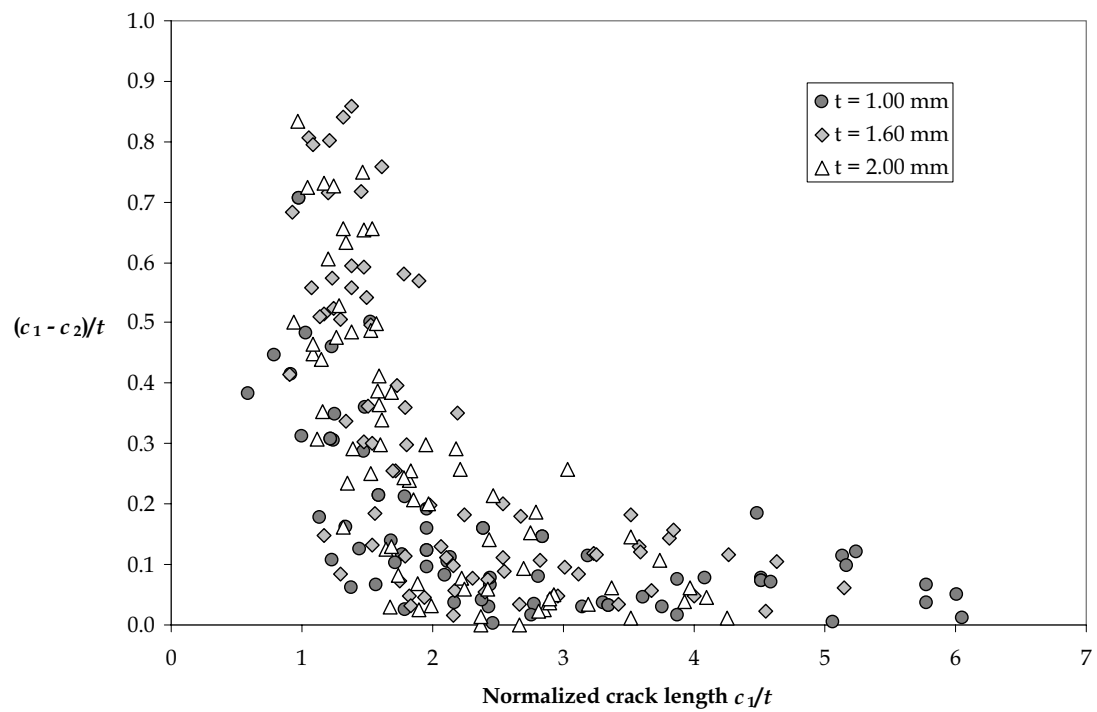
Figure 5-14 Plot showing catching up of the crack length c_2 at the free surface for tensile loading only (from SEM investigation)

Figure 5-14 shows the crack length c_1/t in combination with $(c_1-c_2)/t$, both normalized using the specimen thickness. The behavior of c_2, slowly catching up to c_1 is independent of the specimen thickness. For all specimen thicknesses the obtained data converge to zero ($c_2=c_1$). Crack growth reconstruction of the cracks of the combined tension and bending specimens using the SEM, provides a large amount of crack shape data for the three different thicknesses. The data are compiled in Appendix C and Appendix D.

Figure 5-15 shows a crack shape reconstruction for half a specimen that was loaded under combined tension and bending. In contrast to the tensile crack shape data; the combined loading provides better crack shape correlation to a part-elliptical curve fit. The higher stresses due to the bending at the lower surface cause the crack length c_1 to be longer than in the pure tensile loading. The higher bending stresses eliminate for a large part the influence of the plane stress at the surface causing higher crack growth rates at the lower surface.
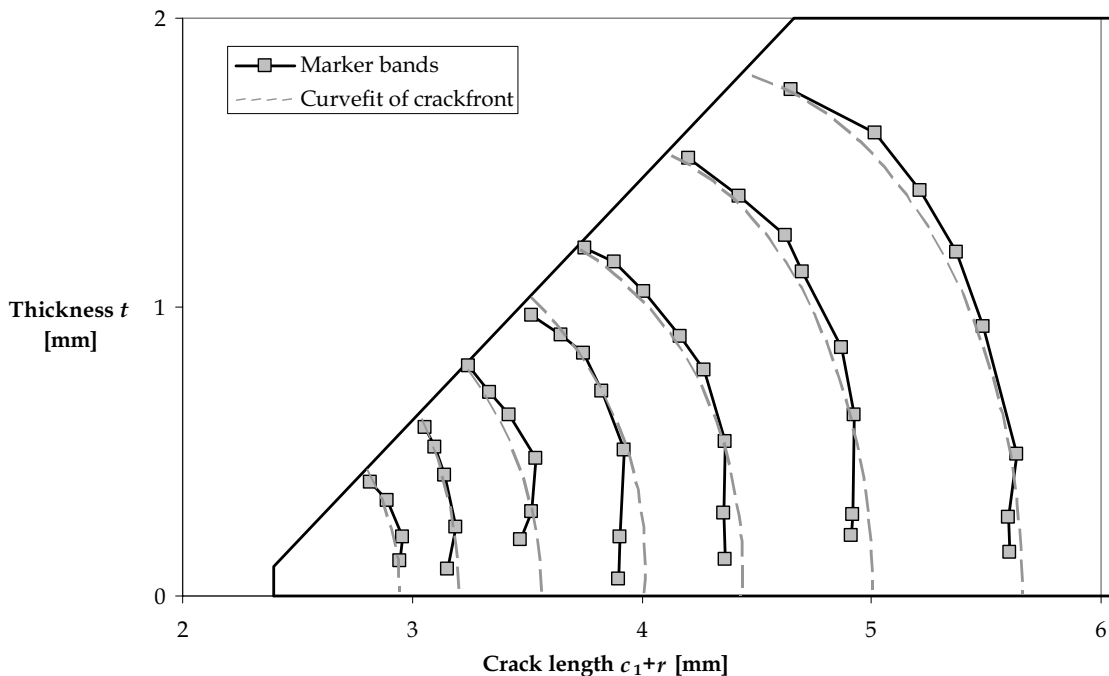
Figure 5-15 Crack front reconstruction for combined loading from the marker bands

The crack shape parameter a/c_1 is also influenced by the bending component in the combined stress field. As shown by the results in Figure 5-16, if compared to Figure 5-14, the crack length c_2 at the free surface is not able to catch up with the crack at the lower surface. The bending stress distribution through the thickness creates a higher stress at the lower surface making it more difficult for the crack tip at the upper surface to catch up to the crack tip at the lower surface. Remember that these specimens are single hole specimens subjected to both tension and bending. Again a large amount of crack front reconstruction data was obtained for these combined

tension and bending specimens. The data as mentioned before is compiled in Appendix C and Appendix D.

The load condition, tension and bending, is similar in lap-splice joints. The influence of multiple holes in a lap-splice joint is also ignored in the combined tension and bending specimens. The fact that a row of fastener holes is present has an effect on the crack growth behavior in joints. Pártl and Schijve [23] showed in a series of fatigue tests of 2024-T3 alloy specimens with a collinear row of open holes subjected to pure tensile loading that some interaction exists. However, this interaction occurred mainly when only half of the remaining ligament between the holes was still present, i.e. usually in the final stages of the fatigue crack growth life.

Similar research by de Rijck [1] showed crack interaction effects in specimens subjected to combined tension and bending. It was found that the crack shape influences the crack interaction effects. Pártl and Schijve investigated straight through the thickness cracks; these cracks can be seen as cracks with a very large a/c_1-ratio.
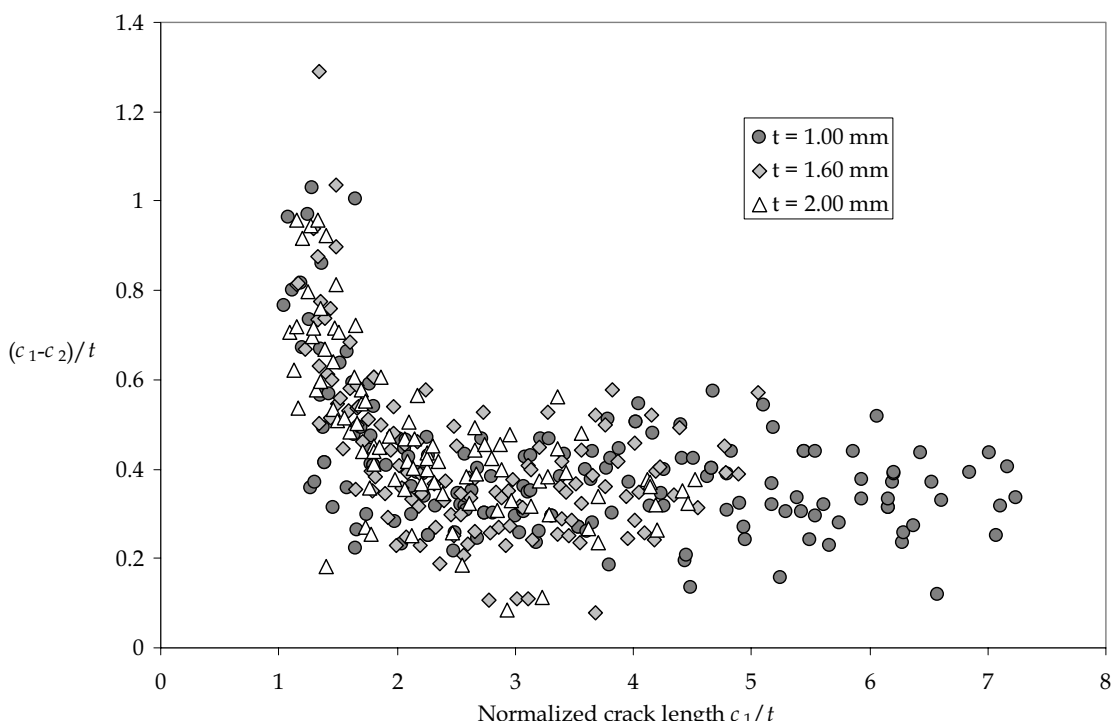
Figure 5-16 Normalized crack shape parameters for cracks in the combined loading specimens. The influence of the bending component is clearly visible

Thus for oblique part-elliptical through cracks with an almost straight crack front ($a \gg c_1$ & $c_1 \approx c_2$) the crack interaction will show the same behavior as straight cracks; the interaction is postponed to the final stages of the fatigue life. Cracks with a more curved crack front ($c_1 \gg c_2$) show less crack interaction effects than the

straight cracks. Part through cracks grow slower towards one another when subjected to similar load conditions [1].

The data in Figure 5-16 for $(c_1-c_2)/t$ seem to converge to a value around 0.3 which applies to tests carried out with a bending $k_b = 0.5$. For the tension specimen without bending the values converged to zero. It should be expected that for larger k_b values ($k_b > 0.5$) that the $(c_1-c_2)/t$ values will converge to still higher values (> 0.3). If k_b would be larger than 1 the nominal bending stress at the lower surface becomes negative, i.e. a compressive stress, see Figure 5-17. Crack growth along the lower surface would become problematic. Fortunately, the bending factor k_b in lap splice joints in a fuselage will generally be lower than one, and it may well be expected that the crack at the outer surface of a lap joint will become detectable by visual inspection.

upper surface

lower surface
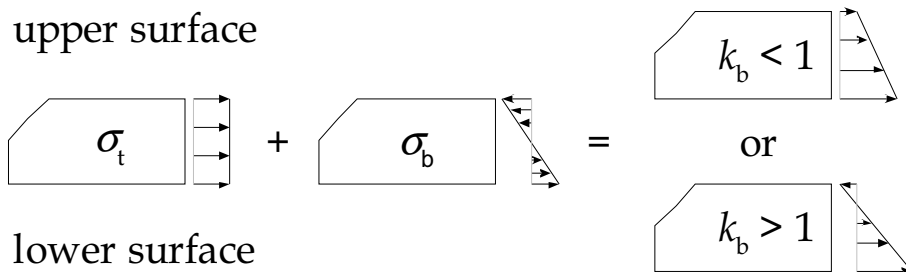
Figure 5-17 Stress distribution through the thickness

5.3   Analytical investigation

The analytical investigation was carried out with finite element analysis techniques. From the experimental investigation, a set of crack shapes and crack growth characteristics was obtained. To reproduce those crack shapes analytically, a finite element model capable of producing data for stress intensity factor calculation is required. The finite element model was created in the following manner. First, a two dimensional model is created allowing for a wide range of cracks for certain t (=thickness), r (=radius), b (=straight shank height) and a/c. The next step is to generate a three dimensional model, by means of session files in MSC/Patran® [24]. The 2D-model is used to generate 3D-models. Since each model contains a number of part-elliptical cracks; both corner and through cracks, a C++ code is used to generate a number of input files for all load cases and data for one crack. ABAQUS® [25] is used for the finite element solution and provides the nodal information needed for the three dimensional virtual crack closure technique used to calculate K. Before finalizing the analytical method a convergence study on the method was performed in Section 5.3.5.

5.3.1 Crack shapes for finite element analysis

The part-elliptical crack shapes used in the finite element analysis are based on data found by Fawaz [2], de Rijck [1] and experimental data in this chapter. All crack shape data obtained by fractographic reconstruction can be found in Appendix D. The a/c_1 data used for the finite element analysis is displayed in Table 5-3. From the data found in Appendix D a small number of a/c_1 had a value under 0.5, therefore this is chosen as a lower limit for the finite elements analysis. For the purpose of validating the calculated K's with the experimental crack growth data more calculations are not required.

Table 5-3   Matrix containing all the crack shape data for finite element analysis

a/c_1	a/t	r/t	b/t
5.00	5 corner cracks on	0.10	0.50
2.00	straight shank part.	0.25	0.25
1.50	10 part-through cracks at	0.50	0.05
1.00	countersunk edge.	0.67	
0.75	Several oblique through	1.00	
0.67	cracks up to $c_1/r = 5.00$.	1.20	
0.50		1.50	
		2.40	

5.3.2 Finite element model generation

Considering the number of crack shape parameters and load cases, a very large number of finite element models must be created. To do this manually, one by one, is a horrendous task that will take too much time and can easily lead to discretization errors. Thus an automated process was developed. The process is automated in such a manner that the steps most prone to error have been eliminated and only limited manual input is required. The first step in the process is generating a 2-dimensional FEM of the entire crack region. This model is constructed in such a manner that the 2D model contains a complete crack trajectory, meaning that K's can be calculated for multiple crack shapes in one model, see Figure 5-18 and Figure 5-19, by simply changing the crack plane boundary conditions.
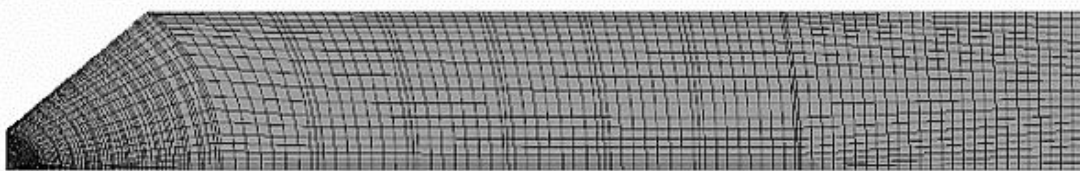
Figure 5-18   A complete 2-dimensional crack shape modeling
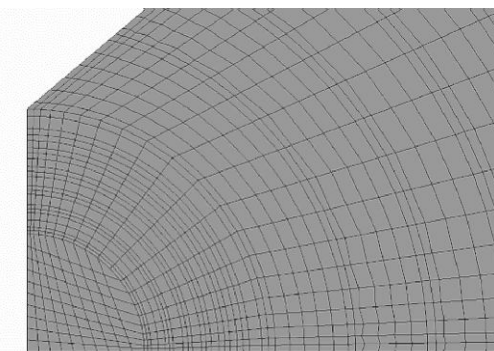
Figure 5-19 Crack shape around the straight shank part of the countersunk hole

For the majority of the 2D models, 25 cracks with an elliptical shape are meshed starting in the straight shank portion of the countersunk hole ending with through the thickness cracks at a distance away from the hole. After the 2D model generation is complete, a 3D model is created by using a "session" file. This session file is a step-by-step record of how a 3D model is generated from the baseline 2D model using MSC/PATRAN®. Any finite element preprocessor with the capabilities to run session files can be used to generate the 3D model. At the end of the 3D model generation, an element connectivity file and a nodal coordinates file is generated as output from MSC/PATRAN® and used for the final step in the model generation. Figure 5-20 shows the first part of the automated mesh generation of a session file. A unconstrained 3D mesh is now generated, with no boundary conditions, load conditions and material properties. The complete quarter plate is generated using a quarter plate with a circular exclusion with the size of the countersunk area shown in Figure 5-20. For the K calculation, the three dimensional virtual crack closure technique is used, which requires nodal displacements and nodal forces as output from the finite element analysis. ABAQUS® has been chosen because the solver is more stable if slightly skewed elements are generated in this automated process.
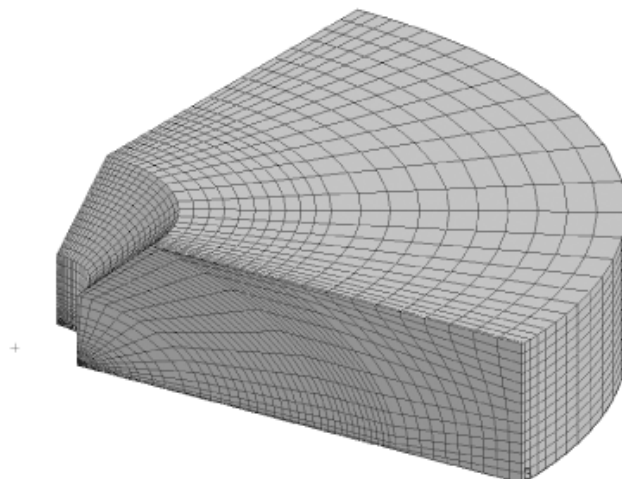
Figure 5-20 Three-dimensional representation of countersunk area of quarter plate. Elliptical crack shapes are visible in the XZ-plane

119

5.3.3 Load cases and boundary conditions

It would be overenthusiastic to include a large variety of combined tension and bending load conditions in the present investigation. Therefore the loading conditions were limited to those relevant for the experiments. Validation of calculated K values is then possible by comparing the crack growth data obtained in the experimental part with crack growth predictions using the new K's.

Figure 5-21 shows three types of applied loads, tension, bending and pin loading on the hole. The pin load condition is also taken into account since the bearing plays an important part in crack growth in joints. The tensile load and the bending load are applied at the top of the plate ($y = h$), the finite element model will only be a quarter of the open hole shown in Figure 5-21. The tensile load is an applied uniform load and the bending stress is assumed to be linearly distributed through the thickness. The pin load is applied to the elements around the bore of the hole using a cos^2 applied pressure distribution. Investigation by several authors, [26],[29], showed this pressure distribution to resemble the applied pressure on the bore of the hole most accurately.
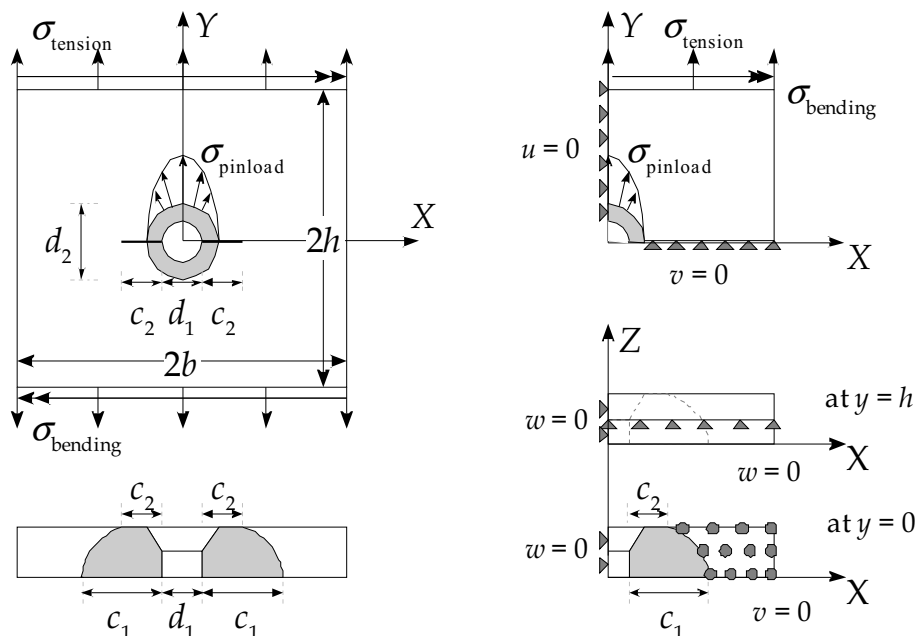
Figure 5-21 Parameter definition of a central countersunk hole subjected to general loading and boundary conditions for finite element model

Since only a quarter plate is used, several boundary conditions need to be applied. The symmetry planes at the $x = 0$ and $y = 0$ in Figure 5-21 dictate the edges of the finite element model. At $x = 0$ the displacements along the X-axis are constrained and at $y = 0$ the different crack shapes are analyzed by releasing nodes along an elliptical curve thereby creating the crack wake.

5.3.4 *The three dimensional virtual crack closure technique*

A variety of methods is available to calculate stress intensity factors for cracked three-dimensional bodies, ranging from rather difficult to more simple methods. Stress intensity factors can be determined using finite element analysis by either direct or indirect methods. The method chosen here is the three-dimensional Virtual Crack Closure Technique (VCCT) in conjunction with the *h-version* finite element method, which is an indirect method, using the energy release rate *G* to calculate the stress intensity factor, *K*. Fawaz [2] and Shivakumar, Tan and Newman [30] showed that using the 3D VCCT avoids most of the problems encountered by using other methods, e.g. in this method no singular elements or elements normal to the crack front are required. This allows the method to be used be any finite element package.

Calculation of the *K* is based on Irwin's crack closure integral [31]. The applicability for finite element use is based on Rybicki-Kanninen's [32] method for the two dimensional crack configurations and extended by Shivakumar, Tan and Newman [30] to three dimensions. The average strain energy release rate G_i can be written as:

$$G_i = \frac{1}{2w_i\Delta} \int_{s_{i-1}}^{s_{i+1}} \int_0^\Delta \sigma_y(r,s)v(\Delta - r,s)dsdr \qquad \text{(5-10)}$$

where
- w_i = Element length along crack front
- Δ_i = Finite element length
- $\sigma_y(r,s)$ = Stress distribution ahead of the crack front
- $v(r,s)$ = Total displacement distribution behind crack front
- r = Distance to crack front
- s = Distance along the crack front

The right hand side of Eqn. (5-10) is equivalent to the product of the nodal forces ahead of the crack front and displacements behind the crack front of the ith segment including contributions from elements on both sides of the crack front. Figure 5-22 illustrates the above mentioned parameters used in the calculation of G_i.
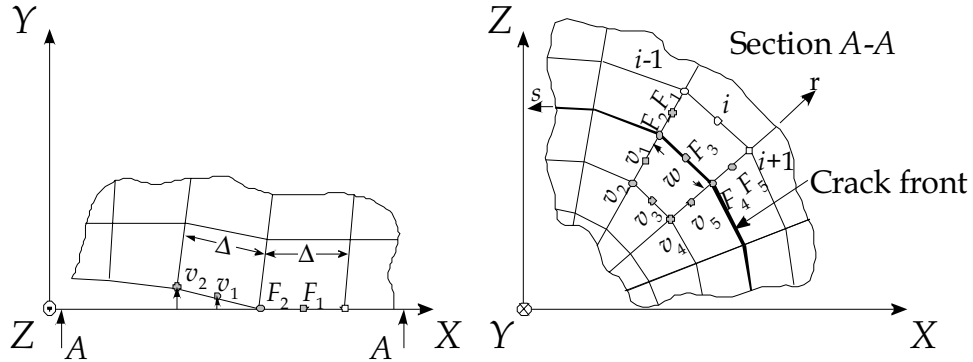
Figure 5-22   Parameters used for G_i calculation

Taking into consideration that twenty node elements are used to model the cracked body, the strain energy release rate G_i for mode I is written as

$$G_i = \frac{1}{2w_i\Delta}\sum_{j=1}^{5} F_j^i v_j \qquad (5\text{-}11)$$

Where v_j are the nodal displacements from the nodes behind the crack front and F_j the forces from nodes at the crack front from the ith segment alone. Eqn. (5-10) is in terms of the ith segment alone and a typical FEA solutions gives nodal quantities, force and displacement contributions from all elements connected to a given node. As a consequence, a method of segmenting or partitioning the nodal forces must be devised. Assuming the nodal forces to be proportional to the element length normal to the crack front [2],[30], Eqn. (5-11) is written as follows

$$G_i = \frac{1}{2w_i\Delta}\sum_{j=1}^{5} C_j F_j v_j \qquad (5\text{-}12)$$

where

$$C_1 = C_2 = \frac{w_i}{w_{i-1} + w_i}$$

$$C_3 = 1$$

$$C_4 = C_5 = \frac{w_i}{w_i + w_{i+1}}$$

Eqn. (5-12) now only depends on the nodal forces and displacements calculated from a finite element analysis. For a uniform applied stress field along the crack, Eqn (5-12) is exact. For non-uniform stress fields Eqn. (5-12) gives an approximation of the strain energy release rate. The G_i calculated using this equation is an average over the width w_i and is assumed to occur at the center of the ith segment. Accuracy

of the calculated results depends on the segmentation of the crack front; a more accurate result can be obtained when the crack front consists of more elements.

The local strain energy release rate G_i will be used to calculate the mode I stress intensity factor K_I

$$K_I = \sqrt{G_i E^*} \qquad \text{(5-13)}$$

where
$\qquad$ E* $\qquad$ = E for plane stress condition
$\qquad$ E* $\qquad$ = E/(1-v^2) for plane strain condition
$\qquad$ E $\qquad$ = Modulus of Elasticity
$\qquad$ v $\qquad$ = Poisson's ratio

The total mode I stress intensity factor is a superposition of the individual stress intensity factors for each load case and can be expressed as

$$K_{TOTAL} = \sum_{i=1}^{n} K_i \qquad \text{(5-14)}$$

Expanding Eqn. (5-14) to the basic definition of the stress intensity factor yields

$$K_{TOTAL} = \left(\sum_{i=1}^{n} \beta_i \sigma_i \right) \sqrt{\pi a} \qquad \text{(5-15)}$$

where
$\qquad$ β_i $\qquad$ = Boundary correction factor for each load case
$\qquad$ σ_i $\qquad$ = Remote stress for each load condition
$\qquad$ a $\qquad$ = Crack length
$\qquad$ n $\qquad$ = Number of load cases

5.3.5 *Convergence study*

A convergence study was performed on the mesh generation procedure described in Section 5.3.2. The results for one crack with crack properties $a/c_1 = 1.00$, $b/t = 0.25$ and $r/t = 1.00$ are shown in Figure 5-23. The baseline finite element mesh contains 68,640 elements, three other finite element meshes are generated having 35,360, 52,000 and 84,760 elements. In sequence of element size the meshes have 915,510, 1,341,750, 1,767,990 and 2,180,910 degrees of freedom. The smallest finite element mesh differs 1.51% from the baseline model. The mesh with 52,000 elements differs 0.82% from the baseline finite element mesh. The larger mesh produces results - 0.27% from the baseline model. From this result, and the small gain that can be achieved by increasing the number of elements and thus the degrees of freedom

with respect to the baseline mesh the *K* solutions produced by this route are converged.
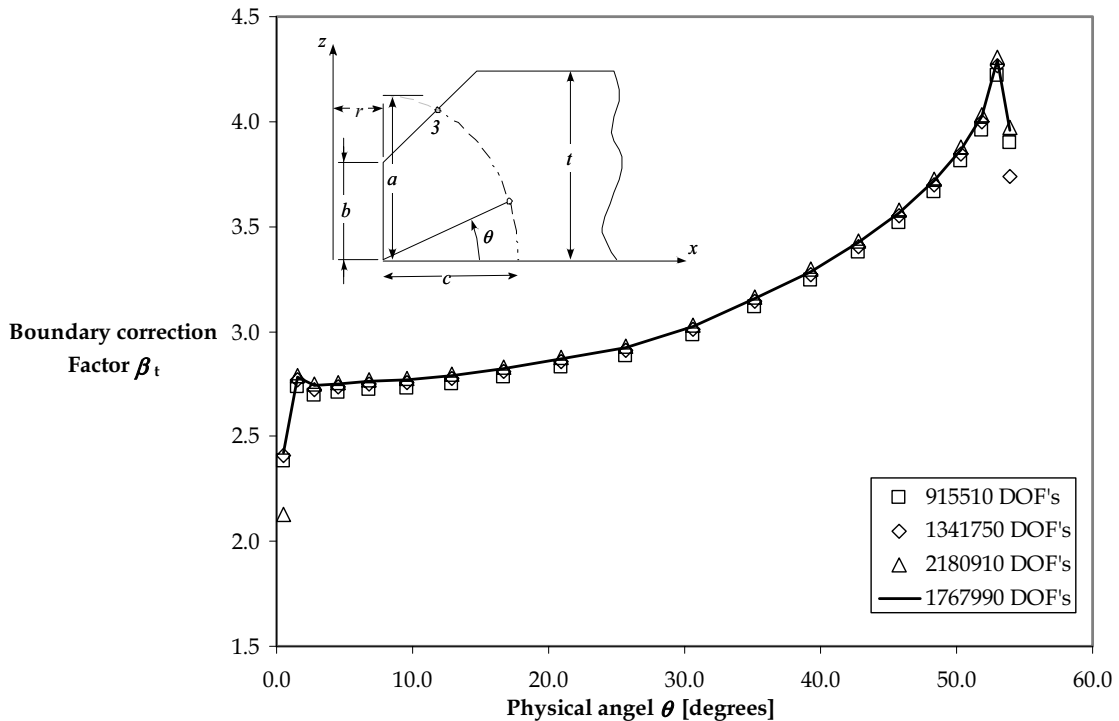
Figure 5-23 Convergence study for crack at countersunk hole subjected to tensile loading

5.4 Comparison of newly calculated *K*'s to the literature

The convergence study has shown that the newly calculated stress intensity factors for countersunk holes, provides solutions that are converged. Validation of the new *SIF* solutions can be done by using the solutions produced by Rahman et al [33]. Their focus was on calculating *SIF* solutions for cracks emanating from countersunk holes subject to tensile, bending and wedge load conditions. A variation of both the geometrical and crack shape parameters results in a number of solutions for all load cases. Three load case results are presented, tension, bending and wedge loading.

5.4.1 Model parameters

The tension loads are uniform through the thickness and applied at the top of the finite element geometry. The bending loads are varied as a uniform linear distribution through the thickness, with only positive loads (at $z/t = 0.0$, the bending load $\sigma_b = 0$, at $z/t = 1.0$ the bending load $\sigma_b = 1.0$). Wedge loading is an applied load at the bore of the countersunk hole. Since the application of the bending loads is significantly different from the bending loads applied in section 5.3.3, the comparison is based upon the tensile load cases only. Figure 5-24 shows the five different crack front locations and the parameters that serve as point of comparison.
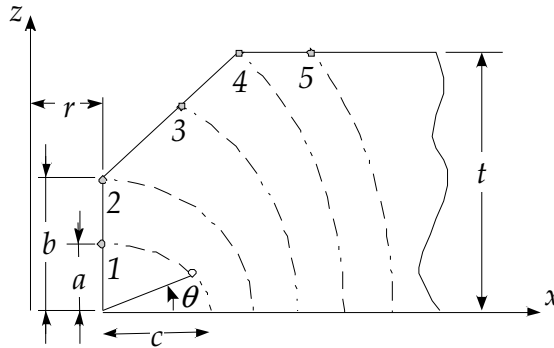
Figure 5-24 Crack shape locations around countersunk hole [33].

Parameters *a*, *b*, *c*, *r* and *t* uniquely define each crack geometry. Three *a*/*c* ratios are used in the Rahman calculations, 1.00, 0.75 and 0.50. For the first crack location *a* = *b*/2, the crack intersects at half the straight shank height. The second crack location *a* = *b*, the crack intersects at the change from the straight shank part to the countersunk part. The third location is determined by the intersection of the crack halfway along the countersunk edge. The fourth crack location marks the dividing line between corner cracks and through the thickness cracks. Crack location five is determined by the parameter *c*/*t* = 3.125, with *t* = 1.00 the crack length *c* = 3.125. The straight shank radius of the countersunk hole with respect to the sheet thickness, *r*/*t* = 1.00 is kept constant. The only other variable is the straight shank height *b*, the ratio *b*/*t* is varied as follows 0.50, 0.25 and 0.05. Where *b*/*t* = 0.50 has a straight shank part half the sheet thickness and *b*/*t* = 0.05 practically simulates a knife-edge condition.

5.4.2 Normalization

The normalization of the stress intensity factors is done according to [34] for ease in comparing *K*. The *K* for any location on the crack front is then written in the following form

$$K_I = \beta_t \sigma_t \sqrt{\frac{\pi a}{Q}} \qquad \textbf{(5-16)}$$

where

β_t = Boundary correction factor for tensile load case
σ_t = Remote stress for tensile load condition
a   = Crack length
Q   = Shape Factor

With the shape factor *Q* known from [34]

$$Q = 1 + 1.464 \left(\frac{a}{c} \right)^{1.65} \quad for \frac{a}{c} \leq 1$$

$$Q = 1 + 1.464 \left(\frac{c}{a} \right)^{1.65} \quad for \frac{a}{c} > 1$$

(5-17)

The boundary correction factor β_t is

$$\beta_t = \frac{K_I}{\sigma_t \sqrt{\dfrac{\pi a}{Q}}}$$

(5-18)

5.4.3 Discussion of the results

The solutions are compared to published K solutions for cracks emanating from countersunk holes by Rahman [33] and for cracks emanating from straight shank holes by Newman Raju [35]. The latter FEA solutions are frequently used in crack growth predictions for corner cracks growing from countersunk holes. The solutions presented by Rahman et al in [33] are obtained using the global intermediate local (*GIL*) finite element approach, using a global model with about 4500 twenty noded solids and with the local model containing 5600 twenty noded solids. Comparing the solutions presented in Figure 5-25 and Figure 5-26 shows distinct differences between the newly calculated K solutions and existing solutions.

The differences between the new K's and the solutions from [33] and [35] are a result from the large difference in the number of degrees of freedom near the crack front. The larger numbers of elements provide a more accurate representation of the stresses around the crack front. Increasing the number of elements, *DOF*'s, around the crack front allows the finite element model to simulate the stress state more accurately. These finite element analysis results represent the plane stress state at crack intersection with the free surface better. Fawaz and Andersson discuss this thoroughly in ref [3]. More *DOF*'s around the crack front represent the constraints in the plain strain and plane stress areas better. This behavior can be seen in both Figure 5-25 and Figure 5-26. Towards the free surface, the K solution drops. This drop in K results in the crack growth lagging at the free surface as was seen in the experimental results in Section 5.2.4.
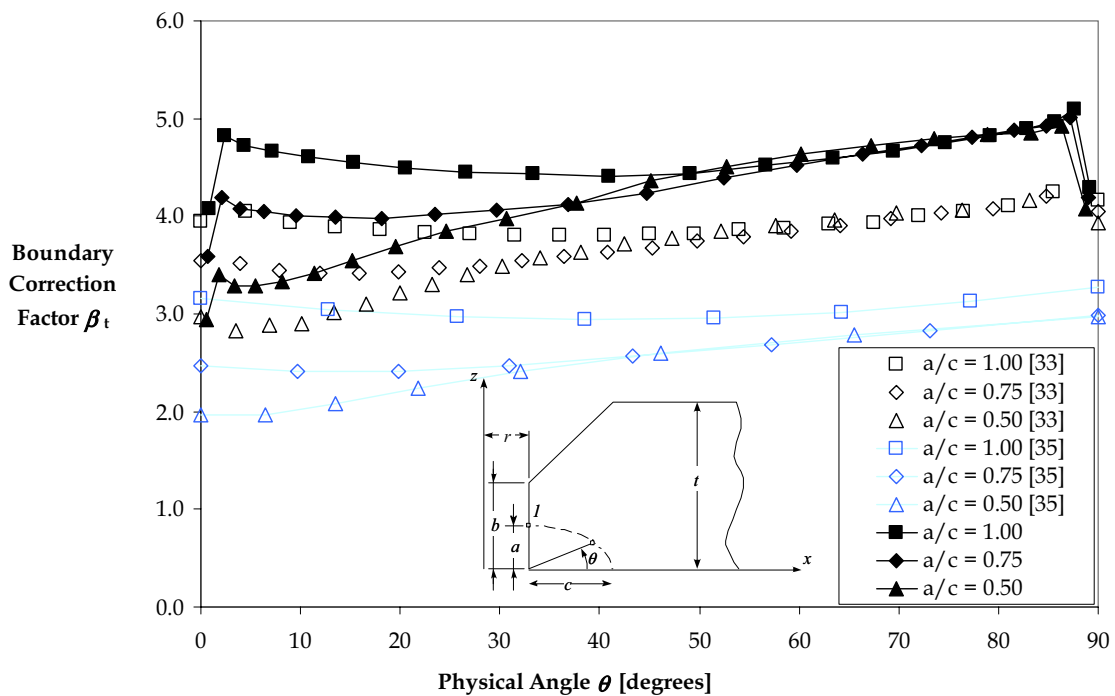
Figure 5-25 Normalized *K*'s for corner crack at crack location 1 subject to tension, *b/t* = 0.50
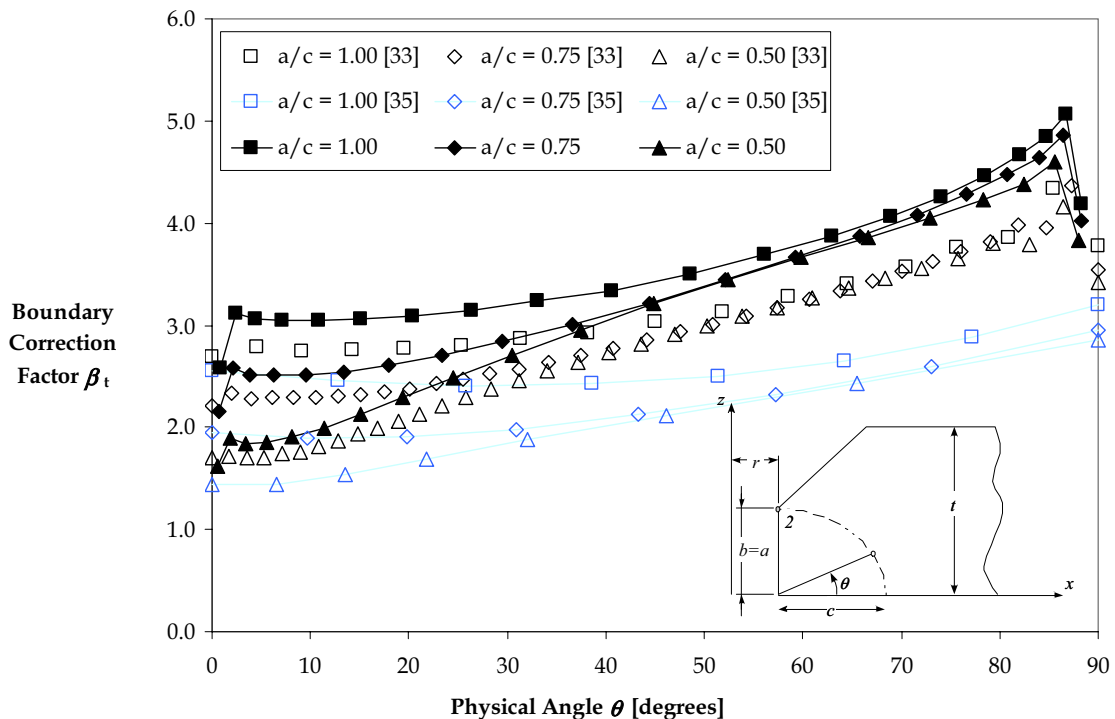
Figure 5-26 Normalized *K*'s for corner crack at crack location 2 subject to tension, *b/t* = 0.25

Comparing the results from the Newman/Raju solutions is done in order to show the influence of the countersunk shape of the fastener hole. For all a/c values in both Figure 5-25 and Figure 5-26, the new K solutions are higher; this difference is attributed to the difference in stress distribution around the fastener hole. Using the Newman/Raju solutions will therefore create an un-conservative life prediction. This can easily be shown using the Paris relation between da/dN and ΔK

$$\frac{da}{dN} = C \, \Delta K^{n}$$

(5-19)

where C and exponent n as material constants. Substitution for K gives the following relation

$$\frac{da}{dN} = C \big(\beta \, \Delta \sigma \sqrt{\pi a} \big)^{n}$$

(5-20)

Inaccuracies in K, will carry through with the exponent n. In case of a corner crack shown in Figure 5-26 where the normalized K's are about 30% higher, the result is an increase in crack growth rate by a factor of 2.2 with $n = 3.3$. The increase in crack growth rate yields a 2.2 times shorter fatigue life. In other words, using the K solutions for corner cracks at a straight shank hole when the hole is actually countersunk is inappropriate and unsafe since the crack growth life is over-predicted!

5.5   Stress intensity factors

Stress intensity factors K are calculated for all crack shapes listed in Table 5-3 using the finite element model from section 5.3.2 and the boundary conditions from section 5.3.3. Seven a/c_1, eight r/t and three b/t values result in 168 finite element models each containing on average twenty crack locations and three load conditions. This results in 10080 stress intensity factor solutions for tension, bending and pin loading.

The K solutions from section 5.4 are normalized using an approximation to the second elliptical integral of the second kind, Q, Eqn. (5-18). This approximation changes with a/c_1, since different a/c_1 values are chosen to describe the crack shapes found during the experimental investigation. To avoid the dependence on Q, the normalization of the K's is done using the following equation, which includes the finite width correction.

$$\beta = \frac{K_I}{\sigma \sqrt{\pi c_1} f_w}$$

(5-21)

Where f_w is the finite width correction according to Newman/Raju [35]:

$$f_w = \sqrt{\sec(\lambda) \cdot \sec\left(\frac{\pi \cdot D}{W/2}\right)}$$

(5-22)

$$\lambda = \frac{\pi}{2} \cdot \sqrt{\frac{a}{t}} \frac{(D + nn \cdot x)}{((W - 2 \cdot x) + nn \cdot x)}$$

(5-23)

The finite element model, shown in Figure 5-21 is a ¼ symmetry model. Due to the boundary conditions applied to the finite element model, the loading conditions are symmetric for all cases; tension, bending and wedge loading. To obtain the bearing load case, which is unsymmetric, linear superposition of several K's are used as shown in Figure 5-27 and in functional form below.

$$K_{P\sigma} + K_{P\sigma} = K_t + K_{2P}$$

(5-24)

Case I and Case II represent the situation for a stress intensity factor for wedge loading

$$K_{P\sigma} = \sigma_{brg} \sqrt{\pi a} \beta_p$$

(5-25)

with $\sigma_{brg} = \dfrac{P}{2rt}$

Case III is representative of the stress intensity factor for tensile loading

$$K_t = \sigma \sqrt{\pi a} \beta_t$$

(5-26)

Case IV represents the stress intensity factor for wedge loading

$$K_{2P} = \sigma_{brg} \sqrt{\pi a} \beta_{2P}$$

(5-27)

Substitution of Eqns. (5-23) – (5-25) into Eqn. (5-22) results in

$$2\sigma_{brg} \sqrt{\pi a} \beta_{P\sigma} = \sigma \sqrt{\pi a} \beta_t + \sigma_{brg} \sqrt{\pi a} \beta_{2P}$$

(5-28)

Substitution of $\sigma = \dfrac{P}{2bt}$ and $\sigma_{brg} = \dfrac{P}{2rt}$ in Eqn. (5-26) results in the normalized stress intensity factor for a pin loaded hole. This can be written as

$$\beta_{P\sigma} = \frac{\dfrac{r}{b}\beta_t + \beta_{2P}}{2} \tag{5-29}$$
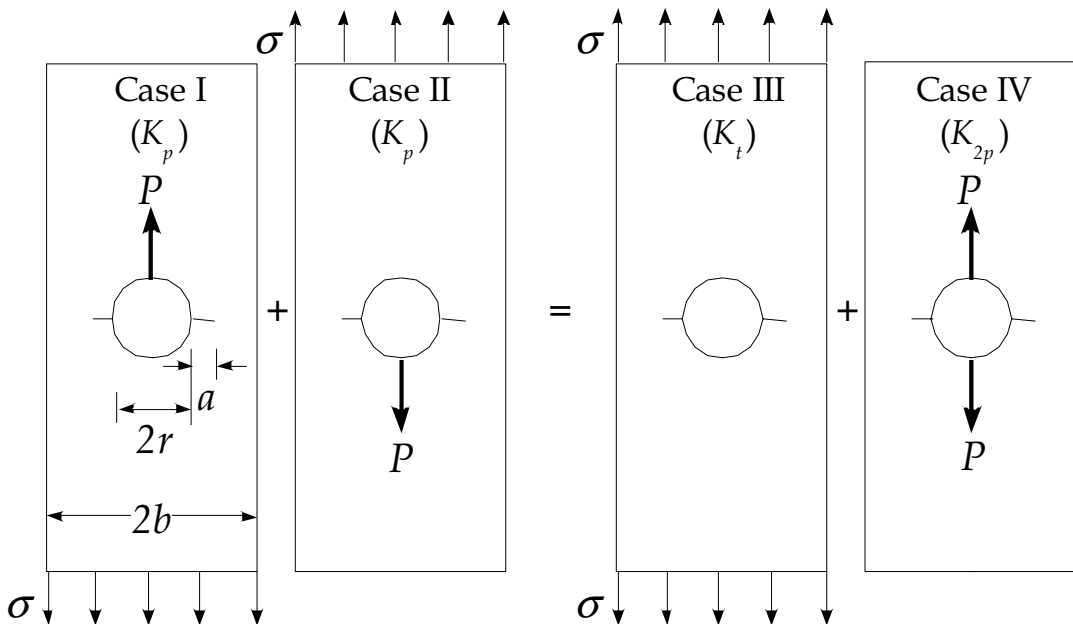
Figure 5-27 Decomposition of unsymmetrical joint loads in symmetrical tensile and wedge loading

Trends describing the relationships between the different crack shape parameters, a/c_1, a/t, b/t and r/t, are shown in the remainder of this section. A description of the crack shape parameters for straight shank holes has already been made by Fawaz [2] and de Rijck [1]. Fawaz described the relation between the parameters for through cracks emanating from a single hole and de Rijck described the parameters for through cracks emanating in a collinear row of holes. It is expected that the relationships for through the thickness cracks resemble those described by Fawaz. The trends for part-through the thickness cracks in the countersunk area are investigated here.

Figure 5-28 shows for several a/c_1 values the normalized K or β solution for a corner crack in the straight shank portion of the countersunk hole. Where x is measured from the edge of the straight shank of the hole. Two trends in β are visible, the behaviour of β along the lower surface and the behaviour of β along the straight

shank hole. The first trend, along the lower surface β decreases with increasing crack length c_1 and decreasing a/c_1.
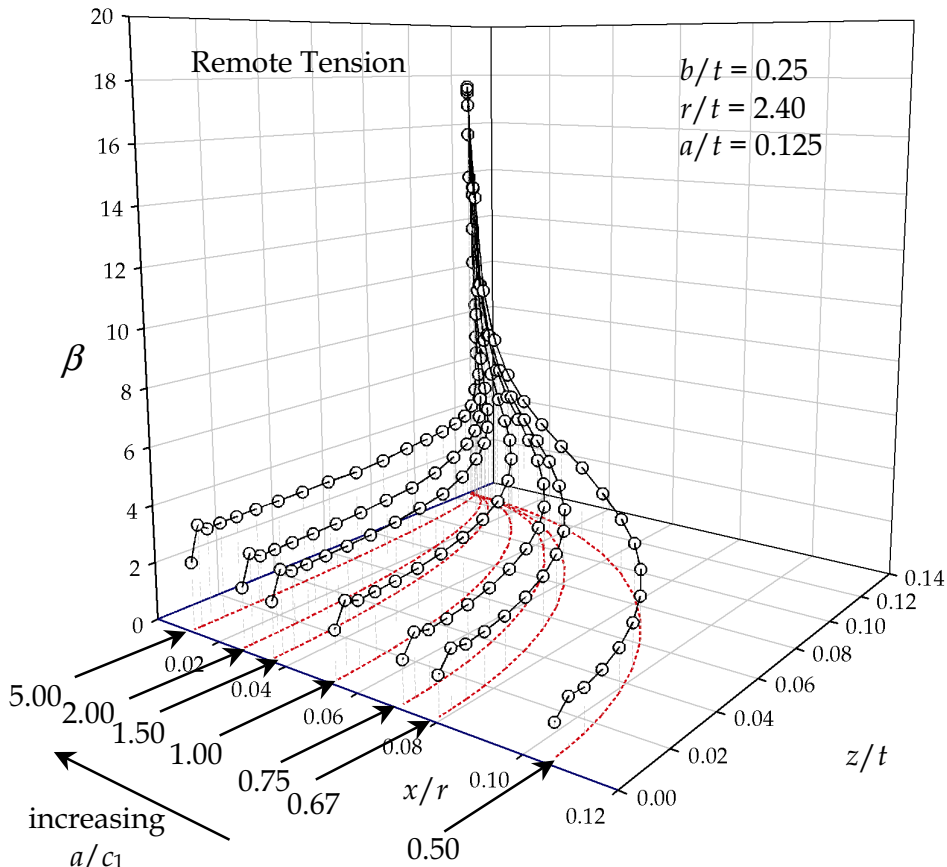
Figure 5-28 Effect of changing a/c_1 on the normalized stress intensity factor for $b/t = 0.25$, $a/t = 0.125$ and $r/t = 2.40$

A small c_1 (with large a/c_1) describes a front that is nearly straight; whereas, a small a/c_1 describes a more curved crack front. The second trend, for a constant crack depth in thickness direction (constant a/t), the β values at the crack-tip intersecting the surface of the straight shank hole increases with a smaller c_1 (decreasing a/c_1). Although shown only for $r/t = 2.40$, for all other r/t ratios the trends for corner cracks is similar. The trends in Figure 5-28 for low c_1 values (high a/c_1) shows a more uniform distribution along the crack front with a sharp rise in β at the bore of the hole. For all a/c_1 the β slowly increases along the entire crack front with finally a sharp rise in β at the bore of the hole.

The following three figures, Figure 5-29 - Figure 5-31 shows the effect of changing a/t for constant a/c_1, b/t, r/t and an increasing crack length c_1. Figure 5-29 shows several corner cracks for $a/c_1 = 1.00$, which implies that the crack front has a quarter circular shape. The value of β for increasing c_1 remains constant along the lower

surface ($z/t = 0$). For all a/c_1 values β increases with increasing a/t, i.e. for deeper cracks. Close to where the crack front intersects the hole surface a large increase of β is observed. Also for increasing a, along the hole edge, an increase of β can be seen. For all other r/t ratios the β behavior for corner cracks is similar.
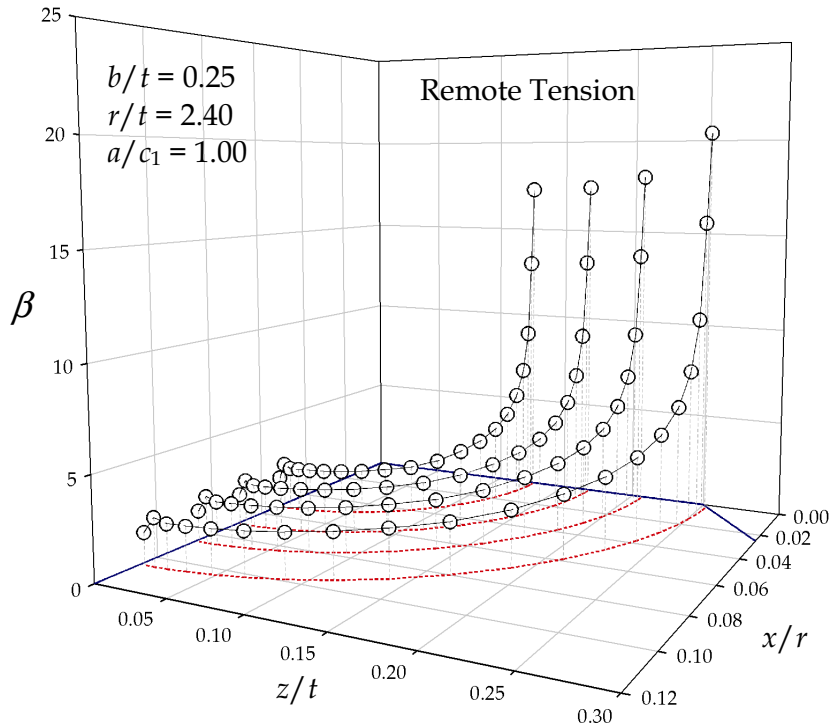
Figure 5-29 Effect of increasing crack length c_1 (changing a/t ratio) for constant $b/t = 0.25$, $r/t = 2.40$ and $a/c_1 = 1.00$ in the straight shank part of the countersunk hole subject to tension

For cracks with $a > b$ (= 0.25) the crack front intersects the countersunk edge. Figure 5-30 and Figure 5-31 show the β values for such situations. A very large drop in β (≈ 20, Figure 5-30) for $z/t = 0.25$ and the next crack location at the penetrated countersunk side at $z/t \approx 0.30$ ($\beta \approx 7$, Figure 5-31). Whereas along the free surface axis the β remains constant for increasing crack length c_1. Along the countersunk edge, the β decreases for increasing a.

Figure 5-31, shows the βs for through the thickness cracks. Once the crack penetrates the opposing side of the sheet, the slow decrease of the β continues. The surface effect on the β values is clearly present in Figure 5-31. Due to the higher flexibility close to the surface of the material, the crack opening will be larger and thus the calculated K–value will be larger. The drop that takes place at the material surface is related Eqn. (5-13). At the material surface the K is calculated using the plane stress Modulus of Elasticity.
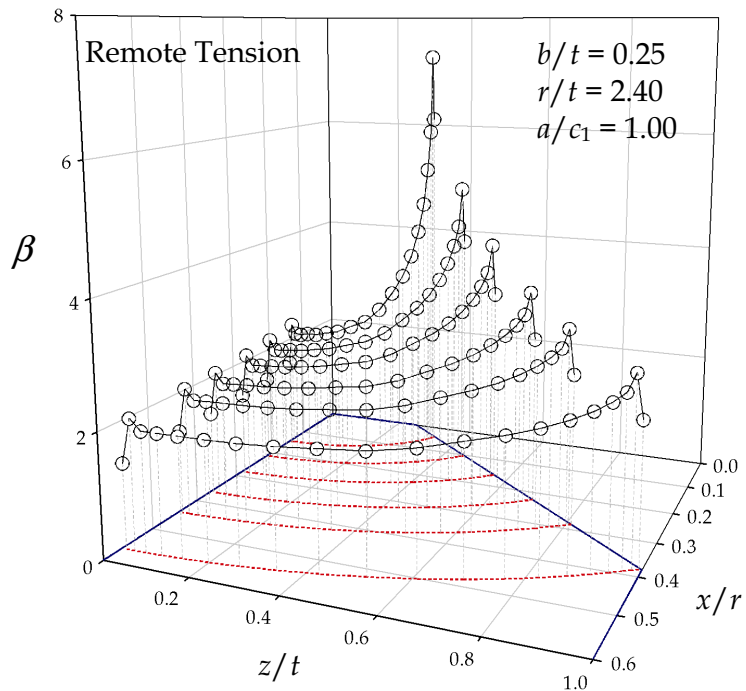
Figure 5-30 Effect of increasing crack length c_1 (changing a/t ratio) for constant $b/t = 0.25$, $r/t = 2.40$ and $a/c_1 = 1.00$ in the countersunk part of countersunk hole subject to tension
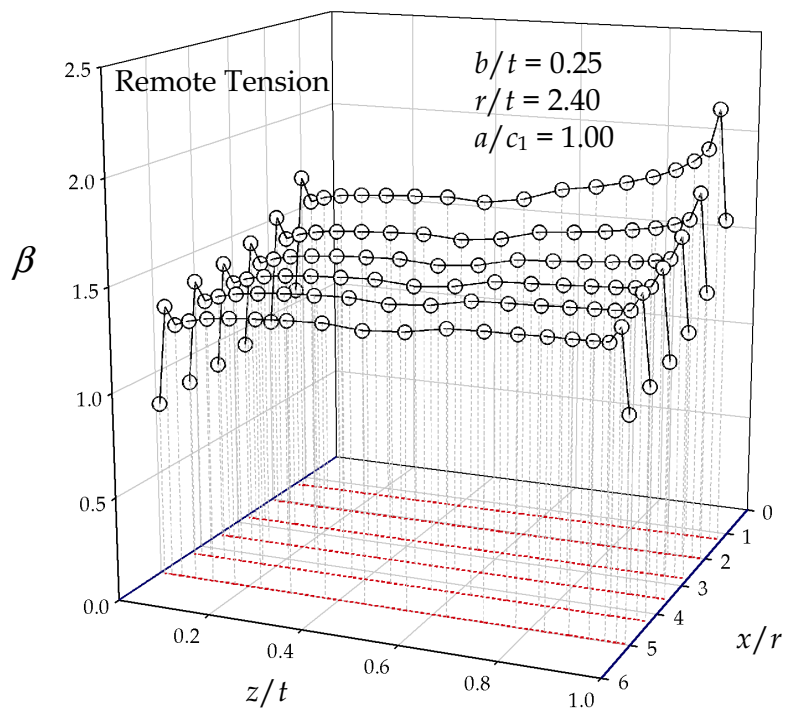
Figure 5-31 Effect of increasing crack length c_1 (changing a/t ratio) for constant $b/t = 0.25$, $r/t = 2.40$ and $a/c_1 = 1.00$ for through the thickness cracks subject to tension

The calculated β's for remote bending are shown in the following three figures, Figure 5-32 - Figure 5-34. Figure 5-32 shows the results for corner crack fronts starting at the lower surface and ending in the straight shank part of the fastener hole. The applied bending stress, linear through the thickness, results in lower β's at the lower surface compared to the remote tension results. For an increasing crack length c_1, the value of β decreases.

The trend in Figure 5-33 for cracks jumping from the straight shank part ($z/t = 0.25$) to the countersunk edge ($z/t > 0.25$) is similar to the remote tension results, a drop in β values once the crack intersects with the countersunk edge. A slow decreasing β at the lower surface with increasing c_1 and a decreasing β for increasing a. The steeper reduction in β is a result of the linear bending stress distribution through the thickness. At the upper surface a compression stress is present, which is opposite to the tensile stress at the lower surface, see Figure 5-17.

Figure 5-34 shows the symmetric behavior of β through the thickness along the crack front. For both the remote tension and bending solutions, the symmetric β solution is possible for almost straight crack fronts, for countersunk holes, when the crack is far enough from the countersunk hole a similar behavior is to be expected.
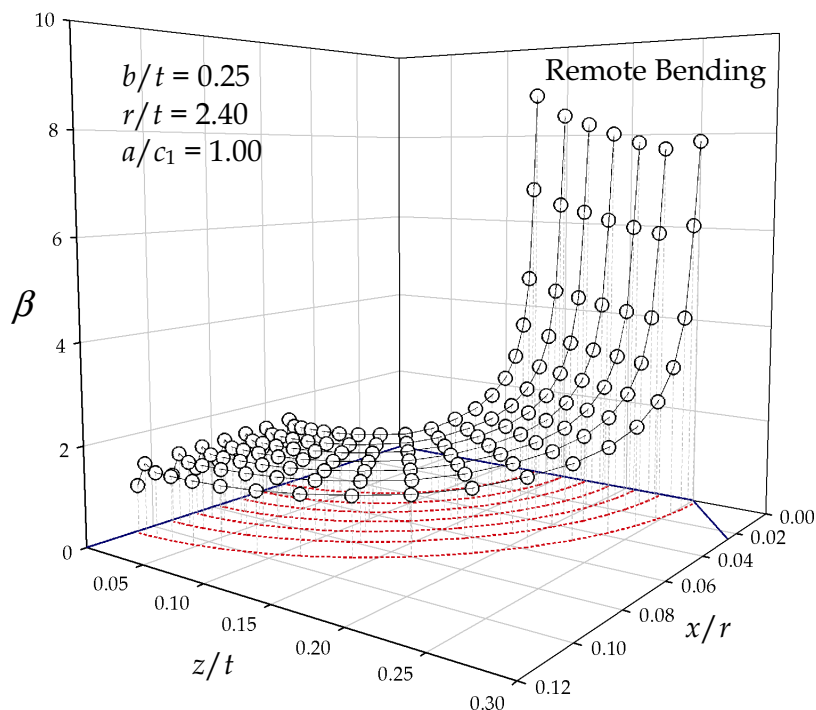
Figure 5-32 **Effect of increasing crack length c_1 (changing a/t ratio) for constant $b/t = 0.25$, $r/t = 2.40$ and $a/c_1 = 1.00$ in the straight shank part of the countersunk hole subject to bending**
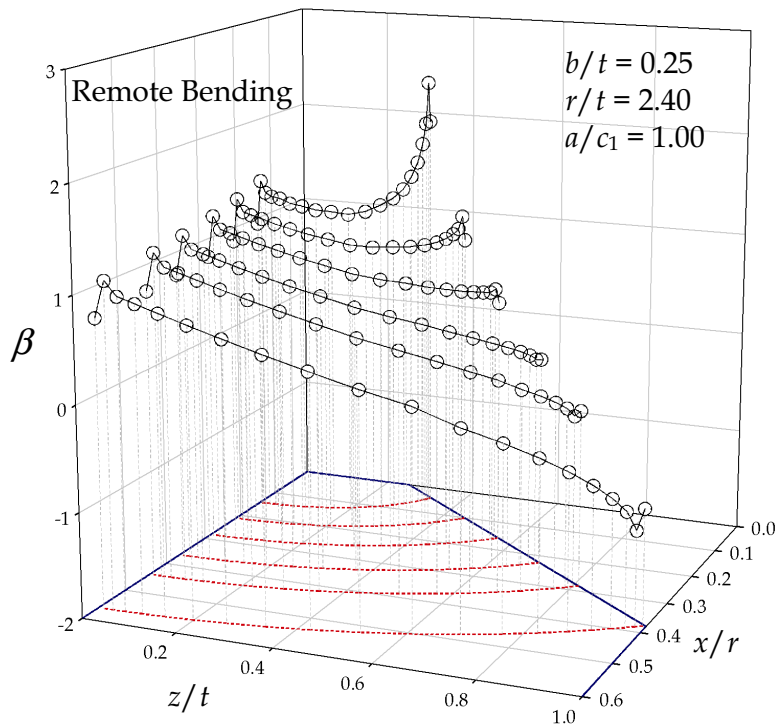
Figure 5-33 Effect of increasing crack length c_1 (changing a/t ratio) for constant $b/t = 0.25$, $r/t = 2.40$ and $a/c_1 = 1.00$ in the countersunk part of countersunk hole subject to bending
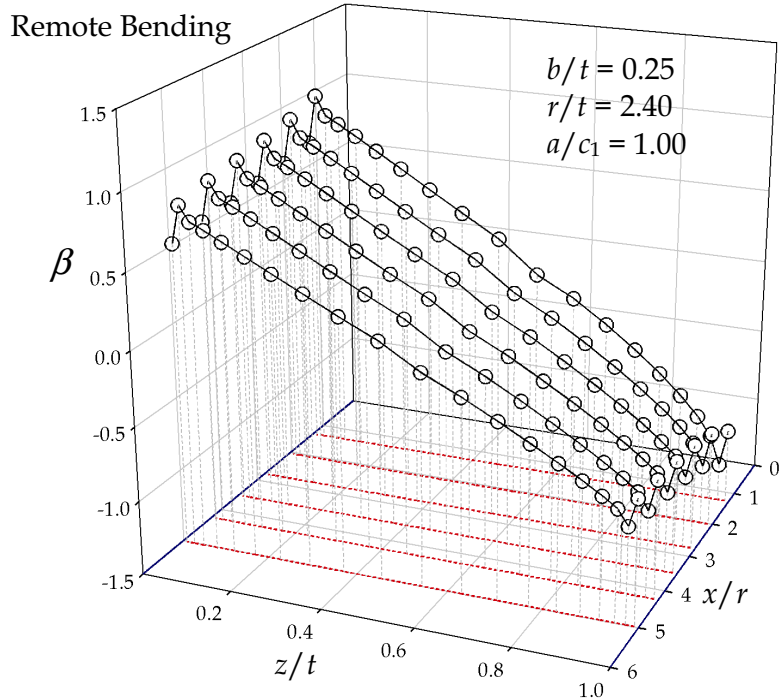
Figure 5-34 Effect of increasing crack length c_1 (changing a/t ratio) for constant $b/t = 0.25$, $r/t = 2.40$ and $a/c_1 = 1.00$ for through the thickness cracks subject to bending

In the straigh shank part of the countersunk hole, the loading is normal to the surface of the hole, the loading at the countersunk part results in a decomposition of the loading wich results in a loading normal to the countersunk surface, see Figure 5-35.
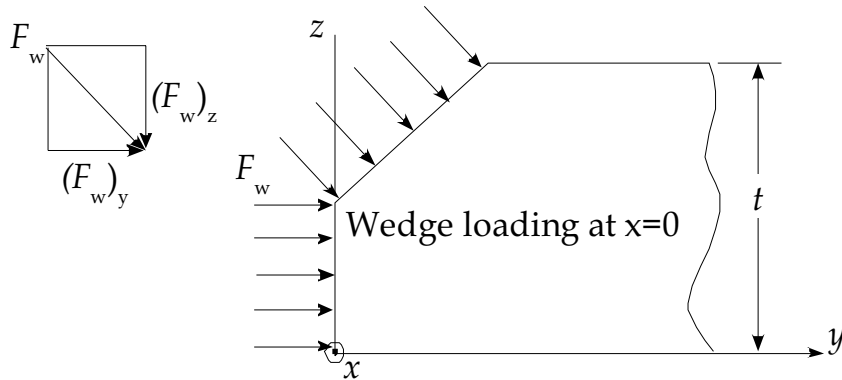
Figure 5-35 Decomposition of wedge loading on countersunk edge at *yz*-symmetry plane (*x* = 0, width direction)

The applied wedge loading creates a loading in thickness direction. At $y = 0$, the location of the crack plane, the displacement of all nodes (excluding the nodes in the crack wake) are constraint by $v = 0$. The loading of the countersunk hole thus creates a different stress intensity factor solution than that of a straigh shank hole.

The calculated β values for pin loading are shown in the following figures, Figure 5-36 Figure 5-38. Figure 5-36 shows the results for corner crack fronts starting at the lower surface and ending in the straight shank part of the fastener hole. The applied pin loading, $\cos^2$ loading at the bore of the countersunk hole, results in higher β values at the lower surface.

The trend in Figure 5-37 for cracks transitioning from the straight shank part ($z/t = 0.25$) to the countersunk edge ($z/t > 0.25$) is similar to the remote tension results, a drop in β values once the crack intersects with the countersunk edge. A slow decreasing β at the lower surface with increasing c_1 and a decreasing β for increasing a. The steeper reduction in β is a result of the through the thickness loading at the countersunk surface. At the upper surface this results in compression stress opposite to the tensile stress at the lower surface.

Figure 5-38 shows the behavior of β through the thickness along the crack front. The behaviour of the β values for pin loading at a countersunk hole is largely dependent on the b/t values. Lower b/t values coincide with a larger countersunk surface, and thus a higer loading in z-direction. For larger b/t values the influence of the loading through the thickness as a result of the pressure loading normal to the countersunk surface decreases, a lower loading in z-direction. Increasing the b/t values to $b = t$, is a straight shank hole. In that case the loading in z-direction has disappeared.
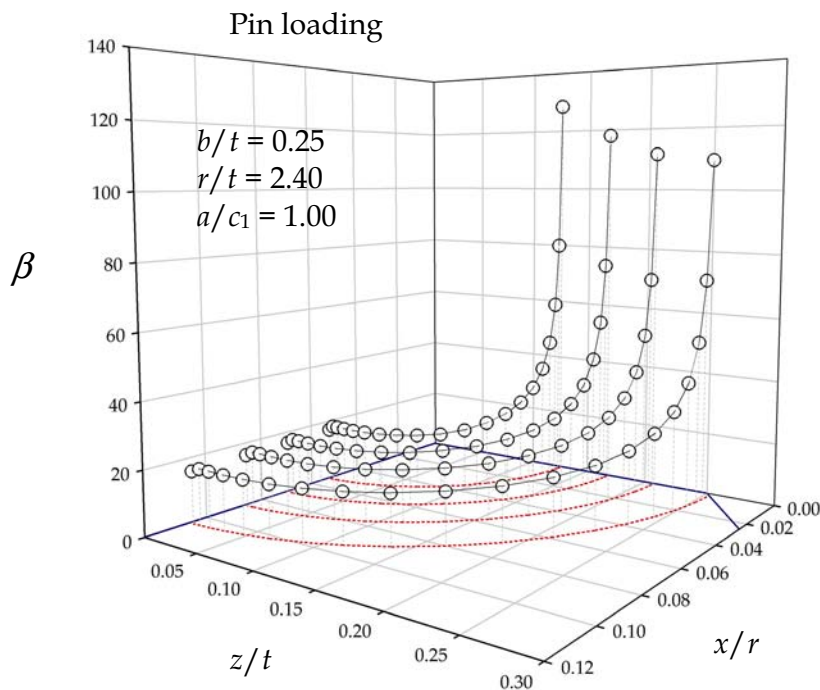
Figure 5-36 Effect of increasing crack length c_1 (changing a/t ratio) for constant b/t = 0.25, r/t = 2.40 and a/c_1 = 1.00 in the straight shank part of the countersunk hole subject to pin loading
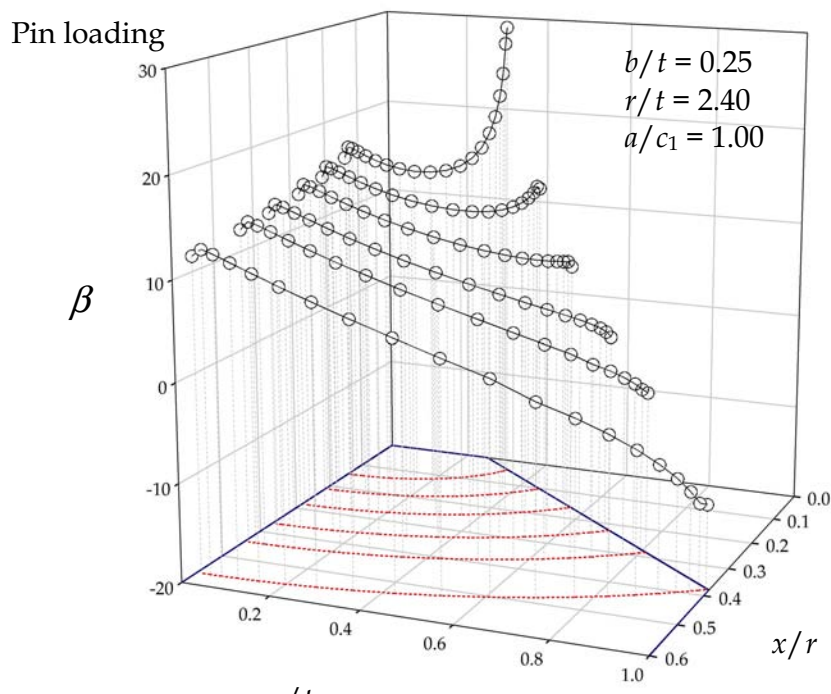
Figure 5-37 Effect of increasing crack length c_1 (changing a/t ratio) for constant b/t = 0.25, r/t = 2.40 and a/c_1 = 1.00 in the countersunk part of countersunk hole subject to pin loading
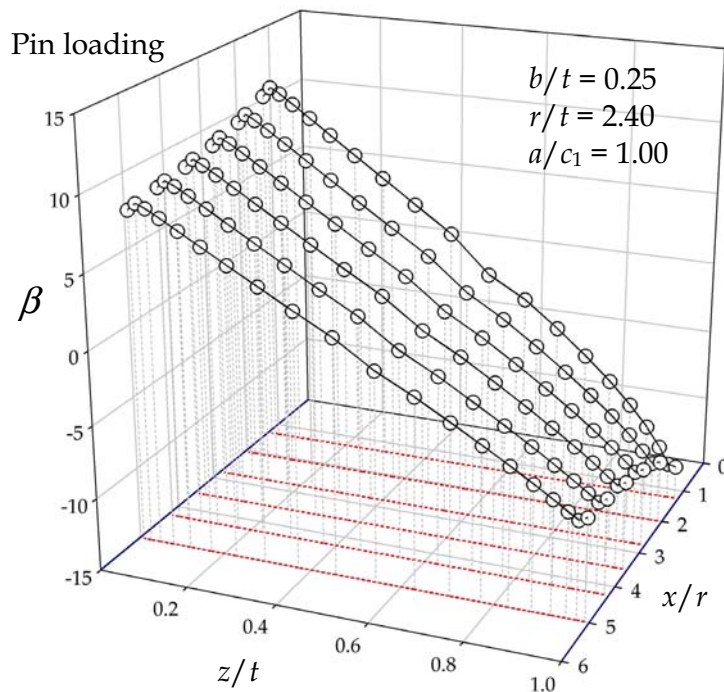
Figure 5-38 Effect of increasing crack length c_1 (changing a/t ratio) for constant b/t = 0.25, r/t = 2.40 and a/c_1 = 1.00 for through the thickness cracks subject to pin loading

Figure 5-39 shows the influence of the countersunk hole geometry for through the thickness cracks with similar crack shape properties. The influence of the countersunk hole is visible at z/t = 1.0. Slightly higher βs are calculated on the upper side of the sheet for increasing b/t. This also confirms that the influence of the countersunk hole decreases for large through the thickness cracks (for $a/t \approx 2.0$ and $c_1/r \approx 2.0$).

In Figure 5-40 the influence of the countersunk hole is more dominant, the β for the countersunk hole are close to intersecting through to the upper surface or are a complete through the thickness crack. The β solution for a through the thickness crack emanating from a straight shank hole has similar crack shape properties as the cracks emanating from the countersunk hole, making a direct comparison possible.

For large through cracks (c_1/r = 5.00) with high a/t values (a/t > 2.0), the influence of the countersunk hole is negligible and values compare very well to the values of normalized stress intensity factor solutions calculated by Fawaz for both the tension and bending [2]. The solutions for pin loading are more influenced by the shape of the fastener hole as was shown before.
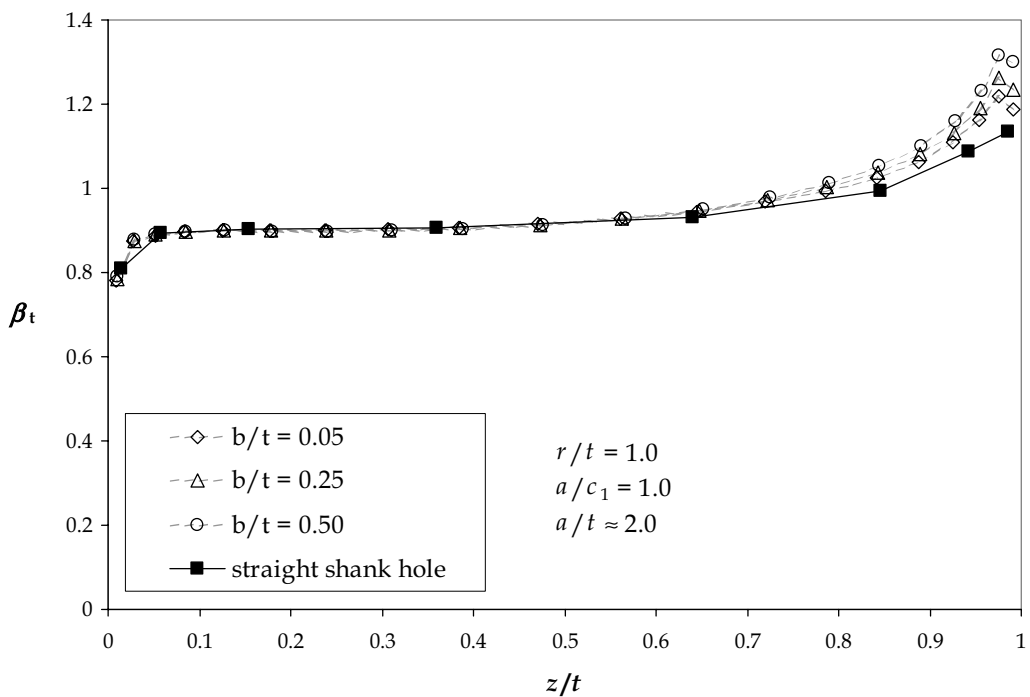
Figure 5-39 Comparison of normalized stress intensity factors for countersunk holes with straight shank hole solutions from Fawaz [2] for a trough the thickness crack
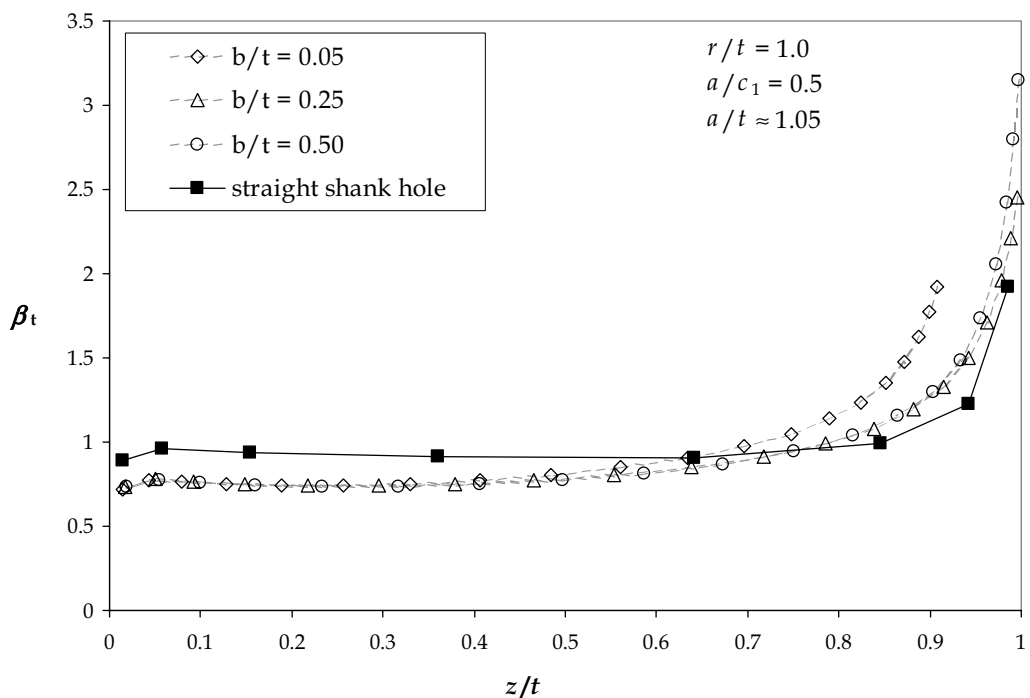
Figure 5-40 Comparison of normalized stress intensity factors for countersunk holes with straight shank hole solutions from Fawaz [2] for a trough the thickness crack close to the countersunk hole

The relation between the crack shape parameters, a/c_1, b/t and r/t, shown in this section is summarized for each part of the countersunk hole for each load case. Starting with pure tension and corner crack in the straight shank part, and progressing through to a through the thickness crack. Global trends that are visible for all crack shapes are:

- Pure Tension
  - Straight shank part
    - For all crack shapes with constant a, increasing β at the straight shank part of the countersunk hole for decreasing a/c_1. Resulting from an increase in crack area, raising the stress at the remaining area at the intersection of the straight shank and countersunk edge of the hole (Figure 5-28).
    - For all crack shapes with constant a, decreasing β at the lower surface as a result of the crack location away from the smallest area around the countersunk hole. At the straight shank part the stress is increased due to the presence of the countersunk edge. Although not shown, for small b/t values this behaviour is more pronounced (Figure 5-28).
    - For crack shapes with constant a/c_1, the β along the lower surface is similar to the behaviour described above. The increase in β along the straight shank is a result of decreasing the un-cracked area towards the countersunk edge, which is a stress raiser (Figure 5-29).
  - Countersunk edge
    - For all a/c_1 values, for increasing c_1, the stress gradient through the thickness excerts less influence on cracks close to the upper surface and thus the β decreases. Close to the switch from straight shank to countersunk edge the β will be higher (Figure 5-30).
  - Through cracks
    - The behaviour for through the thickness cracks is for all a/c_1 values, all r/t similar to the trends described by Fawaz decresing β (Figure 5-31, Figure 5-39 and Figure 5-40).
- Remote Bending
  - Straight shank part
    - For crack shapes with constant a/c_1, the β along the lower surface is similar to the behaviour described for pure tension. At the lower side, the bending stress has a positive unit stress. The decrease in β along the straight shank is a result of decreasing bending stress through the thickness. The effect of decreasing area along the straight shank part (Figure 5-32).

- o Countersunk edge
  - For all a/c_1 values, for increasing c_1, the stress gradient through the thickness excerts less influence on cracks close to the upper surface and thus the β decreases. Close to the switch from straight shank to countersunk edge the β will be higher. This effect described for pure tension is also valid for remote bending, and due to the bending stress through the thickness the effect is magnified (Figure 5-33).
- o Through cracks
  - The behaviour for through the thickness cracks is for all a/c_1 values, all r/t similar to the trends described by Fawaz decreasing β (Figure 5-34).
- Pin Loading
  - o For pin loading, similar trends in β appear as in the summary for remote bending. The influence of the countersunk hole does not decrease with increasing crack length c_1 contrary to the remote tension and bending solutions. The influence of the b/t values is thus dominant for all crack shapes. It is safe to say that the solutions for a large b/t values converge to the solutions for straight shank holes.

In general, the further the crack tip gets away from any hole, the β values will decrease since the crack tip is moving away from the stress riser. For countersunk holes, the case is even worse since the stress riser comes from not only the hole, but the countersunk knuckle as well.

5.6 Crack growth prediction

The crack growth predictions in the present section are all made with the newly calculated K values. These K solutions are contained in several input files, each input file containing the β solutions for a specific load case and r/t values. The input files are used by the crack growth life prediction program. The crack growth predictions are made with the United States Air Force AFGROW computer program developed by Harter [36]. AFGROW is a program that handles predictions for a variety of different fatigue problems, also for oblique part-through and through the thickness cracks. A special release incoorporates the possibility to use the new K values for countersunk holes in AFGROW.

The results of the *SEM* investigation allow a comparison with crack growth predictions. Results will be shown here for two specimens, one specimen loaded under tension only, and a second specimen loaded under combined tension and bending. The results are representative for other specimens as well.

The predictions were started at the first well-defined crack front shape that could be observed on the fracture surface of the two fatigue cracks in the single-hole tension specimen. The predictions were continued until the last crack front shape detected

in the *SEM*. Figure 5-41 shows the crack growth predictions for c_1 at the lower surface of the specimen for the two cracks at the right and left hand side of the countersunk hole edge respectively. The c_1 predictions follow the experimental result very well.
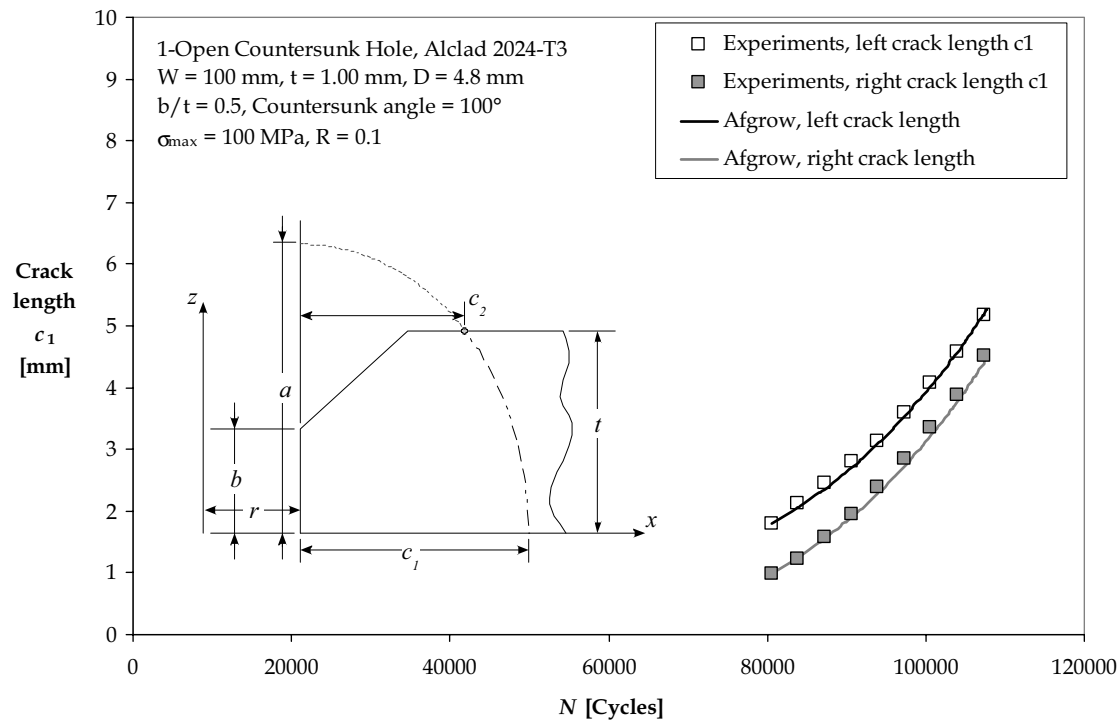
Figure 5-41 Crack growth prediction c_1 in single countersunk open hole specimen T 1024050-2 subject to tension

The crack growth prediction of the crack at the upper surface, crack length c_2, was more difficult since the AFGROW release did not allow to define a through the thickness crack as a initial crack shape. Only corner cracks were allowed for this purpose. The effect of not having the correct shape of the initial crack shape is shown in Figure 5-42. The actual crack shape at the left side of the countersunk hole has dimensions $a = 5.88$ mm and $c_1 = 1.97$ mm. However the crack depth is limited and thus reduced to the sheet thickness. The crack growth prediction of the left crack (starter crack, $a = 1.00$ mm and $c_1 = 1.97$ mm) at the upper surface does not follow the experimental data. For larger crack lengths the prediction catches up with the experimental data. The crack growth prediction of the right crack follows the experimental data from starter crack ($a = 1.04$ mm and $c_1 = 0.98$ mm) to the total number of cycles with good agreement (2% difference in final crack length for the left crack and 2% for the right crack).
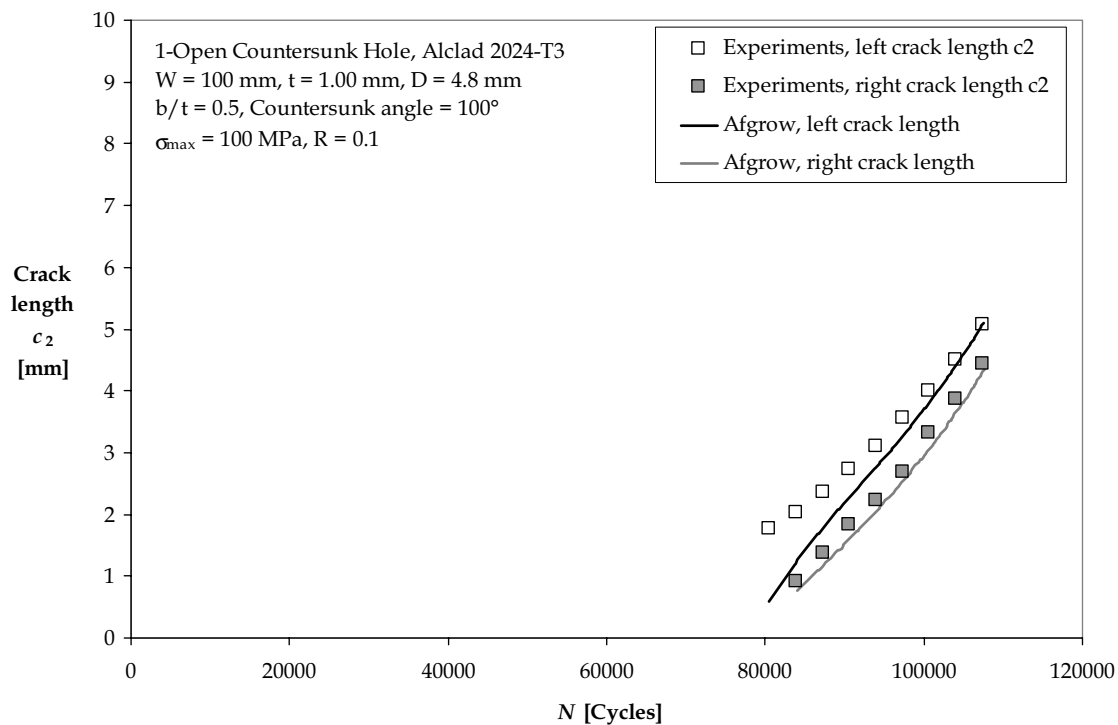
Figure 5-42 Crack growth prediction c_2 in single countersunk open hole specimen T 1024050-2 subject to tension

The prediction of the countersunk open hole specimen subject to tension and bending is shown in Figure 5-43 and Figure 5-44. The predictions in Figure 5-43 for crack length c_1 at the lower surface do not follow the experimental values exactly, but the agreement is still considered to be satisfactory. Figure 5-44 shows the results of the crack length c_2 at the upper surface. For this predition, the initial starter crack front shape was a corner crack at both sides of the countersunk hole. Also in this figure the agreement is satisfactory.

The results of the predictions for the two specimens are representative for the results of all other specimens. For some specimens the prediction results were even more accurate which may also be associated with possible scatter, which is characteristic for fatigue tests. Apparently, the newly calculated K values provide sufficient accuracy for crack growth life predictions of cracks growing from a part through to a through crack at a countersunk hole subjected to tension and combined tension and bending.
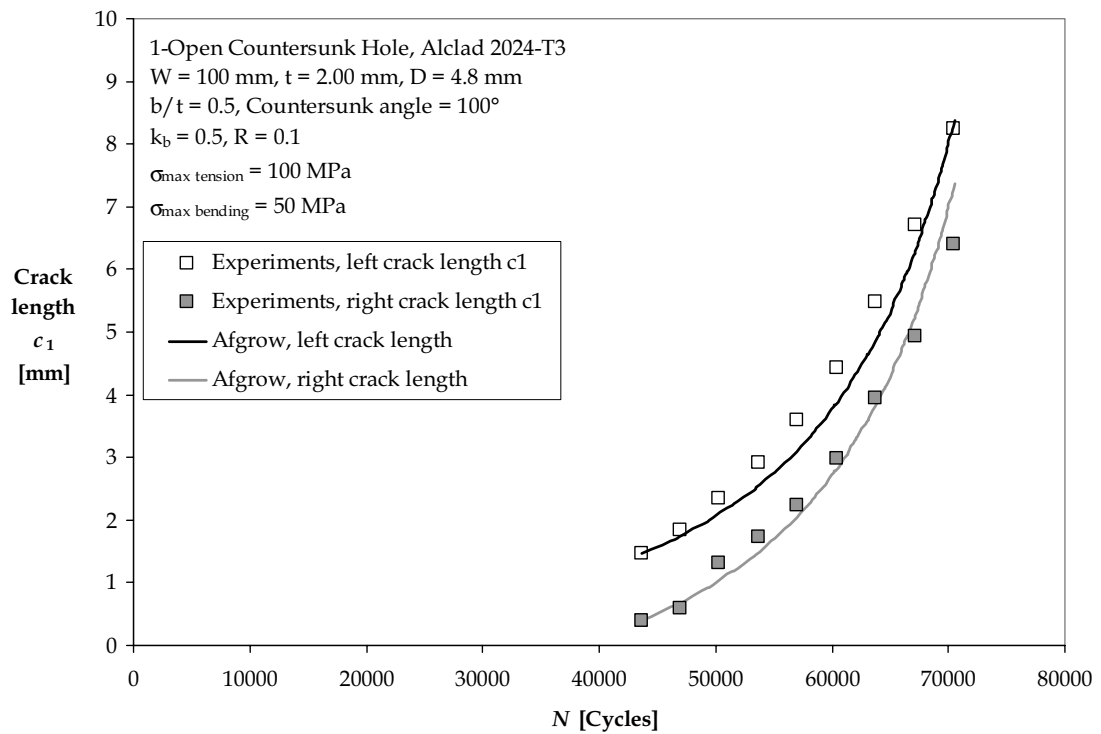
Figure 5-43 Crack growth prediction c_1 in single countersunk open hole specimen TB 2012050-1 subject to combined tension and bending
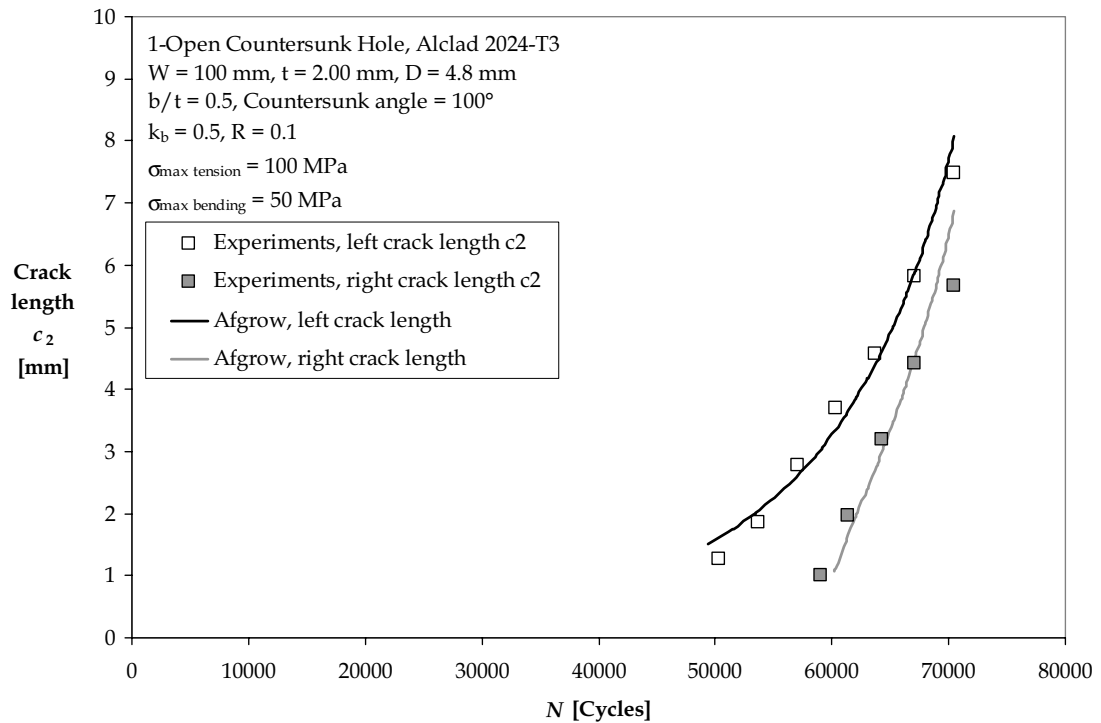
Figure 5-44 Crack growth prediction c_2 in single countersunk open hole specimen TB 2012050-1 subject to combined tension and bending

5.7   Conclusions

The combined tension and bending specimen provides an easy and powerful investigation tool to understand the crack shape and crack growth behavior of cracks subject to combined tension and bending loading. The influence of the secondary bending on the crack shape and crack growth can easily be determined.

The very time consuming fractographic analysis still provides the best fracture surface reconstruction for the larger part of the fatigue crack. The shape of the crack changes throughout the fatigue life, depending on the K values along the crack front. For large K values, the fracture surface is very tortuous making it difficult to detect the marker bands. For low K values, the problem of differentiating the marker bands from the other striations is difficult since both occur at similar ΔK_{eff} values.

Determining the a/c values from fractographic analysis is somewhat troublesome for pure tensile specimens, the uniform stress distribution through the thickness results in lower crack growth rates at the vertices due to the plane stress condition at the crack tip. For combined loading specimens, calculating the a/c is made easier by the extra bending stress component at the lower surface. This allows for a better curve fit through the fractographically obtained crack front locations. These a/c values were used to determine the range of a/c values needed for the K calculations. Comparing the current results with previous works, it turns out that the a/c value, *i.e.* the shape of the crack, is directly related to the applied stress.

The new calculated K values capture the near-the-surface-phenomenon more accurately than the previously published solution due to the increased mesh density.

Crack growth predictions are strongly influenced by small errors in K. A 20% lower K-solution may result in a two times slower crack growth rate, thus over-estimating the fatigue crack growth life considerably. It is imperative to have accurate K solutions.

For through the thickness cracks growing away from the countersunk hole, the normalized stress intensity factors approach the values of the normalized stress intensity factors for cracks emanating from straight shank holes ($c_1/r = 5.00$ with high $a/t > 2.0$). Thus, the effect of the countersunk hole decreases with increasing crack length for both the remote tension and bending solutions. The solutions for the pin loading β values show a dominant influence of the countersunk shape in the b/t values.

The newly calculated K values provide sufficient accuracy for crack growth life predictions for cracks growing from a part through to through crack at a countersunk hole subject to tension and combined tension and bending.

5.8 Literature

[1] de Rijck, J.J.M., *Crack Interaction of Oblique Part-Elliptical Through Cracks*, MSc. Thesis Delft University of Technology, Aerospace Engineering, August 1998

[2] Fawaz, S.A., *Fatigue Crack Growth in Riveted Joints*, Dis. Delft University of Technology, Delft University Press, 1997

[3] Fawaz, S.A., Andersson, B., and J.C. Newman, Jr., *Experimental Verification of Stress Intensity Factor Solutions for Corner Cracks at a Hole Subject to General Loading*, ICAF 2003, Luzern, Switzerland, 2003

[4] Nam, K.W., K. Ando, N. Ogura, and K. Matte, *Fatigue Life and Penetration Behaviour of a Surface Cracked Plate Under Combined Tension and Bending*, Fatigue and Fracture of Engineering Materials and Structures 17, 1994, pp. 873-882

[5] O'Brien, T.K, and G.B. Murri, *Combined Tension and Bending Testing of Tapered Composite Laminates*, Applied Composite Materials, 1995, pp. 401-413

[6] Phillips, E.P., *An Experimental Study of Fatigue Crack Growth in Aluminum Sheet Subjected to Combined Bending and Membrane Stresses*, NASA-TM-4784, 1997

[7] Fawaz, S.A., and J.J.M. de Rijck, *A Thin-Sheet, Combined Tension and Bending Specimen*, Experimental Mechanics, Vol. 39, No. 3, September 1999, pp. 171-176

[8] United States, *Department of Defense, Metallic Materials and Elements for Aerospace Vehicle Structures*, MIL-HDBK-5G, 1 November 1994

[9] Jeong, D. Y., D. P. Roach, J. V. Canha, J. C. Brewer, and T. H. Flournoy, *Strain Fields in Boeing 737 Fuselage Lap Splices: Field and Laboratory Measurements with Analytical Correlations*, DOT/FAA/CT-95/25, FAA Technical Center, Federal Aviation Administration, US Department of Transportation, June 1995

[10] Burgers, A., and P.D. Kempen, *Automatic Crack Length Measurements by the Electrical Potential Drop Method with Computer Control*, Report LR-309, Delft, Netherlands, September 1980

[11] Schijve, J., *Fatigue of Structures and Materials*, Kluwer Acadamic Publishers, Dordrecht, 2001

[12] Pelloux, W.R.A., and J. O'Grady, *Fractographic Analysis of Initiation and Growth of Fatigue Cracks at Rivet Holes*, Eds. S.N. Atluri, S.G. Sampath, and P. Tong, Structural Integrity of Aging Airplanes, Springer Series in Computational Mechanics, Berlin, Springer Verlag, 1991

[13] Schijve, J., *The Significance of Fractography for Investigations of Fatigue Crack Growth under Variable Amplitude Loading*, Fatigue and Fracture of Engineering Materials and Structure, Vol. 22, 1999, pp. 87-99

[14] Piascik, R.S., and S.A. Willard, *The Characterization of Wide Spread Fatigue Damage in the Fuselage Riveted Lap Splice Joint*, NASA-TP-97-206257, 1997

[15] Elber, W., *The Significance of Fatigue Closure*, Damage Tolerance in Aircraft Structures, ASTM STP 486, 1971, pp. 230-242

[16] Paris, P.C., and F. Erdogan, *Critical analysis of crack propagation laws*, Trans. ASME, Series D, Vol. 85, 1963, pp. 528-535

[17] Broek, D., and J. Schijve, *The effect of sheet thickness on the fatigue-crack propagation in 2024-T3 Alclad sheet material*, NLR-TN M.2129, August 1964

[18] Baldwin, J.D., and D.E. Denman, *Stress Intensity Solutions for Countersunk Fuselage Lap Splice Joints*, 20th ICAF Symposium, Seattle, Washington, USA, 1999

[19] Harris, C.E., J.C. Newman, Jr., R.S. Piascik, and J.H. Starnes, Jr., *Analytical Methodology for Predicting the Onset of Widespread Fatigue Damage in Fuselage Structure*, NASA-TM-110293, November 1996

[20] Vlieger, H., and H.H. Ottens, *Uniaxial and Biaxial Tests on Riveted Fuselage Lap Joint Specimens*, DOT/FAA/AR-98/33, October 1998

[21] Schijve, J., *Literature on fatigue crack growth of MSD configurations*, Document b2-01-28, September 2001

[22] Müller, R. P. G., *An Experimental and Analytical Investigation on the Fatigue Behaviour of Fuselage Riveted Lap Joints, The Significance of the Rivet Squeeze Force, and a Comparison of 2024-T3 and Glare 3*. Dis. Delft University of Technology, 1995

[23] Pártl, O., and J. Schijve, *Multiple-site-damage in 2024-T3 alloy sheet*, Report LR-660, Faculty of Aerospace Engineering, January 1992

[24] MSC/Patran®, www.mscsoftware.com

[25] Abaqus®, www.hks.com

[26] Chang, F., Scott, R.A., and G.S. Springer, *Strength of Mechanically Fastened Composite Joints*, Journal of Composite Materials, 16, 1982, pp. 470-494

[27] Crews, J.H., Hong, C.S., and I.S. Raju, *Stress Concentration Factors for Finite Orhtotropic Laminates with a Pinl-Loaded Hole*, NASA-TP-1862, 1981

[28] de Jong, T, *Stresses around Pin-Loaded Holes in Elastically Orthotropic or Isotropic Plates*, Journal of Composite Materials, 11, 1977, pp. 313-331

[29] Eshwar, V.A., Dattaguru, B., and Rao, A.K., *Partial Contact and Friction in Pin Joints*, Report NO. ARDB-STR-5010, Department of Aeronautical Engineering, Indian Institute of Science, 1977

[30] Shivakumar, K.N., Tan, P.W., and J.C. Newman, Jr., *A Virtual Crack Closure Technique for Calculating Stress Intensity Factors for Cracked Three Dimensional Bodies*, International Journal of Fracture, no. 36, 1988, R43-R50

[31] Irwin, G.R., *Analysis of Stresses and Strains Near the End of a Crack Transversing a Plate*, Journal of Applied Mechanics, Trans. ASME. 24, 1957, pp. 361-164

[32] Rybicki, E.F., and M.F. Kanninen, *A Finite Element Calculation of Stress Intensity Factors by a Modified Crack Closure Integral*, Engineering Fracture Mechanics, no. 9, 19977, pp. 931-938

[33] Rahman, A., Bakuckas, J., Jr., Bigelow, C., and P. Tan, *Boundary Correction Factors for Elliptical Surface Cracks Emanating from Countersunk Rivet Holes under Tension, Bending and Wedge loading Conditions*, DOT/FAA/AR-98/37, March 1999

[34] Stress Intensity Factors Handbook

[35] Newman, J.C., Jr., and I.S. Raju, *Stress Intensity Factor Equations for Cracks in Three Dimensional Finite Bodies Subjected to Tension and Bending Loads*, Computational Methods in the Mechanics of Fracture, Ed. S.N. Atluri, Elsevier Publishers B.V., 1986

[36] Harter, J.A., *Afgrow Users Guido and Technical Manual*, Afgrow for Windows 2K/XP, Version 4.0009.12, AFRL-VA-WP-TR-2004-XXXX, June 2004

6 Residual strength of joints

6.1 Introduction

A large experimental investigation of the behavior of crack initiation, crack growth and residual strength of seven different types of Fiber Metal Laminate joints has been carried out. The investigation on fatigue initiation was a combined program of the National Aerospace Laboratory NLR and the Delft University of Technology. The main purpose of this investigation was to support and validate prediction models for fatigue initiation in joints. Fatigue tests were carried out to obtain data for different stress levels. A number of monolithic aluminum lap-splice joints were also tested to provide S-N data on the fatigue crack initiation life as a reference for the Glare joints. Tests were performed at NLR and validated at TUD.

Next to this investigation the specimens were used to perform residual strength tests to validate the residual strength prediction model presented in this thesis. Prior to the residual strength tests fatigue crack growth tests were done to obtain the required crack lengths for the residual strength tests.

The first part of this chapter deals with the background of fatigue in Glare splices, Section 6.2, and residual strength of joints, Section 6.3. The results of the experimental program are presented and discussed in relation to the theoretical methodology, Section 6.4. Conclusions are given in Section 6.5.

6.2 Background of Fatigue in Glare Joints

In the following two sections a summarized background on the development of theoretical models to estimate the crack initiation and crack growth characteristics of Glare splices is presented. The methods presented are at this moment being used or are still under development.

6.2.1 Crack initiation

Crack initiation in Glare joints is based on the same principles as for monolithic aluminum joints [1]. The maximum bending location determines the most critical fastener row, usually the two outer rows. Secondary bending will result in high stresses at the faying surface at these locations. The combination of the stress concentration due to the fastener with the high stress at the faying surface creates the peak stress. Ignoring the influence of the clamping forces or residual stresses introduced by the fastening system, for both the monolithic aluminum and Glare joints, crack initiation will occur at the location of the peak stress. An experimentally validated calculation method for monolithic aluminum, adopted by Fokker Aerostructures several years ago, is used for predicting the fatigue life of riveted joints [2]. As mentioned in section 2.5, the fiber layers in Glare act as a natural crack arresting layers. For each aluminum layer in Glare, the crack which started at the faying surface has to re-initiate into each subsequent aluminum layer. For each

aluminum layer in Glare, the crack initiation can be calculated using the method based on the *Stress Similarity Concept* as described by Homan and Jongebreur in [2].

Since the method assumes that the fatigue crack initiation is entirely determined by the stress cycles in the aluminum, once the stress cycles in the individual layers of aluminum in Glare are known, the fatigue crack initiation can be calculated. This calculation uses the assumption that when two different joints have a similar peak stress system, they will have identical fatigue lives. With this assumption the fatigue life of any joint can be calculated using *S-N* data that are available from the literature or a reference joint. Calculation of the stresses in aluminum layers in Glare is presented in [3], and includes the effects of off-axis loading and curing.

Similar, as for the monolithic joints, the following assumptions have to be made for the method [3]:
- Stresses can be calculated for each individual layer
- The fatigue initiation behavior for individual aluminum layers in Glare is similar to the fatigue initiation of monolithic aluminum
- The same stress concentration factors K_t as for monolithic aluminum can be used
- The reference joints used are standard aluminum joints
- When a variable amplitude load is used, the Miner rule for damage accumulation can be used
- When fatigue cracks initiate away from the fastener hole, not from the net-section, the prediction is conservative.

The peak stress at the hole can be calculated with the following equation obtained from [2].

$$\sigma_{peak} = \frac{s}{s-D}\left[(1-\gamma)K_{t_{hole}} + \gamma K_{t_{pin}} + k_b K_{t_b}\right]\sigma_{Al} \qquad \text{(6-1)}$$

Where:

γ : Load transfer ratio
s : Fastener pitch
D : Fastener diameter
K_t : Stress concentration factor
K_{thole} : K_t for an open hole subject to tension in a finite width sheet
K_{tpin} : K_t for a pin loaded hole in a finite width sheet
K_{tb} : K_t for an open hole subject to bending in a finite width sheet
k_b : Bending factor
σ_{Al} : Stress in aluminum layer including off-axis loading and curing

The load transfer ratio γ can be found in section 3.3.2 and σ_{Al} can be calculated using the methods described in [3].

The following calculation procedure is summarized from [3]:
1. Equating with a reference joint: equal peak stress (both stress amplitude and stress ratio) results in equal fatigue crack initiation life.
2. Calculate the remote stress amplitude for the reference joint.
3. Determine the fatigue initiation life from *S-N* curve for the reference joint.

The bending factor has a significant influence on fatigue crack initiation. The linear bending distribution through the thickness results in different stresses in each aluminum layer. The highest stresses occur in the aluminum layers at the faying surface. Moving away from these layers the bending stress will decrease. The bending factor needs to be adjusted for each individual aluminum layer in the laminate. The number of fatigue cycles for the second aluminum layer to initiate will be higher than the number of cycles for the aluminum layer at the faying surface to initiate.

The fatigue initiation life for the monolithic aluminum joints in this investigation is based on the minimum detectable crack size. Crack growth analysis should be performed using this initial crack size. For Glare, the definition of the fatigue initiation life needs to be done carefully, mainly because the fibers do not affect the fatigue crack growth in Glare in the first small part of the crack growth trajectory. This can vary depending on the lay-up of the fiber metal laminate. Afterwards the fatigue crack growth adapts the characteristic slow crack growth generally observed in Glare.

The crack in the faying surface layer will continue to grow before crack initiation occurs in the second layer. This behavior affects the net-section stress, which requires recalculation of the bending stresses and thus the number of cycles required for crack initiation. In Glare crack initiation and crack growth can and will take place at or around a fastener hole.

6.2.2 Crack growth

The crack growth in a Glare joint will be different from the crack growth characteristics found in open hole fiber metal laminate tension specimens. Due to the secondary bending present in joints the crack initiates at the faying surface of the joint. Similar to crack initiation in monolithic aluminum, the crack initiates at the highest stress concentration at the faying surface. In monolithic aluminum joints, the crack will propagate as a part through crack for a period of time. In Glare, the fiber layers create a natural boundary to prevent crack growth through the thickness. In the subsequent aluminum layer the crack needs to initiate as mentioned in section 6.2.1. For open hole tension specimens, the crack will propagate with a straight crack front through the thickness due to the absence of secondary bending. Each layer in such a specimen will be subjected to a similar stress concentration resulting in a similar crack initiation life. Whereas in a fatigue crack through the thickness, the fibers act as bridging material, in a part through crack the aluminum layers will contribute to the crack bridging effect. And thus creating a different

crack growth behavior, the intact aluminum layers will carry part of the stress and thus lowering the net section stress. This results in a lower stress intensity factor at the crack tip of the cracked aluminum layers.

The crack growth methodology explained below is divided into two different methods summarized by Alderliesten [4]. The first method is based on a combination of stress intensity factor definitions for through cracks and surface cracks. Part through cracks are an intermediate between these two crack configurations: the through the thickness cracks with the highest crack growth rate and the surface cracks with the lowest crack growth rate. It is assumed that the part through cracks will display a crack growth rate between these two extreme cases. The second method is proposed by De Koning [5] and is based on determining the stress intensity factor at the tip of a surface crack. De Koning proposed to treat the stress system responsible for the crack opening as a local stress system near the crack tip, which inadvertently causes the stress intensity at the crack tip and thus the crack growth rate.

Evaluation of several test programs related to crack growth predictions in Glare grades support the method proposed by De Koning [5]. The local stress system includes the effect of secondary bending after the modifications applied by Homan [6].

6.3   Residual strength of Glare joints

Static failure of a joint occurs when that joint is not able to carry the applied load anymore. The type of static failure in joints is based on the loading condition and the joint configuration. The most common static failure modes in monolithic aluminum joints are fastener shear failure, plate tension failure, bearing failure and plate shear failure.

In Glare joints another failure mechanism, fastener pull-through, is often observed. This failure mechanism, explained by Slagter [7], is related to the lower stiffness of Glare in thickness direction, leading to increased tilting of the fasteners and hence increased tensile stresses in the fastener.

Cyclic loading drives fatigue failure modes. Residual strength failure in fatigued joints is in most cases related to the capacity to carry the load through the reduced net section between the fasteners. Just as for static failures, fastener pull-through failure can also occur as a residual strength failure mode in Glare joints.
A method is proposed to calculate the residual strength of joints. Vermeeren [8] and Müller [9] use the remaining net section to calculate the residual strength of monolithic and fiber metal laminates. The residual strength of fiber metal laminates is based on the remaining intact metal layers in combination with the intact fibers based on the blunt notch strength of the un-cracked joint and the metal volume fraction (MVF, see Section 2.4.2).

In the next sections the residual strength methodology is presented, which is based on the MVF approach and the blunt notch strength. The blunt notch strength of Glare and the influence of localized plastic bending on the blunt strength will be discussed. Finally, the residual strength methodology will be presented in the last section.

6.3.1 Blunt notch strength methodology

The strength of a structure containing holes with a stress concentration factor K_t in the range of 1 to 4 is defined as the blunt notch strength [10]. In fuselage joints a large number of fastener holes is present. The blunt notch value of both monolithic aluminum and Glare will be used to calculate the residual strength of the joints. Bosker used the Norris failure criterion and the *MVF* to calculate the blunt notch strength for every possible Glare lay-up [11],[12]. A short summary of the failure criterion and the usage of the *MVF* will be presented.

The Norris failure criterion as presented by Bosker, ref. [11], is obtained from the general Hill theory. This criterion predicts the failure when the following equation is satisfied:

$$\left(\frac{\sigma_{XX}}{\sigma_{XX_{BN}}}\right)^2 - \left(\frac{\sigma_{XX}}{\sigma_{XX_{BN}}}\right)\left(\frac{\sigma_{YY}}{\sigma_{YY_{BN}}}\right) + \left(\frac{\sigma_{YY}}{\sigma_{YY_{BN}}}\right)^2 + \left(\frac{\sigma_{XY}}{\sigma_{XY_{BN}}}\right)^2 > 1 \qquad \text{(6-2)}$$

Where *XX* denotes the *L*-direction and *YY* the *LT*-direction of Glare. The blunt notch strength values $\sigma_{XX_{BN}}$ and $\sigma_{YY_{BN}}$ are obtained through experimentally determined uni-axial blunt notch strengths or indirectly derived from *MVF* values. The shear blunt notch strength $\sigma_{XY_{BN}}$ can be determined by uni-axial off-axis blunt notch experiments [12]. Since all experiments were done uni-axially, these experimental results will have to be transformed to an off-axis stress state in the material rolling direction using the following stress transformation matrix:

$$\begin{bmatrix} \sigma_{XX} \\ \sigma_{YY} \\ \sigma_{XY} \end{bmatrix} = \begin{bmatrix} \cos^2(\gamma) & \sin^2(\gamma) & -2\cos(\gamma)\sin(\gamma) \\ \sin^2(\gamma) & \cos^2(\gamma) & 2\cos(\gamma)\sin(\gamma) \\ \cos(\gamma)\sin(\gamma) & -\cos(\gamma)\sin(\gamma) & \cos^2(\gamma)-\sin^2(\gamma) \end{bmatrix} \begin{bmatrix} \sigma_{XX}' \\ \sigma_{YY}' \\ \sigma_{XY}' \end{bmatrix}$$

$$\text{(6-3)}$$

Where σ_{XX}', σ_{YY}' and σ_{XY}' are applied stresses and γ is the angle between the *L*-direction and the applied load.

To determine the $\sigma_{XY_{BN}}$, experiments under several off-axis loading conditions have been done by Bosker. Rewriting Eqn. (6-2) to an off-axis loading, using Eqn. (6-3), for a 45° angle condition result in:

$$\sigma_{XY_{BN}} > \sqrt{\dfrac{\sigma_{45}^{2}}{4 - \left(\dfrac{\sigma_{45}}{\sigma_{XX_{BN}}}\right)^{2} + \left(\dfrac{\sigma_{45}}{\sigma_{XX_{BN}}}\right)\left(\dfrac{\sigma_{45}}{\sigma_{YY_{BN}}}\right) - \left(\dfrac{\sigma_{45}}{\sigma_{YY_{BN}}}\right)^{2}}} \tag{6-4}$$

σ_{XXBN} and σ_{YYBN} are the net-section strengths from Roebroeks [9] and σ_{45} is the net-section strength from Bosker [12]. With these values known, the σ_{XYBN} can now be calculated using Eqn. (6-4).

Table 6-1   Blunt notch net-section strength parameters, [1] Roebroeks and [2] Bosker

Glare	layer contribution	σ_{XXBN} [1] [MPa]	σ_{YYBN} [1] [MPa]	σ_{XYBN} [2] [MPa]
Glare 2A	Metal	417	394	249
	Fiber	1193	0	52
Glare 2B	Metal	417	394	249
	Fiber	0	1193	52
Glare3	Metal	417	394	249
	Fiber	597	597	52
Glare 4A	Metal	417	394	249
	Fiber	795	398	52
Glare 4B	Metal	417	394	249
	Fiber	398	795	52

As mentioned before, the *MVF* provides the means to calculate the basic properties of any Glare grade using the linear relation rewritten in the form below for the blunt notch strength.

$$\sigma_{i_{BN}} = MVF \cdot \sigma_{i_{al}} + (1 - MVF) \cdot \sigma_{i_{fiber}} \tag{6-5}$$

Where:

σ_{iBN} : XX, YY or XY material direction

σ_{ial} : Aluminum blunt notch strength

σ_{ifiber} : Blunt notch strength of prepreg layer

With this equation and the values for the blunt notch strength shown in Table 6-1 it is possible to calculate the blunt notch values for any given Glare grade.

6.3.2 *Influence of bending on blunt notch strength*

The influence of the bending can be described quantitatively only. All blunt notch testing was done for tensile blunt notch cases. All theoretical and validated blunt notch values are therefore only valid for pure tension load cases. However, as mentioned before, a lap-splice or butt joint is a complex structure subject to several

load cases. Static failure of a material occurs when the nominal stresses in the material exceed the ultimate strength σ_{ult}. In the case of an open hole, the ultimate strength is described by the blunt notch strength σ_{BN}. Due to the stress concentration of the hole, the blunt notch strength will be lower than the ultimate strength of the pristine material ($\sigma_{BN} < \sigma_{ult}$). Due to the lack of blunt notch values for specimens subject to bending, the ultimate strength will be used to give a quantitative description of the influence of the bending on the blunt notch strength.

In case of a uniform tensile stress with no bending present in a sheet of Glare or monolithic aluminum, the maximum stress reached is σ_{ult}. Figure 6-1 shows several calculated curves of the reduction in $\sigma_{tension}$ due to the increase in bending stress [13]. Introducing a bending stress results in a reduction of the maximum tensile stress, since the ultimate stress σ_{ult} remains constant for a specific Glare grade or aluminum alloy.
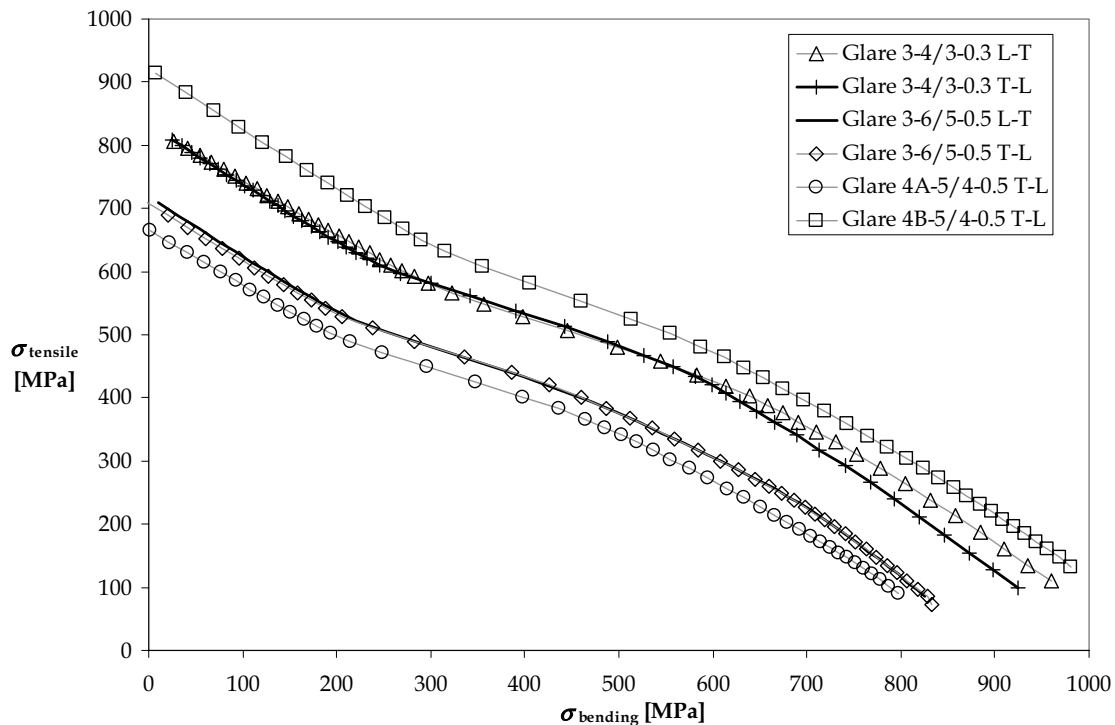
Figure 6-1   **Reduction in maximum tensile stress due to an increase of bending stress for different Glare grades [13]**

From Figure 6-1 the ultimate strength of the Glare laminates used can be found. The relation between σ_{ult} and the blunt notch strength σ_{BN} is assumed to be linear, this allows for a conversion of Figure 6-1 to a relation between blunt notch values for open holes subject to tension and bending. The conversion of the blunt notch values for open holes subject to bending is influenced by the differences in stress concentration factors for open holes. The theoretical stress concentration factor for an open hole subject to tension in an infinite width sheet is 3, for bending the

theoretical stress concentration factor is equal to 2. Therefore the conversion from ultimate tensile stress to blunt notch stress will be as follows:

$$T_{BN_{factor}} = \frac{\sigma_{ult}}{\sigma_{BN}}$$

$$B_{BN_{factor}} = \frac{2}{3} \cdot T_{BN_{factor}} \qquad\qquad \textbf{(6-6)}$$

These two conversion factors allow for the creation of Figure 6-2. It is unfortunate that no test results are available to verify Figure 6-2.
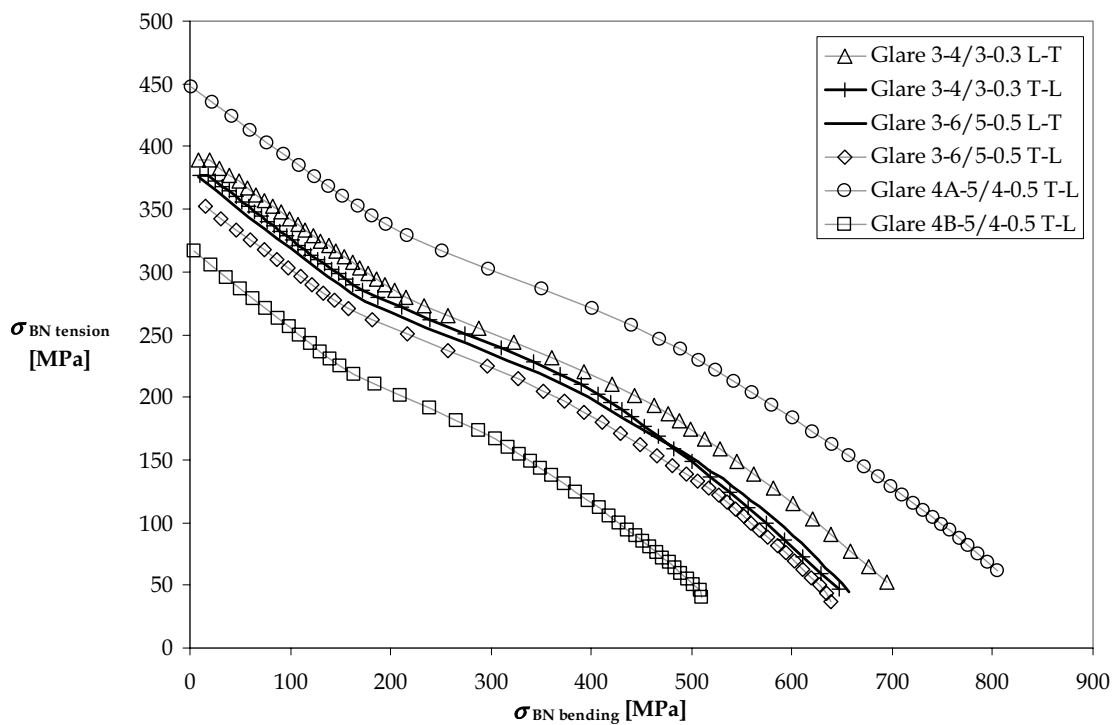
Figure 6-2   Relation between blunt notch values for open holes subject to tension and bending

The behavior of joints when the applied stress exceeds the yield limit of the material is of importance to the residual strength calculation. The calculations of the neutral line model are limited to the elastic region of the joint material. The neutral line model results are the symbols shown in Figure 6-3, the agreement with the strain gage data is as would be expected. This plot shows the stresses calculated from the strain measurements. The tensile stresses show an increasing trend up to the point were the yield stress is exceeded. The increase in tensile stress is reduced due to the plastic behavior of the material. This results in permanent bending at and around the fastener holes, and thus lowering the bending stresses outside the overlap region as shown in Figure 6-3. The bending stresses show, as soon as the yield limit

is reached, a decreasing trend. For both sheet thicknesses the behavior is shown. The sheet with thickness of 2.0 mm shows the first sign of reaching the yield limit as would be expected.

The results show a good agreement between the calculated and the measured stresses. However, the results in Figure 6-3 do not provide the answer to the question what the magnitude of the bending stress is at the location of the fastener row. It does show that a significant reduction in bending stresses outside the overlap region occurs. It is therefore expected that the permanent bending occurs at a bending stress significantly lower then would be calculated with the neutral line model. The neutral line model only used elastic material properties and can not account for plastic material behavior. The tensile stresses present in the sheet exceed the yield limit; a small amount of bending can therefore result in a permanent deformation of the sheets.
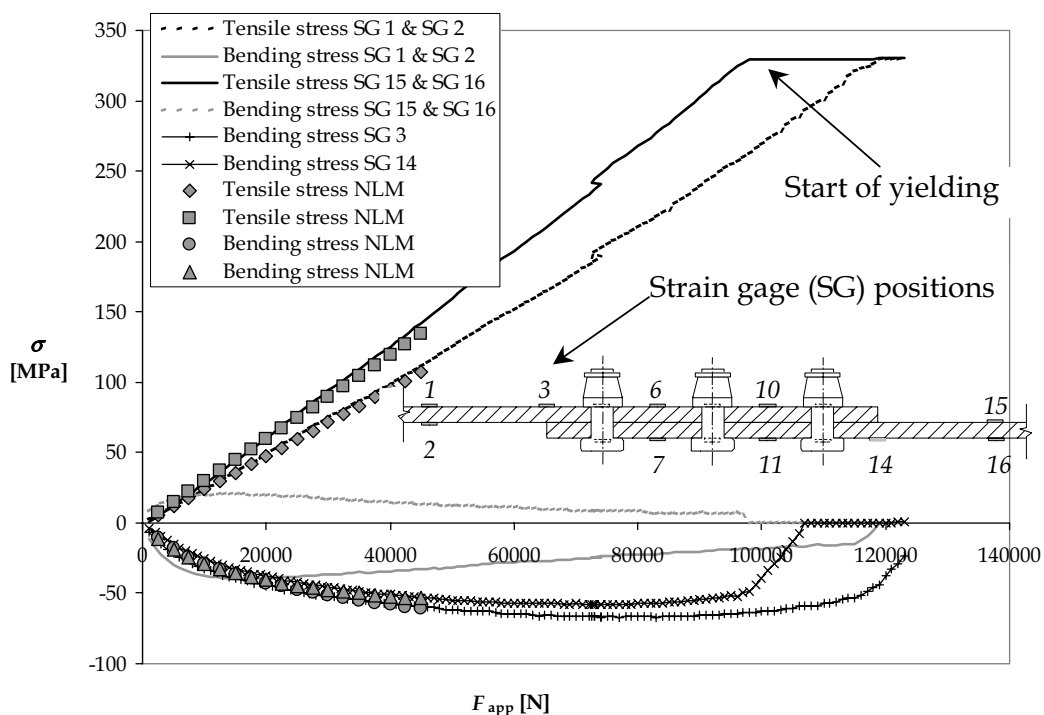
Figure 6-3   Stresses in lap-splice joint (AL_LJ_25_20) measured outside the overlap area

6.3.3   Residual strength methodology

The blunt notch calculation in sections 6.3.1 and 6.3.2 assumes an intact specimen; without fatigue cracks. The residual strength of joints will be significantly affected by fatigue cracks in the net-section and the secondary bending in lap-splice and butt joints. The prediction methodology used by Müller is based on the validation of the blunt notch strength of Glare 3 specimens [9]. The failure mechanism can be described as follows. The stresses in the aluminum layers do not reach the failure stress due to the intact fibers in the Glare laminate. Once the failure stress of the

fibers is reached, the stresses in the aluminum layers drastically increase to failure. Due to the differences in strain properties between the aluminum and prepreg layers, an area of delamination occurs around the highly stressed area. This delamination lowers the stresses in the aluminum layers. The available blunt notch strength is associated with the static strength of an open hole specimen subject to tension. The problem of interest here is a lap-splice or butt joint, joints with multiple holes, load transfer, clamping forces etc. If fatigue cracks are present, the contribution of the aluminum layers to the residual strength changes. Due to the reduced net-section area, the residual strength of the aluminum layers decreases. This concept is used by Müller to develop the following equation for the residual strength [9]:

$$\sigma_{res_{cracked}} = \sigma_{BN_{Glare}} - MVF \cdot \frac{A_{al_{cracked}}}{A_{al_{pristine}}} \sigma_{BN_{al}}$$

$$A_{al_{pristine}} = b \, t_{al} \, n_{al}$$

(6-7)

where:

$\sigma_{res_{cracked}}$	: Residual strength of Glare laminate
$\sigma_{BN_{Glare}}$	: Blunt notch strength from Eqn. (6-5) for pure tension
$\sigma_{BN_{al}}$	: Blunt notch strength from Table 6-1
$A_{al_{cracked}}$	: Total area of aluminum removed due to fatigue cracks
$A_{al_{pristine}}$	: Pristine area of aluminum in Glare
b	: Width of specimen
t_{al}	: Thickness of single aluminum layer
n_{al}	: Number of aluminum layers

Both Soetikno and Müller analyzed Glare 3-3/2-0.3 lap-splice joints. Figure 6-4 shows the results from several residual strength tests on non-fatigued specimens and fatigued specimens. Along the x-axis the amount of cracked aluminum is shown as a percentage. At the left end of the axis with 0 %, all aluminum layers are still intact. No fatigue cracking has taken place. At 100 % all aluminum layers are fully cracked and the fibers solely carry the applied load. The prediction methodology used here differs slightly from the method described by Müller. Müller based his methodology on an empirical determined blunt notch factor, whereas the blunt notch value of Glare in Eqn. (6-7), $\sigma_{BN_{Glare}}$, is based on the metal volume fraction method from section 2.4.2.

It then is not unexpected to obtain such good results in predicting the residual strength of Glare 3-3/2-0.3 specimens. Soetikno also analyzed two other material specification lap-splice joints, several Al 2024-T3 and special Glare 3-3/2-0.3 lap-splice joints [14]. The special Glare 3-3/2-0.3 was not manufactured with the thin aluminum 2024-T3 sheets, but with thin aluminum 7475-T761 sheets. Figure 6-5 shows the good results obtained with the new methodology for other fiber metal laminate specifications and monolithic aluminum.
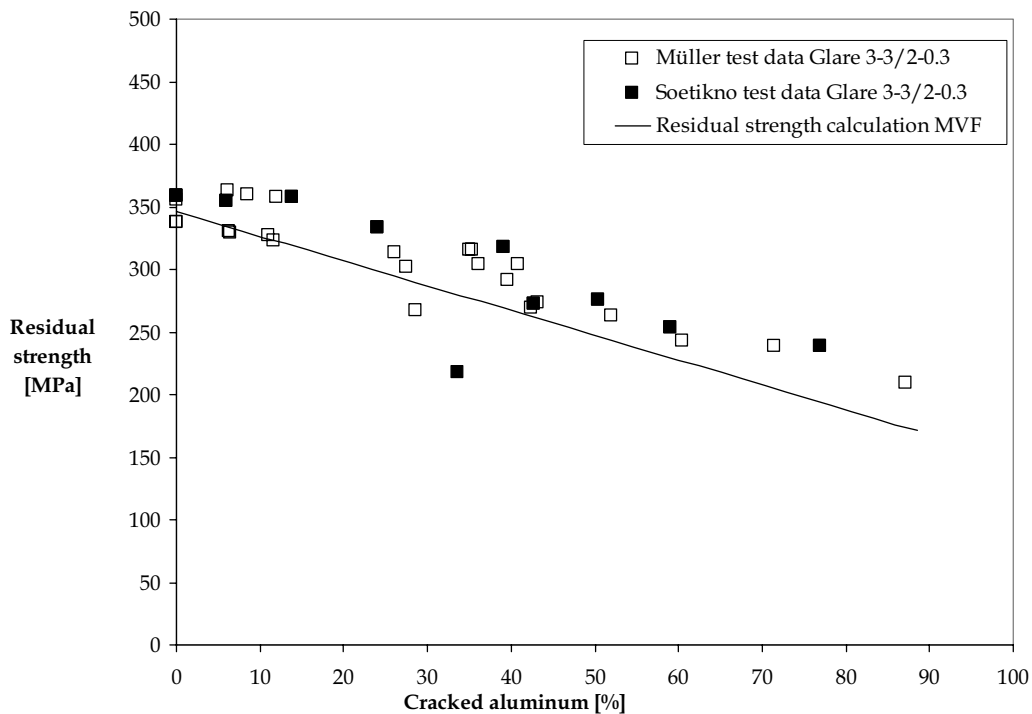
Figure 6-4   Residual strength of Glare 3-3/2-0.3 lap-splice joint [9],[14] based on the specimen gross section
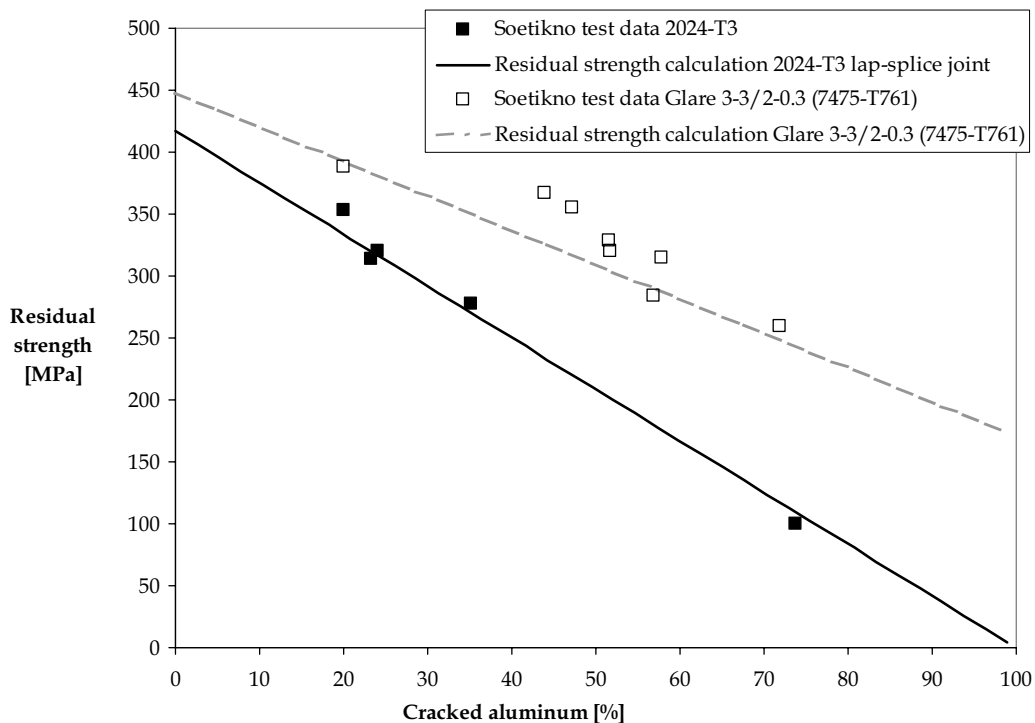
Figure 6-5   Residual strength of Al 2024-T3 and Glare 3-3/2-0.3 (7475-T761) lap-splice joints [14] based on the specimen gross section

6.4 Experimental program

The objective of the test program is to obtain sufficient data for validation of the theoretical methodology described in section 6.2 and 6.3. Table 6-2 and Table 6-3 show an overview of the specimens used in this investigation. The two aluminum 2024-T3 lap-splice joints from Table 6-3 had similar sheets thicknesses as the Glare GL_LJ_B1 and GL_LJ_B2 lap-splice joints, which allows a direct comparison. The theoretical background of the investigation is divided into three parts, crack initiation, crack growth and residual strength in fiber metal laminate joints. The experimental part is divided in the same way. The crack initiation investigation is done by the National Research Laboratory (*NLR*). Both crack growth and residual strength tests are the responsibility of Delft University of Technology. A complete overview of the crack initiation tests can be found in [1].

Table 6-2   Specimen properties for test program glare specimens

Specimen[1]	Sheet material[2]	Thickness [mm]	Strain gage pattern[3]
GL_LJ_B1	$t_1 \rightarrow$ Glare 4A-8/7-0.5 $t_2 \rightarrow$ Glare 3-6/5-0.5	$t_1 = 6.625$ $t_2 = 4.25$	-
GL_LJ_B2	$t_1 \rightarrow$ Glare 3-4/3-0.3 $t_2 \rightarrow$ Glare 4B-4/3-0.3	$t_1 = 1.95$ $t_2 = 2.325$	-
GL_BJ_A1	$t_1 \rightarrow$ Glare 3-6/5-0.5 $t_2 \rightarrow$ Glare 2B-6/5-0.5 $t_3 \rightarrow$ Glare 3-6/5-0.5	$t_1 = 4.25$ $t_2 = 4.25$ $t_3 = 4.25$	Figure E-5
GL_BJ_A2	$t_1 \rightarrow$ Glare 3-8/7-0.3 $t_2 \rightarrow$ Glare 2B-8/7-0.3 $t_3 \rightarrow$ Glare 3-8/7-0.3	$t_1 = 4.15$ $t_2 = 4.15$ $t_3 = 4.15$	Figure E-5
GL_BJ_A3	$t_1 \rightarrow$ Glare 3-4/3-0.3 $t_2 \rightarrow$ Glare 2B-4/3-0.3 $t_3 \rightarrow$ Glare 3-4/3-0.3	$t_1 = 1.95$ $t_2 = 1.95$ $t_3 = 1.95$	-
GL_BJ_A4	$t_1 \rightarrow$ Glare 4A-5/4-0.5 T-L $t_2 \rightarrow$ Glare 2B-6/5-0.5 $t_3 \rightarrow$ Glare 4A-5/4-0.5 T-L	$t_1 = 4.00$ $t_2 = 4.25$ $t_3 = 4.00$	Figure E-5
GL_BJ_A5	$t_1 \rightarrow$ Glare 4B-5/4-0.5 T-L $t_2 \rightarrow$ Glare 2B-6/5-0.5 $t_3 \rightarrow$ Glare 4B-5/4-0.5 T-L	$t_1 = 4.00$ $t_2 = 4.25$ $t_3 = 4.00$	Figure E-5

[1] Lap-splice joint dimensions $\rightarrow$ Figure E-1
   Butt joint dimensions $\rightarrow$ Figure E-2
[2] For *BJ* specimens t_2 corresponds to the butt strap
[3] Type: KYOWA KFG-2-120-C1-23, Gage length: 2.00 mm

Table 6-3   Specimen properties for test program aluminum specimens

Specimen[1]	Sheet material	Thickness [mm]	Strain gage pattern
AL_LJ_B1	$t_1 \rightarrow$ Aluminum 2024-T3 Clad $t_2 \rightarrow$ Aluminum 2024-T3 Clad	$t_1 = 7.00$ $t_2 = 4.50$	-
AL_LJ_B2	$t_1 \rightarrow$ Aluminum 2024-T3 Clad $t_2 \rightarrow$ Aluminum 2024-T3 Clad	$t_1 = 2.00$ $t_2 = 2.40$	-
[1] Lap-splice joint dimensions $\rightarrow$ Figure E-1			

The geometry of the specimens is chosen in order to validate the existing prediction methods. The geometry of each test series is shown in Appendix E, the width of each specimen is 168 mm. Each specimen is manufactured using HL410-V6 SA Hi-loks, titanium fastener with a diameter of 5.6 mm, and HL84-6 collars, each row contains six fasteners. A characteristic property of installing Hi-lok fasteners is that they exert a large amount of clamping around the fastener holes.

The problem of the finite width of the specimen is that the two edge fasteners of a row carry more load than the inner fasteners. This is a consequence of the Poisson contraction in the width direction of the specimen as discussed by Müller [9] and de Rijck [15]. The contraction is larger outside the overlap than in the overlap, and the edge fasteners will carry more load. Crack initiation will then preferably occur at the edge fasteners which is undesirable. There are several tricks to discourage crack initiation at the edge fasteners based on creating special conditions for these fasteners, see discussion by Müller [9] and Fawaz [16]. The most elegant method adopted for the present investigation is to increase the clamping of the edge fasteners. This is possible by the high clamping force which can be obtained by the Hi-lok fastener. The Hi-loks in the edge holes of the outer fastener rows are installed by torquing the nut until the collar fails. A high clamping is then obtained and cracks will initiate outside the hole, situation *a* in Figure 6-6. The nuts of the inner fasteners are not heavily torqued and less clamping is obtained which can still allow crack initiation at the hole, situation *b* in Figure 6-6. Crack initiation at all inner holes becomes possible, which implies multiple site damage, a situation desirable for the present investigation.
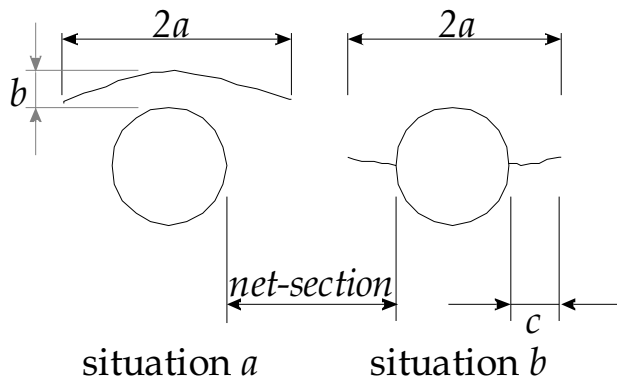
Figure 6-6 **Influence of higher clamping forces on the location of crack initiation around the bore of a fastener hole. Situation *a* due to large clamping forces and situation *b* due to normal clamping forces**

6.4.1 Crack initiation

A summary of the results from the crack initiation tests is presented in Appendix G.2. The results presented indicate the influence of the clamping force of the Hi-loks very well. For all specimens which are assembled using the method described in the previous section a multiple side damage scenario was obtained.

The obtained data from all crack initiation tests is used for validation of the existing methods to predict the fatigue crack initiation of fiber metal laminates using the FML F&DT toolbox [17]. The conclusion reached in the investigation conducted by Schra and Homan, [1], is that a good agreement is reached in predicting the fatigue initiation lives of the fiber metal laminate lap-splice and butt joints. The best agreements could be obtained using *S-N* curves based on fatigue initiation data and not on fatigue failure curves. This will result in overestimation of the fatigue initiation life of joints.

6.4.2 Crack growth

Crack growth measurements during a fatigue test on the joint specimens require that a specimen is periodically disassembled. This has been done for two specimens of test series GL_LJ_B2. The results are presented in Appendix G (Figure G-1 and Figure G-2) which indicates that the cracks were growing with an approximately constant crack growth rate. It implies a linear relation between the crack length and the number of cycles. Because the frequent disassemblies are rather time-consuming it was decided that crack growth for all other specimens would be documented with two measurements only, i.e. one measurement for a small crack length and a second one for a relatively large crack length. The first measurement was made early in the fatigue test to be sure that the crack length was still small. Disassembling was necessary for this measurement. The second measurement did not require disassembling because a crack length measurement was made on the fracture surface at the end of the test before the residual strength test was carried out. The linear relation between the two data points was then used to calculate the fatigue

life at a crack length of 1.0 mm, which was defined as the crack initiation life N_i. This result can then be used for crack growth predictions using the method proposed by De Koning [5] and Homan [7]. Appendix G contains some more data on the crack growth part of the tests, including references to the original test results.

6.4.3   Residual strength

The residual strength tests are done on a MTS computer controlled 100 kN servo-hydraulic test machine. Specimen preparation required bonding tabs at the ends of all specimens. These tabs ensured that the specimen clamping area was sufficiently equipped to withstand the high load transfer from the clevis into the specimen. All residual strength tests were done with a loading rate of 2.00 mm per second to avoid any strain hardening effects of the specimen according to Airbus internal standards.

Preparation of the specimens for crack shape analysis after the residual strength test is done in the following way. The small cut-offs of the residual strength specimens including the fatigue crack surfaces are heated at a temperature of 350 °C for a period of 5 hrs. During this heating process the S_2-glass fibers carbonize and the Glare laminate can be taken apart. This allows for an accurate examination of each individual layer of aluminum of the Glare laminate with a traveling optical microscope and a digital caliper providing an accuracy of 0.01 mm. The crack length can be documented easily due to the differences in structure of the fracture surface between the fatigue crack and the residual strength fracture.

Seven different specimen series were available for the residual strength testing. Table 6-4 and Table 6-5 show the results for all specimens, including the number of cycles accumulated in the crack initiation and crack growth period. The failure load and the calculated residual strength based on the original gross section area is also listed. The crack lengths measured in each individual aluminum layer at each hole are summed to calculate the total cracked area. The failure mode is pre-dominantly net-section failure in a fastener row. Crack growth reduces the load carrying capabilities of the aluminum layers and thus the effective net-section between the fasteners. Fastener pull through occurred in a limited number of joints. The fastener pull-through for the Glare A5 series is associated with the Glare 4B-6/5-0.5 fiber lay-up. These specimens have a 90°/0°/90° fiber lay-up between the aluminum layers. This means that one fiber layer is placed in the rolling direction of the aluminum sheet. The lay-up of Glare 4 laminates increases the load carrying capabilities and reduced the crack growth rate of crack emanating from the fastener holes. Although cracks are present in and around the fastener holes, the net-section strength is not reduced in such a manner that fastener pull-through can be avoided. The fact that the other Glare GL_BJ_A5 series did not have the fastener pull-through problem is related to the higher number of fatigue cycles for GL_BJ_A5-g, GL_BJ_A5-h and GL_BJ_A5-i. Specimens GL_BJ_A5-b, GL_BJ_A5-e and GL_BJ_A5-f accumulated more and longer cracks in the crack initiation program.

Table 6-4   Residual strength results for Glare lap-splice joint specimens

Specimen[3]		Residual strength				
ID	Thickness [mm]	N[1] [Cycles]	F_{res} [kN]	σ_{res} [MPa]	$A_{cracked}$ [mm²]	Failure Mode[2]
GL_LJ_A1-c		50600	240	336		RPT
GL_LJ_A1-d		45200	323	325	3.23	NSF
GL_LJ_A1-e		40200	237	332	5.46	NSF
GL_LJ_A1-f	4.25	30300	226	317	10.69	NSF
GL_LJ_A1-g		75300	229	321	10.09	NSF
GL_LJ_A1-h		10300	177	248	192.28	NSF
GL_LJ_A1-i		70600	228	320	32.88	NSF
GL_LJ_A2-a		55100	210	301	25.83	NSF
GL_LJ_A2-b		50100	210	301	31.71	NSF
GL_LJ_A2-c		35100	205	294	30.90	NSF
GL_LJ_A2-d	4.15	90200	205	294	56.21	NSF
GL_LJ_A2-e		45200	206	295	55.66	NSF
GL_LJ_A2-f		85200	210	301	47.06	NSF
GL_LJ_A2-g		140300	208	298	45.03	NSF
GL_LJ_A2-h		140300	197	283	94.20	NSF
GL_LJ_A3-a		65500	101	308	21.92	NSF
GL_LJ_A3-b		59500	102	311	17.57	NSF
GL_LJ_A3-c		115000	106	324	15.89	NSF
GL_LJ_A3-d		135000	104	317	22.94	NSF
GL_LJ_A3-e	1.95	190000	106	324	20.95	NSF
GL_LJ_A3-f		190000	111	339	20.08	NSF
GL_LJ_A3-g		71500	105	321	16.96	NSF
GL_LJ_A3-h		145000	113	345	20.68	NSF
GL_LJ_A3-i		204000	110	336	19.16	NSF
GL_LJ_A4-a		42100	203	302	19.92	NSF
GL_LJ_A4-b		23100	201	299	17.45	NSF
GL_LJ_A4-c		57100	194	289	20.32	NSF
GL_LJ_A4-d		94100	193	287	26.21	NSF
GL_LJ_A4-e	4.00	32100	187	278	34.20	NSF
GL_LJ_A4-f		44100	187	278	28.67	NSF
GL_LJ_A4-g		78300	166	247	110.60	NSF
GL_LJ_A4-h		108300	169	251	101.10	NSF
GL_LJ_A4-i		61300	136	203	174.74	NSF
[1] Combination of the number of cycles used in the crack initiation and crack growth program [2] *NSF* is net-section failure, *RPT* is rivet pull through failure [3] Width of all specimens is 168 mm						

Specimen[3]		Residual strength				
ID	Thickness [mm]	N[1] [Cycles]	F_{res} [kN]	σ_{res} [MPa]	$A_{cracked}$ [mm^2]	Failure Mode[2]
GL_LJ_A5-a		36800	229	341		RPT
GL_LJ_A5-b		32800	227	338	25.30	NSF
GL_LJ_A5-c		66800	229	340		RPT
GL_LJ_A5-d		31700	234	348		RPT
GL_LJ_A5-e	4.00	43700	233	347	16.63	NSF
GL_LJ_A5-f		38700	230	342	12.35	NSF
GL_LJ_A5-g		87400	232	345	31.01	NSF
GL_LJ_A5-h		97400	227	338	62.36	NSF
GL_LJ_A5-i		87400	227	338	64.22	NSF

[1] Combination of the number of cycles used in the crack initiation and crack growth program
[2] NSF is net-section failure, RPT is rivet pull through failure
[3] Width of all specimens is 168 mm

Table 6-5   Residual strength results for Glare butt joint specimens

Specimen[3]		Residual strength				
ID	Thickness [mm]	N[1] [Cycles]	F_{res} [kN]	σ_{res} [MPa]	$A_{cracked}$ [mm^2]	Failure Mode[2]
GL_BJ_B1-a		151300	196	275	107.79	NSF
GL_BJ_B1-b		106300	206	289	81.80	NSF
GL_BJ_B1-c		86300	223	312	56.77	NSF
GL_BJ_B1-d		87600	177	248	170.46	NSF
GL_BJ_B1-e	4.25	92600	181	254	164.77	NSF
GL_BJ_B1-f		142600	184	258	148.67	NSF
GL_BJ_B1-g		185300	148	207	270.47	NSF
GL_BJ_B1-h		165300	138	194	360.83	NSF
GL_BJ_B1-i		225300	166	323	229.11	NSF
GL_BJ_B2-d		80000	99	295	39.98	NSF
GL_BJ_B2-e		95000	101	301	40.27	NSF
GL_BJ_B2-f	2.00	60000	98	292	57.56	NSF
GL_BJ_B2-g		60000	100	298	41.05	NSF
GL_BJ_B2-i		130000	105	313	32.45	NSF

[1] Combination of the number of cycles used in the crack initiation and crack growth program
[2] NSF is net-section failure, RPT is rivet pull through failure
[3] Width of all specimens is 168 mm

It is difficult to make an estimation on the localized bending that will be present in the lap-splice and butt joints at the critical fastener row. As explained before, the bending outside the overlap region reduces to zero, only leaving the bending at the critical fastener row. This bending is only a small percentage of the bending at that location that will be present when stresses are far below the yield limit of the material. As a result, the blunt notch value will only have to be adapted slightly and in some cases depending on the specimen's geometry and material properties the

bending can entirely be neglected. Looking closely to all the data obtained from all residual strength tests, a reduction of the blunt notch value $\sigma_{BNGlare}$ in Eqn. (6-7) of 10% gives a good approximation of the residual strength prediction if compared to the test results. The following Figure 6-7 to Figure 6-13 are residual strength predictions for the seven Glare specimens taking the total crack length into account.

The test results presented in Figure 6-7 to Figure 6-13 are compared to the residual strength calculations using Eqn. (6-7) with the 10% reduction of $\sigma_{BNGlare}$ as discussed above. The test results in all figures confirm the trend as predicted by Eqn. (6-7). The test results differ from the prediction, and in some extreme cases by +20% and -15%.
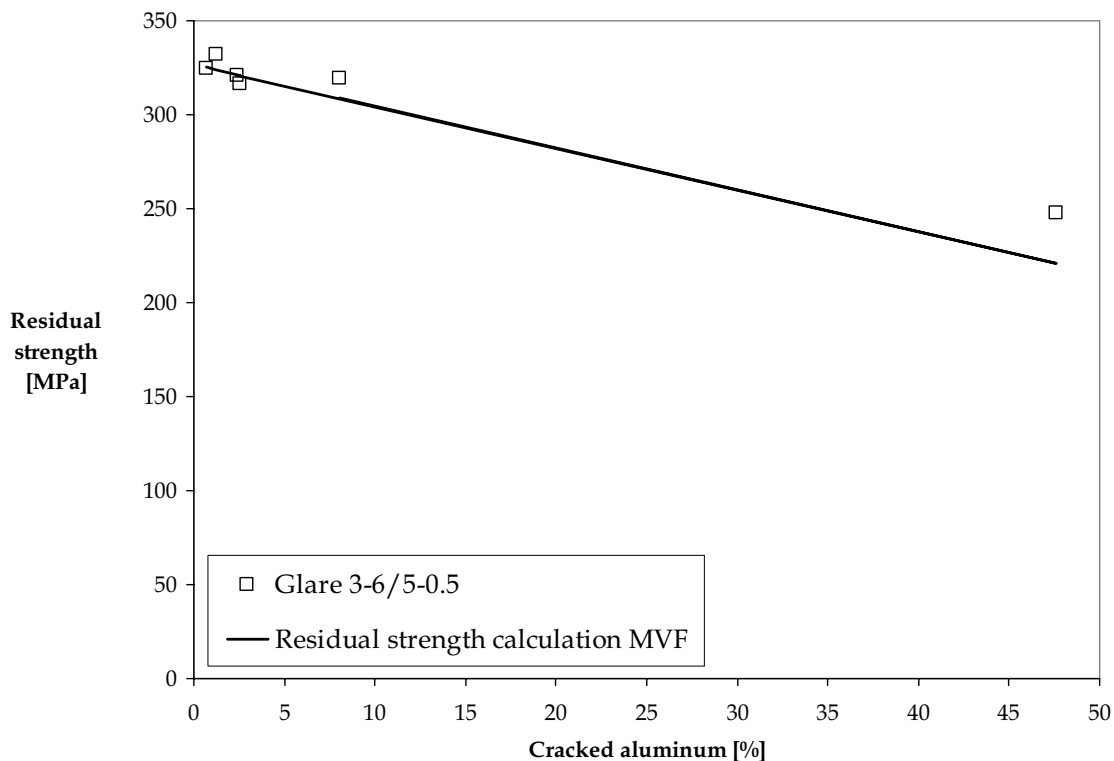
Figure 6-7   **Residual strength prediction and test results of lap-splice joint specimen GL_BJ_A1 for Glare 3-6/5-0.5 based on the specimen gross section**
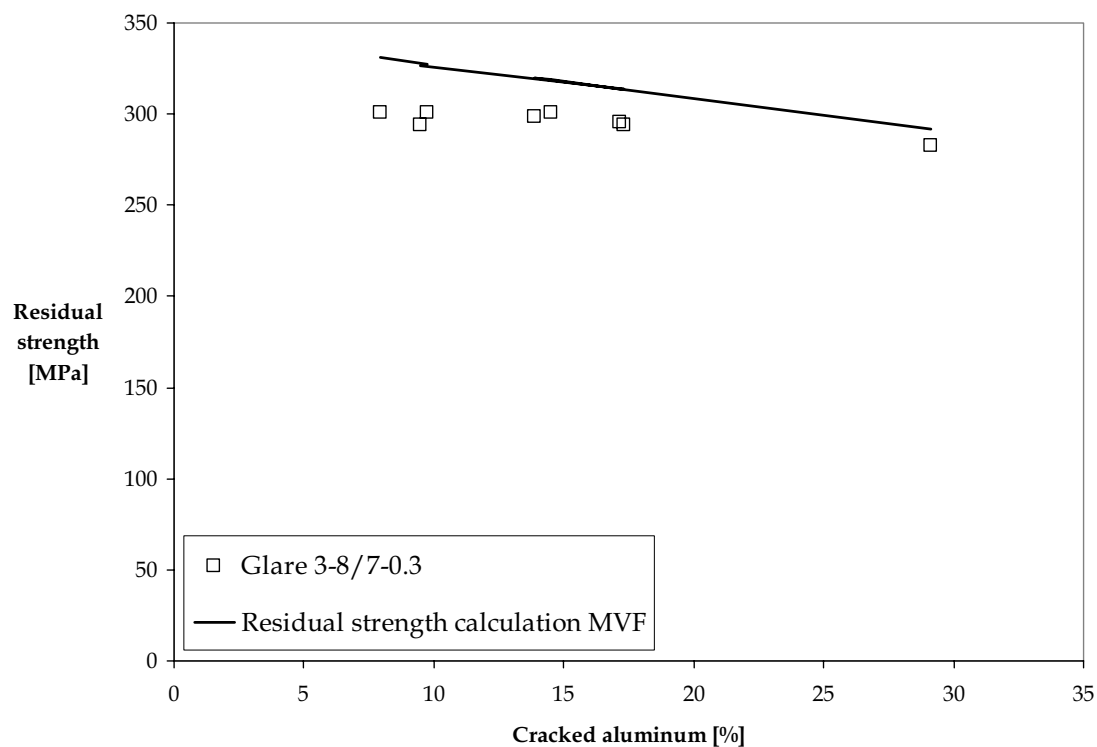
Figure 6-8 **Residual strength prediction and test results of lap-splice joint specimen GL_BJ_A2 for Glare 3-8/7-0.3 based on the specimen gross section**
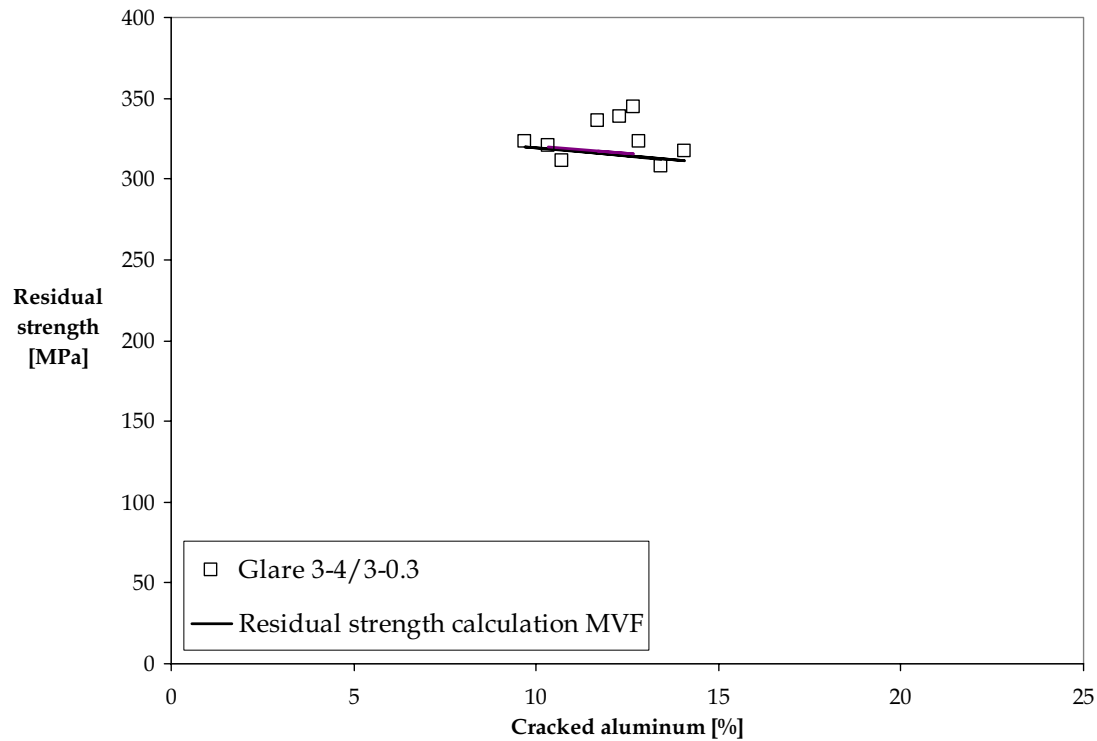
Figure 6-9 **Residual strength prediction and test results of lap-splice joint specimen GL_BJ_A3 for Glare 3-4/3-0.3 based on the specimen gross section**
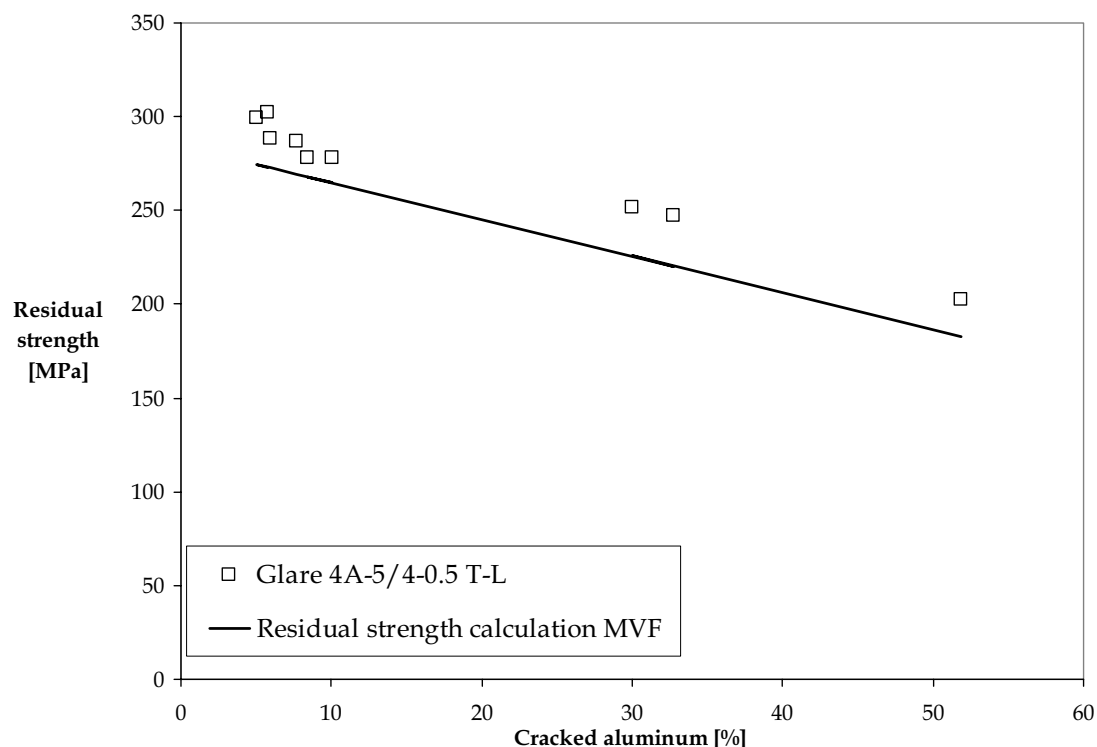
Figure 6-10 Residual strength prediction and test results of lap-splice joint for specimen GL_BJ_A4 Glare 4A-5/4-0.5 based on the specimen gross section
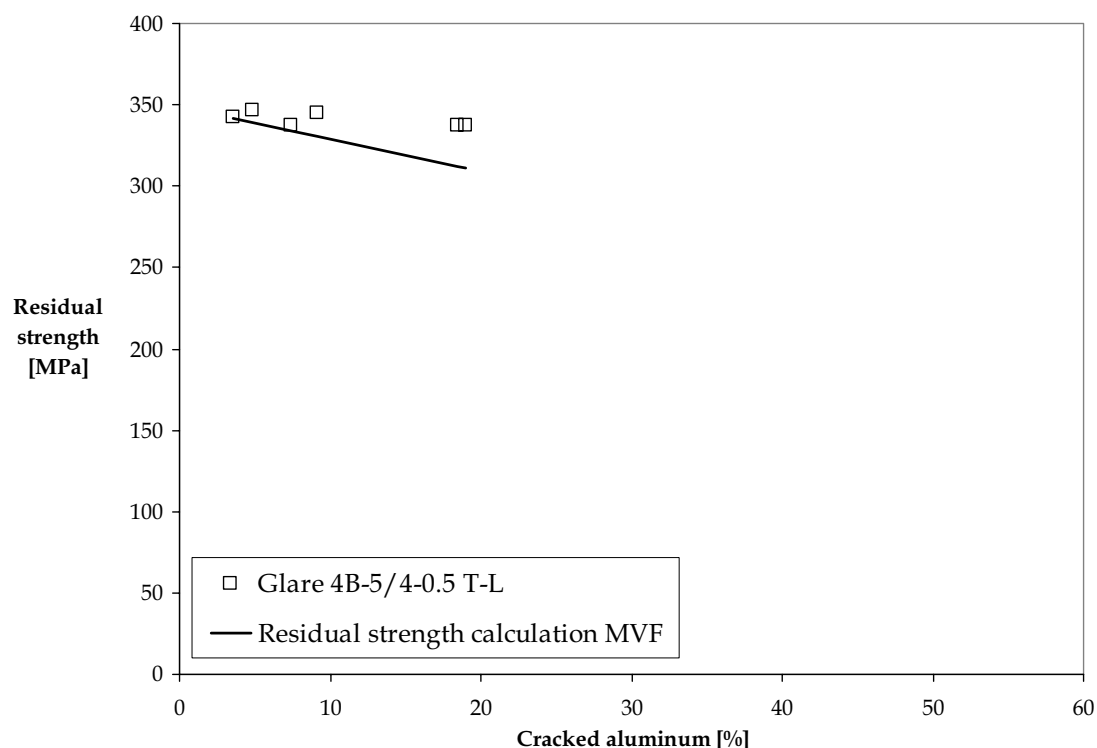
Figure 6-11 Residual strength prediction and test results of lap-splice joint specimen GL_BJ_A5 Glare 4B-5/4-0.5 based on the specimen gross section
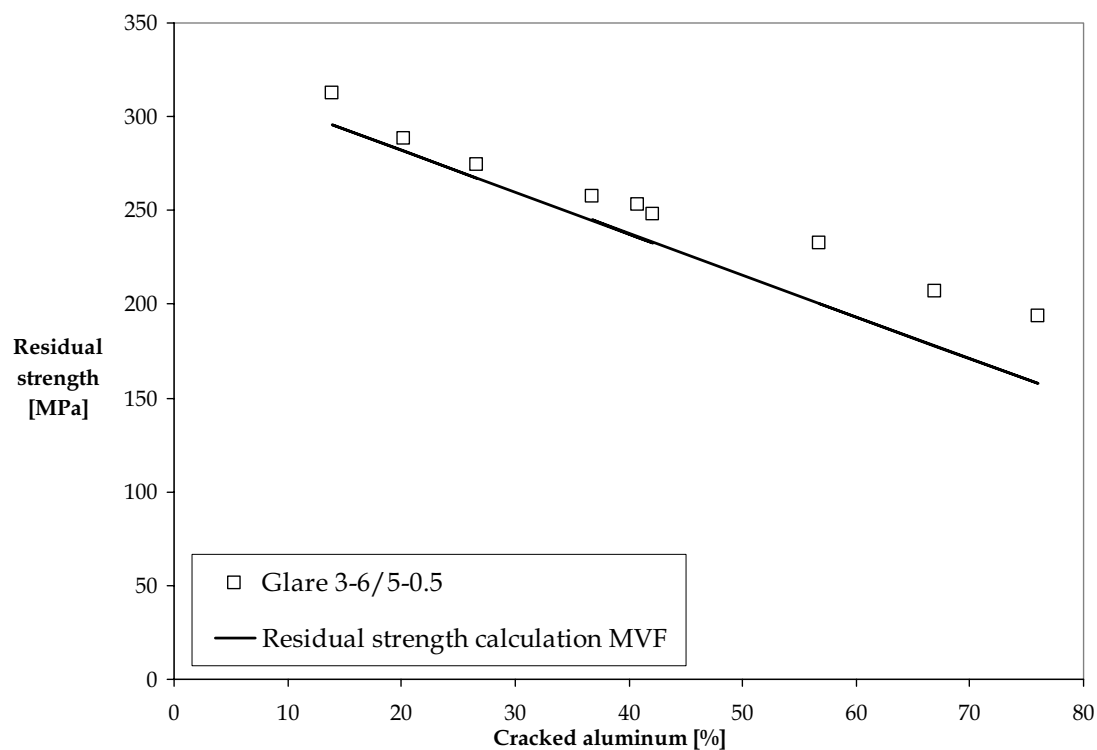
Figure 6-12 **Residual strength prediction and test results of butt joint specimen GL_LJ_B1 for Glare 3-6/5-0.5 based on the specimen gross section**
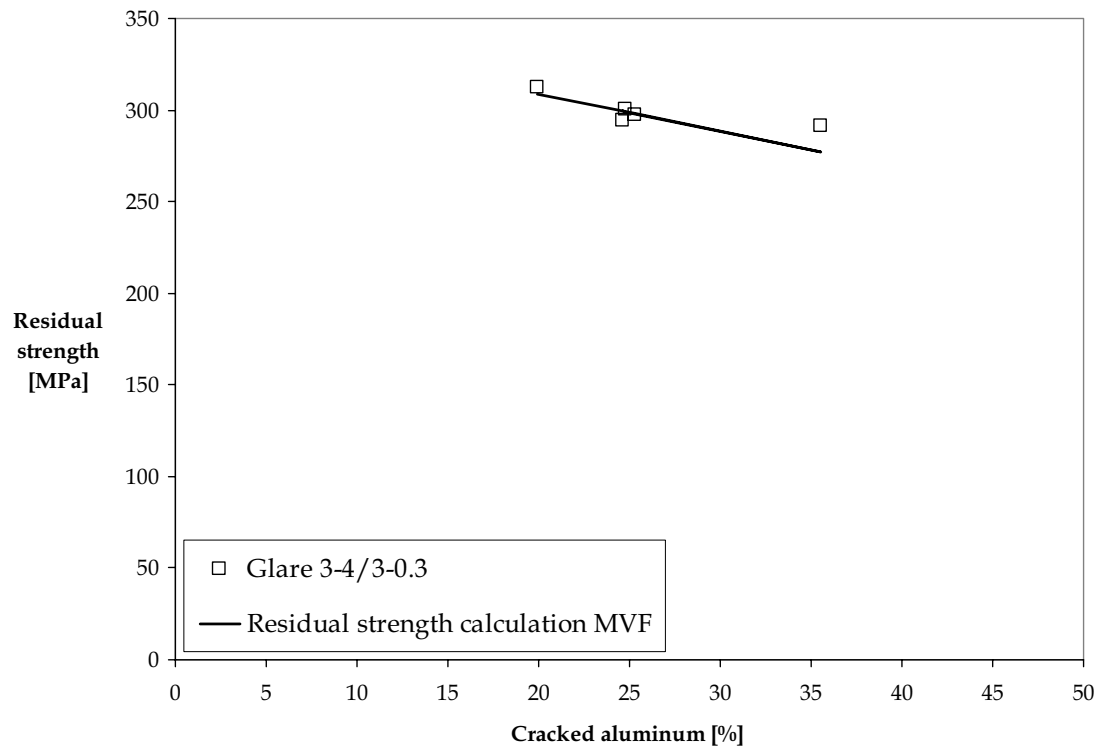
Figure 6-13 **Residual strength prediction and test results of butt joint specimen GL_LJ_B2 for Glare 3-4/3-0.3 based on the specimen gross section**

Each test specimen series was set up in such a way that for each fiber metal laminate, three regions of crack length would be present. Variation of the number of applied load cycles should provide residual strength results over a range of different crack lengths. Due to the arbitrary crack initiation, the number of small cracks is higher then expected. This caused a limited range of residual strength data in Figure 6-9, Figure 6-11 and Figure 6-13. However, with only one residual strength measurement for a large crack without too much deviation from the calculated residual strength, see Figure 6-7, the trend from the measurements and the calculations are similar. The results in Figure 6-8 are more satisfactory with respect to the variety in crack lengths. A satisfactory coverage of different crack length values was also obtained for the results in Figure 6-10 and Figure 6-12. Some other test series already mentioned (Figure 6-9, Figure 6-11 and Figure 6-13) might benefit from additional experiments.

As mentioned before, the residual strength of joints can be estimated by using Eqn. (6-7), but requires a more thorough investigation into the behavior of lap-splice and butt joints when the applied load creates stresses high enough for the material to yield. Until then, a rough estimation of the residual strength can be made only.

6.5 Conclusions

The implementation of the *MVF* in the blunt notch methodology provides the means to calculate the blunt notch strength for any possible Glare grade. It is important to look at the blunt notch values carefully before application in the residual strength calculation. The most significant point to take notice of is the difference in specimen type.

The residual strength calculation suggested by Müller uses the blunt notch values without accounting for the influence of secondary bending. However, secondary bending has a significant influence on the ultimate strength of both Glare and aluminum. The ultimate tensile strength reduces with increasing bending. Since secondary bending is inherent to multi-layer joints it is expected that the blunt notch values available will overestimate the blunt notch strength for specimens subject to both tensile and bending loads.

Strain gage investigation on a monolithic aluminum lap-splice joint showed the applied stress exceeds the yield limit of the material and that the bending stresses outside the overlap region reduces to zero. However, this does not mean that no bending is present above the yield limit of the material. Due to the eccentricity of joints and the accedence of the yield limit, only a small amount of bending will result in permanent plastic deformation at the most critical fastener row and thus will lower the ultimate strength. Taking this into account, an empirically found reduction of 10% of the blunt notch values results in a more accurate representation of the stress system.

Using the 10% reduction of the blunt notch values in combination with the residual strength methodology gives a good approximation of the residual strength of both Glare and aluminum lap-splice and butt joints.

Difficulties arise in determining the amount of plastic deformation due to the bending present at the most critical fastener row, which is influenced by material properties and geometrical properties. More research using a realistic finite element model representing different types of lap-splice and butt joints is recommended. A good estimation of the permanent bending at the most critical fastener row will allow an improved estimation of the blunt notch value for combined tension and bending.

6.6   Literature

[1]   Schra, L., and J.J. Homan, *Fatigue crack initiation in Glare lap joint and butt joint specimens*, GTP Methods Project 2.4.3.5-B, National Aerospace Laboratory NLR, NLR-CR-2003-622, December 2003

[2]   Homan, J.J., and A.A. Jongebreur, *Calculation method for predicting the fatigue life of riveted joints*, ICAF 1993

[3]   Homan, J.J., and L. Schra, *Application of aluminum alloy 2024-T3 fatigue life data to Glare laminates*, GTP Methods Projects 2.4.3.2-B, 2.4.3.3-B and 2.3.3.4-B, NLR report, NLR-CR-2002-185, June 2002

[4]   Alderliesten, R.C., *Fatigue*, In: Vlot, A., Gunnink, J.W. (eds.); Fibre Metal Laminates: an introduction, Kluwer Academic Publishers, Dordrecht, 2001, pp. 155-171

[5]   de Koning, A.U., and L. Schra, *Fatigue crack growth of part through the thickness cracks in Glare 3 and Glare 4B coupons*, Final report GTO subproject 2.4.2, National Aerospace Laboratory NLR, NLR-CR-2000-78, February 2000

[6]   Homan, J.J., *Crack growth in Glare CTB specimens*, Delft University of Technology, Report B2v-03-08, December 2003

[7]   Slagter, W.J., *Static Strength of Riveted Joints in Fibre Metal Laminates*. Diss. Delft University of Technology, Delft: NL, 1994

[8]   Vermeeren, C.A.J.R., *The Blunt Notch Behaviour of Metal Laminates: ARALL and Glare*, LR-617, Aerospace Engineering, Delft University of Technology, January 1990

[9]   Müller, R. P. G., *An Experimental and Analytical Investigation on the Fatigue Behaviour of Fuselage Riveted Lap Joints, The Significance of the Rivet Squeeze Force, and a Comparison of 2024-T3 and Glare 3*. Dis. Delft University of Technology, 1995

[10] De Vries, T.J., *Blunt and sharp notch behaviour of Glare laminates*, Dis. Delft University of Technology, 2001

[11] Bosker, O.J., *Blunt notch strength*, In: Vlot, A., Gunnink, J.W. (eds.); Fibre Metal Laminates: an introduction, Kluwer Academic Publishers, Dordrecht, 2001, pp. 117-131

[12] Bosker, O.J., *Glare uni-axial blunt notch test results*, B2V-99-27, Delft University of Technology, Faculty of Aerospace Engineering, January 2000

[13] de Jong, T.W., *Forming of Laminates*, Dis. Delft University of Technology, 2004

[14] Soetikno, T.P., *Residual strength of the fatigued 3 rows riveted Glare3 longitudinal joint*, MSc. Thesis, Delft University of Technology, Aerospace Engineering Department, May 1992

[15] de Rijck, J.J.M., *Investigation of Load Transfer within a Cracked Lap Joint and Butt Joint*, British Aerospace, R&T/B5607/66238, March 1998

[16] Fawaz, S.A., *Equivalent initial flaw size testing and analysis*, AFRL-VA-WP-TR-2000-3024, June 2000

[17] FML F&DT toolbox v1.11, proprietary of Airbus Germany and Delft University of Technology, 2002

7 Summary and conclusions

7.1 Introduction

In this final chapter, a summary of the research objectives is given in Section 7.2. Then chapter-by-chapter, the conclusions are summarized in Section 7.3.

7.2 Summary of research objective

In the Introduction of this thesis two questions came forward, one question in relation to the crack growth characteristics of multi layer joints of a large aircraft fuselage, and the second one dealing with the design both Glare and aluminum joints. This was combined into one research objective:

> **The development of analytical models, which can predict the behavior of large fuselage joints form simple to complex shaped, laminated, longitudinal lap-splice and circumferential butt joints.**

Several different routes have been taken to answer this question. For Glare and aluminum lap splice and butt joints the mutual focus was directed on a further development of the neutral line model, including more detailed information on fasteners and material properties. In the case of Glare lap splice and butt joints, research was focused on the development of a methodology to calculate the residual strength of Glare joints. For the aluminum lap splice and butt joints, the development of accurate stress intensity factors for cracks emanating from countersunk holes subject to complex loading conditions was the main focus.

7.3 Conclusions

In this section the conclusions of each chapter will be repeated to get a good understanding of the possibilities of each research subject.

7.3.1 Neutral line model (Chapter 3)

Implementation of an internal moment to represent the effect of load transfer through the fasteners in joints improves the stress calculation at the most critical fastener row.

The research into the load transfer of both lap-splice and butt joints revealed an overestimation of the influence of the fastener flexibility. Increasing or decreasing the fastener flexibility significantly has minor influence on the load transfer.

With the additions made to the neutral line model it is now also possible to calculate the displacement of the neutral line more accurately for fiber metal laminates, e.g. Glare. The differences between monolithic aluminum and fiber metal laminates are based on the differences in material build up. Glare build up is based on alternating

layers of thin aluminum and S_2-glass prepreg. Depending on the lay-up the neutral line can by eccentric to the centre of the material. This creates extra eccentricities with respect to secondary bending.

Shown is that the application of stringers and stiffeners to create a more complicated lap-splice or butt joint does not make the usage of the neutral line model more complicated. Through the understanding of the load path and added stiffness a substitution of those extra structural elements can be done.

Mounting stiffeners on a rivet row of a lap splice or butt joint does not make the usage of the neutral line model more complicated. Through the understanding of the load path and added stiffness a substitution of those extra structural elements can be accounted for.

The improved neutral line model is a powerful tool to use in the early stages of joint design. It gives a good picture of the stresses in a joint.

7.3.2   Riveting (Chapter 4)

The riveting process is a highly non-linear deformation process characterized by large plastic strains. The relation between the dimensions of the deformed rivet head and the applied squeeze force determined for several rivet materials gives a good representation of the riveting process. A simple correlation equation was obtained which is useful for evaluating the riveting process when riveting forces are not known. With the initial rivet dimensions and the dimensions of the final shape of the rivet head, the squeeze force can be calculated within 10% accuracy.

If the strength coefficient and the strain-hardening coefficient are known for a rivet material, the correlation equation presented in this chapter should be valid for the rivet material.

7.3.3   Stress intensity factors (Chapter 5)

The combined tension and bending specimen provided an easy and powerful investigative tool to understand the crack shape and crack growth behavior of cracks subjected to combined loading. The influence of the secondary bending on the crack shape and crack growth can easily be determined. With increasing crack growth, the reduction of the minimum net-section increases the locale tensile stress and thus reduces the bending factor and secondary bending.

Although they are very time consuming, observations in the SEM still provide the best fracture surface reconstruction. It was successful for the larger part of the fatigue crack history. Slant and curved crack fronts were recorded, a trend that should be expected for fatigue under continued tension and bending. For large K values occurring near the end of the fatigue life, the fracture surface is very

tortuous. It then is difficult to detect the marker bands. For very low K values, the problem of differentiating the marker bands from the other striations is difficult since both are associated with similar ΔK_{eff} values.

For combined tension and bending specimens, the shape parameters of the elliptical crack fronts (axes a and c) are derived from the fractographic results. These data were used to determine the range of a/c values for the K calculations.

The newly calculated K values capture the free surface phenomenon more accurately than in previously published data. This is associated with the refined mesh density. Accurate K values are essential for crack growth predictions in view of the exponential influence of ΔK on the predicted crack growth rates.

For through the thickness cracks growing away from the countersunk hole, the stress intensity factors approach the stress intensity factor values of cracks emanating from straight shank holes for both the remote tension and bending. The effect of the countersunk hole decreases with increasing crack length. The influence of the countersunk shape (b/t), with respect to pin loading, is dominant for all crack lengths and only approaches the straigh shank hole solutions for b/t-values close to one.

The newly calculated K values provide sufficient accuracy for crack growth life predictions for cracks growing from a part through to through crack at a countersunk hole subject to tension and combined tension and bending.

7.3.4 Residual strength of Joints (Chapter 6)

In the method proposed for the calculation of the residual strength in this thesis, the metal-volume-fraction is implemented into the calculation of the blunt notch strength. However, the blunt notch strength calculations applied to open hole specimens was validated for specimens loaded in tension without bending only. The tests carried out as part of the present thesis indicate that secondary bending reduces the tensile strength of joint specimens from both aluminum and Glare. The reduction depends on the type of specimen and the amount of fatigue damage. On average, the reduction can be accounted for by a 10% reduction of the calculated tensile strength. It should be realized that this is an experimental result. Further research is necessary to arrive at a more realistic concept for determining the residual strength of joint configurations.

A Second order differential equation

A.1 Introduction

The equation obtained from the forces and moments inherent to joints as shown in the neutral line model, are a second order differential equation. Two equations can be obtained, one equation for a linear homogeneous and the second for a non-homogeneous equation. The difference between the two is the influence of the boundary conditions. The non-homogeneous equation takes the clamped edges into account.

A.2 Find a solution for linear homogeneous equation

The homogeneous solution is a solution, were the right-hand side of the equation is zero.

$$\frac{d^2w}{dx^2} - \alpha^2 w = 0 \tag{A-1}$$

This equation can be solved using a more general equation, which has arbitrary real constants.

$$aw'' + bw' + cw = 0 \tag{A-2}$$

From literature [1], for this sort of equations a solution can be obtained by using $w = e^{rx}$, where r is a parameter to be determined. Substitution into Eqn. (A-2) results in:

$$(ar^2 + br + c)e^{rx} = 0$$
$$(ar^2 + br + c) = 0 \wedge e^{rx} \neq 0 \tag{A-3}$$

Eqn. (A-3) is called the 'characteristic equation'. Since Eqn. (A-3) is a quadratic equation with real coefficients (a, b and c), it has for this solution two real and different roots [1]. From Eqn. (A-1) follows $a = 1$, $b = 0$ and $c = -\alpha^2$, combining this with Eqn. (A-2):

$$r^2 - \alpha^2 = 0$$
$$r_1 = \alpha \vee r_2 = -\alpha \tag{A-4}$$

$$w_1 = e^{r_1 x} = e^{\alpha x} \wedge w_2 = e^{r_2 x} = e^{-\alpha x}$$
$$w = C_1 e^{\alpha x} + C_2 e^{-\alpha x} \tag{A-5}$$

Using the Wronskian determinant ($W \neq 0$) gives proof that the found solution is a general solution for solving the set of equations of the neutral line model.

$$W = \begin{vmatrix} w_1 & w_2 \\ w'_1 & w'_2 \end{vmatrix} = w_1 w'_2 - w_2 w'_1 = -2\alpha \tag{A-6}$$

Eqn. (A-5) is for all values with arbitrary coefficients a solution for Eqn. (A-1). Now it is time to find a point in the interval for x were the Wronskian of w_1 and w_2 is non-zero. Then w_1 and w_2 form a fundamental set of solutions.

$$w = \cosh(\alpha x) + \sinh(\alpha x) \tag{A-7}$$

A.3 Find a solution for a non-homogeneous equation

The general solution of a non-homogeneous equation consists of two parts the fundamental set of solutions corresponding to Eqn. (A-1) and a specific solution. Eqn. (A-8) shows on the left-hand side the homogeneous and at the right-hand side the specific solution.

$$\frac{d^2 w}{dx^2} - \alpha^2 w = \alpha^2 \left(D_1 - D_2 x \right) \tag{A-8}$$

To solve the non-homogeneous part of the equation the "Method of undetermined coefficients" is used. Assume that the solution is a polynomial of the same order as the right-hand side of Eqn. (A-8)

$$\begin{aligned} W(x) &= A x^2 + B x + C \\ W'(x) &= 2 A x \\ W''(x) &= 2 A \end{aligned} \tag{A-9}$$

Combining Eqn. (A-8) and Eqn. (A-9)

$$\begin{aligned} 2A - \alpha^2 \left(A x^2 + B x + C \right) &= \alpha^2 \left(D_1 - D_2 x \right) \\ -\alpha^2 A &= 0 \\ -\alpha^2 B + \alpha^2 D_2 &= 0 \\ 2A - \alpha^2 C - \alpha^2 D_1 &= 0 \end{aligned} \tag{A-10}$$

The solution for the non-homogeneous part is

$$W(x) = D_2 x - D_1 \tag{A-11}$$

And the solution for both the homogeneous and non-homogeneous part is

$$w(x) = C_1 e^{\alpha x} + C_2 e^{-\alpha x} - D_1 + D_2 x$$
$$w(x) = A \cosh(\alpha x) + B \sinh(\alpha x) - D_1 + D_2 x \tag{A-12}$$

A.4 Literature

[1] Boyce, W.E., DiPrima, R.C., *Elementary differential equations and boundary value problems*, John Wiley & Sons Inc., Wiley International Edition, 1992

B Marker load spectrum data

A total of six tests are done in order to validate the use of a marker load spectrum. Four marker load tests and two constant amplitude tests are done. The crack lengths are obtained via *in-situ* crack growth measurements using a traveling optical microscope (*TOM*, 40x) and tic-mark ruler with accuracy of 0.125 mm.

$$2a_i = \left(c_{LHS_i} + c_{RHS_i} + d\right) \tag{B-1}$$

$$a_{ave} = \frac{1}{2}\left(a_{i+1} - a_i\right) \tag{B-2}$$

$$\Delta K = \frac{P_{max} - P_{min}}{tW}\sqrt{\pi a_{ave}\sec\left(\frac{\pi a_{ave}}{W}\right)} \tag{B-3}$$

$$\frac{da}{dN} = \frac{a_{i+1} - a_i}{N_{i+1} - N_i} \tag{B-4}$$

Table B-1 and Table B-2 represent the crack growth data for the specimens tested with constant amplitude fatigue cycles, Table B-3 to Table B-6 represent crack growth data for the marker load fatigue cycle tests. The specimen used in this investigation is a simple flat sheet open hole ($d = 4.8$ mm and $t = 1.0$ mm) specimen shown in Figure B-1. Introducing saw cuts in the minimum net-section of the specimen reduces crack initiation time.
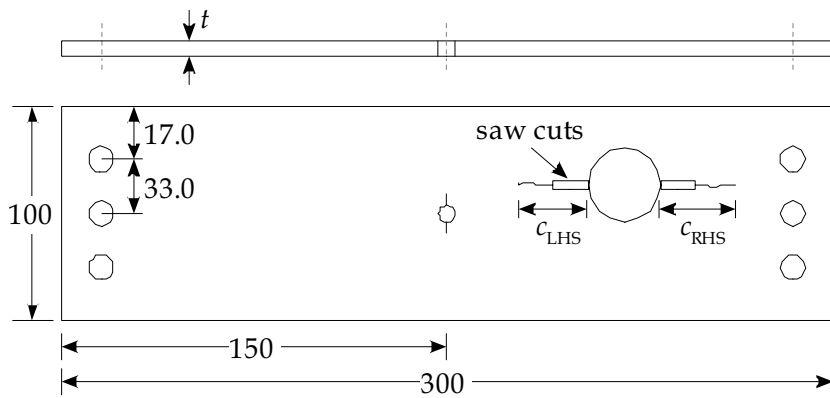
Figure B-1   Open hole specimen with saw cuts on both sides of the hole

All tests are completed using a maximum applied force $P_{max} = 100$ N and $R = 0.1$, this results in a maximum applied stress $\sigma_{max} = 100$ MPa. The test frequency at which all specimens were tested is 15 Hz and the magnification of the traveling optical microscope used to measure the crack lengths is four.

Table B-1 Crack growth results of test with constant amplitude loading. Open hole specimen with two saw-cuts (left = 2.0 mm, right = 2.25 mm)

Test Number	1	Specimen Number	CA1	Temperature (°C) / Humidity (% r.H.)	mean: 22.12 / 30.30	stdev: 0.19 / 0.59

N (cycles)	c_{LHS} (mm)	c_{RHS} (mm)	a_{ave} (mm)	ΔK MPa√m	da/dN (μm/cycle)
8154	2.50	2.75	5.150	11.523	3.551E-01
9562	2.75	3.00	5.650	12.086	2.731E-01
15055	3.50	3.75	6.413	12.905	3.223E-01
19864	4.20	4.60	7.050	13.561	3.943E-01
22400	4.75	5.05	7.600	14.108	3.967E-01
25425	5.25	5.75	8.400	14.880	5.251E-01
29234	6.25	6.75	9.463	15.869	5.818E-01
33101	7.50	7.75	10.463	16.772	5.371E-01
36359	8.25	8.75	11.150	17.380	7.622E-01
37671	8.75	9.25	11.838	17.981	8.020E-01
39853	9.50	10.25	12.588	18.631	1.095E+00
40995	10.00	11.00	13.463	19.382	1.121E+00
43002	11.00	12.25	14.500	20.270	1.295E+00
44469	12.00	13.15	15.288	20.944	1.085E+00
45621	12.65	13.75	16.000	21.555	1.434E+00
46737	13.25	14.75	16.650	22.115	1.931E+00
47255	13.75	15.25	17.150	22.549	2.119E+00
47727	14.25	15.75	17.650	22.985	1.621E+00
48344	14.50	16.50	18.650	23.866	2.571E+00
49511	15.75	18.25	19.775	24.877	2.069E+00
50236	16.25	19.25	20.963	25.971	3.607E+00
51137	17.50	21.25	22.650	27.587	5.279E+00
51800	19.00	23.25	24.838	29.821	7.907E+00
52464	20.75	26.75			

Table B-2 Crack growth results of test with constant amplitude loading. Open hole specimen with two saw-cuts (left = 2.05 mm, right = 2.15 mm)

Test Number	2	Specimen Number	CA1	Temperature (°C) / Humidity (% r.H.)	mean: 22.00 / 30.15	stdev: 0.08 / 0.37

N (cycles)	c_{LHS} (mm)	c_{RHS} (mm)	a_{ave} (mm)	ΔK MPa√m	da/dN (μm/cycle)
11041	3.05	3.15	6.250	12.734	3.342E-01
20017	4.55	4.65	8.000	14.498	4.468E-01
28970	6.55	6.65	9.500	15.904	7.902E-01
31501	7.55	7.65	10.200	16.537	4.972E-01
33110	7.85	8.15	11.525	17.709	7.063E-01
39481	10.15	10.35	13.700	19.586	9.119E-01
44087	12.30	12.40	16.100	21.641	1.409E+00
47920	14.95	15.15	18.038	23.325	2.129E+00
49024	16.05	16.40	19.188	24.346	2.284E+00
50009	17.05	17.65	21.233	26.224	3.889E+00
51534	19.48	21.15	23.608	28.543	5.960E+00
52133	21.05	23.15.			

Table B-3 **Crack growth results of test with marker load spectrum. Open hole specimen with two saw-cuts (left = 2.0 mm, right = 1.75 mm)**

Test Number		3	Specimen Number	ML1	Temperature (°C)	mean	stdev
						21.89	0.25
					Humidity (% r.H.)	33.79	0.55

N (cycles)	N* (cycles)	c_{LHS} (mm)	c_{RHS} (mm)	a_{ave} (mm)	ΔK MPa√m	da/dN (µm/cycle)
10419	6787	2.25	2.25	4.838	11.160	1.277E-01
19016	12660	2.75	2.50	5.350	11.751	3.075E-01
25967	16887	3.30	3.25	6.063	12.534	4.294E-01
31393	20497	4.00	4.10	6.813	13.319	2.305E-01
41082	26788	5.00	4.55	7.600	14.108	3.077E-01
49324	32313	6.00	5.25	8.525	14.998	4.485E-01
56148	36773	7.00	6.25	9.525	15.927	5.399E-01
62270	40478	8.00	7.25	10.650	16.939	5.916E-01
68814	44703	9.50	8.25	11.963	18.090	5.045E-01
76643	50154	11.75	8.75	13.088	19.061	7.518E-01
80627	52482	12.50	9.75	14.275	20.078	9.019E-01
85595	55808	14.75	10.50	15.525	21.147	1.831E+00
87201	56900	15.50	11.75	16.500	21.986	1.830E+00
88811	57939	16.50	12.65	17.375	22.745	2.381E+00
90028	58611	17.50	13.25	18.213	23.479	2.520E+00
91085	59305	18.25	14.25	19.088	24.256	2.267E+00
91857	60077	19.50	14.75	19.963	25.047	2.347E+00
93511	60823	20.75	15.25	21.275	26.264	8.284E+00
93933	61245	23.50	16.00			

Table B-4 **Crack growth results of test with marker load spectrum. Open hole specimen with two saw-cuts (left = 1.8 mm, right = 1.6 mm)**

Test Number		4	Specimen Number	ML2	Temperature (°C)	mean	stdev
						21.89	0.25
					Humidity (% r.H.)	33.79	0.55

N (cycles)	N* (cycles)	c_{LHS} (mm)	c_{RHS} (mm)	a_{ave} (mm)	ΔK MPa√m	da/dN (µm/cycle)
12969	8792	2.30	2.30	5.038	11.393	3.090E-01
21910	14455	3.30	3.30	5.875	12.332	3.236E-01
29388	19400	4.05	4.05	6.900	13.409	3.153E-01
41858	27330	5.40	5.40	8.125	14.618	4.793E-01
49483	32337	6.55	6.55	9.388	15.801	5.046E-01
57565	37589	7.80	7.80	11.075	17.314	6.934E-01
66611	43502	9.80	9.80	13.225	19.179	1.001E+00
73615	47996	11.80	11.80	18.663	23.877	2.297E+00
85106	55505	20.05	20.05	23.413	28.346	7.675E+00
85334	55733	20.80	20.80	24.788	29.768	9.091E+00
86110	56146	22.55	22.55			

Table B-5   Crack growth results of test with marker load spectrum. Open hole specimen with two saw-cuts (left = 2.25 mm, right = 2.0 mm)

Test Number		5	Specimen Number	ML3		mean	stdev
					Temperature (°C)	**21.64**	**0.29**
					Humidity (% r.H.)	**31.71**	**0.86**

N (cycles)	N* (cycles)	c_{LHS} (mm)	c_{RHS} (mm)	a_{ave} (mm)	ΔK MPa√m	da/dN (μm/cycle)
10874	7242	2.30	2.10	5.100	11.466	3.294E-01
20051	13313	3.30	3.10	6.100	12.575	4.274E-01
27618	17993	4.30	4.10	7.100	13.611	3.770E-01
35110	23297	5.30	5.10	7.975	14.473	4.238E-01
41364	26836	6.05	5.85	9.225	15.651	6.343E-01
49567	32354	7.80	7.60	10.725	17.005	6.235E-01
55432	36364	8.80	9.10	11.913	18.047	8.089E-01
60029	39145	10.05	10.10	13.163	19.125	1.098E+00
63986	41649	11.30	11.60	14.463	20.238	1.250E+00
67217	43609	12.40	12.95	16.150	21.684	1.565E+00
70872	46356	14.55	15.10	18.350	23.600	2.368E+00
74225	48256	16.80	17.35	20.213	25.276	4.393E+00
74897	48928	18.30	18.80	21.400	26.382	4.681E+00
75644	49312	19.30	19.60	22.538	27.477	5.908E+00
76110	49778	20.55	21.10	24.075	29.022	9.067E+00
76627	50152	22.05	23.00	25.038	30.035	5.525E+00
77117	50234	22.30	23.20	26.100	31.201	1.350E+01
77756	50516	24.20	25.10			

Table B-6   Crack growth results of test with marker load spectrum. Open hole specimen with two saw-cuts (left = 2.15 mm, right = 2.0 mm)

Test Number		6	Specimen Number	ML4		mean	stdev
					Temperature (°C)	**21.81**	**0.10**
					Humidity (% r.H.)	**30.89**	**0.51**

N (cycles)	N* (cycles)	c_{LHS} (mm)	c_{RHS} (mm)	a_{ave} (mm)	ΔK MPa√m	da/dN (μm/cycle)
12284	8107	2.55	2.35	5.038	11.393	2.028E-01
17798	11805	2.80	2.85	5.688	12.127	3.969E-01
24639	16467	3.80	3.70	6.625	13.126	4.007E-01
32541	21208	4.80	4.60	7.850	14.352	4.138E-01
43531	28458	6.30	6.10	9.225	15.651	6.047E-01
49844	32592	7.55	7.35	10.538	16.839	6.521E-01
56338	36809	8.80	8.85	12.163	18.263	8.785E-01
62870	41078	10.80	10.60	14.100	19.928	1.126E+00
68414	44630	12.80	12.60	17.225	22.614	1.901E+00
75273	49102	17.05	16.85	20.388	25.437	3.561E+00
77279	50267	19.05	19.00	22.038	26.991	4.344E+00
78071	50831	20.30	20.20	23.250	28.183	7.018E+00
78413	51173	21.30	21.60	24.788	29.768	9.271E+00
79363	51578	23.05	23.60	26.663	31.841	1.825E+01
79568	51783	24.80	25.60			

C *In-situ* crack growth data

The following crack growth data are obtained from the *in-situ* crack length measurements of cracks in open hole specimens subject to tensile and bending loading conditions, see Figure 5-2 and Figure 5-4. The tables contain the following crack growth data; the number of cycles N including the marker load cycles can be found in the first column. The second column contains the number of equivalent constant amplitude cycles N^*. The conversion from the marker load cycles to constant amplitude cycles is explained in Section 5.2.2. Measured data for all cracks emanating from the countersunk holes subject to tensile and bending load conditions is available. a_{ave}, ΔK and da/dN are calculated as follows:

$$a_{ave} = \frac{1}{2}\left(a_{i+1} - a_i\right) \tag{C-1}$$

$$\frac{da}{dN} = \frac{a_{i+1} - a_i}{N_{i+1} - N_i} \tag{C-2}$$

The crack measurements are done using a traveling optical microscope (*TOM*, 40x) and a tic-mark ruler with an accuracy of 0.125 mm. Crack measurements are done on both sides of the countersunk hole, the left hand side (a_{LHS}) and right hand side (a_{RHS}) and on both side of the specimen (Back and Front). Two crack growth rates, one for the front side and one for the back side of the specimen are thus obtained with a_i:

$$2a_i = \left(a_{LHSi} + a_{RHS_i} + d\right) \tag{C-3}$$

Table C-1 to Table C-26 are the results of the *in-situ* crack growth measurements for the open hole specimens subject to tensile loading. Table C-27 to Table C-49 represent the measurements for the combined tension and bending specimens. The specimens are numbered in the following manner:

X aabbcc-d
      X   = T refers to tension and TB to combined tension and bending
      aa   = First two digits represent the specimen thickness (1.0, 1.6 or 2.0 mm)
      bb   = Second pair of digits represent the $^{r}/_{t}$-ratio (2.40, 1.50 or 1.20)
      ccc   = Represents the $^{b}/_{t}$-ratio (0.50, 0.25 or 0.05)
      d   = Series number representing specimen with a similar geometry

All specimens are tested with an applied stress $\sigma_{app} = 100$ MPa and $R = 0.1$ at an cycle frequency of 15 Hz. The crack lengths are measured using a traveling optical microscope with magnification of four.

Table C-1   Crack growth measurements and crack growth rate data

								mean	stdev	
Test Number	7	Specimen Number	T 1024005-1	Temperature (^{o}C)				21.75	0.36	
		F_{max} (N) =	27262	Humidity (% r.H.)				14.71	0.56	

N (cycles)	N* (cycles)	Back				Front			
		a_{LHS} (mm)	a_{RHS} (mm)	a_{ave} (mm)	da/dN (μm/cycle)	a_{LHS} (mm)	a_{RHS} (mm)	a_{ave} (mm)	da/dN (μm/cycle)
72420	47276					0.60		2.738	4.456E-02
77582	50642					0.75		2.838	7.275E-02
82814	54078					1.00		2.963	7.504E-02
87942	57410					1.25		3.088	7.335E-02
93146	60818					1.50		3.213	7.466E-02
98291	64167	0.50		3.907	1.494E-01	1.75		3.338	7.472E-02
103433	67513	1.00		4.095	7.410E-02	2.00		3.525	1.482E-01
108603	70887	1.25		4.282	1.480E-01	2.50		3.713	7.398E-02
113778	74266	1.75		4.470	7.362E-02	2.75		4.088	3.681E-01
118970	77662	2.00		4.657	1.491E-01	3.00	1.00	4.588	2.237E-01
124119	81015	2.50		5.157	4.387E-01	3.50	1.25	4.963	2.193E-01
129335	84435	3.00	1.00	5.782	2.936E-01	3.75	1.75	5.400	2.936E-01
134537	87841	3.50	1.50	6.407	3.749E-01	4.00	2.50	6.150	4.999E-01
140334	91842	4.25	2.25	7.032	3.771E-01	5.25	3.25	6.963	4.714E-01
144781	94493	4.75	2.75			6.00	3.75		

Table C-2   Crack growth measurements and crack growth rate data

										mean	stdev
Test Number	8	Specimen Number		T 1024005-2		Temperature (^{o}C)				**21.58**	**0.39**
		F_{max} (N) =		27460		Humidity (% r.H.)				**31.01**	**1.04**
N (cycles)	N* (cycles)	Back				Front					
		a_{LHS} (mm)	a_{RHS} (mm)	a_{ave} (mm)	da/dN (μm/cycle)	a_{LHS} (mm)	a_{RHS} (mm)	a_{ave} (mm)	da/dN (μm/cycle)		
36231	23659					0.5		2.675	2.941E-02		
41427	27059					0.6		2.725	2.993E-02		
46565	30401					0.70		2.881	1.563E-01		
51720	33760					0.73	0.50	3.081	4.078E-02		
62055	40503					0.75	0.75	3.225	8.885E-02		
67228	43880					0.80	1.00	3.475	1.472E-01		
74319	48636					1.00	1.50	3.838	2.890E-01		
78171	51231		0.750	4.157	3.557E-01	1.25	2.00	4.150	1.779E-01		
82778	54042	0.50	1.250	4.657	2.991E-01	1.50	2.25	4.588	3.739E-01		
87917	57385	1.00	1.750	5.157	2.832E-01	2.00	3.00	5.150	2.832E-01		
93244	60916	1.50	2.250	5.782	4.067E-01	2.75	3.25	5.650	2.711E-01		
98729	64605	2.25	3.000	6.470	4.300E-01	3.25	3.75	6.125	3.096E-01		
103432	67512	3.00	3.500	7.157	4.440E-01	3.75	4.15	6.563	2.516E-01		
108606	70890	3.75	4.250	7.970	5.146E-01	4.25	4.50	7.463	8.087E-01		
113803	74291	4.75	5.000			5.50	6.00				

Table C-3   Crack growth measurements and crack growth rate data

										mean	stdev
Test Number	9	Specimen Number		T 1024005-3		Temperature (^{o}C)				**21.39**	**0.15**
		F_{max} (N) =		27667		Humidity (% r.H.)				**32.77**	**0.56**
N (cycles)	N* (cycles)	Back				Front					
		a_{LHS} (mm)	a_{RHS} (mm)	a_{ave} (mm)	da/dN (μm/cycle)	a_{LHS} (mm)	a_{RHS} (mm)	a_{ave} (mm)	da/dN (μm/cycle)		
51714	33754					0.50		2.713	6.884E-02		
57141	37385					0.75		2.963	2.378E-01		
62091	40539					1.50		3.713	6.725E-01		
67233	43885					2.25	1.50	4.525	2.153E-01		
74213	48530	1.00	0.50	4.407	1.397E-01	2.75	2.00	4.963	2.096E-01		
79049	52109	1.25	0.75	4.720	3.961E-01	3.00	2.50	5.338	3.961E-01		
82738	54002	1.75	1.00	5.657	8.144E-01	3.50	2.75	5.775	2.715E-01		
88218	57686	3.25	2.50	6.657	3.266E-01	4.00	3.25	6.400	4.899E-01		
93076	60748	3.75	3.00	7.282	4.104E-01	4.75	4.00	7.150	4.104E-01		
98527	64403	4.50	3.75	8.032	4.850E-01	5.50	4.75	7.838	4.042E-01		
103415	67495	5.25	4.50			6.00	5.50				

Table C-4 Crack growth measurements and crack growth rate data

Test Number	**10**	Specimen Number		**T 1024025-1**	Temperature (°C)	**21.46** mean	**0.23** stdev
		F_{max} (N) =		**26697**	Humidity (% r.H.)	**37.18**	**1.61**

N (cycles)	N* (cycles)	Back a_{LHS} (mm)	a_{RHS} (mm)	a_{ave} (mm)	da/dN (µm/cycle)	Front a_{LHS} (mm)	a_{RHS} (mm)	a_{ave} (mm)	da/dN (µm/cycle)
56897	37141					0.50		2.700	4.672E-02
62974	41422					0.70		2.763	1.700E-02
67712	44364					0.75		2.838	8.485E-02
72454	47310					1.00		2.963	4.222E-02
81069	53231					1.25		3.150	9.468E-02
89583	58512	1.00		3.920	1.073E-01	1.75		3.463	1.609E-01
96398	63172	1.50		4.170	1.152E-01	2.50		3.963	2.881E-01
103432	67512	2.00		4.420	1.187E-01	2.75	1.00	4.525	2.373E-01
109441	71725	2.50		4.795	3.740E-01	3.25	1.50	4.963	2.805E-01
113911	74399	3.00	0.50	5.420	4.622E-01	3.75	1.75	5.400	3.081E-01
118952	77644	3.50	1.50	6.045	2.964E-01	4.25	2.25	5.900	2.964E-01
124122	81018	4.00	2.00	6.608	3.721E-01	4.75	2.75	6.525	4.465E-01
129277	84377	4.50	2.75	7.358	5.172E-01	5.50	3.50	7.213	3.694E-01
134457	87761	5.50	3.50			6.00	4.25		

Table C-5 Crack growth measurements and crack growth rate data

Test Number	**11**	Specimen Number		**T 1024025-2**	Temperature (°C)	**21.17** mean	**0.29** stdev
		F_{max} (N) =		**27362**	Humidity (% r.H.)	**36.34**	**1.68**

N (cycles)	N* (cycles)	Back a_{LHS} (mm)	a_{RHS} (mm)	a_{ave} (mm)	da/dN (µm/cycle)	Front a_{LHS} (mm)	a_{RHS} (mm)	a_{ave} (mm)	da/dN (µm/cycle)
93186	60858	0.75	0.75	4.358	3.815E-01	1.50	2.00	4.338	2.289E-01
98258	64134	1.25	1.50	4.920	2.810E-01	2.00	2.25	4.775	2.810E-01
103613	67693	1.75	2.00	5.795	3.527E-01	2.50	2.75	5.650	3.527E-01
114293	74781	3.00	3.25	6.733	3.907E-01	3.75	4.00	6.588	3.907E-01
119288	77980	3.75	3.75	7.295	3.266E-01	4.50	4.50	7.275	4.900E-01
124146	81042	4.25	4.25	7.983	5.156E-01	5.25	5.25	8.088	5.156E-01
129336	84436	5.00	5.25				6.25		

Table C-6   Crack growth measurements and crack growth rate data

						mean	stdev
Test Number	**12**	Specimen Number	**T 1024025-3**	Temperature (^{o}C)		**21.29**	**0.20**
		F_{max} (N) =	**27525**	Humidity (% r.H.)		**30.87**	**0.68**

N (cycles)	N* (cycles)	Back a_{LHS} (mm)	a_{RHS} (mm)	a_{ave} (mm)	da/dN (μm/cycle)	Front a_{LHS} (mm)	a_{RHS} (mm)	a_{ave} (mm)	da/dN (μm/cycle)
46606	30442					0.60	0.60	3.138	8.209E-02
56898	37142					1.00	0.75	3.588	1.235E-01
72406	47262	0.80	0.25	4.058	2.787E-01	1.75	1.25	4.150	2.934E-01
77610	50670	1.25	0.75	4.545	2.987E-01	2.25	1.75	4.525	1.493E-01
82754	54018	1.75	1.25	5.170	3.382E-01	2.50	2.00	5.025	3.382E-01
88985	58453	2.50	2.00	5.983	3.046E-01	3.25	2.75	5.900	3.482E-01
98322	64198	3.25	3.00	6.733	3.791E-01	4.25	3.75	6.588	2.275E-01
103415	67495	4.00	3.50	7.483	5.149E-01	4.75	4.00	7.338	6.621E-01
108609	70893	5.00	4.25			5.75	5.25		

Table C-7   Crack growth measurements and crack growth rate data

						mean	stdev
Test Number	**13**	Specimen Number	**T 1024050-2**	Temperature (^{o}C)		**21.70**	**0.15**
		F_{max} (N) =	**28203**	Humidity (% r.H.)		**42.05**	**0.65**

N (cycles)	N* (cycles)	Back a_{LHS} (mm)	a_{RHS} (mm)	a_{ave} (mm)	da/dN (μm/cycle)	Front a_{LHS} (mm)	a_{RHS} (mm)	a_{ave} (mm)	da/dN (μm/cycle)
57626	37650					0.50		2.838	2.074E-02
113765	73813	0.50		3.370	7.443E-02	1.25		3.402	2.242E-01
124114	80530	1.00		3.6825	2.239E-01	1.76	1.00	3.908	1.549E-01
129280	83880	1.25	0.50	4.0575	2.175E-01	2.00	1.28	4.281	2.828E-01
134544	87328	1.75	0.75	4.495	3.061E-01	2.50	1.75	4.650	1.531E-01
139626	90594	2.25	1.25	4.995	2.939E-01	2.75	2.00	5.025	2.939E-01
144844	93996	2.75	1.75	5.433	2.278E-01	3.25	2.50	5.463	2.278E-01
149953	97289	3.00	2.25	5.870	2.951E-01	3.75	2.75	5.900	2.951E-01
155158	100678	3.50	2.75	6.433	3.712E-01	4.00	3.50	6.463	3.712E-01
160341	104045	4.00	3.50	6.995	2.993E-01	4.75	4.00	6.963	2.245E-01
165498	107386	4.50	4.00			5.00	4.50		

Table C-8   Crack growth measurements and crack growth rate data

								mean	stdev
Test Number	14	Specimen Number	T 1024050-3	Temperature (^{o}C)				**21.52**	**0.23**
		F_{max} (N) =	28804	Humidity (% r.H.)				**43.09**	**1.15**

N (cycles)	N* (cycles)	Back				Front			
		a_{LHS} (mm)	a_{RHS} (mm)	a_{ave} (mm)	da/dN (μm/cycle)	a_{LHS} (mm)	a_{RHS} (mm)	a_{ave} (mm)	da/dN (μm/cycle)
103426	67106					0.50		2.775	7.429E-02
113788	73836					1.00		3.025	7.417E-02
124161	80577	0.75		3.433	7.454E-02	1.50		3.213	7.454E-02
129331	83931	1.00		3.620	7.519E-02	1.75		3.400	7.519E-02
139613	90581	1.50		4.0575	1.857E-01	2.25		3.588	3.713E-02
149978	97314	2.25	0.5	4.495	1.471E-01	2.50		4.025	4.414E-01
155192	100712	2.50	0.75	4.9325	1.881E-01	3.00	1.00	4.775	2.257E-01
165469	107357	3.25	1.25	5.433	1.119E-01	3.75	1.75	5.275	7.458E-02
175806	114062	3.75	1.5	6.120	5.917E-01	4.00	2.00	5.963	6.657E-01
181002	117442	4.50	2.75			5.00	3.25		

Table C-9   Crack growth measurements and crack growth rate data

								mean	stdev
Test Number	15	Specimen Number	T 1615005-1	Temperature (^{o}C)				**23.78**	**0.28**
		F_{max} (N) =	41618	Humidity (% r.H.)				**30.55**	**2.25**

N (cycles)	N* (cycles)	Back				Front			
		a_{LHS} (mm)	a_{RHS} (mm)	a_{ave} (mm)	da/dN (μm/cycle)	a_{LHS} (mm)	a_{RHS} (mm)	a_{ave} (mm)	da/dN (μm/cycle)
51712	33552					0.75	0.50	3.125	1.187E-01
56897	36921					0.90	0.75	3.263	4.475E-02
62065	40273					1.00	0.80	3.413	1.331E-01
67261	43653					1.25	1.00	3.650	1.500E-01
72411	46987					1.50	1.25	3.863	1.046E-01
77573	50333					1.70	1.40	4.025	8.872E-02
82771	53715					1.90	1.50	4.313	2.560E-01
87907	57035					2.25	2.00	4.650	1.489E-01
93081	60393					2.50	2.25	4.963	2.228E-01
98263	63759	1.00	0.25	5.350	4.503E-01	3.00	2.50	5.525	4.503E-01
103410	67090	1.75	1.00	6.100	4.472E-01	3.75	3.25	6.213	3.726E-01
108581	70445	2.50	1.75	6.975	5.967E-01	4.50	3.75	6.963	5.221E-01
113749	73797	3.50	2.75	7.975	5.969E-01	5.25	4.75	7.900	5.969E-01
118915	77147	4.50	3.75	9.100	7.462E-01	6.25	5.75	9.025	7.462E-01
124082	80498	5.75	5.00			7.50	7.00		

Table C-10   Crack growth measurements and crack growth rate data

Test Number	**16**	Specimen Number		T 1615005-2	Temperature (°C)		mean **25.62**	stdev **0.28**
		F$_{max}$ (N) =		**41503**	Humidity (% r.H.)		**30.54**	**0.76**
N (cycles)	N* (cycles)	Back				Front			
		a$_{LHS}$ (mm)	a$_{RHS}$ (mm)	a$_{ave}$ (mm)	da/dN (µm/cycle)	a$_{LHS}$ (mm)	a$_{RHS}$ (mm)	a$_{ave}$ (mm)	da/dN (µm/cycle)
41378	26850					0.50	0.50	3.125	1.340E-01
51726	33566					1.00	0.90	3.463	1.333E-01
56918	36942					1.25	1.10	3.675	1.204E-01
62056	40264					1.50	1.25	3.900	1.487E-01
67234	43626					1.75	1.50	4.150	1.484E-01
72419	46995					2.00	1.75	4.500	2.693E-01
77577	50337					2.40	2.25	5.000	3.288E-01
82739	53683	0.75	0.25	5.413	6.693E-01	3.00	2.75	5.588	3.719E-01
87917	57045	1.75	1.50	6.838	5.163E-01	3.75	3.25	6.775	5.238E-01
98231	63727	3.60	3.10	8.213	6.097E-01	5.50	5.00	8.088	5.204E-01
103410	67090	4.75	4.00	8.850	1.490E-01	6.50	5.75	9.213	8.197E-01
108581	70445	6.00	3.25			7.75	7.25		

Table C-11   Crack growth measurements and crack growth rate data

Test Number	**17**	Specimen Number		T 1615005-3	Temperature (°C)		mean **26.51**	stdev **0.93**
		F$_{max}$ (N) =		**42256**	Humidity (% r.H.)		**47.21**	**0.83**
N (cycles)	N* (cycles)	Back				Front			
		a$_{LHS}$ (mm)	a$_{RHS}$ (mm)	a$_{ave}$ (mm)	da/dN (µm/cycle)	a$_{LHS}$ (mm)	a$_{RHS}$ (mm)	a$_{ave}$ (mm)	da/dN (µm/cycle)
36225	23513						1.00	2.963	7.464E-02
41390	26862						1.25	3.275	2.333E-01
47492	31148					0.75	1.50	3.563	6.178E-02
51736	33576					0.80	1.60	3.750	1.428E-01
57754	37778					1.00	2.00	4.025	2.004E-01
62065	40273					1.25	2.25	4.275	1.489E-01
67239	43631					1.50	2.50	4.650	3.001E-01
72387	46963		0.75	4.975	2.981E-01	2.00	3.00	5.150	2.981E-01
77558	50318	0.25	1.50	5.663	5.217E-01	2.50	3.50	5.750	4.173E-01
82728	53672	1.25	2.25	6.600	5.966E-01	3.15	4.25	6.563	5.518E-01
87897	57025	2.25	3.25	7.5375	5.219E-01	4.00	5.25	7.525	5.965E-01
93066	60378	3.25	4.00	8.600	7.450E-01	5.00	6.25	8.525	5.960E-01
98237	63733	4.50	5.25			6.00	7.25		

Table C-12 Crack growth measurements and crack growth rate data

									mean	stdev
Test Number	**18**	Specimen Number		**T 1615025-1**	Temperature ($^{\circ}$C)				**24.72**	**0.35**
		F_{max} (N) =		**40362**	Humidity (% r.H.)				**31.30**	**0.61**
N (cycles)	N* (cycles)	Back				Front				
		a_{LHS} (mm)	a_{RHS} (mm)	a_{ave} (mm)	da/dN (μm/cycle)	a_{LHS} (mm)	a_{RHS} (mm)	a_{ave} (mm)	da/dN (μm/cycle)	
113773	73821					1.00	1.25	3.650	1.471E-01	
118987	77219					1.25	1.50	3.938	1.977E-01	
124090	80506					1.65	1.75	4.275	2.089E-01	
129257	83857		0.25	4.688	4.913E-01	2.00	2.10	4.713	3.126E-01	
134431	87215	0.90	1.00	5.463	4.320E-01	2.50	2.65	5.463	5.810E-01	
139604	90572	1.60	1.75	6.213	4.623E-01	3.50	3.60	6.113	1.939E-01	
144772	93924	2.40	2.50	7.125	6.279E-01	3.75	4.00	6.713	5.232E-01	
149933	97269	3.50	3.50	8.100	5.365E-01	4.75	4.75	7.650	5.961E-01	
155104	100624	4.40	4.40	9.125	6.837E-01	5.75	5.75	8.775	7.432E-01	
160284	103988	5.60	5.50	10.425	8.640E-01	7.00	7.00	10.150	8.938E-01	
165456	107344	7.00	7.00			8.50	8.50			

Table C-13 Crack growth measurements and crack growth rate data

									mean	stdev
Test Number	**19**	Specimen Number		**T 1615025-2**	Temperature ($^{\circ}$C)				**23.77**	**0.37**
		F_{max} (N) =		**43298**	Humidity (% r.H.)				**52.30**	**0.41**
N (cycles)	N* (cycles)	Back				Front				
		a_{LHS} (mm)	a_{RHS} (mm)	a_{ave} (mm)	da/dN (μm/cycle)	a_{LHS} (mm)	a_{RHS} (mm)	a_{ave} (mm)	da/dN (μm/cycle)	
99449	64755						0.80	3.775	2.400E-01	
103992	67672					0.50	1.00	4.075	1.794E-01	
108595	70459					0.75	1.25	4.450	1.494E-01	
118922	77154					1.25	1.75	4.888	2.236E-01	
124092	80508					1.50	2.25	5.325	2.992E-01	
129250	83850		1.00	5.025	4.470E-01	2.00	2.75	5.825	2.980E-01	
134422	87206	0.75	1.75	6.338	4.816E-01	2.50	3.25	7.075	5.137E-01	
146233	94992	2.75	3.50	7.525	4.369E-01	4.50	5.25	8.325	4.369E-01	
149945	97281	3.25	4.00	8.400	7.453E-01	5.00	5.75	9.075	5.962E-01	
155115	100635	4.50	5.25			6.00	6.75			

Table C-14 Crack growth measurements and crack growth rate data

Test Number	**20**	Specimen Number		**T 1615025-3**	Temperature (°C)			**24.99** mean	**0.32** stdev
		F_{max} (N) =		**42337**	Humidity (% r.H.)			**50.07**	**0.37**

N (cycles)	N* (cycles)	Back a_{LHS} (mm)	a_{RHS} (mm)	a_{ave} (mm)	da/dN (μm/cycle)	Front a_{LHS} (mm)	a_{RHS} (mm)	a_{ave} (mm)	da/dN (μm/cycle)
72402	46978					0.75		2.963	1.118E-01
82745	53689					1.00	0.50	3.313	1.925E-01
87938	57066					1.25	0.90	3.625	1.795E-01
93096	60408					1.50	1.25	3.938	1.936E-01
98269	63765					1.90	1.50	4.250	1.805E-01
103410	67090	0.50	0.25	4.713	2.236E-01	2.25	1.75	4.600	2.385E-01
108581	70445	1.00	0.50	5.313	4.919E-01	2.60	2.20	5.038	2.832E-01
113751	73799	1.90	1.25	6.563	4.993E-01	3.25	2.50	6.088	4.844E-01
124092	80508	3.50	3.00	7.838	5.217E-01	4.75	4.25	7.400	5.962E-01
129263	83863	4.50	3.75	8.900	7.453E-01	5.75	5.25	8.525	7.453E-01
134433	87217	5.75	5.00			7.00	6.50		

Table C-15 Crack growth measurements and crack growth rate data

Test Number	**21**	Specimen Number		**T 1615050-1**	Temperature (°C)			**24.39** mean	**0.74** stdev
		F_{max} (N) =		**45296**	Humidity (% r.H.)			**31.89**	**2.26**

N (cycles)	N* (cycles)	Back a_{LHS} (mm)	a_{RHS} (mm)	a_{ave} (mm)	da/dN (μm/cycle)	Front a_{LHS} (mm)	a_{RHS} (mm)	a_{ave} (mm)	da/dN (μm/cycle)
271308	176331						1.75	3.400	1.032E-01
279241	181177		0.75	3.966	1.421E-01		2.25	3.650	7.477E-02
289560	187864		1.70	4.466	1.287E-01		2.75	4.025	1.226E-01
301896	196023		2.75	4.854	2.595E-01		3.75	4.338	1.298E-01
305093	197949		3.25	5.041	7.510E-02		4.00	4.525	1.502E-01
310238	201278		3.50	5.279	2.062E-01		4.50	4.775	1.473E-01
315449	204673		4.20	5.591	1.658E-01		5.00	5.025	1.507E-01
320583	207991		4.75	5.854	1.490E-01		5.50	5.275	1.490E-01
325755	211347		5.25	6.104	1.482E-01		6.00	6.025	7.409E-01
330946	214722		5.75	6.666	5.225E-01	1.75	6.75	6.900	2.986E-01
336111	218071	0.75	6.75			2.00	7.50		

Table C-16 Crack growth measurements and crack growth rate data

Test Number	**22**	Specimen Number	**T 1615050-2**			mean	stdev
		F_{max} (N) =	**42964**	Temperature (^{o}C)		**23.57**	**0.46**
				Humidity (% r.H.)		**32.27**	**1.49**

N (cycles)	N (cycles)	Back				Front			
		a_{LHS} (mm)	a_{RHS} (mm)	a_{ave} (mm)	da/dN (µm/cycle)	a_{LHS} (mm)	a_{RHS} (mm)	a_{ave} (mm)	da/dN (µm/cycle)
170637	110709					1.20		3.050	5.955E-02
175811	114067					1.40		3.188	1.024E-01
181047	117487	0.25		3.604	1.442E-01	1.75		3.338	7.209E-02
186331	120955	0.75		3.854	1.570E-01	2.00		3.775	4.711E-01
191331	124139	1.25		4.479	2.987E-01	2.75	0.75	4.525	2.240E-01
201659	130835	2.50	0.75	5.229	2.970E-01	3.25	1.75	5.275	4.455E-01
206842	134202	3.00	1.25	5.916	5.130E-01	4.00	2.50	5.900	2.931E-01
212070	137614	3.75	2.25	7.166	4.910E-01	4.50	3.00	7.275	6.799E-01
222320	144232	5.50	3.75	8.591	7.279E-01	6.25	5.75	8.713	3.714E-01
227502	147598	6.70	5.00			7.50	5.75		

Table C-17 Crack growth measurements and crack growth rate data

Test Number	**23**	Specimen Number	**T 1615050-3**			mean	stdev
		F_{max} (N) =	**42964**	Temperature (^{o}C)		**23.09**	**0.41**
				Humidity (% r.H.)		**39.07**	**2.82**

N (cycles)	N* (cycles)	Back				Front			
		a_{LHS} (mm)	a_{RHS} (mm)	a_{ave} (mm)	da/dN (µm/cycle)	a_{LHS} (mm)	a_{RHS} (mm)	a_{ave} (mm)	da/dN (µm/cycle)
248198	161030					0.75		2.838	7.442E-02
253373	164389					1.00		2.963	7.474E-02
258534	167734					1.25		3.213	1.118E-01
268875	174443	0.75		4.166	1.308E-01	2.00		3.775	1.121E-01
289500	187822	2.50		4.979	1.226E-01	3.50		4.463	1.022E-01
308060	200053	4.00		5.729	3.282E-01	4.75		5.400	5.470E-01
315400	204624	5.00	0.50	6.666	3.353E-01	6.00	1.25	6.650	3.726E-01
325742	211334	6.75	1.00			7.50	2.25		

Table C-18 Crack growth measurements and crack growth rate data

| Test Number | **24** | Specimen Number | **T 2012005-1** | Temperature (°C) | **24.30** mean | **0.29** stdev |
| Fmax (N) = | | | **56381** | Humidity (% r.H.) | **40.51** | **0.51** |

N (cycles)	N* (cycles)	Back a_{LHS} (mm)	a_{RHS} (mm)	a_{ave} (mm)	da/dN (µm/cycle)	Front a_{LHS} (mm)	a_{RHS} (mm)	a_{ave} (mm)	da/dN (µm/cycle)
25896	16816					0.75		2.838	7.536E-02
31029	20133					1.00		3.113	2.532E-01
36202	23490					1.10	0.75	3.675	1.433E-01
50514	33262					1.75	1.50	4.275	2.750E-01
56874	36898					2.25	2.00	4.838	3.731E-01
62040	40248					3.00	2.50	5.650	3.839E-01
69611	45458	1.50	0.75	6.203	5.397E-01	4.00	3.50	6.525	4.907E-01
74484	48515	2.50	1.40	7.015	4.953E-01	4.75	4.25	7.838	1.16E+00
79530	51745	3.50	2.00	8.228	1.104E+00	7.75	5.00	8.963	2.547E-01
83901	54690	4.75	4.00			7.25	6.25		

Table C-19 Crack growth measurements and crack growth rate data

| Test Number | **25** | Specimen Number | **T 2012005-2** | Temperature (°C) | **23.64** mean | **0.17** stdev |
| Fmax (N) = | | | **56381** | Humidity (% r.H.) | **44.37** | **0.65** |

N (cycles)	N* (cycles)	Back a_{LHS} (mm)	a_{RHS} (mm)	a_{ave} (mm)	da/dN (µm/cycle)	Front a_{LHS} (mm)	a_{RHS} (mm)	a_{ave} (mm)	da/dN (µm/cycle)
25868	16788						0.75	3.050	1.640E-01
36207	23495					0.75	1.10	3.488	1.936E-01
41381	26853					1.00	1.50	3.963	1.599E-01
53376	34671					1.50	2.25	4.710	3.101E-01
62074	40282					2.50	2.99	5.175	8.502E-02
64030	41693					2.60	3.01	5.303	3.628E-01
65468	42768					2.75	3.25	5.525	5.949E-01
67217	43609	0.25	0.75	5.703	6.423E-01	3.00	3.50	6.025	4.481E-01
72380	46956	1.40	1.75	6.765	6.250E-01	3.75	4.25	6.838	5.208E-01
77556	50316	2.50	2.75	7.840	6.562E-01	5.00	4.75	7.838	6.711E-01
82725	53669	3.70	3.75	9.1525	9.083E-01	6.25	5.75	9.150	8.934E-01
87899	57027	5.25	5.25			7.50	7.50		

Table C-20   Crack growth measurements and crack growth rate data

						mean	stdev
Test Number	**26**	Specimen Number	**T 2012005-3**	Temperature (°C)		**24.25**	**0.18**
		F_{max} (N) =	**56381**	Humidity (% r.H.)		**42.36**	**0.80**

N (cycles)	N* (cycles)	Back				Front			
		a_{LHS} (mm)	a_{RHS} (mm)	a_{ave} (mm)	da/dN (µm/cycle)	a_{LHS} (mm)	a_{RHS} (mm)	a_{ave} (mm)	da/dN (µm/cycle)
41375	26847					1.50	1.00	3.775	1.485E-01
46559	30215					1.75	1.25	4.463	2.241E-01
62046	40254					3.00	2.25	5.463	3.895E-01
68900	44747	1.25	0.25	5.978	6.630E-01	3.75	3.25	6.400	5.894E-01
74109	48140	2.25	1.50	6.853	5.761E-01	5.00	4.00	7.213	5.761E-01
77545	50310	2.75	2.25	7.790	7.450E-01	5.50	4.75	8.025	5.960E-01
82722	53666	4.00	3.50	9.165	8.949E-01	6.50	5.75	9.338	9.695E-01
87885	57018	5.50	5.00			8.00	7.50		

Table C-21   Crack growth measurements and crack growth rate data

						mean	stdev
Test Number	**27**	Specimen Number	**T 2012025-1**	Temperature (°C)		**25.58**	**1.17**
		F_{max} (N) =	**56381**	Humidity (% r.H.)		**42.29**	**2.67**

N (cycles)	N* (cycles)	Back				Front			
		a_{LHS} (mm)	a_{RHS} (mm)	a_{ave} (mm)	da/dN (µm/cycle)	a_{LHS} (mm)	a_{RHS} (mm)	a_{ave} (mm)	da/dN (µm/cycle)
62065	40273					1.25		3.338	1.242E-01
77576	50336	0.50		4.923	1.119E-01	2.50		3.838	1.119E-01
87913	57041	1.25		5.610	1.990E-01	3.25		4.463	1.741E-01
103410	67090	3.25		6.860	2.959E-01	5.00		5.963	4.192E-01
118996	77228	5.50	0.75	7.735	1.495E-01	7.25	2.00	7.463	5.232E-01
124156	80572	6.50	0.25	8.860	9.287E-01	8.25	2.75	8.713	7.546E-01
130468	84879	8.25	2.50			10.00	4.25		

Table C-22 Crack growth measurements and crack growth rate data

| Test Number | **28** | Specimen Number | **T 2012025-2** | Temperature (°C) | mean **24.90** | stdev **0.39** |
| | | F_{max} (N) = | **56381** | Humidity (% r.H.) | **38.92** | **0.41** |

N (cycles)	N* (cycles)	Back a_{LHS} (mm)	a_{RHS} (mm)	a_{ave} (mm)	da/dN (μm/cycle)	Front a_{LHS} (mm)	a_{RHS} (mm)	a_{ave} (mm)	da/dN (μm/cycle)
77566	50326						1.00	3.213	1.241E-01
93084	60396						2.25	3.713	1.112E-01
103462	67142		0.75	5.173	1.874E-01		3.00	4.150	1.499E-01
113763	73811		2.00	5.860	1.999E-01		4.00	5.000	3.198E-01
124900	81316		3.50	6.548	2.105E-01	1.00	5.40	6.125	3.537E-01
134469	87253		4.75	7.360	5.894E-01	2.00	6.50	7.088	5.158E-01
139678	90646	1.00	5.75	8.298	5.301E-01	2.75	7.50	8.150	7.572E-01
144796	93948	1.75	6.75	9.548	9.738E-01	4.00	8.75	9.463	8.240E-01
149949	97285	3.50	8.25			5.25	10.25		

Table C-23 Crack growth measurements and crack growth rate data

| Test Number | **29** | Specimen Number | **T 2012025-3** | Temperature (°C) | mean **23.64** | stdev **0.32** |
| | | F_{max} (N) = | **56381** | Humidity (% r.H.) | **41.18** | **0.56** |

N (cycles)	N* (cycles)	Back a_{LHS} (mm)	a_{RHS} (mm)	a_{ave} (mm)	da/dN (μm/cycle)	Front a_{LHS} (mm)	a_{RHS} (mm)	a_{ave} (mm)	da/dN (μm/cycle)
113751	73799					1.50	1.00	3.850	2.385E-01
118922	77154					1.90	1.40	4.225	2.094E-01
124080	80496					2.50	1.50	4.588	2.228E-01
129263	83863	0.25		4.923	3.707E-01	2.75	2.00	5.025	2.966E-01
134451	87235	1.25	0.25	5.548	3.727E-01	3.25	2.50	5.650	4.472E-01
139621	90589	2.00	0.75	6.360	5.993E-01	4.00	3.25	6.400	4.494E-01
144774	93926	3.00	1.75	7.548	6.669E-01	4.75	4.00	7.400	6.063E-01
150714	98050	4.25	3.25	8.735	7.768E-01	6.00	5.25	8.463	6.797E-01
155104	100624	5.25	4.25			7.00	6.00		

Table C-24   Crack growth measurements and crack growth rate data

Test Number	30	Specimen Number	T 2012050-1			mean	stdev
		F_{max} (N) =	56381	Temperature (°C)		**23.50**	**0.75**
				Humidity (% r.H.)		**28.54**	**1.27**

N (cycles)	N* (cycles)	Back				Front			
		a_{LHS} (mm)	a_{RHS} (mm)	a_{ave} (mm)	da/dN (µm/cycle)	a_{LHS} (mm)	a_{RHS} (mm)	a_{ave} (mm)	da/dN (µm/cycle)
232708	150988	1.75		5.438	1.494E-01	3.25		4.525	1.992E-01
248197	161029	3.25		6.250	2.595E-01	4.50	0.75	5.588	3.336E-01
258574	167774	4.50	0.50	7.438	4.478E-01	5.75	1.75	7.025	5.224E-01
268905	174473	6.00	2.00			7.50	3.50		

Table C-25   Crack growth measurements and crack growth rate data

Test Number	31	Specimen Number	T 2012050-2			mean	stdev
		F_{max} (N) =	56381	Temperature (°C)		**22.92**	**0.66**
				Humidity (% r.H.)		**45.93**	**2.88**

N (cycles)	N* (cycles)	Back				Front			
		a_{LHS} (mm)	a_{RHS} (mm)	a_{ave} (mm)	da/dN (µm/cycle)	a_{LHS} (mm)	a_{RHS} (mm)	a_{ave} (mm)	da/dN (µm/cycle)
180990	117430						0.75	3.025	7.456E-02
201666	130842						1.75	3.713	1.300E-01
222391	144303		2.00	5.375	2.265E-01		3.50	4.275	1.510E-01
227518	147614		2.75	5.938	1.494E-01		4.00	5.150	2.989E-01
243004	157652		4.25	7.000	4.096E-01	1.25	5.75	6.525	3.723E-01
253350	164366	1.00	6.00	8.375	6.729E-01	2.50	7.00	7.775	6.118E-01
259253	168453	2.50	7.25	9.563	7.613E-01	3.75	8.25	8.900	7.613E-01
263696	171080	3.75	8.00			4.75	9.25		

Table C-26   Crack growth measurements and crack growth rate data

Test Number	32	Specimen Number	T 2012050-3			mean	stdev
		F_{max} (N) =	56381	Temperature (°C)		**25.22**	**0.58**
				Humidity (% r.H.)		**45.63**	**1.12**

N (cycles)	N* (cycles)	Back				Front			
		a_{LHS} (mm)	a_{RHS} (mm)	a_{ave} (mm)	da/dN (µm/cycle)	a_{LHS} (mm)	a_{RHS} (mm)	a_{ave} (mm)	da/dN (µm/cycle)
113751	73799	1.50	2.00	6.375	5.218E-01	3.00	3.50	6.025	4.472E-01
118921	77153	2.50	2.75	7.313	5.976E-01	3.75	4.25	6.838	5.229E-01
124084	80500	3.25	4.00	8.438	7.456E-01	4.50	5.25	7.900	7.456E-01
129253	83853	4.75	5.00	9.813	8.946E-01	5.75	6.50	9.213	8.200E-01
134423	87207	6.25	6.50			7.25	7.75		

Table C-27   Crack growth measurements and crack growth rate data

Test Number	33	Specimen Number	TB 1024005-1	Temperature (^{o}C)		mean **24.76**	stdev **0.13**
		F_{max} (N) =	27329	Humidity (% r.H.)		**55.83**	**0.51**

N (cycles)	N* (cycles)	Back a_{LHS} (mm)	a_{RHS} (mm)	a_{ave} (mm)	da/dN (μm/cycle)	Front a_{LHS} (mm)	a_{RHS} (mm)	a_{ave} (mm)	da/dN (μm/cycle)
10341	10341					0.50	0.50	3.025	4.835E-02
20682	20682					0.75	0.75	3.275	4.835E-02
31023	31023					1.00	1.00	3.650	9.670E-02
41364	41364					1.50	1.50	4.400	1.934E-01
51705	51705	1.00	0.75	5.032	2.418E-01	2.75	2.25	5.463	2.176E-01
62046	62046	2.25	2.00	6.345	2.659E-01	3.75	3.50	6.650	2.418E-01
72387	72387	3.75	3.25	7.620	4.122E-01	5.50	4.25	7.838	3.947E-01
78088	78088	4.85	4.50	8.432	1.940E-01	6.25	5.75	8.900	4.310E-01
82728	82728	5.25	5.00			7.50	6.50		

Table C-28   Crack growth measurements and crack growth rate data

Test Number	34	Specimen Number	TB 1024005-2	Temperature (^{o}C)		mean **26.79**	stdev **0.23**
				Humidity (% r.H.)		**45.83**	**0.62**

N (cycles)	N* (cycles)	Back a_{LHS} (mm)	a_{RHS} (mm)	a_{ave} (mm)	da/dN (μm/cycle)	Front a_{LHS} (mm)	a_{RHS} (mm)	a_{ave} (mm)	da/dN (μm/cycle)
46535	46535					1.00	1.25	3.875	1.354E-01
56876	56876					1.65	2.00	4.688	3.578E-01
62046	62046	0.50	1.00	4.595	2.418E-01	2.50	3.00	5.338	1.451E-01
67217	67217	1.25	1.50	5.157	1.934E-01	2.75	3.50	5.713	1.451E-01
72387	72387	1.50	2.25	5.657	1.934E-01	3.25	3.75	6.088	1.451E-01
77558	77558	2.25	2.50	6.282	2.901E-01	3.50	4.25	6.525	1.934E-01
82728	82728	2.75	3.50	7.095	3.385E-01	4.25	4.50	7.213	3.385E-01
87899	87899	3.75	4.25	7.907	2.901E-01	5.00	5.50	8.025	2.901E-01
93069	93069	4.50	5.00			5.75	6.25		

Table C-29   Crack growth measurements and crack growth rate data

Test Number	35	Specimen Number	TB 1024005-3	Temperature (^{o}C)		mean **27.41**	stdev **0.17**
		F_{max} (N) =	26891	Humidity (% r.H.)		**45.84**	**1.39**

N (cycles)	N* (cycles)	Back a_{LHS} (mm)	a_{RHS} (mm)	a_{ave} (mm)	da/dN (μm/cycle)	Front a_{LHS} (mm)	a_{RHS} (mm)	a_{ave} (mm)	da/dN (μm/cycle)
41364	41364					1.00	1.00	3.650	1.934E-01
46535	46535	0.10	0.10	3.895	2.031E-01	1.50	1.50	4.150	1.934E-01
51705	51705	0.75	0.50	4.395	1.837E-01	2.00	2.00	4.713	2.418E-01
56876	56876	1.20	1.00	5.207	2.224E-01	2.75	2.50	5.588	2.176E-01
67217	67217	2.50	2.00	6.595	3.143E-01	3.75	3.75	6.838	2.659E-01
77558	77558	3.75	4.00	7.782	2.897E-01	5.00	5.25	8.025	3.862E-01
82736	82736	4.50	4.75	8.720	4.358E-01	6.00	6.25	9.025	3.874E-01
87899	87899	5.50	6.00			7.00	7.25		

Table C-30 Crack growth measurements and crack growth rate data

Test Number	**36**	Specimen Number	**TB 1024025-1**	Temperature (°C)		mean **28.72**	stdev **0.51**
		F_{max} (N) =	**26917**	Humidity (% r.H.)		**43.38**	**1.89**

N (cycles)	N* (cycles)	Back				Front			
		a_{LHS} (mm)	a_{RHS} (mm)	a_{ave} (mm)	da/dN (µm/cycle)	a_{LHS} (mm)	a_{RHS} (mm)	a_{ave} (mm)	da/dN (µm/cycle)
51705	33545					0.50	0.50	3.150	1.491E-01
62046	40254					1.00	1.00	3.650	2.981E-01
67217	43609					1.50	1.50	4.650	2.979E-01
82736	53680	1.50	1.50	5.170	4.482E-01	3.00	3.00	5.588	2.241E-01
87899	57027	2.25	2.25	5.783	2.832E-01	3.25	3.50	6.088	3.726E-01
93069	60381	2.75	2.70	6.658	3.801E-01	4.00	4.00	7.025	3.726E-01
103410	67090	4.00	4.00	7.733	5.217E-01	5.25	5.25	8.025	4.472E-01
108581	70445	4.75	5.00	8.545	4.472E-01	6.00	6.00	8.838	5.217E-01
113751	73799	5.50	5.75			6.75	7.00		

Table C-31 Crack growth measurements and crack growth rate data

Test Number	**37**	Specimen Number	**TB 1024025-2**	Temperature (°C)		mean **30.24**	stdev **0.39**
		F_{max} (N) =	**27041**	Humidity (% r.H.)		**40.06**	**0.66**

N (cycles)	N* (cycles)	Back				Front			
		a_{LHS} (mm)	a_{RHS} (mm)	a_{ave} (mm)	da/dN (µm/cycle)	a_{LHS} (mm)	a_{RHS} (mm)	a_{ave} (mm)	da/dN (µm/cycle)
36194	23482					0.50	0.50	2.981	4.844E-02
46535	30191					0.58	0.75	3.119	6.707E-02
51705	33545					0.65	0.90	3.250	8.943E-02
56876	36900					0.75	1.10	3.375	5.962E-02
62046	40254					0.80	1.25	3.538	1.341E-01
67217	43609					1.00	1.50	3.900	2.981E-01
72387	46963					1.50	2.00	4.338	2.236E-01
77558	50318					1.75	2.50	4.688	1.938E-01
82728	53672	0.75	1.50	4.733	3.726E-01	2.00	2.90	5.075	2.683E-01
87899	57027	1.50	2.00	5.295	2.981E-01	2.50	3.30	5.475	2.087E-01
93069	60381	1.75	2.75	5.928	4.561E-01	2.75	3.75	6.025	4.472E-01
98240	63736	2.53	3.50	6.615	3.637E-01	3.50	4.50	6.775	4.472E-01
103410	67090	3.25	4.00	7.233	3.726E-01	4.50	5.00	7.463	3.726E-01
108581	70445	4.00	4.50	7.983	5.217E-01	5.00	5.75	8.150	4.472E-01
113751	73799	4.75	5.50	8.795	4.472E-01	5.75	6.50	9.025	5.962E-01
118922	77154	5.50	6.25			6.75	7.50		

Table C-32 Crack growth measurements and crack growth rate data

Test Number	**38**	Specimen Number	**TB 1024050-1**	Temperature (°C)	mean **25.91**	stdev **0.18**
		F_{max} (N) =	**27670**	Humidity (% r.H.)	**49.61**	**1.04**

N (cycles)	N* (cycles)	Back				Front			
		a_{LHS} (mm)	a_{RHS} (mm)	a_{ave} (mm)	da/dN (µm/cycle)	a_{LHS} (mm)	a_{RHS} (mm)	a_{ave} (mm)	da/dN (µm/cycle)
46535	30191					0.75	0.50	3.150	7.453E-02
56876	36900					1.00	0.75	3.500	8.943E-02
72387	46963	0.25	0.00	3.395	3.279E-01	1.40	1.25	3.975	2.981E-01
77558	50318	0.75	0.60	4.208	3.205E-01	1.90	1.75	4.713	2.907E-01
87899	57027	1.75	1.75	5.370	3.726E-01	3.00	2.60	5.800	3.577E-01
98240	63736	3.00	3.00	7.058	4.223E-01	4.00	4.00	7.400	3.975E-01
113751	73799	5.25	5.00			6.00	6.00		

Table C-33 Crack growth measurements and crack growth rate data

Test Number	**39**	Specimen Number	**TB 1024050-2**	Temperature (°C)	mean **26.37**	stdev **0.24**
				Humidity (% r.H.)	**48.38**	**1.59**

N (cycles)	N* (cycles)	Back				Front			
		a_{LHS} (mm)	a_{RHS} (mm)	a_{ave} (mm)	da/dN (µm/cycle)	a_{LHS} (mm)	a_{RHS} (mm)	a_{ave} (mm)	da/dN (µm/cycle)
56876	36900					0.40	0.50	2.950	1.192E-01
62046	40254					0.50	0.80	3.163	1.341E-01
67217	43609					0.75	1.00	3.438	1.938E-01
72387	46963	0.00	0.25	3.308	2.236E-01	1.00	1.40	3.725	1.491E-01
77558	50318	0.25	0.75	3.745	2.981E-01	1.40	1.50	4.125	3.279E-01
82728	53672	0.75	1.25	4.183	2.236E-01	1.75	2.25	4.588	2.236E-01
87899	57027	1.25	1.50	4.683	3.650E-01	2.25	2.50	5.025	2.920E-01
93139	60451	1.75	2.25	5.433	2.638E-01	2.75	3.00	5.838	3.392E-01
103405	67085	2.75	3.00	6.308	5.209E-01	3.75	4.25	6.650	2.977E-01
108581	70445	3.50	4.00	7.058	3.726E-01	4.25	4.75	7.213	3.726E-01
113751	73799	4.00	4.75	7.808	5.217E-01	4.75	5.50	7.963	5.217E-01
118922	77154	5.00	5.50	8.620	4.472E-01	5.75	6.25	8.900	5.962E-01
124092	80508	5.75	6.25			6.75	7.25		

Table C-34 Crack growth measurements and crack growth rate data

Test Number	**40**	Specimen Number	**TB 1024050-3**	Temperature (°C)	mean **25.94**	stdev **0.27**
		F_{max} (N) =	**27636**	Humidity (% r.H.)	**48.39**	**0.62**

N (cycles)	N* (cycles)	Back				Front			
		a_{LHS} (mm)	a_{RHS} (mm)	a_{ave} (mm)	da/dN (µm/cycle)	a_{LHS} (mm)	a_{RHS} (mm)	a_{ave} (mm)	da/dN (µm/cycle)
51705	33545					0.50	0.75	3.338	1.863E-01
62046	40254	0.1	0.25	3.708	3.205E-01	1.25	1.25	4.088	2.608E-01
72387	46963	1.25	1.25	4.745	2.981E-01	2.25	2.00	5.088	3.354E-01
82728	53672	2.25	2.25	6.120	3.478E-01	3.25	3.25	6.525	3.478E-01
98240	63736	4.00	4.00	7.370	4.472E-01	5.00	5.00	7.775	4.472E-01
103410	67090	4.75	4.75	8.120	4.475E-01	5.75	5.75	8.525	4.475E-01
108578	70442	5.50	5.50			6.50	6.50		

Table C-35 Crack growth measurements and crack growth rate data

							mean	stdev
Test Number	**41**	Specimen Number	**TB 1615005-1**	Temperature (°C)			**21.90**	**0.08**
		F_{max} (N) =	**45600**	Humidity (% r.H.)			**38.99**	**0.64**

N (cycles)	N* (cycles)	Back a_{LHS} (mm)	a_{RHS} (mm)	a_{ave} (mm)	da/dN (µm/cycle)	Front a_{LHS} (mm)	a_{RHS} (mm)	a_{ave} (mm)	da/dN (µm/cycle)
15512	10064					0.40	0.40	2.850	5.964E-02
20681	13417					0.50	0.50	3.025	1.490E-01
25853	16773					0.75	0.75	3.275	1.491E-01
31023	20127					1.00	1.00	3.525	1.491E-01
36194	23482					1.25	1.25	3.775	1.491E-01
41364	26836					1.50	1.50	4.025	1.491E-01
46535	30191					1.75	1.75	4.400	2.981E-01
51705	33545					2.25	2.25	4.963	3.726E-01
56876	36900					2.75	3.00	5.588	3.726E-01
62046	40254					3.25	3.75	6.275	4.472E-01
67217	43609	0.75	1.25	5.900	5.962E-01	4.00	4.50	7.150	5.962E-01
72387	46963	1.75	2.25	6.713	3.726E-01	5.25	5.25	8.025	4.472E-01
77558	50318	2.50	2.75	7.500	5.664E-01	5.75	6.25	8.900	5.962E-01
82728	53672	3.40	3.75			6.75	7.25		

Table C-36 Crack growth measurements and crack growth rate data

							mean	stdev
Test Number	**42**	Specimen Number	**TB 1615005-2**	Temperature (°C)			**21.63**	**0.22**
		F_{max} (N) =	**46613**	Humidity (% r.H.)			**28.37**	**0.85**

N (cycles)	N* (cycles)	Back a_{LHS} (mm)	a_{RHS} (mm)	a_{ave} (mm)	da/dN (µm/cycle)	Front a_{LHS} (mm)	a_{RHS} (mm)	a_{ave} (mm)	da/dN (µm/cycle)
20681	13417					0.50	0.50	3.213	1.242E-01
36194	23482					1.25	1.00	3.650	1.491E-01
41364	26836					1.50	1.25	4.025	2.981E-01
46535	30191					2.00	1.75	4.500	2.683E-01
51705	33545					2.40	2.25	5.000	3.279E-01
56876	36900					3.00	2.75	5.650	4.472E-01
62046	40254	1.25	1.00	6.000	5.664E-01	3.75	3.50	6.400	4.472E-01
67217	43609	2.25	1.90	6.813	4.024E-01	4.50	4.25	7.150	4.472E-01
72387	46963	3.00	2.50	7.588	5.217E-01	5.25	5.00	8.025	5.962E-01
77558	50318	3.75	3.50			6.25	6.00		

Table C-37 Crack growth measurements and crack growth rate data

									mean	stdev
Test Number	**43**	Specimen Number		TB 1615005-3	Temperature (^{o}C)				**21.51**	**0.22**
					Humidity (% r.H.)				**26.37**	**0.57**
N (cycles)	N* (cycles)	Back				Front				
		a_{LHS} (mm)	a_{RHS} (mm)	a_{ave} (mm)	da/dN (μm/cycle)	a_{LHS} (mm)	a_{RHS} (mm)	a_{ave} (mm)	da/dN (μm/cycle)	
25853	16773					0.50	0.50	3.150	1.491E-01	
36194	23482					1.00	1.00	3.650	1.491E-01	
46535	30191					1.50	1.50	4.150	2.981E-01	
51705	33545					2.00	2.00	4.575	2.087E-01	
56876	36900					2.40	2.30	5.100	4.173E-01	
62046	40254	0.25	0.25	5.150	5.962E-01	3.10	3.00	5.700	2.981E-01	
67217	43609	1.25	1.25	6.025	4.472E-01	3.60	3.50	6.425	5.664E-01	
72387	46963	2.00	2.00	7.000	7.155E-01	4.50	4.50	7.338	5.217E-01	
77558	50318	3.20	3.20	8.000	4.770E-01	5.50	5.25	8.338	6.707E-01	
82728	53672	4.00	4.00	8.900	5.962E-01	6.50	6.50	9.400	5.962E-01	
87899	57027	5.00	5.00			7.50	7.50			

Table C-38 Crack growth measurements and crack growth rate data

									mean	stdev
Test Number	**44**	Specimen Number		TB 1615025-1	Temperature (^{o}C)				**21.41**	**0.14**
		F_{max} (N) =		45419	Humidity (% r.H.)				**40.25**	**0.34**
N (cycles)	N* (cycles)	Back				Front				
		a_{LHS} (mm)	a_{RHS} (mm)	a_{ave} (mm)	da/dN (μm/cycle)	a_{LHS} (mm)	a_{RHS} (mm)	a_{ave} (mm)	da/dN (μm/cycle)	
31023	20127					0.50	0.50	2.975	8.943E-02	
36194	23482					0.60	0.70	3.100	5.962E-02	
41364	26836					0.75	0.75	3.275	1.491E-01	
46535	30191					1.00	1.00	3.525	1.491E-01	
51705	33545					1.25	1.25	3.888	2.832E-01	
56876	36900					1.75	1.70	4.288	1.939E-01	
62043	40251					2.00	2.10	4.675	2.681E-01	
67217	43609	0.25	0.25	4.625	4.472E-01	2.50	2.50	5.275	4.472E-01	
72387	46963	1.00	1.00	5.500	5.962E-01	3.25	3.25	6.025	4.472E-01	
77558	50318	2.00	2.00	6.250	2.981E-01	4.00	4.00	6.900	5.962E-01	
82728	53672	2.50	2.50	7.025	6.260E-01	5.00	5.00	7.775	4.472E-01	
87899	57027	3.50	3.60	8.025	5.664E-01	5.75	5.75	8.650	5.962E-01	
93069	60381	4.50	4.50			6.75	6.75			

Table C-39 Crack growth measurements and crack growth rate data

Test Number	**45**	Specimen Number	**TB 1615025-2**	Temperature (°C)		mean **21.72**	stdev **0.18**				
		F_{max} (N) =	**46265**	Humidity (% r.H.)		**39.25**	**0.44**				
N (cycles)	N* (cycles)	Back				Front					
		a_{LHS} (mm)	a_{RHS} (mm)	a_{ave} (mm)	da/dN (µm/cycle)	a_{LHS} (mm)	a_{RHS} (mm)	a_{ave} (mm)	da/dN (µm/cycle)		
25853	16773					0.50	0.30	2.844	5.217E-02		
31023	20127					0.58	0.40	2.931	5.217E-02		
36194	23482					0.65	0.50	3.225	2.981E-01		
41364	26836					1.25	0.90	3.688	1.267E-01		
51705	33545					1.75	1.25	4.088	2.236E-01		
56876	36900					2.25	1.50	4.588	3.726E-01		
62046	40254	0.25		4.438	3.726E-01	3.00	2.00	5.150	2.981E-01		
67217	43609	1.25	0.25	5.063	3.726E-01	3.50	2.50	5.713	3.726E-01		
72387	46963	1.75	1.00	6.250	5.217E-01	4.00	3.25	6.775	4.472E-01		
82728	53672	3.50	2.75	7.625	5.962E-01	5.50	4.75	8.025	5.962E-01		
87899	57027	4.50	3.75			6.50	5.75				

Table C-40 Crack growth measurements and crack growth rate data

Test Number	**46**	Specimen Number	**TB 1615025-3**	Temperature (°C)		mean **21.54**	stdev **0.89**				
		F_{max} (N) =	**44511**	Humidity (% r.H.)		**29.39**	**2.22**				
N (cycles)	N* (cycles)	Back				Front					
		a_{LHS} (mm)	a_{RHS} (mm)	a_{ave} (mm)	da/dN (µm/cycle)	a_{LHS} (mm)	a_{RHS} (mm)	a_{ave} (mm)	da/dN (µm/cycle)		
31023	20127					0.50	0.75	3.206	7.204E-02		
46535	30191					0.58	1.40	3.619	1.379E-01		
56876	36900					0.65	2.25	4.438	7.006E-01		
62046	40254					2.50	2.75	5.338	3.726E-01		
67217	43609	0.75	1.00	5.350	5.664E-01	3.00	3.50	6.025	4.472E-01		
72387	46963	1.75	1.90	6.288	5.515E-01	4.00	4.00	6.838	5.217E-01		
77558	50318	2.75	2.75	7.150	4.770E-01	4.75	5.00	7.675	4.770E-01		
82728	53672	3.50	3.60	8.025	5.664E-01	5.60	5.75	8.613	6.409E-01		
87899	57027	4.50	4.50	9.113	7.304E-01	6.50	7.00	9.713	6.707E-01		
93069	60381	5.70	5.75			7.75	8.00				

Table C-41   Crack growth measurements and crack growth rate data

									mean	stdev
Test Number	**47**	Specimen Number	**TB 1615050-1**	Temperature (^{o}C)					**21.86**	**0.13**
		F_{max} (N) =	**45998**	Humidity (% r.H.)					**45.89**	**0.23**
N (cycles)	N* (cycles)	Back				Front				
		a_{LHS} (mm)	a_{RHS} (mm)	a_{ave} (mm)	da/dN (μm/cycle)	a_{LHS} (mm)	a_{RHS} (mm)	a_{ave} (mm)	da/dN (μm/cycle)	
30764	20082					0.40	0.70	3.113	3.876E-02	
56616	36853					0.75	1.00	3.388	1.342E-01	
61787	40207					1.00	1.20	3.888	2.311E-01	
72128	46915					1.75	2.00	4.863	3.503E-01	
82469	53623	1.25	1.25	5.157	4.472E-01	3.00	3.10	5.863	4.919E-01	
87639	56977	2.00	2.00	5.907	4.472E-01	3.75	4.00	6.650	4.472E-01	
92810	60331	2.75	2.75	6.657	4.472E-01	4.50	4.75	7.338	3.727E-01	
97980	63685	3.50	3.50	7.532	5.963E-01	5.25	5.25	8.213	6.708E-01	
103151	67039	4.50	4.50			6.25	6.50			

Table C-42   Crack growth measurements and crack growth rate data

									mean	stdev
Test Number	**48**	Specimen Number	**TB 1615050-2**	Temperature (^{o}C)					**21.60**	**0.13**
		F_{max} (N) =	**47261**	Humidity (% r.H.)					**47.01**	**0.60**
N (cycles)	N* (cycles)	Back				Front				
		a_{LHS} (mm)	a_{RHS} (mm)	a_{ave} (mm)	da/dN (μm/cycle)	a_{LHS} (mm)	a_{RHS} (mm)	a_{ave} (mm)	da/dN (μm/cycle)	
51705	33545					0.40	0.70	3.238	1.714E-01	
62046	40254					1.00	1.25	3.713	2.236E-01	
67217	43609					1.25	1.75	4.025	1.491E-01	
72387	46963					1.50	2.00	4.488	4.024E-01	
77558	50318					2.25	2.60	5.188	4.316E-01	
82733	53677	1.00	1.75	5.257	4.180E-01	2.80	3.50	5.975	5.075E-01	
87899	57027	1.75	2.40	6.507	5.366E-01	3.75	4.25	7.275	5.217E-01	
98240	63736	3.50	4.25			5.50	6.00			

Table C-43   Crack growth measurements and crack growth rate data

Test Number	**49**	Specimen Number	**TB 1615050-3**	Temperature (^{o}C)		mean **21.35**	stdev **0.26**
		F_{max} (N) =	**47188**	Humidity (% r.H.)		**42.20**	**1.16**

N (cycles)	N* (cycles)	Back a_{LHS} (mm)	a_{RHS} (mm)	a_{ave} (mm)	da/dN (μm/cycle)	Front a_{LHS} (mm)	a_{RHS} (mm)	a_{ave} (mm)	da/dN (μm/cycle)
51705	33545					0.60	0.75	3.175	1.192E-01
56876	36900					0.85	0.90	3.500	2.683E-01
62046	40254					1.25	1.40	3.913	2.236E-01
67217	43609					1.50	1.90	4.213	1.341E-01
72387	46963					1.75	2.10	4.613	3.433E-01
77553	50313	0.25	0.75	4.470	5.209E-01	2.50	2.50	5.213	3.721E-01
82728	53672	1.25	1.50	5.220	3.726E-01	3.00	3.25	5.900	4.472E-01
87899	57027	1.75	2.25	6.032	5.962E-01	3.75	4.00	6.525	2.981E-01
93069	60381	2.75	3.25	6.970	5.217E-01	4.25	4.50	7.338	6.707E-01
98240	63736	3.75	4.00			5.25	5.75		

Table C-44   Crack growth measurements and crack growth rate data

Test Number	**50**	Specimen Number	**TB 2012005-1**	Temperature (^{o}C)		mean **24.75**	stdev **0.28**
		F_{max} (N) =	**56381**	Humidity (% r.H.)		**34.28**	**0.70**

N (cycles)	N* (cycles)	Back a_{LHS} (mm)	a_{RHS} (mm)	a_{ave} (mm)	da/dN (μm/cycle)	Front a_{LHS} (mm)	a_{RHS} (mm)	a_{ave} (mm)	da/dN (μm/cycle)
31023	20127					1.25	1.25	3.800	1.789E-01
36194	23482					1.40	1.70	4.113	1.938E-01
41364	26836					1.75	2.00	4.588	3.726E-01
46535	30191					2.25	2.75	5.088	2.236E-01
51705	33545					2.75	3.00	5.838	6.707E-01
56876	36900	0.60	1.10	6.090	6.856E-01	3.75	4.25	6.900	5.962E-01
62046	40254	1.75	2.25	7.290	7.453E-01	4.75	5.25	8.338	1.12E+00
67217	43609	3.00	3.50			7.75	6.00		

Table C-45   Crack growth measurements and crack growth rate data

Test Number	**51**	Specimen Number	**TB 2012005-2**	Temperature (^{o}C)		mean **28.63**	stdev **0.29**
		F_{max} (N) =	**56381**	Humidity (% r.H.)		**37.15**	**0.42**

N (cycles)	N* (cycles)	Back a_{LHS} (mm)	a_{RHS} (mm)	a_{ave} (mm)	da/dN (μm/cycle)	Front a_{LHS} (mm)	a_{RHS} (mm)	a_{ave} (mm)	da/dN (μm/cycle)
31214	20318					1.00	1.00	3.525	1.575E-01
36204	23492					1.25	1.25	3.950	3.589E-01
41364	26836					1.95	1.75	4.450	2.012E-01
47157	30813					2.50	2.00	5.338	4.518E-01
56876	36900	0.50	0.75	6.478	7.082E-01	3.75	3.50	7.150	6.709E-01
67215	43607	3.00	3.00	8.540	9.305E-01	5.75	6.00	9.088	8.640E-01
72793	47369	4.75	4.75			7.50	7.50		

Table C-46   Crack growth measurements and crack growth rate data

| Test Number | **52** | Specimen Number | **TB 2012005-3** | Temperature (°C) | | mean **29.88** | stdev **0.43** |
| | | F_{max} (N) = | **56381** | Humidity (% r.H.) | | **35.68** | **0.92** |

N (cycles)	N* (cycles)	Back				Front			
		a_{LHS} (mm)	a_{RHS} (mm)	a_{ave} (mm)	da/dN (µm/cycle)	a_{LHS} (mm)	a_{RHS} (mm)	a_{ave} (mm)	da/dN (µm/cycle)
36204	23492					1.50	1.50	4.150	3.069E-01
40864	26750					2.00	2.00	5.088	4.047E-01
51705	33545					3.25	3.50	6.900	6.707E-01
62046	40254	2.50	2.75	9.228	1.155E+00	5.50	5.75	9.713	1.01E+00
72387	46963	6.25	6.75			9.00	9.00		

Table C-47   Crack growth measurements and crack growth rate data

| Test Number | **53** | Specimen Number | **TB 2012025-1** | Temperature (°C) | | mean **24.15** | stdev **0.13** |
| | | F_{max} (N) = | **56381** | Humidity (% r.H.) | | **36.04** | **0.53** |

N (cycles)	N* (cycles)	Back				Front			
		a_{LHS} (mm)	a_{RHS} (mm)	a_{ave} (mm)	da/dN (µm/cycle)	a_{LHS} (mm)	a_{RHS} (mm)	a_{ave} (mm)	da/dN (µm/cycle)
31023	20127					0.40	0.90	3.375	1.938E-01
41364	26836					1.00	1.60	3.950	2.514E-01
47157	30813					1.50	2.10	4.425	3.294E-01
51705	33545					1.75	2.75	4.963	3.726E-01
56876	36900					2.50	3.25	5.713	5.217E-01
62046	40254	0.50	1.50	6.110	7.453E-01	3.50	4.00	6.713	6.707E-01
67217	43609	1.75	2.75	7.360	7.453E-01	4.50	5.25	7.900	7.453E-01
72387	46963	3.00	4.00			5.75	6.50		

Table C-48   Crack growth measurements and crack growth rate data

| Test Number | **54** | Specimen Number | **TB 2012025-2** | Temperature (°C) | | mean **26.98** | stdev **0.23** |
| | | F_{max} (N) = | **56381** | Humidity (% r.H.) | | **37.69** | **0.39** |

N (cycles)	N* (cycles)	Back				Front			
		a_{LHS} (mm)	a_{RHS} (mm)	a_{ave} (mm)	da/dN (µm/cycle)	a_{LHS} (mm)	a_{RHS} (mm)	a_{ave} (mm)	da/dN (µm/cycle)
25853	16773					0.50	0.75	3.150	1.181E-01
31904	21008					0.75	1.00	3.838	2.295E-01
47157	30813					2.00	2.00	4.650	3.660E-01
51705	33545					2.50	2.50	5.275	4.472E-01
56876	36900					3.25	3.25	6.150	4.980E-01
62708	40916	1.50	1.50	7.110	7.441E-01	4.25	4.25	7.775	7.441E-01
72387	46963	3.75	3.75	9.235	1.192E+00	6.50	6.50	9.775	1.04E+00
77558	50318	5.75	5.75			8.25	8.25		

Table C-49 Crack growth measurements and crack growth rate data

N (cycles)	N* (cycles)	Back a_{LHS} (mm)	a_{RHS} (mm)	a_{ave} (mm)	da/dN (µm/cycle)	Front a_{LHS} (mm)	a_{RHS} (mm)	a_{ave} (mm)	da/dN (µm/cycle)
Test Number	**55**	Specimen Number	**TB 2012025-3**		Temperature (°C) **27.65** mean		Humidity (% r.H.) **37.50**	0.21 stdev	0.29
26310	17230					0.00	0.50	3.063	2.635E-01
36204	23492					1.25	0.90	3.813	1.844E-01
47157	30813					2.00	1.50	4.775	4.107E-01
56876	36900					3.25	2.75	5.988	5.583E-01
62901	41109	1.75	1.25	6.360	6.004E-01	4.50	3.85	6.950	6.004E-01
67215	43607	2.50	2.00	8.235	8.941E-01	5.25	4.60	11.300	2.37E+00
77558	50318	5.50	5.00			13.25	12.50		

Header block: Test Number **55**; F_{max} (N) = **56381**; Temperature (°C) mean **27.65** stdev **0.21**; Humidity (% r.H.) mean **37.50** stdev **0.29**.

Table C-50 Crack growth measurements and crack growth rate data

Header block: Test Number **56**; Specimen Number **TB 2012050-1**; F_{max} (N) = **56381**; Temperature (°C) mean **25.49** stdev **0.19**; Humidity (% r.H.) mean **41.13** stdev **0.45**.

N (cycles)	N* (cycles)	Back a_{LHS} (mm)	a_{RHS} (mm)	a_{ave} (mm)	da/dN (µm/cycle)	Front a_{LHS} (mm)	a_{RHS} (mm)	a_{ave} (mm)	da/dN (µm/cycle)
46535	30191					0.50	0.50	3.025	6.045E-02
58983	38462					0.75	0.75	3.175	1.943E-02
67217	43609					0.40	1.20	3.488	3.428E-01
72387	46963					1.00	1.75	3.963	2.236E-01
77558	50318					1.25	2.25	4.463	3.726E-01
82728	53672					1.75	3.00	5.025	2.989E-01
87889	57018					2.25	3.50	5.650	4.460E-01
93069	60381	0.25	2.00	5.875	6.707E-01	3.00	4.25	6.525	5.962E-01
98240	63736	1.50	3.00	7.000	6.708E-01	4.00	5.25	7.713	8.199E-01
103410	67090	2.75	4.00	8.250	8.197E-01	5.25	6.75	9.025	7.452E-01
108581	70445	4.00	5.50			6.50	8.00		

Table C-51   Crack growth measurements and crack growth rate data

Test Number	57	Specimen Number	TB 2012050-2	Temperature (°C)			mean **26.04**	stdev **0.16**
		F_{max} (N) =	56381	Humidity (% r.H.)			**37.08**	**1.13**
N (cycles)	N* (cycles)	Back				Front		
		a_{LHS} (mm)	a_{RHS} (mm)	a_{ave} (mm)	da/dN (µm/cycle)	a_{LHS} (mm)	a_{RHS} (mm)	a_{ave} (mm)	da/dN (µm/cycle)
58183	37941					0.40	0.50	2.925	1.297E-01
62046	40254					0.60	0.60	3.325	1.762E-01
73058	47634					1.00	1.50	3.713	6.692E-02
78900	51369					1.00	1.75	3.963	3.257E-01
82728	53672					1.25	2.25	4.525	4.472E-01
87899	57027					2.00	3.00	5.088	2.236E-01
93069	60381					2.50	3.25	5.775	5.138E-01
98778	64274	1.25	2.00	6.313	6.563E-01	3.50	4.25	6.650	4.922E-01
103641	67321	2.25	3.00	7.438	8.004E-01	3.75	5.50	7.400	4.802E-01
108581	70445	3.50	4.25	8.563	5.962E-01	4.25	6.50	9.088	1.57E+00
113751	73799	5.00	4.75			7.75	8.25		

Table C-52   Crack growth measurements and crack growth rate data

Test Number	58	Specimen Number	TB 2012050-3	Temperature (°C)			mean **27.05**	stdev **0.33**
		F_{max} (N) =	56381	Humidity (% r.H.)			**33.11**	**1.41**
N (cycles)	N* (cycles)	Back				Front		
		a_{LHS} (mm)	a_{RHS} (mm)	a_{ave} (mm)	da/dN (µm/cycle)	a_{LHS} (mm)	a_{RHS} (mm)	a_{ave} (mm)	da/dN (µm/cycle)
46535	30191					0.50	0.50	3.213	1.863E-01
56876	36900					1.25	1.00	3.713	2.236E-01
62046	40254					1.75	1.25	4.188	3.428E-01
67217	43609					2.25	1.90	4.813	4.024E-01
72387	46963					3.00	2.50	5.425	3.279E-01
77558	50318	1.00	0.50	5.438	5.962E-01	3.50	3.10	6.238	6.409E-01
82728	53672	2.00	1.50	6.563	7.453E-01	4.75	4.00	7.338	6.707E-01
87899	57027	3.25	2.75	7.875	8.198E-01	5.75	5.25	8.525	7.453E-01
93069	60381	4.50	4.25	9.4375	1.043E+00	7.00	6.50	10.150	1.19E+00
98240	63736	6.25	6.00			8.75	8.75		

D *SEM* crack shape data

To support the crack shapes used in calculating accurate stress intensity factors for crack emanating from countersunk holes an extensive scanning electron microscope (*SEM*) investigation of the fracture surface has been performed. Due to the effect of using a marker load spectrum, which allows a fractographic reconstruction of the fracture surface. A complete crack shape and crack growth history can be documented. For this purpose a JEOL JSM-840A scanning electron microscope is used. Figure D-1 shows a detail of the final crack shape obtained for a specimen subject to combined loading. The elliptical crack shape is evolving into a straight through crack due to the increase of the tensile loading in the decreasing net-section. The bending factor k_b decreases and the tensile loading creates a more straight crack front.
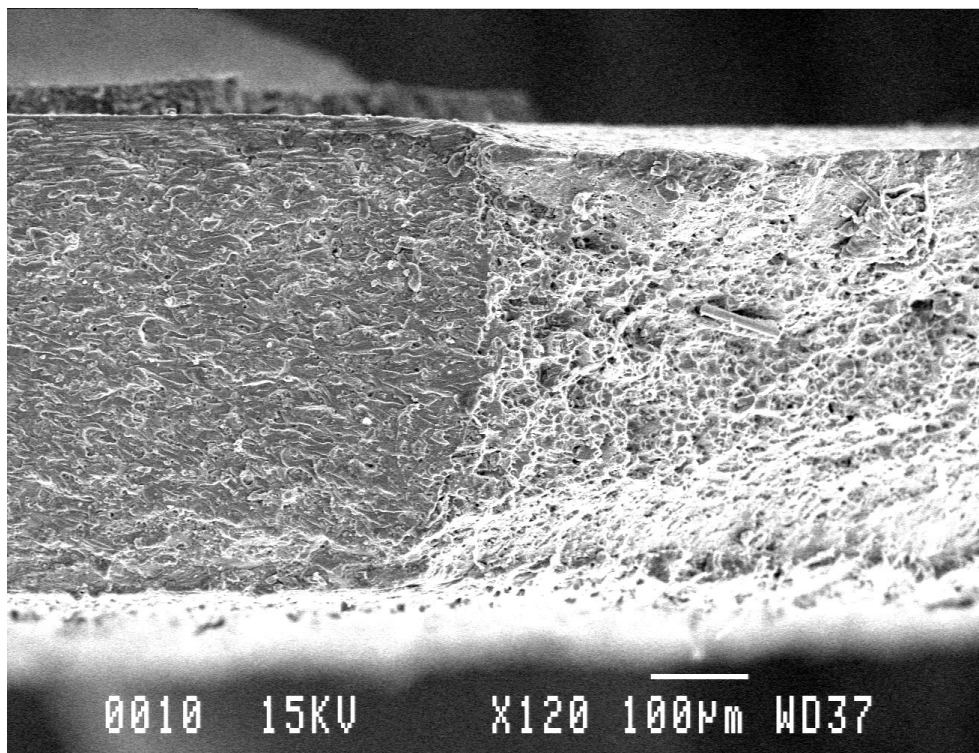
Figure D-1 Aluminum specimen in *SEM*, transition between fatigue area on the left and static failure on the right characterized by necking

The fracture surface can show a variety of features, Figure D-2 shows some striations between the tortuous surface characterized by micro voids and differences in depth on the fracture surface. These 'obstructions' can hide the striations and it can be difficult to locate the continuation of the striations. Mapping these striations through the thickness gives the crack front shape at a certain point in the fatigue life of the specimen by using an elliptical curve fit through these marker load striations.

211
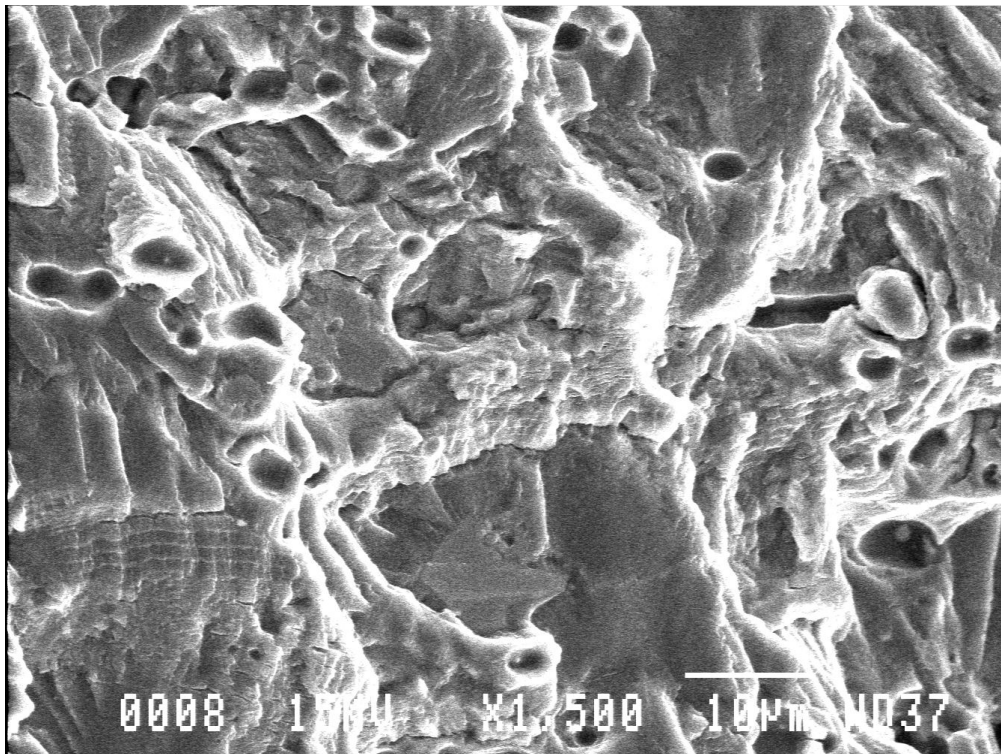
Figure D-2   Striations between micro voids and differences in depth of the fracture surface

The results of the measurements on the fracture surface can be found in Table D-1 to Table D-19 for the open hole specimens subject to tensile loading and in Table D-20 to Table D-45 for specimens subject to combined loading. Specimen specifications can be found in section 5.2.1. Figure D-3 shows the crack shape parameters for the *SEM* crack history reconstruction, cracks where table does not provide a crack length for c_2 is a part-through the thickness crack.
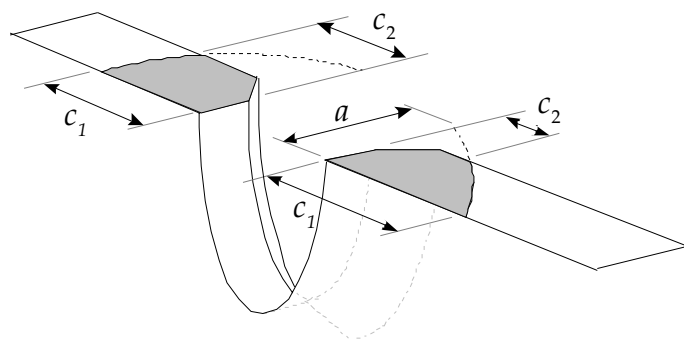
Figure D-3   Crack shape a, c_1 and c_2 definitions for countersunk holes

The results from the fractographic crack shape reconstruction are shown in Figure D-4 to Figure D-41 for the tensile specimens and Figure D-42 to Figure D-92 are the crack shapes for the combined tensions and bending specimens.

D.1 Crack length measurements for all specimens

Table D-1 Crack shape parameters for crack emanating from a countersunk hole subject to tensile loading, with $t = 1.00$ mm, $r/t = 2.40$ and $b/t = 0.05$

Test Number			7		Specimen Number			T 1024005-1	
		left					right		
N (cycles)	a (mm)	c_1 (mm)	c_2 (mm)	a/c_1	N (cycles)	a (mm)	c_1 (mm)	c_2 (mm)	a/c_1
					43862	0.610	0.724		0.843
					47236	0.656	0.850		0.772
					50610	0.823	0.935		0.880
					53984	1.062	1.048	0.353	1.013
					57358	1.281	1.228	0.767	1.043
					60732	1.531	1.485	1.124	1.031
					64106	2.805	1.763	1.647	1.591
67480	0.721	0.462		1.560	67480	3.216	2.112	2.007	1.523
70854	0.664	0.724		0.917	70854	6.326	2.434	2.403	2.599
74228	0.813	0.915		0.889	74228	50.000	2.783	2.782	17.968
77602	0.993	1.173		0.846	77602	50.000	2.877	2.876	17.381
80976	1.687	1.472	1.185	1.146	80976	50.000	3.538	3.537	14.133
84350	2.535	1.960	1.801	1.294	84350	50.000	3.928	3.927	12.729
87724	32.016	2.462	2.461	13.002	87724	50.000	4.458	4.457	11.217
91098	50.000	3.080	3.079	16.235	91098	4.760	5.138	5.024	0.926
94472	11.023	3.875	3.859	2.845	94472	8.865	5.780	5.743	1.534

Table D-2 Crack shape parameters for crack emanating from a countersunk hole subject to tensile loading, with $t = 1.00$ mm, $r/t = 2.40$ and $b/t = 0.05$

Test Number			8		Specimen Number			T 1024005-2	
		left					right		
N (cycles)	a (mm)	c_1 (mm)	c_2 (mm)	a/c_1	N (cycles)	a (mm)	c_1 (mm)	c_2 (mm)	a/c_1
37114	1.524	1.240	0.935	1.229					
40488	1.352	1.529	1.029	0.884					
43862	2.112	1.786	1.573	1.182					
47236	3.600	2.097	2.015	1.717					
50610	4.316	2.446	2.379	1.765					
53984	6.451	2.779	2.746	2.321	53984	0.804	0.896		0.897
57358	50.000	3.149	3.149	15.876	57358	0.996	1.183		0.841
60732	50.000	3.494	3.493	14.310	60732	2.458	1.438	1.314	1.709
64106	50.000	3.893	3.892	12.843	64106	2.319	1.961	1.770	1.182
67480	50.000	4.466	4.465	11.196	67480	50.000	2.413	2.413	20.718
70854	24.413	5.060	5.056	4.824	70854	50.000	3.067	3.066	16.302
74228	6.599	5.774	5.707	1.143	74228	50.000	3.789	3.788	13.196

Table D-3   Crack shape parameters for crack emanating from a countersunk hole subject to tensile loading, with t = 1.00 mm, r/t = 2.40 and b/t = 0.25

Test Number		**11**			Specimen Number			**T 1024025-2**	
	left					right			
N (cycles)	a (mm)	c_1 (mm)	c_2 (mm)	a/c_1	N (cycles)	a (mm)	c_1 (mm)	c_2 (mm)	a/c_1
					47236	50.000	0.704	0.704	71.001
50610	1.067	0.587	0.205	1.818	50610	1.378	0.997	0.686	1.381
53984	1.112	0.792	0.346	1.405	53984	2.445	1.232	1.124	1.985
57358	1.182	1.036	0.552	1.141	57358	3.504	1.569	1.503	2.234
60732	2.101	1.333	1.173	1.576	60732	3.221	1.955	1.858	1.648
64106	2.928	1.717	1.613	1.705	64106	5.405	2.380	2.339	2.271
67480	50.000	2.090	2.090	23.922	67480	9.281	2.763	2.747	3.359
70854	50.000	2.591	2.591	19.296	70854	6.758	3.304	3.267	2.046
74228	3.785	3.194	3.081	1.185	74228	5.140	3.878	3.803	1.326
77602	7.937	3.763	3.733	2.109	77602	5.395	4.511	4.433	1.196
80976	3.520	4.485	4.300	0.785	80976	4.674	5.247	5.125	0.891
84350	7.826	6.015	5.965	1.301	84350	17.122	6.049	6.039	2.830

Table D-4   Crack shape parameters for crack emanating from a countersunk hole subject to tensile loading, with t = 1.00 mm, r/t = 2.40 and b/t = 0.50

Test Number		**13**			Specimen Number			**T 1024050-2**	
	left					right			
N (cycles)	a (mm)	c_1 (mm)	c_2 (mm)	a/c_1	N (cycles)	a (mm)	c_1 (mm)	c_2 (mm)	a/c_1
73788	1.445	1.252	0.903	1.154					
77142					77142	0.744	0.791		0.941
80496	5.877	1.790	1.764	3.284	80496	1.041	0.977	0.271	1.066
83850	3.151	2.138	2.027	1.474	83850	1.510	1.225	0.918	1.233
87204	4.000	2.446	2.368	1.635	87204	1.994	1.585	1.372	1.258
90558	4.247	2.807	2.728	1.513	90558	2.864	1.961	1.837	1.460
93912	7.434	3.146	3.117	2.363	93912	2.782	2.387	2.227	1.166
97266	6.262	3.607	3.561	1.736	97266	3.175	2.845	2.700	1.116
100620	5.160	4.080	4.003	1.265	100620	7.217	3.350	3.317	2.155
103974	5.724	4.589	4.518	1.247	103974	50.000	3.872	3.871	12.912
107328	5.142	5.173	5.074	0.994	107328	5.568	4.518	4.444	1.233

Table D-5 **Crack shape parameters for crack emanating from a countersunk hole subject to tensile loading, with t = 1.00 mm, r/t = 2.40 and b/t = 0.50**

Test Number			**14**		Specimen Number			**T 1024050-3**	
	left					right			
N (cycles)	a (mm)	c_1 (mm)	c_2 (mm)	a/c_1	N (cycles)	a (mm)	c_1 (mm)	c_2 (mm)	a/c_1
60300	0.516	0.385		1.338					
63650	0.668	0.495		1.348					
67000	0.804	0.602		1.337					
70350	0.956	0.737		1.297					
73700	1.193	0.913	0.498	1.306					
77050	1.861	1.139	0.960	1.635					
80400	3.396	1.377	1.316	2.467					
83750	2.511	1.680	1.541	1.494					
87100	50.000	1.875	1.874	26.673	87100	0.744	0.791		0.941
90450	5.556	2.165	2.129	2.567	90450	1.041	0.977	0.271	1.066
93800	50.000	2.413	2.412	20.725	93800	1.510	1.225	0.918	1.233
97150	50.000	2.671	2.670	18.723	97150	1.994	1.585	1.372	1.258
100500	50.000	2.995	2.994	16.695	100500	2.864	1.961	1.837	1.460
103850	50.000	3.321	3.321	15.054	103850	2.782	2.387	2.227	1.166
107200	50.000	3.669	3.669	13.626	107200	3.175	2.845	2.700	1.116
110550	50.000	4.118	4.118	12.141	110550	7.217	3.350	3.317	2.155
113900	50.000	4.523	4.522	11.056	113900	50.000	3.872	3.871	12.912
117250	50.000	4.980	4.979	10.040	117250	5.568	4.518	4.444	1.233

Table D-6 **Crack shape parameters for crack emanating from a countersunk hole subject to tensile loading, with t = 1.60 mm, r/t = 1.50 and b/t = 0.05**

Test Number			**15**		Specimen Number			**T 1615005-1**	
	left					right			
N (cycles)	a (mm)	c_1 (mm)	c_2 (mm)	a/c_1	N (cycles)	a (mm)	c_1 (mm)	c_2 (mm)	a/c_1
					43550	1.247	1.400		0.891
					46900	1.453	1.601		0.907
50250	0.984	1.258		0.782	50250	1.568	1.833		0.856
53600	1.173	1.456		0.805	53600	1.717	2.113	0.767	0.813
56950	1.426	1.699		0.839	56950	2.074	2.385	1.517	0.870
60300	1.698	1.932	0.648	0.879	60300	3.058	2.752	2.345	1.111
63650	1.855	2.324	1.175	0.798	63650	4.567	3.303	3.093	1.383
67000	2.510	2.758	2.125	0.910	67000	50.000	3.872	3.870	12.913
70350	6.087	4.079	3.936	1.492	70350	50.000	4.659	4.656	10.733
73700	6.909	4.991	4.855	1.384	73700	50.000	5.527	5.525	9.046
77050	5.903	6.096	5.868	0.968	77050	50.000	6.517	6.514	7.672
80400	16.255	7.272	7.237	2.235	80400	50.000	7.604	7.601	6.575

Table D-7 **Crack shape parameters for crack emanating from a countersunk hole subject to tensile loading, with t = 1.60 mm, r/t = 1.50 and b/t = 0.05**

Test Number		**16**			Specimen Number			**T 1615005-2**	
	left					right			
N (cycles)	a (mm)	c_1 (mm)	c_2 (mm)	a/c_1	N (cycles)	a (mm)	c_1 (mm)	c_2 (mm)	a/c_1
					30186	0.789	0.838		0.942
33540	0.839	1.101		0.762	33540	50.000	0.947		52.806
36894	1.154	1.324		0.872	36894	1.444	1.147		1.259
40248	1.347	1.566		0.861	40248	1.257	1.440		0.873
43602	1.610	1.832	0.206	0.879	43602	1.411	1.698		0.831
46956	1.944	2.202	1.251	0.883	46956	4.530	2.075	1.942	2.183
50310	2.166	2.846	1.918	0.761	50310	2.170	2.445	1.651	0.888
53664	3.671	3.162	2.845	1.161	53664	2.899	2.877	2.399	1.007
57018	7.500	3.848	3.759	1.949	57018	12.760	3.460	3.433	3.688
60372	8.909	4.688	4.612	1.900	60372	10.004	4.259	4.204	2.349
63726	6.220	5.740	5.546	1.084	63726	50.000	4.619	4.616	10.826
67080	6.908	6.829	6.643	1.012	67080	5.660	6.145	5.895	0.921
70434	10.431	8.244	8.146	1.265	70434	50.000	7.161	7.158	6.982

Table D-8 **Crack shape parameters for crack emanating from a countersunk hole subject to tensile loading, with t = 1.60 mm, r/t = 1.50 and b/t = 0.05**

Test Number		**17**			Specimen Number			**T 1615005-3**	
	left					right			
N (cycles)	a (mm)	c_1 (mm)	c_2 (mm)	a/c_1	N (cycles)	a (mm)	c_1 (mm)	c_2 (mm)	a/c_1
					30186	1.062	0.870		1.221
33540	1.394	1.681		0.829	33540	1.210	1.066		1.135
36894	1.927	1.862	1.038	1.035	36894	1.137	1.367		0.832
40248	1.728	2.210	0.834	0.782	40248	1.290	1.676		0.770
43602	1.887	2.582	1.368	0.731	43602	1.747	1.912	0.767	0.913
46956	2.237	3.024	2.113	0.740	46956	1.996	2.358	1.410	0.846
50310	2.946	3.502	2.941	0.841	50310	2.661	2.870	2.293	0.927
53664	4.105	4.051	3.731	1.013	53664	4.050	3.595	3.302	1.127
57018	8.906	4.737	4.660	1.880	57018	5.850	4.512	4.340	1.296
60372	5.995	5.733	5.525	1.046	60372	5.047	5.630	5.340	0.896
63726	50.000	7.764	7.760	6.440	63726	50.000	6.644	6.641	7.526

Table D-9 Crack shape parameters for crack emanating from a countersunk hole subject to tensile loading, with t = 1.60 mm, $^r/_t$ = 1.50 and $^b/_t$ = 0.25

Test Number		18			Specimen Number			T 1615025-1	
	left					right			
N (cycles)	a (mm)	c_1 (mm)	c_2 (mm)	a/c_1	N (cycles)	a (mm)	c_1 (mm)	c_2 (mm)	a/c_1
					67080	1.828	5.507	2.663	0.332
					70434	2.643	5.644	4.492	0.468
73788	3.261	5.692	4.960	0.573	73788	2.016	5.940	3.614	0.339
77142	2.388	5.972	4.433	0.400	77142	2.633	6.074	4.824	0.433
80496	2.775	6.192	5.059	0.448	80496	3.067	6.323	5.394	0.485
83850	3.420	6.467	5.716	0.529	83850	3.367	6.647	5.849	0.507
87204	3.498	6.940	6.171	0.504	87204	4.431	6.970	6.500	0.636
90558	4.598	7.452	6.986	0.617	90558	6.588	7.464	7.240	0.883
93912	5.220	8.094	7.705	0.645	93912	10.292	8.097	7.999	1.271
97266	13.466	8.781	8.719	1.534	97266	50.000	8.849	8.845	5.650
100620	50.000	9.604	9.599	5.206	100620	50.000	9.638	9.633	5.188
103974	2.004	12.164	7.326	0.165	103974	50.000	10.634	10.629	4.702
107328	50.000	13.342	13.336	3.747	107328	50.000	13.247	13.240	3.775

Table D-10 Crack shape parameters for crack emanating from a countersunk hole subject to tensile loading, with t = 1.60 mm, $^r/_t$ = 1.50 and $^b/_t$ = 0.25

Test Number		19			Specimen Number			T 1615025-2	
	left					right			
N (cycles)	a (mm)	c_1 (mm)	c_2 (mm)	a/c_1	N (cycles)	a (mm)	c_1 (mm)	c_2 (mm)	a/c_1
					53664	0.830	0.422		1.968
					57018	0.891	0.553		1.610
60372	0.472	0.474		0.996	60372	1.329	0.710		1.871
63726	1.028	0.523		1.965	63726	1.260	0.911		1.382
67080	1.016	0.672		1.511	67080	1.316	1.164		1.131
70434	1.241	0.825		1.503	70434	1.638	1.353	0.291	1.211
73788	1.234	1.104		1.117	73788	1.646	1.690	0.398	0.974
77142	1.488	1.338		1.112	77142	1.961	1.986	1.148	0.988
80496	1.660	1.732	0.461	0.959	80496	2.630	2.353	1.867	1.118
83850	1.989	2.202	1.308	0.903	83850	5.595	2.790	2.673	2.006
87204	3.025	2.704	2.295	1.119	87204	5.380	3.452	3.296	1.558
90558	4.964	3.376	3.196	1.470	90558	50.000	4.030	4.028	12.407
93912	4.448	4.276	3.990	1.040	93912	50.000	4.824	4.821	10.365
97266	6.057	5.205	5.020	1.164	97266	50.000	5.674	5.671	8.813
100620	8.730	6.330	6.223	1.379	100620	50.000	6.661	6.657	7.507

Table D-11 Crack shape parameters for crack emanating from a countersunk hole subject to tensile loading, with t = 1.60 mm, r/t = 1.50 and b/t = 0.25

Test Number		20			Specimen Number			T 1615025-3	
	left					right			
N (cycles)	a (mm)	c_1 (mm)	c_2 (mm)	a/c_1	N (cycles)	a (mm)	c_1 (mm)	c_2 (mm)	a/c_1
					36894	0.552	0.575		0.960
					40248	0.930	0.642		1.450
					43602	1.105	0.809		1.366
46956	0.753	0.535		1.408	46956	1.128	1.021		1.105
50310	0.925	0.663		1.396	50310	1.343	1.202		1.117
53664	1.070	0.843		1.269	53664	1.549	1.407		1.102
57018	1.202	1.051		1.143	57018	1.825	1.717	0.825	1.063
60372	1.324	1.336		0.991	60372	2.020	2.075	1.267	0.974
63726	1.576	1.629		0.968	63726	2.689	2.460	1.977	1.093
67080	1.890	1.968	1.048	0.960	67080	4.557	2.855	2.673	1.596
70434	2.460	2.407	1.828	1.022	70434	50.000	3.440	3.438	14.536
73788	6.970	2.922	2.844	2.386	73788	50.000	4.241	4.239	11.790
77142	6.212	3.687	3.562	1.685	77142	5.971	5.168	4.979	1.155
80496	50.000	4.483	4.481	11.153	80496	13.740	6.086	6.045	2.257
83850	50.000	5.552	5.550	9.005	83850	9.806	6.493	6.406	1.510
87204	50.000	6.623	6.619	7.550	87204	10.519	7.201	7.117	1.461

Table D-12 Crack shape parameters for crack emanating from a countersunk hole subject to tensile loading, with t = 1.60 mm, r/t = 1.50 and b/t = 0.50

Test Number		22			Specimen Number			T 1615050-2	
	left					right			
N (cycles)	a (mm)	c_1 (mm)	c_2 (mm)	a/c_1	N (cycles)	a (mm)	c_1 (mm)	c_2 (mm)	a/c_1
					23478	0.864	0.778		1.111
					26832	0.957	1.021		0.937
					30186	1.131	1.134		0.998
					33540	1.354	1.295		1.046
					36894	1.658	1.482	0.388	1.118
					40248	1.918	1.819	1.003	1.055
43602	2.155	0.662	0.444	3.255	43602	2.409	2.135	1.596	1.128
46956	1.994	0.982	0.586	2.030	46956	3.386	2.500	2.204	1.354
50310	1.905	1.454	0.789	1.310	50310	8.511	2.939	2.887	2.896
53664	3.291	1.867	1.632	1.762	53664	6.993	3.461	3.369	2.020
57018	3.955	2.455	2.245	1.611	57018	5.476	4.060	3.883	1.349
60372	7.461	3.099	3.027	2.407	60372	50.000	4.742	4.739	10.544
63726	6.422	3.869	3.747	1.660	63726	11.322	5.476	5.421	2.067
67080	6.362	4.814	4.659	1.322	67080	10.309	6.400	6.323	1.611
70434	9.164	5.876	5.786	1.560	70434	7.561	7.409	7.241	1.021

Table D-13 Crack shape parameters for crack emanating from a countersunk hole subject to tensile loading, with t = 2.00 mm, r/t = 1.20 and b/t = 0.05

Test Number		24			Specimen Number		T 2012005-1		
	left					right			
N (cycles)	a (mm)	c_1 (mm)	c_2 (mm)	a/c_1	N (cycles)	a (mm)	c_1 (mm)	c_2 (mm)	a/c_1
16770	0.767	0.799		0.961					
20124	0.937	0.967		0.969	20124	0.765	0.720		1.062
23478	1.165	1.208		0.965	23478	0.945	0.914		1.035
26832	1.401	1.455		0.963	26832	1.381	1.118		1.235
30186	1.668	1.799		0.927	30186	1.434	1.395		1.028
33540	2.029	2.135	0.357	0.950	33540	1.775	1.706		1.040
36894	2.559	2.528	1.577	1.012	36894	2.126	2.106	0.713	1.009
40248	2.730	3.052	2.078	0.895	40248	2.473	2.566	1.509	0.964
43602	4.045	3.643	3.167	1.110	43602	3.051	3.154	2.382	0.967
46956	7.627	4.437	4.282	1.719	46956	12.628	3.797	3.750	3.325
50310	5.559	5.579	5.206	0.996	50310	4.897	4.925	4.496	0.994
53664	10.526	6.741	6.618	1.561					

Table D-14 Crack shape parameters for crack emanating from a countersunk hole subject to tensile loading, with t = 2.00 mm, r/t = 1.20 and b/t = 0.05

Test Number		25			Specimen Number		T 2012005-2		
	left					right			
N (cycles)	a (mm)	c_1 (mm)	c_2 (mm)	a/c_1	N (cycles)	a (mm)	c_1 (mm)	c_2 (mm)	a/c_1
16770	0.406	0.502		0.809					
20124	0.690	0.652		1.059					
23478	0.899	0.852		1.056					
26832	1.506	1.044		1.442	26832	0.939	1.022		0.920
30186	1.560	1.314		1.188	30186	1.343	1.212		1.108
33540	1.807	1.686		1.072	33540	1.526	1.511		1.010
36894	2.051	2.107	0.466	0.973	36894	1.655	1.910		0.867
40248	2.311	2.633	1.319	0.878	40248	1.898	2.277		0.834
43602	3.133	3.174	2.443	0.987	43602	2.351	2.665	1.400	0.882
46956	4.549	3.928	3.528	1.158	46956	2.737	3.139	2.143	0.872
50310	5.970	4.859	4.578	1.229	50310	3.922	3.664	3.152	1.070
53664	4.961	6.066	5.552	0.818	53664	50.000	4.295	4.292	11.641
57018	8.371	7.472	7.255	1.120	57018	14.227	7.846	7.768	1.813

Table D-15 Crack shape parameters for crack emanating from a countersunk hole subject to tensile loading, with t = 2.00 mm, $^r/_t$ = 1.20 and $^b/_t$ = 0.25

Test Number		27			Specimen Number		T 2012025-1		
	left					right			
N (cycles)	a (mm)	c_1 (mm)	c_2 (mm)	a/c_1	N (cycles)	a (mm)	c_1 (mm)	c_2 (mm)	a/c_1
16770	0.876	0.943		0.928					
20124	50.000	1.090		45.882					
23478	1.449	1.457		0.994					
26832	1.926	1.744		1.104					
30186	2.099	2.079	0.631	1.010					
33540	2.201	2.490	1.039	0.884					
36894	2.405	2.938	1.631	0.818					
40248	3.146	3.377	2.606	0.932					
43602	7.470	3.767	3.629	1.983					
46956	50.000	4.359	4.355	11.471					
50310	2.761	5.323	3.669	0.519	50310	50.000	0.418		119.530
53664	15.389	5.707	5.659	2.696	53664	1.144	0.940		1.217
57018	50.000	6.422	6.417	7.786	57018	2.522	1.438	0.876	1.754
60372	2.348	7.765	4.067	0.302	60372	2.475	2.178	1.283	1.136
63726	50.000	8.110	8.103	6.165	63726	3.638	3.057	2.553	1.190
67080	50.000	8.877	8.870	5.633	67080	50.000	4.271	4.268	11.707
70434	50.000	10.480	10.472	4.771	70434	9.183	4.848	4.731	1.894

Table D-16 Crack shape parameters for crack emanating from a countersunk hole subject to tensile loading, with t = 2.00 mm, $^r/_t$ = 1.20 and $^b/_t$ = 0.25

Test Number		28			Specimen Number		T 2012025-2		
	left					right			
N (cycles)	a (mm)	c_1 (mm)	c_2 (mm)	a/c_1	N (cycles)	a (mm)	c_1 (mm)	c_2 (mm)	a/c_1
					46956	50.000	0.807	0.806	61.994
					50310	50.000	0.706	0.705	70.847
					53664	50.000	0.887	0.887	56.341
					57018	50.000	1.056	1.055	47.350
					60372	50.000	1.294	1.293	38.645
					63726	50.000	1.316	1.315	38.000
					67080	50.000	1.457	1.456	34.309
					70434	50.000	1.714	1.712	29.176
73788	0.739	0.745		0.993	73788	50.000	1.992	1.990	25.106
77142	1.493	1.107		1.349	77142	50.000	2.446	2.444	20.440
80496	2.130	1.633	0.562	1.305	80496	50.000	2.482	2.480	20.147
83850	2.547	2.305	1.427	1.105	83850	12.464	5.786	5.711	2.154
87204	2.976	3.170	2.347	0.939	87204	50.000	6.438	6.433	7.766
90558	4.012	4.365	3.784	0.919	90558	50.000	7.245	7.239	6.901
93912	2.908	4.733	3.436	0.614	93912	50.000	7.964	7.957	6.279
97266	10.833	5.859	5.759	1.849	97266	10.665	10.913	10.720	0.977

Table D-17 Crack shape parameters for crack emanating from a countersunk hole subject to tensile loading, with t = 2.00 mm, r/t = 1.20 and b/t = 0.25

Test Number		29			Specimen Number		T 2012025-3		
	left					right			
N (cycles)	a (mm)	c_1 (mm)	c_2 (mm)	a/c_1	N (cycles)	a (mm)	c_1 (mm)	c_2 (mm)	a/c_1
					57018	0.321	0.632		0.509
					60372	50.000	0.551		90.821
					63726	1.407	0.752		1.871
67080	1.077	0.767		1.405	67080	1.344	0.988		1.360
70434	1.154	1.017		1.135	70434	1.458	1.294		1.127
73788	1.610	1.265		1.273	73788	1.647	1.627		1.012
77142	1.613	1.595		1.011	77142	2.263	1.882	0.881	1.203
80496	2.018	1.926	0.260	1.048	80496	2.157	2.339	0.877	0.922
83850	2.299	2.393	1.180	0.960	83850	2.626	2.758	1.787	0.952
87204	2.438	3.067	1.753	0.795	87204	3.252	3.213	2.534	1.012
90558	3.961	3.566	3.078	1.111	90558	3.767	3.902	3.306	0.965
93912	4.274	4.431	3.916	0.964	93912	8.709	4.486	4.366	1.941
97266	6.081	5.489	5.184	1.108	97266	7.631	5.396	5.207	1.414
100620	50.000	6.774	6.768	7.382	100620	69.737	7.798	7.795	8.942

Table D-18 Crack shape parameters for crack emanating from a countersunk hole subject to tensile loading, with t = 2.00 mm, r/t = 1.20 and b/t = 0.50

Test Number		30			Specimen Number		T 2012050-1		
	left					right			
N (cycles)	a (mm)	c_1 (mm)	c_2 (mm)	a/c_1	N (cycles)	a (mm)	c_1 (mm)	c_2 (mm)	a/c_1
					124098	1.188	1.024		1.161
					127452	1.335	1.225		1.089
					130806	1.670	1.432		1.166
					134160	1.915	1.704		1.124
					137514	2.212	2.030	0.867	1.089
					140868	2.786	2.325	1.619	1.198
					144222	2.290	2.925	1.424	0.783
					147576	3.432	3.191	2.593	1.076
					150930	6.615	3.482	3.319	1.900
					154284	11.048	3.977	3.911	2.778
					157638	50.000	4.234	4.230	11.810
160992	0.923	1.031		0.896	160992	50.000	5.030	5.026	9.941
164346	1.482	1.438		1.030	164346	16.098	5.613	5.569	2.868
167700	1.984	2.043		0.971	167700	50.000	5.742	5.737	8.708
171054	3.263	2.783	2.199	1.173	171054	23.753	7.034	7.009	3.377
174408	4.356	3.702	3.289	1.177	174408	13.281	8.186	8.093	1.622

Table D-19 Crack shape parameters for crack emanating from a countersunk hole subject to tensile loading, with t = 2.00 mm, $^r/_t$ = 1.20 and $^b/_t$ = 0.50

Test Number			32		Specimen Number			T 2012050-3	
		left					right		
N (cycles)	a (mm)	c_1 (mm)	c_2 (mm)	a/c_1	N (cycles)	a (mm)	c_1 (mm)	c_2 (mm)	a/c_1
46956	1.450	1.011		1.434					
50310	4.608	1.208		3.815	50310	0.834	1.330		0.627
53664	1.768	1.589		1.113	53664	1.301	1.003		1.297
57018	2.239	1.881	0.846	1.190	57018	1.604	1.262		1.271
60372	2.901	2.239	1.622	1.296	60372	1.950	1.688		1.156
63726	3.544	2.702	2.231	1.312	63726	2.439	2.177	1.246	1.120
67080	5.199	3.276	3.024	1.587	67080	4.163	2.633	2.309	1.582
70434	50.000	3.897	3.894	12.829	70434	5.193	3.374	3.113	1.539
73788	19.412	4.733	4.708	4.101	73788	10.779	3.352	3.294	3.215
77142	11.745	5.786	5.702	2.030	77142	50.000	4.098	4.095	12.200
80496	50.000	6.147	6.142	8.134	80496	50.000	5.092	5.088	9.818
83850	7.026	7.033	6.742	0.999	83850	13.513	6.376	6.306	2.119
87204	26.575	8.511	8.487	3.122	87204	11.344	7.940	7.816	1.429

Table D-20 Crack shape parameters for crack emanating from a countersunk hole subject to combined loading, with t = 1.00 mm, $^r/_t$ = 2.40 and $^b/_t$ = 0.05

Test Number			33		Specimen Number			TB 1024005-1	
		left					right		
N (cycles)	a (mm)	c_1 (mm)	c_2 (mm)	a/c_1	N (cycles)	a (mm)	c_1 (mm)	c_2 (mm)	a/c_1
13416	0.517	0.841		0.614					
16770	0.648	1.091		0.595	16770	0.675	0.922		0.732
20124	0.861	1.402		0.614	20124	0.917	1.052		0.871
23478	0.980	1.527		0.642	23478	1.077	1.367	0.506	0.788
26832	1.086	1.645	0.641	0.660	26832	1.340	1.770	1.179	0.757
30186	1.401	1.798	1.259	0.779	30186	1.767	2.219	1.830	0.796
33540	1.705	2.266	1.836	0.753	33540	1.783	2.715	2.247	0.657
36894	1.979	2.800	2.416	0.707	36894	1.944	3.283	2.815	0.592
40248	2.055	3.422	2.989	0.601	40248	2.571	3.820	3.519	0.673
43602	1.993	4.053	3.506	0.492	43602	3.328	4.456	4.250	0.747
46956	2.534	4.797	4.408	0.528	46956	2.893	5.175	4.856	0.559
50310	3.106	5.545	5.250	0.560	50310	3.034	5.930	5.598	0.512
53664	2.767	6.437	6.002	0.430	53664	2.996	6.851	6.458	0.437

Table D-21 Crack shape parameters for crack emanating from a countersunk hole subject to combined loading, with $t = 1.00$ mm, $^r/_t = 2.40$ and $^b/_t = 0.05$

Test Number		34			Specimen Number			TB 1024005-2	
		left					right		
N (cycles)	a (mm)	c_1 (mm)	c_2 (mm)	a/c_1	N (cycles)	a (mm)	c_1 (mm)	c_2 (mm)	a/c_1
					20124	0.549	0.694		0.791
23478	0.976	0.872		1.119	23478	0.767	0.768		0.998
26832	0.915	1.112		0.822	26832	0.848	0.985		0.861
30186	1.158	1.352	0.682	0.857	30186	1.098	1.254	0.519	0.876
33540	1.419	1.692	1.200	0.838	33540	1.579	1.577	1.220	1.001
36894	1.656	2.101	1.675	0.788	36894	1.475	1.785	1.312	0.826
40248	2.075	2.571	2.253	0.807	40248	1.586	2.082	1.617	0.762
43602	2.169	3.105	2.755	0.699	43602	2.453	2.479	2.263	0.990
46956	2.262	3.644	3.268	0.621	46956	2.480	3.034	2.776	0.817
50310	2.363	4.257	3.857	0.555	50310	2.686	3.603	3.344	0.745
53664	2.802	4.898	4.576	0.572	53664	2.531	4.236	3.891	0.598
57018	3.011	5.619	5.300	0.536	57018	3.244	4.945	4.704	0.656
60372	3.448	6.379	6.105	0.541	60372	3.240	5.739	5.459	0.565

Table D-22 Crack shape parameters for crack emanating from a countersunk hole subject to combined loading, with $t = 1.00$ mm, $^r/_t = 2.40$ and $^b/_t = 0.05$

Test Number		35			Specimen Number			TB 1024005-3	
		left					right		
N (cycles)	a (mm)	c_1 (mm)	c_2 (mm)	a/c_1	N (cycles)	a (mm)	c_1 (mm)	c_2 (mm)	a/c_1
					13416	0.377	0.412		0.915
16770	0.445	0.559		0.796	16770	0.533	0.649		0.820
20124	0.693	0.784		0.884	20124	0.681	0.787		0.865
23478	0.850	1.006		0.845	23478	0.888	0.969		0.916
26832	1.020	1.283	0.252	0.795	26832	1.026	1.251	0.281	0.821
30186	1.295	1.625	1.033	0.797	30186	1.228	1.577	0.916	0.779
33540	1.611	2.065	1.619	0.780	33540	1.563	2.017	1.550	0.775
36894	1.798	2.571	2.137	0.699	36894	1.982	2.519	2.175	0.787
40248	1.966	3.083	2.654	0.638	40248	1.976	3.129	2.698	0.632
43602	2.107	3.659	3.220	0.576	43602	2.225	3.780	3.377	0.589
46956	2.163	4.405	3.906	0.491	46956	2.361	4.512	4.087	0.523
50310	2.353	5.190	4.698	0.453	50310	2.986	5.296	4.990	0.564
53664	2.472	6.069	5.550	0.407	53664	2.855	6.213	5.819	0.459
57018	2.882	7.010	6.575	0.411	57018	3.327	7.239	6.904	0.460

Table D-23 Crack shape parameters for crack emanating from a countersunk hole subject to combined loading, with t = 1.00 mm, $^r/_t$ = 2.40 and $^b/_t$ = 0.25

Test Number		36			Specimen Number			TB 1024025-1	
	left					right			
N (cycles)	a (mm)	c_1 (mm)	c_2 (mm)	a/c_1	N (cycles)	a (mm)	c_1 (mm)	c_2 (mm)	a/c_1
33540	0.523	0.563		0.929					
36894	0.724	0.741		0.976	36894	0.985	0.814		1.210
40248	1.053	1.189	0.372	0.885	40248	1.038	1.046	0.281	0.992
43602	1.228	1.516	0.880	0.810	43602	1.230	1.353	0.787	0.909
46956	1.623	1.915	1.509	0.847	46956	1.511	1.766	1.324	0.856
50310	1.981	2.327	2.009	0.851	50310	1.885	2.232	1.892	0.845
53664	2.220	2.818	2.516	0.788	53664	2.391	2.680	2.434	0.892
57018	2.161	3.378	2.994	0.640	57018	2.657	3.182	2.948	0.835
60372	2.365	3.962	3.591	0.597	60372	3.254	3.799	3.615	0.857
63726	2.506	4.630	4.245	0.541	63726	3.418	4.436	4.242	0.770
67080	2.875	5.393	5.057	0.533	67080	2.704	5.175	4.809	0.522
70434	2.941	6.197	5.828	0.475	70434	2.850	5.929	5.553	0.481
73788	3.796	7.071	6.821	0.537	73788	5.263	6.581	6.461	0.800

Table D-24 Crack shape parameters for crack emanating from a countersunk hole subject to combined loading, with t = 1.00 mm, $^r/_t$ = 2.40 and $^b/_t$ = 0.25

Test Number		37			Specimen Number			TB 1024025-2	
	left					right			
N (cycles)	a (mm)	c_1 (mm)	c_2 (mm)	a/c_1	N (cycles)	a (mm)	c_1 (mm)	c_2 (mm)	a/c_1
30186	0.628	0.290		2.165					
33540	0.925	0.706		1.310					
36894	1.125	0.993	0.455	1.133					
40248	1.433	1.307	0.936	1.096	40248	0.459	0.218		2.105
43602	1.995	1.650	1.428	1.209	43602	0.621	0.430		1.446
46956	2.160	2.047	1.814	1.055	46956	0.792	0.745		1.063
50310	2.055	2.539	2.219	0.809	50310	1.042	1.110	0.310	0.938
53664	2.310	2.999	2.704	0.770	53664	1.615	1.460	1.146	1.106
57018	2.610	3.535	3.266	0.738	57018	1.944	1.981	1.699	0.981
60372	2.604	3.535	3.264	0.737	60372	2.264	2.495	2.238	0.907
63726	2.605	4.140	3.822	0.629	63726	2.309	3.075	2.771	0.751
67080	2.832	4.797	4.488	0.590	67080	2.178	3.808	3.383	0.572
70434	3.408	5.501	5.259	0.620	70434	4.127	4.483	4.350	0.921
73788	3.695	6.274	6.039	0.589	73788	4.115	5.249	5.092	0.784
77142	3.391	7.106	6.790	0.477	77142	3.080	6.163	5.829	0.500

Table D-25 Crack shape parameters for crack emanating from a countersunk hole subject to combined loading, with t = 1.00 mm, $^r/_t$ = 2.40 and $^b/_t$ = 0.50

Test Number		38			Specimen Number			TB 1024050-1	
	left					right			
N (cycles)	a (mm)	c_1 (mm)	c_2 (mm)	a/c_1	N (cycles)	a (mm)	c_1 (mm)	c_2 (mm)	a/c_1
33540	0.387	0.390		0.993	33540	0.481	0.459		1.049
36894	0.505	0.517		0.977	36894	0.646	0.577		1.119
40248	0.713	0.625		1.141	40248	0.769	0.787		0.977
43602	1.085	0.761	0.296	1.427	43602	0.978	1.090		0.898
46956	1.112	1.194	0.522	0.931	46956	1.401	1.384	0.969	1.012
50310	1.420	1.642	1.166	0.865	50310	1.580	1.807	1.399	0.874
53664	1.792	2.121	1.760	0.845	53664	2.178	2.262	2.009	0.963
57018	1.999	2.632	2.279	0.759	57018	2.195	2.746	2.445	0.800
60372	2.534	3.200	2.940	0.792	60372	2.428	3.308	3.014	0.734
63726	2.151	3.878	3.433	0.555	63726	2.061	4.023	3.517	0.512
67080	2.080	4.673	4.098	0.445	67080	2.460	4.666	4.263	0.527
70434	3.027	5.424	5.119	0.558	70434	2.540	5.452	5.012	0.466
73788	2.874	6.209	5.821	0.463	73788	3.179	6.160	5.847	0.516

Table D-26 Crack shape parameters for crack emanating from a countersunk hole subject to combined loading, with t = 1.00 mm, $^r/_t$ = 2.40 and $^b/_t$ = 0.50

Test Number		39			Specimen Number			TB 1024050-2	
	left					right			
N (cycles)	a (mm)	c_1 (mm)	c_2 (mm)	a/c_1	N (cycles)	a (mm)	c_1 (mm)	c_2 (mm)	a/c_1
30186	0.477	0.426		1.121					
33540	0.574	0.489		1.174					
36894	0.618	0.670		0.923					
40248	0.802	0.856		0.938					
43602	1.006	1.083	0.118	0.929					
46956	1.305	1.377	0.884	0.948	46956	1.016	0.939	0.167	1.082
50310	1.784	1.744	1.444	1.023	50310	1.436	1.269	0.911	1.131
53664	1.742	2.166	1.774	0.804	53664	1.846	1.661	1.396	1.111
57018	2.111	2.583	2.275	0.817	57018	1.959	2.126	1.828	0.922
60372	2.122	3.069	2.707	0.692	60372	2.022	2.586	2.247	0.782
63726	2.185	3.593	3.195	0.608	63726	2.167	3.128	2.775	0.693
67080	2.150	4.171	3.692	0.515	67080	2.610	3.652	3.373	0.715
70434	2.398	4.827	4.388	0.497	70434	2.645	4.257	3.941	0.621
73788	2.564	5.544	5.105	0.462	73788	3.069	4.938	4.669	0.621
77142	3.523	6.291	6.032	0.560	77142	3.542	5.660	5.430	0.626
80496	3.017	7.166	6.761	0.421	80496	3.007	6.525	6.154	0.461

Table D-27 **Crack shape parameters for crack emanating from a countersunk hole subject to combined loading, with** t **= 1.00 mm,** $^r/_t$ **= 2.40 and** $^b/_t$ **= 0.50**

Test Number		40			Specimen Number		TB 1024050-3		
		left					right		
N (cycles)	a (mm)	c_1 (mm)	c_2 (mm)	a/c_1	N (cycles)	a (mm)	c_1 (mm)	c_2 (mm)	a/c_1
13416	0.456	0.491		0.927					
16770	0.553	0.646		0.855	16770	0.481	0.459		1.049
20124	0.741	0.847		0.874	20124	0.646	0.577		1.119
23478	0.898	1.152		0.780	23478	0.769	0.787		0.977
26832	1.250	1.425	0.856	0.877	26832	0.978	1.090		0.898
30186	1.563	1.780	1.368	0.878	30186	1.401	1.384	0.969	1.012
33540	1.637	2.258	1.787	0.725	33540	1.580	1.807	1.399	0.874
36894	1.898	2.683	2.281	0.707	36894	2.178	2.262	2.009	0.963
40248	1.924	3.211	2.743	0.599	40248	2.195	2.746	2.445	0.800
43602	1.995	3.788	3.278	0.527	43602	2.428	3.308	3.014	0.734
46956	2.337	4.417	3.992	0.529	46956	2.061	4.023	3.517	0.512
50310	2.232	5.109	4.568	0.437	50310	2.460	4.666	4.263	0.527
53664	2.636	5.866	5.427	0.449	53664	2.540	5.452	5.012	0.466
57018	3.209	6.610	6.280	0.485	57018	3.179	6.160	5.847	0.516

Table D-28 **Crack shape parameters for crack emanating from a countersunk hole subject to combined loading, with** t **= 1.60 mm,** $^r/_t$ **= 1.50 and** $^b/_t$ **= 0.05**

Test Number		41			Specimen Number		TB 1615005-1		
		left					right		
N (cycles)	a (mm)	c_1 (mm)	c_2 (mm)	a/c_1	N (cycles)	a (mm)	c_1 (mm)	c_2 (mm)	a/c_1
					10062	0.249	0.559		0.445
					13416	0.724	0.699		1.036
16770	0.223	0.830		0.269	16770	0.860	0.879		0.978
20124	0.862	0.879		0.981	20124	1.059	1.116		0.949
23478	1.154	1.321		0.873	23478	1.196	1.412		0.847
26832	1.691	1.584		1.067	26832	1.488	1.737		0.856
30186	1.585	2.075		0.764	30186	1.601	2.152	0.088	0.744
33540	1.954	2.573	1.477	0.759	33540	2.142	2.539	1.688	0.844
36894	2.448	3.156	2.388	0.776	36894	2.326	3.157	2.291	0.737
40248	2.669	3.972	3.179	0.672	40248	2.990	3.851	3.253	0.776
43602	3.374	4.713	4.150	0.716	43602	3.411	4.610	4.071	0.740
46956	4.025	5.566	5.107	0.723	46956	3.644	5.493	4.935	0.663
50310	4.592	6.554	6.143	0.701	50310	3.937	6.474	5.915	0.608
53664	4.038	7.652	7.026	0.528	53664	3.762	7.636	6.910	0.493

Table D-29 Crack shape parameters for crack emanating from a countersunk hole subject to combined loading, with t = 1.60 mm, $^r/_t$ = 1.50 and $^b/_t$ = 0.05

Test Number		42			Specimen Number		TB 1615005-2		
	left					right			
N (cycles)	a (mm)	c_1 (mm)	c_2 (mm)	a/c_1	N (cycles)	a (mm)	c_1 (mm)	c_2 (mm)	a/c_1
					20124	0.960	0.995		0.966
23478	0.677	0.917		0.738	23478	1.119	1.240		0.903
26832	0.789	1.173		0.673	26832	1.336	1.514		0.882
30186	1.164	1.626		0.716	30186	1.547	1.840		0.840
33540	1.312	1.887		0.695	33540	1.811	2.222	1.041	0.815
36894	1.678	2.370	0.714	0.708	36894	2.241	2.667	1.868	0.840
40248	2.140	2.886	1.917	0.741	40248	2.657	3.232	2.580	0.822
43602	2.387	3.581	2.657	0.666	43602	3.354	3.939	3.462	0.851
46956	2.707	4.365	3.521	0.620	46956	4.115	4.671	4.304	0.881
50310	2.939	5.235	4.392	0.561	50310	4.261	5.523	5.119	0.772
53664	3.540	6.197	5.528	0.571	53664	3.449	6.423	5.690	0.537

Table D-30 Crack shape parameters for crack emanating from a countersunk hole subject to combined loading, with t = 1.60 mm, $^r/_t$ = 1.50 and $^b/_t$ = 0.05

Test Number		43			Specimen Number		TB 1615005-3		
	left					right			
N (cycles)	a (mm)	c_1 (mm)	c_2 (mm)	a/c_1	N (cycles)	a (mm)	c_1 (mm)	c_2 (mm)	a/c_1
					13416	0.601	0.675		0.890
					16770	1.058	0.772		1.370
					20124	0.822	0.928		0.886
23478	0.555	0.725		0.766	23478	0.742	1.123		0.660
26832	0.911	1.154		0.789	26832	1.415	1.322		1.070
30186	1.206	1.488		0.810	30186	1.643	1.658	0.376	0.991
33540	1.494	1.712		0.872	33540	1.702	2.123	0.722	0.802
36894	1.331	2.491		0.534	36894	2.077	2.559	1.631	0.812
40248	2.099	2.658	1.720	0.790	40248	2.520	3.119	2.409	0.808
43602	2.831	3.275	2.702	0.864	43602	3.159	3.834	3.306	0.824
46956	3.395	4.057	3.578	0.837	46956	5.839	4.436	4.266	1.316
50310	3.636	4.900	4.400	0.742	50310	4.198	5.378	4.972	0.781
53664	3.124	5.896	5.064	0.530	53664	4.610	6.327	5.933	0.729
57018	3.773	6.698	6.066	0.563	57018	4.389	7.283	6.782	0.603

Table D-31 Crack shape parameters for crack emanating from a countersunk hole subject to combined loading, with t = 1.60 mm, $^r/_t$ = 1.50 and $^b/_t$ = 0.25

Test Number		44			Specimen Number		TB 1615025-1		
	left					right			
N (cycles)	a (mm)	c_1 (mm)	c_2 (mm)	a/c_1	N (cycles)	a (mm)	c_1 (mm)	c_2 (mm)	a/c_1
23478	0.901	0.630		1.430					
26832	0.907	0.876		1.036					
30186	1.035	1.168		0.886	30186	1.349	1.111		1.214
33540	1.263	1.427		0.885	33540	1.294	1.455		0.890
36894	1.589	1.840		0.864	36894	1.506	1.783		0.845
40248	1.815	2.301	1.086	0.789	40248	2.051	2.140	1.339	0.958
43602	2.264	2.801	1.982	0.808	43602	2.588	2.640	2.075	0.980
46956	2.596	3.482	2.743	0.746	46956	3.444	3.195	2.829	1.078
50310	3.078	4.185	3.575	0.736	50310	3.656	3.962	3.562	0.923
53664	3.278	5.011	4.373	0.654	53664	3.819	4.734	4.298	0.807
57018	3.218	6.019	5.223	0.535	57018	3.592	5.613	5.026	0.640
60372	4.103	6.942	6.393	0.591	60372	4.325	6.421	5.966	0.674

Table D-32 Crack shape parameters for crack emanating from a countersunk hole subject to combined loading, with t = 1.60 mm, $^r/_t$ = 1.50 and $^b/_t$ = 0.25

Test Number		45			Specimen Number		TB 1615025-2		
	left					right			
N (cycles)	a (mm)	c_1 (mm)	c_2 (mm)	a/c_1	N (cycles)	a (mm)	c_1 (mm)	c_2 (mm)	a/c_1
20124	0.718	0.824		0.872					
23478	0.932	1.051		0.887					
26832	0.918	1.366		0.672	26832	0.536	0.739		0.725
30186	1.470	1.601		0.918	30186	0.983	0.986		0.997
33540	1.663	2.066	0.564	0.805	33540	1.283	1.301		0.986
36894	2.069	2.392	1.517	0.865	36894	1.427	1.709		0.835
40248	2.348	2.981	2.182	0.788	40248	1.769	2.160	0.921	0.819
43602	3.088	3.498	2.992	0.883	43602	2.339	2.727	1.990	0.858
46956	3.259	4.191	3.651	0.778	46956	2.987	3.408	2.878	0.876
50310	3.228	4.984	4.329	0.648	50310	3.866	4.168	3.794	0.927
53664	3.579	5.858	5.240	0.611	53664	6.031	4.971	4.793	1.213
57018	3.749	6.763	6.116	0.554	57018	3.745	6.025	5.447	0.622

Table D-33 **Crack shape parameters for crack emanating from a countersunk hole subject to combined loading, with t = 1.60 mm, r/t = 1.50 and b/t = 0.25**

Test Number		46			Specimen Number		TB 1615025-3		
		left					right		
N (cycles)	a (mm)	c_1 (mm)	c_2 (mm)	a/c_1	N (cycles)	a (mm)	c_1 (mm)	c_2 (mm)	a/c_1
					16770	0.403	0.574		0.702
					20124	0.815	0.776		1.050
23478	1.008	1.229		0.821	23478	1.097	1.016		1.080
26832	1.338	1.522		0.880	26832	1.167	1.353		0.863
30186	3.149	1.738	1.497	1.811	30186	1.675	1.672	0.495	1.002
33540	1.743	2.376	0.941	0.733	33540	1.789	2.131	0.954	0.840
36894	2.143	2.888	1.921	0.742	36894	2.172	2.651	1.793	0.819
40248	2.814	3.517	2.893	0.800	40248	2.744	3.344	2.717	0.821
43602	3.109	4.263	3.655	0.729	43602	3.175	4.055	3.503	0.783
46956	3.137	5.132	4.414	0.611	46956	3.602	4.868	4.361	0.740
50310	3.026	6.119	5.193	0.494	50310	4.458	5.684	5.306	0.784
53664	3.476	7.030	6.241	0.494	53664	4.781	6.681	6.296	0.716
57018	3.465	8.097	7.182	0.428	57018	4.090	7.818	7.195	0.523

Table D-34 **Crack shape parameters for crack emanating from a countersunk hole subject to combined loading, with t = 1.60 mm, r/t = 1.50 and b/t = 0.50**

Test Number		47			Specimen Number		TB 1615050-1		
		left					right		
N (cycles)	a (mm)	c_1 (mm)	c_2 (mm)	a/c_1	N (cycles)	a (mm)	c_1 (mm)	c_2 (mm)	a/c_1
					30186	0.591	0.584		1.013
					33540	1.165	0.874		1.333
36894	0.691	0.807		0.857	36894	1.080	1.199		0.901
40248	1.264	0.995		1.270	40248	1.323	1.548		0.855
43602	1.283	1.302		0.986	43602	1.798	1.965	0.897	0.915
46956	3.184	1.650	1.426	1.930	46956	2.273	2.468	1.753	0.921
50310	2.177	2.681	1.818	0.812	50310	3.025	3.081	2.615	0.982
53664	2.558	3.314	2.585	0.772	53664	3.379	3.318	2.922	1.018
57018	2.793	4.012	3.289	0.696	57018	4.102	3.772	3.473	1.087
60372	3.287	4.765	4.163	0.690	60372	3.776	4.573	4.142	0.826
63726	3.308	5.698	4.987	0.581	63726	3.958	5.428	4.965	0.729
67080	3.301	6.641	5.808	0.497	67080	3.937	6.301	5.757	0.625

Table D-35 Crack shape parameters for crack emanating from a countersunk hole subject to combined loading, with t = 1.60 mm, $^r/_t$ = 1.50 and $^b/_t$ = 0.50

Test Number		48			Specimen Number		TB 1615050-2		
		left					right		
N (cycles)	a (mm)	c_1 (mm)	c_2 (mm)	a/c_1	N (cycles)	a (mm)	c_1 (mm)	c_2 (mm)	a/c_1
					30186	0.706	0.570		1.238
33540	0.534	0.544		0.982	33540	0.854	0.794		1.075
36894	0.797	0.748		1.066	36894	1.127	1.042		1.082
40248	0.960	1.032		0.930	40248	1.527	1.416		1.078
43602	1.231	1.318		0.933	43602	1.677	1.866	0.558	0.899
46956	1.517	1.749		0.867	46956	2.085	2.299	1.474	0.907
50310	1.942	2.265	1.284	0.857	50310	2.695	2.874	2.313	0.938
53664	2.600	2.905	2.290	0.895	53664	3.603	3.514	3.149	1.025
57018	2.959	3.705	3.117	0.799	57018	3.711	4.251	3.836	0.873
60372	3.817	4.466	4.054	0.855	60372	4.159	5.032	4.645	0.826
63726	3.336	5.441	4.774	0.613	63726	7.723	5.879	5.751	1.314

Table D-36 Crack shape parameters for crack emanating from a countersunk hole subject to combined loading, with t = 1.60 mm, $^r/_t$ = 1.50 and $^b/_t$ = 0.50

Test Number		49			Specimen Number		TB 1615050-3		
		left					right		
N (cycles)	a (mm)	c_1 (mm)	c_2 (mm)	a/c_1	N (cycles)	a (mm)	c_1 (mm)	c_2 (mm)	a/c_1
					30186	0.854	0.647		1.319
33540	0.714	0.610		1.172	33540	0.856	0.883		0.970
36894	1.419	0.748		1.898	36894	1.535	1.078		1.424
40248	1.191	1.153		1.032	40248	1.453	1.477		0.984
43602	1.461	1.486		0.983	43602	1.676	1.850	0.551	0.906
46956	1.886	2.147	1.137	0.878	46956	1.973	2.312	1.353	0.854
50310	2.064	2.434	1.538	0.848	50310	2.553	2.856	2.226	0.894
53664	2.784	3.038	2.486	0.916	53664	2.977	3.537	2.983	0.842
57018	3.418	3.718	3.286	0.919	57018	4.059	4.097	3.765	0.991
60372	3.330	4.530	3.973	0.735	60372	5.973	4.827	4.651	1.237
63726	3.565	5.413	4.837	0.659	63726	3.844	5.693	5.177	0.675

Table D-37 Crack shape parameters for crack emanating from a countersunk hole subject to combined loading, with t = 2.00 mm, $^r/_t$ = 1.20 and $^b/_t$ = 0.05

Test Number		50			Specimen Number		TB 2012005-1		
		left					right		
N (cycles)	a (mm)	c_1 (mm)	c_2 (mm)	a/c_1	N (cycles)	a (mm)	c_1 (mm)	c_2 (mm)	a/c_1
13416	0.591	0.580		1.019					
16770	1.102	0.788		1.398	16770	0.763	0.780		0.978
20124	1.228	1.158		1.061	20124	1.146	1.070		1.071
23478	1.531	1.555		0.984	23478	1.357	1.416		0.958
26832	1.701	2.029		0.838	26832	1.753	1.793		0.977
30186	2.238	2.597	1.165	0.862	30186	2.158	2.307	0.867	0.936
33540	2.578	3.274	2.065	0.787	33540	4.072	2.802	2.440	1.454
36894	3.074	4.193	3.184	0.733	36894	2.713	3.726	2.517	0.728
40248	3.821	5.184	4.417	0.737	40248	2.976	4.346	3.218	0.685
43602	4.561	6.262	5.628	0.728	43602	4.432	5.689	5.076	0.779

Table D-38 Crack shape parameters for crack emanating from a countersunk hole subject to combined loading, with t = 2.00 mm, $^r/_t$ = 1.20 and $^b/_t$ = 0.05

Test Number		51			Specimen Number			TB 2012005-2	
	left					right			
N (cycles)	a (mm)	c_1 (mm)	c_2 (mm)	a/c_1	N (cycles)	a (mm)	c_1 (mm)	c_2 (mm)	a/c_1
					6708	0.481	0.459		1.049
					10062	0.646	0.577		1.119
13416	0.728	0.625		1.165	13416	0.769	0.787		0.977
16770	0.995	0.835		1.192	16770	0.532	0.437		1.218
20124	1.129	1.178		0.958	20124	0.547	0.528		1.036
23478	1.635	1.523		1.074	23478	0.705	0.654		1.078
26832	1.789	1.956		0.915	26832	1.163	0.886		1.313
30186	2.142	2.484	0.889	0.862	30186	1.938	1.252		1.548
33540	2.689	3.102	2.073	0.867	33540	1.629	1.720		0.947
36894	3.056	3.877	2.932	0.788	36894	1.936	2.239		0.865
40248	3.852	4.774	4.080	0.807	40248	2.332	2.941	1.512	0.793
43602	8.350	5.869	5.698	1.423	43602	3.884	3.567	3.058	1.089
46956	5.689	7.407	6.935	0.768	46956	5.304	7.232	6.698	0.733

Table D-39 Crack shape parameters for crack emanating from a countersunk hole subject to combined loading, with t = 2.00 mm, $^r/_t$ = 1.20 and $^b/_t$ = 0.05

Test Number		52			Specimen Number			TB 2012005-3	
	left					right			
N (cycles)	a (mm)	c_1 (mm)	c_2 (mm)	a/c_1	N (cycles)	a (mm)	c_1 (mm)	c_2 (mm)	a/c_1
13416	0.286	0.395		0.724					
16770	0.601	0.458		1.313					
20124	0.768	0.607		1.265	20124	0.809	0.584		1.386
23478	0.967	0.879		1.099	23478	0.878	0.859		1.021
26832	1.260	1.202		1.048	26832	1.137	1.109		1.026
30186	1.506	1.641		0.918	30186	1.497	1.519		0.985
33540	1.892	2.116		0.894	33540	1.816	1.982		0.916
36894	2.126	2.798	0.950	0.760	36894	2.250	2.567	1.175	0.877
40248	3.736	3.463	2.925	1.079	40248	2.792	3.320	2.316	0.841
43602	3.429	4.514	3.667	0.760	43602	4.249	4.259	3.758	0.998
46956	5.355	8.918	8.273	0.600	46956	5.012	9.034	8.284	0.555

Table D-40 Crack shape parameters for crack emanating from a countersunk hole subject to combined loading, with t = 2.00 mm, $^r/_t$ = 1.20 and $^b/_t$ = 0.25

Test Number		53			Specimen Number			TB 2012025-1	
	left					right			
N (cycles)	a (mm)	c_1 (mm)	c_2 (mm)	a/c_1	N (cycles)	a (mm)	c_1 (mm)	c_2 (mm)	a/c_1
					13416	0.479	0.480		0.998
16770	0.373	0.326		1.146	16770	0.726	0.661		1.099
20124	0.557	0.509		1.095	20124	1.097	0.920		1.193
23478	0.799	0.738		1.083	23478	0.417	0.649		0.643
26832	1.052	1.076		0.978	26832	1.653	1.718		0.962
30186	1.546	1.461		1.058	30186	2.138	2.181	0.770	0.980
33540	2.003	1.922	0.101	1.042	33540	2.335	2.766	1.428	0.844
36894	2.083	2.657	0.743	0.784	36894	2.993	3.426	2.548	0.874
40248	2.737	3.473	2.371	0.788	40248	3.430	4.273	3.471	0.803
43602	3.384	4.512	3.639	0.750	43602	4.146	5.220	4.573	0.794
46956	3.944	5.765	4.969	0.684	46956	4.2544	6.5429	5.775	0.650

Table D-41 Crack shape parameters for crack emanating from a countersunk hole subject to combined loading, with t = 2.00 mm, r/t = 1.20 and b/t = 0.25

Test Number		54			Specimen Number		TB 2012025-2		
		left					right		
N (cycles)	a (mm)	c_1 (mm)	c_2 (mm)	a/c_1	N (cycles)	a (mm)	c_1 (mm)	c_2 (mm)	a/c_1
10062	0.376	0.411		0.915					
13416	0.569	0.567		1.004					
16770	0.814	0.804		1.012	16770	0.442	0.424		1.043
20124	1.418	1.079		1.313	20124	0.686	0.609		1.126
23478	1.318	1.534		0.859	23478	1.027	0.871		1.179
26832	1.658	1.972		0.840	26832	1.379	1.161		1.188
30186	1.686	1.965		0.858	30186	1.705	1.498		1.138
33540	2.069	2.539	0.649	0.815	33540	2.062	2.011	0.491	1.025
36894	2.416	3.290	1.846	0.734	36894	2.418	2.636	1.481	0.917
40248	3.159	4.138	3.203	0.763	40248	2.665	3.402	2.248	0.784
43602	3.449	5.310	4.326	0.649	43602	3.335	4.188	3.351	0.796
46956	3.609	6.713	5.587	0.538	46956	3.618	5.311	4.426	0.681
50310	4.834	8.275	7.533	0.584	50310	4.907	8.279	7.560	0.593

Table D-42 Crack shape parameters for crack emanating from a countersunk hole subject to combined loading, with t = 2.00 mm, r/t = 1.20 and b/t = 0.25

Test Number		55			Specimen Number		TB 2012025-3		
		left					right		
N (cycles)	a (mm)	c_1 (mm)	c_2 (mm)	a/c_1	N (cycles)	a (mm)	c_1 (mm)	c_2 (mm)	a/c_1
50310	5.186	8.228		0.630					
13416	0.694	0.443		1.566					
16770	0.666	0.634		1.050					
20124	0.874	0.941		0.929					
23478	1.220	1.174		1.039	23478	1.204	0.892		1.350
26832	1.535	1.573		0.976	26832	1.815	1.225		1.482
30186	1.833	2.108		0.869	30186	1.556	1.713		0.908
33540	2.223	2.697	1.177	0.824	33540	1.993	2.246		0.887
36894	2.716	3.387	2.292	0.802	36894	2.240	2.959	1.333	0.757
40248	3.205	4.290	3.352	0.747	40248	3.056	3.694	2.794	0.827
43602	3.850	5.334	4.558	0.722	43602	3.512	4.701	3.864	0.747
46956	7.592	6.463	6.235	1.175	46956	4.372	5.932	5.275	0.737

Table D-43 Crack shape parameters for crack emanating from a countersunk hole subject to combined loading, with t = 2.00 mm, r/t = 1.20 and b/t = 0.50

Test Number			56		Specimen Number			TB 2012050-1	
	left					right			
N (cycles)	a (mm)	c_1 (mm)	c_2 (mm)	a/c_1	N (cycles)	a (mm)	c_1 (mm)	c_2 (mm)	a/c_1
30186	0.409	0.433		0.944					
33540	0.624	0.572		1.091					
36894	0.956	0.785		1.219					
40248	1.152	1.091		1.056					
43602	1.410	1.467		0.961	43602	0.466	0.391		1.192
46956	1.991	1.841		1.082	46956	0.776	0.582		1.332
50310	2.378	2.337	1.265	1.017	50310	1.323	1.307		1.012
53664	2.588	2.916	1.850	0.887	53664	1.716	1.740		0.986
57018	3.144	3.599	2.777	0.874	57018	2.234	2.247	1.002	0.994
60372	3.626	4.422	3.688	0.820	60372	2.659	2.983	1.966	0.891
63726	3.629	5.492	4.582	0.661	63726	3.409	3.957	3.204	0.862
67080	4.016	6.721	5.828	0.598	67080	4.503	4.938	4.424	0.912
70434	4.785	8.241	7.487	0.581	70434	4.269	6.411	5.664	0.666

Table D-44 Crack shape parameters for crack emanating from a countersunk hole subject to combined loading, with t = 2.00 mm, r/t = 1.20 and b/t = 0.50

Test Number			57		Specimen Number			TB 2012050-2	
	left					right			
N (cycles)	a (mm)	c_1 (mm)	c_2 (mm)	a/c_1	N (cycles)	a (mm)	c_1 (mm)	c_2 (mm)	a/c_1
36894	0.890	0.485		1.835					
40248	0.884	0.865		1.023					
43602	1.399	1.102		1.270	43602	0.555	0.530		1.046
46956	1.539	1.509		1.020	46956	0.909	0.747		1.218
50310	2.000	1.890		1.058	50310	1.128	1.110		1.016
53664	2.060	2.407	0.576	0.856	53664	1.499	1.551		0.967
57018	2.359	3.009	1.595	0.784	57018	2.010	2.021	0.199	0.995
60372	3.020	3.612	2.706	0.836	60372	2.413	2.710	1.517	0.890
63726	3.523	4.499	3.704	0.783	63726	3.317	3.529	2.815	0.940
67080	3.779	5.609	4.759	0.674	67080	3.678	4.618	3.875	0.796
70434	4.304	6.851	6.067	0.628	70434	3.671	5.908	4.954	0.621
73788	5.207	8.376	7.733	0.622	73788	4.791	7.411	6.734	0.646

Table D-45 Crack shape parameters for crack emanating from a countersunk hole subject to combined loading, with *t* = 2.00 mm, $^r/_t$ = 1.20 and $^b/_t$ = 0.50

Test Number			58		Specimen Number			TB 2012050-3	
	left					right			
N (cycles)	a (mm)	c_1 (mm)	c_2 (mm)	a/c_1	N (cycles)	a (mm)	c_1 (mm)	c_2 (mm)	a/c_1
26832	0.761	0.408		1.867					
30186	0.798	0.695		1.147					
33540	1.105	1.009		1.095	33540	1.108	0.983		1.127
36894	1.399	1.385		1.010	36894	1.727	1.301		1.328
40248	1.764	1.789		0.986	40248	1.789	1.881		0.951
43602	2.029	2.303	0.391	0.881	43602	2.086	2.027		1.029
46956	2.415	2.918	1.635	0.828	46956	1.995	2.529		0.789
50310	3.058	3.613	2.733	0.846	50310	2.789	3.196	2.227	0.872
53664	3.360	4.605	3.700	0.730	53664	3.560	4.121	3.409	0.864
57018	3.706	5.744	4.836	0.645	57018	5.367	5.108	4.740	1.051
60372	3.982	7.112	6.150	0.560	60372	4.802	6.567	5.971	0.731
63726	5.115	8.831	8.127	0.579	63726	5.751	8.403	7.879	0.684

D.2 Fractographic reconstruction

The following figures contain all the *SEM* crack location measurements. The axis origin of the figures is located in at the centerline of the countersunk hole. Along the x-axis, the specimens start at x equals the hole radius. Along the *y*-axis the measurements in thickness direction are found.
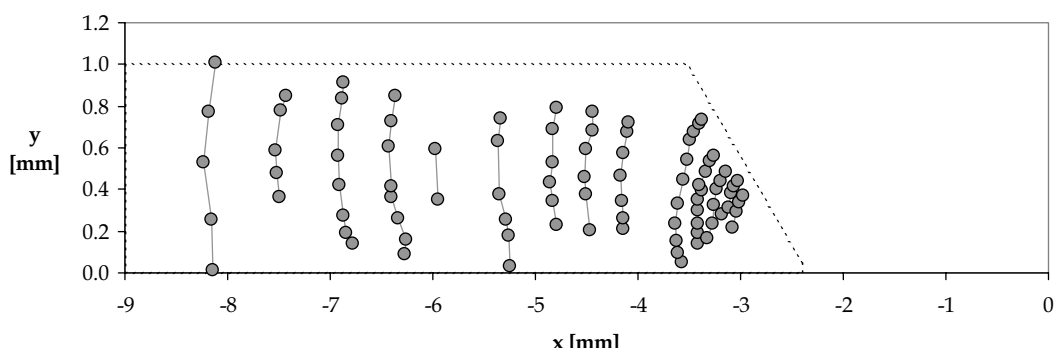
Figure D-4   T 1024005-1 *SEM* crack measurements for left side of countersunk hole
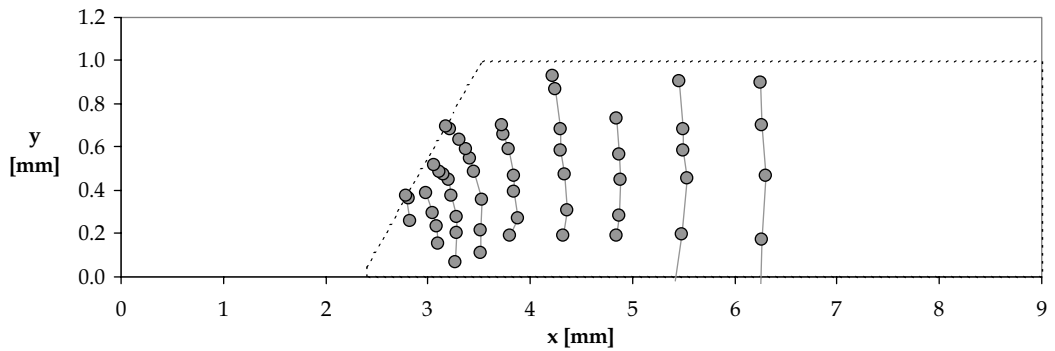
Figure D-5   T 1024005-1 *SEM* **crack measurements for right side of countersunk hole**
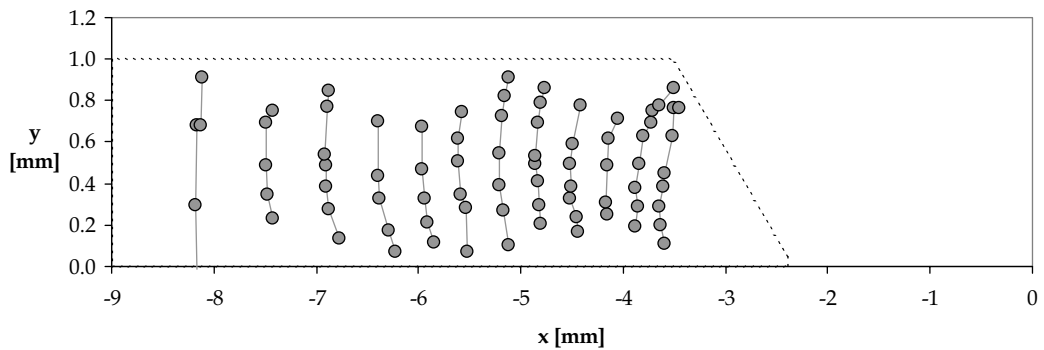
**Figure D-6   T 1024005-2** *SEM* **crack measurements for left side of countersunk hole**
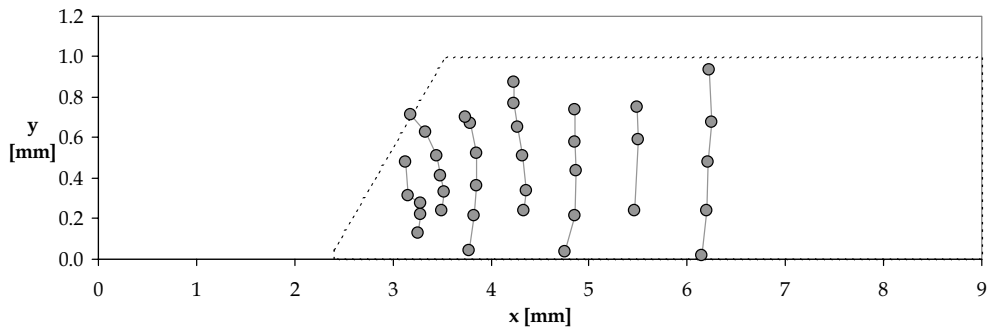
Figure D-7   T 1024005-2 *SEM* **crack measurements for right side of countersunk hole**
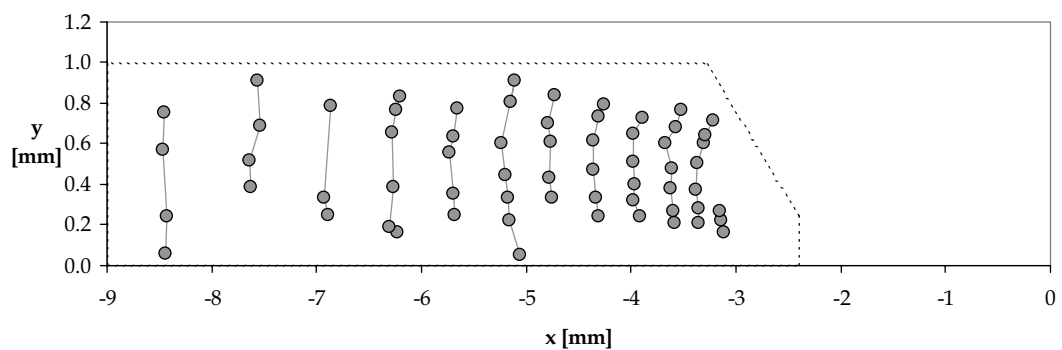
**Figure D-8   T 1024025-2** *SEM* **crack measurements for left side of countersunk hole**
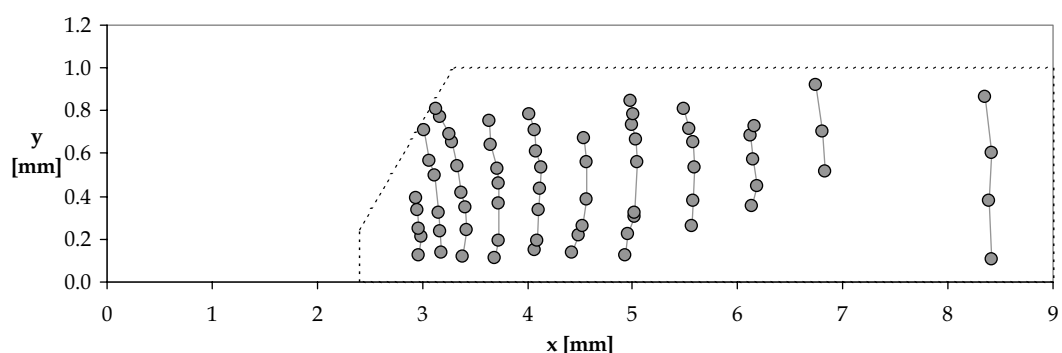
**Figure D-9   T 1024025-2** *SEM* **crack measurements for right side of countersunk hole**
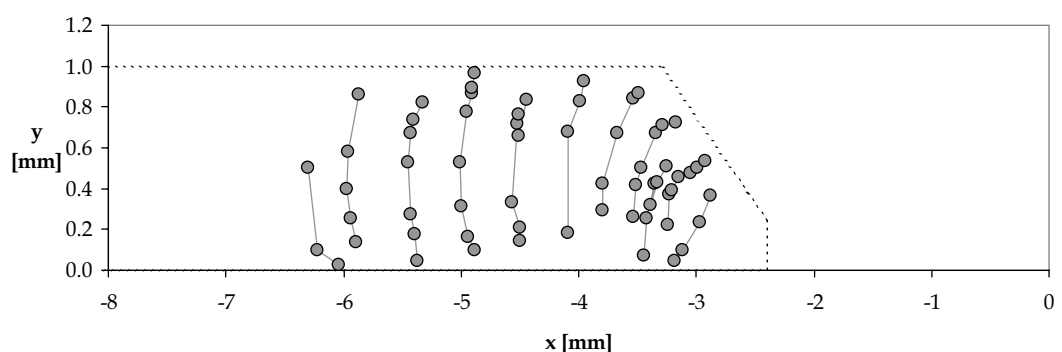
Figure D-10 T 1024050-1 *SEM* **crack measurements for left side of countersunk hole**
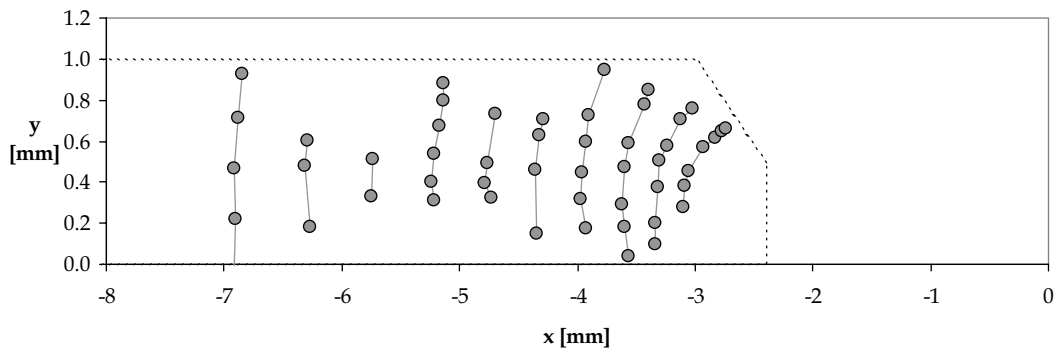
Figure D-11 T 1024050-2 *SEM* **crack measurements for left side of countersunk hole**
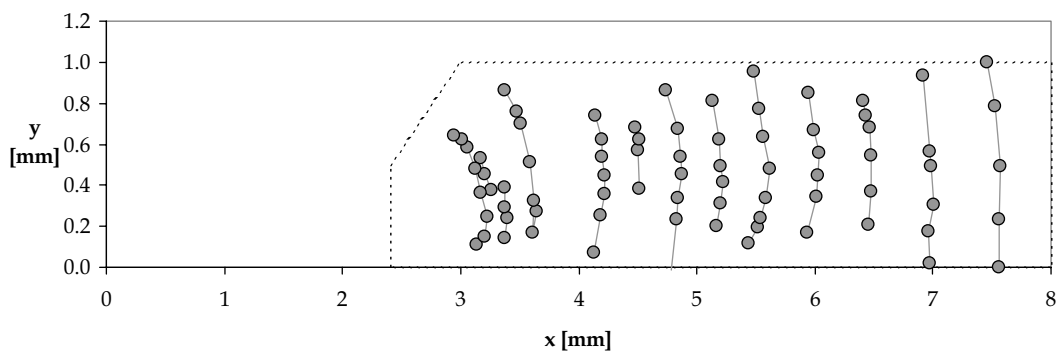
Figure D-12 T 1024050-2 *SEM* **crack measurements for right side of countersunk hole**
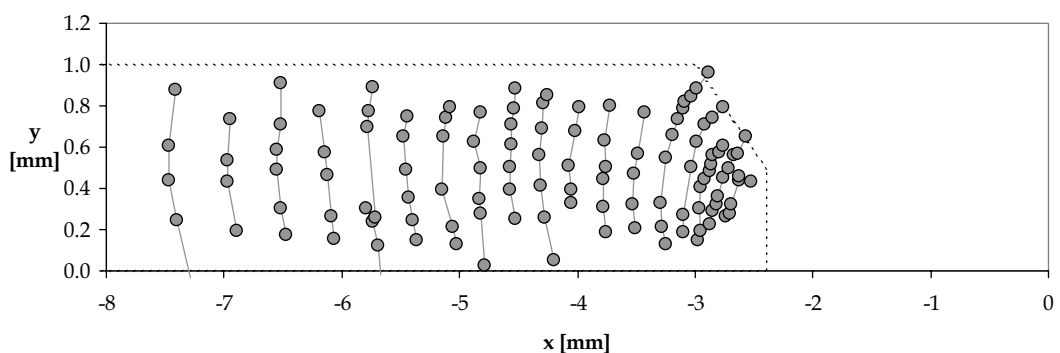
Figure D-13 T 1024050-3 *SEM* **crack measurements for left side of countersunk hole**
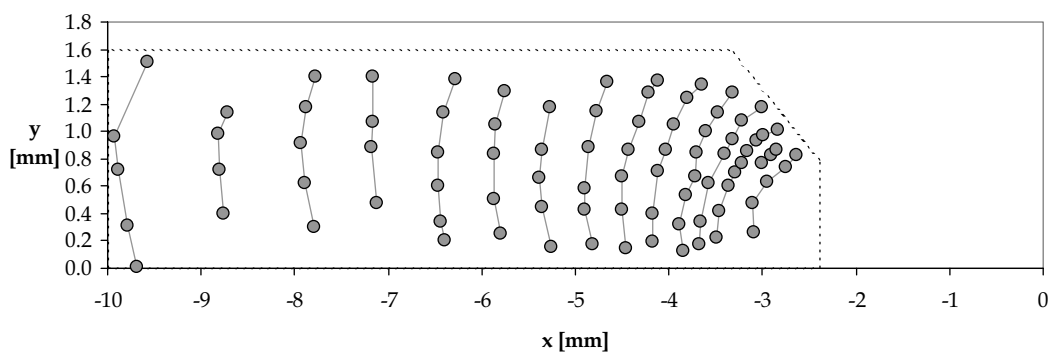
Figure D-14 T 1615050-2 *SEM* **crack measurements for left side of countersunk hole**
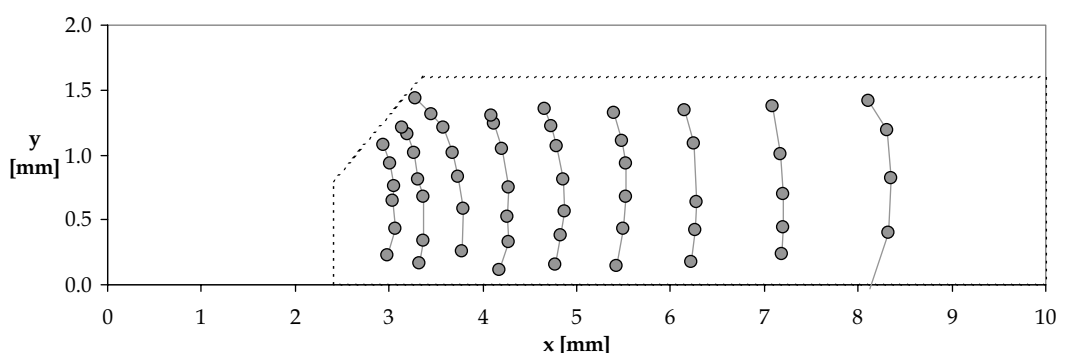
**Figure D-15 T 1615050-2** *SEM* **crack measurements for right side of countersunk hole**
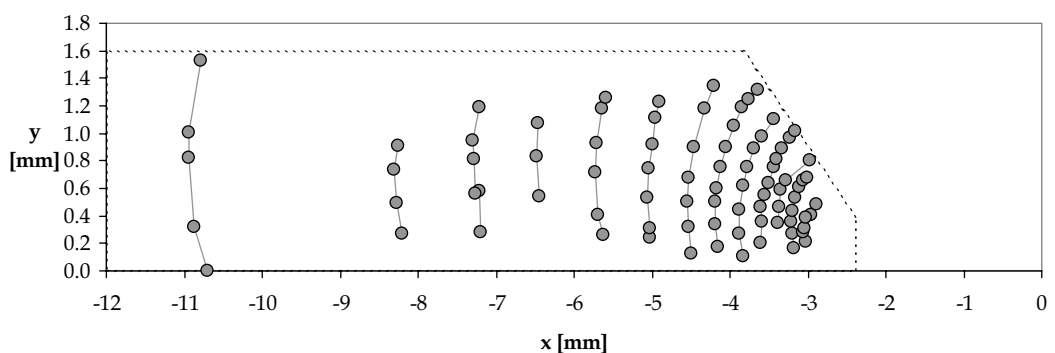
**Figure D-16 T 1615025-1** *SEM* **crack measurements for left side of countersunk hole**
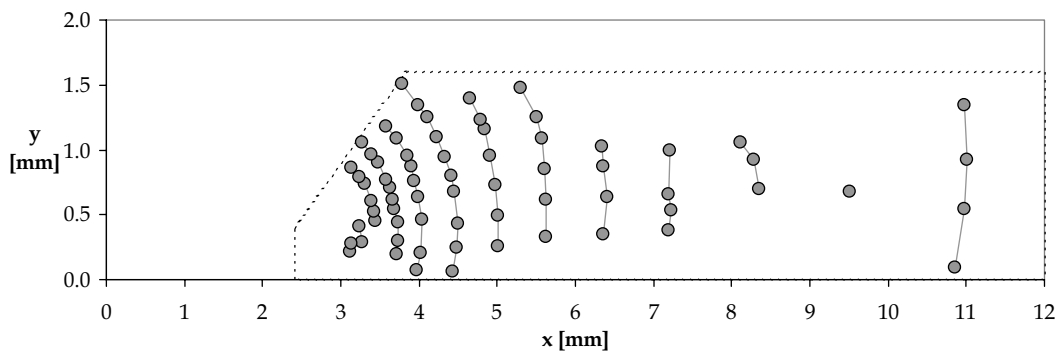
Figure D-17 T 1615025-1 *SEM* **crack measurements for right side of countersunk hole**
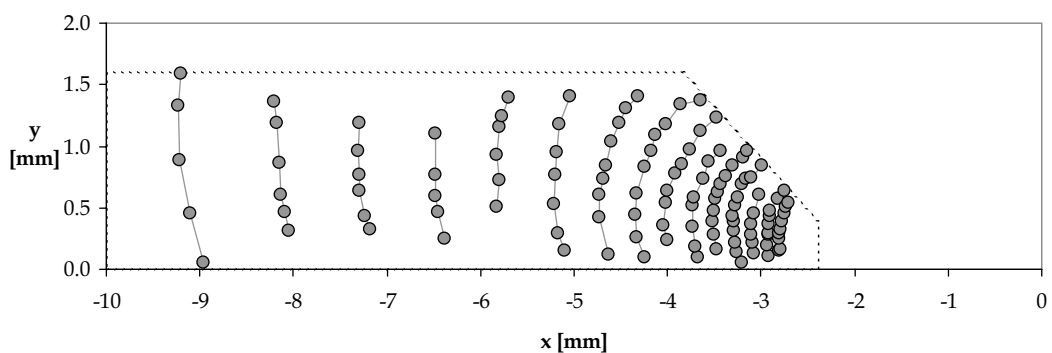
Figure D-18 T 1615025-2 *SEM* **crack measurements for left side of countersunk hole**
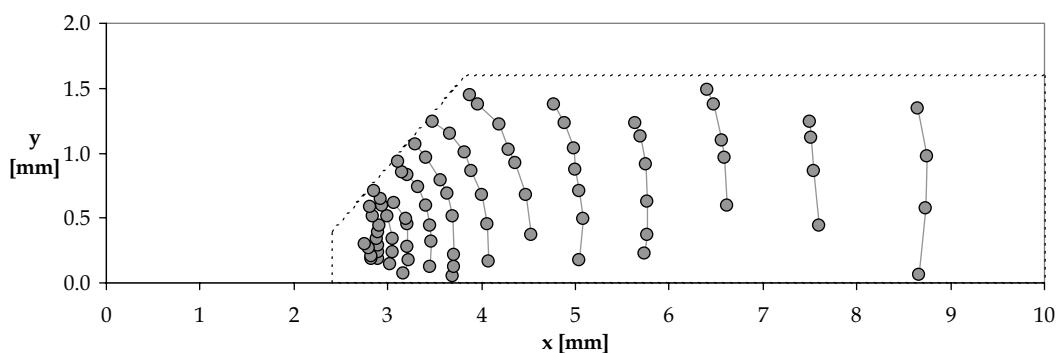
Figure D-19 T 1615025-2 *SEM* **crack measurements for right side of countersunk hole**
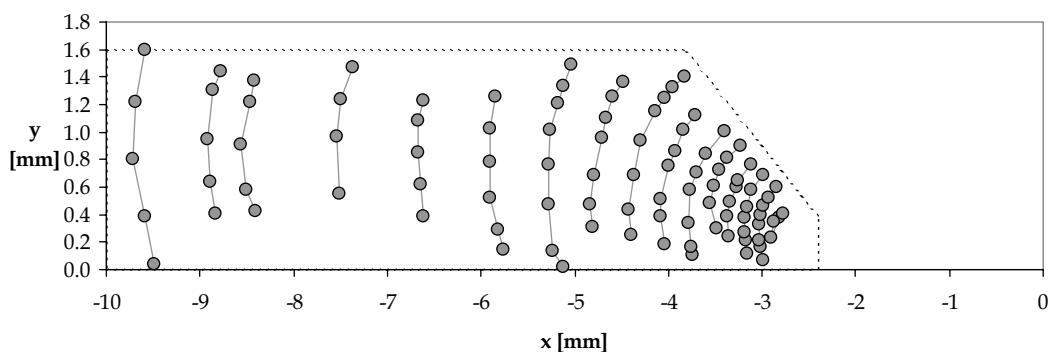
Figure D-20 T 1615025-3 *SEM* crack measurements for left side of countersunk hole
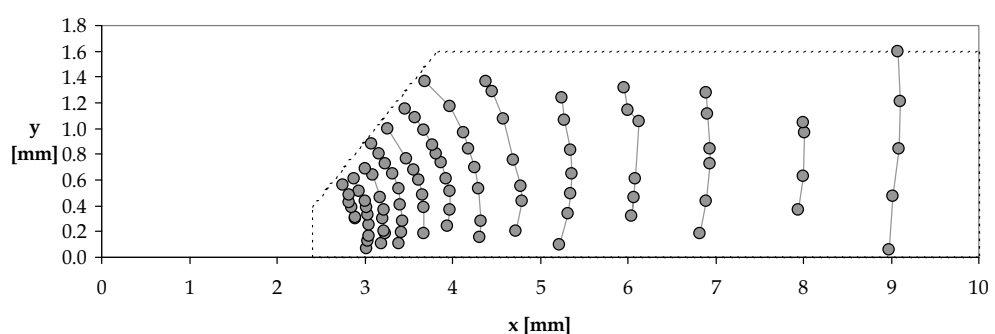
**Figure D-21 T 1615025-3 *SEM* crack measurements for right side of countersunk hole**
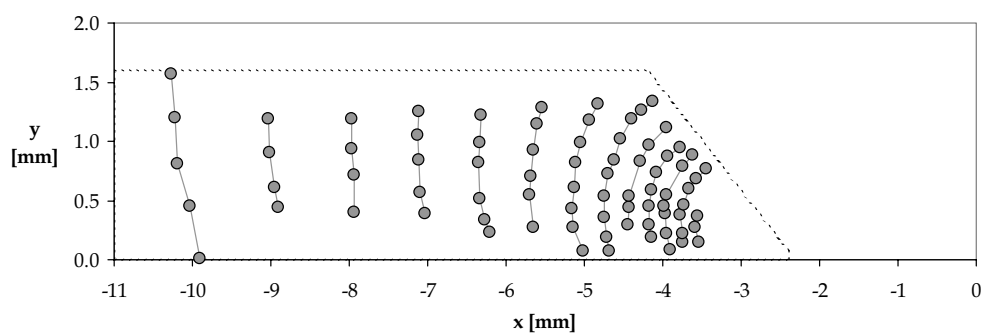
Figure D-22 T 1615005-1 *SEM* crack measurements for left side of countersunk hole
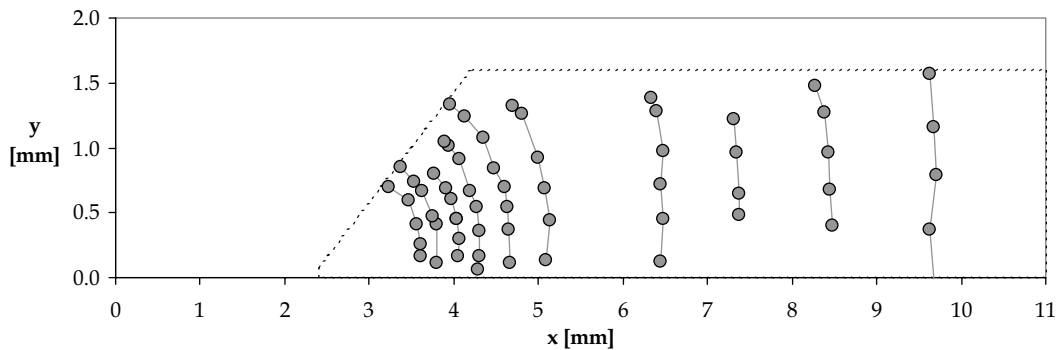
Figure D-23 T 1615005-1 *SEM* **crack measurements for right side of countersunk hole**
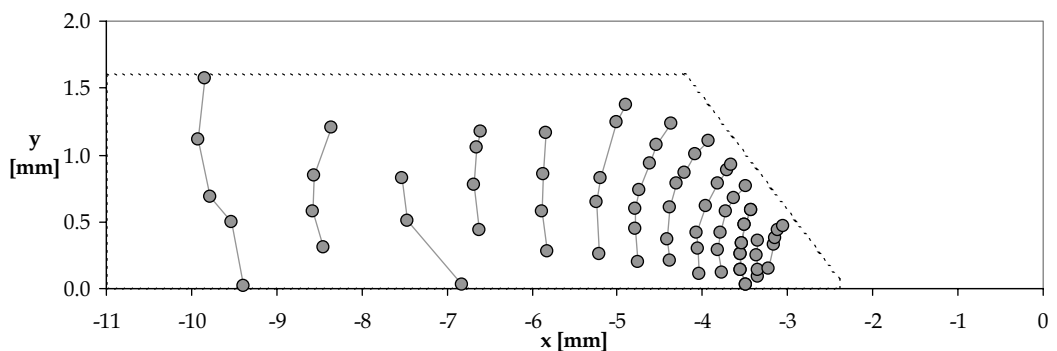
Figure D-24 T 1615005-2 *SEM* **crack measurements for left side of countersunk hole**
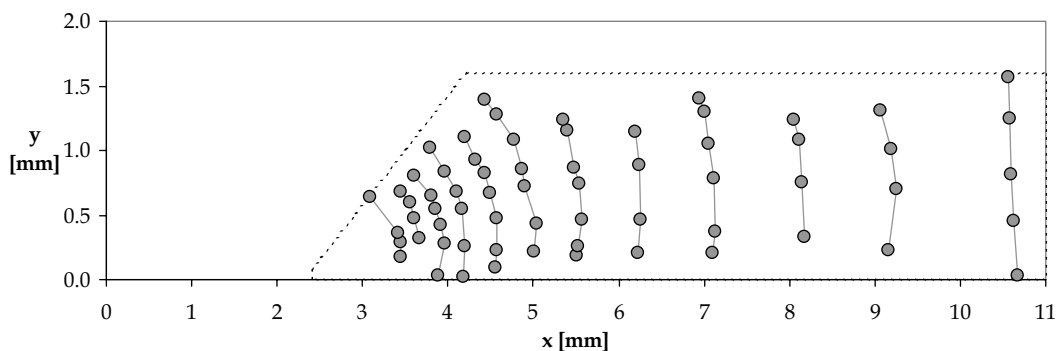
Figure D-25 T 1615005-2 *SEM* **crack measurements for right side of countersunk hole**
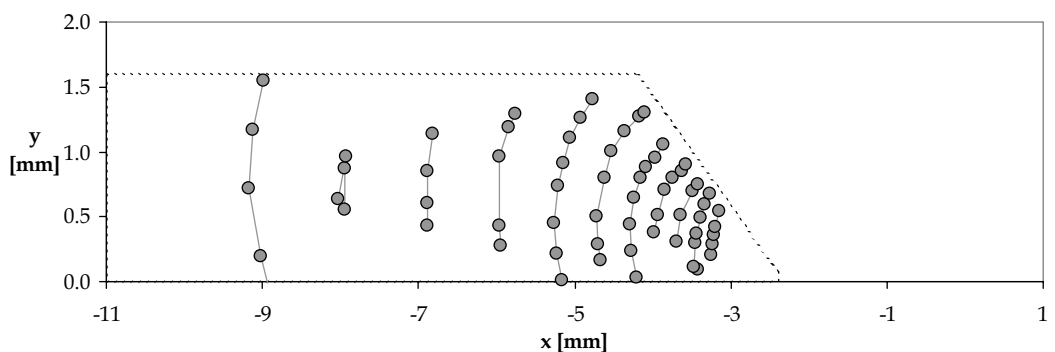
Figure D-26 T 1615005-3 *SEM* **crack measurements for left side of countersunk hole**
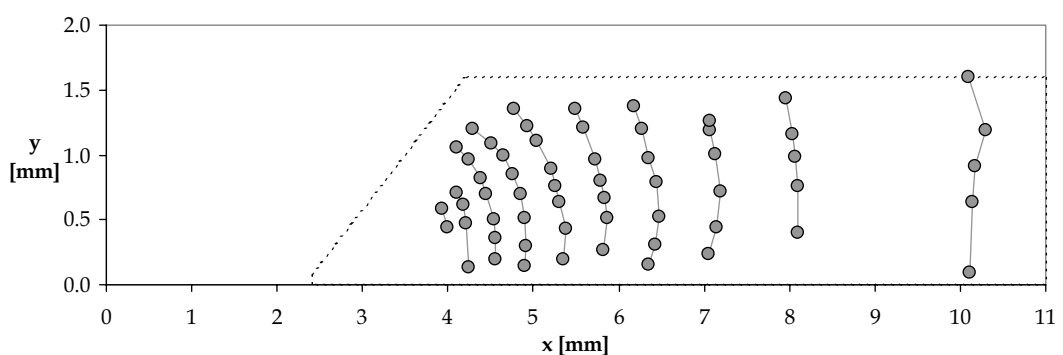
Figure D-27 T 1615005-3 *SEM* **crack measurements for right side of countersunk hole**
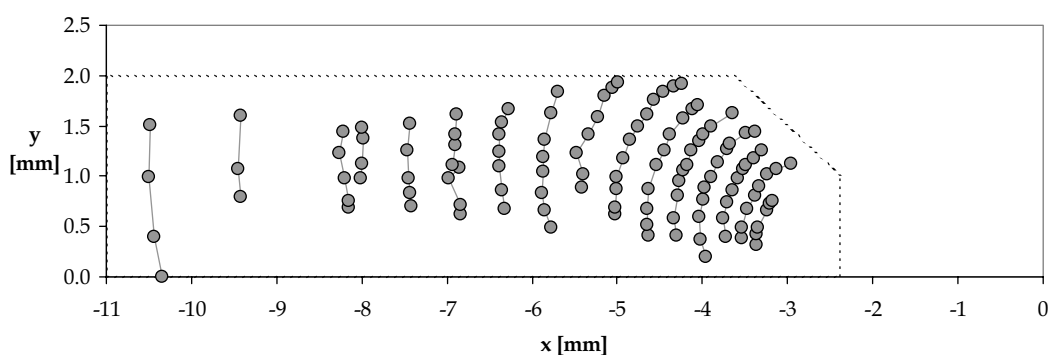
Figure D-28 T 2012050-1 *SEM* **crack measurements for left side of countersunk hole**
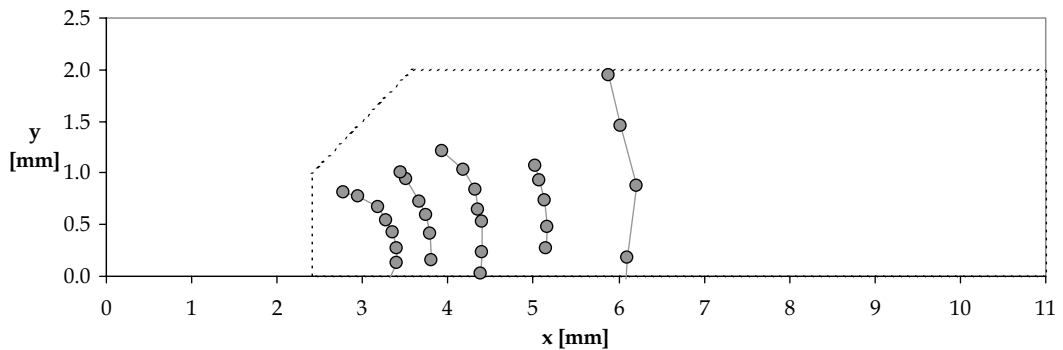
Figure D-29 T 2012050-1 *SEM* **crack measurements for right side of countersunk hole**
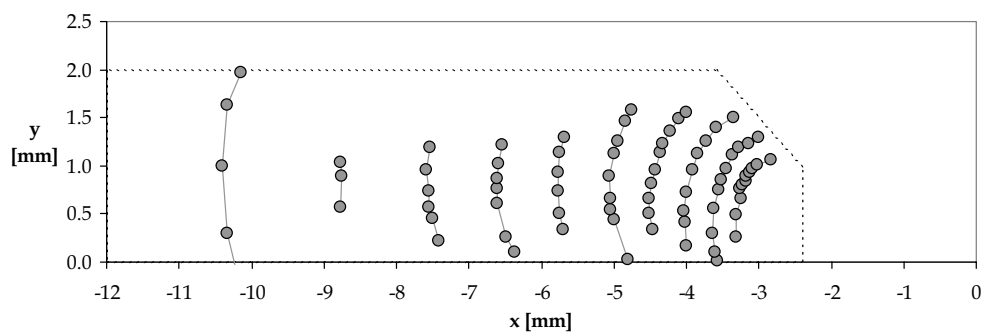
**Figure D-30 T 2012050-3** *SEM* **crack measurements for left side of countersunk hole**
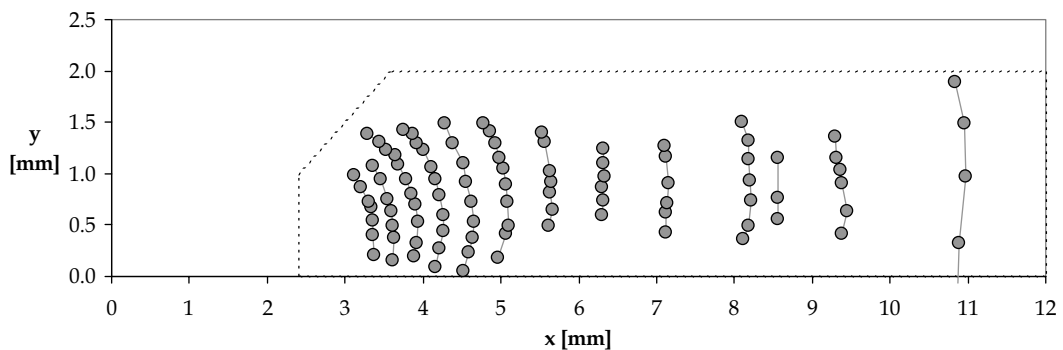
Figure D-31 T 2012050-3 *SEM* **crack measurements for right side of countersunk hole**
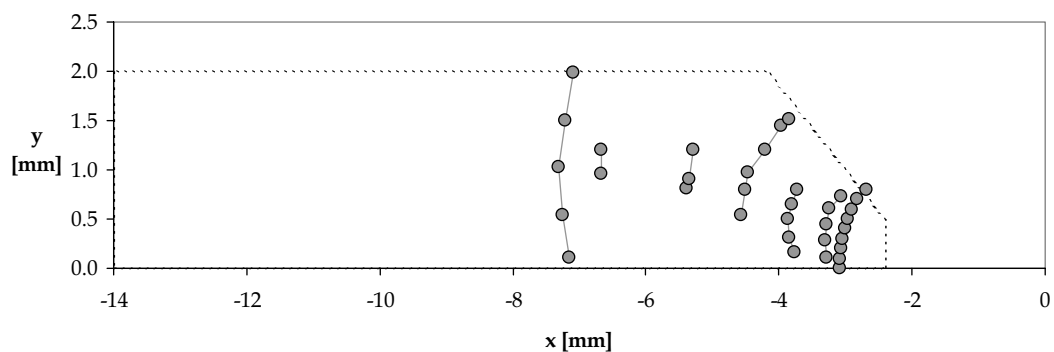
**Figure D-32 T 2012025-1** *SEM* **crack measurements for left side of countersunk hole**
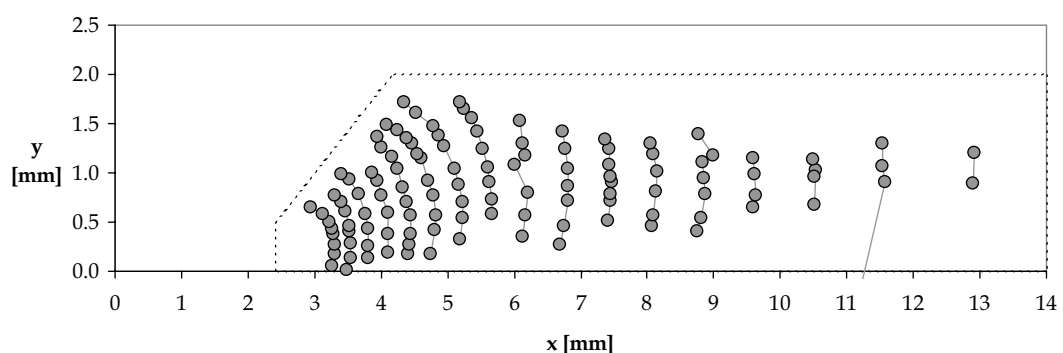
Figure D-33 T 2012025-1 *SEM* **crack measurements for right side of countersunk hole**
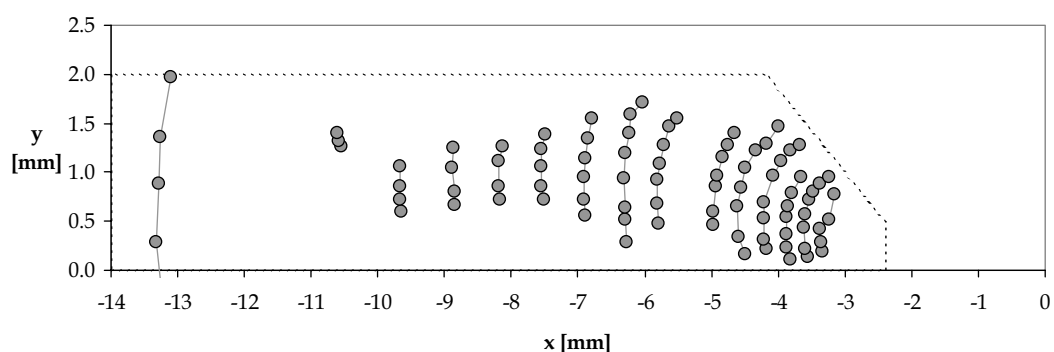
Figure D-34 T 2012025-2 *SEM* **crack measurements for left side of countersunk hole**
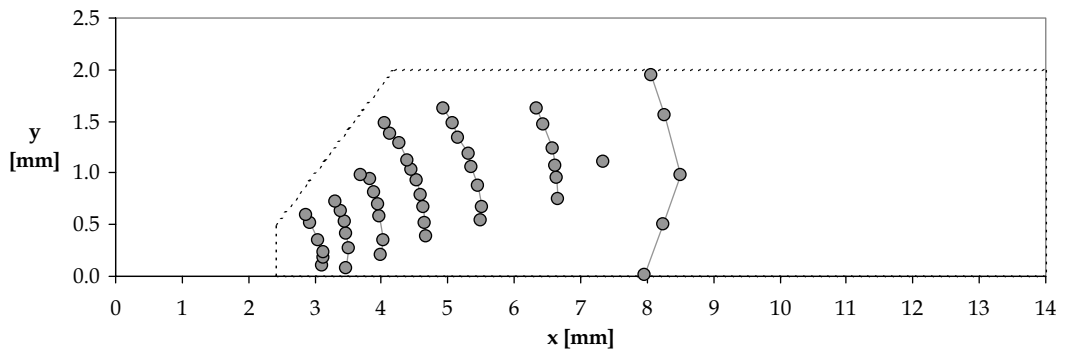
Figure D-35 T 2012025-2 *SEM* crack measurements for right side of countersunk hole
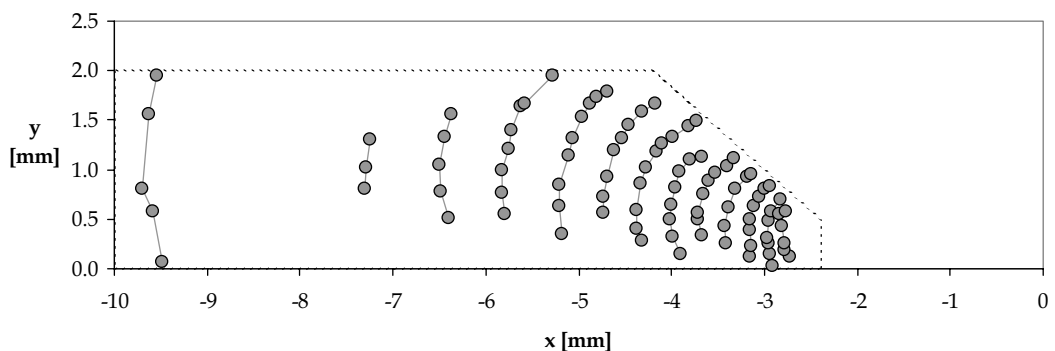
Figure D-36 T 2012025-3 *SEM* crack measurements for left side of countersunk hole
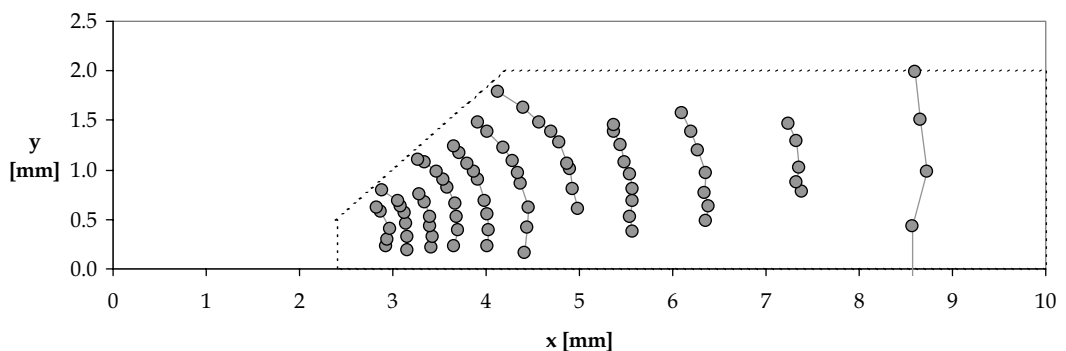
Figure D-37 T 2012025-3 *SEM* crack measurements for right side of countersunk hole
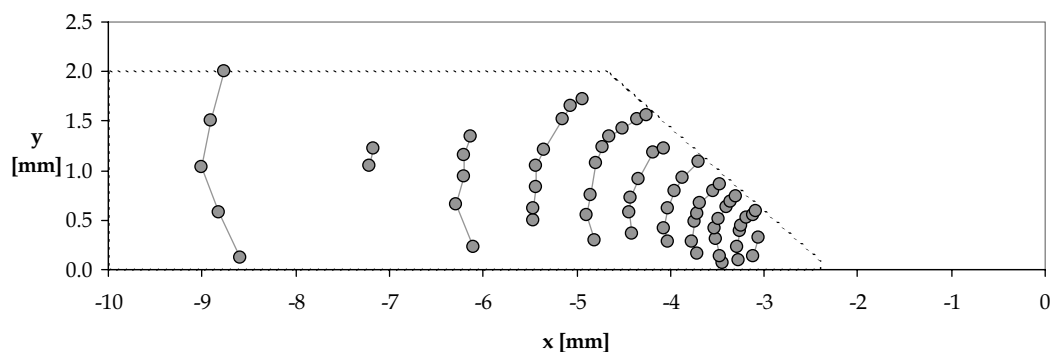
Figure D-38 T 2012005-1 *SEM* **crack measurements for left side of countersunk hole**
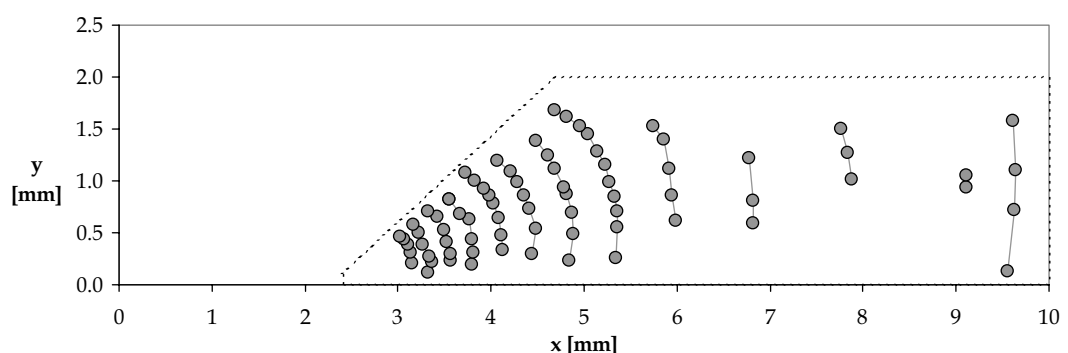

Figure D-39 T 2012005-1 *SEM* **crack measurements for right side of countersunk hole**
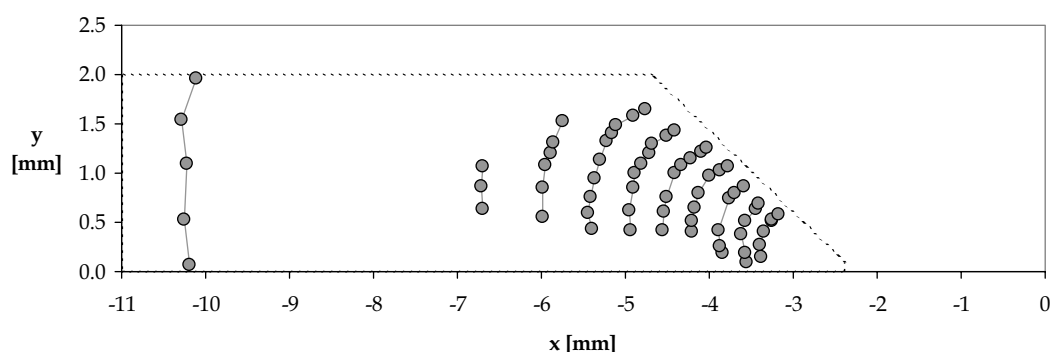
Figure D-40 T 2012005-2 *SEM* **crack measurements for left side of countersunk hole**
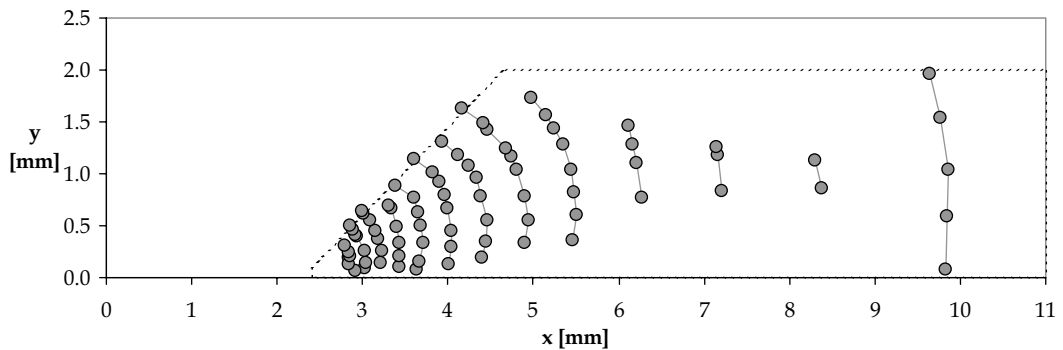
Figure D-41 T 2012005-2 *SEM* **crack measurements for right side of countersunk hole**
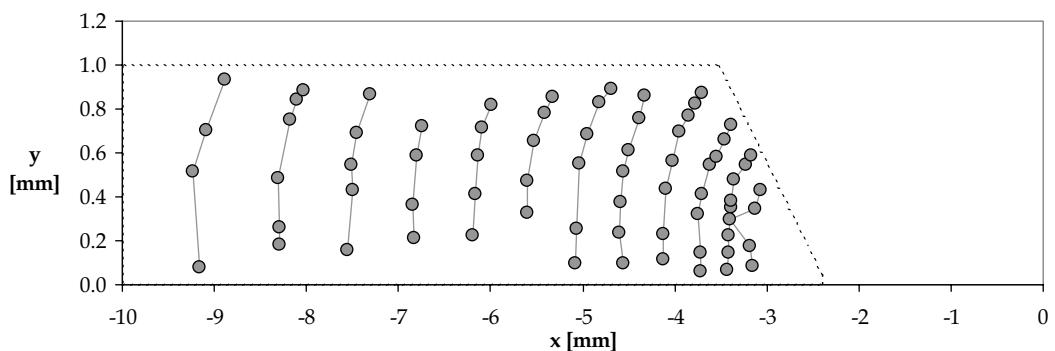
Figure D-42 TB 1024005-1 *SEM* **crack measurements for left side of countersunk hole**
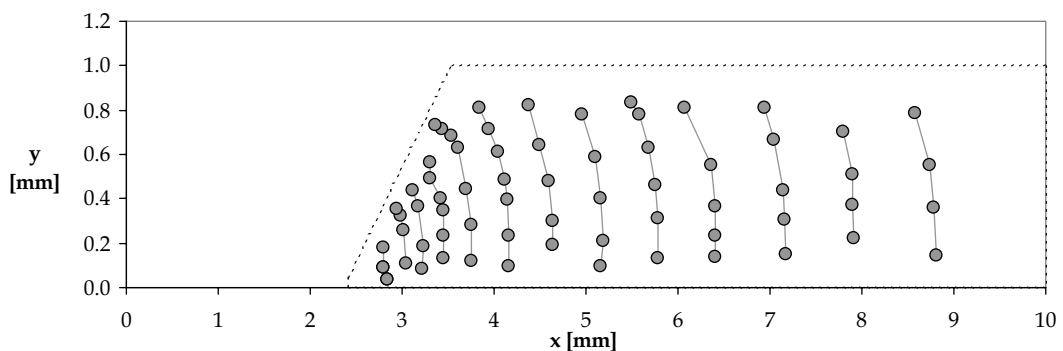
Figure D-43 TB 1024005-1 *SEM* **crack measurements for right side of countersunk hole**
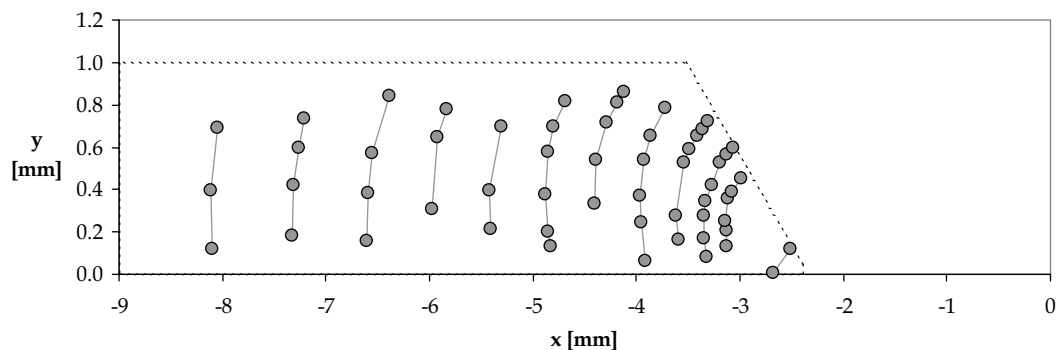
Figure D-44 TB 1024005-2 *SEM* crack measurements for left side of countersunk hole
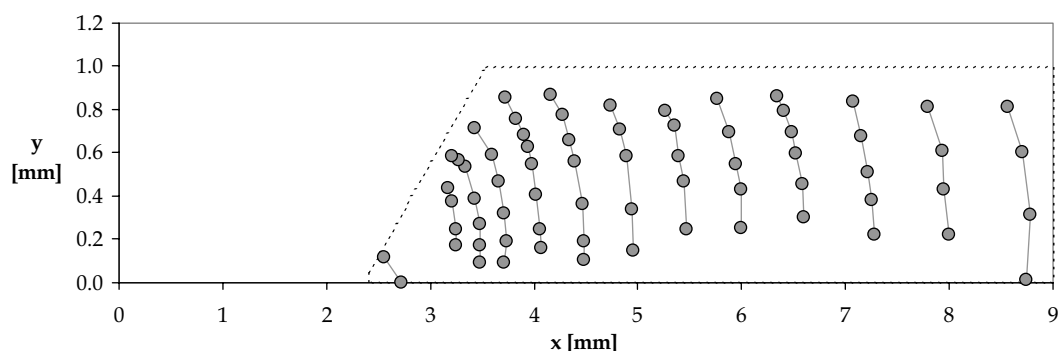
Table D-46　TB 1024005-2 *SEM* crack measurements for right side of countersunk hole
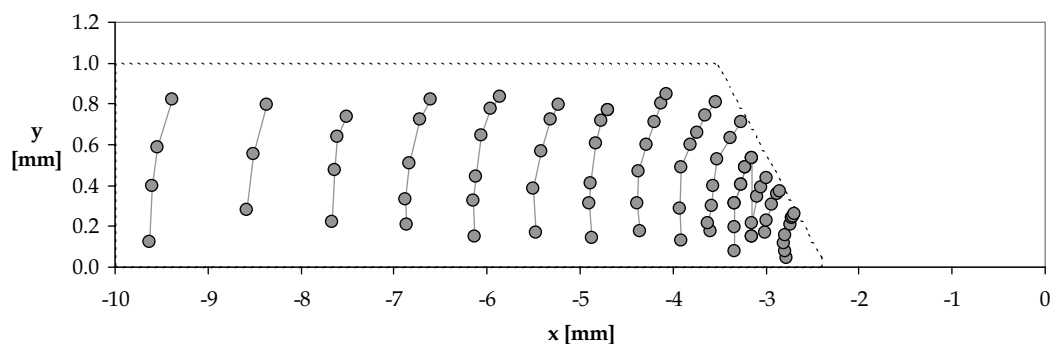
Figure D-45 TB 1024005-3 *SEM* crack measurements for left side of countersunk hole
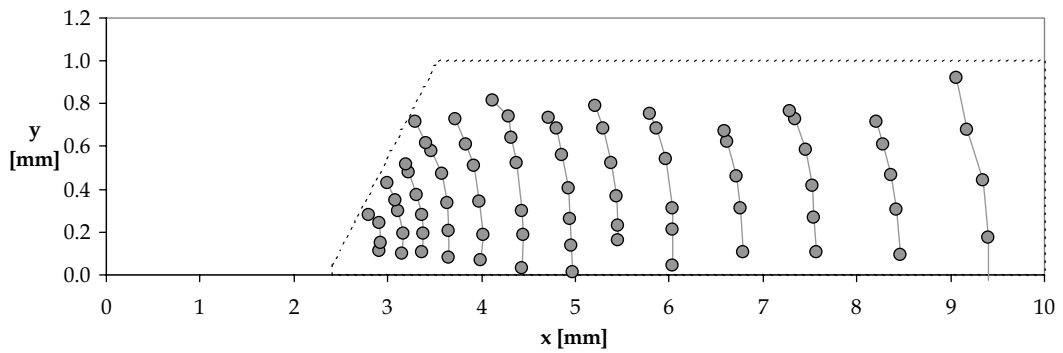
**Figure D-46 TB 1024005-3 *SEM* crack measurements for right side of countersunk hole**
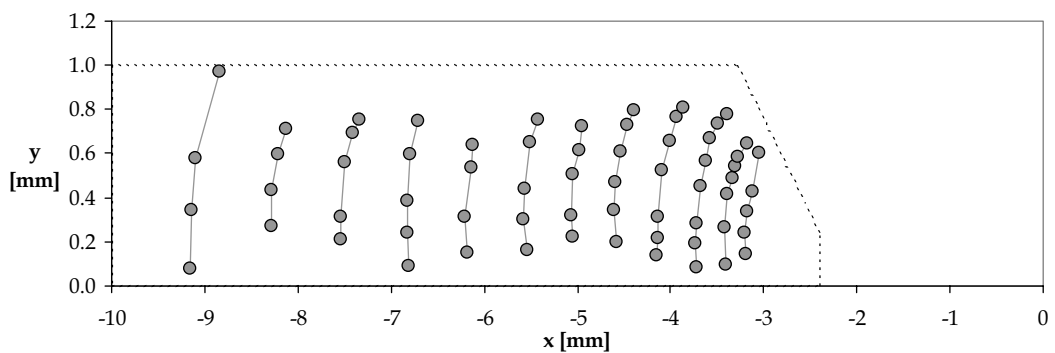

Figure D-47 TB 1024025-1 *SEM* crack measurements for left side of countersunk hole
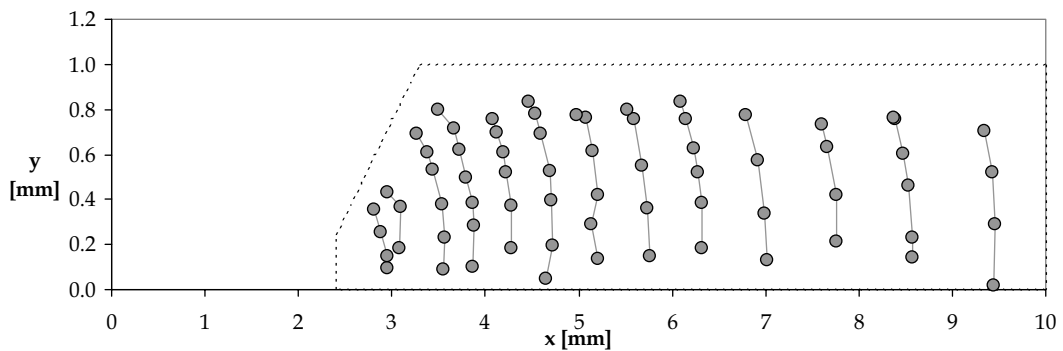
Figure D-48 TB 1024025-1 *SEM* crack measurements for right side of countersunk hole
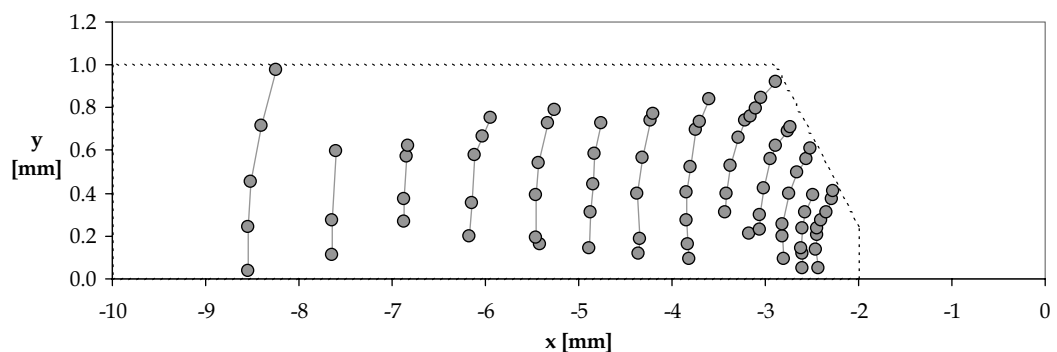
Figure D-49 TB 1024025-2 *SEM* **crack measurements for left side of countersunk hole**
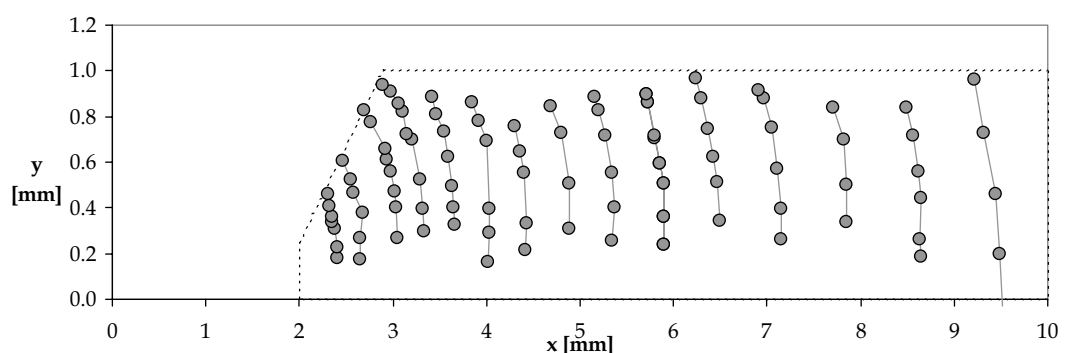

Figure D-50 TB 1024025-2 *SEM* **crack measurements for right side of countersunk hole**
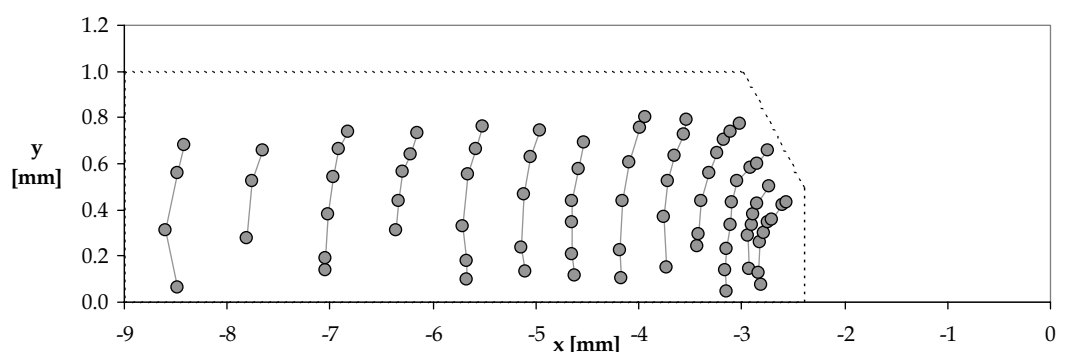
Figure D-51 TB 1024050-1 *SEM* **crack measurements for left side of countersunk hole**
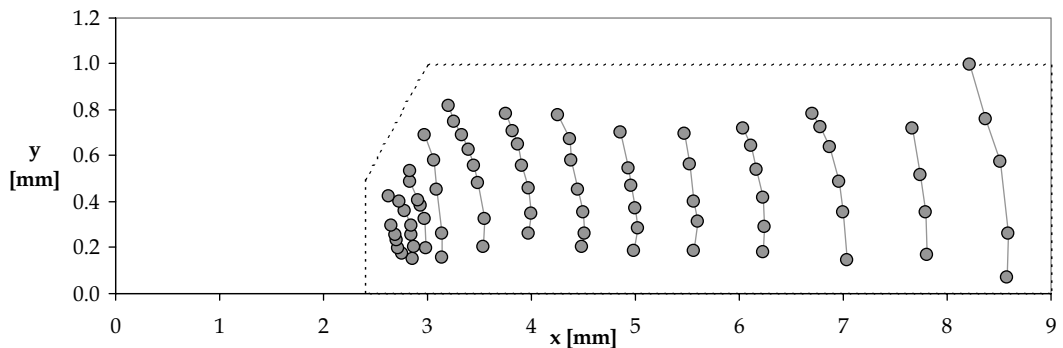
Figure D-52 TB 1024050-1 *SEM* **crack measurements for right side of countersunk hole**
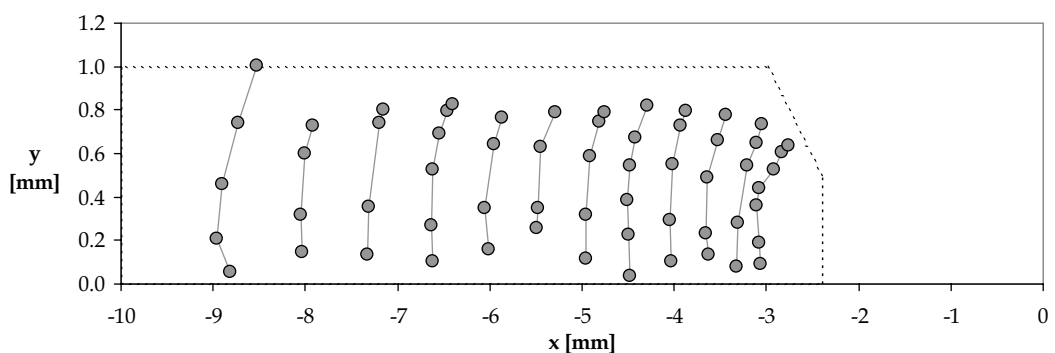
Figure D-53 TB 1024050-2 *SEM* **crack measurements for left side of countersunk hole**
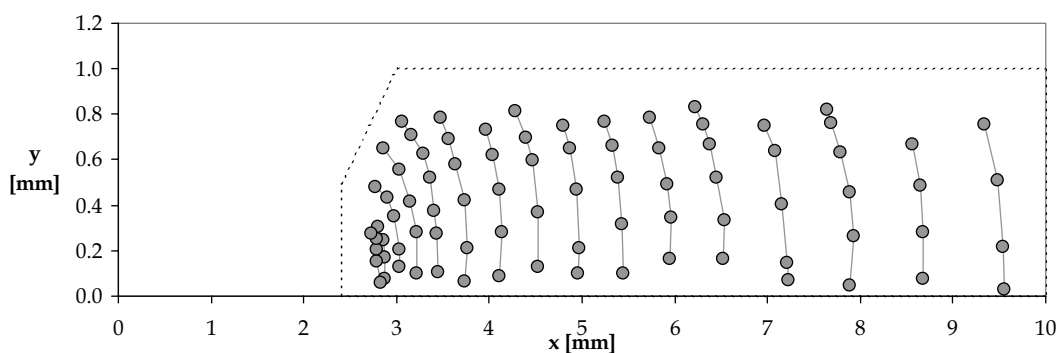
**Figure D-54 TB 1024050-2** *SEM* **crack measurements for right side of countersunk hole**
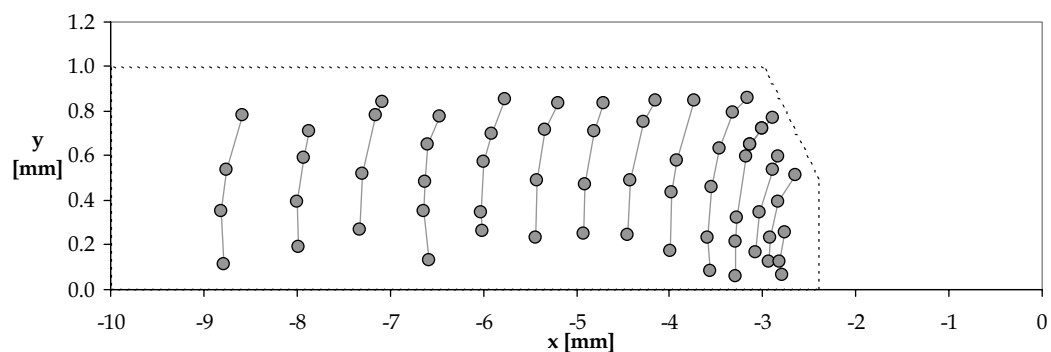
Figure D-55 TB 1024050-3 *SEM* crack measurements for left side of countersunk hole
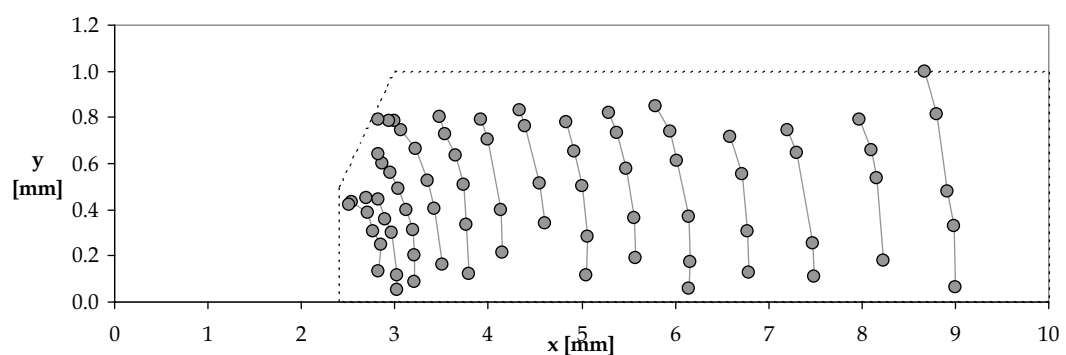

Figure D-56 TB 1024050-3 *SEM* crack measurements for right side of countersunk hole
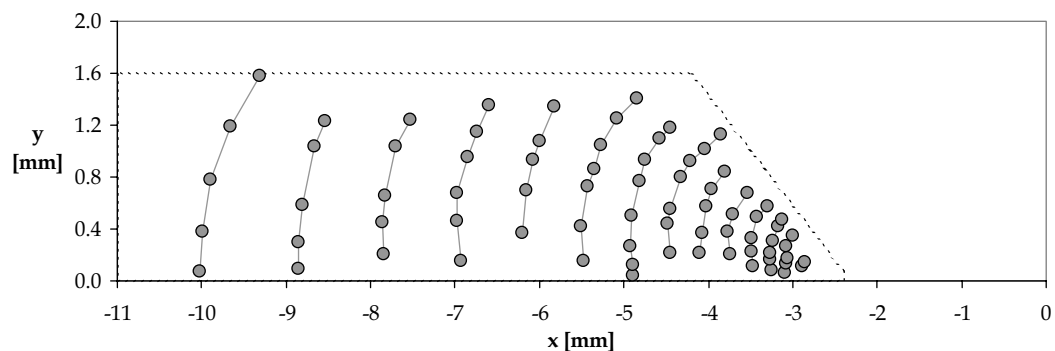
Figure D-57 TB 1615005-1 *SEM* crack measurements for left side of countersunk hole
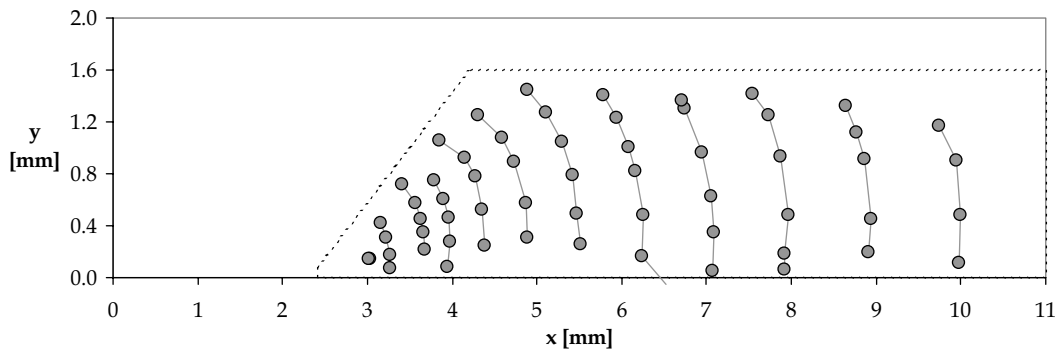
Figure D-58 TB 1615005-1 *SEM* crack measurements for right side of countersunk hole
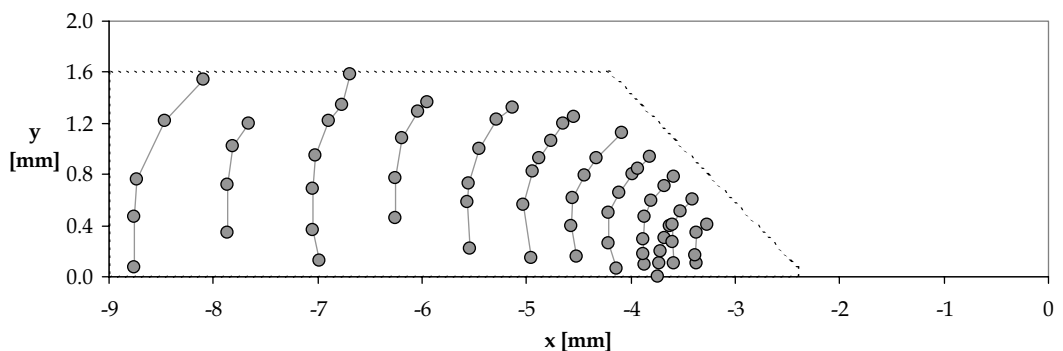

Figure D-59 TB 1615005-2 *SEM* crack measurements for left side of countersunk hole
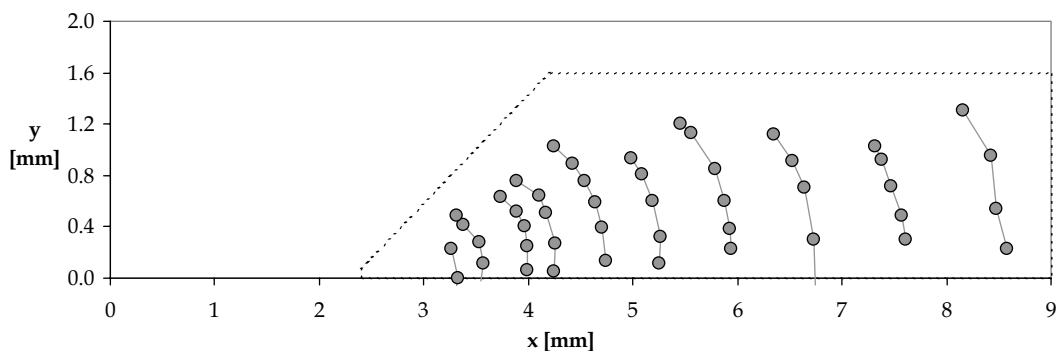
Figure D-60 TB 1615005-2 *SEM* crack measurements for right side of countersunk hole
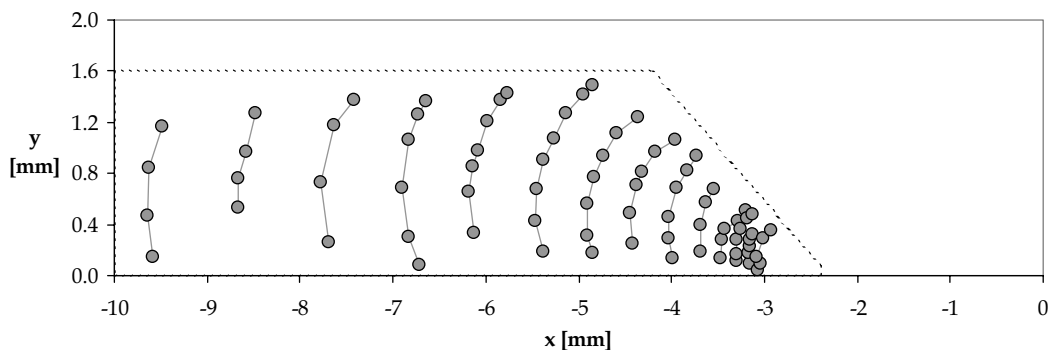
Figure D-61 TB 1615005-3 *SEM* crack measurements for left side of countersunk hole
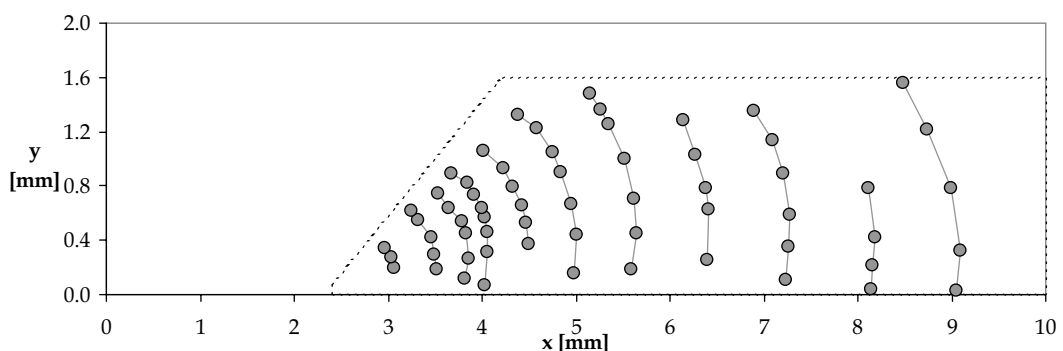
Figure D-62 TB 1615005-3 *SEM* crack measurements for right side of countersunk hole
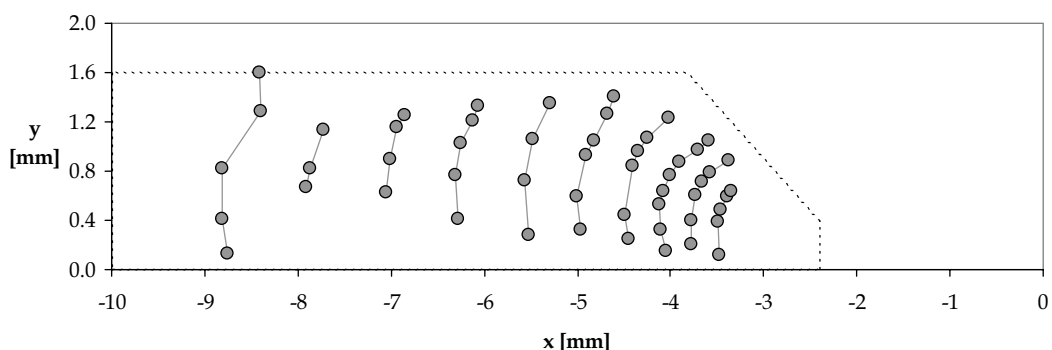
**Figure D-63 TB 1615025-1 *SEM* crack measurements for left side of countersunk hole**
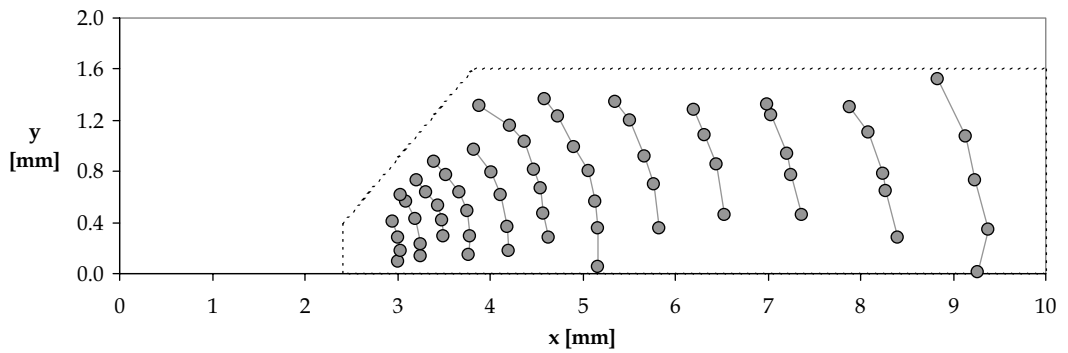
Figure D-64 TB 1615025-1 *SEM* crack measurements for right side of countersunk hole
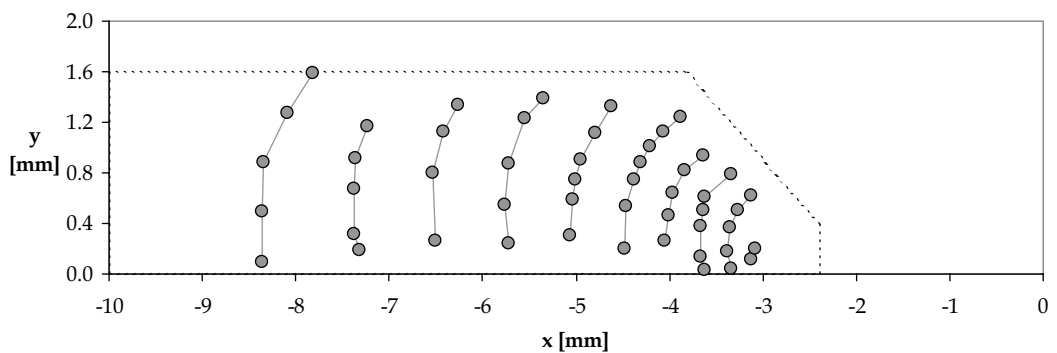

Figure D-65 TB 1615025-2 *SEM* crack measurements for left side of countersunk hole
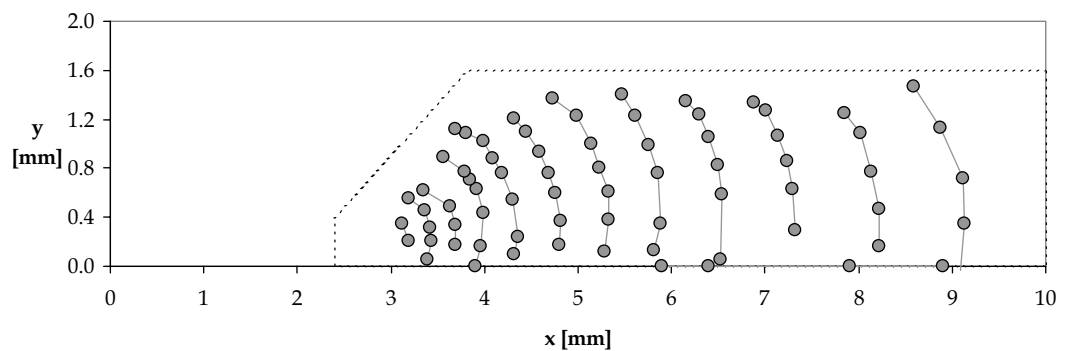
Figure D-66 TB 1615025-2 *SEM* crack measurements for right side of countersunk hole
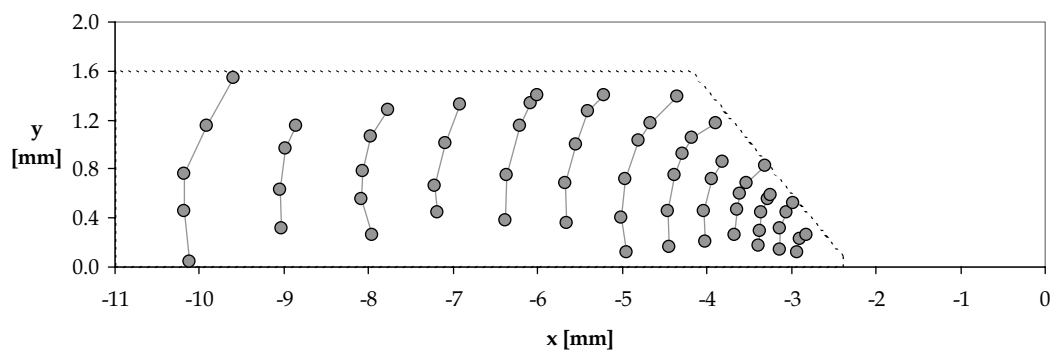
Figure D-67 TB 1615025-3 *SEM* crack measurements for left side of countersunk hole
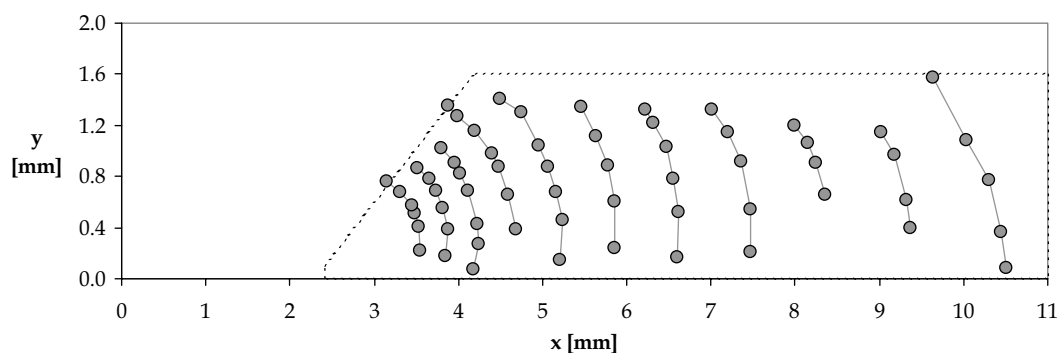
Figure D-68 TB 1615025-3 *SEM* crack measurements for right side of countersunk hole
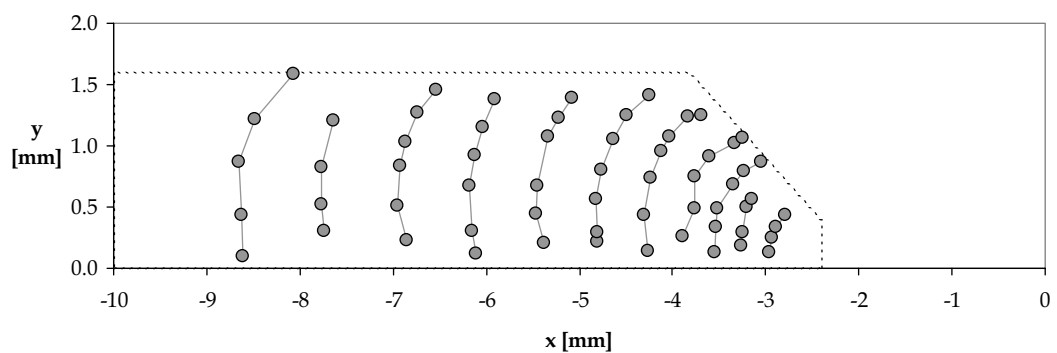
**Figure D-69 TB 1615050-1 *SEM* crack measurements for left side of countersunk hole**
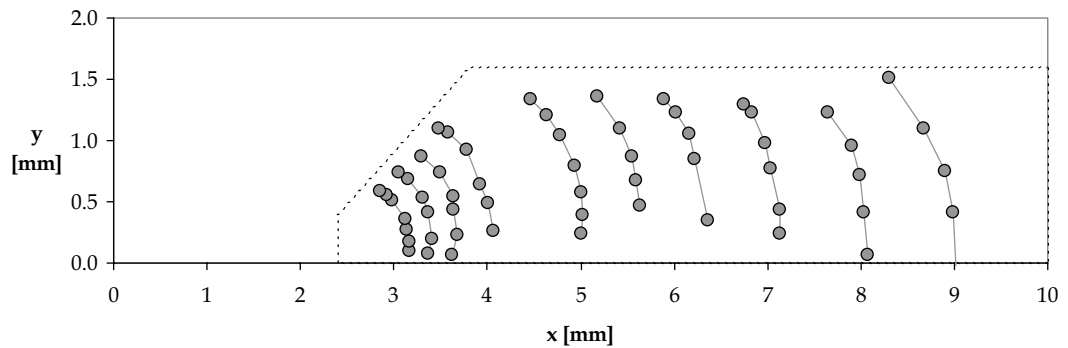
Figure D-70 TB 1615050-1 *SEM* **crack measurements for right side of countersunk hole**
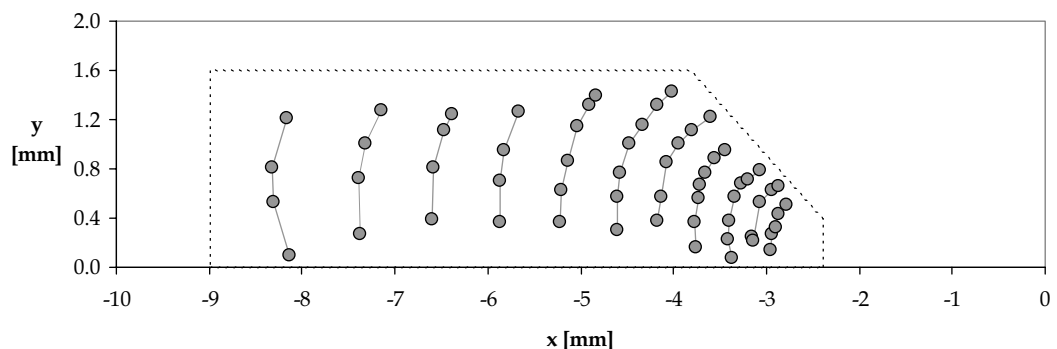
Figure D-71 TB 1615050-2 *SEM* **crack measurements for left side of countersunk hole**
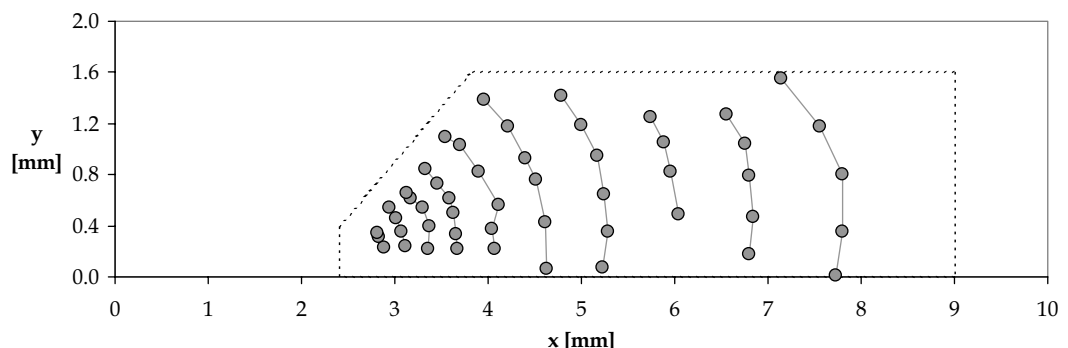
Figure D-72 TB 1615050-2 *SEM* **crack measurements for right side of countersunk hole**
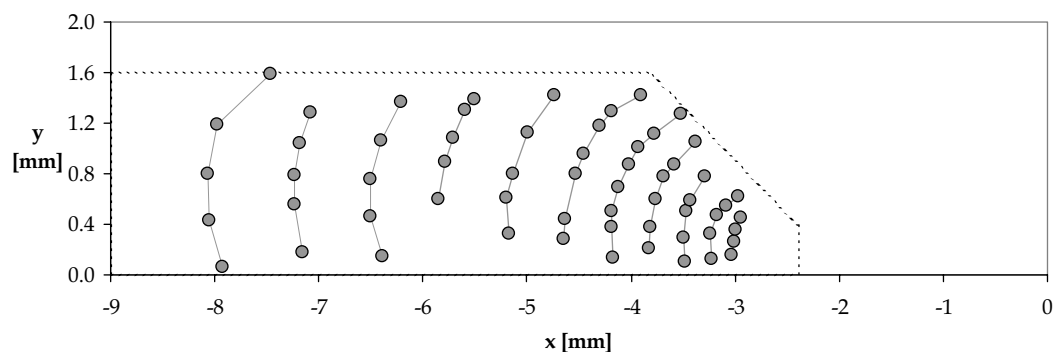
**Figure D-73 TB 1615050-3 *SEM* crack measurements for left side of countersunk hole**
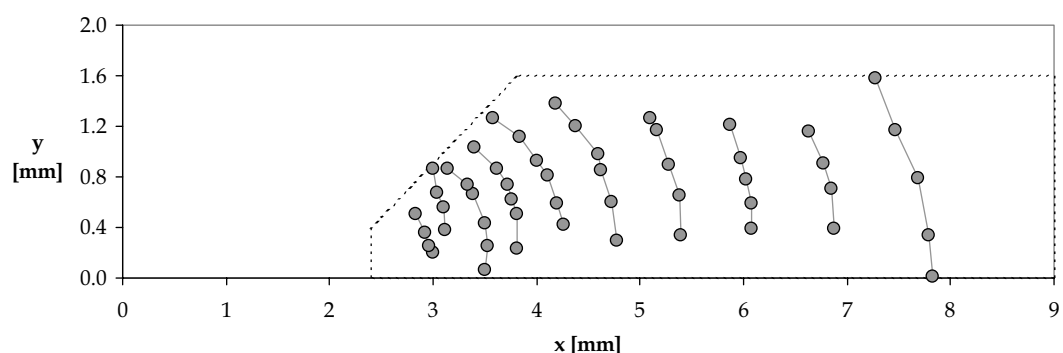
Figure D-74 TB 1615050-3 *SEM* crack measurements for right side of countersunk hole
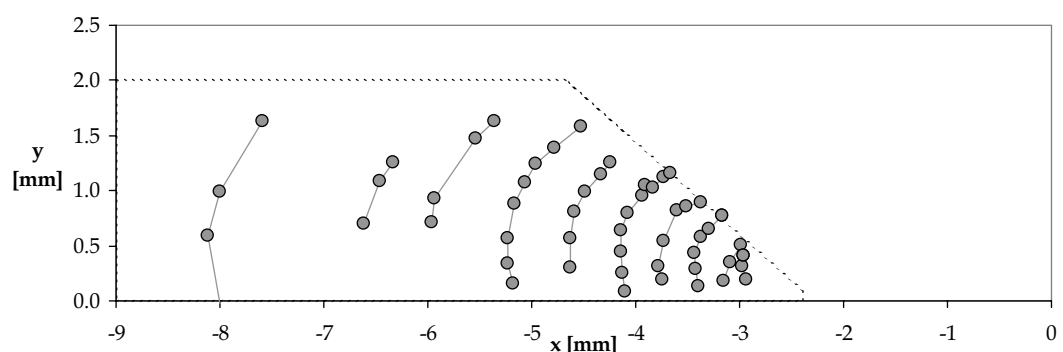
Figure D-75 TB 2012005-1 *SEM* crack measurements for left side of countersunk hole
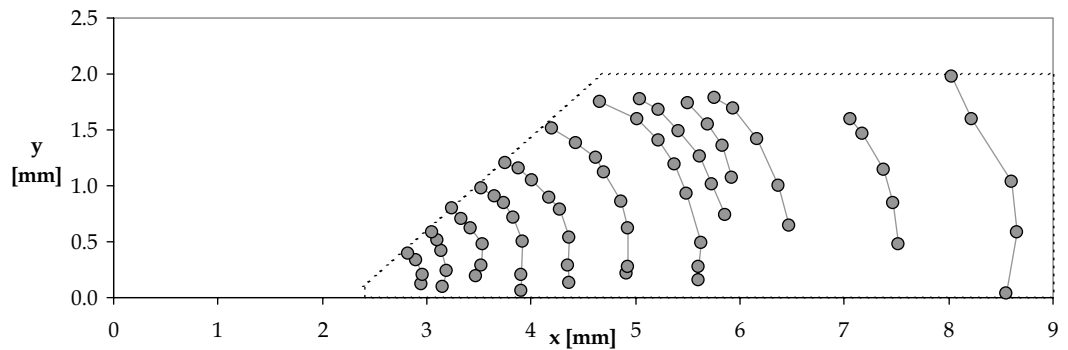
Figure D-76 TB 2012005-1 *SEM* crack measurements for right side of countersunk hole
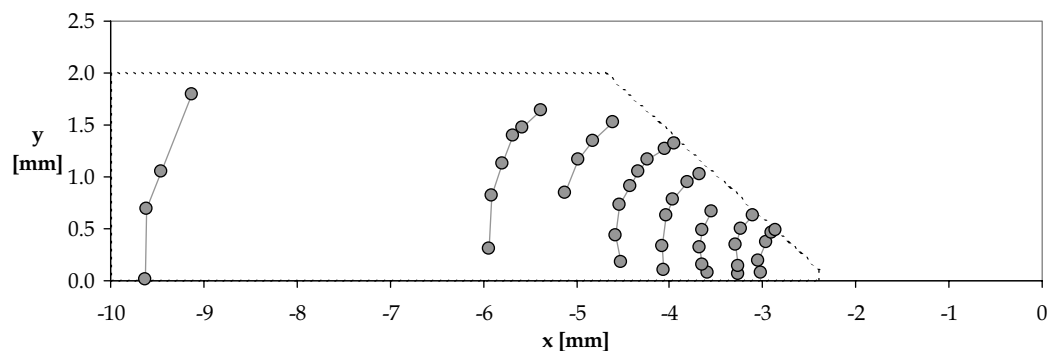

Figure D-77 TB 2012005-2 *SEM* crack measurements for left side of countersunk hole
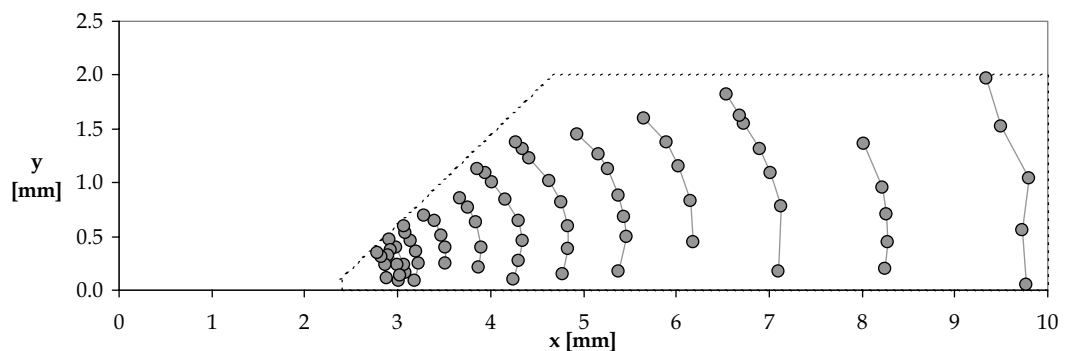
Figure D-78 TB 2012005-2 *SEM* crack measurements for right side of countersunk hole
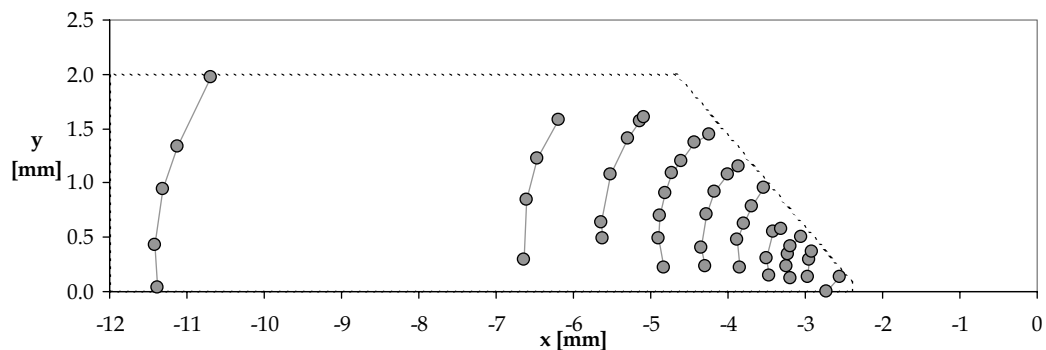
Figure D-79 TB 2012005-3 *SEM* crack measurements for left side of countersunk hole
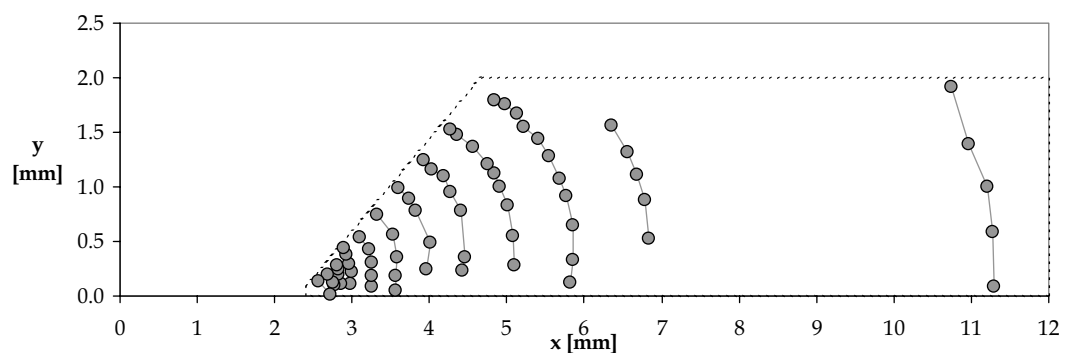
Figure D-80 TB 2012005-3 *SEM* crack measurements for right side of countersunk hole
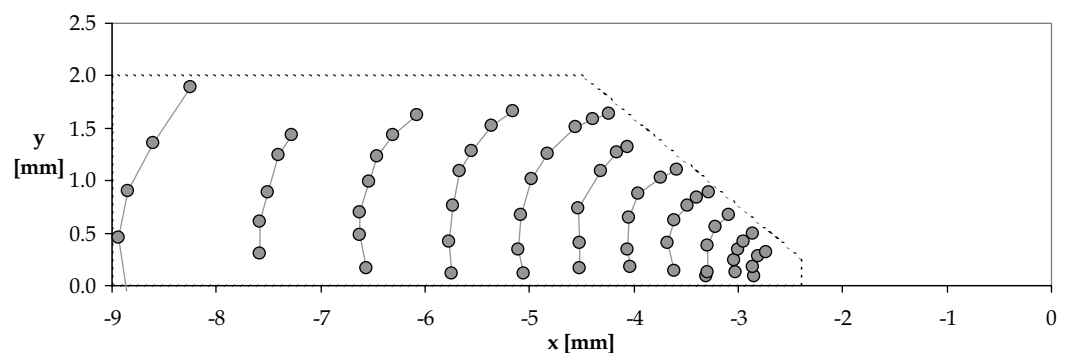
Figure D-81 TB 2012025-1 *SEM* crack measurements for left side of countersunk hole
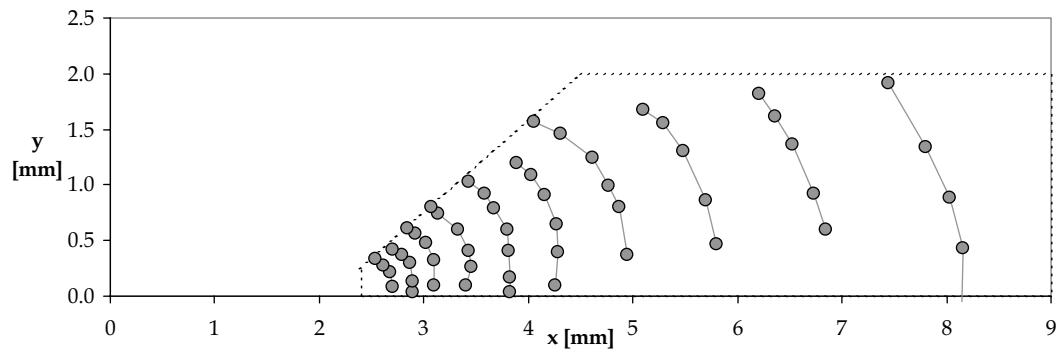
Figure D-82 TB 2012025-1 *SEM* crack measurements for right side of countersunk hole
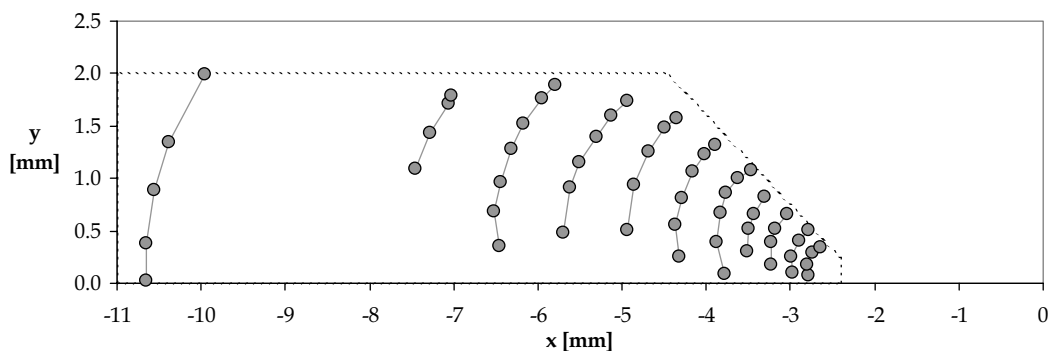

Figure D-83 TB 2012025-2 *SEM* crack measurements for left side of countersunk hole
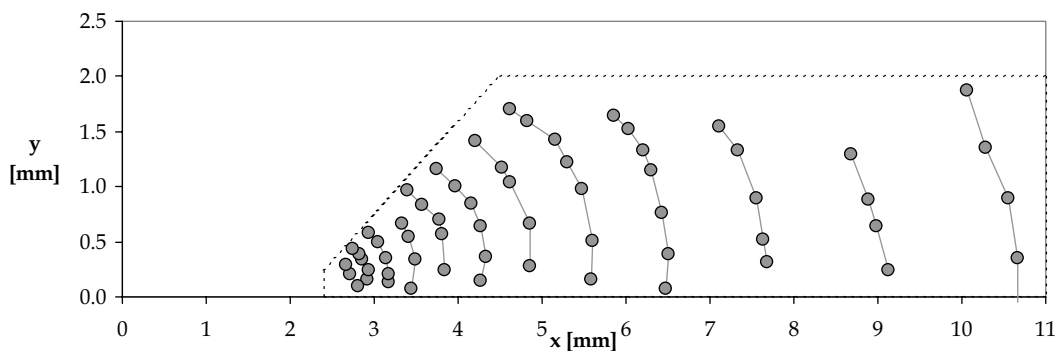
Figure D-84 TB 2012025-2 *SEM* crack measurements for right side of countersunk hole
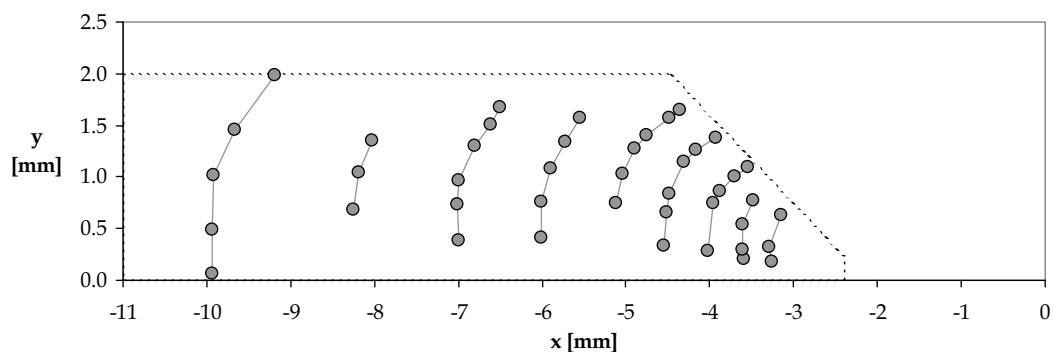
Figure D-85 TB 2012025-3 *SEM* crack measurements for left side of countersunk hole
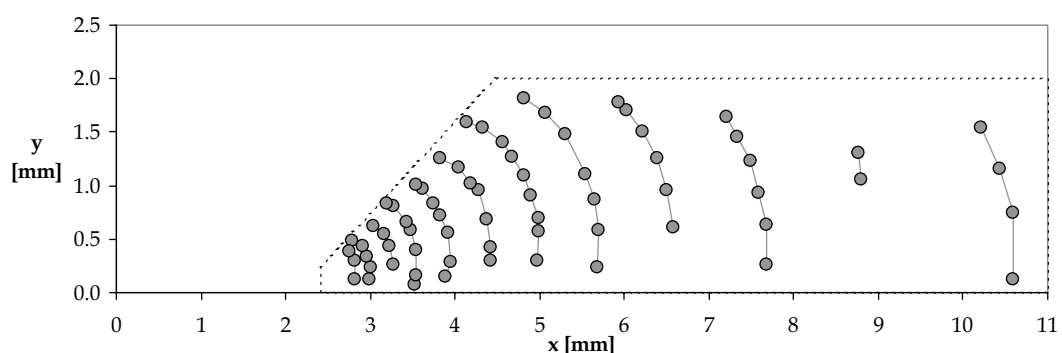

Figure D-86 TB 2012025-3 *SEM* crack measurements for right side of countersunk hole
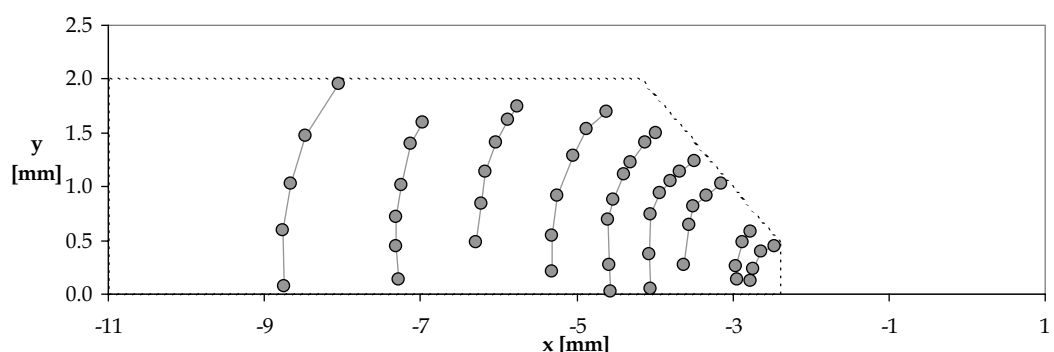

Figure D-87 TB 2012050-1 *SEM* crack measurements for left side of countersunk hole
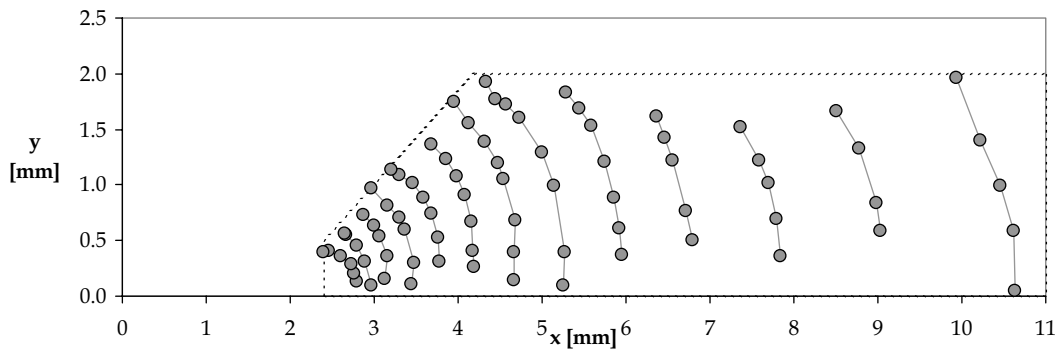
Figure D-88 TB 2012050-1 *SEM* **crack measurements for right side of countersunk hole**
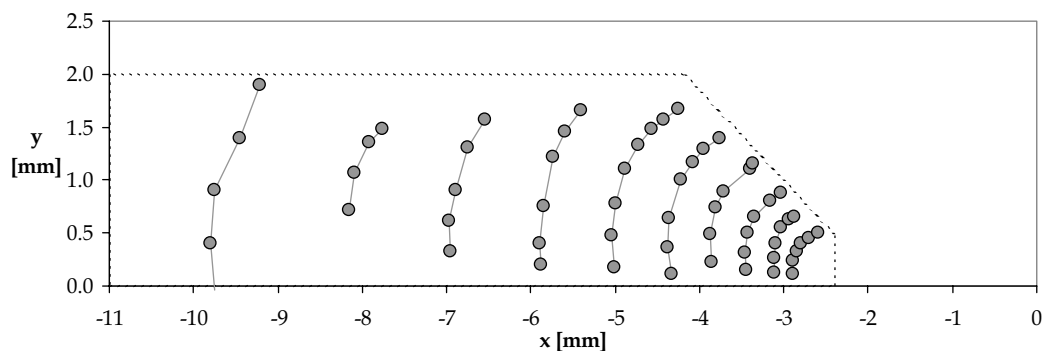
Figure D-89 TB 2012050-2 *SEM* **crack measurements for left side of countersunk hole**
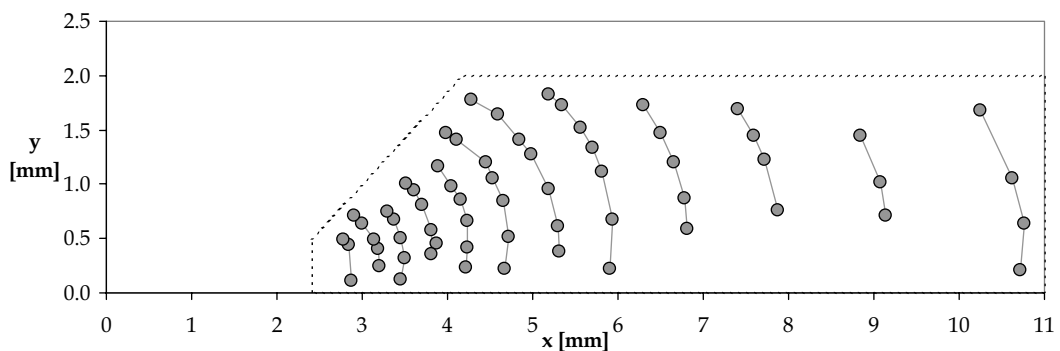
Figure D-90 TB 2012050-2 *SEM* **crack measurements for right side of countersunk hole**
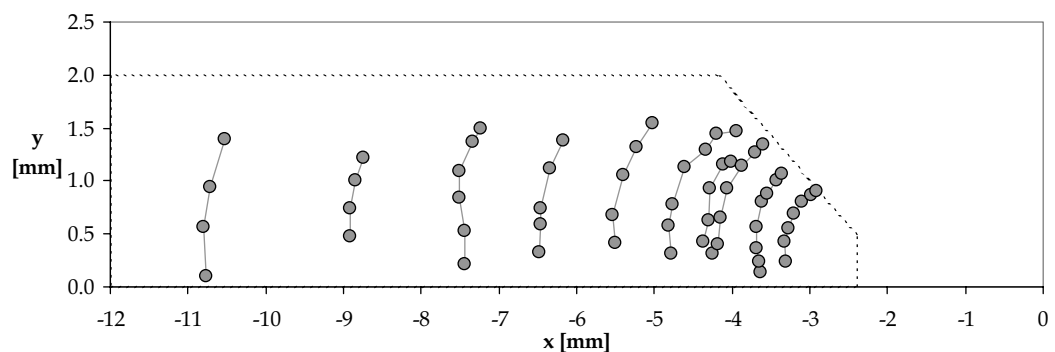
**Figure D-91 TB 20121050-3 *SEM* crack measurements for left side of countersunk hole**
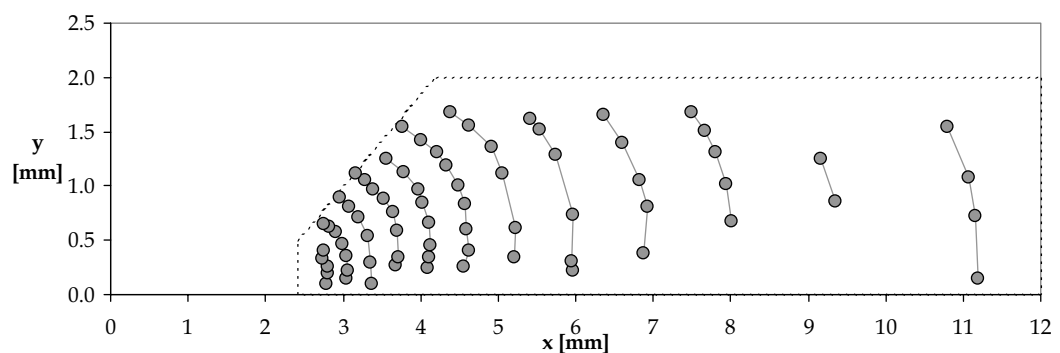
Figure D-92 TB 2012050-3 *SEM* crack measurements for right side of countersunk hole

E Lap-splice and butt joint specimens

A large number of lap-splice and butt joint specimens were used in this investigation. Most joints were used to obtain a variety of data; such as crack initiation, crack growth, residual strength and strain data. Strain data are required for validation of the neutral line model as described in Chapter 3. The strain data are used to calculate the stresses at several locations on the joints. Crack initiation, crack growth and residual strength data obtained through different tests are also used to validate the methods available for Glare.

Table E-1 shows the aluminum specimens with specific sheet thicknesses and the strain gage pattern used in the tests. Table E-2 contains the same information albeit for glare specimen. A variety of different thicknesses has been chosen to represent large fuselage joints and to have significant differences to validate the neutral line model.

Figure E-1 and Figure E-2 show the geometry of both the lap-splice and butt joints, Figure E-3 to Figure E-6 show the strain gage patterns used in the investigation.

Table E-1   **Specimen properties for test program of the aluminum specimens. Sheet material 2024-T3 clad**

Specimen[1]	Thickness [mm][2]	Strain gage pattern[3]
AL_LJ_25_20	$t_1 = 2.50$ $t_2 = 2.00$	Figure E-4
AL_LJ_40_64	$t_1 = 4.00$ $t_2 = 6.40$	Figure E-3
AL_BJ_20_20_20	$t_1 = 2.00$ $t_2 = 2.00$	Figure E-5
AL_BJ_40_40_40	$t_1 = 4.00$ $t_2 = 4.00$	Figure E-6
AL_LJ_B1	$t_1 = 7.00$ $t_2 = 4.50$	X
AL_LJ_B2	$t_1 = 2.00$ $t_2 = 2.40$	X
[1] Lap-splice joint dimensions → Figure E-1 Butt joint dimensions → Figure E-2 [2] For *BJ* specimens t_2 corresponds to the butt strap [3] Type: KYOWA KFG-2-120-C1-23, Gage length: 2.00 mm		

Table E-2   Specimen properties for test program glare specimens

Specimen[1]	Sheet material[2]	Thickness [mm]	Strain gage pattern[3]
GL_LJ_B1	$t_1 \rightarrow$ Glare 4A-8/7-0.5 $t_2 \rightarrow$ Glare 3-6/5-0.5	$t_1 = 6.625$ $t_2 = 4.25$	X
GL_LJ_B2	$t_1 \rightarrow$ Glare 3-4/3-0.3 $t_2 \rightarrow$ Glare 4B-4/3-0.3	$t_1 = 1.95$ $t_2 = 2.325$	X
GL_BJ_A1	$t_1 \rightarrow$ Glare 3-6/5-0.5 $t_2 \rightarrow$ Glare 2B-6/5-0.5 $t_3 \rightarrow$ Glare 3-6/5-0.5	$t_1 = 4.25$ $t_2 = 4.25$ $t_3 = 4.25$	Figure E-5
GL_BJ_A2	$t_1 \rightarrow$ Glare 3-8/7-0.3 $t_2 \rightarrow$ Glare 2B-8/7-0.3 $t_3 \rightarrow$ Glare 3-8/7-0.3	$t_1 = 4.15$ $t_2 = 4.15$ $t_3 = 4.15$	Figure E-5
GL_BJ_A3	$t_1 \rightarrow$ Glare 3-4/3-0.3 $t_2 \rightarrow$ Glare 2B-4/3-0.3 $t_3 \rightarrow$ Glare 3-4/3-0.3	$t_1 = 1.95$ $t_2 = 1.95$ $t_3 = 1.95$	X
GL_BJ_A4	$t_1 \rightarrow$ Glare 4A-5/4-0.5 $t_2 \rightarrow$ Glare 2B-6/5-0.5 $t_3 \rightarrow$ Glare 4A-5/4-0.5	$t_1 = 4.00$ $t_2 = 4.25$ $t_3 = 4.00$	Figure E-5
GL_BJ_A5	$t_1 \rightarrow$ Glare 4B-5/4-0.5 $t_2 \rightarrow$ Glare 2B-6/5-0.5 $t_3 \rightarrow$ Glare 4B-5/4-0.5	$t_1 = 4.00$ $t_2 = 4.25$ $t_3 = 4.00$	Figure E-5

[1] Lap-splice joint dimensions → Figure E-1
   Butt joint dimensions → Figure E-2
[2] For *BJ* specimens t_2 corresponds to the butt strap
[3] Type: KYOWA KFG-2-120-C1-23, Gage length: 2.00 mm
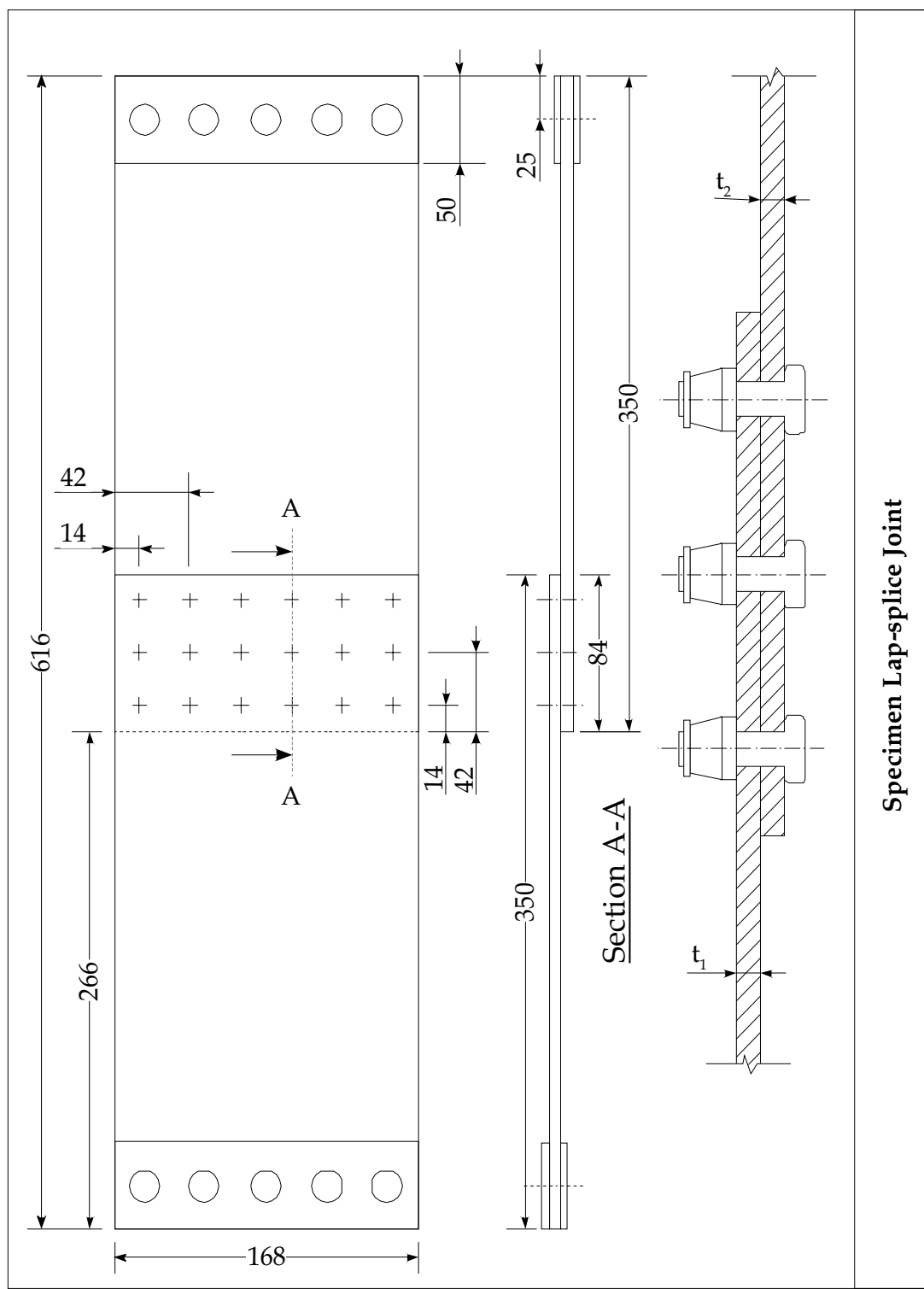
Figure E-1   Geometry of lap-splice joints
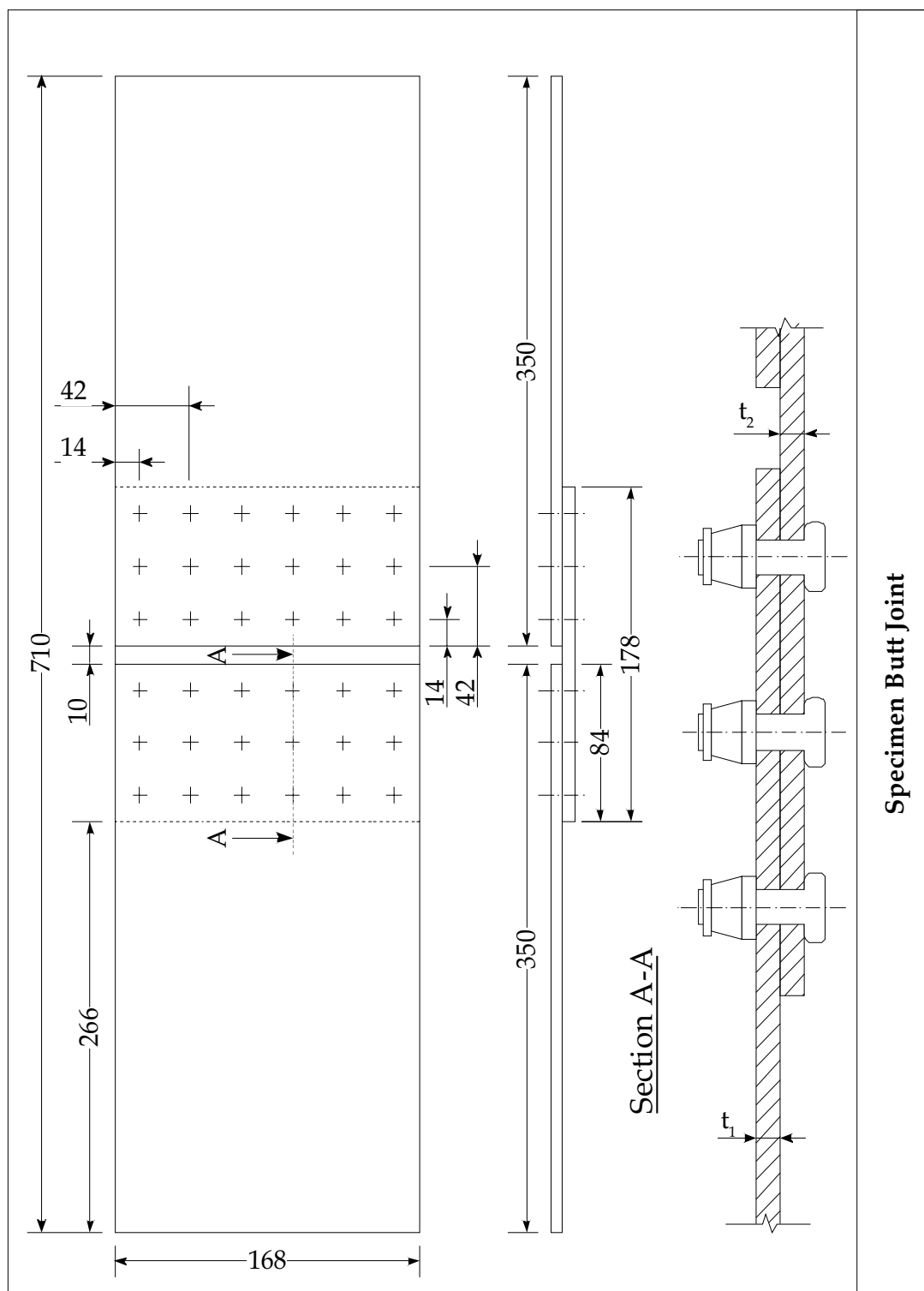
Figure E-2   Geometry of butt joints
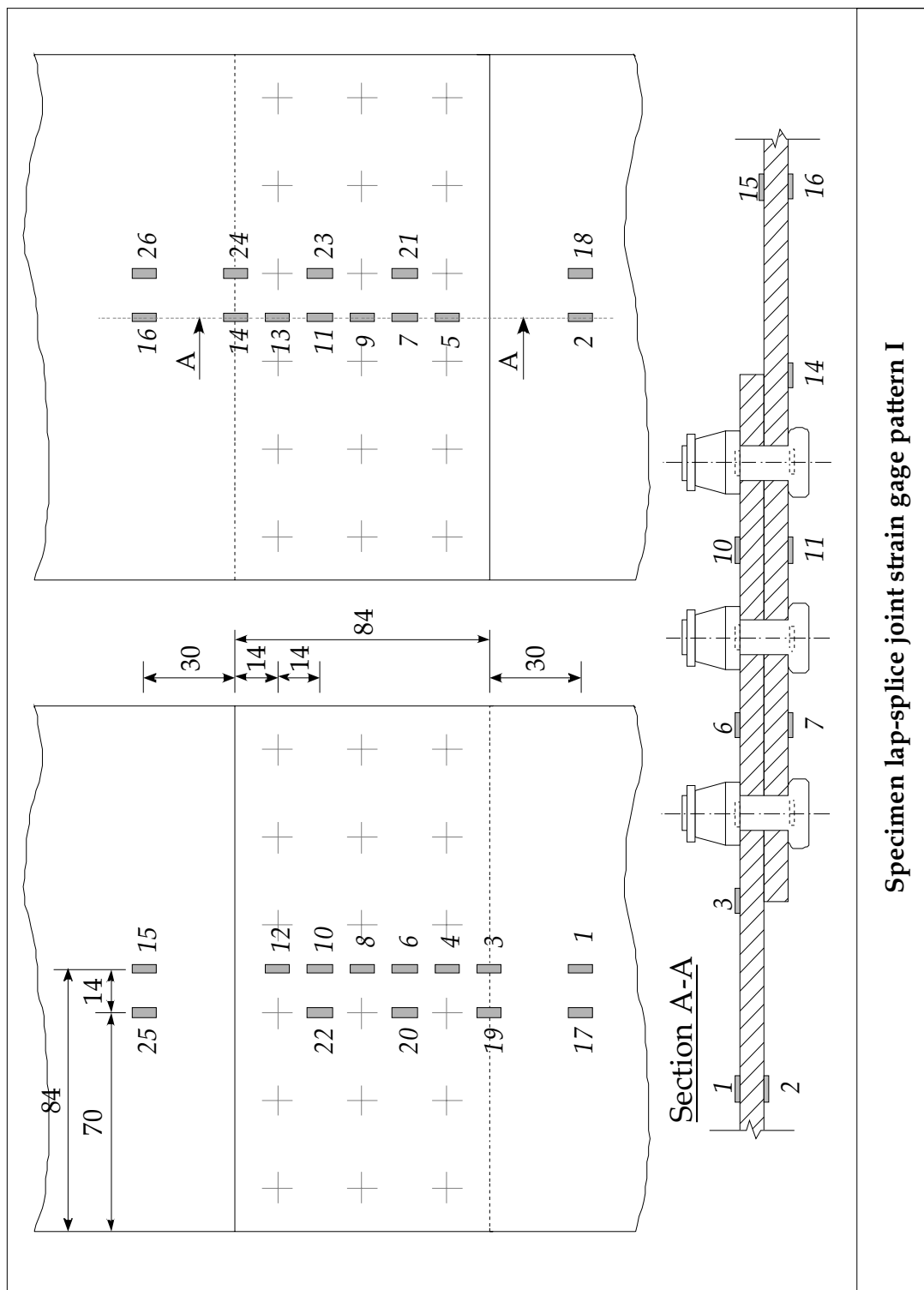
Figure E-3   Location of strain gage on lap-splice joints
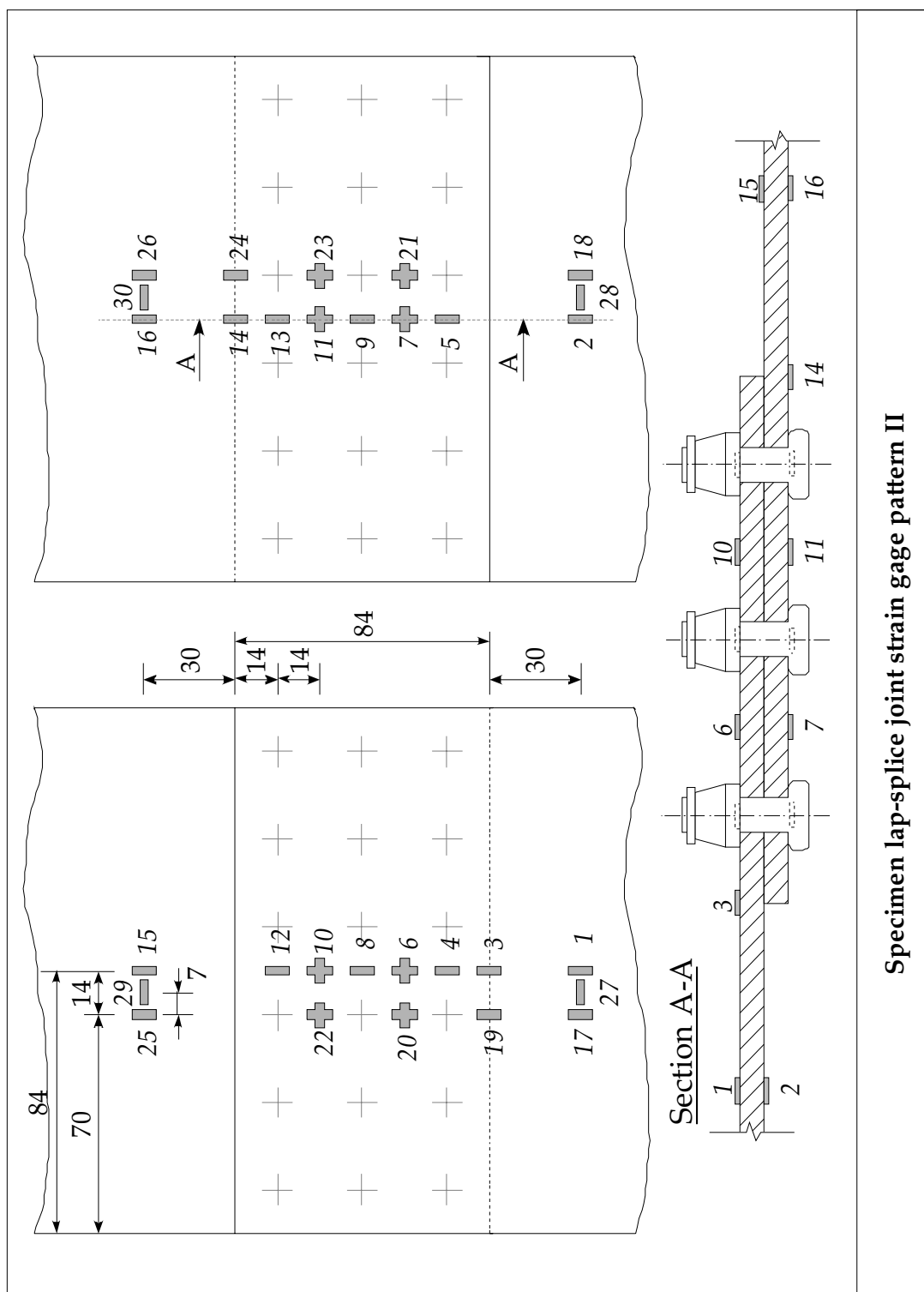
Figure E-4   Location of strain gage on lap-splice joints
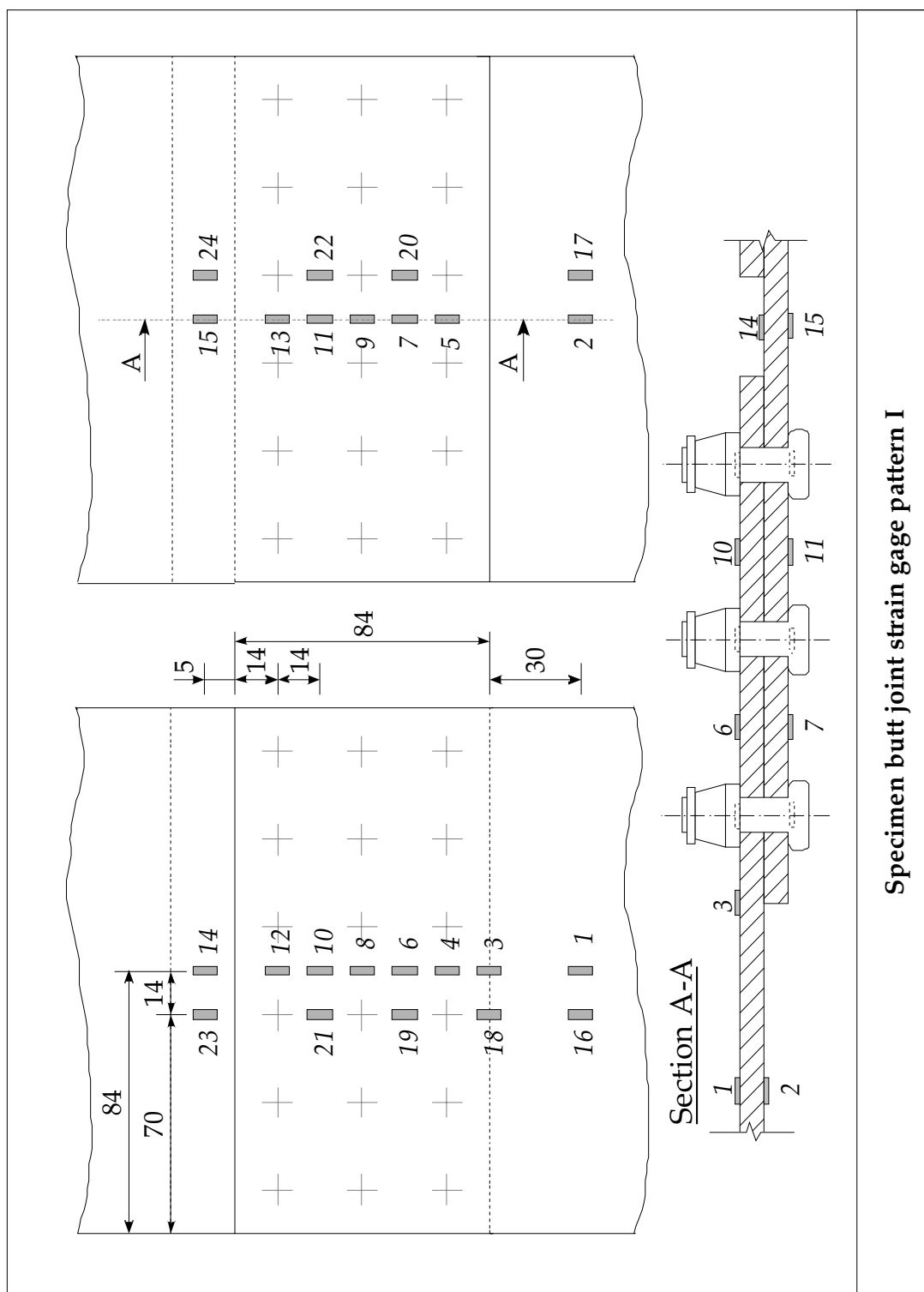
Figure E-5   Location of strain gage on butt joints
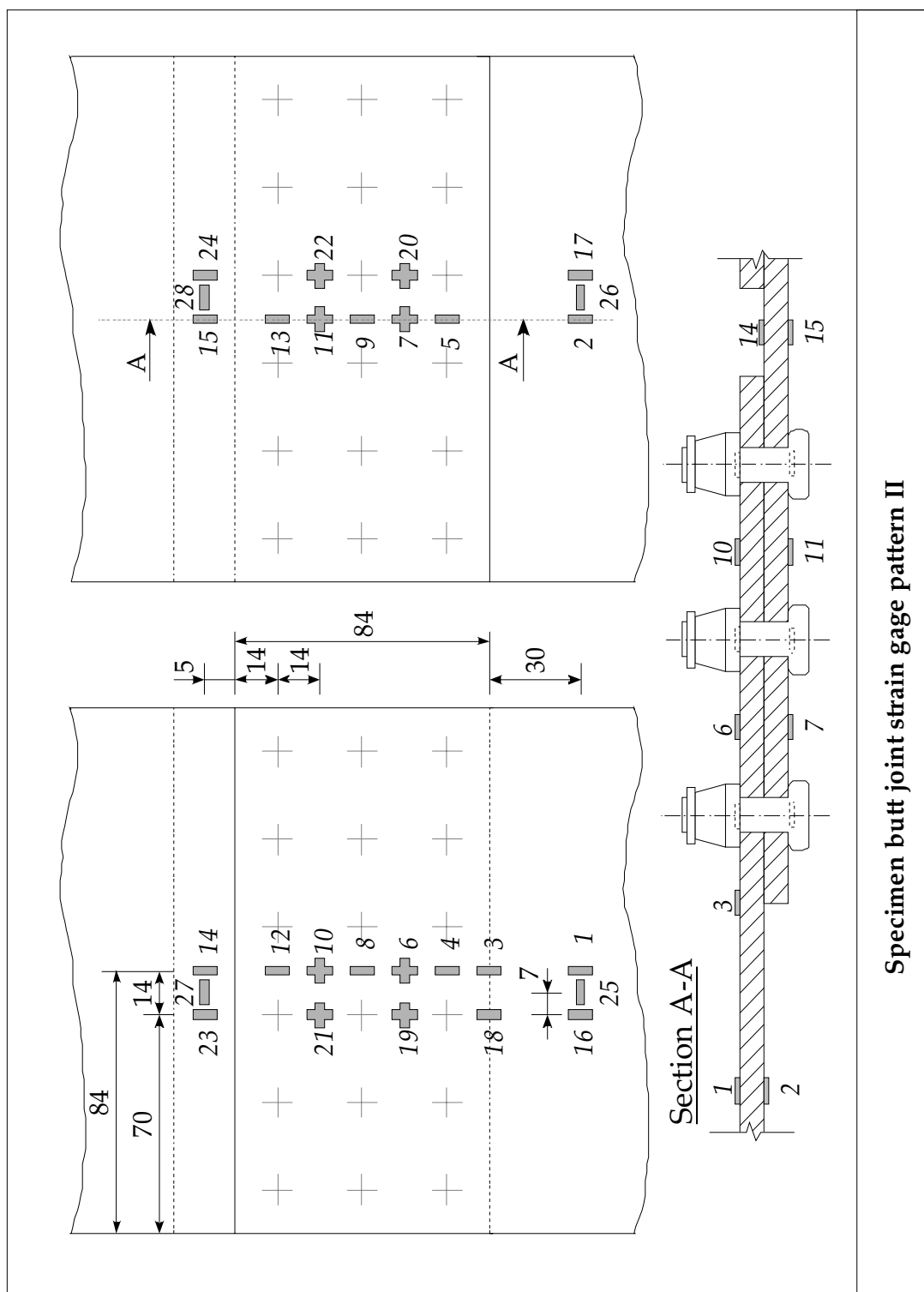
Figure E-6   Location of strain gage on butt joints

F Riveting data

F.1   Introduction

Several types of rivets were used in the investigation of Chapter 4; the different types described in section F.2. Four different standards are used; the *NAS* rivets are based on an American standard for rivets. The *DIN* and *LN* nomination for rivets indicates a German standard. The last standard is a Fokker standard. In section F.3 the results from the rivet head measurements are listed in the following tables. Table F-1 to Table F-13 present data obtained from the aluminum specimens. Table F-14 to Table F-22 contain data from the measurements on the Glare specimens. In section F.4 calculated and measured squeeze forces as a function of the protruding rivet head H_{ave} is shown in Table F-23 to Table F-44.

F.2   Rivet types

NAS 1097 *AD* x_d-xx_l (NAS 1097 *AD* 5-6)

        NAS   = National Aerospace Standard
        1097 = Reduced countersunk head rivet
        AD   = Material designation (*AD* = 2117-T3 aluminum alloy)
        x_d = Diameter code (D_0 = 5/32″)
        xx_l = Length code (L_0 = 6/16″)

LN 9198 x_d xx_l *C F*   (LN 9198 40 20 *C F*)

        LN   = Luft- und Raumfahrt norm
        9198 = Reduced countersunk head rivet
        C   = Material designation (2017*A* aluminum alloy)
        F   = Surface treatment
        x_d = Diameter code (D_0 = 40/10 mm)
        xx_l = Length code (L_0 = f(D_0))

MS20470 *D* x_d - xx_l (MS20470 *D* 6-10)

        MS   = Military Standard specification
        20470 = Universal head
        C   = Material designation (2017*A* aluminum alloy)
        F   = Surface treatment
        x_d = Diameter code (D_0 = 40/10 mm)
        xx_l = Length code (L_0 = f(D_0))

EN6101 D x_d - xx_l (6101D 7-10)

EN	= European norm
D	= Material designation (2017-T4 aluminum alloy)
x_d	= Diameter code (D_0 = 7/32")
xx_l	= Length code (L_0 = f(D_0))

F.3 Measurements of driven rivet heads

Three measurements of the driven rivet head were made at each load step, two measurements of the diameter and one of the height of the driven rivet head. The two measurements of the diameter are taken at an angle of 90°. This results in the average diameter D_{ave} in the third column.

Table F-1 Specimen A.1, 2024-T3 clad, t = 4.07 mm, NAS 1097 AD 5-6, D_0 = 3.96, H_0 = 5.45, H_0/D_0 = 1.38

A.1		
F_{sq} [kN]	D_{ave} [mm]	H_{ave} [mm]
0.00	3.96	5.46
5.00	4.22	4.48
7.50	4.68	3.63
10.00	5.16	2.97
12.50	5.58	2.56
15.00	5.96	2.23
17.50	6.21	2.04
20.00	6.43	1.91
22.50	6.65	1.73

Table F-2 Specimen A.2, 2024-T3 clad, t = 4.06 mm, NAS 1097 AD 6-7, D_0 = 4.76, H_0 = 7.02, H_0/D_0 = 1.48

A.2		
F_{sq} [kN]	D_{ave} [mm]	H_{ave} [mm]
0.00	4.76	7.02
5.00	4.94	6.42
10.00	5.74	4.89
15.00	6.65	3.69
20.00	7.27	3.08
25.00	7.72	2.70
30.00	8.11	2.38
35.00	8.41	2.13
40.00	8.70	1.89

Table F-3 Specimen A.3, 2024-T3 clad, t = 6.37 mm, EN 6101 D 7-10, D_0 = 5.52, H_0 = 9.86, H_0/D_0 = 1.79

A.3		
F_{sq} [kN]	D_{ave} [mm]	H_{ave} [mm]
0.00	5.52	9.79
10.00	6.09	7.80
20.00	7.79	4.96
25.00	8.37	4.29
30.00	8.87	3.81
35.00	9.25	3.51
40.00	9.58	3.23
45.00	9.90	2.98
49.00	10.13	2.83

Table F-4 Specimen A.4, 2024-T3 clad, t = 4.01 mm, NAS 1097 D 5-6, D_0 = 3.98, H_0 = 5.68, H_0/D_0 = 1.43

A.4		
F_{sq} [kN]	D_{ave} [mm]	H_{ave} [mm]
0.00	3.98	5.69
5.00	4.43	4.33
7.50	5.02	3.38
10.00	5.53	2.78
12.50	5.88	2.43
15.00	6.19	2.18
17.50	6.50	1.95
20.00	6.74	1.80
22.50	6.92	1.68

Table F-5 Specimen A.5, 2024-T3 clad, t = 4.01 mm, EN 6101 AD 5-6, D_0 = 4.01, H_0 = 4.18, H_0/D_0 = 1.04

A.5		
F_{sq} [kN]	D_{ave} [mm]	H_{ave} [mm]
0.00	4.01	4.24
5.00	4.29	3.60
7.50	4.62	3.05
10.00	5.10	2.50
12.50	5.55	2.11
15.00	5.90	1.89
17.50	6.16	1.69
20.00	6.35	1.59
22.50	6.53	1.44

Table F-6 Specimen A.6, 2024-T3 clad, t = 4.00 mm, EN 6101 AD 5-5, D_0 = 4.01, H_0 = 5.3, H_0/D_0 = 1.32

A.6		
F_{sq} [kN]	D_{ave} [mm]	H_{ave} [mm]
0.00	4.01	5.36
5.00	4.25	4.64
7.50	4.69	3.85
10.00	5.27	3.08
12.50	5.73	2.64
15.00	6.11	2.28
17.50	6.40	2.07
20.00	6.63	1.90
22.50	6.85	1.77

Table F-7 Specimen A.7, 2024-T3 clad, t = 4.02 mm, EN 6101 D 5-6-5, D_0 = 3.95, H_0 = 6.11, H_0/D_0 = 1.55

A.7		
F_{sq} [kN]	D_{ave} [mm]	H_{ave} [mm]
0.00	3.95	6.09
5.00	4.37	4.64
7.50	5.07	3.50
10.00	5.56	2.90
12.50	5.94	2.51
15.00	6.30	2.22
17.50	6.58	2.02
20.00	6.75	1.90
22.50	6.98	1.76

Table F-8 Specimen A.8, 2024-T3 clad, t = 4.00 mm, MS20470 AD 5-5-5, D_0 = 3.95, H_0 = 5.11, H_0/D_0 = 1.29

A.8		
F_{sq} [kN]	D_{ave} [mm]	H_{ave} [mm]
0.00	3.95	5.17
5.00	4.20	4.16
7.50	4.66	3.52
10.00	5.21	2.82
12.50	5.65	2.38
15.00	6.02	2.14
17.50	6.32	1.88
20.00	6.55	1.77
22.50	6.77	1.66

Table F-9 Specimen A.9, 2024-T3 clad, t = 4.01 mm, EN 6101 D 6-7, D_0 = 4.78, H_0 = 7.10, H_0/D_0 = 1.48

A.9		
F_{sq} [kN]	D_{ave} [mm]	H_{ave} [mm]
0.00	4.78	7.07
5.00	4.96	6.42
10.00	5.97	4.67
15.00	6.84	3.49
20.00	7.45	2.91
25.00	7.91	2.54
30.00	8.31	2.24
35.00	8.63	2.00
40.00	8.90	1.72

Table F-10 Specimen A.10, 2024-T3 clad, t = 4.01 mm, EN 6101 AD 6-7, D_0 = 4.79, H_0 = 7.01, H_0/D_0 = 1.46

A.10		
F_{sq} [kN]	D_{ave} [mm]	H_{ave} [mm]
0.00	4.79	7.06
5.00	2.44	3.37
10.00	5.50	5.47
15.00	6.49	4.03
20.00	7.23	3.18
25.00	7.74	2.76
30.00	8.16	2.45
35.00	8.52	2.13
40.00	8.83	1.91

Table F-11 Specimen A.11, 2024-T3 clad, t = 4.01 mm, NAS 1097 *AD* 6-7, D_0 = 4.78, H_0 = 7.00, H_0/D_0 = 1.46

A.11		
F_{sq} [kN]	D_{ave} [mm]	H_{ave} [mm]
0.00	4.78	7.05
5.00	4.88	6.62
10.00	5.57	5.14
15.00	6.50	3.87
20.00	7.18	3.11
25.00	7.69	2.69
30.00	8.14	2.38
35.00	8.46	2.14
40.00	8.75	1.97

Table F-12 Specimen A.12, 2024-T3 clad, t = 4.04 mm, EN 6101 *AD* 6-5-5, D_0 = 4.79, H_0 = 5.27, H_0/D_0 = 1.1

A.12		
F_{sq} [kN]	D_{ave} [mm]	H_{ave} [mm]
0.00	4.79	5.23
5.00	4.88	5.01
10.00	5.42	4.10
15.00	6.26	3.11
20.00	6.95	2.50
25.00	7.42	2.16
30.00	7.79	1.87
35.00	8.09	1.60
40.00	8.28	1.41

Table F-13 Specimen A.13, 2024-T3 clad, t = 4.00 mm, MS20470 *AD* 6-6-5, D_0 = 4.75, H_0 = 6.08, H_0/D_0 = 1.28

A.13		
F_{sq} [kN]	D_{ave} [mm]	H_{ave} [mm]
0.00	4.75	6.08
5.00	4.85	5.54
10.00	5.44	4.47
15.00	6.35	3.32
20.00	7.05	2.53
25.00	7.53	2.28
30.00	7.92	2.07
35.00	8.28	1.89
40.00	8.55	1.71

Table F-14 Specimen G.1, Glare 3-3/2-0.3, t = 2.80 mm, MS20470 *D* 6-6-5, D_0 = 4.75, H_0 = 6.95, H_0/D_0 = 1.46

G.1		
F_{sq} [kN]	D_{ave} [mm]	H_{ave} [mm]
0.00	4.75	7.13
5.00	4.94	7.14
10.00	5.82	5.08
15.00	6.71	3.96
20.00	7.38	3.31
25.00	7.85	2.85
30.00	8.11	2.21
35.00	8.59	1.97
40.00	9.04	

Table F-15 Specimen G.2, Glare 3-6/5-0.4, t = 7.30 mm, MS20470 *D* 6-8, D_0 = 4.75, H_0 = 5.47, H_0/D_0 = 1.15

G.2		
F_{sq} [kN]	D_{ave} [mm]	H_{ave} [mm]
0.00	4.75	5.55
5.00	4.94	4.71
10.00	5.75	3.50
15.00	6.51	2.72
20.00	7.01	2.26
25.00	7.41	1.99
30.00	7.74	1.71
35.00	8.04	1.60
40.00	8.30	1.35

Table F-16 Specimen G.3, Glare 3-6/5-0.4, t = 7.30 mm, MS20470 *D* 6-10, D_0 = 4.75, H_0 = 8.56, H_0/D_0 = 1.80

G.3		
F_{sq} [kN]	D_{ave} [mm]	H_{ave} [mm]
0.00	4.75	8.65
5.00	4.93	7.59
10.00	5.78	5.77
15.00	6.74	4.21
20.00	7.42	3.46
25.00	7.93	2.95
30.00	8.37	2.57
35.00	8.70	2.37
40.00	8.96	2.24

Table F-17 Specimen G.4, Glare 3-8/7-0.5, $t = 11.50$ mm, MS20470 D 6-10, $D_0 = 4.76$, $H_0 = 4.27$, $H_0/D_0 = 0.90$

G.4		
F_{sq} [kN]	D_{ave} [mm]	H_{ave} [mm]
0.00	4.76	4.44
5.00	4.92	3.32
10.00	5.65	2.40
15.00	6.26	1.99
20.00	6.69	1.65
25.00	7.02	1.40
30.00	7.33	1.26
35.00	7.56	1.01
40.00	7.78	0.82

Table F-18 Specimen G.5, Glare 3-8/7-0.5, $t = 11.50$ mm, MS20470 D 6-12-5, $D_0 = 4.75$, $H_0 = 8.21$, $H_0/D_0 = 1.73$

G.5		
F_{sq} [kN]	D_{ave} [mm]	H_{ave} [mm]
0.00	4.75	8.37
5.00	4.91	7.10
10.00	5.83	4.92
15.00	6.83	3.79
20.00	7.56	3.01
25.00	8.02	2.64
30.00	8.43	2.34
35.00	8.66	1.96
40.00	9.03	1.96

Table F-19 Specimen G.6, Glare 4B-3/2-0.3, $t = 11.50$ mm, EN 6101 D 7-9, $D_0 = 5.56$, $H_0 = 9.68$, $H_0/D_0 = 1.74$

G.6		
F_{sq} [kN]	D_{ave} [mm]	H_{ave} [mm]
0.00	5.56	9.68
10.00	6.12	8.11
20.00	7.84	5.10
25.00	8.46	4.30
30.00	8.96	3.80
35.00	9.36	3.42
40.00	9.70	3.14
45.00	10.01	2.85
49.00	10.21	2.69

Table F-20 Specimen G.7, Glare 3-3/2-0.3, $t = 3.04$ mm, EN 6101 D 7-8, $D_0 = 5.56$, $H_0 = 10.13$, $H_0/D_0 = 1.82$

G.7		
F_{sq} [kN]	D_{ave} [mm]	H_{ave} [mm]
0.00	5.56	10.05
10.00	6.15	8.37
20.00	7.84	5.33
25.00	8.48	4.53
30.00	8.97	3.98
35.00	9.39	3.61
40.00	9.76	3.26
45.00	10.06	2.97
49.00	10.29	2.71

Table F-21 Specimen G.8, Glare 3-6/5-0.4, $t = 7.39$ mm, EN 6101 D 7-8, $D_0 = 5.56$, $H_0 = 5.69$, $H_0/D_0 = 1.02$

G.8		
F_{sq} [kN]	D_{ave} [mm]	H_{ave} [mm]
0.00	5.56	5.69
10.00	6.16	4.46
20.00	7.50	2.96
25.00	7.94	2.63
30.00	8.33	2.31
35.00	8.65	2.15
40.00	8.91	1.93
45.00	9.10	1.77
49.00	9.31	1.63

Table F-22 Specimen G.9, Glare 4B-6/5-0.5, $t = 10.17$ mm, EN 6101 D 7-10, $D_0 = 5.56$, $H_0 = 5.91$, $H_0/D_0 = 1.07$

G.9		
F_{sq} [kN]	D_{ave} [mm]	H_{ave} [mm]
0.00	5.56	5.89
10.00	6.09	4.42
20.00	7.38	2.95
25.00	7.84	2.63
30.00	8.18	2.35
35.00	8.47	2.10
40.00	8.72	1.91
45.00	8.96	1.71
49.00	9.11	1.52

F.4 Calculated squeeze force

Table F-23 to Table F-44 show the results of all the measured rivet height H vs. rivet squeeze force F_{sq} and the calculated squeeze force $F_{sq\ calc}$. All results compare well within 0 - 10% with the exception of specimens G.2, G.4, G.8 and G.9, for these specimens the difference between the measured data and calculated values differ up to 25%.

Table F-23 Results of measured forces and Eqn. (4-9)

A.1		
H_{ave} [mm]	F_{sq} [kN]	$F_{sq\ calc}$ [kN]
5.46	0.00	0.00
4.48	5.00	5.17
3.63	7.50	7.89
2.97	10.00	10.80
2.56	12.50	13.49
2.23	15.00	16.17
2.04	17.50	18.07
1.91	20.00	19.76
1.73	22.50	21.73

Table F-24 Results of measured forces and Eqn. (4-9)

A.2		
H_{ave} [mm]	F_{sq} [kN]	$F_{sq\ calc}$ [kN]
7.02	0.00	0.00
6.42	5.00	3.88
4.89	10.00	9.84
3.69	15.00	17.09
3.08	20.00	22.80
2.70	25.00	27.49
2.38	30.00	32.15
2.13	35.00	36.03
1.89	40.00	40.31

Table F-25 Results of measured forces and Eqn. (4-9)

A.3		
H_{ave} [mm]	F_{sq} [kN]	$F_{sq\ calc}$ [kN]
9.79	0.00	0.00
7.80	10.00	8.99
4.96	20.00	24.02
4.29	25.00	30.29
3.81	30.00	36.14
3.51	35.00	40.76
3.23	40.00	45.28
2.98	45.00	49.88
2.83	49.00	53.29

Table F-26 Results of measured forces and Eqn. (4-9)

A.4		
H_{ave} [mm]	F_{sq} [kN]	$F_{sq\ calc}$ [kN]
5.69	0.00	0.00
4.33	5.00	5.15
3.38	7.50	8.87
2.78	10.00	12.42
2.43	12.50	15.15
2.18	15.00	17.72
1.95	17.50	20.50
1.80	20.00	22.77
1.68	22.50	24.69

Table F-27   Results of measured forces and Eqn. (4-9)

A.5		
H_{ave} [mm]	F_{sq} [kN]	$F_{sq\ calc}$ [kN]
4.24	0.00	0.00
3.60	5.00	5.07
3.05	7.50	7.21
2.50	10.00	10.15
2.11	12.50	13.05
1.89	15.00	15.37
1.69	17.50	17.44
1.59	20.00	18.90
1.44	22.50	20.59

Table F-28   Results of measured forces and Eqn. (4-9)

A.6		
H_{ave} [mm]	F_{sq} [kN]	$F_{sq\ calc}$ [kN]
5.36	0.00	0.00
4.64	5.00	4.77
3.85	7.50	7.42
3.08	10.00	10.94
2.64	12.50	13.93
2.28	15.00	16.78
2.07	17.50	19.03
1.90	20.00	20.96
1.77	22.50	22.84

Table F-29   Results of measured forces and Eqn. (4-9)

A.7		
H_{ave} [mm]	F_{sq} [kN]	$F_{sq\ calc}$ [kN]
6.09	0.00	0.00
4.64	5.00	5.01
3.50	7.50	9.29
2.90	10.00	12.73
2.51	12.50	15.74
2.22	15.00	18.82
2.02	17.50	21.28
1.90	20.00	22.96
1.76	22.50	25.35

Table F-30   Results of measured forces and Eqn. (4-9)

A.8		
H_{ave} [mm]	F_{sq} [kN]	$F_{sq\ calc}$ [kN]
5.17	0.00	0.00
4.16	5.00	5.26
3.52	7.50	7.68
2.82	10.00	11.00
2.38	12.50	13.93
2.14	15.00	16.42
1.88	17.50	18.86
1.77	20.00	20.67
1.66	22.50	22.44

Table F-31   Results of measured forces and Eqn. (4-9)

A.9		
H_{ave} [mm]	F_{sq} [kN]	$F_{sq\ calc}$ [kN]
7.07	0.00	0.00
6.42	5.00	4.03
4.67	10.00	11.27
3.49	15.00	18.84
2.91	20.00	24.80
2.54	25.00	29.77
2.24	30.00	34.69
2.00	35.00	38.93
1.72	40.00	43.62

Table F-32   Results of measured forces and Eqn. (4-9)

A.10		
H_{ave} [mm]	F_{sq} [kN]	$F_{sq\ calc}$ [kN]
7.06	0.00	0.00
3.37	5.00	2.56
5.47	10.00	9.46
4.03	15.00	16.67
3.18	20.00	23.03
2.76	25.00	27.67
2.45	30.00	31.91
2.13	35.00	36.11
1.91	40.00	39.84

Table F-33 Results of measured forces and Eqn. (4-9)

A.11		
H_{ave} [mm]	F_{sq} [kN]	$F_{sq\,calc}$ [kN]
7.05	0.00	0.00
6.62	5.00	4.89
5.14	10.00	10.35
3.87	15.00	17.09
3.11	20.00	22.84
2.69	25.00	27.57
2.38	30.00	32.04
2.14	35.00	35.55
1.97	40.00	38.76

Table F-34 Results of measured forces and Eqn. (4-9)

A.12		
H_{ave} [mm]	F_{sq} [kN]	$F_{sq\,calc}$ [kN]
5.23	0.00	0.00
5.01	5.00	4.33
4.10	10.00	9.04
3.11	15.00	15.17
2.50	20.00	20.79
2.16	25.00	24.96
1.87	30.00	28.84
1.60	35.00	32.44
1.41	40.00	35.08

Table F-35 Results of measured forces and Eqn. (4-9)

A.13		
H_{ave} [mm]	F_{sq} [kN]	$F_{sq\,calc}$ [kN]
6.08	0.00	0.00
5.54	5.00	5.44
4.47	10.00	9.80
3.32	15.00	16.35
2.53	20.00	22.52
2.28	25.00	26.58
2.07	30.00	30.19
1.89	35.00	33.90
1.71	40.00	37.00

Table F-36 Results of measured forces and Eqn. (4-9)

G.1		
H_{ave} [mm]	F_{sq} [kN]	$F_{sq\,calc}$ [kN]
7.13	0.00	0.00
7.14	5.00	0.00
5.08	10.00	10.57
3.96	15.00	16.58
3.31	20.00	21.75
2.85	25.00	25.97
2.21	30.00	29.77
1.97	35.00	34.40

Table F-37 Results of measured forces and Eqn. (4-9)

G.2		
H_{ave} [mm]	F_{sq} [kN]	$F_{sq\,calc}$ [kN]
5.55	0.00	0.00
4.71	5.00	6.13
3.50	10.00	11.33
2.72	15.00	16.55
2.26	20.00	20.54
1.99	25.00	23.88
1.71	30.00	27.16
1.60	35.00	29.80
1.35	40.00	33.00

Table F-38 Results of measured forces and Eqn. (4-9)

G.3		
H_{ave} [mm]	F_{sq} [kN]	$F_{sq\,calc}$ [kN]
8.65	0.00	0.00
7.59	5.00	5.70
5.77	10.00	10.99
4.21	15.00	17.78
3.46	20.00	23.19
2.95	25.00	27.77
2.57	30.00	32.05
2.37	35.00	35.33
2.24	40.00	38.00

Table F-39 Results of measured forces and Eqn. (4-9)

G.4		
H_{ave} [mm]	F_{sq} [kN]	$F_{sq\ calc}$ [kN]
4.44	0.00	0.00
3.32	5.00	7.23
2.40	10.00	11.94
1.99	15.00	15.85
1.65	20.00	19.27
1.40	25.00	22.23
1.26	30.00	24.84
1.01	35.00	27.82
0.82	40.00	30.61

Table F-40 Results of measured forces and Eqn. (4-9)

G.5		
H_{ave} [mm]	F_{sq} [kN]	$F_{sq\ calc}$ [kN]
8.37	0.00	0.00
7.10	5.00	6.06
4.92	10.00	12.12
3.79	15.00	18.81
3.01	20.00	24.87
2.64	25.00	29.02
2.34	30.00	33.03
1.96	35.00	36.21
1.96	40.00	39.37

Table F-41 Results of measured forces and Eqn. (4-9)

G.6		
H_{ave} [mm]	F_{sq} [kN]	$F_{sq\ calc}$ [kN]
9.68	0.00	0.00
8.11	10.00	9.61
5.10	20.00	23.23
4.30	25.00	29.01
3.80	30.00	33.95
3.42	35.00	38.31
3.14	40.00	42.09
2.85	45.00	45.97
2.69	49.00	48.52

Table F-42 Results of measured forces and Eqn. (4-9)

G.7		
H_{ave} [mm]	F_{sq} [kN]	$F_{sq\ calc}$ [kN]
10.05	0.00	0.00
8.37	10.00	9.82
5.33	20.00	23.15
4.53	25.00	28.99
3.98	30.00	33.98
3.61	35.00	38.35
3.26	40.00	42.63
2.97	45.00	46.34
2.71	49.00	49.58

Table F-43 Results of measured forces and Eqn. (4-9)

G.8		
H_{ave} [mm]	F_{sq} [kN]	$F_{sq\ calc}$ [kN]
5.69	0.00	0.00
4.46	10.00	10.74
2.96	20.00	21.39
2.63	25.00	25.17
2.31	30.00	29.04
2.15	35.00	32.07
1.93	40.00	35.14
1.77	45.00	37.48
1.63	49.00	40.02

Table F-44 Results of measured forces and Eqn. (4-9)

G.9		
H_{ave} [mm]	F_{sq} [kN]	$F_{sq\ calc}$ [kN]
5.89	0.00	0.00
4.42	10.00	11.03
2.95	20.00	21.08
2.63	25.00	24.88
2.35	30.00	28.15
2.10	35.00	31.27
1.91	40.00	34.03
1.71	45.00	37.01
1.52	49.00	39.27

G Experimental results Glare joints

G.1 Introduction

In the following two sections a short summary of the experiments done by both the *NLR* and Delft University of Technology are presented. All crack initiation tests and evaluation of those tests was done at the *NLR*. With the results from those tests the crack growth tests and evaluation is done at Delft University of Technology.

G.2 Crack initiation

The initiation life is normally defined as the number of cycles at which there is a transition from micro cracking to macro cracking. For fiber metal laminates, the crack initiation is also based on the presence of the prepreg layers and the detectability of cracks using non-destructive investigations. Since the point of transition is difficult to determine a crack length that could easily be established by eddy-current is chosen; $a_I = 1.00$ mm. The results of the crack initiation program run by the *NLR* are shown in Table G-1 to Table G-7. For each specimen, if available, the maximum applied stress, the number of cycles and the number of detected initiation cracks in the specimens. For Table G-1, the number of cracks in the upper sheet is two with a length between 1.0 and 2.0 mm.

Table G-1   **Results of butt joint series GL_BJ_A1, with Glare 3-6/5-0.5 sheets and Glare 2B-6/5-0.5 butt strap. Only cracks at the four inner Hi-loks are considered, all cracks initiated close or in the smallest net-section area between the fasteners. The inner Hi-loks are torqued with 1.7 – 1.8 Nm**

Specimen	σ_{max} [MPa]	N [kCycles]	Cracks at 4 inner Hi-Loks							
			Upper sheet		Lower sheet		Upper butt strap		Lower butt strap	
			Number	Length [mm]	Number	Length [mm]	Number	Length [mm]	Number	Length [mm]
A1-f	70	20	2	1.0 - 2.0	2	1.0 - 1.5	7	1.0 - 3.0	7	1.0 - 3.0
A1-h										
A1-c	60	30	0		1	1.0	0		1	1.0
A1-d		40	0		1	3.0	6	1.0 - 1.5	7	2.0 - 3.0
A1-d		35	2	1.5	0		4	1.0 - 1.5	5	1.0 - 2.5
A1-g	50	65	0		1	1.2	7	1.0 - 4.5	8	2.0 - 4.0
A1-i		50	1	2.0	1	1.2	3	1.2 - 1.5	1	2.0

Table G-2   **Results of butt joint series GL_BJ_A2, with Glare 3-8/7-0.3 sheets and Glare 2B-8/7-0.3 butt strap. Only cracks at the four inner Hi-loks are considered, all cracks initiated close or in the smallest net-section area between the fasteners. The inner Hi-loks are torqued with 1.7 – 1.8 Nm**

Specimen	σ_{max} [MPa]	N [kCycles]	Cracks at 4 inner Hi-Loks							
			Upper sheet		Lower sheet		Upper butt strap		Lower butt strap	
			Number	Length [mm]	Number	Length [mm]	Number	Length [mm]	Number	Length [mm]
A2-c	70	20	8	1.0 - 2.5	7	1.5 - 2.5	8	1.5 - 2.5	8	1.0 - 2.0
A2-e		15	5	1.0 - 2.0	4	1.0 - 1.5	6	1.0 - 1.5	7	1.0 - 2.0
A2-a	60	40	4	2.0 - 3.0	5	1.8 - 2.0	7	1.5 - 2.0	8	1.0 - 3.0
A2-b		35	6	1.0 - 2.0	7	1.0 - 2.0	8	1.5 - 2.5	7	1.0 - 2.0
A2-d	50	60	2	1.0 - 3.0	6	1.0 - 2.0	6	1.5 - 3.0	6	1.0 - 2.5
A2-f		55	4	1.0 - 2.0	4	1.0 - 2.5	7	1.0 - 2.0	8	1.0 - 2.0
A2-g	40	80	1	1.0	0	-	3	1.0 - 2.0	5	1.0 - 2.0
A2-h		80	1	1.5	1	1.0	5	1.0 - 2.0	4	1.0 - 3.0

Table G-3   **Results of butt joint series GL_BJ_A3, with Glare 3-4/3-0.3 sheets and Glare 2B-4/3-0.3 butt strap. Only cracks at the four inner Hi-loks are considered. The inner Hi-loks are torqued with 2.2 – 2.3 Nm. Combination of cracks initiating at the bore of the hole or away from the hole. [1] Initiation away from the hole**

Specimen	σ_{max} [MPa]	N [kCycles]	Cracks at 4 inner Hi-Loks							
			Upper sheet		Lower sheet		Upper butt strap		Lower butt strap	
			Number	Length [mm]	Number	Length [mm]	Number	Length [mm]	Number	Length [mm]
A3-a	120	24	2	1.0 - 1.3	4	1.0 - 1.3	0		0	
A3-b		21	3	1.0 - 1.5	5	1.0 - 2.2	0		0	
A3-g		27	1 [1]	1.0	6	1.0 - 1.8	1 [1]	1.15	0	
A3-c	100	40	3	1.0 - 1.5	1	1.3	0		0	
A3-d		50	3	1.0 - 1.75	4	1.7 - 2.1	0		0	
A3-h		55	1 - 4 [1]	1.15 - 2.1	2 [1]	1.5 - 2.0	2 [1]	1.2 - 1.35	0	
A3-e	90	65	6	1.4 - 1.78	7	1.14 - 1.75	0		0	
A3-f		65	1	1	5	2.0 - 2.2	0		0	
A3-i		72	1 - 1 [1]	1.4 - 2.0	3	1.25 - 1.5	0		0	

Table G-4   **Results of butt joint series GL_BJ_A4, with Glare 4A-6/5-0.5 T-L sheets and Glare 2B-6/5-0.5 butt strap. Only cracks at the four inner Hi-loks are considered, all cracks initiated close or in the smallest net-section area between the fasteners. The inner Hi-loks are torqued with 1.7 – 1.8 Nm**

Specimen	σ_{max} [MPa]	N [kCycles]	Cracks at 4 inner Hi-Loks							
			Upper sheet		Lower sheet		Upper butt strap		Lower butt strap	
			Number	Length [mm]	Number	Length [mm]	Number	Length [mm]	Number	Length [mm]
A4-b	70	16	4	1.5 - 2.0	2	1.5	3	1.0 - 1.5	3	1.5
A4-e		18	1	2.0	1	1.5	3	1.0 - 1.5	1	1.5
A4-a	60	35	2	1.5	3	2.0 - 2.5	2	2.0 - 2.5	5	1.5 - 2.0
A4-f		30	0		1	1.0	1	1.0	0	
A4-i		33	2	1.5 - 2.5	1	1.0	2	1.0	0	
A4-c	50	50	0		0		4	1.0 - 2.0	1	1.5
A4-g		50	0		2	1.0 - 1.5	1	1.0	2	1.0 - 1.5
A4-d	40	80	0		1	1.0	2	1.0 - 1.5	3	1.0 - 1.5
A4-h		80	0		1	1.5	1	2.0	2	2.0

Table G-5 Results of butt joint series GL_BJ_A5, with Glare 4B-6/5-0.5 T-L sheets and Glare 2B-6/5-0.5 butt strap. Only cracks at the four inner Hi-loks are considered, all cracks initiated close or in the smallest net-section area between the fasteners. The inner Hi-loks are torqued with 1.7 – 1.8 Nm

Specimen	σ_{max} [MPa]	N [kCycles]	Cracks at 4 inner Hi-Loks							
			Upper sheet		Lower sheet		Upper butt strap		Lower butt strap	
			Number	Length [mm]	Number	Length [mm]	Number	Length [mm]	Number	Length [mm]
A5-a	70	30	2	1.0 - 1.7	3	1.5 - 2.0	4	1.5 - 1.7	5	1.6 - 2.5
A5-b		26	2	1.6 - 3.0	5	1.5 - 3.0	8	1.5 - 3.0	8	1.5 - 3.5
A5-d		18	2	1.0	3	1.0 - 2.0	4	1.5 - 2.0	7	1.0 - 2.2
A5-c	60	60	5	2.5 - 3.0	7	2.0 - 4.0	8	3.0 - 7.0	8	2.5 - 5.0
A5-e		30	3	1.0 - 1.5	2	1.0	1	1.0	8	1.0 - 2.5
A5-f		25	1	1.0	3	1.5 - 2.0	2	1.2 - 2.0	4	1.0 - 2.0
A5-g	50	60	1	1.0	1	1.0	2	2.0 - 2.5	2	1.0 - 1.5
A5-h		70	2	1.0 - 1.2	2	2.0 - 3.0	7	1.0 - 3.0	4	1.0 - 2.5
A5-i		60	1	2.0	0		2	1.5	3	1.0 - 3.0

Table G-6 Results of lap-splice joint series GL_LJ_B1, with Glare 4A-8/7-0.5 upper sheet and Glare 3-6/5-0.5 lower sheet. Only cracks at the four inner Hi-loks are considered. The inner Hi-loks are torqued with 2.2 – 2.3 Nm. Combination of cracks initiating at the bore of the hole or away from the hole

Specimen	σ_{max} [MPa]	N [kCycles]	Cracks at 4 inner Hi-Loks			
			Upper sheet		Lower sheet	
			Number	Length [mm]	Number	Length [mm]
B1-a	60	125	6	1.3 - 3.4	1	1.4
B1-b		80	7	1.0 - 1.8	1	1.3
B1-c		60	1	1.4	0	
B1-h		60	2	1.0	1	1.0
B1-d	70	35	2	1.0	1	1.0
B1-e		40	4	1.0 - 1.5	3	1.5
B1-f	55	90	4	1.0 - 2.3	0	
B1-g		80	2	1.0	0	
B1-i		120	3	1.0 - 1.2	0	

Table G-7 Results of lap-splice joint series GL_LJ_B2, with Glare 4B-4/3-0.3 upper sheet and Glare 3-4/3-0.3 lower sheet. Only cracks at the four inner Hi-loks are considered. The inner Hi-loks are torqued with 2.2 – 2.3 Nm. Combination of cracks initiating at the bore of the hole or away from the hole

Specimen	σ_{max} [MPa]	N [kCycles]	Cracks at 4 inner Hi-Loks			
			Upper sheet		Lower sheet	
			Number	Length [mm]	Number	Length [mm]
B2-f	120	25	2	1.0	5	1.0 - 1.2
B2-g		25	0		0	
B2-d	100	45	2	1.5	1	1.1
B2-e		40	2	1.0 -1.5	0	
B2-j		40	0		0	
B2-h	90	40	2	1.0 - 1.3	0	
B2-i		40	1	1.5	0	

Because an optimal torque was established during testing, the order in which all specimens are tested is of influence on the results of the crack initiation detection. The first series tested is the lap-splice joint GL_LJ_B1, the torque applied is based upon tests from reference [1]. The two outer Hi-Lok columns are torqued at 80 % of the collar head break-off point; the four inner Hi-Lok columns are torqued at 65 % of the torque at collar break-off. As expected the cracks in the outer Hi-Lok columns initiated away from the hole, however these cracks also grew to a larger length then the cracks at the four inner columns. This is related to finite width effect of the specimens as explained. With the results from the first series, the outer Hi-Lok fasteners will be torqued to collar break-off.

The results obtained from the lap-splice GL_LJ_B2 crack initiation tests showed the positive effect of the break-off of the collar heads for the outer columns. Investigation of these specimens showed a retardation of the crack initiation at the outer fastener columns, and crack initiation of the four inner columns close to or at the minimum net-section between the fasteners.

Due to the differences in bending behavior of the butt joints, the results of the next series, GL_BJ_A3, tested showed problems using the same torque forces used for the GL_LJ_B2 specimens. For the GL_BJ_A3 series the torque applied to the four inner Hi-Lok columns appeared to be to high, cracks initiated for the Glare 3-4/3-0.3 sheets close to the minimum net-section between the fasteners and away from the hole. For the Glare 2B-4/3-0.3 butt strap all cracks initiated away from the hole. For all specimens to be tested the torque load for the four inner Hi-Lok columns was reduced to 1.7 - 1.8 Nm. At this torque for the inner Hi-Loks, the sheets are just clamped together. Using this method of assembly, the GL_BJ_A1, GL_BJ_A2, GL_BJ_A4 and GL_BJ_A5 series had crack initiation at the fastener holes in or close to the minimum net-section between the fasteners.

The obtained data from all crack initiation tests is used for validation of the existing methods to predict the fatigue crack initiation of fiber metal laminates using the FML F&DT toolbox [2]. The conclusion reached in the investigation conducted by Schra and Homan, [1], is that a good agreement is reached in predicting the fatigue initiation lives of the fiber metal laminate lap-splice and butt joints. The best agreements could be obtained using *S-N* curves based on fatigue initiation data and not on fatigue failure curves. This will result in overestimation of the fatigue initiation life of joints.

G.3 Crack growth

All specimens are fatigue tested until a predetermined number of cycles with one exception, series GL_LJ_B2. This set of specimens has been tested and investigated visually and by means of eddy-current inspections at certain intervals [1],[3]. For the eddy-current inspections the specimen was dismantled and remounted for each inspection. Due to the large amount of time needed to dismantle, visually inspect the specimens and rebuild the specimens, all other specimens were tested until they

reached a certain amount of cycles, which resulted in a variety of different crack lengths. Determining the final crack length is done by means of crack length measurement after the residual strength testing. Crack growth rates are then established from eddy-current inspections and the final crack length. The crack growth rates are assumed to be constant during the whole crack growth life.

The GL_LJ_B2 lap-splice joint series with the periodic inspections provides a large amount of crack growth data to validate the method proposed by De Koning [5] and adapted by Homan [4]. After the crack initiation tests at the NLR, the specimens off all other series have been tested until a predetermined number of cycles. For these crack growth tests it was assumed, that in all specimens cracks had initiated from the fastener holes. Table G-8 and Table G-9 shows the number of fatigue cycles that were applied to all series. It is clear that for each applied load and specimen geometry a different number of cycles was required to initiate a crack that provides a starting point for the crack growth analysis. Thus all successive cycles are applied to get an accurate crack growth history of the Glare joints. With the exception of series GL_LJ_B2 and GL_BJ_A3, all specimens were tested with σ_{max} = 100 MPa and R = 0.05. Series GL_LJ_B2 and GL_BJ_A3 were tested at similar stress levels as used in the crack initiation tests.

The fatigue crack initiation data represents the definition of crack initiation length, namely 1.00 mm and the fatigue crack initiation life N_i in the aluminum surface layer. This definition has been determined by back calculation of several different crack initiation lengths to one value. Specimen series GL_LJ_B2 lap-splice joint consisted of two Glare materials, both resulting in different crack growth rates. Using the method proposed by Homan [4], looking at both Figure G-1 for the Glare 3-4/3-0.3 and Figure G-2 for the Glare 4B-4/3-0.3 sheets show a good correlation between several crack measurements and the crack growth prediction curves for cracks emanating from the fastener holes in the minimum net-section. With the test data available, crack initiation data and the crack length after the residual strength tests, there are two options to validate the crack growth analysis. First, a back calculation from the crack length measurements done after the residual strength tests, or a calculation of the fatigue crack growth using the fatigue crack initiation length as a starting point. The latter method was used for the crack growth prediction in Table G-8 and Table G-9.

Although the crack growth curves shown in Figure G-1 and Figure G-2 show a good resemblance between the measured and predicted curves, some predictions showed differences up to 30%. Three categories can be established, results of the crack growth prediction and measurements are within 0 - 10%, 10 - 20% and 20 - 30%. The following predicted crack growth curves are within 10% of the measured data, *a*2, *a*7, *a*8, *a*9, *b*1, *b*4, *b*5, *b*7, *b*9, *b*11 and *b*12. Within 10 – 20%, *a*1, *a*3, *a*5, *a*10, *a*11, *a*12, *b*2, *b*3 and *b*8. Within 20 – 30% are the following, *a*4, *b*6 and *b*10. The percentages differences for each of the curves are valid for each point on the curve. Although it

might appear that the differences are smaller for the smaller crack lengths, percentage wise the differences are comparable to the final crack length differences.

Table G-8   Number of fatigue cycles for both crack initiation and crack growth for Glare butt joint specimens

Specimen[2]		Crack initiation		Crack growth	
ID	Thickness [mm]	σ_{max}[1] [MPa]	N [Cycles]	σ_{max}[1] [MPa]	N [Cycles]
GL_BJ_A1-c		60	30000	100	20600
GL_BJ_A1-d		60	40000	100	5200
GL_BJ_A1-e		60	35000	100	5200
GL_BJ_A1-f	4.25	70	20000	100	10300
GL_BJ_A1-g		50	65000	100	10300
GL_BJ_A1-h				100	10300
GL_BJ_A1-i		50	50000	100	20600
GL_BJ_A2-a		60	40000	100	15100
GL_BJ_A2-b		60	35000	100	15100
GL_BJ_A2-c		70	20000	100	15100
GL_BJ_A2-d	4.15	50	60000	100	30200
GL_BJ_A2-e		70	15000	100	30200
GL_BJ_A2-f		50	55000	100	30200
GL_BJ_A2-g		40	80000	100	60300
GL_BJ_A2-h		40	80000	100	60300
GL_BJ_A3-a		120	24000	120	41500
GL_BJ_A3-b		120	21000	120	38500
GL_BJ_A3-c		100	40000	100	75000
GL_BJ_A3-d		100	50000	100	85000
GL_BJ_A3-e	1.95	90	65000	90	125000
GL_BJ_A3-f		90	65000	90	125000
GL_BJ_A3-g		120	27000	120	44500
GL_BJ_A3-h		100	55000	100	90000
GL_BJ_A3-i		90	72000	90	132000
GL_BJ_A4-a		60	35000	100	7100
GL_BJ_A4-b		70	16000	100	7100
GL_BJ_A4-c		50	50000	100	7100
GL_BJ_A4-d		40	80000	100	14100
GL_BJ_A4-e	4.00	70	18000	100	14100
GL_BJ_A4-f		60	30000	100	14100
GL_BJ_A4-g		50	50000	100	28300
GL_BJ_A4-h		40	80000	100	28300
GL_BJ_A4-i		60	33000	100	28300
GL_BJ_A5-a		70	30000	100	6800
GL_BJ_A5-b		70	26000	100	6800
GL_BJ_A5-c		60	60000	100	6800
GL_BJ_A5-d		70	18000	100	13700
GL_BJ_A5-e	4.00	60	30000	100	13700
GL_BJ_A5-f		60	25000	100	13700
GL_BJ_A5-g		50	60000	100	27400
GL_BJ_A5-h		50	70000	100	27400
GL_BJ_A5-i		50	60000	100	27400

[1] R-ratio used 0.05
[2] Width of all specimens is 168 mm

Table G-9 **Number of fatigue cycles for both crack initiation and crack growth for Glare lap-splice joint specimens**

Specimen[2]		Crack initiation		Crack growth	
ID	Thickness [mm]	σ_{max}[1] [MPa]	N [Cycles]	σ_{max}[1] [MPa]	N [Cycles]
GL_LJ_B1-a		60	125000	100	26300
GL_LJ_B1-b		60	80000	100	26300
GL_LJ_B1-c		60	60000	100	26300
GL_LJ_B1-d		70	35000	100	52600
GL_LJ_B1-e	4.25	70	40000	100	52600
GL_LJ_B1-f		70	90000	100	52600
GL_LJ_B1-g		55	80000	100	105300
GL_LJ_B1-h		55	60000	100	105300
GL_LJ_B1-i		55	120000	100	105300
GL_LJ_B2-d		100	10000	100	70000
GL_LJ_B2-e		100	10000	100	85000
GL_LJ_B2-f	2.00	120	10000	120	50000
GL_LJ_B2-g		120	10000	120	50000
GL_LJ_B2-i		90	10000	90	120000

[1] R-ratio used 0.05
[2] Width of all specimens is 168 mm
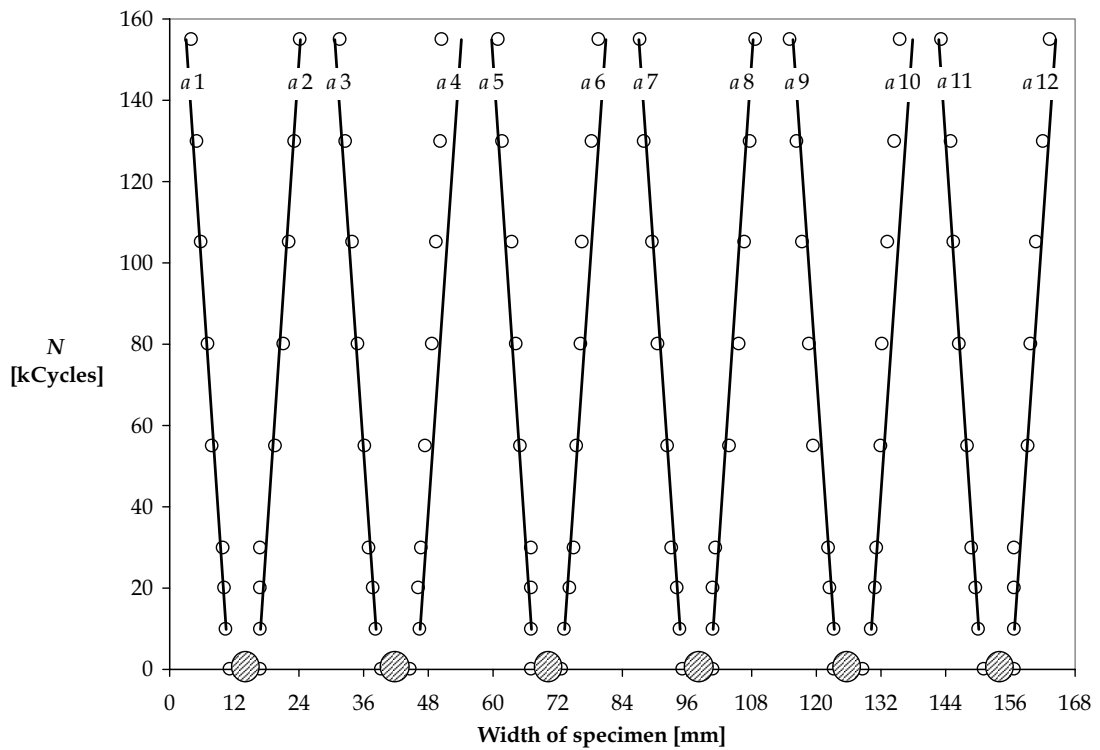
Figure G-1 Crack growth in Glare 3-4/3-0.3 for cracks emanating from fastener holes lap-splice joint series GL_LJ_B2. σ_{max} = 90 MPa, R = 0.05
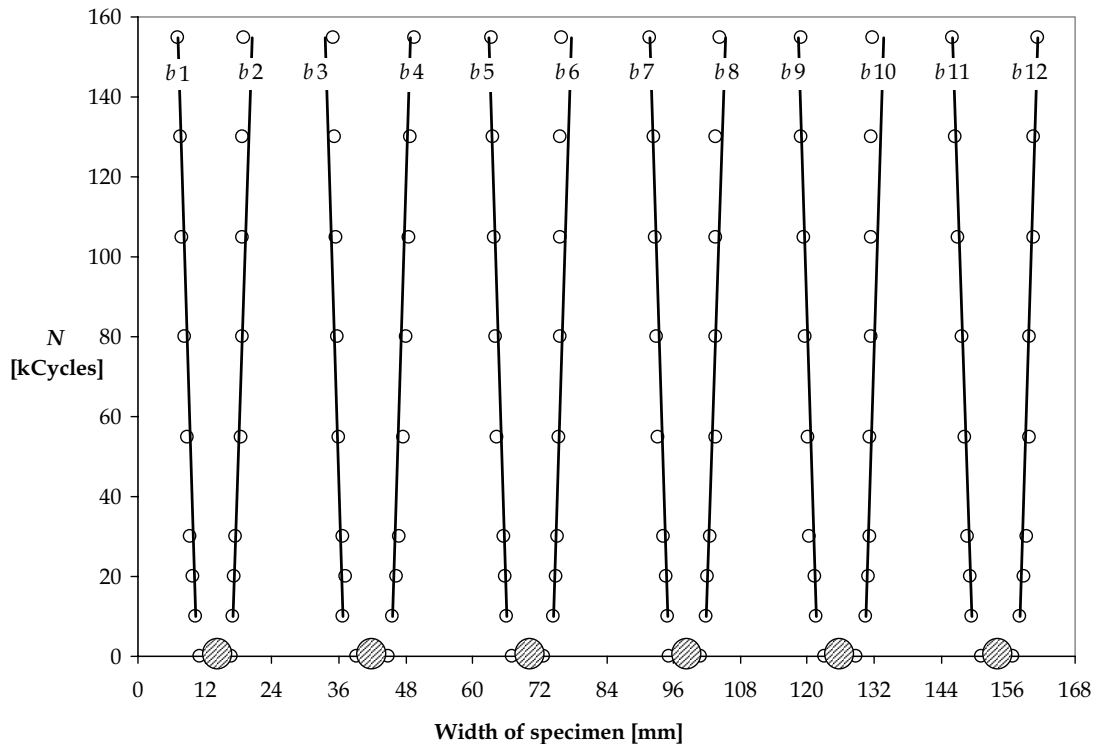

Figure G-2 Crack growth in Glare 4B-4/3-0.3 for cracks emanating from fastener holes lap-splice joint series GL_LJ_B2. σ_{max} = 75 MPa, R = 0.05

291

G.4 Literature

[1] Schra, L., and J.J. Homan, *Fatigue crack initiation in Glare lap joint and butt joint specimens*, GTP Methods Project 2.4.3.5-B, National Aerospace Laboratory NLR, NLR-CR-2003-622, December 2003

[2] FML F&DT toolbox v1.11, proprietary of Airbus Germany and Delft University of Technology, 2002

[3] Schra, L. and H.J. ten Hoeve, *Feasibility of Eddy Current inspection for detection of fatigue crack initiation in Glare joints, and a comparison of crack length measuring techniques*, National Aerospace Laboratory NLR, NLR-CR-2001-565, 2001

[4] Homan, J.J., *Crack growth in Glare CTB specimens*, Delft University of Technology, Report B2v-03-08, December 2003

[5] de Koning, A.U., and L. Schra, *Fatigue crack growth of part through the thickness cracks in Glare 3 and Glare 4B coupons*, Final report GTO subproject 2.4.2, National Aerospace Laboratory NLR, NLR-CR-2000-78, February 2000

Curriculum Vitae

The Author was born on 25 January 1973 in Leiderdorp, The Netherlands. After graduation Gymnasium in 1991 at Katholieke Scholengemeenschap Etten Leur e.o., he started his Aerospace Engineering study at Delft University of Technology. In the Structures and Materials Laboratory he started the research under supervision of Scott Fawaz on the subject of fatigue crack growth in monolithic aluminum. In support of his master thesis he conducted a practical training in Filton at British Aerospace Airbus at the Damage Tolerance department for six months. Returning to finish his master thesis in 1998 with the title of "Crack Interaction of Oblique Part Elliptical Through Cracks".

In the same year he started his PhD research at the Structures and Materials Laboratory in Delft on the subject of joining techniques for laminates, supported by the Netherlands Institute for Metals Research and Delft University of Technology. Before completing his PhD research, he was employed, on 1 April 2004, as a researcher Mechanical Performance of Products at the Automotive Applications Center of Corus Research, Development & Technology in IJmuiden, The Netherlands. At the same time he continued to work on his PhD, resulting in this thesis.

Summary

Stress Analysis of Fatigue Cracks in Mechanically
Fastened Joints

An analytical and experimental investigation

by J.J.M. de Rijck

Introduction

The two historical fuselage failures, Comet in 1954 and Aloha in 1988, illustrate that similar accidents must be avoided which requires a profound understanding of the fatigue mechanisms involved, including analytical models to predict the fatigue behavior of riveted joints of a fuselage structure. The scope of the research project covers a variety of joint types and joining techniques for both monolithic and laminated sheet materials. The fuselage structure is a rather complicated system of parts consisting of skin sheets, tear-straps, stringers, frames and doublers. These parts are interconnected by mechanically fastened and bonded joints, or a combination of both. The complex fuselage structure in the present research is reduced to specimen level size for laboratory testing and theoretical analysis.

The major topics of the thesis are:
- Calculations of the combined tension and bending stress distribution in joints, which implies an extension of the so-called secondary bending model (Chapter 3).
- Find a direct and simple relation between the formed rivet head and squeeze force. (Chapter 4).
- Development of stress intensity factors for fatigue cracks in joints loaded under combined tension and application to fatigue crack growth results (Chapter 5).
- Fractographic observations with the scanning electron microscope of crack front shapes occurring in riveted joints under combined tension and bending (Chapter 5).
- Analysis of the residual strength of joints with fatigue cracks (Chapter 6).

Neutral line model

For mechanically fastened lap-splice and butt joints in a fuselage structure, a dominant load is introduced by the Ground-Air-Ground (*GAG*) pressurization cycle. The hoop load is transferred from one skin panel to the next via the fasteners in the joint. The hoop load is offset by eccentricities in the load path, which causes

secondary bending. The bending stress is a non-linear function of the applied tension load. The stress system in the joint then encompasses the membrane stress, the secondary bending stress and the bearing stress associated with the fastener loads on the holes. The secondary bending is highly depending on the magnitude of the eccentricity and the flexural rigidity of the joint between the fastener rows. The theory used to derive the bending stresses is based on the advanced beam theory. A further development of the neutral line model incorporates the internal moment, which is a useful representation of the load transfer occurring in multiple row joints. The calculation of the load transfer can be made for complicated lap splice and butt joints. With the developments of the present research, the neutral line model is still a very powerful tool to use in the early stages of joint design. It gives a good picture of the stresses in a joint.

Riveting

Solid rivets and more advanced fasteners are still widely used in aircraft fuselage design efforts. The fasteners are characterized by various parameters associated with the fastener material and geometry, sheet material and installation process. The present investigation focuses on solid rivets installed in aluminum and Glare. The expansion of a solid rivet in a rivet hole is important with respect to the fatigue properties of joints. The expanding rivet inside a fastener hole will create a compressive residual stress around the hole and this will delay fatigue crack nucleation. It is important to know the correct squeeze force used to form the driven head of a rivet. Measurements of the formed rivet head (diameter or protruding height) can be used to obtain information about the applied squeezing force. The riveting process is a non-linear deformation process characterized by large plastic strains. Simple equations based on constant volume of the rivet and the Holloman model for uniform plastic deformation, were adopted to evaluate the riveting process. Useful results were obtained about the correlation between the rivet head deformation and the applied squeezing force.

Stress intensity factors

As a result of combined tension and secondary bending in a lap joint, fatigue cracks at the edge of a hole start at one side of the sheet only. Initially these cracks at the edge of a hole are growing as a part through the thickness corner crack, which later become a through the thickness crack, a so called through crack. But also for a through crack, the shape of the crack front is usually curved and the crack length measured at both sides of the sheet will be different. In view of fatigue crack growth predictions it then is necessary to obtain stress intensity factors for such slant and curved crack fronts. In the present investigation this problem has been explored for a simple configuration, which is an open hole in a sheet specimen subjected to combined tension and bending. Fatigue tests were carried out on specimens of AL 2024-T3 clad sheet material with three different thicknesses (1.0, 1.6 and 2.0 mm). In each specimen a single open countersunk hole was present. The

development of the crack front is these specimens could be recorded because so-called marker load cycles were applied in these tests. It then was possible to observe the crack fronts in the scanning electron microscope, which still was a rather strenuous work. Reconstruction of the crack growth could be done for the larger part of the fatigue cracks.

K-values were obtained for a large variety of crack front shapes and crack sizes. Comparison of the new calculated *K* values with existing solutions showed that the new solutions capture near the surface phenomenon more accurately than the previously published data. The improvement is a result of using an increased mesh density. For through the thickness cracks growing away from the countersunk hole, the normalized stress intensity factors approach the values of the normalized stress intensity factors for cracks emanating from a straight shank hole. Thus, the effect of the countersunk hole decreases with increasing crack length. The solutions for the pin loading β values show a dominant influence of the countersunk shape in the b/t values.

Residual strength

Static failure of a joint occurs when that joint is not able to carry the applied load anymore. The type of static failure in joints depends on the loading condition and the joint configuration. The most common static failure modes in monolithic aluminum joints are fastener shear failure, plate tension failure, bearing failure and plate shear failure. In Glare joints another failure mechanism, fastener pull-through, is often observed. This failure mechanism is related to the lower stiffness of Glare in thickness direction, leading to increased tilting of the fasteners and hence increased tensile stresses in the fastener.

In the present thesis, a method is proposed to calculate the residual strength of joints of monolithic and fiber metal laminates. The method uses the remaining net section. For the fiber metal laminates the net section includes the remaining intact metal layers in combination with the intact fibers. The method starts with the blunt notch strength of the un-cracked joint and the metal volume fraction for the fiber-metal laminates. The Norris failure criterion and the metal volume fraction are used to calculate the blunt notch strength for any possible Glare lay up. Secondary bending has a significant influence on the ultimate strength of both Glare and aluminum. The ultimate tensile strength reduces with increasing bending. Taking this into account, an empirically found reduction of 10% of the blunt notch values results in a more accurate representation of the stress system. Difficulties arise if significant plastic deformation occurs at the most critical fastener row, and further research using a finite element model is recommended.

Samenvatting

Spanning Analyse van Vermoeiingsscheuren in
Klinkverbindingen

Een analytisch en experimenteel onderzoek

door J.J.M. de Rijck

Inleiding

Twee historische catastrofale ongelukken als gevolg van vermoeiingscheuren in de vliegtuigromp van de Comet in 1954 en de Aloha 737 in 1988 illustreren dat gelijksoortige ongelukken vermeden moeten worden. Dat vereist een diepgaand begrip van het vermoeiingsmechanisme en van analytische modellen om het vermoeiingsgedrag van geklonken verbindingen in vliegtuigrompen te bepalen. Het onderzoek van dit proefschrift bestrijkt verschillende verbindingstypen en verbindingstechnieken voor zowel monolithisch als gelamineerd plaatmateriaal (Glare). De vliegtuigromp bestaat uit een complex systeem van onderdelen, zoals huidplaten, scheurstoppers, verstijvers, spanten en doublers. Deze onderdelen zijn onderling met elkaar verbonden via mechanische of gelijmde verbindingen, of een combinatie van beide. De complexe structuur van een vliegtuigromp is in het onderzoek vereenvoudigd tot een proefstuk geschikt voor laboratoriumproeven en theoretische analyse.

De belangrijkste onderwerpen in dit proefschrift zijn:
- Berekeningen van buig- en trekspanningsverdeling in verbindingen. Daarvoor is een uitbreiding nodig van het zogenaamde secondaire buigings model (Hoofdstuk 3)
- Het vinden van een directe relatie tussen de klinknagelvervorming en de kracht die daarvoor nodig is (Hoofdstuk 4)
- Berekening van spanningsintensiteitfactoren voor vermoeiingsscheuren in verbindingen die gedomineerd worden door buig- en trekspanningen en het doen van scheurgroeivoorspellingen (Hoofdstuk 5)
- Fractografisch onderzoek met de elektronen microscoop van opeenvolgenden scheurgroeifronten ontstaan door een spanningssysteem van buiging en trek (Hoofdstuk 5)
- Analyse van reststerkte van verbindingen met vermoeiingsscheuren (Hoofdstuk 6)

Neutrale lijn model

Voor verbindingen in een vliegtuigromp is de dominante wisselbelasting het gevolg van de cabinedruk. De belasting in omtreksrichting wordt beïnvloed door excentriciteiten in de verbindingen wat secondaire buiging veroorzaakt. De buigspanning is een niet lineaire functie van de aangebrachte trekbelasting. Het spanningsysteem in de verbinding bestaat dan uit de membraanspanning, secondaire buigspanning en de gatdruk van klinknagels of bouten. De secondaire buiging is sterk afhankelijk van de excentriciteiten en de flexibiliteit van de verbindingselementen. De gebruikte theorie om de buigspanning te berekenen is gebaseerd op de 'advanced beam' theorie. Een verdere ontwikkeling van het neutrale lijn model beschouwt de invloed van het interne moment dat representatief is voor de krachtoverdracht in verbindingen. De berekening van de krachtsoverdracht kan voor eenvoudige maar ook voor gecompliceerde verbindingen worden gedaan. Met de ontwikkelingen in het huidige onderzoek blijkt dat het neutrale lijn model een krachtig en eenvoudig gereedschap is om te gebruiken bij de eerste stappen in het ontwerpproces van een verbinding. Er wordt een goed beeld verkregen van de spanningen in een verbinding.

Klinken

Klinknagels en geavanceerde bouten worden nog steeds op omvangrijke schaal gebruikt in de vliegtuigindustrie. De klinkverbinding wordt gekarakteriseerd door verschillende parameters zoals het nagelmateriaal, plaat materiaal en installatie proces. Het installeren van klinknagels in platen van aluminium en Glare is onderzocht. De expansie van de klinknagel in het nagelgat is belangrijk voor de vermoeiingseigenschappen van de verbinding. Het uitzetten van de klinknagel in het nagelgat veroorzaakt een drukspanning in het materiaal om het nagelgat heen. Hierdoor wordt de scheurinitiatie vertraagd. Daarom is het belangrijk om te weten welke klinkkracht gebruikt is om de klinknagelkop in zijn uiteindelijke vorm te brengen. Uit de afmetingen van de gevormde klinknagelkop (hoogte en diameter) kan hierover informatie worden verkregen. Het klinkproces is een niet lineair proces gekarakteriseerd door grote plastische vervormingen. Eenvoudige vergelijkingen gebaseerd op een constant nagelvolume bij de vervormingen en het Holloman model voor uniforme plastische deformatie zijn gebruikt om het klinkproces te evalueren. Hiermee werd een bruikbare relatie tussen de vervorming van de klinknagelkop en de toegepaste klinkkracht verkregen.

Spanningsintensiteitfactoren

Door de aanwezigheid van een combinatie van trek en secondaire buigspanningen in een verbinding zullen vermoeiingscheuren aan een zijde van de huidplaat initiëren. Deze kleine scheuren met een kwartelliptisch scheurfront zijn nog niet door de gehele plaatdikte heen gegroeid. Bij groter wordende scheuren zullen deze uitbreiden en door de gehele dikte heen groeien. Ook voor deze grotere scheuren blijft het gekromde scheurfront een elliptische vorm behouden. Dit resulteert in een

verschil in scheurlengte aan beide zijden van de huidplaat. In het licht van scheurgroei voorspellingen is het nodig om over spanningsintensiteitfactoren voor dergelijke driedimensionale scheuren te beschikken. In het huidige onderzoek is dit probleem onderzocht voor de simpele configuratie van een open gat proefstuk belast door een combinatie van trek- en buigspanning. Vermoeiingsproeven zijn uitgevoerd op proefstukken van Al 2024-T3 clad plaatmateriaal met drie verschillende diktes (1.0, 1.6 and 2.0 mm). In ieder proefstuk is een open verzonken gat aanwezig. De ontwikkeling van het scheurfront in deze proefstukken kon worden geregistreerd door het toepassen van zgn. markerloads. Daarmee was het mogelijk om de progressie van de scheurfronten te bepalen met onderzoek van het scheuroppervlak in de elektronen microscoop, een opgave die wel veel inspanning vergt. Op deze manier kon een groot deel van de scheurgroei gereconstrueerd worden.

K oplossingen zijn verkregen voor een groot aantal verschillende scheurvormen en scheurlengtes. Vergelijking van deze nieuwe resultaten met gepubliceerde resultaten laat zien dat de nieuwe resultaten de oppervlakte eigenschappen beter beschrijven. De verbetering is een resultaat van een fijnere elementendichtheid aan het oppervlak. Voor door de dikte scheuren, die gegroeid zijn tot een ruime afstand van het verzonken gat, benaderen de spanningsintensiteitfactoren voor een recht gat die van het verzonken gat. De invloed van de vorm van het gat neemt af met toenemende scheurlengte. De spanningsintensiteitsfactoren die berekend zijn met behulp van een belasting in het gat, laten zien dat de invloed van het verzonken gat afneemt met toenemen b/t verhouding en dus niet met toenemende scheurlengte.

Reststerkte

De reststerkte van een verbinding is het statisch bezwijken wanneer de verbinding de aangebrachte belasting niet meer kan dragen. De statische bezwijkvorm is afhankelijk van de belasting en de configuratie van de verbinding. De meest voorkomende statische bezwijkvormen in monolithisch aluminium zijn nagelafschuiving, plaatafschuiving, vlaktedrukdeformatie en het bezwijken van de netto doorsnede. In een Glare verbinding is een bezwijkvorm mogelijk waarbij de nagel door de plaat heen getrokken wordt. Dit is gerelateerd aan de lagere stijfheid van Glare in dikte richting, waardoor meer nagelrotatie mogelijk is en een hogere trekspanningen in de nagel.

In dit onderzoek is een methode voorgesteld om de reststerkte van zowel monolithisch aluminium als vezel metaal laminaten te berekenen. De methode gebruikt de minimale breedte tussen de nagelgaten bij aanwezigheid van vermoeiingscheuren. Voor vezel metaal laminaten is de minimale breedte een combinatie van overgebleven intacte aluminium lagen en de vezellagen. De methode is gebaseerd op de blunt notch sterkte en de 'metal volume fraction' (*MVF*) voor vezel metaal laminaten. Met behulp van het Norris bezwijkcriterium en de *MVF* kan de blunt notch sterkte berekend worden voor iedere willekeurige Glare variant. Secondaire buiging heeft invloed op de reststerkte van zowel Glare als aluminium verbindingen. De maximale trekstrekte neemt af bij aanwezigheid van

buigspanning. De proefresultaten geven aan dat die invloed bij benadering verdisconteerd kan worden met een empirische reductie van de berekende blunt notch sterkte met 10%. Moeilijkheden ontstaan wanneer er zeer grote plastische vervormingen bij de kritieke nagel rij ontstaan. Verder onderzoek naar deze invloed wordt aanbevolen.